How Francis Collins put his stamp on NIH *p. 632*

Glial cells for sensing pain in the skin *pp. 641 & 695*

Orbiting a supermassive black hole *p. 664*

Science

$15
16 AUGUST 2019
sciencemag.org

AAAS

WALK-TO-RUN EXOSUIT

Adaptive technology reduces metabolic cost of locomotion

pp. 636 & 668

CONTENTS

16 AUGUST 2019 • VOLUME 365 • ISSUE 6454

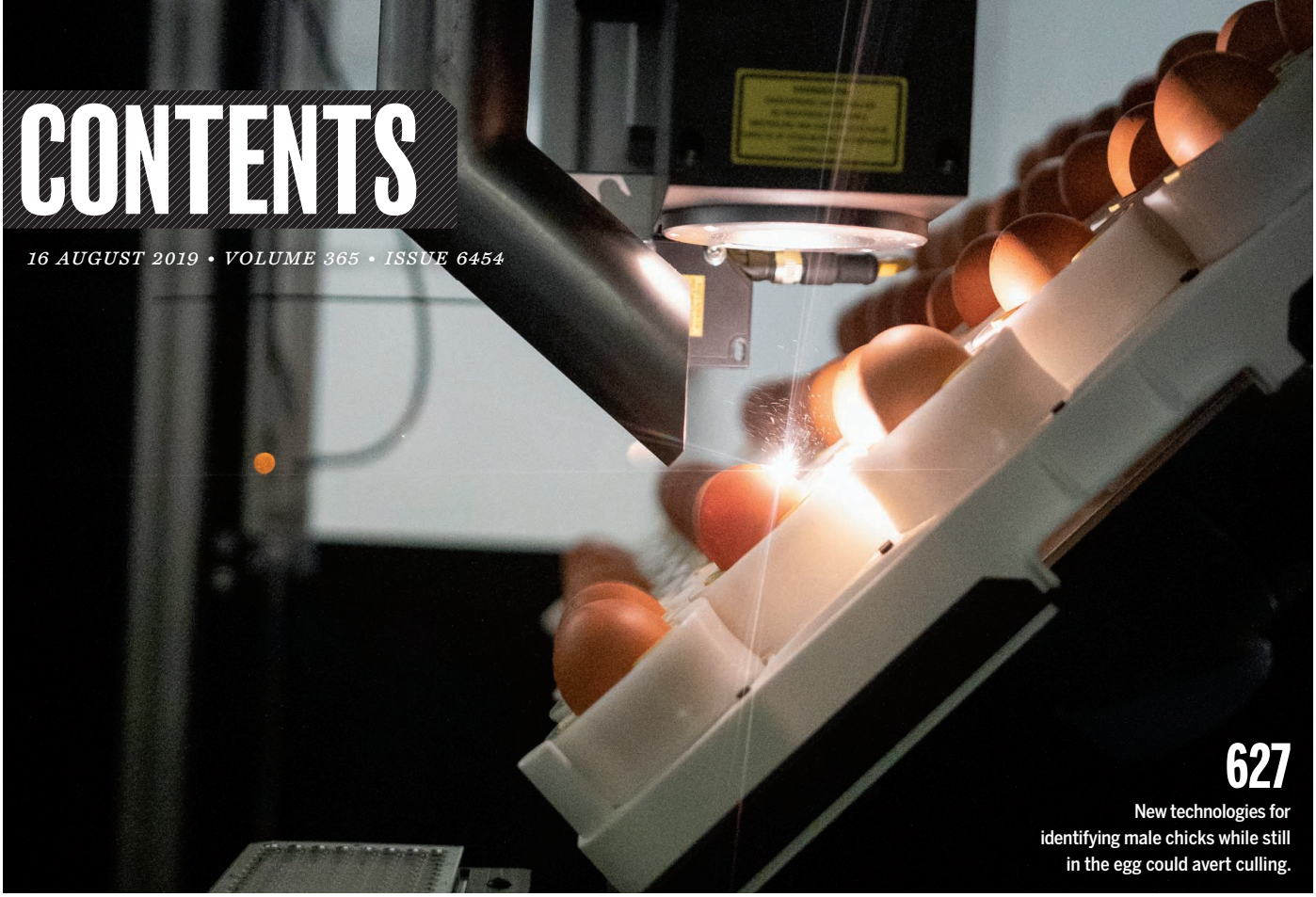

627
New technologies for identifying male chicks while still in the egg could avert culling.

PHOTO: SELEGGT

NEWS

IN BRIEF

IN DEPTH

FEATURES

INSIGHTS

PERSPECTIVES

POLICY FORUM

Published by AAAS

ON THE COVER

A portable exosuit that attaches to the waist and thighs reduces the energy required for walking and running by delivering hip extension assistance for the wearer's hip extensor muscles. The exosuit's minimally restrictive design allows the user to move naturally, and it switches seamlessly between the two gaits, paving the way for future applications that require dynamic and adaptive assistance. See pages 636 and 668. *Illustration: V. Altounian/* Science*; 3D model: Harvard Biodesign Lab*

SCIENCE (ISSN 0036-8075) is published weekly on Friday, except last week in December, by the American Association for the Advancement of Science, 1200 New York Avenue, NW, Washington, DC 20005. Periodicals mail postage (publication No. 484460) paid at Washington, DC, and additional mailing offices. Copyright © 2019 by the American Association for the Advancement of Science. The title SCIENCE is a registered trademark of the AAAS. Domestic individual membership, including subscription (12 months): $165 ($74 allocated to subscription). Domestic institutional subscription (51 issues): $1971; Foreign postage extra: Mexico, Caribbean (surface mail) $55; other countries (air assist delivery): $98. First class, airmail, student, and emeritus rates on request. Canadian rates with GST available upon request, GST #125488122. Publications Mail Agreement Number 1069624. **Printed in the U.S.A.**
Change of address: Allow 4 weeks, giving old and new addresses and 8-digit account number. **Postmaster:** Send change of address to AAAS, P.O. Box 96178, Washington, DC 20090–6178. **Single-copy sales:** $15 each plus shipping and handling; bulk rate on request. **Authorization to reproduce** material for internal or personal use under circumstances not falling within the fair use provisions of the Copyright Act can be obtained through the Copyright Clearance Center (CCC), www.copyright.com. The identification code for *Science* is 0036-8075. *Science* is indexed in the *Reader's Guide to Periodical Literature* and in several specialized indexes.

ILLUSTRATION: ROBERT NEUBECKER

Published by AAAS

Science AAAS

Editor-in-Chief Jeremy Berg, jberg@aaas.org

Executive Editor Monica M. Bradford

Editors, Research Valda Vinson, Jake S. Yeston **Editor, Insights** Lisa D. Chong

DEPUTY EDITORS Julia Fahrenkamp-Uppenbrink (UK), Stella M. Hurtley (UK), Phillip D. Szuromi, Sacha Vignieri **SR. EDITORIAL FELLOW** Andrew M. Sugden (UK) **SR. EDITORS** Gemma Alderton (UK), Caroline Ash (UK), Brent Grocholski, Pamela J. Hines, Paula A. Kiberstis, Marc S. Lavine (Canada), Steve Mao, Ian S. Osborne (UK), Beverly A. Purnell, L. Bryan Ray, H. Jesse Smith, Jelena Stajic, Peter Stern (UK), Valerie B. Thompson, Brad Wible, Laura M. Zahn **ASSOCIATE EDITORS** Michael A. Funk, Priscilla N. Kelly, Tage S. Rai, Seth Thomas Scanlon (UK), Keith T. Smith (UK), Yury V. Suleymanov **LETTERS EDITOR** Jennifer Sills **LEAD CONTENT PRODUCTION EDITORS** Harry Jach, Lauren Kmec **CONTENT PRODUCTION EDITORS** Amelia Beyna, Jeffrey E. Cook, Chris Filiatreau, Nida Masiulis, Suzanne M. White **SR. EDITORIAL COORDINATORS** Carolyn Kyle, Beverly Shields **EDITORIAL COORDINATORS** Aneera Dobbins, Joi S. Granger, Jeffrey Hearn, Lisa Johnson, Maryrose Madrid, Ope Martins, Shannon McMahon, Jerry Richardson, Alana Warnke, Alice Whaley (UK), Anita Wynn **PUBLICATIONS ASSISTANTS** Jeremy Dow, Alexander Kief, Ronmel Navas, Hilary Stewart (UK), Brian White **EXECUTIVE ASSISTANT** Jessica Slater **ASI DIRECTOR, OPERATIONS** Janet Clements (UK) **ASI SR. OFFICE ADMINISTRATOR** Jessica Waldock (UK)

News Editor Tim Appenzeller

NEWS MANAGING EDITOR John Travis **INTERNATIONAL EDITOR** Martin Enserink **DEPUTY NEWS EDITORS** Elizabeth Culotta, Lila Guterman, David Grimm, Eric Hand (Europe), David Malakoff **SR. CORRESPONDENTS** Daniel Clery (UK), Jon Cohen, Jeffrey Mervis, Elizabeth Pennisi **ASSOCIATE EDITORS** Jeffrey Brainard, Catherine Matacic **NEWS REPORTERS** Adrian Cho, Jennifer Couzin-Frankel, Jocelyn Kaiser, Kelly Servick, Robert F. Service, Erik Stokstad (Cambridge, UK), Paul Voosen, Meredith Wadman **INTERN** Alex Fox **CONTRIBUTING CORRESPONDENTS** Warren Cornwall, Ann Gibbons, Mara Hvistendahl, Sam Kean, Eli Kintisch, Kai Kupferschmidt (Berlin), Andrew Lawler, Mitch Leslie, Eliot Marshall, Virginia Morell, Dennis Normile (Shanghai), Elisabeth Pain (Careers), Charles Piller, Michael Price, Tania Rabesandratana (Barcelona), Emily Underwood, Gretchen Vogel (Berlin), Lizzie Wade (Mexico City) **CAREERS** Donisha Adams, Rachel Bernstein (Editor), Katie Langin **COPY EDITORS** Julia Cole (Senior Copy Editor), Cyra Master (Copy Chief) **ADMINISTRATIVE SUPPORT** Meagan Weiland

Creative Director Beth Rakouskas

DESIGN MANAGING EDITOR Marcy Atarod **GRAPHICS MANAGING EDITOR** Alberto Cuadra **PHOTOGRAPHY MANAGING EDITOR** William Douthitt **WEB CONTENT STRATEGY MANAGER** Kara Estelle-Powers **SENIOR DESIGNER** Chrystal Smith **DESIGNER** Christina Aycock **PHOTO EDITOR** Emily Petersen **GRAPHICS EDITOR** Nirja Desai **SENIOR SCIENTIFIC ILLUSTRATORS** Valerie Altounian, Chris Bickel **SCIENTIFIC ILLUSTRATOR** Alice Kitterman **SENIOR GRAPHICS SPECIALISTS** Holly Bishop, Nathalie Cary

Interim Chief Executive Officer and Executive Publisher Alan Leshner

Publisher, Science Family of Journals Bill Moran

DIRECTOR, BUSINESS SYSTEMS AND FINANCIAL ANALYSIS Randy Yi **DIRECTOR, BUSINESS OPERATIONS & ANALYSIS** Eric Knott **DIRECTOR OF ANALYTICS** Enrique Gonzales **MANAGER, BUSINESS OPERATIONS** Jessica Tierney **SENIOR BUSINESS ANALYST** Cory Lipman, Meron Kebede **FINANCIAL ANALYST** Alexander Lee **ADVERTISING SYSTEM ADMINISTRATOR** Tina Burks **SENIOR SALES COORDINATOR** Shirley Young **DIGITAL/PRINT STRATEGY MANAGER** Jason Hillman **QUALITY TECHNICAL MANAGER** Marcus Spiegler **ASSISTANT MANAGER DIGITAL/PRINT** Rebecca Doshi **SENIOR CONTENT SPECIALISTS** Steve Forrester, Jacob Hedrick, Antoinette Hodal, Lori Murphy **DIGITAL PRODUCTION MANAGER** Lisa Stanford **CONTENT SPECIALIST** Kimberley Oster **DIGITAL AD-OPS SPECIALIST** Patrick Gerrits **ADVERTISING PRODUCTION OPERATIONS MANAGER** Deborah Tompkins **DESIGNER, CUSTOM PUBLISHING** Jeremy Huntsinger **SR. TRAFFIC ASSOCIATE** Christine Hall **SPECIAL PROJECTS ASSOCIATE** Sarah Dhere

ASSOCIATE DIRECTOR, BUSINESS DEVELOPMENT Justin Sawyers **GLOBAL MARKETING MANAGER** Allison Pritchard **DIGITAL MARKETING MANAGER** Aimee Aponte **MARKETING MANAGER** Shawana Arnold **MARKETING ASSOCIATES** Tori Velasquez, Mike Romano, Ashley Hylton **SENIOR DESIGNER** Kim Huynh **TRADE SHOW AND MEETINGS ASSOCIATE** Andrew Clamp

DIRECTOR AND SENIOR EDITOR, CUSTOM PUBLISHING Sean Sanders **ASSISTANT EDITOR, CUSTOM PUBLISHING** Jackie Oberst

DIRECTOR, BUSINESS STRATEGY AND PORTFOLIO MANAGEMENT Sarah Whalen **ASSOCIATE DIRECTOR, PRODUCT MANAGMENT** Kris Bishop **ASSOCIATE DIRECTOR, PRODUCT DEVELOPMENT AND SPJ** Hannah Heckner **SR. PRODUCT ASSOCIATE** Robert Koepke **DIGITAL PRODUCT STRATEGIST** Michael Hardesty **SPJ ASSOCIATE** Samantha Bruno Fuller

DIRECTOR, INSTITUTIONAL LICENSING Iquo Edim **ASSOCIATE DIRECTOR, RESEARCH & DEVELOPMENT** Elisabeth Leonard **SENIOR INSTITUTIONAL LICENSING MANAGER** Ryan Rexroth **INSTITUTIONAL LICENSING MANAGERS** Marco Castellan, Christos Skoutas **MANAGER, SYSTEMS AND OPERATIONS** Brian Holiahn **MANAGER, AGENT RELATIONS & CUSTOMER SUCCESS** Judy Lillibridge **SENIOR OPERATIONS ANALYST** Lana Guz **FULFILLMENT COORDINATOR** Melody Stringer

DIRECTOR, GLOBAL SALES Tracy Holmes **ASSOCIATE DIRECTOR, ADVERTISING SALES, US** Laurie Faraday **US EAST COAST AND MID WEST SALES** Glen Cox **US WEST COAST SALES** Lynne Stickrod **US SALES MANAGER, SCIENCE CAREERS** Claudia Paulsen-Young **US SALES REP, SCIENCE CAREERS** Tracy Anderson **ASSOCIATE DIRECTOR, ROW** Roger Goncalves **SALES REP, ROW** Sarah Lelarge **SALES ADMIN ASSISTANT, ROW** Bryony Cousins **DIRECTOR OF GLOBAL COLLABORATION AND ACADEMIC PUBLISHING RELATIONS, ASIA** Xiaoying Chu **ASSOCIATE DIRECTOR, INTERNATIONAL COLLABORATION** Grace Yao **SALES MANAGER** Danny Zhao **PROJECT MANAGER** Kilo Lan **ASCA CORPORATION, JAPAN** Kaoru Sasaki (Tokyo), Miyuki Tani (Osaka) **COLLABORATION/CUSTOM PUBLICATIONS/JAPAN** Adarsh Sandhu

DIRECTOR, COPYRIGHT, LICENSING AND SPECIAL PROJECTS Emilie David **RIGHTS AND LICENSING COORDINATOR** Jessica Adams **RIGHTS AND PERMISSIONS ASSOCIATE** Elizabeth Sandler **CONTRACTS AND LICENSING ASSOCIATE** Lili Catlett

---

MAIN HEADQUARTERS
Science/AAAS
1200 New York Ave. NW
Washington, DC 20005

SCIENCE INTERNATIONAL
Clarendon House
Clarendon Road
Cambridge, CB2 8FH, UK

SCIENCE CHINA
Room 1004, Culture Square
No. 59 Zhongguancun St.
Haidian District, Beijing, 100872

SCIENCE JAPAN
ASCA Corporation
Sibaura TY Bldg. 4F, 1-14-5
Shibaura Minato-ku
Tokyo, 108-0073 Japan

EDITORIAL
science_editors@aaas.org

NEWS
science_news@aaas.org

INFORMATION FOR AUTHORS
sciencemag.org/authors/science-information-authors

REPRINTS AND PERMISSIONS
sciencemag.org/help/reprints-and-permissions

MEDIA CONTACTS
scipak@aaas.org

MULTIMEDIA CONTACTS
SciencePodcast@aaas.org
ScienceVideo@aaas.org

INSTITUTIONAL SALES AND SITE LICENSES
sciencemag.org/librarian

PRODUCT ADVERTISING & CUSTOM PUBLISHING
advertising.sciencemag.org/products-services
science_advertising@aaas.org

CLASSIFIED ADVERTISING
advertising.sciencemag.org/science-careers
advertise@sciencecareers.org

JOB POSTING CUSTOMER SERVICE
employers.sciencecareers.org
support@sciencecareers.org

MEMBERSHIP AND INDIVIDUAL SUBSCRIPTIONS
sciencemag.org/subscriptions

MEMBER BENEFITS
aaas.org/membercentral

AAAS BOARD OF DIRECTORS
CHAIR Margaret A. Hamburg
PRESIDENT Steven Chu
PRESIDENT-ELECT Claire M. Fraser
TREASURER Carolyn N. Ainslie
INTERIM CHIEF EXECUTIVE OFFICER Alan Leshner
BOARD Cynthia M. Beall, May R. Berenbaum, Rosina M. Bierbaum, Ann Bostrom, Stephen P. A. Fodor, S. James Gates, Jr., Laura H. Greene, Kaye Husbands Fealing, Maria Klawe, Robert B. Millard, William D. Provine

Science serves as a forum for discussion of important issues related to the advancement of science by publishing material on which a consensus has been reached as well as including the presentation of minority or conflicting points of view. Accordingly, all articles published in *Science*—including editorials, news and comment, and book reviews—are signed and reflect the individual views of the authors and not official points of view adopted by AAAS or the institutions with which the authors are affiliated.

BOARD OF REVIEWING EDITORS (Statistics board members indicated with **S**)

Adriano Aguzzi, *U. Hospital Zürich*
Takuzo Aida, *U. of Tokyo*
Leslie Aiello, *Wenner-Gren Foundation*
Judith Allen, *U. of Manchester*
Sebastian Amigorena, *Institut Curie*
James Analytis, *U. of California, Berkeley*
Paola Arlotta, *Harvard U.*
Johan Auwerx, *EPFL*
David Awschalom, *U. of Chicago*
Clare Baker, *U. of Cambridge*
Nenad Ban, *ETH Zürich*
Franz Bauer, *Pontificia Universidad Católica de Chile*
Ray H. Baughman, *U. of Texas at Dallas*
Peter Bearman, *Columbia U.*
Carlo Beenakker, *Leiden U.*
Yasmine Belkaid, *NIAID, NIH*
Philip Benfey, *Duke U.*
Gabriele Bergers, *VIB*
Bradley Bernstein, *Mass. General Hospital*
Alessandra Biffi, *Harvard Med. School*
Peer Bork, *EMBL*
Chris Bowler, *École Normale Supérieure*
Ian Boyd, *U. of St. Andrews*
Emily Brodsky, *U. of California, Santa Cruz*
Ron Brookmeyer, *U. of California, Los Angeles* (**S**)
Christian Büchel, *UKE Hamburg*
Dennis Burton, *Scripps Research*
Carter Tribley Butts, *U. of California, Irvine*
György Buzsáki, *New York U. School of Med.*
Blanche Capel, *Duke U.*
Annmarie Carlton, *U. of California, Irvine*
Lars-Erik Cederman, *ETH Zürich*
Nick Chater, *U. of Warwick*
Zhijian Chen, *UT Southwestern Med. Ctr.*
Ib Chorkendorff, *Denmark TU*
James J. Collins, *MIT*
Robert Cook-Deegan, *Arizona State U.*
Alan Cowman, *Walter & Eliza Hall Inst.*
Carolyn Coyne, *U. of Pittsburgh*
Roberta Croce, *VU Amsterdam*
Jeff L. Dangl, *U. of North Carolina*
Tom Daniel, *U. of Washington*
Chiara Daraio, *Caltech*
Nicolas Dauphas, *U. of Chicago*
Frans de Waal, *Emory U.*
Claude Desplan, *New York U.*
Sandra Díaz, *Universidad Nacional de Córdoba*
Hong Ding, *Inst. of Physics, CAS*
Jennifer Dionne, *Stanford U.*
Dennis Discher, *U. of Penn.*
Jennifer A. Doudna, *U. of California, Berkeley*
Bruce Dunn, *U. of California, Los Angeles*
William Dunphy, *Caltech*
Christopher Dye, *U. of Oxford*
Todd Ehlers, *U. of Tübingen*
Jennifer Elisseeff, *Johns Hopkins U.*
Tim Elston, *U. of North Carolina*
Andrea Encalada, *U. San Francisco de Quito*
Nader Engheta, *U. of Penn.*
Karen Ersche, *U. of Cambridge*
Barry Everitt, *U. of Cambridge*
Vanessa Ezenwa, *U. of Georgia*
Michael Feuer, *The George Washington U.*
Toren Finkel, *U. of Pittsburgh Med. Ctr.*
Gwenn Flowers, *Simon Fraser U.*
Peter Fratzl, *Max Planck Inst. Potsdam*
Elaine Fuchs, *Rockefeller U.*
Eileen Furlong, *EMBL*
Jay Gallagher, *U. of Wisconsin*
Susan Gelman, *U. of Michigan*
Daniel Geschwind, *U. of California, Los Angeles*
Karl-Heinz Glassmeier, *TU Braunschweig*
Ramon Gonzalez, *Rice U.*
Elizabeth Grove, *U. of Chicago*
Nicolas Gruber, *ETH Zürich*
Kip Guy, *U. of Kentucky College of Pharmacy*
Taekjip Ha, *Johns Hopkins U.*
Christian Haass, *Ludwig Maximilians U.*
Sharon Hammes-Schiffer, *Yale U.*
Wolf-Dietrich Hardt, *ETH Zürich*
Louise Harra, *U. College London*
Jian He, *Clemson U.*
Carl-Philipp Heisenberg, *IST Austria*
Ykä Helariutta, *U. of Cambridge*
Janet G. Hering, *Eawag*
Hans Hilgenkamp, *U. of Twente*
Kai-Uwe Hinrichs, *U. of Bremen*
David Hodell, *U. of Cambridge*
Lora Hooper, *UT Southwestern Med. Ctr.*
Fred Hughson, *Princeton U.*
Randall Hulet, *Rice U.*
Auke Ijspeert, *EPFL*
Akiko Iwasaki, *Yale U.*
Stephen Jackson, *USGS and U. of Arizona*
Kai Johnsson, *EPFL*
Peter Jonas, *IST Austria*
Matt Kaeberlein, *U. of Washington*
William Kaelin Jr., *Dana-Farber Cancer Inst.*
Daniel Kammen, *U. of California, Berkeley*
Abby Kavner, *U. of California, Los Angeles*
V. Narry Kim, *Seoul Nat. U.*
Robert Kingston, *Harvard Med. School*
Nancy Knowlton, *Smithsonian Institution*
Etienne Koechlin, *École Normale Supérieure*
Alexander Kolodkin, *Johns Hopkins U.*
Thomas Langer, *U. of Cologne*
Mitchell A. Lazar, *U. of Penn.*
Ottoline Leyser, *U. of Cambridge*
Wendell Lim, *U. of California, San Francisco*
Marcia C. Linn, *U. of California, Berkeley*
Jianguo Liu, *Michigan State U.*
Luis Liz-Marzán, *CIC biomaGUNE*
Jonathan Losos, *Washington U. in St. Louis*
Ke Lu, *Chinese Acad. of Sciences*
Christian Lüscher, *U. of Geneva*
Fabienne Mackay, *U. of Melbourne*
Anne Magurran, *U. of St. Andrews*
Oscar Marín, *King's College London*
Charles Marshall, *U. of California, Berkeley*
Christopher Marx, *U. of Idaho*
Geraldine Masson, *CNRS*
C. Robertson McClung, *Dartmouth College*
Rodrigo Medellín, *U. of Mexico*
Graham Medley, *London School of Hygiene & Tropical Med.*
Jane Memmott, *U. of Bristol*
Edward Miguel, *U. of California, Berkeley*
Tom Misteli, *NCI, NIH*
Yasushi Miyashita, *U. of Tokyo*
Alison Motsinger-Reif, *NC State U.* (**S**)
Daniel Nettle, *Newcastle U.*
Daniel Neumark, *U. of California, Berkeley*
Beatriz Noheda, *U. of Groningen*
Helga Nowotny, *Austrian Council*
Rachel O'Reilly, *U. of Warwick*
Harry Orr, *U. of Minnesota*
Pilar Ossorio, *U. of Wisconsin*
Andrew Oswald, *U. of Warwick*
Isabella Pagano, *Istituto Nazionale di Astrofisica*
Margaret Palmer, *U. of Maryland*
Elizabeth Levy Paluck, *Princeton U.*
Jane Parker, *Max Planck Inst. Cologne*
Giovanni Parmigiani, *Dana-Farber Cancer Inst.* (**S**)
Samuel Pfaff, *Salk Inst. for Biological Studies*
Julie Pfeiffer, *UT Southwestern Med. Ctr.*
Matthieu Piel, *Institut Curie*
Kathrin Plath, *U. of California, Los Angeles*
Martin Plenio, *Ulm U.*
Elvira Poloczanska, *Alfred-Wegener-Inst.*
Julia Pongratz, *Ludwig Maximilians U.*
Philippe Poulin, *CNRS*
Jonathan Pritchard, *Stanford U.*
David Randall, *Colorado State U.*
Félix A. Rey, *Institut Pasteur*
Trevor Robbins, *U. of Cambridge*
Amy Rosenzweig, *Northwestern U.*
Mike Ryan, *U. of Texas at Austin*
Mitinori Saitou, *Kyoto U.*
Shimon Sakaguchi, *Osaka U.*
Miquel Salmeron, *Lawrence Berkeley Nat. Lab*
Nitin Samarth, *Penn. State U.*
Jürgen Sandkühler, *Med. U. of Vienna*
Alexander Schier, *Harvard U.*
Wolfram Schlenker, *Columbia U.*
Susannah Scott, *U. of California, Santa Barbara*
Rebecca Sear, *London School of Hygiene & Tropical Med.*
Vladimir Shalaev, *Purdue U.*
Jie Shan, *Cornell U.*
Beth Shapiro, *U. of California, Santa Cruz*
Jay Shendure, *U. of Washington*
Brian Shoichet, *U. of California, San Francisco*
Robert Siliciano, *Johns Hopkins U. School of Med.*
Lucia Sivilotti, *U. College London*
Alison Smith, *John Innes Centre*
Richard Smith, *U. of North Carolina* (**S**)
Mark Smyth, *QIMR Berghofer*
Pam Soltis, *U. of Florida*
John Speakman, *U. of Aberdeen*
Tara Spires-Jones, *U. of Edinburgh*
Allan C. Spradling, *Carnegie Institution for Science*
V. S. Subrahmanian, *U. of Maryland*
Ira Tabas, *Columbia U.*
Sarah Teichmann, *U. of Cambridge*
Rocio Titiunik, *Princeton U.*
Shubha Tole, *Tata Inst. of Fundamental Research*
Wim van der Putten, *Netherlands Inst. of Ecology*
Reinhilde Veugelers, *KU Leuven*
Bert Vogelstein, *Johns Hopkins U.*
Kathleen Vohs, *U. of Minnesota*
David Wallach, *Weizmann Inst. of Science*
Jane-Ling Wang, *U. of California, Davis* (**S**)
David Waxman, *Fudan U.*
Jonathan Weissman, *U. of California, San Francisco*
Chris Wikle, *U. of Missouri* (**S**)
Terrie Williams, *U. of California, Santa Cruz*
Ian A. Wilson, *Scripps Research* (**S**)
Yu Xie, *Princeton U.*
Jan Zaanen, *Leiden U.*
Kenneth Zaret, *U. of Penn. School of Med.*
Jonathan Zehr, *U. of California, Santa Cruz*
Maria Zuber, *MIT*

Published by AAAS

EDITORIAL

Stop blaming mental illness

The United States is experiencing a public health epidemic of mass shootings and other forms of gun violence. A convenient response seems to be blaming mental illness; after all, "who in their right mind would do this?" This is utterly wrong. Mental illnesses, certainly severe mental illnesses, are not the major cause of mass shootings. It also is dangerously stigmatizing to people who suffer from these devastating disorders and can subject them to inappropriate restrictions. According to the National Council for Behavioral Health, the best estimates are that individuals with mental illnesses are responsible for less than 4% of all violent crimes in the United States, and less than a third of people who commit mass shootings are diagnosably mentally ill. Moreover, a large majority of individuals with mental illnesses are not at high risk for committing violent acts. Continuing to blame mental illness distracts from finding the real causes of mass shootings and addressing them directly.

<4%
violent crimes
in the United States are caused by individuals with mental illnesses

<1/3
people
who commit mass shootings are diagnosably mentally ill

Mental illness is, regrettably, a rather loosely defined and loosely used term, and this contributes to the problem. According to the American Psychiatric Association, "Mental illnesses are health conditions involving changes in emotion, thinking or behavior…associated with distress and/or problems functioning in social, work or family activities." That broad definition can arguably be applied to many life stresses and situations. However, what most people likely mean when they attribute mass shootings to mental illness are what mental health professionals call "serious or severe mental illnesses," such as schizophrenia, bipolar disorder, or major depression. Other frequently cited causes of mass shootings—hate, employee disgruntlement, being disaffected with society or disappointed with one's life—are not defined clinically as serious mental illnesses themselves. And because they have not been studied systematically, we do not know if these purported other causes really apply, let alone what to do about them if true.

Unfortunately, it has been difficult to determine precisely the causes of mass shootings and the appropriate approaches to preventing them, largely because of a dearth of public funding for this line of research. The U.S. Centers for Disease Control and Prevention (CDC) had historically been the major funder of the public health aspects of firearm-related violence research, and much was being learned. But in 1996, Congress passed the so-called "Dickey Amendment" to the appropriations bill for the CDC, which was interpreted by the agency as prohibiting support for any firearm-related studies, and therefore the agency stopped funding this research. Although agencies including the National Institutes of Health (NIH) and the National Science Foundation have devoted small amounts to studies related to firearm violence, Congressional actions over the last few years have discouraged such investment, and both agencies have virtually stopped funding that kind of work.

There is now a new opportunity to apply science to the problem of mass shootings. In June 2019, the funding bill passed by the U.S. House of Representatives included $50 million for the Department of Health and Human Services, split between the NIH and CDC, to support research on firearm violence. It is not a lot of money, given the scope of the problem, but surely a start. The Institute of Medicine and the National Research Council (now parts of the National Academies of Sciences, Engineering, and Medicine) laid out a detailed research agenda in 2013 for investigating firearm-related violence that could easily be updated. The Senate and the White House should agree to this funding bill, and the country should stop scapegoating people who suffer from mental illnesses and get on with determining the real causes of mass shootings.

–Alan I. Leshner

Alan I. Leshner *is the interim chief executive officer of the American Association for the Advancement of Science (AAAS) and executive publisher of* Science. *He is a former deputy director and acting director of the National Institute of Mental Health at the NIH in Bethesda, MD, USA. aleshner@aaas.org*

PHOTO: PROFESSIONAL IMAGES PHOTOGRAPHY

10.1126/science.aaz0997

Published by AAAS

NEWS

> “The striking advances [in science] come from people on the fringes, being playful.”
>
> **Polymerase chain reaction inventor Kary Mullis,** to *The Post and Courier* in 1993. Mullis, who won a Nobel Prize but held controversial views, died last week at age 74.

IN BRIEF

Edited by **Catherine Matacic**

ASTRONOMY

Mauna Kea telescopes reopen

After more than 3 weeks, astronomers on 10 August returned to work at 12 observatories atop Mauna Kea in Hawaii, thanks to a deal between state officials and protesters blocking construction of the $1.4 billion, 18-story Thirty Meter Telescope (TMT) on what they say is a sacred site. After protesters set up camp on the summit access road on 15 July, the Mauna Kea observatories shuttered to protect staff. The standoff has remained peaceful, however, and the protest camp now hosts shops, cafeterias, and even visits by Hollywood celebrities. But for astronomers, it has been the longest shutdown in the 5 decades since the mountaintop observatory opened in 1967. The deal involved building a temporary roadway around the camp, over hardened lava. Law enforcement will give protesters an advance list of all vehicles going up and down—to show that they are not associated with the TMT.

Banana fungus hits Colombia

AGRICULTURE | Colombia declared a national state of emergency on 8 August, following confirmation of a dread fungus on banana plantations. This is the first time that Fusarium wilt tropical race 4 (TR4), which has devastated banana harvests in Asia, has been confirmed in Latin America (*Science*, 19 July, p. 207). Signs of the fungus were first spotted in June in northern Colombia, putting the region on high alert. After eradicating trees on nearly 170 hectares of quarantined cropland, the Colombian Agricultural Institute announced plans to expand biosecurity efforts. On 5 August, agricultural ministers from across Latin America met in Quito to discuss plans to prevent further outbreaks. TR4, for which there is no treatment, kills plants by disrupting their vascular systems, and it can persist in soil for decades.

New rules for at-risk species

POLICY | U.S. President Donald Trump’s administration this week overhauled the Endangered Species Act, curbing protections for some at-risk species and making it easier to develop in critical habitats. The new rules would also let federal officials consider—for the first time—economic factors, not just scientific ones, in deciding whether to protect a species. The changes are needed to make the rules “clear, consistent, and efficient,” Secretary of the Interior David Bernhardt said. But conservation groups say they will sue to block the new policies, which could go into effect as early as next month. “Science must guide our decisions, not dollar signs,” says Rebecca Riley, an attorney with the Natural Resources Defense Council in Chicago, Illinois.

U.K. to speed scientist visas

POLICY | U.K. Prime Minister Boris Johnson last week announced plans to make it easier for foreign scientists to work in the United Kingdom after Brexit. Research advocates welcomed the news, because EU citizens—the biggest source of nonnative scientific talent in the United Kingdom—will need visas, which are costly and cumbersome to obtain. The

PHOTO: THOMAS JAHN/ALAMY STOCK PHOTO

Published by AAAS

BIOLOGY

World's biggest frogs build their own ponds

The world's biggest frogs, as long as a human foot, may have become so brawny in order to dig swimming pools for their young. That's what Mark-Oliver Rödel, a herpetologist at the Berlin Museum of Natural History, and colleagues concluded after discovering tadpoles of the Goliath frog (*Conraua goliath*) swimming in pools that the animals, which can weigh up to 3.3 kilograms, had apparently dug themselves along the banks of the Mpoula River in western Cameroon. The researchers never saw the frogs at work, but they saw signs of excavation: Day by day, gravel and stones weighing up to 2 kilograms were gradually moved to create meter-wide pools—some of which contained up to 3000 eggs or tadpoles of different ages, Rödel's team reported last week in the *Journal of Natural History*. A camera recorded a single frog parent guarding each pool at night. The bigger the frog, the researchers say, the bigger the pools they can build for their vulnerable youngsters.

PHOTO: DANIEL HEUCLIN/NATURE PICTURE LIBRARY/GETTY IMAGES

new system, to be launched this year, will be open to researchers of all career stages and will allow scientists' family members to work in the United Kingdom. Scientific societies have urged the government to make the new system simple, cheap, and flexible, but have also warned that the economic disruption of a chaotic Brexit could still set back research. If an exit deal is not approved, the United Kingdom will crash out of the European Union on 31 October.

'Aggressive' surveillance decried

ACADEMIC ESPIONAGE | The United States should not emulate China in tracking ethnic minorities in order to thwart academic espionage, writes a coalition of 19 Asian and higher education organizations in an open letter released this week. The groups, which range from the American Association of University Professors to the Chinese American Citizens Alliance, chided the Federal Bureau of Investigation (FBI) for an initiative, first reported by NPR, to urge university officials to monitor the activities of Chinese students and Chinese-born researchers on their campuses. Despite "the mounting global reach of Beijing's tech-enabled authoritarianism" and the Chinese government's "aggressive use of surveillance," the groups write, U.S. authorities "must not mimic the very tactics it professes to reject." Senator Mark Warner (D–VA), who has organized several meetings between FBI and university officials, says the United States should not "engage in racial profiling" as it combats the "creative ways [used by] the Chinese Communist Party to access and steal our technologies."

Blast in Russia kills five

WEAPONS | An 8 August blast at a Russian naval range in the White Sea killed five scientists and injured three others as they were working on a missile engine, according to the Russian State Atomic Energy Corporation (Rosatom). The explosion also appears to have released radiation into the environment—Russia's Federal Service for Hydrometeorology and Environmental Monitoring reported a brief spike in gamma radiation in the nearby port city of Severodvinsk, according to the TASS news agency. According to Rosatom, the missile was a conventional liquid-fueled rocket that used batteries that derive energy from radioactive materials. However, U.S. intelligence officials—and some Russian media outlets—speculate that the researchers were testing a nuclear-powered cruise missile.

Drone ship circles Antarctica

OCEANOGRAPHY | Earlier this month, a robotic ship became the first to circumnavigate Antarctica, Saildrone in Alameda, California, reported. The company, which is seeking to revolutionize oceanography with its sensor-laden marine drones (*Science*, 9 March 2018, p. 1082), had previously attempted such a feat twice, only to have its robots' high sails damaged by the freezing, 15-meter-high waves and strong winds of the Southern Ocean. The successful drone, which took 196 days to complete its 22,000-kilometer voyage on 3 August, was outfitted with a stout, square sail that, although unwieldy, was broad enough to navigate downwind. Some of

Published by AAAS

its preliminary measurements agree with recent data that indicate the Southern Ocean—long thought to be a carbon sink—may instead be emitting carbon dioxide, puzzling and worrying scientists.

Cosmic ray scope to look down

ASTROPHYSICS | On any given night, dozens of Earth-based telescopes peer up into the sky watching for the fluorescent glow of particle showers produced by high-energy cosmic rays slamming into the atmosphere. On 22 August, an international team will launch the first telescope that will watch for those glows by looking *down*, from a window on the International Space Station (ISS). By monitoring a larger piece of the sky, the Mini–Extreme Universe Space Observatory (Mini-EUSO) telescope could detect more high-energy events than telescopes on the ground, yielding clues to the origins of cosmic rays. Scientists hope its performance will lead to larger instruments that would be attached to the ISS or orbiting spacecraft. The Mini-EUSO will also watch for lightning and the flash of meteoroids entering the atmosphere.

UC scientists quit journals

PUBLISHING | Thirty scientists in the University of California (UC) system announced last week that they will resign from Cell Press editorial boards to protest a 5-month impasse with the owner, publishing giant Elsevier, over costs. The researchers include Jennifer Doudna, co-inventor of the CRISPR-Cas9 gene-editing technology, and Elizabeth Blackburn, co-recipient of the 2009 Nobel Prize in Physiology or Medicine. The protesters are a minority of the approximately 110 UC faculty members on Cell Press editorial boards and the more than 900 on the boards of other Elsevier journals. UC has sought a deal with Elsevier that would make all UC-authored articles immediately free to readers while lowering total costs for its access to paywalled content.

Antibiotics in U.S. poultry drop

AGRICULTURE | Antibiotic use in chickens and turkeys has fallen sharply since 2013, according to the first analysis of U.S. industry data. The share of U.S. hatchery chicks that receive antibiotics—typically to prevent *Escherichia coli* infections—fell from 93% to 17% between 2013 and 2017, for example, according to a study produced by the Mindwalk Consulting Group in Falcon Heights, Minnesota, and funded by the U.S. Food and Drug Administration and the U.S. Poultry & Egg Association. The reductions, largely due to responsible use and consumer demand, follow an industry-led phaseout of medically important antibiotics for boosting growth, says study author Randall Singer of the University of Minnesota in Saint Paul.

Star biochemist out at Scripps

WORKPLACE | The Scripps Research Institute (TSRI) in San Diego, California, has ousted prominent biochemist Floyd Romesberg for undisclosed reasons. The high-profile biology research hub, recently renamed Scripps Research, confirmed Romesberg's mid-June departure. In a statement last week, Scripps Research said it had investigated but found no violation of Title IX, the 1972 law forbidding gender discrimination by academic institutions receiving federal funds. "However, Dr. Romesberg is no longer with TSRI, we are winding down his lab at the institute, and we will not comment on any personnel decision," the statement said. Romesberg made his name by creating a pair of novel DNA bases and adding them to the genetic code of a bacterium that then produced novel proteins. He did not respond to repeated interview requests.

Computer joins exascale trio

ADVANCED COMPUTING | Officials at the U.S. Department of Energy this week announced plans to build a third U.S. supercomputer operating at unprecedented "exascale" speeds. The machine, dubbed El Capitan, will reach 1.5 exaflops, or 1.5 quintillion calculations per second. That's more than seven times faster than Summit, the current supercomputing record holder, at Oak Ridge National Laboratory (ORNL) in Tennessee. El Capitan is expected to be completed in late 2022 at a cost of $600 million. Housed at Lawrence Livermore National Laboratory in California, the machine will help the National Nuclear Security Administration ensure the safety and effectiveness of U.S. nuclear weapons. Two other exascale machines, dubbed Aurora and Frontier, are already scheduled for delivery at Argonne National Laboratory and ORNL, beginning in 2021.

A Filipino boy with dengue rests under a mosquito net.

PHOTO: LEO SOLINAP/EPA-EFE/SHUTTERSTOCK

PUBLIC HEALTH

Dengue emergency declared in the Philippines

Dengue was declared a national epidemic in the Philippines on 6 August. The island country has already logged 146,062 cases and 622 deaths this year—nearly twice the number of cases and deaths during the same period in 2018, according to the Department of Health. Most of the deaths have occurred in children. In response to the rapid spread, the government is stepping up efforts to find and destroy mosquito breeding sites. In 2016, the Philippines was one of the first countries to begin widespread use of a new dengue vaccine, Dengvaxia, in children, but that campaign abruptly ended in November 2017 after the manufacturer revealed the shot increased the risk of severe disease through an unusual mechanism called antibody-dependent enhancement. About 1 million Filipino children received the vaccine, which is particularly dangerous for those who have never been infected with the virus.

S SCIENCEMAG.ORG/NEWS
Read more news from *Science* online.

Published by AAAS

IN DEPTH

Chickens have been genetically engineered to produce male eggs that are fluorescent.

PHOTO: EGGXYT LTD.

AGRICULTURAL TECHNOLOGY

'Ethical' eggs could save day-old chicks from slaughter

Scientists find ways to count male chicks before they hatch

By **Gretchen Vogel**, *in Berlin*

In hundreds of grocery stores here, shoppers can pay a few extra cents for eggs stamped with a heart and the word *respeggt*—to show that they were laid by hens that did not hatch alongside male chicks destined for slaughter. This week, the eggs will be available for the first time in stores outside of Berlin. By the end of the year, they will appear all across Germany—a sign that scientists are getting closer to solving a tricky chick-and-egg problem.

Modern laying hens have been bred to produce huge numbers of eggs, but their brothers are useless. They don't put on weight fast enough to be raised for meat. So hatchery workers—specialized "sexers"—sort day-old chicks by hand, squeezing open their anal vents for a sign of their sex. Females are sold to farms. Males—roughly 7 billion per year worldwide, according to industry estimates—are fed into a shredder or gassed.

Sorting males from females before chicks hatch at 21 days wouldn't just avoid the massacre. Hatcheries would no longer need to employ sexers, they wouldn't waste space and energy incubating male eggs, and they could sell those eggs as a raw material for animal feed producers, the cosmetics industry, or vaccine manufacturers. The United Egg Producers, a U.S. cooperative, says it wants to be cull-free by 2020, and the German government has said it will outlaw the practice. "Everyone wants the same thing, and the right piece of technology could solve this right now," says Timothy Kurt, scientific program director at the U.S. Department of Agriculture's Foundation for Food and Agriculture Research (FFAR) in Washington, D.C.

One contender is the technology behind the *respeggt* eggs, which sorts them based on sex hormones. Funding from governments and industry has prompted an abundance of other ideas—from laser spectroscopy to MRI scans to genetic engineering. And next month, FFAR will announce seed funding for six finalists—selected from 21 entries from 10 countries—for an EggTech Prize competing for up to $6 million for a workable method.

Almuth Einspanier, a veterinary endocrinologist at Leipzig University in Germany, and her colleagues laid the groundwork for the *respeggt* brand. They found that by day 9 of development, female embryos produce a hormone called estrone sulfate that can be detected reliably in fluid that builds up in the egg—"essentially the embryo's pee," Einspanier says. The German grocery chain Rewe and HatchTech, a Dutch hatchery equipment supplier, founded Seleggt, a spinoff based in Cologne, Germany, to market the technique. The company built a robot that fires a laser to open a hole in the shell much smaller than a pinhead. It sucks out a minuscule drop of the fluid and adds it to a solution that turns blue in the presence of the female hormone. Female eggs go to the incubator and male eggs are sent off to be frozen and processed into powder for animal feed.

Ludger Breloh, Seleggt's managing director, says that the system is sorting up to 3000 eggs an hour in a Dutch hatchery. As those hens reach laying age, Seleggt will be able to supply eggs to more than 5000 grocery stores across Germany. But large hatcheries process as many as 50,000 eggs an hour, which would overwhelm the current system. Some animal welfare advocates raise a more fundamental problem, claiming that a 9-day embryo might feel pain. And hatcheries must pay for 9 days of incubation costs.

Gerald Steiner, an expert in medical imaging at the Technical University of Dresden in Germany, helped find a test that works at day 4. His team shines a laser through a thumbnail-size hole in the eggshell and measures fluorescent signals from the blood cells. The signals are different for male and female embryos, likely because males develop slightly faster and form certain blood cells sooner. In female eggs, the hole is sealed with medical tape, and the egg is returned to incubation. The group is working with Agri Advanced Technologies (AAT), a German subsidiary of one of Europe's largest chicken breeders, to develop a prototype system. So far, says Jörg Hurlin, managing director at AAT in Visbek, sorting accuracy is high,

Published by AAAS

but "we are not yet where we need to be."

Ovabrite, a U.S company in Austin, is chasing a technique that would leave the eggshell intact and sort eggs before incubation. Mass spectrometers would capture and analyze sex-specific volatile molecules that leak through the eggshell. Scientists suspect the molecules, first discovered in quail eggs, may allow parent birds to smell clues about an embryo's development and sex. But it is still a challenge to reliably detect such a faint signal from preincubation eggs, which must be refrigerated, says Ovabrite President Jonathan Hoopes.

Some predict that genetic engineering could help do away with complicated robots. Groups in Australia and Israel have used the CRISPR gene-editing technique to modify hens' sex chromosomes so that their sons carry a marker gene that makes male eggs glow under fluorescent light. That would allow hatcheries to sort out the fluorescent male eggs with a simple detector. Finding a marker that produces a strong enough signal in early embryos is a challenge, says Yehuda Elram, CEO of eggXYt (pronounced "exit") in Jerusalem. He says eggXYt has found a solution, but declined to say whether it is close to hatchery tests.

Public opposition to genetic modification in Europe means the approach is unlikely to catch on there. But Mark Tizard, a geneticist at the Australian Animal Health Laboratory in Geelong, who is also working on the technology, says his group's social science research suggests consumers in North America and Australia might accept it. Neither the layer hens nor the eggs sold for consumption would contain modified genes, because only males carry the inserted marker gene, he notes.

Other noninvasive ideas are still in the running: Scientists in Turkey reported that with the help of machine learning they could detect subtle differences between male and female egg shapes. German researchers have examined MRI scans of intact eggs for sex differences.

Meanwhile, the political pressure continues. In June, a German court ruled that culling day-old chicks violates the country's laws against killing animals without a justifiable reason. The court allowed hatcheries an exception "until a feasible alternative is available," but politicians are still considering a law to ban culling.

Researchers, feeling they are close to commercial breakthroughs, don't want that to happen—yet. "A ban now would do more harm than good," Einspanier says—mostly by driving hatcheries to neighboring countries with less strict laws. With a bit more time, she says, her field should be able to finally crack the problem. ■

A health worker puts on protective gear at an Ebola treatment center in Beni, Democratic Republic of the Congo.

PHOTO: REUTERS/BAZ RATNER

INFECTIOUS DISEASES

Successful Ebola treatments promise to tame outbreak

Antibody preparations that cut the death rate dramatically will become available to all patients in Congo

By **Kai Kupferschmidt**

In 2006, two survivors of an Ebola outbreak 11 years earlier in Kikwit, Democratic Republic of the Congo (DRC), were flown to the National Institute of Allergy and Infectious Diseases (NIAID) in Bethesda, Maryland. There, scientists took blood samples and from one of the patients isolated what might be the secret to his survival: a potent antibody against the virus, which they named mAb114. Now, in the DRC's latest and largest Ebola outbreak, mAb114 and another monoclonal antibody preparation, REGN-EB3, have yielded something unprecedented for people infected with the deadly virus: hope.

In November 2018, 3 months into the current outbreak, researchers started a trial using mAb114 and two other potential treatments for people infected with Ebola; 1 month later, they added a fourth treatment, REGN-EB3, developed in mice with "humanized" immune systems by scientists at Regeneron Pharmaceuticals in Tarrytown, New York. Last week, that study was stopped early after an interim analysis showed that both mAb114 and REGN-EB3 boost patients' chance of survival dramatically.

All patients at Ebola treatment centers in the DRC will now receive one of these two drugs, whereas the use of the other two experimental therapies will be discontinued, researchers said at a 12 August press conference where the results were announced. "This will undoubtedly save lives," Jeremy Farrar, head of the Wellcome Trust in London—which was not involved in the study—said in a statement. Mike Ryan, executive director of the Health Emergencies Programme at the World Health Organization (WHO) in Geneva, Switzerland, calls the news "fantastic."

The findings should help allay the suspicion and fatalism with which many DRC citizens view the Ebola response, Congolese virologist Jean-Jacques Muyembe-Tamfum said at the press conference. "People think that if you enter a treatment center, you'll leave in a coffin," said Muyembe, who heads the DRC's National Institute for Biomedical Research in Kinshasa, a partner in the trial, and took command of the Ebola fight on 22 July (*Science*, 9 August, p. 526). Now, "We have a great message," Muyembe said: "A treatment center is a place where you can recover and that you leave alive."

So far, no drugs exist for Ebola; in the current outbreak, centered in the eastern DRC, 67% of all known cases have died. Scientists tested several drugs during the West African Ebola epidemic of 2013–16, but none proved

Published by AAAS

effective (*Science*, 1 January 2016, p. 12). Some had high hopes for an antibody cocktail named ZMapp, but a trial in 71 patients didn't show a significant effect on mortality. Still, the ZMapp data were considered encouraging enough for researchers to use it as a control in the new trial, named PALM, short for the Swahili expression *pamoja tulinde maisha*, or "together save lives."

PALM randomized patients at four Ebola treatment centers to ZMapp, REGN-EB3, mAb114, or remdesivir, an antiviral drug developed by Gilead Sciences in Foster City, California. The goal was to enroll 725 patients. But on 9 August, an independent data and safety monitoring board reviewed data for 499 patients and found that only 29% of patients on REGN-EB3 had died, compared with 49% on ZMapp and 53% on remdesivir. That result was good enough, according to predetermined criteria, that the trial had to end, because it's unethical to withhold proven treatments from patients. The mortality rate in patients given mAb114 was 34%, close enough to REGN-EB3 to continue its use as well.

The two preparations did even better in the 41% of trial participants who had lower levels of Ebola virus in their blood because they had sought treatment early. In those people, mortality plummeted to 6% in the REGN-EB3 group and to 11% with mAb114. (The numbers for ZMapp and remdesivir were 24% and 33%, respectively.) Patients with a high viral load faced a bleaker outlook, however: a death rate of 60% or more. Muyembe hopes these numbers will persuade future patients to seek help early.

The success is remarkable given that the trial took place in a remote, conflict-torn area—"the worst possible conditions," says Anthony Fauci, who heads NIAID, a partner in the trial. "And the beauty of it is that you can now immediately apply it in the field."

Indeed, patients in the four treatment centers will now be randomized either to REGN-EB3 or mAb114, in an extension of the original trial. Under an ethical framework developed by WHO, patients in all other DRC treatment centers will also be eligible to receive one of the two new treatments, even though they are not yet licensed. Regeneron and Ridgeback Biotherapeutics in Miami, Florida, which produces mAb114, have stockpiled enough doses to cover all patients, Fauci says.

Muyembe, who helped discover Ebola during the first outbreak in 1976 and tried to save Kikwit patients using survivors' blood in 1995, said he never thought he'd live to see the announcement of such hopeful data. "Today, we have started a new chapter," he told reporters. "From now on, we will no longer say that Ebola is not curable." ■

SCIENTIFIC PUBLISHING

Open access takes root at National Cancer Institute

Cancer Moonshot program requires grantees to provide immediate free access to papers they publish

By **Jocelyn Kaiser**

The long-standing debate over open access to research results has been marked by a geographic divide. In Europe, some public funders have launched a high-profile open-access initiative, dubbed Plan S, that would ultimately require grantees to publish only in journals that immediately make papers free to all. But in the United States, federal agencies have stuck to a decade-old policy that allows grantees to publish in journals that keep papers behind a paywall for up to 1 year. Now, the divide is starting to blur, with one prominent U.S. research program starting to require immediate open access to the peer-reviewed publications it funds.

The policy is part of the Cancer Moonshot program at the National Cancer Institute (NCI) in Bethesda, Maryland, the 7-year, $1.8 billion research initiative spearheaded in 2016 by then–Vice President Joe Biden after his son Beau died of brain cancer. Biden felt that broader data sharing would speed cancer research, and after hearing from open-access advocates he backed the concept for all cancer research papers. NCI officials then drafted rules that require moonshot grantees to submit a plan for making their publications "immediately and broadly available to the public."

> ***"People aren't going to look at everybody else's website" for moonshot papers.***
>
> **Dinah Singer**, National Cancer Institute

That is a big change from the current policy at the National Institutes of Health, NCI's parent agency. NIH requires only that final papers be available through NIH's full-text PubMedCentral site within 12 months of publication—a delay that publishers cherish, saying that it safeguards subscription revenues and keeps journals viable.

NCI began to flesh out the moonshot open-access policy this summer after learning that what it believed was a moonshot paper—one of perhaps two dozen so far—had appeared in *Cell*, which is paywalled, says NCI Deputy Director for Scientific Strategy and Development Dinah Singer. (The agency later realized this paper hadn't been funded by the moonshot.) At first, NCI considered accepting two free sharing strategies allowed by many paywalled journals: Researchers can either publish a draft manuscript in an online preprint repository or post the final accepted paper on their own website. But officials decided that "people aren't going to look at everybody else's website" for papers, Singer says. Instead, NCI opted for a "strictly" open-access policy, with rare exceptions.

The policy says moonshot authors can publish in either a fully open-access journal or a hybrid journal that publishes both free and paywalled papers. The authors can also include in their grant budgets the fees that open-access journals charge for peer review and other costs, usually about $2000 to $3000 per paper.

NCI says it wants to enable grantees to publish in highly selective journals, including *Nature*, *Science*, and *Cell*, that don't offer open access, and it has been discussing options with such journals. *Cell* says it expects to negotiate ways to make moonshot papers free, and *Nature* says it will consider the issue on a case-by-case basis. *Science* says it will allow authors to post accepted moonshot manuscripts on PubMedCentral as soon as the papers are published, and will make the papers immediately open access, as part of its policy of making papers "related to public health" freely available.

Singer says that, for now, NCI won't expand the moonshot's open-access requirement to other programs run by the $5.7 billion institute. "We consider this a pilot program and depending on [its] success … we'll determine the next steps," she says. But Heather Joseph, executive director of the Scholarly Publishing and Academic Resources Coalition in Washington, D.C., hopes the agency will go further. "It's great that this policy is in effect for this small slice of public research," she says. "But obviously we'd like to see it for all research." ■

Published by AAAS

WORKFORCE

Grad students struggle with rising fees

Hefty bills at some U.S. public universities strain STEM students' finances

By **Katie Langin**

To help offset declines in state funding, many U.S. public universities are billing their graduate students for thousands of dollars of university fees. The charges, many of them new or recently increased, frequently come as a shock to master's and Ph.D. students in science, technology, engineering, and math fields who expect their years of training to be financially feasible because they do not pay tuition and receive modest stipends for their research and teaching work.

At Louisiana State University (LSU) in Baton Rouge, for example, grad students are charged $4900 per year in student fees—a sum that has more than doubled in 5 years. "We are not here to be rich," but grad students who work for the university expect to be able to make ends meet, says Luis Santiago-Rosario, a biology Ph.D. student at LSU who—like many in his situation—wasn't aware of the fees until he started his program. He's had to take out $6000 in federal student loans each of the 2 years he's been in grad school because his teaching stipend—roughly $22,000—isn't enough to cover the fees as well as living expenses. "[Our pay] is not enough; it's absolutely not enough after the fees."

"It's really hard to be a student here," adds Erin Good, a physics Ph.D. student at the university who points out that LSU policy bars graduate assistants from seeking outside employment to supplement their income. "I know a ton of people who are relying on food banks; … it's really getting untenable." LSU isn't alone in issuing hefty bills. Many other institutions across the country—including private ones—charge fees ranging from less than $100 to a few thousand dollars. But LSU's fees are especially steep.

An LSU spokesperson wrote that the university is aware of the squeeze on its grad students. "We continue to evaluate resources to further support our graduate students, as we work within the constraints of the university's operating budget," the statement said. On other campuses, students and faculty are also demanding action through strikes and petitions.

Cutbacks in public funding at a time when student numbers are growing and the cost of education is rising have left universities looking for new revenue. "Higher education is being shoved out of state budgets," says David Feldman, a professor of economics at the College of William & Mary in Williamsburg, Virginia. In response, many public universities have raised tuition. But some states limit tuition hikes. "Fees have been used as this wiggle room way to increase funding if you can't increase tuition," says Sophia Laderman, a senior policy analyst at the State Higher Education Executive Officers Association, a nonprofit organization based in Boulder, Colorado.

At LSU, for example, the university instituted a "student excellence fee" in 2016—saying the money would be used to hire instructors and teaching assistants, among other things. At first, grad students were charged roughly $500 per year, but this year the bill is more than $2200, making it the highest of the university's current fees. The fact that grad students seem to be charged for a service they themselves provide—teaching—is bewildering, says Good, who has advocated for fee changes on behalf of LSU's grad students.

There are some hopeful signs for grad students who are struggling. At the University of Illinois in Chicago, the graduate student union initiated a strike largely to protest fees, says Sagen Cocklin, a physics Ph.D. student who pays $1200 per year in student fees and serves as co-president of the union's steering committee. Two weeks into the strike, which led to the cancellation of hundreds of classes, the university agreed to cut the international student fee—$260 per year—in half and increase stipend levels to offset other fees.

Elsewhere, grad students are hoping for similar progress. At the University of Colorado in Boulder, for instance, more than 1600 people—including grad students, faculty members, and state and federal legislators—signed a petition calling for $1700 in annual fees to be waived for graduate teaching and research assistants. At the Georgia Institute of Technology (Georgia Tech) in Atlanta, the most controversial fee—the $1000 per year "special institutional fee"—is set by the state, not the university, so waivers are less feasible. Instead, grad students, who face fees totaling $2800 per year, are proposing steps to offset the burden, such as reducing the cost of on-campus housing and making it easier for professors to raise stipend levels. "We are trying to seek creative solutions," says Narayan Shirolker, a materials science and engineering Ph.D. student at Georgia Tech who serves as president of the grad student association.

Georgia Tech professor Joshua Weitz, who directs the quantitative biosciences graduate program, has gathered information about fees at 67 universities. In March he wrote an op-ed for *The Atlanta Journal-Constitution* arguing that the fees create financial stress for existing students and make it challenging for faculty to recruit new students, particularly those with limited financial resources. "Graduate students are benefiting the institute in a fundamental way," Weitz says. "I think it will take some time, but we should aim in the direction of eliminating [their] fees." But Feldman, the economist, notes that given the budget pressures on universities, that may not be easy. ■

Growing student burden

Over the past 20 years, costs for students—including undergraduate, graduate, and professional students—at U.S. public universities and colleges have grown as state funding has generally decreased, with some fluctuations in response to economic trends. (Numbers are adjusted for inflation.)

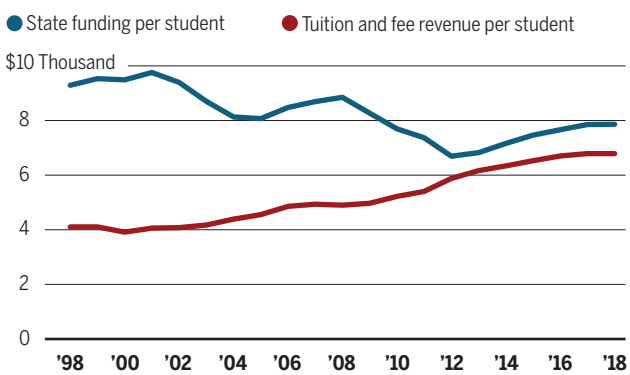

CREDITS: (GRAPHIC) K. LANGIN/*SCIENCE*; (DATA) STATE HIGHER EDUCATION EXECUTIVE OFFICERS ASSOCIATION

Published by AAAS

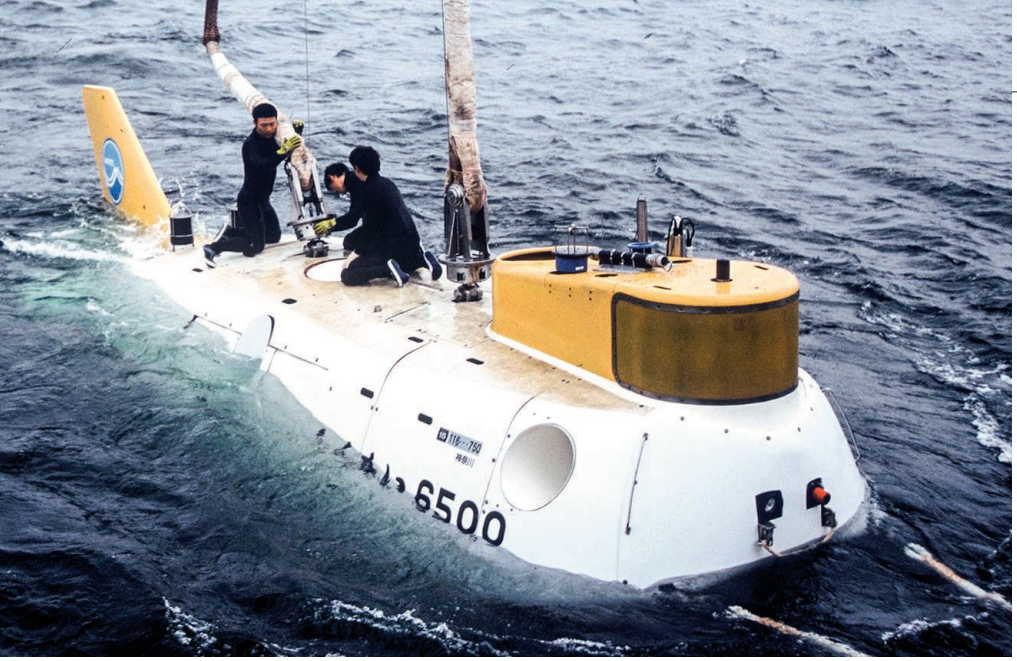

A Japanese submersible brought up a seabed sample from which a microbe was grown.

PHOTO: THE ASAHI SHIMBUN/GETTY IMAGES

BIOLOGY

Tentacled microbe hints at how simple cells became complex

A "gargantuan" effort grew archaea from deep-sea mud

By **Elizabeth Pennisi**

After 12 years of dogged effort, a team in Japan has grown an organism from seafloor mud that it says could explain how simple microbes evolved into eukaryotes—organisms with complex, nucleated cells, including animals, plants, and ourselves. The microbe sports unusual branched appendages, leading the group to suggest that an ancestral version long ago used similar tentacles to corral and envelop the symbiotic bacteria that gave rise to mitochondria, the energy-producing organelles characteristic of eukaryotic cells.

"This is the work that many people in the field have been waiting for," says Thijs Ettema, an evolutionary microbiologist at Wageningen University in the Netherlands. The finding has not yet been published in a peer-reviewed journal, but on Twitter, other scientists have described a preprint on the work as the "paper of the year" and the "moon landing for microbial ecology."

The tree of life has three major branches: eukaryotes, plus bacteria and archaea, which both lack nuclei, mitochondria, and internal membranes. Biologists have long debated the origins of those branches, with some proposing that they sprang from a single common ancestor and others saying eukaryotes branched off archaea, making those microbes our direct ancestors.

That "two domain idea" was bolstered when Ettema and colleagues sieved fragments of DNA from seafloor mud that revealed a new class of microbes with some genetic features resembling eukaryotes: the so-called Asgard archaea. But to explore that possible link, researchers needed to isolate and grow them—a tall order, as the archaea live in oxygen-deprived environments deep in the seabed and grow very slowly.

Hiroyuki Imachi and Ken Takai, microbiologists at the Japan Agency for Marine-Earth Science and Technology in Yokosuka, and their colleagues persisted. For 2000 days, they kept mud from a core sample extracted from a depth of 2500 meters off the coast of Japan in bioreactors fed continuously with methane, a gas common in deep-sea mud. The team then incubated samples of the mud in glass tubes supplied with a wide variety of nutrients and other substances. A year later, they detected microbes in one of the tubes.

DNA analyses indicated the tube held an Asgard archaeon. It took about 20 days for its numbers to double—bacteria commonly double in less than an hour—but eventually, the team grew enough of the organism to study it. "It was really a gargantuan task," says David Baum, an evolutionary biologist at the University of Wisconsin in Madison.

The Japanese researchers, who declined to comment while a journal reviews their manuscript, named the microbe *Prometheoarchaeum syntrophicum*, after the Greek titan Prometheus, who created humans out of mud. The researchers confirmed last week in their preprint, posted on bioRxiv, that some of the microbe's genes look like those found in eukaryotes. It's as if the microbe "were primed to become eukaryotes," Ettema says.

Electron microscope images revealed another suggestive feature: multiple branched appendages. The team hypothesizes that early in the history of life, the protrusions of an ancient member of the same archaeon family encircled the bacterial ancestor of mitochondria—an organism that could convert oxygen to energy. The researchers propose that as the concentration of oxygen increased on early Earth, the oxygen-using partners gave a *Prometheoarchaeum*-like host an advantage, and eukaryotic life took off.

"This is exactly what we predicted," Baum says. In 2014, he and a colleague published this idea, called the "inside out" theory. Previously, most researchers had assumed that the mitochondria were pulled into their archaeal hosts—the "outside in" theory, with the cell's internal membrane-bound compartments evolving from cell membrane folded inward. Baum proposed instead that appendages on the original host cell encased the protomitochondria, then merged to form the body of the early eukaryotic cell. *Prometheoarchaeum*'s tentacles support the idea, he says.

Ettema cautions that the archaeal ancestor to eukaryotic cells may not have looked and acted just like *Prometheoarchaeum*. Moreover, DNA studies indicate that other archaea are more closely related to eukaryotes than this one. He expects, however, that the team's work will help him and others grow related archaea: "I'm sure it will not take 12 years to get the next Asgard into culture."

As impressive as the work is, the culturing of this Asgard—or others—doesn't answer whether there are two kingdoms or three, says Patrick Forterre, a microbiologist at the Pasteur Institute in Paris. Based on his group's extensive DNA studies of the microbes, Forterre argues that Asgard archaea are not close kin to eukaryotes. He maintains that its eukaryotelike genes were borrowed from the real eukaryotic ancestors, which evolved from a common ancestor to both archaea and eukaryotes. "They don't look like [an] 'intermediate' cell between prokaryote and eukaryote but 100% as a classical (but very small) archaeon," he wrote in an email.

But even if Asgard archaea don't prove to be the ancestor of eukaryotes, the new work "reveals all kinds of exciting biology," says Willem van Schaik, a microbiologist at the University of Birmingham in the United Kingdom. "It feels like this will go into microbial textbooks immediately." ■

Published by AAAS

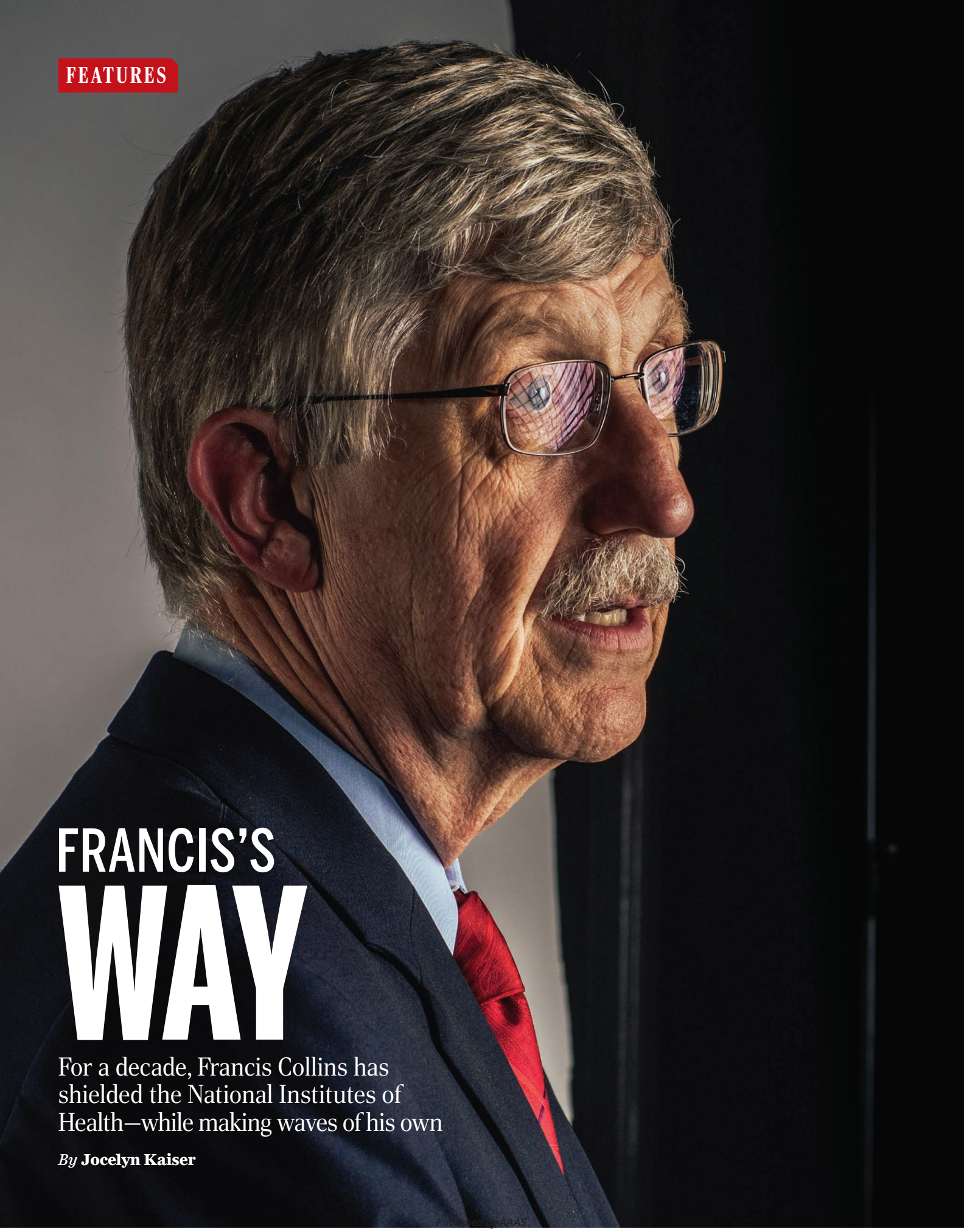

FRANCIS'S WAY

For a decade, Francis Collins has shielded the National Institutes of Health—while making waves of his own

By **Jocelyn Kaiser**

Published by AAAS

For months after President Donald Trump's inauguration in January 2017, biomedical scientists were on edge. The White House had asked geneticist Francis Collins to stay on as director of the National Institutes of Health (NIH) in Bethesda, Maryland, but nobody knew for how long. Some unconventional candidates for the NIH post, including a surgeon-turned-entrepreneur and a Tea Party member of Congress, provoked "major angst," recalls NIH observer Tony Mazzaschi, policy director for the Association of Schools and Programs of Public Health in Washington, D.C. Soon, Trump proposed slashing the agency's budget by 22%.

But in early June 2017, relief came when the White House announced that Collins would remain NIH director. Two years later, biomedical scientists are counting themselves lucky. Collins has helped shield NIH from threatened budget cuts as well as the upheaval that has shaken many other federal agencies under the Trump administration. As he completes a decade as NIH director this month, Collins, 69, has been a survivor—he's one of a few top-level holdovers from former President Barack Obama's administration and has served longer than any other NIH head in 50 years. Observers say Collins has also been one of the most influential directors ever to shape NIH, which with a budget of $39 billion this year is the world's largest biomedical research agency.

The plainspoken, guitar-playing, motorcycle-riding scientist—who took the helm of NIH after 15 years as director of NIH's genome institute—has used charm to rally Congress to restore growth to NIH's budget after more than a decade of stagnation. He has launched ambitious research initiatives in cancer, neuroscience, and precision medicine. He has tackled, with mixed results, vexing community problems, such as a lack of minorities in science, the struggles of young scientists to gain funding, and sexual harassment. With two key exceptions—the recent curtailment of fetal tissue research by Trump officials and pressure to scrutinize foreign scientists' ties to their home countries—NIH has largely escaped political interference during his tenure.

"He's had multifaceted successes. … He's always probing to do bigger and better things," says Anthony Fauci, director of NIH's National Institute of Allergy and Infectious Diseases since 1984. "He likes large initiatives that challenge the status quo, which is exactly what you want in an NIH director," says Elias Zerhouni, Collins's predecessor.

Yet Collins has detractors on NIH's campus and among the 300,000 researchers supported with NIH grants. Beneath a relaxed, affable public persona and a knack for conveying excitement about biomedical research in simple terms to the public and lawmakers, he is driven to achieve his priorities, whether pushing basic discoveries toward treatments or crafting policies to promote diversity in science. That drive has sometimes meant charging ahead without buy-in from those around him.

Early in his tenure, he ruffled feathers by shuttering a workhorse NIH research center and creating a new one to speed drug development. Some academic researchers have complained that his centrally managed projects aimed at generating large amounts of data drain resources from curiosity-driven individual grants. Still, even some former critics have come around. University of California (UC), Berkeley, evolutionary biologist and *eLife* Editor-in-Chief Michael Eisen, who had decried Collins's "big science" initiatives and called for him to be replaced soon after Trump was elected, has changed his mind. "He is trying to do the right thing for the institution. You also appreciate that he's probably a bulwark against worse things for science," Eisen says.

> **"He's always probing to do bigger and better things."**
> **Anthony Fauci**, National Institute of Allergy and Infectious Diseases

Collins's intense focus on what he believes in can come across as arrogance, says biochemist Mark Lively of Wake Forest University's School of Medicine in Winston-Salem, North Carolina. But overall the biomedical research community has benefited from his leadership, Lively says: "I'm glad he's still there."

And Collins is, too. "I didn't expect to [still] be here," he says. But, he adds, "It is a privilege, indeed, to be able to stay at the helm of this remarkable institution with such an incredible mission. So I'm happy to be here. I hope I'm still doing a good job."

ON A WARM JULY DAY as Collins prepares to hand out employee awards in an NIH auditorium, he reaches for his guitar, decorated with silver strands representing DNA. He has just told the story of a young man pictured on a giant screen behind him, who died this spring at NIH after 4 years of treatment for a rare kidney cancer. Collins says the patient's death shows that "our solutions don't always work." He then sings an Andy Grammer song that the patient liked: "I'm not givin' up, I'm not givin' up, givin' up." After applause, he tells his staff: "You don't give up. … You figure out how to move science forward."

It's "vintage Francis Collins," says veteran NIH cancer researcher Stephen Chanock at a reception after the ceremony. "He's wonderful, an old-fashioned kind of person," Chanock says. Collins grew up home-schooled in rural Virginia in a family that sang and staged plays. After earning a Ph.D. in chemistry and then a medical degree, he headed a lab at the University of Michigan, where he and collaborators used a gene-hunting technique he'd developed to identify the cystic fibrosis gene. At NIH, he led the Human Genome Project to its completion in 2003. But Collins drew criticism then—and still occasionally does—for hyping the payoff from genomic medicine. When Obama named him NIH director, some researchers worried Collins would favor data-intensive, big biology projects; another concern was that his outspoken Christian faith would influence his leadership.

His religion never became an issue—he followed Obama's order to loosen rules for stem cell research, which some Christians oppose, and has defended fetal tissue research despite criticism from antiabortion groups. But he has run NIH with the same firm hand with which he led the genome institute's sequencing projects. ("It's Francis's way or no way," says an NIH senior scientist who asked not to be named.) In 2010, with almost no discussion, he proposed dismantling the National Center for Research Resources, a cherished NIH center that helped pay for expensive resources such as primate centers and electron microscopes. In its place, he launched a new center that would "reengineer" drug development. The creation of the National Center for Advancing Translational Sciences (NCATS) rankled investigators, lawmakers, and some NIH institute directors. Drug company executives scoffed at the idea that NIH could improve on the success rate of industry, which spends billions of dollars on drug development.

"I'm a physician [and] also a basic scientist. I'm impatient about figuring out how basic science discoveries can find their way into clinical benefits," Collins says now. He maintains that 7 years after its launch, NCATS "has a pretty strong track record."

Former Eli Lilly scientist Bernard Munos agrees. NCATS is hampered by having to spend most of its budget on a program it inherited that funds large translational

Francis Collins has led the National Institutes of Health with a firm hand.

PHOTO: (OPPOSITE PAGE) STEPHEN VOSS

Published by AAAS

Francis Collins's good relationships with key congressional leaders have led to a string of healthy budget increases for the National Institutes of Health since 2016, reversing a 12-year erosion.

PHOTO: CHIP SOMODEVILLA/GETTY IMAGES

grants at academic health centers. Even so, he says, it has produced tools, such as tissue chips, 3D bioprinting, and stem cell technologies, that will help industry. NCATS is "still a work in progress," but "much of the early opposition has waned," says Munos, now a consultant in Indianapolis.

Even scientists who spoke out against abolishing the National Center for Research Resources say its programs, now managed by other institutes, are running smoothly. The reorganization "wasn't necessary, but it worked out," Lively says.

COLLINS'S LEGACY also includes three big biology projects announced by Obama, starting in 2013 with the 10-year Brain Research through Advancing Innovative Neurotechnologies (BRAIN) Initiative. Neuroscientists conceived of the project, which develops tools to probe how neural circuits control thoughts and movement. So far, its fruits include a brain cell census and a device that converts brain activity into speech.

"BRAIN seized the moment extremely well" by bringing together scientists from various disciplines to harness new approaches, says neuroscientist Karl Deisseroth at Stanford University in Palo Alto, California. "The field has become even more complex and exciting."

The Cancer Moonshot, launched in 2016 at the behest of then–Vice President Joe Biden after his son Beau died from brain cancer, also emphasizes large collaborations and big data. Collins's signature project, however, is the 2015 Precision Medicine Initiative that led to All of Us, an effort to amass a trove of data on the genomic basis of disease by collecting health records and DNA sequences from 1 million volunteers.

"I am totally over-the-moon excited about All of Us and the transformation that it's going to create as a platform for figuring out how do people stay healthy and how do you manage chronic illness when it happens," says Collins, who first proposed the project in 2004 as head of the genome institute. Zerhouni, who vetoed that proposal because of costs, says it's unclear whether All of Us, which is pooling disparate health records and could see a high dropout rate, will measure up to similar projects run by U.S. health providers and the United Kingdom's national health system. All of Us has so far enrolled more than 180,000 participants, and NIH says it is on schedule.

Although some scientists grumble that Collins prioritizes such projects over investigator-initiated grants, the criticism has subsided as the NIH budget has improved. The numbers were bleak in the first years of Collins's leadership. In 2011, after years of flat budgets, NIH was funding less than one in five of the grant applications it received, a record low. Two years later, as part of a government-wide retrenchment, the agency's budget fell by 5%. But in 2016, Congress began to ease tight overall spending caps. The 21st Century Cures Act, passed by Congress that year, created a $4.8 billion fund over 10 years for Obama's three science initiatives. And since Trump's election, Collins has helped persuade Congress to reverse repeated presidential proposals to slash NIH's budget. In June, the House of Representatives voted to give NIH its fifth consecutive $2 billion raise, which would bring its budget to $41 billion in 2020.

Collins has been "able to gain and maintain the support of Congress," says biologist Keith Yamamoto of UC San Francisco. Adds Kathy Hudson, a consultant in Washington, D.C., who was Collins's policy chief until late 2016: "He has managed to cultivate a huge number of very important friends on [Capitol] Hill, and I think that has to do with personal interactions."

COLLINS HAS ALSO SHAPED the agency's leadership and policies. "One of his legacies will be that he will have appointed a huge number of institute directors," says Story Landis, a former director of NIH's National Institute of Neurological Disorders and Stroke. Mazzaschi says Collins has "had just a stellar record of recruiting noted scientific minds." Of the current 27 institute and center directors, Collins has appointed 16, six of them women.

Addressing a lack of diversity among NIH investigators became a Collins priority in 2011, when a study reported that from 2000 to 2006, black investigators, who submitted only 1.3% of all grant proposals, were 13 percentage points less likely than whites to win NIH's standard R01 awards. NIH responded by pouring $250 million over 5 years into a new investigator mentoring network and an undergraduate program for minorities. Collins also created a Scientific Workforce Diversity office headed by Hannah Valantine, a black cardiologist and researcher who had led diversity efforts at Stanford. At a meeting of Collins's board in June, Valantine reported modest improvements: The difference in grant success rates between black applicants and whites dropped to seven points in the years 2013 to 2018, and the annual number of awards to black investigators more than doubled over that period to 113.

"There is progress being made, but … there's still way, way, way more to do," said Roy Wilson at the board meeting. Wilson chairs NIH's diversity working group and is president of Wayne State University in Detroit, Michigan. But Collins is encouraged: "For the first time, it made me feel like we may be on the right track," he says.

Another stubborn problem is that the average age of first-time Ph.D. investigators has hovered at 42 years for 2 decades, up from 36 in 1980. Collins's remedy starting in 2017 was to set aside money each year

Published by AAAS

A decade at the top

Francis Collins has led the National Institutes of Health (NIH) through lean times and plenty, always following a personal compass toward big biology and translational research.

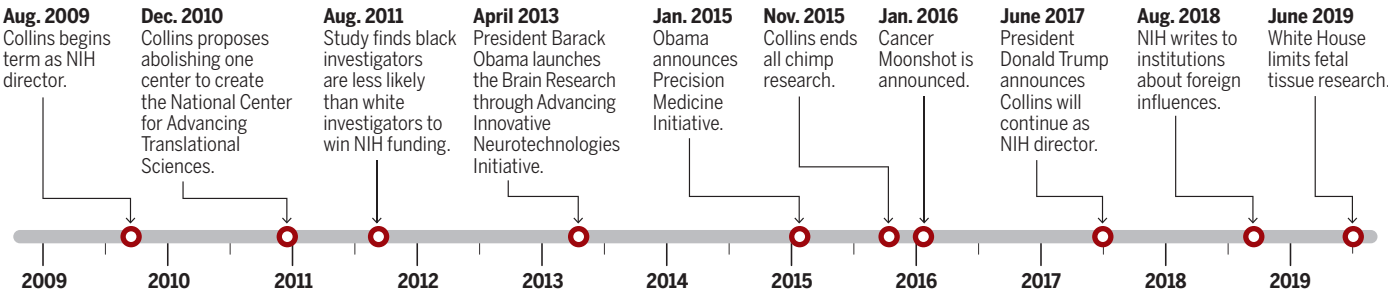

to fund 200 additional young investigators' first research grants. For each of the past 2 years, the number of early-stage investigators supported by the agency has risen, reaching 1287 awards last year.

But that approach is a "Band-Aid," says Gary McDowell, who recently stepped down as executive director of Future of Research, a nonprofit in Abington, Massachusetts, that represents young scientists. The grants do nothing to address what McDowell says is the deeper problem: an oversupply of young scientists with little hope of winning tenure track jobs, who often serve as cheap labor in labs. "What I really would have liked Collins to do is pivot away from this constant expansion and address how to make things sustainable" by limiting the number of trainees NIH supports, McDowell says. "There is no long-term view."

THE #METOOSTEM movement criticized Collins last year for failing to beef up NIH's policies after news reports of several alleged incidents of sexual harassment by NIH-funded investigators. After months of criticism, Collins announced tougher measures in June, saying he hopes to follow a working group's recommendation that institutions and grant applicants be required to report sexual harassment findings to NIH. "I am regretful that we did not take firmer action sooner," he says, for which he partly blames legal advice that such cases be left to investigators' institutions. "I think people who look at it now ought to be feeling somewhat reassured that we get it," he says.

Collins recently won praise for vowing not to serve on all-male panels at scientific meetings. Diversity in science is "associated with greater productivity," he says. His dismissal of "manels," he says, is not "just a nice thing to do. … It's driven by a desire to see science flourish."

Collins's strategy for protecting NIH in the Trump era has been to keep a low profile—and it has largely succeeded, agency observers say. But Collins suffered a rare loss in June, when the Trump administration clamped down on research that uses fetal tissue donated after elective abortions. In December 2018, Collins had defended the research as ethical when done properly and called it a mainstay. Instead, the Department of Health and Human Services, NIH's parent agency, announced it was ending intramural studies using fetal tissue and would require lengthy special ethics reviews for new extramural grants and renewals.

Francis Collins (left) works with Idowu Aimola, a postdoctoral fellow from Nigeria participating in a new training program for African researchers.

Reports that the White House overruled him and Secretary of Health and Human Services Alex Azar are "basically accurate," Collins says. He adds that even applications for a new $20 million NIH program to find alternatives to fetal tissue in research, which "the pro-life community very much wanted us to do," will need to go through the ethics review because the studies will use fetal tissue as a comparator. Although he opposed the policy, he adds, "I understand the sincerity and the passion of those who felt that fetal tissue research crosses an ethical line."

Collins has also faced pressure from Congress and the Trump administration to crack down on foreign scientists believed to be stealing the fruits of federally funded research, with China portrayed as a major threat. After NIH called out more than 60 grantee institutions for possible violations of NIH rules, at least two universities dismissed faculty members, all of Asian descent, for allegedly failing to report foreign funding or sharing confidential grant proposals. "This has been a painful experience," he says. "Foreign nationals who are wonderful contributors to our medical workforce … are feeling as if they are being targeted or even profiled." But, he adds, "I don't think people are getting fired for trivial reasons."

Many researchers, however, fear that the campaign—perceived to target foreign-born scientists—will damage U.S. science in the long run. One former NIH official suggests that instead of pushing back against the White House, Collins "caved" to keep his job.

After 10 years, Collins has plenty on his to-do list. He wants to expand NIH's support of artificial intelligence and machine learning and is looking to hire a data czar, probably from Silicon Valley. He's also excited about gene therapy, which is finally reaching the clinic for some inherited childhood diseases. Collins has used NIH's Common Fund, a pot of money that Zerhouni created for initiatives that cut across institutes, to support industry and academic scientists who are devising better ways to get gene-editing tools such as CRISPR into patients' tissues.

Investigators may not be inclined to propose such applied research, but Collins says it's "something we should pull out all the stops to do." It's an example of why he still works 100-hour weeks. "You do have the ability to steer science in pretty powerful ways, by identifying things that just aren't going to happen without a push." ■

PHOTO: NATIONAL INSTITUTES OF HEALTH

Published by AAAS

ROBOTICS

Witnessing a wearables transition

Assistive robots must mimic human dynamics and move toward neural-interface control

By **José L. Pons**[1,2,3]

Wearable robots, such as exoskeletons and soft exosuits, can augment normal function or serve as prostheses for missing limbs. In both cases, they extend, complement, substitute, or enhance human functions and capability and can empower or replace human limbs. Cognitive and physical interactions between human and robot are key for these robots to seamlessly deliver assistance when required. The physical interaction between a robot and its wearer generates forces to overcome the wearer's physical limits, and cognitive interactions allow the wearer to guide and control the robot at all times. On page 668 of this issue, Kim *et al.* (*1*) report on a soft exosuit that switches assistance profiles for different physical interaction strategies—in this case, walking versus running—through a versatile cognitive interaction in which algorithms accurately determine and detect the wearer's gait.

Early wearable robots and exosuits were used to assist healthy wearers by reducing the metabolic cost of walking or running and, in the health care arena, to assist physical therapy for individuals with neurological disorders. In health care, they promote motor recovery or assist locomotion through assistive force to the patients, but how can assistive forces be efficiently delivered? Kim *et al.* showed that by assisting hip extension at key walking and running phases, metabolic cost is reduced (see the figure). The soft exosuit kept added mass as close to the wearer as possible, which reduced the number of joint movements restricted by the robot. Assisting hip extension can aid both walking and running, and a robust online classification algorithm helped the suit switch between walking and running assistive modes.

Previous studies have highlighted the impact of neuromechanics and dynamic properties of human limbs in achieving efficient locomotion and to adapt locomotion modes over a wide speed range (*2*). To a large extent, efficient locomotion in humans is based on exploiting our passive lower-extremity dynamics, but several problems with wearable robots and exosuits can compromise these dynamics. Anatomical and artificial joints can become misaligned, the robot or exosuit exerts forces that oppose rather than assist the movements intended by the wearer, or the inertial characteristics of body segments can be modified in unfamiliar ways by the added mass (for example, the movements can feel sluggish or top-heavy).

In spite of these altered neuromechanics, the effect of wearing a wearable robot on human motor coordination is small (*3*), which supports the use of these technologies to assist human movement. Moreno *et al.* (*3*) observed that the dimensionality of motor control when using a wearable robot—how many independent components in the muscle space of wearers are required to explain how muscles are activated—did not change for different walking speeds or amount of assistive force. They also showed that the timing impulsive motor structure—that is, the gait cycle phase and timing at which muscle groups are recruited during locomotion—was maintained along a broad range of walking conditions (flat surfaces as well as uneven terrain). These findings support the value of robotic-based strategies, both with rigid wearable robots and with

[1]*Legs + Walking AbilityLab, Shirley Ryan AbilityLab, Chicago, IL, USA.* [2]*Department of Physical Medicine and Rehabilitation, Department of Biomedical Engineering, and Department of Mechanical Engineering, Northwestern University, Chicago, IL, USA.* [3]*Neural Rehabilitation Group, Cajal Institute, Spanish National Research Council, Madrid, Spain. Email: jpons@sralab.org*

ILLUSTRATION: V. ALTOUNIAN/*SCIENCE*; (MOTION CAPTURE DATA) HARVARD BIODESIGN LAB

Published by AAAS

Toward more responsive robots

The soft exosuit reported by Kim *et al.* represents a transition from more restrictive hard exosuits to future wearables that will respond to nervous system commands.

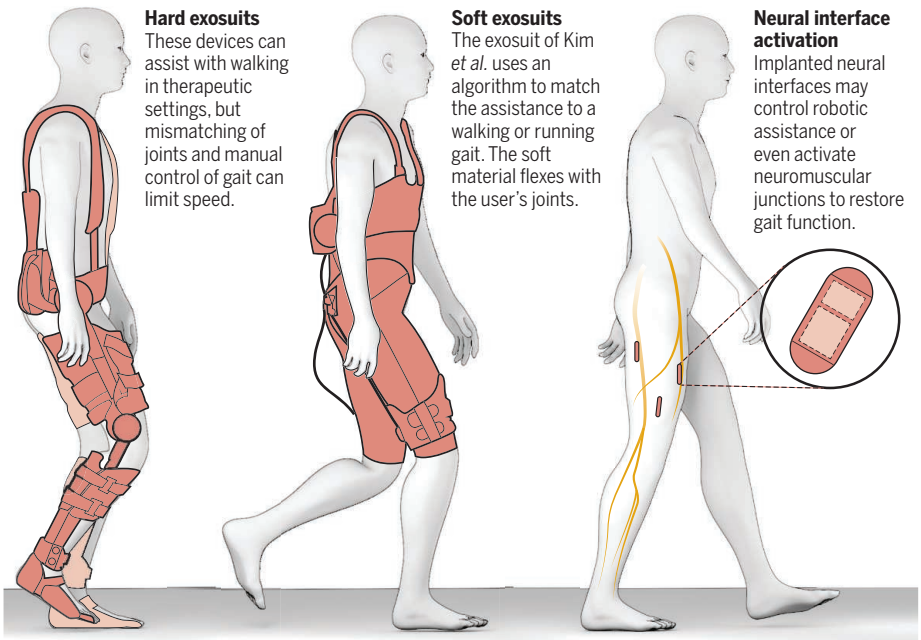

GRAPHIC: ADAPTED BY V. ALTOUNIAN/*SCIENCE* FROM A. PONS-GRAU

exosuits, aimed at assisting locomotion in healthy wearers and at healing or assisting neurological patients.

How can assistance be seamlessly delivered with wearable robots and exosuits according to the wearer-intended behavior? The work by Kim *et al.* shows an elegant and robust gait classification algorithm based on transitions between potential and kinetic energy that can detect whether the wearer is walking or running. However, the detection of actual user movement or movement intent can be much more challenging. When proportional control of wearable robots with multiple degrees of freedom is attempted—for example, in hand prosthetics—a more elaborated strategy to seamlessly command the robots is needed.

Under these circumstances, robot commands are usually obtained from decoding neural and bioelectrical signals by using classification algorithms. A variety of input signals have been considered, including both invasive and noninvasive neural interfaces, and recorded from either the central nervous system (CNS, the brain and spinal cord) or the peripheral nervous system (PNS, the muscle or peripheral nerve electrical activity) (*4*). Ideally, a neural interface would require simple connections to human neural structures, versatile operation with no calibration, high spatiotemporal resolution, sampling of a population of neural cells to associate their activity to relevant motor functions, and long-term stability.

None of the currently available recording and signal processing strategies fully meet these requirements, and new interface technologies will need to be developed. Given the relatively lower complexity of the PNS compared with the CNS, and recent developments in decoding the neural drive to muscles (*5*, *6*), it is realistic to think that we will witness, in the next several years, the development of robust human-robot interfaces to command wearable robotics based on the decoding of a representative part of the neural code of movement in humans. The need for wearable technologies that minimally alter human biomechanics will result in a transition from rigid wearable robots to soft exosuits such as the one reported by Kim *et al.*, and, eventually, to implantable neuroprostheses that can influence or assist human movement. The need for preserving human neuromechanics while using assistive technology will likely lead to implantable and networked recording and stimulation neuroprostheses. Such devices would implement effective interfaces to decode the wearer's movement intent and influence it when necessary to enhance human performance (*7*). ■

REFERENCES AND NOTES

1. J. Kim *et al.*, *Science* **365**, 668 (2019).
2. J. L. Pons, Ed., *Wearable Robots: Biomechatronic Exoskeletons* (Wiley, 2008).
3. J. C. Moreno *et al.*, *J. Neuroeng. Rehabil.* **10**, 79 (2013).
4. J. R. Wolpaw *et al.*, *Clin. Neurophysiol.* **113**, 767 (2002).
5. F. Negro, S. Muceli, A. M. Castronovo, A. Holobar, D. Farina, *J. Neural Eng.* **13**, 026027 (2016).
6. A. Holobar *et al.*, *J. Neural Eng.* **11**, 016008 (2014).
7. Bidirectional Hyper-Connected Neural System, the EXTEND project; https://extend-project.eu.

10.1126/science.aaw9407

ECOLOGY

Changing nutrients, changing rivers

Phosphorus removal from freshwater systems has wide-ranging ecological consequences

By **Carles Ibáñez**[1] *and* **Josep Peñuelas**[2,3]

Eutrophication—the excessive enrichment of a body of water with nutrients such as nitrogen (N) and phosphorus (P)—is Earth's most widespread problem for water quality (*1*, *2*). Growing evidence suggests a global trend toward reversing eutrophication. However, in rivers and estuaries of developed countries and in lakes of emerging economies, the ongoing reduction in nutrient inputs—termed reoligotrophication—is much larger for P than for N (*3*, *4*). Although the rapid emergence of this phenomenon has hindered detailed monitoring of the ecological effects, a few studies have documented an abrupt shift from green to clear waters and consequently from phytoplankton to macrophytes as dominant primary producers in response to reoligotrophication in rivers and estuaries (*5*–*7*). However, the improvement in water quality due to P decline does not imply a return to pristine ecological conditions, because high N:P ratios trigger undesirable changes in the ecosystem (*8*).

Understanding of the effects of eutrophication and reoligotrophication mainly comes from studies of shallow lakes, which can be in two alternative states: turbid, dominated by phytoplankton, and characterized by low diversity and poor water quality; or clear, dominated by macrophytes, and characterized by higher diversity. Anthropogenic eutrophication or reoligotrophication causes abrupt shifts between these states (*9*). Many American and European lakes have recovered from eutrophication following the control of phosphorus inputs, providing a

[1]*IRTA, Department of Marine and Continental Waters, 43540 Sant Carles de la Ràpita, Catalonia, Spain.* [2]*CSIC, Global Ecology Unit CREAF-CSIC-UAB, 08193 Bellaterra, Catalonia, Spain.* [3]*CREAF, 08193 Cerdanyola del Vallès, Catalonia, Spain. Email: carles.ibanez@irta.cat; josep.penuelas@uab.cat*

Published by AAAS

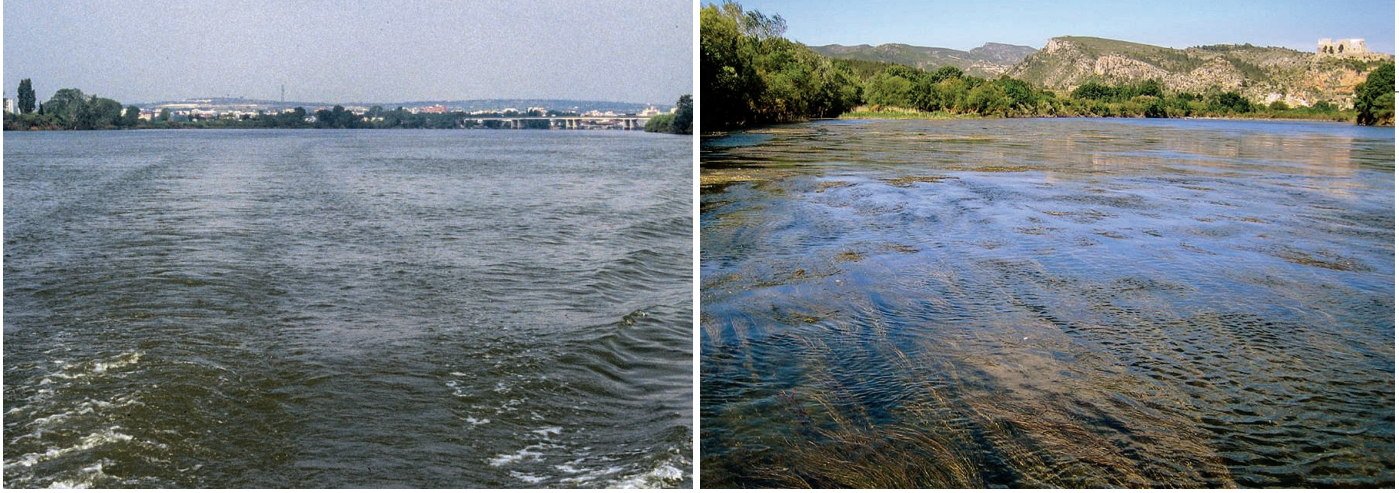

In 1992, the lower Ebre River (Catalonia, Spain) was in the eutrophic state, dominated by phytoplankton (left). In 2000, the river became transparent and has remained in this state of reoligotrophication, triggering the rapid proliferation of macrophytes, as seen in the photo to the right, taken in 2009.

paradigm of successful environmental management (*1*, *10*). This trend is also beginning to emerge in lakes throughout the world—for example, in urban regions in China—linked mostly to rapid advances in the treatment of municipal wastewater (*11*).

Eutrophication changes in rivers and estuaries around the world are less well understood than those in lakes, but research is beginning to address this (*12*). During the second half of the 20th century, nutrient loads in rivers and estuaries rose in Europe and the United States, mostly due to fertilizers, manure, industrial pollution, and release of urban wastewater. In the past 20 to 30 years, P (and in some cases N) inputs have decreased in some eutrophicated rivers because of improved water treatment and crop management (*3*, *4*).

One reason why the effects of eutrophication and reoligotrophication in rivers are not fully understood is that most studies have focused on streams, where phytoplankton cannot be a relevant component owing to a shallow water column and high water turnover. Several studies have, nevertheless, helped to clarify the impacts of reoligotrophication in rivers. These studies have reported declines in chlorophyll concentrations or phytoplankton populations in rivers caused by P removal following the introduction of wastewater-treatment plants and P-free detergents (table S1). The larger the river, the closer the relationship between P and phytoplankton becomes to that of lakes. Fewer data are available for reoligotrophication of coastal areas, but data are available for Danish estuaries (*5*) and a few other locations (table S2). Two river studies have shown that the decrease in fluvial P concentrations triggered an abrupt ecosystem shift, with the collapse of phytoplankton populations and the subsequent increase in water transparency allowing the spread of macrophytes (*6*, *7*).

These results suggest that the shallow-lake model of alternative equilibria can be adapted to lowland and dammed rivers, where the model predicts that reoligotrophication should lead to abrupt changes between states of turbid and clear water (*6*). The results in (*6*, *7*) thus support the view that lake and river ecosystems respond similarly to P enrichment. However, the abundance of phytoplankton per unit of total P is lower in rivers than in lakes because of the higher water turnover rates in rivers. Besides phytoplankton decline, factors such as river depth, pulsing flow, load of suspended sediments, and substrate type may determine the spread of submerged macrophytes in rivers. It is possible that macrophytes are spreading in many rivers without being monitored. Long-term monitoring of phytoplankton and macrophytes in rivers is thus strongly warranted.

Long-term river data series often include dissolved nutrients, less frequently particulate nutrients, and rarely chlorophyll, phytoplankton, or macrophytes, making it difficult to assess the extent of ongoing reoligotrophication. This problem could be addressed with remote-sensing data from satellites. Moreover, not only the effects of P decline but also of the changes in stoichiometric imbalances between N and P must be considered to better understand the ecological effects. In this respect, past research on lakes can be valuable, but research on cascading effects on rivers and estuaries is also warranted. This is now under way in a few rivers, such as the lower Ebre River in Spain (see the photo). For instance, the decline in phytoplankton and the spread of macrophytes have triggered massive black fly blooms, the decline of massive mayfly blooms in the river, and the recovery of biological communities in the estuary (*7*, *13*).

The responses of small, medium, and large rivers to reoligotrophication are likely to differ, as will the responses of rivers with distinct river basin substrates, such as limestone or granite. The applicability of possible measures for managing river restoration, land use, and water flow to avoid negative impacts of stoichiometric imbalances between N and P must be assessed through monitoring, controlled experiments, and models. For example, improved monitoring and modeling of reservoirs can help to better understand their role in N and P retention and release (*14*).

The ecological effects of P decline and N/P imbalances on the structure and function of natural and managed ecosystem are pervasive around the globe (*8*), but the consequences for aquatic systems are not well understood (*15*). Moreover, the interactions with other global changes such as global warming, hydrological alteration, and invasive species are complex. However, the recent results on reoligotrophication of rivers and estuaries in developed countries and the resulting cascading effects on the physicochemistry of water and the trophic web show that the implications of reoligotrophication and increasing N:P ratios for ecosystem structure and function, and therefore for environmental management, are profound. Reoligotrophication is good news in terms of water quality, but the effects on structure and composition of biological communities are complex and present a fundamental environmental management challenge. ■

REFERENCES AND NOTES

1. D. W. Schindler, *Proc. Biol. Sci.* **279**, 4322 (2012).
2. C. J. Stevens, *Science* **363**, 578 (2019).
3. S. Cozzi, C. Ibáñez, L. Lazar, P. Raimbault, M. Giani, *Water* **11**, 1 (2019).
4. R. M. Kreiling, J. N. Houser, *Environ. Monit. Assess.* **188**, 454 (2016).
5. B. Riemann *et al.*, *Estuaries Coasts* **39**, 82 (2016).
6. S. Hilt, J. Köhler, H. P. Kozerski, E. H. van Nes, M. Scheffer, *Oikos* **120**, 766 (2011).
7. C. Ibáñez *et al.*, *Sci. Total Environ.* **416**, 314 (2012).
8. J. Peñuelas *et al.*, *Nat. Commun.* **4**, 2934 (2013).
9. M. Scheffer, E. Jeppesen, *Ecosystems (N. Y.)* **10**, 1 (2007).
10. K. Sand-Jensen, H. H. Bruun, L. Baastrup-Spohr, *J. Ecol.* **105**, 690 (2017).
11. Y. Tong *et al.*, *Nat. Geosci.* **10**, 507 (2017).
12. M. T. O'Hare *et al.*, *Front. Plant Sci.* **9**, 451 (2018).
13. A. Nebra *et al.*, *Sci. Mar.* **75**, 577 (2011).
14. T. Maavara et al., *Proc. Natl. Acad. Sci. U.S.A.* **112**, 15603 (2015).
15. Z. Yan *et al.*, *Ecol. Lett.* **19**, 1237 (2016).

SUPPLEMENTARY MATERIALS

science.sciencemag.org/content/365/6454/637/suppl/DC1

10.1126/science.aay2723

PHOTOS: (LEFT TO RIGHT) C. IBAÑEZ; IRTA

Published by AAAS

EARLY UNIVERSE

First molecule still animates astronomers

A study of the helium hydride ion stirs up primordial astrochemistry

By **Stefano Bovino**[1] *and* **Daniele Galli**[2]

The reason why astronomers find the helium hydride ion (HeH^+) so intriguing is simple: This light, highly reactive molecule with strong acid character binds together hydrogen and helium, the first and most abundant elements in the Universe. The first clear detection of HeH^+ in a nebula, earlier this year, has only intensified interest in the primordial molecule. On page 676 of this issue, Novotný *et al.* (*1*) studied HeH^+ under conditions designed to mimic those of the early Universe. Their work offers insight into the chemical composition of the Universe before formation of the first stars.

Discovered in the laboratory as early as 1925 (*2*), HeH^+ has long been suspected to be present in the interstellar medium. Astronomers engaged in a decades-long search for HeH^+ in interstellar regions that house hot gas, an environment wherein the simultaneous presence of ionized hydrogen and neutral helium favors HeH^+ formation. Unsuccessful attempts have been made in planetary nebulae (bubbles of hot gas surrounding a dying star) (*3*, *4*), supernova ejecta (material expanding from star explosion) (*5*), and quasars (supermassive galactic objects thought to contain a black hole) (*6*).

This search finally came to an end in April 2019, when HeH^+ was unambiguously detected in the hot gas of the planetary nebula NGC 7027 (*7*). In a complementary laboratory experiment, Novotný *et al.* collided a beam of HeH^+ with a beam of electrons at a very low temperature to elucidate the characteristics of HeH^+ during the epoch that preceded formation of the first stars and galaxies (i.e., the cosmological "dark ages," ~400,000 years after the Big Bang) (see the figure). The low experimental temperature was used to mimic conditions of the early Universe.

But when and how did the first molecules appear in the hot, harsh environment of the expanding early Universe? Three minutes after the Big Bang, the Universe consisted of a mixture of hydrogen, helium, and trace amounts of deuterium and lithium ions. These positively charged nuclei progressively combined with electrons to form neutral atoms: first helium and then hydrogen and the other elements. Because of the expansion of the Universe, only 99.99% of the hydrogen ions present after the Big Bang could complete this process. The tiny but crucial leftover free protons (H^+) and electrons (e^-) acted as catalysts for the first gas-phase chemical reactions among the dominant neutral species (*8*). This marks the dawn of chemistry, during which the first-ever molecular bond was formed to create HeH^+.

Compared with the thousands of reactions and the hundreds of species needed to model the chemistry of the present-day interstellar medium, an understanding of the chemistry of the early Universe should be easily won. Because of the simplicity of the reactants and the lack of complex phenomena, such as magnetic fields, turbulence, and stellar radiation, the field of primordial chemistry has received special attention and become the test bed for astrochemical kinetic models that describe the evolution of chemical species under interstellar medium conditions. The chemistry of helium has been the focus of several recent investigations (*9*, *10*).

Early Universe, first molecules

Hydrogen recombination began after the generation of cosmic microwave background radiation.

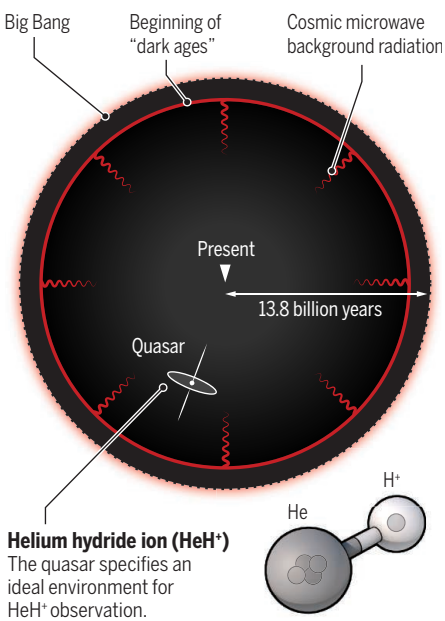

Helium hydride ion (HeH^+)
The quasar specifies an ideal environment for HeH^+ observation.

Despite these developments, the necessary support from experimental data for the majority of chemical reactions remains sparse. Important progress was achieved in two recent laboratory experiments that solved a long-standing controversy on the destruction of H_3^+ by collisions with electrons (*11*, *12*), a crucial reaction for the chemistry of interstellar clouds. The experiment by Novotný *et al.* fits perfectly within these efforts to provide reliable data for deciphering the chemistry of the Universe. The authors made use of the newly completed electrostatic cryogenic ion storage ring CSR at the Max Planck Institute for Nuclear Physics, which has made it possible to measure the efficiency of the destruction of cold HeH^+ by collisions with electrons. Novotný *et al.* measured a substantial reduction, relative to previous findings (*13*), in the velocity at which this reaction occurs at low temperatures. This implies a higher abundance of HeH^+ in the early Universe than previously estimated (*10*) and thus a stronger interaction with the cosmic microwave background radiation. Further observational developments might facilitate detection of HeH^+ in the first galaxies, an important step in reconstructing the chemical history of the Universe.

Other molecules relevant to astrochemistry can now be studied with the new CSR. These experiments, coupled with newly devised theoretical calculations and other laboratory studies being done worldwide, signal a bright future for astrochemistry, which is essential for unraveling complex processes such as star and planet formation and the origins of life. ■

[1]*Departamento de Astronomía, Facultad Ciencias Física y Matemaícas, Universidad de Concepción, Concepción, Chile.*
[2]*INAF-Osservatorio Astrofisico di Arcetri, Firenze, Italy.*
Email: stefanobovino@astro-udec.cl; galli@arcetri.astro.it

REFERENCES AND NOTES

1. O. Novotný *et al.*, *Science* **365**, 676 (2019).
2. T. R. Hogness, E. G. Lunn, *Phys. Rev.* **26**, 44 (1925).
3. C. Cecchi-Pestellini, A. Dalgarno, *Astrophys. J.* **413**, 611 (1993).
4. X. W. Liu *et al.*, *Mon. Not. R. Astron. Soc.* **290**, L71 (1997).
5. S. Miller *et al.*, *Nature* **355**, 420 (1992).
6. I. Zinchenko, V. Dubrovich, C. Henkel, *Mon. Not. R. Astron. Soc.* **415**, L78 (2011).
7. R. Güsten *et al.*, *Nature* **568**, 357 (2019).
8. D. Galli, F. Palla, *Annu. Rev. Astron. Astrophys.* **51**, 163 (2013).
9. D. R. G. Schleicher *et al.*, *Astron. Astrophys.* **490**, 521 (2008).
10. S. Bovino *et al.*, *Astron. Astrophys.* **529**, A140 (2011).
11. B. J. McCall *et al.*, *Phys. Rev. A* **70**, 052716 (2004).
12. H. Kreckel *et al.*, *Phys. Rev. Lett.* **95**, 263201 (2005).
13. C. Strömholm *et al.*, *Phys. Rev. A* **54**, 3086 (1996).

ACKNOWLEDGMENTS

We thank D. Schleicher, N. Leigh, and our late colleague F. Palla for stimulating discussions about early-Universe astrochemistry.

10.1126/science.aay5825

GRAPHIC: C. BICKEL/*SCIENCE*

Published by AAAS

CROPS

Using wild relatives to improve maize

Altering maize leaf angle increases yield under high-density planting

By **Sarah Hake** *and* **Annis Richardson**

Human-mediated selection allows for the rapid evolution of crops with desired characteristics during domestication. These traits make the crops easier for humans to grow, gather, and eat (*1*). The iterative selection process during domestication restricts the diversity available in modern crop varieties for future generations of selection. Wild relatives of modern crops can therefore be a rich resource to mine for useful variants lost during domestication. Maize (*Zea mays* spp. *mays*) is one of the world's staple food and energy crops. The ancestor of maize, teosinte (*Zea mays* spp. *parviglumis*) (*2*, *3*), grows in the wild in Mexico and can be crossed with maize. On page 658 of this issue, Tian *et al.* (*4*) elegantly use the genetic diversity in teosinte to discover a useful genetic sequence that can directly increase maize yields in field conditions. This suggests that redomestication of crops may identify other useful traits hidden in crop ancestors.

Maize yields have increased throughout the past half century, in part because plants have been grown at increasing densities (*5*). This increase in yield also comes from changes in plant architecture. Increasing the density of maize has required more upright leaves to enhance their overall photosynthetic capacity and hence their ability to grow optimally (*6*, *7*). The angle of a leaf is determined by a boundary region that separates the blade from the sheath (see the figure). The blade leans away from the plant to intercept light, and the sheath wraps around the shoot to protect younger leaves and provide stiffness to the stem. The boundary region contains a ligule, an epidermal fringe that wraps tightly against the inner leaves, and the auricles on either side of the midrib, which allow the blade to lean away from the stem.

To continue to boost yield through maximizing field planting density, the maize leaf angle needs to be reduced further. Previous work in maize genetics has identified several genes that influence leaf angle. Mutations in these genes can affect leaf angle in three ways. Removing the ligule and auricles, such as in the *liguleless1* (*lg1*), *lg2*, and *liguleless narrow* mutants, results in a very upright leaf angle (*8*). Similarly, modulation of the size of the auricle, as observed when brassinosteroid (BR) hormone signaling is altered, can affect leaf angle. The application of BR to seedlings leads to larger auricles and a wide leaf angle, whereas loss of BR (or of BR signaling) leads to small leaf angles (*9*, *10*). The thickness of the leaf at the midvein (the midrib) can also affect leaf angle. For example, *drooping leaf* (*drl*) mutants lack a midrib, resulting in floppy leaves with wide leaf angles (*11*). However, in all cases, these mutants have additional effects that have a negative impact on floral patterning or overall plant stature. Therefore, despite the positive effects on leaf angle, the additional pleiotropic effects of these mutants mean that incorporating any of them into a breeding program would not be beneficial for overall crop yield. To further modulate leaf angle in crops, alternative sources of leaf angle regulation are required.

Greater genetic variation exists in teosinte because of the genetic bottlenecks that arise from domestication as certain alleles are selected and many are discarded (*12*). Tian *et al.* created recombinant inbred lines between maize and teosinte. They measured leaf angle in these lines and found two loci, *Upright Plant Architecture1* (*UPA1*) and *UPA2*, that quantitatively affect leaf angle. They identified *UPA2* as an upstream regulatory sequence. Two nucleotides are present at this location in the teosinte parent that are missing in the maize parent. Indeed, they found that no maize lines carry these two nucleotides and that only a few teosinte lines do. A more upright leaf angle is achieved when the teosinte version of *UPA2* is added to the maize version. In contrast to the *liguleless* or BR biosynthetic mutants, maize plants carrying the teosinte *UPA2* allele have normal plant height and floral branch number with only a quantitative reduction in auricle size.

Evolutionary change often acts at cis-regulatory sequences, thereby modulating gene expression levels or affecting the timing or location of gene action (*13*). The two-nucleotide difference is within a distant cis-regulatory element nine kilobases upstream of a gene that encodes the maize ortholog of RAV-LIKE 1 (RAVL1) (*14*). RAVL1 is

Regulation of maize leaf angle

Tian *et al.* found a leaf regulatory network by comparing maize crop and parental teosinte genomes. The cis-regulatory element *UPA2* is bound by DRL, which directly inhibits LG1. LG1 binds to the promoter of *RAVL1* and induces its expression. RAVL1 binds to the promoter of *UPA1*, which encodes an enzyme that regulates the last step in BR synthesis. BR promotes auricle expansion, which regulates leaf angle.

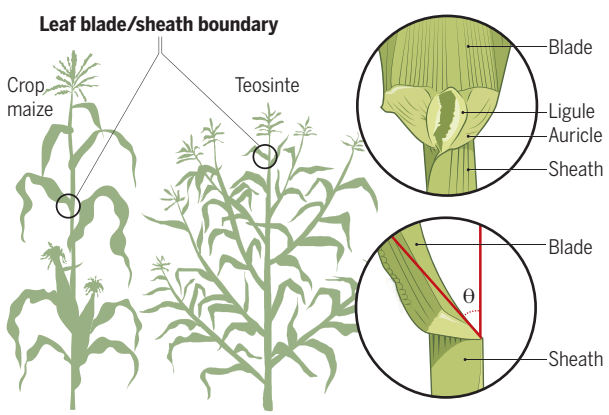

The maize *UPA2* (*mUPA2*) sequence is weakly bound by DRL; adding teosinte *UPA2* (*tUPA2*) in maize increases DRL binding, resulting in less *RAVL1* expression and more upright leaves.

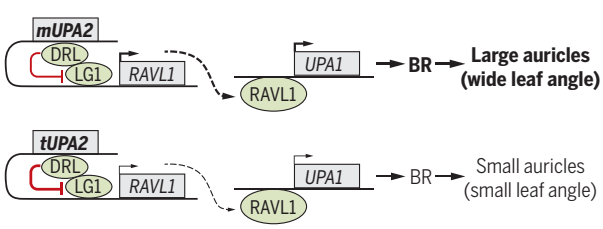

BR, brassinosteroid; DRL, DROOPING LEAF; LG1, LIGULELESS1; *RAVL1*, *RAV-LIKE 1*; *UPA2*, *Upright Plant Architecture2*.

GRAPHIC: N. CARY/*SCIENCE*

Plant Gene Expression Center, USDA-ARS and Department of Plant and Microbial Biology, University of California, Berkeley, CA 94710, USA. Email: hake@berkeley.edu

Published by AAAS

expressed at lower levels in teosinte than in maize. Tian *et al.* reasoned that differential regulation operating at this cis-regulatory element caused the difference in expression, and perhaps the difference in leaf angle. Indeed, when RAVL1 expression was knocked down, maize leaves were more upright. The region containing this key cis element carries a C2C2 transcription factor binding motif, which is also bound by DRL. The promoter also carries a LG1 binding site. Tian *et al.* found that DRL interacts with LG1 and dampens its positive effect on RAVL1 expression, thereby fine-tuning leaf angle. Downstream of *RAVL1* is *UPA1*, which encodes the final enzyme in BR biosynthesis (*15*). Maize lines that carry teosinte *UPA1* have larger leaf angles. Thus, by identifying two loci from teosinte, the authors were able to elucidate part of the leaf angle regulatory network, ultimately linking elements long proposed to be involved in leaf angle but with no previously known direct connections to each other.

Tian *et al.* found that the maize line in which *RAVL1* is mutated and the near-isogenic maize line carrying the teosinte *UPA2* allele have higher yields than control maize lines under high-density field conditions. They also transferred the sequences into elite crop lines, showing an increase in yield at the highest planting densities. This work highlights the power of small cis-regulatory variations, lost during domestication, to make large differences in crop yields under modern planting conditions. Overall, the hidden genetic variation in wild ancestors is revealed by generating recombinant lines and recaptured through near-isogenic lines. ■

REFERENCES AND NOTES

1. J. F. Doebley, B. S. Gaut, B. D. Smith, *Cell* **127**, 1309 (2006).
2. Y. Matsuoka *et al.*, *Proc. Natl. Acad. Sci. U.S.A.* **99**, 6080 (2002).
3. D. R. Piperno, A. J. Ranere, I. Holst, J. Iriarte, R. Dickau, *Proc. Natl. Acad. Sci. U.S.A.* **106**, 5019 (2009).
4. J. Tian *et al.*, *Science* **365**, 658 (2019).
5. D. N. Duvick, *Maydica* **50**, 193 (2005).
6. J. W. Pendleton, G. E. Smith, S. R. Winter, T. J. Johnston, *Agron. J.* **60**, 422 (1968).
7. R. J. Lambert, R. R. Johnson, *Crop Sci.* **18**, 499 (1978).
8. A. Richardson, S. Hake, *Plants* **8**, 4 (2019).
9. H. Tong *et al.*, *Plant Cell* **24**, 2562 (2012).
10. Z. Hong, M. Ueguchi-Tanaka, M. Matsuoka, *J. Pestic. Sci.* **29**, 184 (2004).
11. J. Strable *et al.*, *Plant Cell* **29**, 1622 (2017).
12. M. B. Hufford *et al.*, *Nat. Genet.* **44**, 808 (2012).
13. A. Studer, Q. Zhao, J. Ross-Ibarra, J. Doebley, *Nat. Genet.* **43**, 1160 (2011).
14. B. I. Je *et al.*, *Plant Cell* **22**, 1777 (2010).
15. I. Makarevitch, A. Thompson, G. J. Muehlbauer, N. M. Springer, *PLOS ONE* **7**, e30798 (2012).

ACKNOWLEDGMENTS

A.R. is supported by NSF grant ECA-PGR: 1733606. S.H. is supported by the Agricultural Research Service.

10.1126/science.aay5299

GRAPHIC: N. DESAI/*SCIENCE*

NEUROSCIENCE

Glia in the skin activate pain responses

A newly discovered cell type forms a network that senses painful stimuli

By **Ryan A. Doan** *and* **Kelly R. Monk**

The ability to rapidly perceive and react to damaging stimuli is essential for survival. In the vertebrate nervous system, specialized neural crest–derived sensory neurons in the skin, called nociceptors, detect and send signals to the brain after potentially harmful encounters. The cell bodies and axons of these nociceptors are associated with glia, non-neuronal cells that perform myriad functions in the nervous system. However, it has been a long-standing belief that nociceptors lose glial ensheathment when they cross the basement membrane into the epidermis, leaving only the free endings of unmyelinated axons as nociceptive sensors (*1*). On page 695 of this issue, Abdo *et al.* (*2*) provide evidence of a previously unrecognized specialized glial cell type, called nociceptive Schwann cells, that in direct association with nociceptive fibers project into the epidermis, where they initiate the sensation of pain. This discovery may offer new insights into future treatments for chronic pain.

Vollum Institute, Oregon Health & Science University, Portland, OR 97221, USA. Email: monk@ohsu.edu

Cutaneous sensory neurons are classified into myelinated A fibers with large-diameter axons and unmyelinated C fibers with small-diameter axons. A fibers are wrapped with myelin by specialized Schwann cells to promote fast nerve impulse propagation, whereas C fibers are organized into "Remak bundles" by nonmyelinating Remak Schwann cells (*3*). C fibers are more abundant than A fibers in the skin (*4*) and can respond to many forms of noxious stimuli, including mechanical, heat, and chemical. The lack of myelination may afford greater plasticity in C fibers as compared with A fibers, which is especially important in the skin, where physical insults and injuries are common (*5*). Both A and C fibers have long been thought to terminate as free endings in the skin, and non-neuronal cells in the epidermis, such as skin cells called keratinocytes, can modulate nociception (*6*, *7*). Abdo *et al.* set out to understand the relationship between non-neuronal cutaneous Schwann cells and nociceptive nerve terminals in the epidermis and found that nociceptive fibers form an intricate, mesh-like network with nociceptive Schwann cells. Notably, this network extends from the dermis into the epidermal layers of the skin (see the figure).

Detecting painful mechanical stimuli

Abdo *et al.* discovered a specialized glial cell that is directly associated with nociceptive nerve fibers that project into the epidermis. These nociceptive Schwann cells form a meshwork in the skin that activates pain responses to mechanical stimuli.

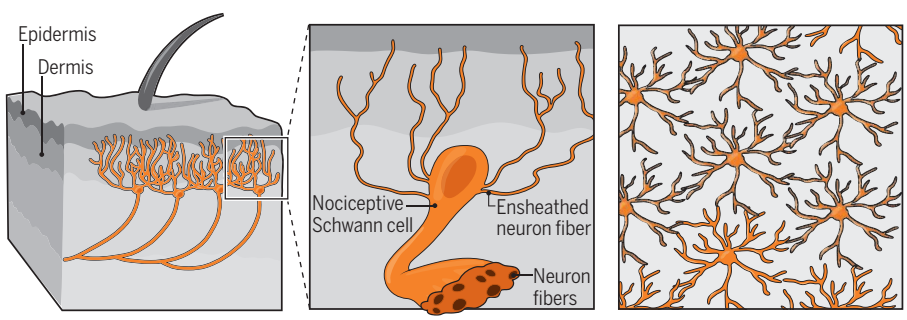

Published by AAAS

Nociceptive neurons typically lie in an electrically inactive state under resting conditions (*8*). Upon activation by noxious stimuli, nociceptive signals are transduced and sent to the brain through neurons in the form of an electrical impulse (*1*). To investigate a potential role for the newly described nociceptive Schwann cells in the detection of pain-inducing stimuli, the authors used a technique called optogenetics to modulate the activity of these cells with light. Taking advantage of the superficial location of the nociceptive Schwann cell–nociceptor network on the foot pads of mice, Abdo *et al.* found that light stimulation of nociceptive Schwann cells produced a light intensity–dependent limb withdrawal coupled with an increase in nociceptor firing rates.

Although limb withdrawal under conditions of nociceptive Schwann cell–specific stimulation supports the idea that these cells are sensing pain, the behavioral response could also be in reaction to a touch or pressure sensation. Certain behaviors, such as licking or shaking coupled with paw withdrawal or guarding upon or shortly after stimulation, are considered pain-specific responses (*9*). Stimulation of the nociceptive Schwann cells in mice using optogenetics led to significant increases in all of these pain behaviors.

Pain can be caused by a variety of insults, ranging from pressure and touch to extreme heat or cold. To elucidate specific stimuli to which nociceptive Schwann cells are sensitive, subthreshold light stimulation was used to sensitize physiological stimuli: cold, heat, and mechanical stimuli. This resulted in responsiveness to all three stimuli. Moreover, although inhibition of nociceptive Schwann cell signaling did not reduce cold or heat sensitivity, mechanical thresholds were significantly increased when mouse foot pads were poked with filaments. Complementary electrophysiological investigations indicated that cultured nociceptive Schwann cells responded to changes in force very quickly and adapted to sustained force over time. These results indicate that nociceptive Schwann cells physiologically contribute to the sensation of mechanical pain.

Nociception plays a crucial role in how animals interact with the environment, providing an enhanced awareness of surroundings as well as ensuring safety and well-being. When this essential system does not function as expected, however, unpleasant and debilitating side effects such as pain can occur. Chronic pain has become a focus of attention as opioid addiction continues to debilitate lives and cause mortality. From diseases such as osteoarthritis to diabetes, the development of chronic pain resulting from injury to the nociceptive network is a challenge for which therapeutics remain problematic. The long-standing belief has been that nociception is an axonally driven process, with perception occurring in the most distal nerve endings, which were previously thought to be free of any glial ensheathment. The discovery by Abdo *et al.* of nociceptive Schwann cells that cross the basement membrane into the epidermis, where they form a mesh-like nociceptive network with the axonal field, changes this view and provides a new potential target cell for pain medication.

The nociceptive Schwann cells function in conjunction with sensory nerve fibers to transduce and signal tactile sensations. Further studies to tease apart how these nociceptive Schwann cells signal to sensory nerves will improve understanding of these glial cells and their role in nociception. Previous RNA-sequencing studies suggest that Schwann cells along peripheral nerves express mechanosensitive Piezo ion channels (*10*); understanding how mechanical stimuli influence Schwann cell biology is an area of growing interest (*11*). In the future, it will be interesting to determine whether and how Piezo channels function in nociceptive Schwann cells to initiate pain sensation. Given that nonglial skin cells can clear debris after axon damage (*12*), it will be important to investigate how these nociceptive Schwann cells respond to axon injury and function in disease states. Further investigation of this new sensory network cell discovered by Abdo *et al.* will provide a clearer understanding of how the body perceives pain and may lay the foundation for more targeted and effective therapeutics. ■

REFERENCES AND NOTES

1. A. E. Dubin, A. Patapoutian, *J. Clin. Invest.* **120**, 3760 (2010).
2. H. Abdo *et al.*, *Science* **365**, 695 (2019).
3. B. L. Harty, K. R. Monk, *Curr. Opin. Neurobiol.* **47**, 131 (2017).
4. G. R. Lewin, R. Moshourab, *J. Neurobiol.* **61**, 30 (2004).
5. J. W. Griffin, W. J. Thompson, *Glia* **56**, 1518 (2008).
6. Z. Pang *et al.*, *Pain* **156**, 656 (2015).
7. K. M. Baumbauer *et al.*, *eLife* **4**, e09674 (2015).
8. D. M. Cain, S. G. Khasabov, D. A. Simone, *J. Neurophysiol.* **85**, 1561 (2001).
9. J. R. Deuis, L. S. Dvorakova, I. Vetter, *Front. Mol. Neurosci.* **10**, 284 (2017).
10. S. D. Ackerman, C. Garcia, X. Piao, D. H. Gutmann, K. R. Monk, *Nat. Commun.* **6**, 6122 (2015).
11. S. Belin, K. L. Zuloaga, Y. Poitelon, *Front. Cell. Neurosci.* **11**, 347 (2017).
12. J. P. Rasmussen, G. S. Sack, S. M. Martin, A. Sagasti, *J. Neurosci.* **35**, 559 (2015).

ACKNOWLEDGMENTS

We thank K. Wright for helpful discussions. R.A.D. acknowledges funding from National Institute of Neurological Disorders and Stroke training grant T32NS007446.

10.1126/science.aay6144

CELL BIOLOGY

Marching out of the crypt

Intestinal epithelial cells actively migrate up the villus, challenging a long-held view

By **Marnix Jansen**

The surface of the intestines comprises epithelial cells arranged in villi, at the base of which are the crypts where intestinal stem cells that produce the epithelial cells are located. These crypts have become the cell biologist's favorite model system for understanding epithelial stem cell biology and lineage differentiation. In stark contrast, the biophysical underpinnings of crypt-villus biology have received considerably less attention. The simple model that has been accepted for many years is one of epithelial cells passively moving along a conveyor from the crypt to the top of the villus, pushed forward by stem cells continuously producing daughter cells at the base of the crypt. On page 705 of this issue, Krndija *et al.* (*1*) reveal that this model is incorrect and that instead, mouse intestinal epithelial cells actively crawl up the villus after they exit the crypt.

Studies using either induced labeling or naturally occurring markers of stem cell lineage in mice and humans, respectively, have shown that intestinal epithelial cells leave the crypt and move up the villus in an orderly manner (*2*, *3*). These migratory streams of cells can be observed as tightly arranged ribbons along the villus, indicating that epithelial cells move in cohorts and rarely break formation (*4*, *5*). Once epithelial cells reach the villus tip, they are actively extruded from the epithelial sheet, and the rate of elimination is dependent on the degree of crowding (*6*). This dynamic behavior is largely invisible without external manipulation and must be tightly regulated to facilitate nutrient absorption and avoid defects in the epithelial barrier.

Krndija *et al.* arrive at their conclusion through a set of fascinating experiments combined with mathematical modeling. They first injected mice with hydroxyurea, an

UCL Cancer Institute, University College London, UK.
Email: m.jansen@ucl.ac.uk

Published by AAAS

agent that blocks cell division when used in low doses. Intestinal stem cell proliferation and differentiation occur along well-defined axes and renewal is rapid, meaning that empirical data can be collected within relatively short time frames. If cellular migration along the villus occurs passively, driven by a pushing force resulting from mitosis in the crypts, then blocking cell division with hydroxyurea should reduce or eliminate cell movement. The authors found that cell movement along the villus is not affected by hydroxyurea treatment, which suggests that cell migration up the villus may instead be actively regulated.

The authors then built a mathematical model to independently assess the contributing forces of mitotic pushing and migratory pulling. The mathematical model predicted dynamic changes to cell density and migratory speed as pushing forces begin to decline moving away from the crypt and pulling forces increase toward the villus tip. Direct observation of cell density revealed a bimodal distribution along intestinal villi in mice, with cell packing first decreasing along the lower part of the villus and then increasing toward the villus tip. To assess differences in migration speed along the villus, Krndija *et al.* used mouse gut explants, tissue slices of small bowel mucosa that can be maintained ex vivo for several hours, to assess cell migration through live imaging in a controlled environment (see the image). By tracing individual cells marked by green fluorescent protein moving along the villus, Krndija *et al.* found that cells accelerate as they move toward the villus tip.

Further analyses using gut explants in which some cells expressed a reporter molecule attached to actin, a cytoskeletal protein that underpins cell shape and migration, revealed that villus epithelial cells demonstrate basal protrusions, much like little feet, that allow intestinal columnar epithelial cells to crawl up the villus. Chemically blocking these protrusions also disrupted cell migration and caused cell crowding toward the villus tip. This revelation also indicates that in addition to a cellular polarity axis from the apical part of the cell that is exposed to the intestinal lumen and the basal end that is attached to the basement membrane, intestinal epithelial cells also maintain a front-rear polarity axis from villus to crypt. Together, the experimental data confirm the theoretical predictions and show that cell movement up the villus is dominated by passive pushing forces in the crypt and lower villus and active pulling forces through migration along the remainder of the villus.

The data of Krndija *et al.* reveal an unexpected aspect of intestinal epithelial homeostasis that had been overlooked for many years. The long-held view of an epithelial sheet passively responding to forces emanating from the crypt seemed to fit with the coordinated behavior of intestinal epithelial cells traveling up the villus in tight ribbons. In an extension to their model, Krndija *et al.* reveal that coordinated epithelial cell movement up the villus is due to strong intercellular connections that ensure the epithelium experiences a strong tensile spring force. Therefore, active migratory pulling of individual cells and tight intercellular connections together ensure that the epithelium moves as a coordinated sheet.

The study of Krndija *et al.* suggests many avenues for further research to investigate how this active migratory mechanism might be linked to human disease. For example, the rare pediatric disorder congenital tufting enteropathy presents with early-onset severe and intractable diarrhea, which leads to irreversible intestinal failure. The disease is linked to germline mutations in the epithelial cell adhesion molecule (*EPCAM*) gene, and intestinal biopsies of affected patients demonstrate characteristic protruding tufts of epithelial cells, typically at the villus tip. These defects in villous maturation lead to malabsorption of nutrients, which provokes severe diarrhea. *EPCAM* mutations are paradoxically linked to increased cell migration (*7*), which, according to the biophysical model presented by Krndija *et al.*, would further increase crowding at the villus tip, possibly precipitating the characteristic epithelial tufts associated with this disease. Similarly, colorectal adenomas, the benign precursor lesions of colorectal cancer, often expand their territory by actively pushing out neighboring epithelium. The adenomatous epithelium grows top-down into neighboring crypts, gradually replacing the normal intestinal crypt epithelium by growing underneath it. Similar biophysical models could be applied to disentangle the clonal contribution of passive pushing and active pulling forces in this tug of war between normal and precancerous epithelium. ■

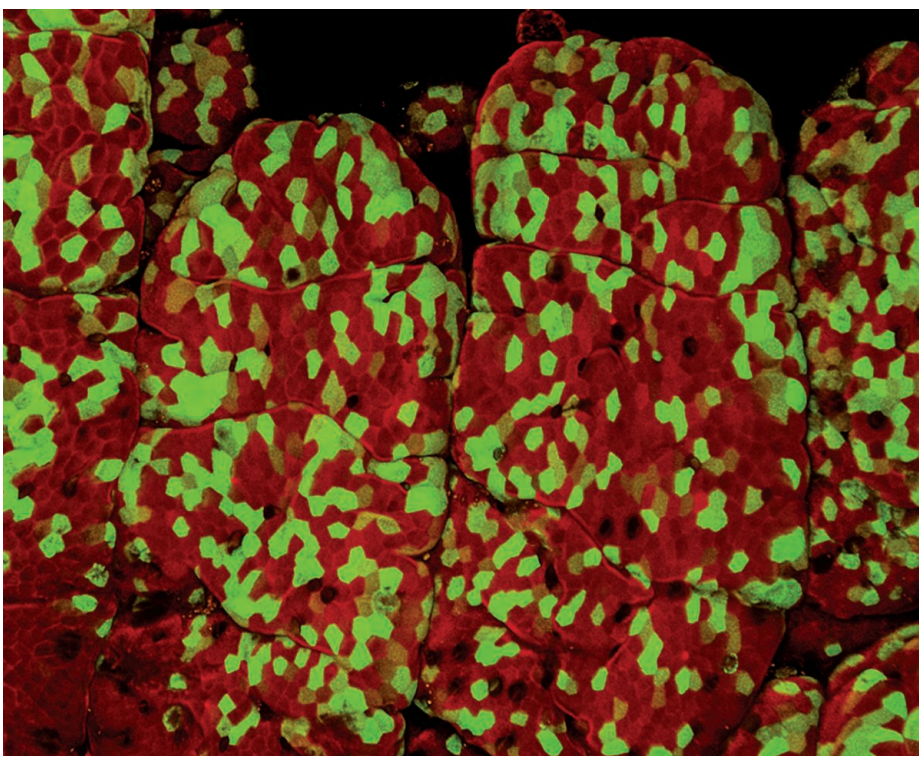

Mouse intestinal villi of a gut explant show scattered epithelial cells marked by green fluorescent protein. Live imaging of these explants allows the movement of individual epithelial cells to be recorded over time.

PHOTO: D. KRNDIJA *ET AL.* (*1*)

REFERENCES AND NOTES

1. D. Krndija *et al.*, *Science* **365**, 705 (2019).
2. D. J. Winton, M. A. Blount, B. A. Ponder, *Nature* **333**, 463 (1988).
3. L. Gutierrez-Gonzalez *et al.*, *J. Pathol.* **217**, 489 (2009).
4. H. J. Snippert *et al.*, *Cell* **143**, 134 (2010).
5. T. A. Graham *et al.*, *Gastroenterology* **140**, 1241 (2011).
6. G. T. Eisenhoffer *et al.*, *Nature* **484**, 546 (2012).
7. J. L. Mueller, M. D. McGeough, C. A. Peña, M. Sivagnanam, *Am. J. Physiol. Gastrointest. Liver Physiol.* **306**, G278 (2014).

ACKNOWLEDGMENTS

Work in my laboratory is supported by Cancer Research UK.

10.1126/science.aay5861

Published by AAAS

POLICY FORUM

REGULATION

Downgrading of regulation in regenerative medicine

What should be a firm commitment to product efficacy is threatened by economic competition

By **Douglas Sipp**[1,2,3,4] *and* **Margaret Sleeboom-Faulkner**[5]

Science is fundamental to ensuring the safety and demonstrating the efficacy of newly developed medicines. Government agencies play a key role in establishing standards for safety and efficacy. But in a climate of international economic competition, this function comes under frequent scrutiny and pressure. We suggest that in response to this competitive pressure, regulations in some countries have become more permissive. Drawing on controversies over the regulation of regenerative medicine products in Japan and elsewhere, we consider whether the policies that have developed from such tensions can simultaneously protect patients, strengthen health markets, and enhance national competitiveness. These developments shed light on global drivers of a policy phenomenon we call "regulatory brokerage" (*1*). We argue that when regulation does not support the scientific effort to establish the safety and efficacy of medical products, it may be brokered by interest groups, including industry, particular groups of scientists and patients, and policy-makers. In an international context, regulatory changes for short-term economic or political reasons in one country can have a cascading effect, leading to unforeseeable, detrimental consequences for the field of regenerative medicine at the global level.

The field of regenerative medicine may be particularly susceptible to regulatory brokerage because of its economic promise, the huge investment already made in the field, and the hope of relief for growing public health budgets in aging societies. Stem cell–based medicines have always presented a regulatory conundrum because many of the principles used in the standardization, review, characterization, and testing of small-molecule drugs and other chemical entities are of little help in evaluating the use of living cells. But even though standards for product identity, purity, dose, and toxicity may require substantial adjustments to account for the distinct properties of products made from living cells (*2*), the critical feature in which such products should not differ from other drugs is efficacy—the ability to measurably and reliably produce a desired therapeutic effect.

DEGENERATIVE POLICY

Even as countries around the world contend with the problem of direct-to-consumer marketing of unproven stem cell–based interventions by what are seen as "rogue" operators, the field has seen a trend toward loosening the rules for market authorization. This is creating an opaque area of regulatory policy, where it is unclear whether

[1]*RIKEN Center for Biosystems Dynamics, Kobe, Japan.* [2]*Keio University School of Medicine, Tokyo, Japan.* [3]*Keio University Global Research Institute, Tokyo, Japan.* [4]*RIKEN Advanced Intelligence Project, Tokyo, Japan.* [5]*Department of Anthropology, School of Global Studies, University of Sussex, Brighton, UK. Email: m.sleeboom-faulkner@sussex.ac.uk*

ILLUSTRATION: STEPHAN SCHMITZ/FOLIO ART

Published by AAAS

deregulation serves competition, science, or patients. South Korea was perhaps the first country to give preferential regulatory treatment to stem cell medicine. In 2011–2012, the Korean Food and Drug Administration issued a flurry of three approvals of the world's first stem cell–based medical products, adding a fourth in 2014. However, only one of the four products is reimbursed by the national health insurance system because of concerns about the strength of efficacy data from premarket trials.

The Korean approvals attracted international skepticism for sacrificing clinical data standards to expedience. But they made a different impact in Japan, which had embarked on a multibillion-dollar initiative to lead the world in regenerative medicine research and commercialization. Japan had already identified the United States as a major competitor in the race to commercialize; Korea's streamlined approval of cell biologics made it a leading contender as well. A 2012 presentation to a Japanese cabinet committee on regulation and regulatory reform highlighted how South Korea had approved five times as many cell biologics as Japan between 2010 and 2012 as an indicator of a purported innovation gap (*3*).

This emphasis on regulatory competition is also reflected in documents of the Research Institute of Economy, Trade and Industry (RIETI), a policy-making organization of the Ministry of Economy, Trade and Industry (METI). The report opens with the observation: "Though Japan has surpassed South Korea in terms of R&D in the area of regenerative medicine, South Korea has been more successful at commercialization" (*4*). The report further cites "tremendous regulatory disparities between Japan and other economies," asserting that "the low number of market approvals is caused by the low number of clinical trials," which the authors attribute to regulatory differences.

In 2013, Japan's government responded to this competitive challenge by amending the Pharmaceutical Affairs Act to create a new category of medicines ("regenerative medicine products") and a review pathway designed to grant such products faster market entry in the form of "conditional approval." These legal changes have drawn both envy and critique from outside Japan. Whereas the Korean approvals represented de facto policy without changes to the legal code, Japan's reforms involved actual changes to law.

The first product to take advantage of Japan's new accelerated pathway was a sheet of skeletal muscle cells intended for use in severe heart failure. Since its 2015 approval, the product has not fared well. The cardiologist who led the small, open-label study that led to its conditional approval subsequently expressed doubts that the product would be adequate to repair severely damaged hearts (*2*). In December 2018, the Health Ministry announced that it would extend the conditional approval period by 3 years because sufficient numbers of patients had not yet been enrolled in postmarket testing (*5*).

Also in December 2018, Japan's drug regulator issued a second conditional approval, for a stem cell biologic for the treatment of spinal cord injury. That decision has also sparked controversy, as it was based on a single, small, uncontrolled, and unpublished study (*6*). In February 2019, the Central Social Insurance Medical Council agreed to reimburse the product at a price of nearly 15 million yen (~$140,000) per treatment course, making it one of the country's most expensive drugs.

DRUG LAG, AN ENDLESS RACE

The perception of regulatory shortcomings or excesses as responsible for national differences in drug approval rates has a long history in the concept of "drug lag." The notion was first introduced in 1973, in a comparison of drug approval times in the United States and the United Kingdom (UK) (*7*). The study's author found the latter country to be faster and suggested that the slower time to decision in the United States harmed both patients and companies. Drug lag soon became a cudgel in the hands of free-market policy organizations, which since the 1970s have embarked on a campaign to weaken the power of the U.S. Food and Drug Administration (FDA).

At the global level, drug lag arguments promote perpetual comparisons between regulatory jurisdictions, in which the regime with faster approvals is often deemed superior to the one favoring a slower, more cautious approach. Solutions proposed by those alleging drug lag almost invariably call for weaker regulation, in the form of easier market entry enabled by faster, and looser, premarket testing. States that fail to relax their health product quality standards risk being accused of bureaucratic sluggishness and obstructionism. Although there is always scope to further refine regulatory codes, sacrificing efficacy requirements for speed is unwise. Unproven and ineffective products can sell well in markets that do not require advance evidence of efficacy (e.g., dietary supplements, homeopathic products). Creating new regulatory carveouts for regenerative medicines is likely to lead to similar outcomes: preemption of adequate treatment, wastage of public funds, and undermining of public trust. Moreover, deregulation in one country may lead international competitors to follow suit.

To our knowledge, the Japanese case is the first instance in which the lowering of market entry standards has been targeted to a medical product on the basis of its material composition. Previous examples of preferential treatment have focused instead on disease severity (e.g., "breakthrough therapy" designation in the United States), incidence (e.g., orphan drug laws), geographical prevalence (e.g., drug development incentive programs for tropical diseases), or mitigation of terrorism (e.g., the FDA Animal Efficacy Rule).

CALLS FOR REGULATORY ROLLBACK

Although Japan's policy experiment has attracted international attention, few are aware that the key principles adopted in Japan's deregulation of regenerative medicine were previously outlined by a free-market policy institute, the Illinois-based Heartland Institute, in the form of a book-length proposal titled *Free to Choose Medicine* (FTCM) (*8*). Although we do not maintain that Heartland Institute is the sole driver behind Japan's regulatory changes, we suggest that it is an important illustration of how attempts by private policy groups in one country may influence lawmaking in another, with consequences that may be disadvantageous to the publics they are intended to serve.

The core concept in FTCM is that clinical trial sponsors should be allowed to begin selling the investigational product to patients while phase 2 studies are still under way. Normally, products must complete a definitive efficacy test in a much larger and more rigorous phase 3 trial prior to sale. This FTCM scheme, which undercuts the need to develop robust evidence of efficacy prior to sale, initially gained little traction at the national level in the United States. Its proponents then began to look farther afield. For example, during the national controversy surrounding so-called "stamina therapy" in Italy, two American scientists and a former FDA commissioner submitted a letter to Italian health authorities, suggesting that Italy could resolve the issue by adopting FTCM. This unsolicited overture, which was immediately rebuffed, prompted a letter of protest from the head of AIFA, the Italian drug regulatory agency, to the then-current FDA commissioner over the attempted interference by U.S. persons in a matter of Italian national interest (*9*).

In Japan, FTCM found more fertile ground. An early version of the proposal was translated into Japanese by the president of the free-market organization Japanese for Tax Reform (*10*), who proceeded to lobby it to members of the Japanese government. The current administration in Japan has

Published by AAAS

made regulatory reform a core component of its national economic strategy and has made regenerative medicine one of the cornerstones of its medical innovation agenda. This convergence of interests was not missed by key players in the regenerative medicine industry or the policy-making arena.

In 2012, the Japanese Society for Regenerative Medicine began to call for regulatory reforms aimed at accelerating approvals through revisiting clinical testing standards (*11*). By 2013, mentions of FTCM began to appear in presentations made by staff in Japan's drug regulatory agency, the Pharmaceuticals and Medical Devices Agency. The same year, the conditional approvals pathway for regenerative medicine products was introduced. The author of FTCM has since thanked the translator for helping to make his ideas into law in Japan.

GLOBAL IMPACT

One would expect the controversies surrounding the first conditionally approved regenerative medicine products to be a warning to other regulatory jurisdictions. But some regulators have responded to Japan's new regulatory regime as a competitive challenge. In India, the national drug regulatory authority cited the Japanese model in justifying its first conditional approval of a stem cell product in 2015 (*12*). In 2014, a report by the Regenerative Medicine Expert Group convened by the UK government noted Japan's new law as placing the UK at a competitive disadvantage (*13*).

In 2015, a Japanese industry group signed a memorandum of understanding with the Alliance for Regenerative Medicine, a U.S.-based industry organization. By aligning with this international organization, which advocates "clear, predictable, and efficient regulatory and review pathways," Japan gained recognition for its new policies. Numerous joint ventures subsequently sought permission to initiate clinical trials in Japan. In the same year, the California Institute for Regenerative Medicine cited the Japanese system in its annual prospectus, calling for the United States to adopt similar lenient standards (*14*).

In 2016, the Washington, DC–based Bipartisan Policy Center published model legislation that led to the REGROW Act, a bill seeking to allow regenerative medicine products onto the U.S. market upon completion of a phase 2 study—a stage at which robust statistical evidence of efficacy has not been obtained. The group stated that "Europe and Japan have outpaced the United States in modernizing their policies to grant patient access to safe cell therapies." Although the REGROW bill died in committee, months later new language on speeding regenerative medicine approvals was added in an amendment to the 21st Century Cures Act, leading to the introduction of a new FDA regulatory designation for "Regenerative Medicine Advanced Therapies." In January 2019, the FDA projected that by 2025 it would be approving 10 to 20 new cell and gene therapy products per year (for comparison, the FDA had not approved any cell/gene therapy product until December 2017; to date, it still has not approved any stem cell products).

In May 2019, four Republican senators called on the FDA to expand "parallel track" market access for unapproved drugs targeting "critical" diseases (*15*). Their proposal followed a March statement by the Heartland Institute calling for the same measure, which cited Japan's deregulation of regenerative medicine as a successful case. Heartland had previously described FTCM in Japan as "a model for America" (*10*). The push for deregulation, as promoted by FTCM supporters, is beginning to extend beyond stem cells.

The examples above illustrate how sensitivity to international competition can make regulators receptive to lowering regulatory thresholds, without giving sufficient consideration to the long-term effects for patients and health care budgets—and perhaps unaware of the consequences that deregulation can have on a global level. Japan's citizens may be alarmed that stem cell products approved under its relaxed standards are now the subject of widespread skepticism among global scientific communities. Other countries, such as Italy and India, have experienced firsthand how economic agendas, cloaked in the language of serving patients, can undermine standards intended to ensure that new drugs deliver measurable therapeutic benefits. Observers should remain on the alert for policy proposals that seek to accelerate approvals to a speed that makes it impossible to determine whether a product is worth marketing.

"Although there is always scope to further refine regulatory codes, sacrificing efficacy requirements for speed is unwise."

To begin addressing the problem of regulatory brokerage in pursuit of short-term economic advantage, voters and taxpayers need to be informed when public health budgets are spent on medicines that have not undergone sufficient scientific and regulatory review. Patient groups must stay informed and alert to the fact that regulatory permissiveness is often geared as much to expediting profit and prestige for private and state-backed firms as it is to accelerating access. And international science and health organizations must be more proactive in sounding the alarm about how the weakening of regulatory protections can lead to the squandering of public money and erosion of trust in scientific research. ■

REFERENCES AND NOTES

1. M. Sleeboom-Faulkner, *Soc. Stud. Sci.* **49**, 355 (2019).
2. D. Cyranoski, *Nature* **557**, 619 (2018).
3. *Saisei iryou sangyouka sokushin e no kadai* [Issues in accelerating the commercialization of regenerative medicine], presentation by industry group Forum for Innovative Regenerative Medicine to Cabinet Committee on Regulation and Reform, 29 November 2012; www.cao.go.jp/sasshin/kisei-seido/meeting/2012/togi/life/121129/item2.pdf. [In Japanese]
4. K. Kurata, Y.-H. Choi, "Dissemination of Regenerative Medicine in Japan: Promoting commercialization under the regulatory system." Research Institute of Economy, Trade and Industry, January 2012; www.rieti.go.jp/jp/publications/dp/12e004.pdf.
5. *Shinzou-byou wo chiryou suru "ha-to shi-to" kenshou wo 3-nen enchou ...chiryou yuukousei no shourei tarizu* [Validation of HeartSheet for heart disease extended by 3 years; insufficient cases showing clinical efficacy]. YomiDr., 3 December 2018; https://yomidr.yomiuri.co.jp/article/20181203-OYTET50054/. [In Japanese]
6. D. Cyranoski, *Nature* **565**, 544 (2019).
7. W. M. Wardell, *Clin. Pharmacol. Ther.* **14**, 773 (1973).
8. B. Madden, *Free to Choose Medicine: How Faster Access to New Drugs Would Save Countless Lives and End Needless Suffering* (Heartland Institute, 2010).
9. Letter from Luca Pani, Director-General of AIFA, to FDA Commissioner Margaret Hamburg, concerning "FDA role on Italian stem cell fraud case and possible involvement of U.S.-based partners," 22 January 2014; www.senato.it/application/xmanager/projects/leg17/attachments/documento_evento_procedura_commissione/files/000/001/759/20.pdf.pdf.
10. E. Hudgins, "How Extending the AIDS Drug Access Model to Other Diseases Would Save Lives." Heartland Institute Policy Brief, 8 March 2019; www.heartland.org/publications-resources/publications/how-extending-the-aids-drug-access-model-to-other-diseases-would-save-lives.
11. *Yokohama sengen* [Yokohama Declaration]. Japanese Society for Regenerative Medicine, 13 June 2012; www.jsrm.jp/news/news-659/. [In Japanese]
12. Central Drugs Standard Control Organisation, Minutes of the 26th Meeting of the APEX Committee Held on 10-12-2015 Under Chairmanship of Secretary of Health and Family Welfare for Supervising Clinical Trials on New Chemical Entities in the Light of the Directions of the Hon'ble Supreme Court of India, Dated 03-01-2013. Dec. 12, 2015; https://cdsco.gov.in/opencms/opencms/system/modules/CDSCO.WEB/elements/common_download.jsp?num_id_pk=Njcz.
13. UK Regenerative Medicine Expert Group, "Building on our own potential: A UK pathway for regenerative medicine" (December 2014); https://assets.publishing.service.gov.uk/government/uploads/system/uploads/attachment_data/file/415919/build-on-potential.pdf.
14. California Institute for Regenerative Medicine, "Proposed Strategic Plan: 2016 & Beyond" (8 December 2015); www.cirm.ca.gov/sites/default/files/files/agenda/151217_Agenda_7_CIRM_StratPlan_final_120815.pdf.
15. T. Cruz, M. Braun, R. Paul, M. Lee, Letter to FDA Acting Commissioner Sharpless, 17 May 2019; www.cruz.senate.gov/files/documents/Letters/2019.05.20%20Cruz%20Braun%20Paul%20Lee%20FDA%20Letter.pdf.

ACKNOWLEDGMENTS

Supported by European Research Council grant 283219 and Economic and Social Science Research Council grant ES/I018107/1.

10.1126/science.aax6184

Published by AAAS

BOOKS *et al.*

Workers harvest strawberries in Carlsbad, California.

PHOTO: ZUMA PRESS INC/ALAMY STOCK PHOTO

AGRICULTURAL TOXICOLOGY

Berry blues

Strawberry growers seek a sustainable path forward without go-to fungicides

By **Emily Monosson**

How do conventional, corporate berries that have traveled more than 2000 miles compare with local, organic berries? They are certainly more affordable and taste just as good—but at what cost?

In her new book, *Wilted*, Julie Guthman explores the strawberry industry, from its origins in the mid-1800s to our kitchen tables today. But her focus is not limited to the berries themselves. She also examines the influence of pathogens and chemicals on the human shippers, growers, and workers that underlies the berry industry, all while revealing how planting, tending, and harvesting berries in California can cost a grower more than $60,000 per acre (*1*).

In the starring role of this story is a common and intransigent pathogen called *Verticillium dahliae*, or wilt. Playing opposite is a duo of chemicals: methyl bromide—the silver-bullet fungicide—and chloropicrin, also known as tear gas.

Verticillium is a soilborne fungus that transforms vigorous green leaves into dry brown litter. The pathogen can survive dormant in soil for years. When triggered to germinate, it moves into plant roots and eventually into vessels that carry water and nutrients to the shoots. In response, a plant may cut off its own water circulation. Eventually, it will wilt and die.

As a soil pathogen, *Verticillium* is under the influence of the local soil microbiome. If the microbiome is robust, the pathogen may be controlled by other microbes in the system. Conversely, in highly disturbed soils or soils that host the same crop year after year, a lack of diversity may enable the pathogen to run rampant. Unless, that is, the soil is forced into submission. Enter methyl bromide, stage left.

The brominated hydrocarbon has been an industry standard for more than 65 years. When administered in combination with chloropicrin, it essentially sterilizes the soil, killing off bacteria, nematodes, and weeds. But it also seems to boost growth, which makes it even more useful.

Being gaseous and light, methyl bromide quickly wafts from soil into the air, and any left in the soil degrades within a couple of months. (Of the dozens of trace pesticides that land strawberries on the Environmental Working Group's dirty dozen each year, surprisingly, this is not one of them.)

At the height of its reign, nearly 20,000 tons of methyl bromide were used on various U.S. crops. Unfortunately, it not only kills pests, it also destroys ozone.

Several years after the Montreal Protocol agreement banning chlorofluorocarbons was signed in 1987, an amendment that targets other halogenated hydrocarbons, including methyl bromide, was added. It took the strawberry industry nearly three decades to capitulate. For years, the industry applied for, and received, critical-use exemptions. Officially, methyl bromide's use on strawberry fields ended in 2016 (its application to strawberry rootstock or starts is another story also covered in Guthman's book).

Often in such stories, there are stand-in chemicals waiting in the wings. They may not be ideal, and some may be more toxic than the compound they are replacing, but they are usually there. In this case, there are no clear alternatives.

Growers can apply chloropicrin on its own, but it is less effective and, because of its toxicity, may require buffer zones to protect human health. Methyl iodide, meanwhile, was pulled from the market under protest over concerns for consumer, worker, and community health before it ever hit the field. There are also a range of nonchemical techniques under exploration, including taking the organic route. None of these alternatives offers an easy out. Organic farming, for example, requires growing smarter, tighter, and more hygienically. It also takes more land in a state where land is costly.

But solutions do not have to be all or none, organic or conventional. The best approach may be some combination: the development of less toxic fumigants combined with the cultivation of helpful soil microbes; steam treatment (killing soilborne organisms with heat) and anaerobic soil disinfestation; breeding disease-resistant plants.

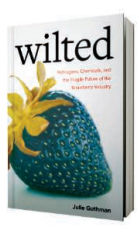

Wilted
Julie Guthman
University of California Press, 2019. 322 pp.

As Guthman writes, "readers should not assume the existence of an optimal pathway. Solutions that are efficacious, reasonably harmless, and economically viable remain elusive." And she notes that sustainable solutions must be accessible rather than monopolized.

Wilted provides a detailed case study for a strategy that I imagine could be applied to many other coevolved systems that arose as a result of our post–World War II love affair with chemicals. From antibiotics to pesticides, we are only now realizing the pitfalls of this approach (resistance, toxicity, and systems built on chemicals that are destined to fail, at some point.)

The strawberry industry's predicament is just one example of how our strategy of dominating ecological systems and focusing on increased output at all cost is short-sighted, with diminishing returns. Recent efforts to work with, rather than against, natural systems suggest a path forward. ■

The reviewer is at the Ronin Institute, Montclair, NJ 07043, USA, and the author of Natural Defense: Enlisting Bugs and Germs to Protect Our Food and Health *(Island Press, 2017). Email: emonosson@gmail.com*

REFERENCES AND NOTES

1. M. P. Bolda *et al.*, *Sample Costs to Produce and Harvest Strawberries* (University of California Agriculture and Natural Resources Cooperative Extension and Agricultural Issue Center, UC Davis Department of Agricultural and Resource Economics, 2016).

10.1126/science.aay1461

Published by AAAS

COGNITIVE SCIENCE

Choosing wisely

A high IQ isn't the liability this book suggests, but we can all learn to make better decisions

The Intelligence Trap
Why Smart People Make Dumb Mistakes
David Robson
Norton, 2019. 331 pp.

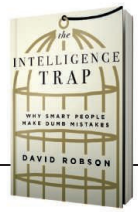

By **Aron K. Barbey**

Examining "why smart people make dumb mistakes," *The Intelligence Trap* presents an accessible and engaging discussion of the nature of human intelligence. The reason for this paradox, suggests author David Robson, is that people with a high IQ are often unaware of the limits of their understanding and are therefore susceptible to poor judgment.

Robson reviews research that examines the relationship between IQ and decision-making (*1*). This work presents evidence that standard IQ tests fail to measure critical thinking skills that are at the heart of decision-making, and as a result, high IQ does not guarantee competent decisions.

To illustrate the role of critical thought in decision-making, consider the following example from the Cognitive Reflection Test (*2*) presented in the book: "A bat and a ball cost $1.10. The bat costs $1.00 more than the ball. How much does the ball cost?" Although "10 cents" immediately comes to mind, the application of logic and mathematics allows us to generate the correct solution (5 cents).

The importance of critical thinking for decision-making is well established (*3*) and supports inferences about the value of an outcome (value assessment), the likelihood of an event (belief assessment), and the capacity to combine this information to make an adaptive choice (information integration). Measurement tools to assess these essential competencies of decision-making have recently been developed and support the direct comparison of decision-making and IQ.

In a seminal study, published in 2007, Baruch Fischhoff and colleagues developed the "Adult Decision-Making Competence Test" (A-DMC) and demonstrated that performance on this measure predicts real-world decision outcomes even after controlling for IQ (*4*). This finding contributes to a growing body of evidence that suggests that standard IQ tests may fail to capture critical thinking skills that are essential to decision-making.

This conclusion, however, is difficult to reconcile with the broad predictive power of IQ and the well-established association between IQ and performance on tests of reasoning and problem-solving (*5*). Researchers have therefore conducted experiments to further examine the nature of the association between IQ and decision-making.

Mindfulness meditation can help enhance decision-making abilities.

In a recent study, Nikki Blacksmith and colleagues found that scores on the A-DMC were largely indistinguishable from IQ, with a construct-level correlation of 0.91 (*6*). It is also well known that performance on measures of critical thinking, such as the Cognitive Reflection Test, is positively correlated with IQ (0.43) (*2*). Thus, the question of whether IQ and decision-making can be empirically dissociated remains the focus of ongoing research and debate.

Critically, however, *The Intelligence Trap* argues not that IQ fails to capture essential facets of decision-making but that a high IQ is a liability for decision-making. Robson's thesis is that "smart people are not only just as prone to making mistakes as everyone else—they may even be *more* susceptible to them."

To support this view, evidence would need to suggest that a high IQ makes people more susceptible to errors in decision-making. This, however, is inconsistent with the high positive correlation observed in Blacksmith's recent study (0.91) (*6*) and the positive associations found in studies of the Cognitive Reflection Test (0.43) (*2*) and in research that Robson reviews from Stanovich and his colleagues (0.47) (*1*). In contrast to the book's premise, this suggests that IQ and decision-making are positively correlated and that a high IQ may be associated with better decisions.

Anecdotes abound of individuals with a high IQ who have made substantial blunders. But in terms of where the field stands, scientists are currently grappling with the question of whether IQ and decision-making can even be disentangled—rather than whether they are in opposition.

Robson dedicates the majority of the book to an engaging discussion of how to improve decision-making, surveying a broad landscape of research on "evidence-based wisdom," emphasizing the importance of critical thought and self-reflection, and reviewing promising new areas of research [e.g., (*7*)]. Despite my concerns about the book's central premise, I found the presentation of topics and wealth of evidence reviewed to be impressively accessible, with engaging storytelling, depth of discussion, and counterintuitive conclusions that are sure to engage the reader's capacity for critical thought and intelligent decision-making. ■

The reviewer is director of the Center for Brain Plasticity, Beckman Institute for Advanced Science and Technology, University of Illinois at Urbana-Champaign, Urbana, IL 61801, USA. Email: barbey@illinois.edu

REFERENCES AND NOTES

1. K. E. Stanovich *et al.*, *The Rationality Quotient: Toward a Test of Rational Thinking* (MIT Press, 2016).
2. S. Frederick, *J. Econ. Perspect.* **19**, 25 (2005).
3. D. Kahneman *et al.*, *Judgment Under Uncertainty: Heuristics and Biases* (Cambridge Univ. Press, 1982).
4. W. Bruine de Bruin *et al.*, *J. Personal. Soc. Psychol.* **92**, 938 (2007).
5. A. R. Jensen, *The g Factor: The Science of Mental Ability* (Praeger, 1998).
6. N. Blacksmith *et al.*, *Pers. Indiv. Differ.* **138**, 305 (2019).
7. C. E. Zwilling *et al.*, *NPJ Sci. Learn.* **4**, 11 (2019).

10.1126/science.aay4327

PHOTO: HERO IMAGES INC./ALAMY STOCK PHOTO

Published by AAAS

LETTERS

To conserve threatened biodiversity, southeast Asia will need more protected areas like Thailand's Khao Sok National Park.

PHOTO: LUCY BROWN - LOCA4MOTION/ISTOCK.COM

Edited by **Jennifer Sills**

A bold successor to Aichi Target 11

In their Policy Forum "Protected area targets post-2020" (19 April, p. 239), P. Visconti *et al.* argue that focusing on areas of biodiversity importance and emphasizing monitoring outcomes would strengthen a successor to Aichi Target 11 of the Convention on Biological Diversity (CBD). We agree but believe that the authors misrepresent Aichi 11 and the potential of a percentage coverage target in establishing valuable protected areas.

Visconti *et al.* claim that Target 11 focuses only on areal protection without regard for what is protected, but its description explicitly mentions "areas of particular importance for biodiversity" (*1*). Their suggestion that Target 11 "may have contributed to global biodiversity loss" is unsubstantiated. By using an out-of-date dataset for 2010 to 2014, the authors have ignored recent gains under Target 11, including a massive increase in marine protection from 2.5 to 7.6% since 2010 (*2*). Visconti *et al.* argue that there is little concrete evidence that percentage targets work, but reports from a variety of countries indicate that such targets do indeed provide incentives for governments to protect important new areas on both land and sea (*3*). For example, Canada has increased its marine protected and conserved areas between 2012 and 2019 from 0.8% to 8.3%, with the majority of sites being targeted in high-value conservation areas (*4*, *5*).

The global priorities proposed by Visconti *et al.* would add a relatively small percentage of Earth. For example, adding all known unprotected Key Biodiversity Areas would add only 1.3% of the land and 1.6% of the ocean (*6*). Many of the other suggested priorities, including World Heritage Sites, Ramsar sites, Natura 2000 sites, and many Ecologically or Biologically Significant Marine Areas, are already protected so would not constitute any conservation gain.

Visconti *et al.* choose not to include in their revised target other fundamental elements such as spatial connectivity and social equity of protected areas. Yet these issues were stressed in Aichi 11 (*1*) because many governments fail to consider them. With climate change, most conservation features will not hold their value without connectivity (*7*). The dismissal of social safeguards risks alienating those wary of protected areas due to human rights concerns. Visconti *et al.* also overlook ecosystem services, missing the imperative of the CBD to benefit people.

Visconti *et al.* are incorrect in stating that protected area management effectiveness (PAME) deals only with inputs (such as staff) and outputs (such as management). Most PAME tools (*8*), as well as the International Union for Conservation of Nature (IUCN) Green List of Protected and Conserved Areas (*9*), also focus on biodiversity outcomes. Additionally, positive biodiversity outcomes are correlated with good management (*10*, *11*).

Setting post-2020 targets is not a choice between focusing on biodiversity importance or spatial percentage protection targets. We need both, as well as clear ways of holding governments accountable. Target 11 is the most successful of all the 20 Aichi Targets (*12*). Suggestions to replace it with a narrow, technocratic target misunderstand the broader policy context and realities on the ground. We need a bold conservation target that demands successful outcomes, focuses on biodiversity, respects benefits to people, and considers carbon values to help achieve the Paris climate goals.

Stephen Woodley[1]*, Jonathan E. M. Baillie[2], Nigel Dudley[1], Marc Hockings[1,3], Naomi Kingston[4], Dan Laffoley[1], Harvey Locke[1], Jane Lubchenco[5], Kathy MacKinnon[1], Imen Meliane[1], Enric Sala[2], Mark Spalding[6,7]

[1]World Commission on Protected Areas, International Union for Conservation of Nature, 1196 Gland, Switzerland. [2]National Geographic Society, Washington, DC 20001, USA. [3]School of Earth and Environmental Sciences, University of Queensland, St. Lucia, QLD 4067, Australia. [4]United Nations Environment Programme World Conservation Monitoring Centre, Cambridge, UK. [5]Oregon State University, Corvallis, OR 97331. USA. [6]The Nature Conservancy, Arlington, VA 22208, USA. [7]Department of Zoology, University of Cambridge, Cambridge CB2 3EJ, UK.
*Corresponding author.
Email: stephen.woodley@wcpa.iucn.org

REFERENCES AND NOTES

1. CBD, Aichi Target 11 (www.cbd.int/aichi-targets/target/11).
2. UNEP-WCMC, IUCN, "Protected Planet: The World Database on Protected Areas (WDPA)" (2019); www.protectedplanet.net.

Published by AAAS

3. CBD, "Compilation of national experiences in achieving Aichi Biodiversity Target 11 in marine and coastal areas, including area-based management measures used in marine fisheries and other ocean sectors" (2018), Table 1, pp 21–36; www.cbd.int/doc/c/d4c9/9cae/909c9460303adf1b0dca5f9c/sbstta-22-inf-27-en.pdf.
4. N. Lopoukhine, "The current state of marine protected areas in Canada" (2013); http://thepearsoncentre.ca/wp-content/uploads/2014/01/State-of-Canadian-Marine-Protected-Areas1.pdf.
5. Department of Fisheries and Oceans, Canada, "Canada's marine protected and conserved areas" (2019); www.dfo-mpo.gc.ca/oceans/conservation/achievement-reussite-eng.html.
6. E. Dinerstein *et al.*, *Sci. Adv.* **5**, eaaw2869 (2019).
7. M. Krosby, J. Tewksbury, N. M. Haddad, J. Hoekstra, *Conserv. Biol.* **24**, 1686 (2010).
8. L. Coad *et al.*, *Philos. Trans. R. Soc. London B Biol. Sci.* **370**, 20140281 (2015).
9. IUCN, World Commission on Protected Areas, "IUCN green list of protected and conserved areas: Standard, version 1.1." (IUCN, Gland, Switzerland, 2017).
10. D. A. Gill *et al.*, *Nature* **543**, 665 (2017).
11. W. F. Laurance *et al.*, *Nature* **489**, 290 (2012).
12. P. Gannon *et al.*, *Parks* **23.2**, 13 (2017).

10.1126/science.aay2131

Response

Woodley *et al.* claim that percentage targets incentivize governments to protect important sites for biodiversity. They are correct that protected area (PA) coverage has increased since 2010, yet the evidence overwhelmingly suggests that many of these additional PAs have contributed little to biodiversity conservation. For example, PA extent in southeast Asia, a global hotspot of endemism and threatened biodiversity across all major taxonomic groups (*1*), increased by 24% between 2000 and 2010 but only 3% since then (*2*). Globally, the percentage of threatened amphibians, mammals, and birds whose ranges were sufficiently covered by PAs saw a modest increase from 8.5% to 9% from 2014 to 2019, despite a higher increase in PA extent (*3*). Similarly, in 2010, 20 to 30% of protected areas covered sites of international biodiversity importance [Figure 3 in (*4*)]; in 2019, this percentage has declined to 17 to 18% (*2*, *5*). These up-to-date analyses support the contention that PA growth since 2010 has not led to proportionally better biodiversity outcomes. Target 11 could be deemed the most successful Aichi Target only if one measured success by the areal extent gained.

Woodley *et al.* contend that marine protection has substantially improved since 2010. Globally, however, marine protected areas established since 2010 have broadly targeted quantity over quality. They have generally avoided areas with high fish catch, despite overfishing being the most important threat to biodiversity that marine protected areas can address (*6*).

Woodley *et al.* assert that our proposed target would increase PAs by a trivial amount, but these percentages will increase as implementation of the new standard progresses. Additionally, we state that the effective conservation of all sites of documented global importance for biodiversity should be included. For example, unprotected Ecologically or Biologically Significant Areas cover 17.9% of the ocean (*7*), and there is increasing evidence that many marine and terrestrial sites of high ecological integrity and global biodiversity importance are unprotected (*8*); both of these are included in our proposal.

We do not dismiss connectivity and social equity, as Woodley *et al.* assert. On the contrary, we say that to achieve positive outcomes, area-based approaches must inherently address these issues. The target we propose would require functional connectivity, and its adequacy would be evaluated through regular assessments of the state of biodiversity at locations of sites of global importance, which may change with climate change. We also specifically state that other targets that address ecosystem services will need to complement ours.

We agree with Woodley *et al.* that monitoring management effectiveness is important, but we maintain that existing systems largely track processes rather than outcomes. The focus on process is reflected by the fact that the only available global indicator of management effectiveness relates to the number of protected areas with assessments (*9*), not the adequacy of management or the biodiversity outcomes it delivers. We are not alone in recognizing that current monitoring and indicators of management effectiveness are useful but inadequate nor in calling for outcome-based conservation targets and indicators (*10*–*12*).

We do not claim that Aichi 11 "may have contributed to global biodiversity loss" but rather that the four shortcomings we identify may have done so. We agree with Woodley *et al.* that site conservation post-2020 should not be defined by "a narrow, technocratic target"; indeed, our suggestion is broad (incentivizing the safeguard of all biodiversity at the site scale) and inspirational (focused on outcomes rather than activities). Biodiversity outcomes would define the effective implementation and target achievement rather than arbitrary percentages of area. We should demand no less of the world's protected and conserved areas.

Piero Visconti[1]*, Stuart H. M. Butchart[2,3], Thomas M. Brooks[4], Penny F. Langhammer[5,6,7], Daniel Marnewick[8], Sheila Vergara[9], Alberto Yanosky[10], Olivia Crowe[2], James E. M. Watson[11,12]
[1]International Institute for Applied Systems Analysis (IIASA), A-2361 Laxenburg, Austria. [2]BirdLife International, Cambridge CB2 3QZ, UK. [3]Department of Zoology, University of Cambridge, Cambridge CB2 3EJ, UK. [4]International Union for Conservation of Nature, 1196 Gland, Switzerland. [5]Global Wildlife Conservation, Austin, TX 78767, USA. [6]Amphibian Survival Alliance, London SW7 2HQ, UK. [7]School of Life Sciences, Arizona State University, Tempe, AZ 85287-4501, USA. [8]BirdLife South Africa, Dunkeld West 2196, South Africa. [9]ASEAN Center for Biodiversity, Laguna, Philippines.

NEXTGEN VOICES: SUBMIT NOW

Peer mentoring: Your advice needed!

Add your voice to *Science*! In this NextGen Voices survey, a reader asks for your advice! Have you been in this situation or one like it? Do you have any tips that you would like to share? Become a NextGen Voices peer mentor by contributing your thoughts!

Dear NextGen Voices peer mentors,
One of my lab responsibilities as a graduate student is to train another graduate student to do certain parts of the team's research. The graduate student often neglects his duties, which means I have to do the work myself. Despite meeting with him to demonstrate exactly how to do the tasks, offering to answer any questions he has, and reminding him that many of these tasks are time sensitive, I have not been able to persuade him to complete his assignments. I always cover for him, both because failure to do these tasks puts my own research at risk and because my PI has trusted me to train this student, so his failures reflect poorly on me. How can I more effectively train this student and also protect my research and my reputation as a manager?

Sincerely,
Trying to Manage

To submit, go to www.sciencemag.org/nextgen-voices
Deadline for submissions is 30 August. A selection of the best responses will be published in an October issue of *Science*. Submissions should be 150 words or less. Anonymous submissions will not be considered.

Published by AAAS

The yellow-breasted bunting population has rapidly declined in recent years.

PHOTO: FLPA/ALAMY STOCK PHOTO

[10]Guyra Paraguay–CONACYT, 20 Asunción, Paraguay. [11]School of Earth and Environmental Sciences, The University of Queensland, St. Lucia, QLD 4072, Australia. [12]Wildlife Conservation Society, Global Conservation Program, Bronx, NY 10460-1068, USA. *Corresponding author. Email: visconti@iiasa.ac.at

REFERENCES AND NOTES

1. N. S. Sodhi *et al.*, *Biodivers. Conserv.* **19**, 317 (2010).
2. UNEP-WCMC, IUCN, "Protected Planet: The World Database on Protected Areas (WDPA)" (2019); www.protectedplanet.net.
3. S. Mogg, C. Fastre, M. Jung, P. Visconti, *bioRxiv* 10.1101/608992 (2019).
4. S. H. M. Butchart *et al.*, *PLOS One* **7**, e32529 (2012).
5. BirdLife International, "Digital boundaries of Key Biodiversity Areas from the World Database of Key Biodiversity Areas" (2019); www.keybiodiversityareas.org/site/requestgis.
6. C. D. Kuempel, K. R. Jones, J. E. M. Watson, H. P. Possingham, *Conserv. Biol.* 10.1111/cobi.13340 (2019).
7. D. C. Dunn *et al.*, *Mar. Pol.* **49**, 137 (2014).
8. J. E. Watson *et al.*, *Nature* **563**, 27 (2018).
9. IPBES, "Summary for policymakers of the global assessment report on biodiversity and ecosystem services of the Intergovernmental Science-Policy Platform on Biodiversity and Ecosystem Services" (Paris, France, 2019).
10. L. Boitani *et al.*, *PLOS Biol.* **6**, 0436 (2008).
11. M. D. Barnes, L. Glew, C. Wyborn, I. D. Craigie, *Nat. Ecol. Evol.* **2**, 759 (2018).
12. J. Eklund, L. Coad, J. Geldmann, M. Cabeza, *Conserv. Sci. Pract.* 10.1111/CSP2.107 (2019).

10.1126/science.aay2768

Save China's yellow-breasted bunting

The previously widespread yellow-breasted bunting, a migratory bird that was recently classified as Critically Endangered on the International Union for Conservation of Nature's Red List (*1*, *2*), declined in number by about 90% globally between 1980 and 2013 (*3*). The species has disappeared in most areas of Eastern Europe, Japan, and Russia, its range shrinking by 5000 km (*3*–*5*). The rapid and continued population decline is primarily driven by excessive hunting (*3*, *6*).

In the 1990s, rumors began in southern China that the yellow-breasted bunting could be used as a medical supplement (*7*). To meet this demand, hunting of the bird as it migrated through the country became increasingly common, despite a 1997 law making it illegal (*5*). In 2001, it was estimated that 1 million yellow-breasted buntings were consumed in China's Guangdong province (*8*). Only a few tens of thousands of buntings remain globally (*1*, *3*), and the recent steep population decline indicates that they could soon dwindle to critically low numbers.

In China, commercial hunting of the yellow-breasted bunting is still rampant (*9*). To preserve this species, the Chinese government must step up protection efforts, including strengthening protection regulation, cracking down on illegal hunting, and inhibiting illegal trade. To make these efforts more effective, the government should expedite the update of the special state protection list (*10*, *11*), where the yellow-breasted bunting is still categorized as only a class III protected species (*11*), as opposed to the first-class protection level that its vulnerability warrants. China should also better publicize the importance of wildlife protection and help the public understand that consuming this bird could lead to its extinction.

Yali Wang[1], Wenjing Xue[2], Hongjie Wang[1]*
[1]Xiong'an Institute of Eco-Environment, Hebei University, Baoding 071002, China. [2]College of Environmental Science and Engineering, Hunan University, Changsha 410082, China.
*Corresponding author. Email: wanghj@hbu.edu.cn

REFERENCES AND NOTES

1. BirdLife International, *Emberiza aureola* (Yellow-breasted bunting), IUCN Red List (2017); www.iucnredlist.org/species/22720966/119335690.
2. J. Kamp *et al.*, *Conserv. Biol.* **29**, 1684 (2015).
3. J. Westrip, "Archived 2017 topics: Yellow-breasted bunting (*Emberiza aureola*): Urgent request for information" (2017); http://globally-threatened-bird-forums.birdlife.org/2017/06/yellow-breasted-bunting-emberiza-aureola-urgent-request-for-information.
4. "Yellow-breasted bunting," WhatBird (2019); https://identify.whatbird.com/obj/689/overview/Yellow-breasted_Bunting.aspx.
5. M. Fowlie, "Yellow-breasted Bunting declined by 90%," BirdLife International (2015); www.birdlife.org/asia/news/yellow-breasted-bunting-declined-90.
6. S. Chan, "Is the yellow-breasted bunting the next passenger pigeon?," BirdLife International (2017); www.birdlife.org/worldwide/news/yellow-breasted-bunting-next-passenger-pigeon.
7. "Heart-broken! In just 13 years, they almost were eaten to extinction by Chinese diners" (2017); http://n.cztv.com/news/12759250.html?spm=zm5173-001.0.0.1.6Wl21f [in Chinese].
8. S. Chan "A bird to watch: Yellow-breasted bunting" *BirdingASIA* **1**, 16 (2004).
9. W. Fei *et al.*, *Forktail* **31**, 47 (2015).
10. "Wildlife under special state protection list" (2009); www.forestry.gov.cn/main/1078/content-115089.html [in Chinese].
11. "Lists of terrestrial wildlife under state protection, which are beneficial or of important economic or scientific value" (2000); www.forestry.gov.cn/main/151/content-635711.html [in Chinese].

10.1126/science.aay6909

TECHNICAL COMMENT ABSTRACTS

Comment on "Impacts of historical warming on marine fisheries production"

Cody Szuwalski

Free *et al.* (Reports, 1 March 2019, p. 979) linked sea surface temperature (SST) to surplus production and estimated a 4% decline in maximum sustainable yield (MSY) since 1930. Changes in MSY are expected when fitting production models to age-structured data, so attributing observed changes to SST is problematic. Analyses of recruitment (a metric of productivity in the same database) showed increases in global productivity.
Full text: dx.doi.org/10.1126/science.aax5721

Response to Comment on "Impacts of historical warming on marine fisheries production"

Christopher M. Free, James T. Thorson, Malin L. Pinsky, Kiva L. Oken, John Wiedenmann, Olaf P. Jensen

Szuwalski argues that varying age structure can affect surplus production and that recruitment is a better metric of productivity. We explain how our null model controlled for age structure and other processes as explanations for the temperature-production relationship. Surplus production includes growth, recruitment, and other processes and provides a more complete description of food production impacts than does recruitment alone.
Full text: dx.doi.org/10.1126/science.aax7170

Published by AAAS

RESEARCH

Visualizing memory recall in the brain

Norman et al., *p. 657*

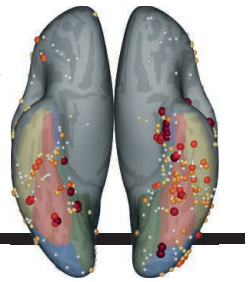

IN *SCIENCE* JOURNALS

Edited by **Michael Funk**

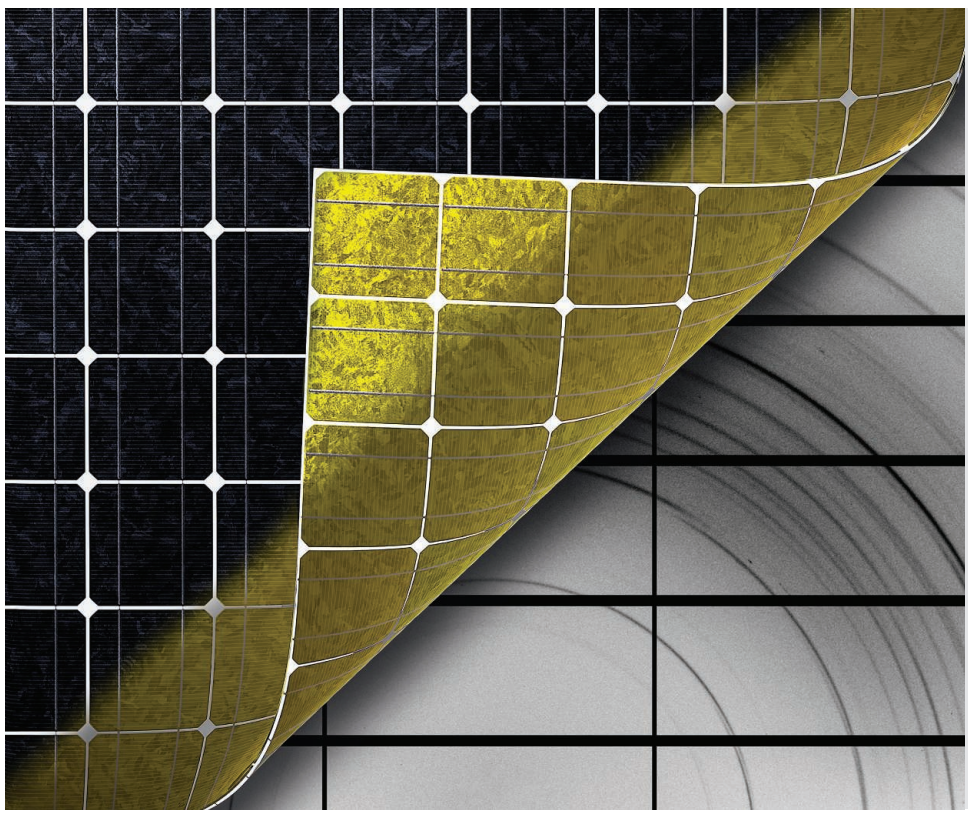

X-ray scattering images of a perovskite material (under) used in solar cells (overlay)

PEROVSKITES

Strain-stabilized perovskites

The perovskite materials used for solar cells and light-emitting diodes (which are black in color) are generally less stable at room temperature than the electronically inactive nonperovskite phases (which are yellow in color). Steele *et al*. show that for $CsPbI_3$, strain induced in a thin film after annealing the material to 330°C and then rapidly cooling it to room temperature kinetically trapped the black phase. Grazing-incidence wide-angle x-ray scattering revealed the crystal distortions and texture formation created by interfacial strain. —PDS

Science, this issue p. 679

GRAVITATION

Gravitational redshift in the Galactic Center

General relativity predicts that light emitted by an object in a strong gravitational field—for example, close to a black hole—should be shifted to longer wavelengths. This gravitational redshift does not exist in the Newtonian theory of gravity. Do *et al*. monitored the position and spectrum of the star S0-2 as it passed Sagittarius A*, the supermassive black hole at the center of the Milky Way. Around the closest part of S0-2's 16-year orbit, they detected the effect of gravitational redshift on its spectrum. These results are more consistent with general relativity than Newtonian gravity at the 5σ level. —KTS

Science, this issue p. 664

OPTICS

Switching on quantum dot lasers

The optical properties of quantum dots can be tailored with alterations to their size and composition. Developing quantum dots as low-threshold laser sources requires overcoming problems associated with carrier recombination and stability. Kozlov *et al*. report success in this direction by demonstrating that a mix of processing and postsynthesis charging can overcome these problems. Synthesis of compositionally graded core-shell quantum dots followed by a carrier charging step provides stable, slow-threshold lasing. —ISO

Science, this issue p. 672

GEOCHEMISTRY

Diamond window into the deep mantle

Helium isotopes provide a window into the very deepest and oldest parts of Earth's voluminous mantle. However, several processes tend to obscure the helium isotope signal from reservoirs in basaltic lavas that have erupted at the surface. Timmerman *et al*. identified a set of diamonds that formed deep within Earth and were rapidly erupted, which have avoided near-surface contamination. They find evidence for a deep, primordial rock source along with mixing of sediments from old subducting plates. The signatures extracted from these diamonds have implications for chemical and dynamic models of Earth. —BG

Science, this issue p. 692

CREDITS (FROM TOP): NORMAN *ET AL.*; IMAGE: RICHARD TROUVE

Published by AAAS

IN OTHER JOURNALS

Edited by **Caroline Ash** *and* **Jesse Smith**

NEUROSCIENCE

Visualizing neuronal activity in vivo

Imaging the changes in fluorescence of voltage-sensitive reagents would enable monitoring of the activity of neurons in vivo. Abdelfattah *et al*. created such a voltage indicator by designing a protein that combines the voltage sensor domain from microbial rhodopsin with a domain that captures a dye molecule with exceptional brightness and photostability. When the protein was expressed in mice, flies, or zebrafish, they could monitor single action potentials in dozens of neurons simultaneously for many minutes. —LBR

Science, this issue p. 699

METABOLISM

Malleable muscle metabolism

The effect of sex on physiological processes such as metabolism has not been sufficiently studied, despite signs that cellular-level processes can be sexually dimorphic. During fasting, skeletal muscles switch from using carbohydrates to fatty acids as a fuel source. Yang *et al*. found that fasting induced skeletal muscle in female mice to produce brain-derived neurotrophic factor (BDNF), a protein known for its role in synaptic plasticity and neuronal survival. Skeletal muscle deficiency of BDNF in female mice, but not in male mice, prevented this metabolic switch and resulted in myofiber necrosis and reduced muscle strength. —WW

Sci. Signal. **12**, eaau1468 (2019).

ENGINEERING

Decoding sweat to monitor health

Our sweat carries biomolecules, such as electrolytes, metabolites, and hormones, that can be used probe the state of our bodies at a chemical level. Nyein *et al.* developed a wearable microfluidic patch that captures sweat, which they used to predict whole-body fluid and electrolyte loss during exercise. Secretion rate and sodium levels show a positive correlation across regions of the body and among study subjects. Correlation between regional fluid loss and whole-body water loss could be used to track hydration status. —JR

Sci. Adv. 10.1126/sciadv.aaw9906 (2019).

ROBOTICS

Lowering locomotion's metabolic cost

Walking and running require different gaits, with each type of motion putting a greater bias on different muscles and joints. Kim *et al.* developed a soft, fully portable, lightweight exosuit that is able to reduce the metabolic rate for both running and walking by assisting each motion via the hip extension (see the Perspective by Pons). A waist belt holds most of the mass, thus reducing the cost of carrying the suit. By tracking the motion of the user, the suit is able to switch modes between the two types of motion automatically. —MSL

Science, this issue p. 668; see also p. 636

PLANT SCIENCE

Less space but greater maize yield

To meet increasing demands for food, modern agriculture works with increasingly dense plantings. Tian *et al*. identified a gene in teosinte, the wild ancestor of maize, and used it to alter maize such that the plant has a narrower architecture that nonetheless allows leaves access to sunlight (see the Perspective by Hake and Richardson). The yield advantage only becomes evident with the high-density plantings characteristic of modern agriculture, perhaps explaining why this gene was not brought into the fold during the previous millennia of maize domestication. —PJH

Science, this issue p. 658; see also p. 640

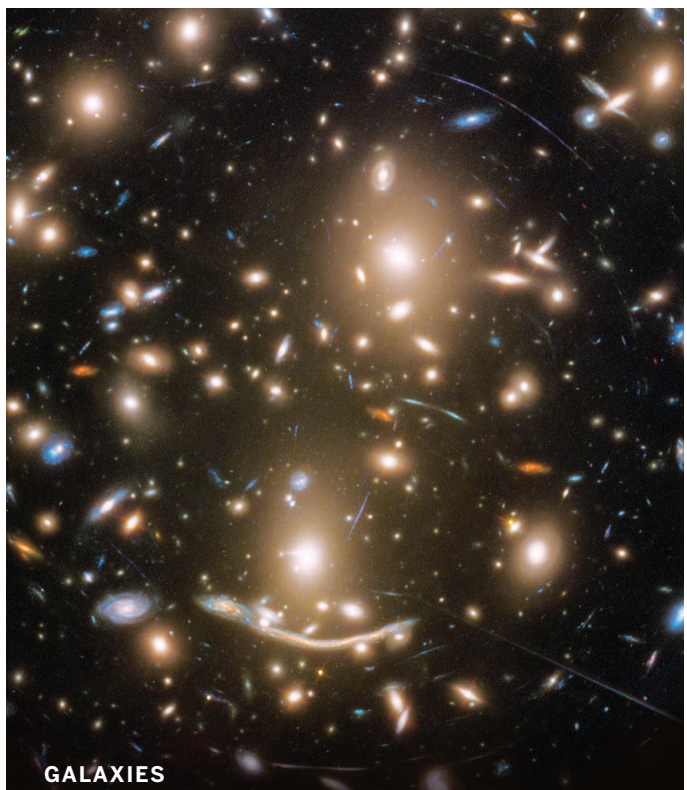

PHOTO: NASA GODDARD

GALAXIES

Dust declines after a starburst

Post-starburst (PSB) galaxies recently experienced a short episode of vigorous star formation, which has now ceased. Li *et al.* have studied 58 PSB galaxies whose starbursts ended 100 million to 800 million years ago. By combining data from the ultraviolet to the far infrared, they measure the mass of dust in PSB galaxies and find that it declines approximately exponentially with time since the starburst. The decline is too fast to be the result of the residual star formation, so it may reflect dust destruction by an active galactic nucleus. The dust and gas levels would evolve to typical levels for early-type galaxies about a billion years after the starburst. —KTS

Astrophys. J. **879**, 131 (2019).

The mass of dust in galaxies decreases exponentially with time since the end of their star formation phase.

NEUROSCIENCE

Social isolation biases rodent data

Rodents are social animals, and social isolation and barren environments are stressful for them. However, experimental protocols sometimes insist on single housing to obtain accurate measurements of biological parameters or to avoid damage to monitoring apparatus, such as severing of EEG wires, or to prevent aggressive behavior from others. Manouze *et al.* investigated the consequences of animal housing conditions on stress response and epilepsy severity in rats and mice. Isolated

Published by AAAS

AGRICULTURAL ECOLOGY

Benefits of diversity

Increasingly, our planet's landscapes are becoming homogenized into large areas of monoculture of very few species. This renders food security vulnerable to pests, disease, and natural disasters. Increasing biodiversity by encouraging seminatural patches in a landscape improves crop resilience by harboring natural predators and pollinators. By sampling a variety of agricultural landscapes across North America and Europe, Sirami *et al.* show that making fields smaller and crops more diverse has an even stronger effect on resilience than just leaving seminatural areas between crops. This is because crop diversity provides multiple refuges for predatory animals. Policies to increase crop heterogeneity may improve biodiversity in agricultural landscapes without taking land out of production. —CA

Proc. Natl. Acad. Sci. U.S.A. 10.1073/pnas.1906419116 (2019).

Smaller fields and diverse crops improve the biodiversity and resilience of farmed landscapes.

healthy individuals showed higher stress and anxiety levels compared with socially housed animals. Epileptic rats and mice also had more severe seizures when they were isolated. Hence, materials and methods should systematically report housing conditions and all efforts should be made to maintain social interaction during experimentation whenever possible. —PRS

eNeuro **6**, ENEURO.0179-18.2019 (2019).

OVARIAN DYSFUNCTION

Microbiota and polycystic ovaries

Polycystic ovary syndrome (PCOS) is a common hormonal disorder that mainly affects women of reproductive age. It results in small ovarian cysts that can affect fertility, as well as metabolic conditions such as insulin resistance and obesity. Finding an increased presence of the bacterium *Bacteroides vulgatus* in PCOS patients, Qi *et al.* report a link between the gut microbiome and PCOS. Enhanced abundance of *B. vulgatus* was associated with alterations in gut bile acid metabolites, which up-regulated interleukin-22 (IL-22) expression via TGR5-GATA3 signaling. Therapeutic administration of IL-22 perturbed browning of adipose tissue and improved insulin sensitivity and ovarian function in mouse models. —PNK

Nat. Med. **25**, 1225 (2019).

IMMUNOLOGY

Class (II) warfare

Natural killer (NK) cells are cytotoxic lymphocytes that recognize virus-infected, stressed cells and tumor cells with both activating and inhibitory receptors. Many NK cell receptors bind human leukocyte antigen (HLA) class I, which presents self-peptides but which is often lost within tumors and during infection. Whether and how NK cells might then bind HLA class II molecules, which are required for adaptive immunity, remains unclear. Niehrs *et al*. report a direct functional interaction between the NK cell receptor NKp44 and a subset of commonly expressed HLA-DP molecules, including HLA-DP401. Intriguingly, the strength of NK cell binding and activation was both peptide- and HLA allotype–dependent. This work may help explain previously reported associations between certain HLA allotypes and some autoimmune, viral, and graft-versus-host disease outcomes. —STS

Nat. Immunol. 10.1038/s41590-019-0448-4 (2019).

ORGANIC CHEMISTRY

An *E*-*Z* resolution

Compounds with carbon-carbon double bonds can adopt two distinct geometries, designated *E* or *Z* on the basis of whether the largest substituents on each carbon are across from or adjacent to each other. Majhi *et al.* report a method to transform a mixture of *E* and *Z* reactants into a single *E*-configured alkylated product. This dynamic kinetic resolution process relies on deprotonating the carbon next to the double bond to facilitate the rotation. Modeling highlights a coordinative role of the base's sodium counterion after deprotonation. —JSY

J. Am. Chem. Soc. **141**, 11770 (2019).

PSYCHOLOGY

Training to reduce cognitive biases

Human beings are susceptible to cognitive biases, such as the tendency to seek out information that confirms their prior beliefs. Sellier *et al.* examined whether a single debiasing training intervention could reduce confirmation bias outside of the training setting. Students assigned to solve a business case exercise were less likely to choose the inferior confirmatory solution when they had previously undergone the debiasing intervention. These results stand in contrast to prior work, which had failed to find evidence that debiasing training could transfer to other settings and have implications for improving decision-making. —TSR

Psychol. Sci. 10.1177/0956797619861429 (2019).

PHOTO: BLOM/GETTY IMAGES

Published by AAAS

ALSO IN *SCIENCE* JOURNALS

Edited by **Michael Funk**

MITOCHONDRIA

Putting a price on the powerhouse

Mitochondria—the so-called powerhouse of the cell—are derived from bacterial endosymbionts. This history provides opportunities and challenges for their host cells, particularly metazoans, including humans. Youle reviews the interplay between host and mitochondrial biology and highlights how mitochondrial ancestry has influenced innate immune responses. Keeping mitochondria both healthy and in check is key to organismal health and, when perturbed, leads to a variety of pathologies, including Parkinson's disease and inflammation. —SMH

Science, this issue p. 655

ASTROCHEMISTRY

Enhanced abundance of primordial HeH^+

Though only recently detected in space, the helium hydride ion (HeH^+) is thought to be the first molecule ever to have formed in the early Universe. Novotný *et al*. report state-specific rate coefficients for the dissociative reaction of HeH^+ with electrons, obtained using a cryogenic ion storage ring combined with a merged electron beam (see the Perspective by Bovino and Galli). They detect substantial rotational dependence and a decrease of the rates for the lowest states of HeH^+, far below the values listed in astrochemistry databases and those previously applied in early-Universe models. These results suggest high abundance of this important primordial molecule at redshifts of first star and galaxy formation. —YS

Science, this issue p. 676; see also p. 639

SUPERCONDUCTIVITY

An unusual superconductor

In conventional, and in many unconventional, superconductors, the electrons that form Cooper pairs have spins pointing in opposite directions. An applied magnetic field can easily "break" such pairs—and destroy superconductivity—by aligning both spins in the same direction. In contrast, spin-triplet superconductors are much more resilient to magnetic fields. Very few candidates for such materials have been discovered. Ran *et al*. add to this select group by observing signatures of spin-triplet superconductivity, including a very large and anisotropic upper critical magnetic field, in the material UTe_2. Because spin-triplet superconductors may naturally exhibit topological superconductivity, this material may also be of interest in quantum computing. —JS

Science, this issue p. 684

SOLAR CELLS

Strong perovskite interfaces

The weak bonding in the crystal lattice of hybrid perovskites used in solar cells promotes surface decomposition and interferes with the formation of stable heterostructures with the charge carrier layers. Y. Wang *et al*. show that strong bonds are formed between lead and both chlorine and oxygen atoms in a film with a lead-rich surface and a chlorinated graphene oxide layer. This interface was used with common hole-transporting materials to fabricate solar cells that maintained 90% of their initial efficiency of 21% after operation at 60°C for 1000 hours. —PDS

Science, this issue p. 687

NEUROSCIENCE

A newly discovered cell type for pain perception

Pain has been thought to be initiated by activation of free nerve endings without end organs in the skin. In contrast to this paradigm, Abdo *et al*. discovered a previously unknown meshlike organ covering the skin that senses dangerous environmental stimuli (see the Perspective by Doan and Monk). This organ is built from specialized glial cells located in the epidermal-dermal border and is sufficient and required for initiation of mechanical pain transduction. —PRS

Science, this issue p. 695; see also p. 641

CELL BIOLOGY

Active migration renews gut epithelia

Epithelial tissues are continuously renewed throughout adult life, and the gut epithelium is the fastest self-renewing tissue in mammals. Over 3 days or so, epithelial cells migrate from the crypts, where they are born, to the tips of the villi, where they die. It is commonly believed that migration is strictly passive, driven by mitotic pressure in crypts—as cells divide, they push their neighbors upward. Krndija *et al*. now challenge this concept and show that cells migrate actively, using actin-rich basal protrusions oriented in the direction of migration (see the Perspective by Jansen). —SMH

Science, this issue p. 705; see also p. 642

IMMUNE SIGNALING

A nuclear sensor of viral DNA?

A signaling pathway in eukaryotes known as cGAS–STING recognizes the presence of cytosolic DNA, which alerts the immune system to viral infection or cellular damage. However, the majority of DNA viruses direct their genomic DNA into nuclei, suggesting that nuclear-specific sensing is also needed. L. Wang *et al*. find that during herpes simplex virus–1 infection, heterogeneous nuclear ribonucleoprotein A2B1 forms a complex with viral DNA, homodimerizes, and is demethylated. These events result in translocation of the complex to the cytosol and activation of the immune system through type I interferon signaling. Additionally, the complex promotes N^6-methyladenosine modification and translocation of cGAS–STING–related mRNAs after DNA virus infection, further amplifying the immune response. —STS

Science, this issue p. 656

ENVIRONMENT

Watch out for river nutrient imbalances

Input of excess nutrients, such as nitrogen and phosphorus, into a body of water can cause excessive growth of algae. This eutrophication has occurred in fresh waters all around the world as a result of human activities. Efforts to reduce nutrient inputs have been effective, but as Ibáñez and Peñuelas explain in a Perspective, greater reductions in phosphorus than in nitrogen are leading to nutrient imbalances that can also have negative ecological impacts. Most studies have focused on lakes or smaller streams, but recent work is beginning to explore the profound effects of these changes in rivers. —JFU

Science, this issue p. 637

CANCER IMMUNOLOGY

Enhanced inhibitor

Epidermal growth factor receptor tyrosine kinase inhibitors (EGFR TKIs) block oncogenic receptor signaling and are used as a first-line treatment for EGFR-mutated non–small cell lung cancer. Resistance to EGFR TKIs, including the

Published by AAAS

standard hyperfractionated EGFR TKI treatment (HyperTKI), is a problem that has driven the development of next-generation inhibitors. Liu *et al.* describe the improved efficacy of hypofractionated EGFR TKI treatment (HypoTKI) relative to HyperTKI in triggering antitumor T cell responses and preventing relapse in a TKI-sensitive syngeneic murine tumor model through a mechanism involving immune signaling pathways. Coadministration of HypoTKI with an immunotherapy antibody further improved antitumor responses and reduced tumor relapse, thus suggesting that this combined therapy may be a potential alternative to existing treatment regimens. —CNF

Sci. Immunol. **4**, eaav6473 (2019).

ALZHEIMER'S DISEASE

An appetite for memory

The hippocampus serves a critical role in memory formation and cognition. Hippocampal lesions are among the earliest changes in Alzheimer's disease (AD); however, the molecular mechanisms responsible for these alterations remain unclear. Using autoptic brain samples from patients with AD and a mouse model of AD, Tian *et al*. show that in the hippocampus, pathologic β-amyloid directly binds and inhibits the receptor for the "hunger hormone" ghrelin (GHSR1α). In the animal model, the binding blocked the GHSR1α-mediated dopamine receptor D1 (DRD1) activation, leading to synaptic plasticity impairments and memory loss. Simultaneous pharmacological activation of GHSR1α and DRD1 rescued synaptic plasticity and spatial memory in AD mice. —MM

Sci. Transl. Med. **11**, eaav6278 (2019).

NEUROSCIENCE

Sharp-wave ripples in the hippocampus

What are the brain mechanisms responsible for episodic memory retrieval? Norman *et al*. investigated epilepsy patients who had electrodes implanted in the hippocampus and a variety of cortical areas. Using a visual learning paradigm, they examined the temporal relationship between the incidence of hippocampal sharp-wave ripples and recall. Effective encoding of visual information was associated with higher incidence of ripples. Successful recall was preceded by an increased probability of ripples, which were also associated with transient reemergence of activation patterns in higher visual cortical areas. Hippocampal ripples may thus boost recollections during episodic memory retrieval. —PRS

Science, this issue p. 657

Published by AAAS

REVIEW SUMMARY

MITOCHONDRIA

Mitochondria—Striking a balance between host and endosymbiont

Richard J. Youle*

BACKGROUND: Evolution generally trundles along by selecting for mutations or by leveraging the new realms generated from chromosomal amplifications and the transfer of genes between organisms through vectors such as viruses. However, a few times 1 billion to 2 billion years ago, endosymbiosis between bacteria and Archaea yielded relatively huge bursts of divergent gene transfers, leading to the fungi, plants, and animals that we have today. One obvious benefit of endosymbiosis for Eukaryota centers on energy production. Mitochondria derived from α-proteobacteria efficiently generate adenosine triphosphate (ATP) from reduced carbon sources. Mitochondria also perform numerous key metabolic reactions and synthesize essential iron-sulfur compounds that serve as enzyme cofactors. Although most α-proteobacterial genes have transfered to the eukaryotic nucleus, mitochondria retain their own genome encoding for the ribosomal and transfer RNAs needed for the translation of the few protein-coding genes retained in their DNA. Although endosymbiosis offers tremendous evolutionary opportunities, mitochondria, particularly in animals, have some downsides. Here, I describe some of the drawbacks of mitochondria and the patches that metazoans have developed to resolve them.

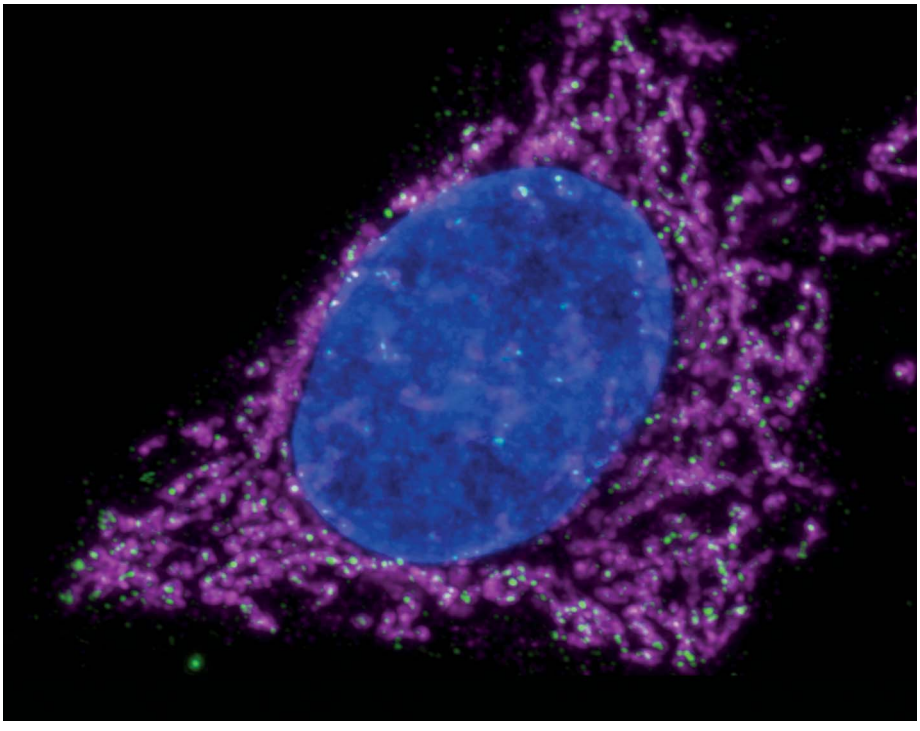

Mitochondria (magenta) in a single cell surround the nucleus (blue). Mitochondria adopt divergent morphologies in different tissues and frequently fuse and divide. They have an outer membrane that surrounds an inner membrane, which houses the electron transport and ATP-synthesizing machinery. In one cell, there are hundreds to thousands of mitochondrial genomes packaged in nucleoids (green) dispersed throughout the organelle network that coordinate expression of proteins with the nuclear genome. Mitochondria were stained with antibody to Tom20, the nucleus was stained with 4′,6-diamidino-2-phenylindole, and nucleoids were stained with antibodies to transcription factor A, mitochondrial.

ADVANCES: Mitochondrial electron transport complexes involved in oxidative phosphorylation are composed of proteins encoded in both the mitochondrial and nuclear genomes. How these genomes coordinate the expression levels of their respective proteins has been recently deciphered. The newest advances reveal previously unknown pathways of mitochondria quality control—including nuclear genome RNA synthesis regulation, mitochondrial encoded protein synthesis control, regulated proteolysis, and selective autophagy—that deal with the challenges of the second genome of mitochondria in our cells. Animals have also developed ways to eliminate mutant mitochondrial DNA (mtDNA) and assure that progeny have a single, homoplasmic, and functional mitochondrial genome. Another emerging issue for mammals is that mitochondrial stress or failure of quality control processes can trigger inflammation. Mitochondria are involved in innate immunity at many levels, from mitochondrial antiviral signaling (MAVS) signaling of interferon-β production, to damage-associated molecular pattern (DAMP) release triggering unwanted inflammation, to mitigating virus spread through apoptosis of infected cells. Programmed cell death involves a pathway using mitochondria as a trigger for apoptosis, which resembles an inflammatory response.

ON OUR WEBSITE

Read the full article at http://dx.doi.org/10.1126/science.aaw9855

OUTLOOK: Understanding how cells and tissues handle the problems of endosymbiosis enhances our understanding of disease etiology. When mitochondria experience inordinate stress or when quality control processes fail, cell-, tissue-, and even organism-wide responses are enacted. Mitochondrial dysfunction contributes to metabolic and neurological disorders. For example, people who lack a form of mitochondrial protein quality control develop ataxia, and those who lack compartmental quality control may develop Parkinson's disease. Although debated, accumulation of mutations and deletions in mitochondrial DNA may be a key aspect of age-associated animal decline. Mitochondria also require careful maintenance because they share molecular patterns with bacteria and viruses that may activate innate immune pathways and inadvertently contribute to inflammatory disorders. An increasing number of human disease etiologies can be attributed to a wide range of mitochondrial defects, and efforts to treat mitochondrial disorders are advancing rapidly. ■

Surgical Neurology Branch, National Institute of Neurological Disorders and Stroke, NIH, Bethesda, MD 20892, USA.
*Corresponding author. Email: youler@ninds.nih.gov
Cite this article as R. Youle, *Science* **365**, eaaw9855 (2019). DOI: 10.1126/science.aaw9855

REVIEW

MITOCHONDRIA

Mitochondria–Striking a balance between host and endosymbiont

Richard J. Youle*

Mitochondria are organelles with their own genome that arose from α-proteobacteria living within single-celled Archaea more than a billion years ago. This step of endosymbiosis offered tremendous opportunities for energy production and metabolism and allowed the evolution of fungi, plants, and animals. However, less appreciated are the downsides of this endosymbiosis. Coordinating gene expression between the mitochondrial genomes and the nuclear genome is imprecise and can lead to proteotoxic stress. The clonal reproduction of mitochondrial DNA requires workarounds to avoid mutational meltdown. In metazoans that developed innate immune pathways to thwart bacterial and viral infections, mitochondrial components can cross-react with pathogen sensors and invoke inflammation. Here, I focus on the numerous and elegant quality control processes that compensate for or mitigate these challenges of endosymbiosis.

One challenge for eukaryotes centers around the coordination of gene expression from multiple distinct genomes (*1*, *2*). Although most of the protein-coding genes from the α-proteobacterial ancestors of mitochondria have been lost or migrated into the nuclear genome, a few remain along with genes for tRNAs and ribosomal RNAs required for organellar translation of the remaining protein-coding genes. Mitochondria contain large, multisubunit protein complexes involved in electron transport and adenosine 5′-triphosphate (ATP) synthesis that, ancestrally, were entirely encoded in the endosymbiont genome, which are now encoded partly in the nuclear and partly in the organellar DNA. In addition to the inherent difficulty in coordinating gene expression between two genomes in different compartments, the large excess of mitochondrial genomes relative to the diploid nuclear genome in each cell (on the order of 1000:1 in most mammalian cells) adds to potential error in producing the proper stoichiometry of nuclear and mitochondrial encoded protein subunits. Thus, imprecision in coordinating expression between the nuclear and organelle genomes promotes incorrect stoichiometries of the subunits in protein complexes and invokes proteotoxic stress. Balancing subunit stoichiometry is dealt with by coordinating RNA transcription in the nucleus with protein translation in the mitochondrial matrix and by degrading extraneous protein subunits.

Another problem, at least for metazoan animals, is that their innate immune response pathways may recognize bacterially derived mitochondrial components as pathogen-associated molecular patterns (PAMPs) and generate inflammatory responses (*3*, *4*). Careful segregation of mitochondrial PAMPs from innate immune sensors within the cytosol and on cell surfaces and efficient disposal of damaged mitochondria are required to avoid autoinflammation.

Exacerbating the potential threats of proteotoxic stress and PAMP release to innate immune effectors, mitochondria are the center of the controlled burn of nutrients to carbon dioxide and water, generating ATP (*5*). Electrons from reduced nicotinamide adenine dinucleotide and flavin adenine dinucleotide, tunneling through inner mitochondrial membrane transport complexes to reduce molecular oxygen to water, occasionally escape and generate oxyradicals that can oxidize lipids and proteins in the mitochondrial membranes, especially those proximal to the electron transport channels. Thus, oxidative damage adds further demand for mitochondrial quality control mechanisms.

Mitochondrial DNA (mtDNA) is also subject to oxidative damage, mutations, and deletions. Within individual human cells, hundreds to thousands of mitochondrial genomes are packaged into nucleoids within the matrix compartment, surrounded by the inner and outer mitochondrial membranes (Fig. 1). In contrast to the one or two copies of the nuclear DNA that reproduces in mammals through sexual admixture of two parents' genomes and can recombine to mitigate mutation accumulation, mitochondria reproduce asexually. In contrast to bacteria, which can conjugate to exchange DNA and allow mutation removal, mitochondria in mammals are not known to do this with any efficiency. Thus, the largely clonal expansion of mtDNA carries the risk of mutational meltdown, which is known as Muller's ratchet, with scant mechanisms to revert mutations to wild-type sequences. The meltdown problem is exacerbated because mtDNA has higher DNA mutation rates than that of nuclear DNA owing to greater replication rates yielding inherent errors, as well as the proximity of mtDNA to electron transport-generated oxyradicals, which can lead to DNA mutations. Mitochondrial genomes are invariably passed down essentially uniparentally-maternally in mammals—presumably, to avoid competition among genetically variant mitochondria or more direct deleterious consequences of two distinct mtDNA genomes occupying the same cytoplasm, which is known as heteroplasmy (*6*). Although it is clear that the ontogeny of the female germ line selects the least mutated mitochondria for transmission to the next generation (*7*–*9*), it is less certain whether some processes, such as apoptosis or autophagy, which can eliminate damaged cells and mitochondria,

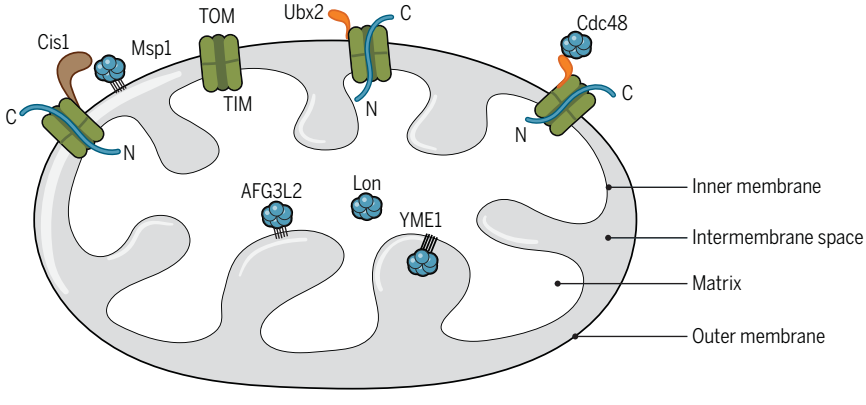

Fig. 1. The mitochondria has several distinct compartments that require distinct protein quality control processes. Mitochondria have an inner membrane that contains the electron transport machinery surrounding the Matrix compartment, which houses TCA cycle enzymes and the mtDNA. An outer membrane surrounds the intermembrane space. TOM and TIM import complexes transport proteins through the outer and inner membranes, respectively. Proteotoxic stress is mitigated by AAA proteases LON, YME1, and AFG3L2/SPG7 that degrade misfolded and superfluous proteins. The AAA ATPases p97/Cdc48 and ATAD1/Msp1 extract mislocalized proteins from the outer mitochondrial membrane and clogged import channels.

Surgical Neurology Branch, National Institute of Neurological Disorders and Stroke, NIH, Bethesda, MD 20892, USA.
***Corresponding author. Email: youler@ninds.nih.gov**

respectively, might also counteract this inexorable mutation accumulation in somatic cells.

Quality control processes to cope with mitochondrial burdens

Of the original α-proteobacterial genes, most of those that survived migrated to the nucleus over time. Of the thousand or so mitochondrial proteins in mammals, only 13 remain encoded in the mtDNA today. Perhaps one driver for gene migration from the mitochondrial genome to the nucleus is to coordinate protein expression transcriptionally and minimize proteotoxic disproportionality among proteins working together in the same pathway. Alternatively, gene transfer to the nucleus could leave less mtDNA vulnerable to Muller's ratchet (*10*). The 13 mtDNA protein-coding genes remaining in humans encode subunits of four large multisubunit protein complexes (named I, III, IV, and V) embedded in the inner mitochondrial membrane that are involved in oxidative phosphorylation (Ox/Phos). Why these few genes remain encoded in mtDNA is not clear; hypotheses center around challenges of transferring hydrophobic membrane proteins through the hydrophilic channels of the translocator of the outer membrane (TOM) and translocator of the inner membrane (TIM) protein import channels (Fig. 1), or mechanisms to insert hydrophobic proteins central to large protein complexes in the inner membrane (*11*). All the soluble metabolic and tricarboxylic acid (TCA) cycle enzymes located in the mitochondrial matrix are encoded in the nucleus, where their expression is coordinated. Recent work shows that mtDNA-encoded Ox/Phos subunit expression is indeed coordinated with nuclear encoded Ox/Phos protein expression and is regulated mainly at the translational level (*2*, *12*), and that mtDNA protein expression is tuned unidirectionally based on expression levels of nuclear encoded mitochondrial proteins (*13*). How mtDNA-encoded protein translation is linked to nuclear encoded protein complex assembly is becoming more clear (*14*).

Beyond regulation of RNA transcription and protein translation, backup processes on the degradation side of protein homeostasis deal with ensuing proteotoxic stress in several different compartments: the cytosol, the mitochondrial matrix, and in the two mitochondrial membranes (Fig. 1). Proteolysis in the mitochondrial matrix largely rebalances protein complex subunit stoichiometry by eliminating excess proteins imported from cytosolic translation of nuclear genes or translated in the matrix from mtDNA-encoded genes that misfold in the absence of interacting partners from the alternate genome (*15*). Piecemeal autophagy of mitochondrial subregions or fragments (Fig. 2A) may also play a role in extreme cases of protein misfolding, and mitochondria-derived vesicles may directly target outer mitochondrial membrane proteins to lysosomes (*16*–*19*).

Aspects of mitochondrial protein quality control have been known for many years. The proteases Lon and ClpX/P in the matrix, Yme1 anchored to the mitochondrial inner membrane facing the intermembrane space, and AFG3L2/SPG7 anchored to the mitochondrial inner membrane facing the matrix are at the center of protein quality control proteolysis (*15*). They are all ATP-dependent, AAA adenosine triphosphatase (ATPase) proteases with unfoldase activity that degrade misfolded and superfluous proteins. These AAA ATPases are all conserved in bacteria and represent primordial quality control mechanisms (*20*).

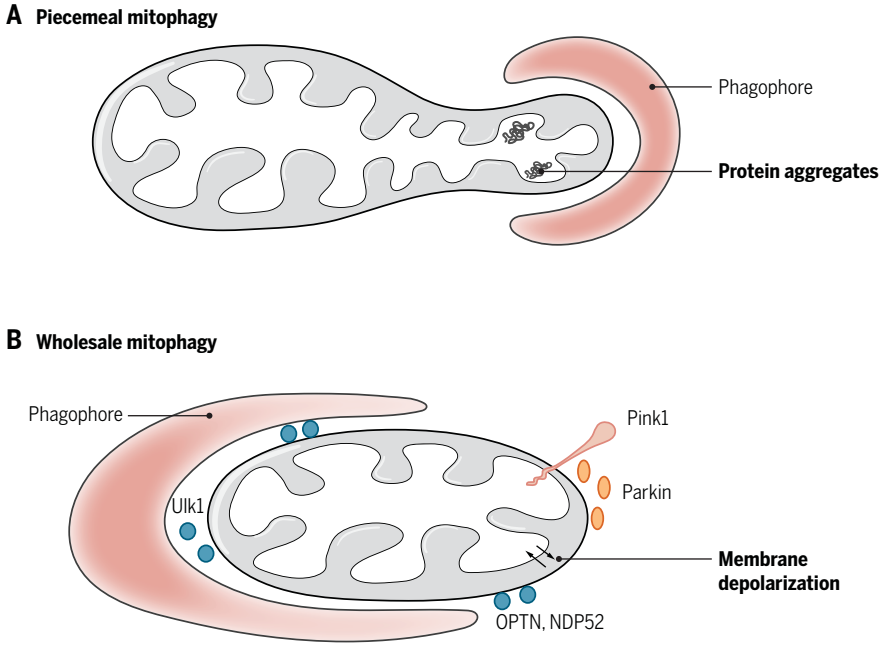

Fig. 2. Selective autophagy of mitochondrial proteins is a quality control process. (**A**) Piecemeal, also called bit by bit, mitophagy removes mitochondrial subdomains, which can selectively eliminate protein aggregates in the matrix. (**B**) Wholesale mitophagy of damaged and depolarized mitochondria mediated by PINK1/Parkin is suggested to mediate quality control and elimination of mitochondrial DAMPs to avoid inflammation.

A recent series of studies has revealed other pathways that deal with unfolded or misfolded matrix proteins and mitochondrial import defects. Transcription of certain nuclear encoded mitochondrial proteins is regulated by mitochondrial proteotoxic stress, leading to increased expression of mitochondrial chaperones that help fold proteins and proteases that degrade misfolded proteins. The original mammalian model to induce a mitochondrial unfolded protein response used overexpression of a deletion mutant of a mitochondrial protein, ornithine transcarbamylase (ΔOTC), which becomes insoluble in the matrix (*21*). ΔOTC expression in mammalian cells activates expression of the HSP60 chaperonin and protease ClpP in mitochondria (*21*). Chemical inhibition of Lon protease or the Hsp90 chaperone in mammalian cells also induces HSP60 expression (*22*). Autophagy can also eliminate misfolded ΔOTC selectively relative to other mitochondrial proteins (*23*). This would be consistent with a piecemeal or bit-by-bit mitophagy of mitochondrial subdomains (Fig. 2A) (*18*, *24*).

In *Caenorhabditis elegans*, mechanistic understanding of how the mitochondrial unfolded protein response activates transcription has been delineated (*25*). A transcription factor, ATFS-1, has both a mitochondrial import signal and a nuclear localization signal and is normally imported into mitochondria, degraded, and thereby repressed (*26*). Upon proteotoxic stress or other stresses that impair mitochondrial protein import, such as loss of mitochondrial membrane potential, ATFS-1 escapes elimination through mitochondrial import and traffics to the nucleus to induce transcription of a variety of mitochondrial genes, including the chaperonin HSP60 (Fig. 3). As mitochondria recover from proteotoxic stress, they proceed to down-regulate ATFS-1 through import and degradation. Atf4 and Atf5 have roles in mitochondrial stress maintenance and appear to function as mammalian orthologs of ATFS-1 (*22*, *27*, *28*). In mammals, mammalian target of rapamycin complex 1 (mTORC1) orchestrates a transcriptional response to myopathy caused by mtDNA deletions. Atf4 and Atf5, one-carbon metabolism leading to tetrahydrofolate formylation, and the metabolic cytokine FGF21 are all induced by this form of mitochondrial stress (*29*).

Using yeast, a series of recent studies explored the consequences of mitochondrial protein import blockade or mitochondrial membrane protein misfolding. A decrease in cytosolic protein translation occurs upon mitochondrial proteotoxic stress as well as improved proteasome subunit assembly, which is required for cells to cope with the proteotoxic stress (*30*, *31*). When hydrophobic inner mitochondrial membrane proteins are overexpressed, they may clog the TOM/TIM import channels. Cis1 and Msp1 bind to the TOM complex and clear excess import intermediates (Fig. 1) (*32*). Msp1 in yeast and the ortholog ATAD1 in mammals also

dislodge at least some tail-anchored proteins, such as Pex15, from the outer mitochondrial membrane, allowing protein retargeting to their proper location in the peroxisomal membrane (*33*, *34*). Clogging of mitochondrial import channels induces the heat shock factor Hsf1, which increases Rpn4, a transcription factor that increases proteasome subunit expression (*35*). Consistent with (*32*), Pdr3, which induces transcription of CIS1, is another downstream target of Rpn4. Hsf1 also induces a number of cytosolic chaperones and represses cytosolic protein translation. Interestingly, clogging mitochondrial import represses nuclear encoded TCA cycle and Ox/Phos gene transcription. Ox/Phos protein repression is mediated through inhibition of the HAP transcription complex. How HAP is inhibited, which is suggested to be posttranslational, remains unclear. As for mtDNA-encoded proteins, mitochondrial translation machinery and translation itself (but not transcription) is markedly down-regulated after clogging (*35*). This would help balance mtDNA-encoded protein production with the loss of import of nuclear encoded proteins, which is consistent with other studies that use Lon inhibition in mammalian cells (*22*), and during mitochondrial biogenesis in yeast (*13*). Removal of proteins stuck in the TOM channel uses the AAA ATPase Cdc48 and an adaptor Ubx2 that is constitutively bound to the TOM complex. This work also implicates ubiquitination of stuck substrates, although the ubiquitin ligase that mediates ubiquitination remains unknown (*36*). If mitochondrial proteins are stalled during translation, Vms1 prevents protein aggregation that would occur in the matrix compartment downstream of ribosome quality control modifications (*37*). In mammalian cells, a protein family with ubiquitin-like domains and ubiquitin-binding domains, called ubiquilins, bind to tail-anchored outer mitochondrial membrane proteins and redirect at least matrix proteins unable to enter the mitochondria for proteosomal degradation (*38*).

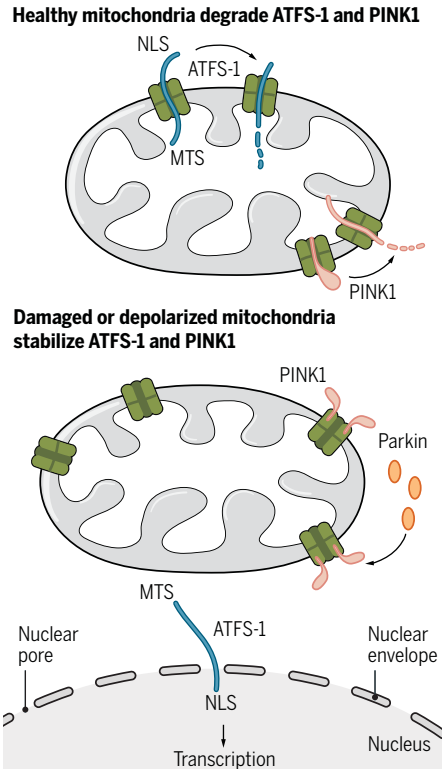

Fig. 3. Mitochondrial protein import regulates two quality control processes. The transcription factor ATFS-1 and the ubiquitin kinase PINK1 are regulated through mitochondrial fidelity. (**Top**) Healthy mitochondria degrade ATFS-1 and PINK1. When mitochondria are damaged and fail to import ATFS-1 and PINK1, their degradation is prevented. ATFS-1 then traffics to the nucleus and induces the transcription of mitochondrial chaperones and proteases. PINK1 accumulates bound to the outer mitochondrial membrane TOM complex, where it phosphorylates ubiquitin already attached to outer mitochondrial membrane proteins. (**Bottom**) These phospho-ubiquitin chains recruit Parkin from the cytosol and activate Parkin E3 ubiquitin ligase activity. Parkin ubiquitinates more mitochondrial proteins for PINK1 to phosphorylate, forming an amplification loop. These ubiquitin chains recruit autophagy receptors that induce autophagosomal engulfment selective for the damaged mitochondria.

Thus, numerous processes maintain endosymbiont proteostasis, including (i) increasing transcription of chaperones; (ii) inhibition of mtDNA gene translation; (iii) inhibition of nuclear encoded mitochondrial gene transcription; (iv) proteolysis of mislocalized and misfolded mitochondrial proteins in several compartments, including the cytosol and mitochondrial subcompartments; (v) mitochondrial-derived vesicles; and (vi) autophagy, both piecemeal and likely wholesale. When these processes fail, mitochondria can lose metabolic capacity, leading to numerous diseases commonly linked to the nervous system (*39*). Additionally, a failure of quality control leading to mitochondrial breakdown may also activate inflammation, with severe consequences.

Mitophagy at the mtDNA level

Mitochondria accumulate mutations during aging and are purified during maternal oocyte development, starting each generation of mammals with a homogenous (homoplastic) and fully functional mitochondrial genome. In *Drosophila*, deleterious mtDNA mutations are sensed based on mitochondrial function, and impaired mitochondria are eliminated through mitophagy (*9*). In *C. elegans* and in mammals, paternal mtDNA in sperm is eliminated upon fertilization, at least in part through autophagy of the paternal mitochondria (*40*–*42*).

It is not clear whether quality control exists at the level of mtDNA in somatic cells. Neither mouse liver hepatocytes nor human colonic epithelial cells display purifying selection against the accumulation of deleterious mtDNA mutations (*7*, *43*). However, inherited mtDNA mutations, in contrast to sporadic mutations, can be selected against in proliferating tissues (*44*, *45*). Whether this selection occurs intracellularly at the mtDNA level or through the death of stem cells with high mutation loads is not yet clear. In *Drosophila*, there is also evidence against purifying selection in somatic tissues (*46*). Studies of cultured mammalian cell lines that contain a mixture of wild-type and mutant mtDNA, called cybrids, indicate that mitophagy has the potential to select against certain deleterious mtDNA mutations but not others (*47*, *48*). Because mitochondria continuously fuse and divide in many tissues and cultured cells (*49*), mixing their contents, physical links between a deleterious gene product and the mtDNA encoding the mutant gene appear to be tenuous. Thus, wild-type and mutant mtDNA, when both are present in heteroplasmic cells, would be challenging to distinguish on the basis of their gene products that become mixed throughout the mitochondriome. Furthermore, more rapidly diffusible mitochondrial components such as tRNA would be harder to physically link to mutant mtDNA nucleoids than to large membrane-spanning electron transport complexes, and thus more challenging to select against under heteroplasmic conditions. Consistently, mutations in tRNA genes are substantially overrepresented among heteroplasmic mtDNA mutation disease patients relative to protein-coding mutations. Not only may mutant DNA be selected against, mitochondrial proteins in yeast and human cells can be segregated and, in human cells, destroyed, cleansing the mitochondriome of debris (*18*, *50*). This may be related to processes in bacteria in which daughter cells differentially inherit damaged proteins to avoid a posttranscriptional form of meltdown with the gradual accumulation of protein aggregates over generations (*51*).

Mitochondria share PAMPs with bacteria

Another challenge for mitochondria is to maintain sequestration of their contents from cytosolic and extracellular innate immune sensors. During metazoan evolution, immune pathways arose in invertebrates that innately recognize virus and bacterial PAMPs. These pathways involve Toll-like receptors (TLRs), nucleotide-binding oligomerization domain-containing protein (NOD) receptors, and certain G protein–coupled receptors that recognize bacterial components, such as the bacterial cell wall lipopolysaccharide. Activation of innate immune pathways by PAMPs triggers intracellular signaling pathways to induce chemotaxis of monocytes, secretion of cytokines, and type 1 interferons, which transmit the danger signal to neighboring cells. Pathways downstream of innate immune signaling further link inflammation to adaptive immune responses in vertebrates (*52*).

Viral double-stranded DNA (dsDNA) in the cytosol is recognized by the cyclic guanosine monophosphate–adenosine monophosphate (cGAMP) synthase (cGAS)–stimulator of inferon genes (STING) pathway and the absent in melanoma 2 (AIM2) inflammasome, whereas extracellular or

phagocytosed DNA is recognized by TLR9 (*53*–*55*). Viral double-stranded RNA (dsRNA) is recognized by the relatives RIG I and MDA5 (*56*) and by the oligoadenylate synthetase (OAS)/ribonuclease L (RNase L) antiviral pathway (*57*). Interestingly, cGAS that binds dsDNA is evolutionarily related to OAS that binds dsRNA (*58*). They both synthesize 2′5′–linked nucleotides upon double-stranded polynucleotide binding to activate downstream effectors: STING to induce interferon-β (IFNβ) and RNase L to degrade RNA, respectively. Furthermore, the type III CRISPR-Cas system shares overlapping mechanisms. In bacteria, upon the CRISPR interference complex binding to invader RNA, the Cas10 subunit links ATP into a 3′-5′–linked cyclic hexaadenylate that in turn activates the RNase activity of Csm6. Thus, some nucleic acid–sensing pathways of mammalian innate immunity appear to have evolved from primordial bacterial defense mechanisms (*59*, *60*).

Not surprisingly, some antibacterial innate immune receptors can cross-react with molecules that mitochondria share with bacteria, called damage-associated molecular patterns (DAMPs). Mitochondrial DAMPs are associated with poor prognosis in cardiovascular disease (*61*), acute respiratory distress syndrome (*62*), and several other disorders (*63*). The innate immune receptors are known for several mitochondrial DAMPs, suggesting pathways that may be targeted to ameliorate disease.

Bacterial protein translation depends on *N*-formylmethonine as a start codon, distinct from cytosolic eukaryotic translation but shared with the mitochondrial matrix translation machinery. Two G protein–coupled receptors, FPR1 and FPR2, reside on the plasma membrane of neutrophils and macrophages facing the extracellular space that bind and signal the presence of *N*-formyl peptides, inducing chemotaxis of the white blood cells toward the *N*-formyl peptide source—either bacterial or mitochondrial (*64*). This innate immune pathway would detect mitochondrial *N*-formyl peptides after cell and tissue damage that release the DAMP into the extracellular space (*65*). Cardiolipin, a dimeric phospholipid found in bacteria and in the mitochondrial inner membrane, is also a potential DAMP linked to inflammation. NLRP3 appears to directly interact with cardiolipin, and inflammasome activation has been correlated with cardiolipin levels in macrophages (*66*).

Among several stress signals, NLRP3 also recognizes mitochondrial damage that stems from reactive oxygen radicals (ROS) during Ox/Phos; although the mechanism of how ROS can activate NLRP3 remains unclear, it may involve changes in cytosolic potassium levels (*67*). Upon activation, NLRP3 forms a heptameric ring that binds ASC and procaspase 1, cleaving and activating caspase 1 based on proximity, which in turn processes the proforms of cytokines interleukin-1β (IL-1β) and IL-18 to initiate inflammation (Fig. 4A). When mitochondria are damaged, they are normally eliminated by the phosphatase and tensin homolog (PTEN)–induced putative kinase protein 1 (PINK1)/Parkin mitophagy pathway in macrophages (Fig. 2B). Loss of Parkin or p62, the ubiquitin-binding autophagy receptor, in macrophages causes an accumulation of damaged mitochondria and excessive activation of the NLRP3 inflammasome (*68*). Oxidized mtDNA in the cytosol binds and activates the NLRP3 (*69*) but not the AIM2 inflammasome (*68*), adding to the broad molecular diversity of NLRP3 activators (*70*). Mitochondrial ROS is thought to lead to the oxidization of the mtDNA. In contrast to the NLRP3 inflammasome activation in macrophages, mtDNA activates the cGAS/STING pathway of IFNβ induction in other cell types. When the mtDNA nucleoid is disrupted, mtDNA is released to the cytosol, where it activates cGAS and STING-induced inflammation (*71*). Preventing mitochondrial fusion in muscle tissue activates TLR9 and nuclear factor κB (NF-κB) expression, apparently from release of mtDNA and activation of macrophages cell-nonautonomously (*72*). In *C. elegans*, the mitochondrial proteotoxic stress sensor ATFS-1 induces innate immune gene expression (*73*). In some of the above scenarios, mtDNA is thought to actively participate in mammalian innate immunity and host defense and not to simply represent deleterious off-target inflammatory response to be avoided. Such models are hard to test in vivo because mtDNA cannot be removed from most cells in mammals except in cultured cell lines.

In early stages of apoptosis, if caspases are blocked (Fig. 4), mtDNA can be released from mitochondria when the proapoptotic Bcl-2 family members Bax and Bak permeabilize the outer membrane. First the inner membrane herniates through Bax pores in the outer membrane and then ruptures to release cytosolic mtDNA. This mtDNA activates cGAS and STING induction of IFNβ expression (*74*, *75*). Normally, apoptosis is immunologically silent as caspases eliminate the cGAS induction of interferon. However, low-level activation of Bax and Bak without caspase activation can induce cytokine expression and bacterial resistance (*76*).

Mitochondrial dsRNA also activates IFNβ production if its catabolism within mitochondria is inhibited (*77*). Mitochondrial dsRNA appears to escape mitochondria by way of Bax and Bak pores and then binds MDA5, which activates mitochondrial antiviral signaling (MAVS) and subsequent IFNβ production. Interestingly, MAVS has a C-terminal hydrophobic tail that localizes it to the mitochondrial outer membrane, and without mitochondrial localization, MAVS fails to signal cytokine production (*78*). However, the role of mitochondrial localization of MAVS remains unclear.

Control of mitochondrial DAMPs

One pathway that removes mitochondrial DAMPs involves mitophagy and lysosomal degradation. Mouse cardiomyocytes that lack lysosomal deoxyribonuclease II fail to degrade mitochondria, leading to extracellular mtDNA activating TLR9

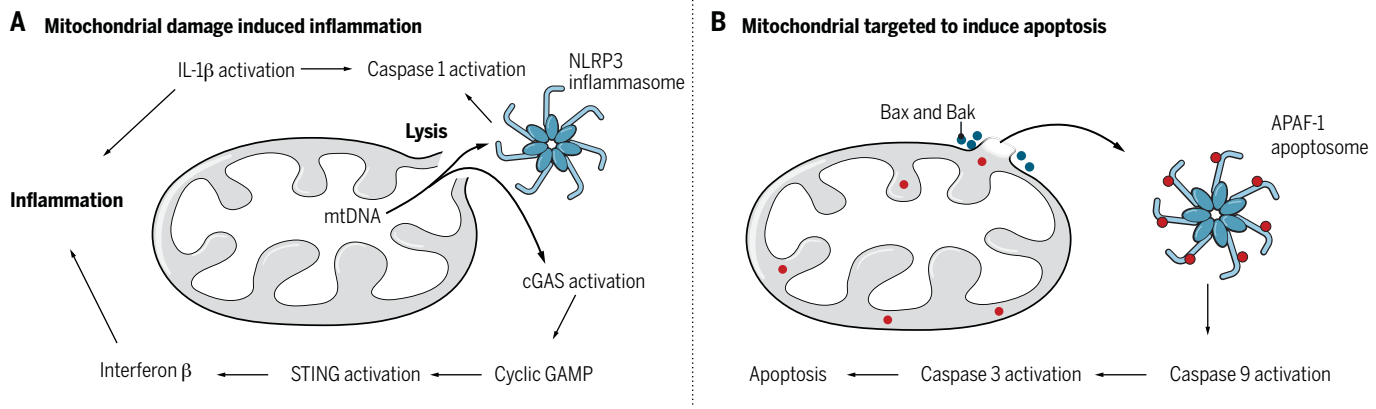

Fig. 4. mtDNA activation of inflammation has similarities to apoptosis. (**A**) When mitochondria are sufficiently damaged to break the membranes, mtDNA leaks into the cytoplasm, where it can activate the NLRP3 inflammasome in macrophages and cGAS in other cell types. This leads to IL-1β and IFN-β cytokine activation, respectively, and inflammation. (**B**) The apoptosome, which resembles the inflammasome, induces apoptosis and a form of innate immunity. When the outer mitochondrial membrane is permeabilized by BCL-2 family proteins (blue circles), cytochrome c (red circles) is released, which activates the apoptosome. The apoptosome, a relative of the inflammasome, activates Caspase 9 to induce apoptotic cell death. This pathway is another innate defense mechanism to prevent the spread of viruses in mammalian tissues.

and inflammation (79). A well-characterized pathway that selectively removes damaged mitochondria involves the ubiquitin kinase PINK1 and the ubiquitin ligase Parkin (Fig. 3). Like the transcription factor ATFS-1—which is rescued from degradation by mitochondrial stress, leading to the loss of membrane potential—PINK1 is normally imported into mitochondria, clipped by the protease PARL embedded in the inner mitochondrial membrane, and degraded by the N-end rule for proteosomal proteolysis (80). Damage to mitochondria that prevents protein import prevents PINK1 degradation, allowing it to accumulate bound to the outer mitochondrial membrane (81). There, it phosphorylates ubiquitin that has been previously attached to outer mitochondrial membrane proteins that face the cytosol, which serve as receptors for cytosolic Parkin. Parkin binding to phospho-ubiquitin on mitochondria activates Parkin ubiquitin ligase activity, yielding more ubiquitin chains on outer-membrane proteins for PINK1 to phosphorylate. This yields a powerful amplification loop (80). The ubiquitin chains on mitochondria recruit autophagy receptors such as NDP52 that can directly recruit the Ulk1 kinase complex to induce autophagosome biogenesis (82). Importantly, the loss of either PINK1 or Parkin induces early onset Parkinson's disease. The fact that damaged mitochondria are selectively degraded suggests that mitochondrial quality control may be important for protecting dopaminergic neurons that are lost in Parkinson's disease. This model is compatible with a variety of other evidence that mitochondrial defects are involved in Parkinson's disease (83).

Mice that lack either PINK1 or Parkin do not display parkinsonism-related phenotypes unless stressed from mtDNA mutation accumulation (84). Under such conditions, mice display an increase in serum amounts of mtDNA and the cytokines IL-6 and IFNβ mediated by the cGAS STING DNA–sensing pathway (85). Because evidence is accumulating that inflammation may lead to Parkinson's disease (86), a key finding is that blocking the inflammation in Parkin-null mice through loss of STING activity prevents neurodegeneration (85). These results lead to the model that PINK1/Parkin–mediated mitophagy is important to prevent mtDNA from activating the innate immunity that can lead to neuron loss. Because cGAMP can transfer between cells (87–89), it will be important to understand what cell types release the mtDNA and cGAS activation and which cell types express STING and secrete the cytokines, ultimately causing neuron death. After the inflammatory stress of chronic exposure to lipopolysaccharide, a classical PAMP, mice in which Parkin was deleted display neurodegeneration (90). Mice in which Parkin or PINK1 was deleted also display an increased immune response to a mitochondrial antigen (91). It is thought that Parkin-mediated autophagy mitigates self-reactivity, and interestingly bacterial infection of mice in which PINK1 was deleted leads to impaired dopaminergic neuron function (92).

STING's primordial function in metazoans appears to induce autophagy and not interferon production (93). Autophagy that leads to lysosomal destruction of bacteria can be considered another branch of innate immunity and shares some common molecular mechanisms with mitophagy, such as using the autophagy receptors Optineurin and NDP52 and the kinase Tbk1 (94). Although Tbk1 is also required for STING activation of interferon regulatory factor–3 (IRF3) to drive IFNβ expression, STING appeared in metazoan evolution as an autophagy inducer before acquiring the Tbk1 interaction domain. cGAS also appeared with the earliest metazoans, such as anemones (58). However, the DNA-binding domain of cGAS was not apparent until vertebrates, when IFN defense pathways appeared during evolution. It remains unclear what may activate insect and more primitive cGAS homologs. Similarly, OAS appeared in sponges, whereas RNase L did not appear until much later in vertebrate evolution (in birds and mammals) (95). PINK1 and Parkin appeared somewhat later in evolution than cGAS and STING, not appearing in sponges or anemones but in nematodes, insects, and vertebrates. Both *C. elegans* and *Drosophila*, lacking Parkin, display increased expression of innate immune genes (73, 96, 97), supporting the proposed link between mitophagy and DAMP removal. Thus, this mitophagy pathway may be a relatively late evolutionarily patch to mitigate innate immune signaling by mtDNA.

Mitochondrial induced apoptosis—Another innate immune mechanism

Mitochondrial cytochrome c, the Ox/Phos electron carrier located between the outer and inner membranes, could be considered the ultimate DAMP. It is released into the cytosol by Bax and Bak to induce apoptosis. Once in the cytosol, cytochrome c binds to monomeric apoptotic peptidase activating factor 1 (APAF-1), triggering it to form the heptameric apoptosome, a complex similar to the NLRP3 inflammasome (Fig. 4B). The assembled apoptosome recruits caspase 9, where induced proximity of this protease effects self-cleavage and proteolytic activation and subsequent activation of caspase 3 and apoptosis. This is similar to the related NLRP3 inflammasome activation caspase 1, which processes IL-1β to promote inflammation. Many viruses express proteins that block apoptosis (98), indicating that apoptosis is a form of innate immunity. Cytochrome c is conserved in bacteria, and apoptosis may have evolved from an innate immune bacterial sensor to induce cell death after mitochondrial damage. However, cytochrome c activation of APAF-1 does not induce inflammation but prevents it through elimination of mitochondrial DAMPs and other cell debris to avoid inflammation through the sterile death process of apoptosis (99).

Future perspectives

Mitochondria are central to our energy supply and metabolism. Understanding the particular challenges for mitochondria that stem from their endosymbiont origin is advancing rapidly and includes how gene expression is coordinating between two genomes, how the integrity of the mitochondrial genome is maintained, and how inflammation caused by loss of mitochondrial integrity is avoided. How some of these challenges are mitigated in yeast is becoming clear, but how these pathways and others work in the variety of different cell types in humans—in vivo, with very different energy and metabolic demands—remains to be elucidated. Disruptions to mitochondrial homeostasis caused by excessive damage or insufficient repair lead to a wide array of human diseases, many with muscle and/or neuron phenotypes, and understanding how failures in mitochondrial maintenance lead to human diseases is in its infancy. There are undoubtedly more medical consequences to the risks associated with endosymbiosis than are currently appreciated. mtDNA mutations and inflammation increase during normal human aging. Whether mitochondrial dysfunction contributes to inflammaging would be important to know. The rapid progress on these topics in the past few years will continue to unveil how the delicate balance between host and endosymbiont is maintained.

REFERENCES AND NOTES

1. J. D. Woodson, J. Chory, Coordination of gene expression between organellar and nuclear genomes. *Nat. Rev. Genet.* **9**, 383–395 (2008). doi: 10.1038/nrg2348; pmid: 18368053
2. R. S. Isaac, E. McShane, L. S. Churchman, The multiple levels of mitonuclear coregulation. *Annu. Rev. Genet.* **52**, 511–533 (2018). doi: 10.1146/annurev-genet-120417-031709; pmid: 30230928
3. A. P. West, G. S. Shadel, Mitochondrial DNA in innate immune responses and inflammatory pathology. *Nat. Rev. Immunol.* **17**, 363–375 (2017). doi: 10.1038/nri.2017.21; pmid: 28393922
4. S. E. Weinberg, L. A. Sena, N. S. Chandel, Mitochondria in the regulation of innate and adaptive immunity. *Immunity* **42**, 406–417 (2015). doi: 10.1016/j.immuni.2015.02.002; pmid: 25786173
5. J. Nunnari, A. Suomalainen, Mitochondria: In sickness and in health. *Cell* **148**, 1145–1159 (2012). doi: 10.1016/j.cell.2012.02.035; pmid: 22424226
6. M. S. Sharpley *et al*., Heteroplasmy of mouse mtDNA is genetically unstable and results in altered behavior and cognition. *Cell* **151**, 333–343 (2012). doi: 10.1016/j.cell.2012.09.004; pmid: 23063123
7. J. B. Stewart *et al*., Strong purifying selection in transmission of mammalian mitochondrial DNA. *PLOS Biol.* **6**, e10 (2008). doi: 10.1371/journal.pbio.0060010; pmid: 18232733
8. V. I. Floros *et al*., Segregation of mitochondrial DNA heteroplasmy through a developmental genetic bottleneck in human embryos. *Nat. Cell Biol.* **20**, 144–151 (2018). doi: 10.1038/s41556-017-0017-8; pmid: 29335530
9. T. Lieber, S. P. Jeedigunta, J. M. Palozzi, R. Lehmann, T. R. Hurd, Mitochondrial fragmentation drives selective removal of deleterious mtDNA in the germline. *Nature* **570**, 380–384 (2019). doi: 10.1038/s41586-019-1213-4; pmid: 31092924
10. O. G. Berg, C. G. Kurland, Why mitochondrial genes are most often found in nuclei. *Mol. Biol. Evol.* **17**, 951–961 (2000). doi: 10.1093/oxfordjournals.molbev.a026376; pmid: 10833202
11. K. L. Adams, J. D. Palmer, Evolution of mitochondrial gene content: Gene loss and transfer to the nucleus. *Mol. Phylogenet. Evol.* **29**, 380–395 (2003). doi: 10.1016/S1055-7903(03)00194-5; pmid: 14615181
12. D. U. Mick, T. D. Fox, P. Rehling, Inventory control: Cytochrome c oxidase assembly regulates mitochondrial translation. *Nat. Rev. Mol. Cell Biol.* **12**, 14–20 (2011). doi: 10.1038/nrm3029; pmid: 21179059
13. M. T. Couvillion, I. C. Soto, G. Shipkovenska, L. S. Churchman, Synchronized mitochondrial and cytosolic translation programs. *Nature* **533**, 499–503 (2016). doi: 10.1038/nature18015; pmid: 27225121
14. R. Richter-Dennerlein *et al*., Mitochondrial protein synthesis adapts to influx of nuclear-encoded protein. *Cell* **167**, 471–483. e10 (2016). doi: 10.1016/j.cell.2016.09.003; pmid: 27693358

15. M. Koppen, T. Langer, Protein degradation within mitochondria: Versatile activities of AAA proteases and other peptidases. *Crit. Rev. Biochem. Mol. Biol.* **42**, 221–242 (2007). doi: 10.1080/10409230701380452; pmid: 17562452
16. V. Soubannier *et al*., A vesicular transport pathway shuttles cargo from mitochondria to lysosomes. *Curr. Biol.* **22**, 135–141 (2012). doi: 10.1016/j.cub.2011.11.057; pmid: 22226745
17. F. Le Guerroué *et al*., Autophagosomal content profiling reveals an LC3C-dependent piecemeal mitophagy pathway. *Mol. Cell* **68**, 786–796.e6 (2017). doi: 10.1016/j.molcel.2017.10.029; pmid: 29149599
18. J. L. Burman *et al*., Mitochondrial fission facilitates the selective mitophagy of protein aggregates. *J. Cell Biol.* **216**, 3231–3247 (2017). doi: 10.1083/jcb.201612106; pmid: 28893839
19. E. S. Vincow *et al*., Autophagy accounts for approximately one-third of mitochondrial protein turnover and is protein selective. *Autophagy* **2019**, 1–14 (2019). doi: 10.1080/15548627.2019.1586258; pmid: 30865561
20. R. T. Sauer, T. A. Baker, AAA^+ proteases: ATP-fueled machines of protein destruction. *Annu. Rev. Biochem.* **80**, 587–612 (2011). doi: 10.1146/annurev-biochem-060408-172623; pmid: 21469952
21. Q. Zhao *et al*., A mitochondrial specific stress response in mammalian cells. *EMBO J.* **21**, 4411–4419 (2002). doi: 10.1093/emboj/cdf445; pmid: 12198143
22. C. Münch, J. W. Harper, Mitochondrial unfolded protein response controls matrix pre-RNA processing and translation. *Nature* **534**, 710–713 (2016). doi: 10.1038/nature18302; pmid: 27350246
23. S. M. Jin, R. J. Youle, The accumulation of misfolded proteins in the mitochondrial matrix is sensed by PINK1 to induce PARK2/Parkin-mediated mitophagy of polarized mitochondria. *Autophagy* **9**, 1750–1757 (2013). doi: 10.4161/auto.26122; pmid: 24149988
24. J. Y. Yang, W. Y. Yang, Bit-by-bit autophagic removal of parkin-labelled mitochondria. *Nat. Commun.* **4**, 2428 (2013). doi: 10.1038/ncomms3428; pmid: 24013556
25. A. Melber, C. M. Haynes, UPR^{mt} regulation and output: A stress response mediated by mitochondrial-nuclear communication. *Cell Res.* **28**, 281–295 (2018). doi: 10.1038/cr.2018.16; pmid: 29424373
26. A. M. Nargund, M. W. Pellegrino, C. J. Fiorese, B. M. Baker, C. M. Haynes, Mitochondrial import efficiency of ATFS-1 regulates mitochondrial UPR activation. *Science* **337**, 587–590 (2012). doi: 10.1126/science.1223560; pmid: 22700657
27. P. M. Quirós *et al*., Multi-omics analysis identifies ATF4 as a key regulator of the mitochondrial stress response in mammals. *J. Cell Biol.* **216**, 2027–2045 (2017). doi: 10.1083/jcb.201702058; pmid: 28566324
28. C. J. Fiorese *et al*., The transcription factor ATF5 mediates a mammalian mitochondrial UPR. *Curr. Biol.* **26**, 2037–2043 (2016). doi: 10.1016/j.cub.2016.06.002; pmid: 27426517
29. N. A. Khan *et al*., mTORC1 regulates mitochondrial integrated stress response and mitochondrial myopathy progression. *Cell Metab.* **26**, 419–428.e5 (2017). doi: 10.1016/j.cmet.2017.07.007; pmid: 28768179
30. L. Wrobel *et al*., Mistargeted mitochondrial proteins activate a proteostatic response in the cytosol. *Nature* **524**, 485–488 (2015). doi: 10.1038/nature14951; pmid: 26245374
31. X. Wang, X. J. Chen, A cytosolic network suppressing mitochondria-mediated proteostatic stress and cell death. *Nature* **524**, 481–484 (2015). doi: 10.1038/nature14859; pmid: 26192197
32. H. Weidberg, A. Amon, MitoCPR-A surveillance pathway that protects mitochondria in response to protein import stress. *Science* **360**, eaan4146 (2018). doi: 10.1126/science.aan4146; pmid: 29650645
33. V. Okreglak, P. Walter, The conserved AAA-ATPase Msp1 confers organelle specificity to tail-anchored proteins. *Proc. Natl. Acad. Sci. U.S.A.* **111**, 8019–8024 (2014). doi: 10.1073/pnas.1405755111; pmid: 24821790
34. Y. C. Chen *et al*., Msp1/ATAD1 maintains mitochondrial function by facilitating the degradation of mislocalized tail-anchored proteins. *EMBO J.* **33**, 1548–1564 (2014). doi: 10.15252/embj.201487943; pmid: 24843043
35. F. Boos *et al*., Mitochondrial protein-induced stress triggers a global adaptive transcriptional programme. *Nat. Cell Biol.* **21**, 442–451 (2019). doi: 10.1038/s41556-019-0294-5; pmid: 30886345
36. C. U. Mårtensson *et al*., Mitochondrial protein translocation-associated degradation. *Nature* **569**, 679–683 (2019). doi: 10.1038/s41586-019-1227-y; pmid: 31118508
37. T. Izawa, S. H. Park, L. Zhao, F. U. Hartl, W. Neupert, Cytosolic protein Vms1 links ribosome quality control to mitochondrial and cellular homeostasis. *Cell* **171**, 890–903.e18 (2017). doi: 10.1016/j.cell.2017.10.002; pmid: 29107329
38. E. Itakura *et al*., Ubiquilins chaperone and triage mitochondrial membrane proteins for degradation. *Mol. Cell* **63**, 21–33 (2016). doi: 10.1016/j.molcel.2016.05.020; pmid: 27345149
39. M. Patron, H. G. Sprenger, T. Langer, m-AAA proteases, mitochondrial calcium homeostasis and neurodegeneration. *Cell Res.* **28**, 296–306 (2018). doi: 10.1038/cr.2018.17; pmid: 29451229
40. R. Rojansky, M. Y. Cha, D. C. Chan, Elimination of paternal mitochondria in mouse embryos occurs through autophagic degradation dependent on PARKIN and MUL1. *eLife* **5**, e17896 (2016). doi: 10.7554/eLife.17896; pmid: 27852436
41. M. Sato, K. Sato, Degradation of paternal mitochondria by fertilization-triggered autophagy in C. elegans embryos. *Science* **334**, 1141–1144 (2011). doi: 10.1126/science.1210333; pmid: 21998252
42. S. Al Rawi *et al*., Postfertilization autophagy of sperm organelles prevents paternal mitochondrial DNA transmission. *Science* **334**, 1144–1147 (2011). doi: 10.1126/science.1211878; pmid: 22033522
43. L. C. Greaves *et al*., Comparison of mitochondrial mutation spectra in ageing human colonic epithelium and disease: Absence of evidence for purifying selection in somatic mitochondrial DNA point mutations. *PLOS Genet.* **8**, e1003082 (2012). doi: 10.1371/journal.pgen.1003082; pmid: 23166522
44. R. Filograna *et al*., Modulation of mtDNA copy number ameliorates the pathological consequences of a heteroplasmic mtDNA mutation in the mouse. *Sci. Adv.* **5**, eaav9824 (2019). doi: 10.1126/sciadv.aav9824; pmid: 30949583
45. T. Su *et al*., Inherited pathogenic mitochondrial DNA mutations and gastrointestinal stem cell populations. *J. Pathol.* **246**, 427–432 (2018). doi: 10.1002/path.5156; pmid: 30146801
46. C. L. Samstag *et al*., Deleterious mitochondrial DNA point mutations are overrepresented in *Drosophila* expressing a proofreading-defective DNA polymerase γ. *PLOS Genet.* **14**, e1007805 (2018). doi: 10.1371/journal.pgen.1007805; pmid: 30452458
47. D. F. Suen, D. P. Narendra, A. Tanaka, G. Manfredi, R. J. Youle, Parkin overexpression selects against a deleterious mtDNA mutation in heteroplasmic cybrid cells. *Proc. Natl. Acad. Sci. U.S.A.* **107**, 11835–11840 (2010). doi: 10.1073/pnas.0914569107; pmid: 20547844
48. R. W. Gilkerson *et al*., Mitochondrial autophagy in cells with mtDNA mutations results from synergistic loss of transmembrane potential and mTORC1 inhibition. *Hum. Mol. Genet.* **21**, 978–990 (2012). doi: 10.1093/hmg/ddr529; pmid: 22080835
49. J. R. Friedman, J. Nunnari, Mitochondrial form and function. *Nature* **505**, 335–343 (2014). doi: 10.1038/nature12985; pmid: 24429632
50. A. L. Hughes, C. E. Hughes, K. A. Henderson, N. Yazvenko, D. E. Gottschling, Selective sorting and destruction of mitochondrial membrane proteins in aged yeast. *eLife* **5**, e13943 (2016). doi: 10.7554/eLife.13943; pmid: 27097106
51. A. B. Lindner, R. Madden, A. Demarez, E. J. Stewart, F. Taddei, Asymmetric segregation of protein aggregates is associated with cellular aging and rejuvenation. *Proc. Natl. Acad. Sci. U.S.A.* **105**, 3076–3081 (2008). doi: 10.1073/pnas.0708931105; pmid: 18287048
52. A. Iwasaki, R. Medzhitov, Control of adaptive immunity by the innate immune system. *Nat. Immunol.* **16**, 343–353 (2015). doi: 10.1038/ni.3123; pmid: 25789684
53. J. Lugrin, F. Martinon, The AIM2 inflammasome: Sensor of pathogens and cellular perturbations. *Immunol. Rev.* **281**, 99–114 (2018). doi: 10.1111/imr.12618; pmid: 29247998
54. G. N. Barber, STING: Infection, inflammation and cancer. *Nat. Rev. Immunol.* **15**, 760–770 (2015). doi: 10.1038/nri3921; pmid: 26603901
55. A. Ablasser, Z. J. Chen, cGAS in action: Expanding roles in immunity and inflammation. *Science* **363**, eaat8657 (2019). doi: 10.1126/science.aat8657; pmid: 30846571
56. H. Kato, T. Fujita, RIG-I-like receptors and autoimmune diseases. *Curr. Opin. Immunol.* **37**, 40–45 (2015). doi: 10.1016/j.coi.2015.10.002; pmid: 26530735
57. R. H. Silverman, Viral encounters with 2′,5′-oligoadenylate synthetase and RNase L during the interferon antiviral response. *J. Virol.* **81**, 12720–12729 (2007). doi: 10.1128/JVI.01471-07; pmid: 17804500
58. S. R. Margolis, S. C. Wilson, R. E. Vance, Evolutionary origins of cGAS-STING signaling. *Trends Immunol.* **38**, 733–743 (2017). doi: 10.1016/j.it.2017.03.004; pmid: 28416447
59. M. Kazlauskiene, G. Kostiuk, Č. Venclovas, G. Tamulaitis, V. Siksnys, A cyclic oligonucleotide signaling pathway in type III CRISPR-Cas systems. *Science* **357**, 605–609 (2017). doi: 10.1126/science.aao0100; pmid: 28663439
60. O. Niewoehner *et al*., Type III CRISPR-Cas systems produce cyclic oligoadenylate second messengers. *Nature* **548**, 543–548 (2017). doi: 10.1038/nature23467; pmid: 28722012
61. H. Nakayama, K. Otsu, Mitochondrial DNA as an inflammatory mediator in cardiovascular diseases. *Biochem. J.* **475**, 839–852 (2018). doi: 10.1042/BCJ20170714; pmid: 29511093
62. L. B. Tolle, T. J. Standiford, Danger-associated molecular patterns (DAMPs) in acute lung injury. *J. Pathol.* **229**, 145–156 (2013). doi: 10.1002/path.4124; pmid: 23097158
63. K. Nakahira, S. Hisata, A. M. Choi, The roles of mitochondrial damage-associated molecular patterns in diseases. *Antioxid. Redox Signal.* **23**, 1329–1350 (2015). doi: 10.1089/ars.2015.6407; pmid: 26067258
64. C. Dahlgren, M. Gabl, A. Holdfeldt, M. Winther, H. Forsman, Basic characteristics of the neutrophil receptors that recognize formylated peptides, a danger-associated molecular pattern generated by bacteria and mitochondria. *Biochem. Pharmacol.* **114**, 22–39 (2016). doi: 10.1016/j.bcp.2016.04.014; pmid: 27131862
65. H. Carp, Mitochondrial *N*-formylmethionyl proteins as chemoattractants for neutrophils. *J. Exp. Med.* **155**, 264–275 (1982). doi: 10.1084/jem.155.1.264; pmid: 6274994
66. S. S. Iyer *et al*., Mitochondrial cardiolipin is required for Nlrp3 inflammasome activation. *Immunity* **39**, 311–323 (2013). doi: 10.1016/j.immuni.2013.08.001; pmid: 23954133
67. J. Tschopp, Mitochondria: Sovereign of inflammation? *Eur. J. Immunol.* **41**, 1196–1202 (2011). doi: 10.1002/eji.201141436; pmid: 21469137
68. Z. Zhong *et al*., NF-κB restricts inflammasome activation via elimination of damaged mitochondria. *Cell* **164**, 896–910 (2016). doi: 10.1016/j.cell.2015.12.057; pmid: 26919428
69. K. Shimada *et al*., Oxidized mitochondrial DNA activates the NLRP3 inflammasome during apoptosis. *Immunity* **36**, 401–414 (2012). doi: 10.1016/j.immuni.2012.01.009; pmid: 22342844
70. A. Liston, S. L. Masters, Homeostasis-altering molecular processes as mechanisms of inflammasome activation. *Nat. Rev. Immunol.* **17**, 208–214 (2017). doi: 10.1038/nri.2016.151; pmid: 28163301
71. A. P. West *et al*., Mitochondrial DNA stress primes the antiviral innate immune response. *Nature* **520**, 553–557 (2015). doi: 10.1038/nature14156; pmid: 25642965
72. A. Rodríguez-Nuevo *et al*., Mitochondrial DNA and TLR9 drive muscle inflammation upon Opa1 deficiency. *EMBO J.* **37**, e96553 (2018). doi: 10.15252/embj.201796553; pmid: 29632021
73. M. W. Pellegrino *et al*., Mitochondrial UPR-regulated innate immunity provides resistance to pathogen infection. *Nature* **516**, 414–417 (2014). doi: 10.1038/nature13818; pmid: 25274306
74. K. McArthur *et al*., BAK/BAX macropores facilitate mitochondrial herniation and mtDNA efflux during apoptosis. *Science* **359**, eaao6047 (2018). doi: 10.1126/science.aao6047; pmid: 29472455
75. J. S. Riley *et al*., Mitochondrial inner membrane permeabilisation enables mtDNA release during apoptosis. *EMBO J.* **37**, e99238 (2018). doi: 10.15252/embj.201899238; pmid: 30049712
76. D. Brokatzky *et al*., A non-death function of the mitochondrial apoptosis apparatus in immunity. *EMBO J.* **38**, e100907 (2019). doi: 10.15252/embj.2018100907; pmid: 30979778
77. A. Dhir *et al*., Mitochondrial double-stranded RNA triggers antiviral signalling in humans. *Nature* **560**, 238–242 (2018). doi: 10.1038/s41586-018-0363-0; pmid: 30046113
78. R. B. Seth, L. Sun, C. K. Ea, Z. J. Chen, Identification and characterization of MAVS, a mitochondrial antiviral signaling protein that activates NF-kappaB and IRF 3. *Cell* **122**, 669–682 (2005). doi: 10.1016/j.cell.2005.08.012; pmid: 16125763
79. T. Oka *et al*., Mitochondrial DNA that escapes from autophagy causes inflammation and heart failure. *Nature* **485**, 251–255 (2012). doi: 10.1038/nature10992; pmid: 22535248
80. S. Sekine, R. J. Youle, PINK1 import regulation: A fine system to convey mitochondrial stress to the cytosol. *BMC Biol.* **16**, 2 (2018). doi: 10.1186/s12915-017-0470-7; pmid: 29325568
81. D. P. Narendra *et al*., PINK1 is selectively stabilized on impaired mitochondria to activate Parkin. *PLOS Biol.* **8**, e1000298 (2010). doi: 10.1371/journal.pbio.1000298; pmid: 20126261
82. J. N. S. Vargas *et al*., Spatiotemporal Control of ULK1 Activation by NDP52 and TBK1 during Selective Autophagy. *Mol. Cell* **74**, 347–362.e6 (2019). doi: 10.1016/j.molcel.2019.02.010; pmid: 30853401

83. M. P. Giannoccaro, C. La Morgia, G. Rizzo, V. Carelli, Mitochondrial DNA and primary mitochondrial dysfunction in Parkinson's disease. *Mov. Disord.* **32**, 346–363 (2017). doi: 10.1002/mds.26966; pmid: 28251677
84. A. M. Pickrell, R. J. Youle, The roles of PINK1, parkin, and mitochondrial fidelity in Parkinson's disease. *Neuron* **85**, 257–273 (2015). doi: 10.1016/j.neuron.2014.12.007; pmid: 25611507
85. D. A. Sliter *et al*., Parkin and PINK1 mitigate STING-induced inflammation. *Nature* **561**, 258–262 (2018). doi: 10.1038/s41586-018-0448-9; pmid: 30135585
86. N. Dzamko, C. L. Geczy, G. M. Halliday, Inflammation is genetically implicated in Parkinson's disease. *Neuroscience* **302**, 89–102 (2015). doi: 10.1016/j.neuroscience.2014.10.028; pmid: 25450953
87. A. F. Cordova, C. Ritchie, G. T. Hess, M. C. Bassik, L. Li, SLC19A1 is an importer of the immunotransmitter cGAMP. *bioRxiv* (2019). doi: 10.1101/539247
88. R. Luteijn *et al*., SLC19A1 is a cyclic dinucleotide transporter. *bioRxiv* (2019). doi: 10.1101/539767
89. A. Ablasser *et al*., Cell intrinsic immunity spreads to bystander cells via the intercellular transfer of cGAMP. *Nature* **503**, 530–534 (2013). doi: 10.1038/nature12640; pmid: 24077100
90. T. C. Frank-Cannon *et al*., Parkin deficiency increases vulnerability to inflammation-related nigral degeneration. *J. Neurosci.* **28**, 10825–10834 (2008). doi: 10.1523/JNEUROSCI.3001-08.2008; pmid: 18945890
91. D. Matheoud *et al*., Parkinson's disease-related proteins PINK1 and Parkin repress mitochondrial antigen presentation. *Cell* **166**, 314–327 (2016). doi: 10.1016/j.cell.2016.05.039; pmid: 27345367
92. D. Matheoud *et al*., Intestinal infection triggers Parkinson's disease-like symptoms in Pink1$^{-/-}$ mice. *Nature* **571**, 565–569 (2019). doi: 10.1038/s41586-019-1405-y; pmid: 31316206
93. X. Gui *et al*., Autophagy induction via STING trafficking is a primordial function of the cGAS pathway. *Nature* **567**, 262–266 (2019). doi: 10.1038/s41586-019-1006-9; pmid: 30842662
94. F. Randow, R. J. Youle, Self and nonself: How autophagy targets mitochondria and bacteria. *Cell Host Microbe* **15**, 403–411 (2014). doi: 10.1016/j.chom.2014.03.012 pmid: 24721569
95. J. Hu *et al*., Origin and development of oligoadenylate synthetase immune system. *BMC Evol. Biol.* **18**, 201 (2018). doi: 10.1186/s12862-018-1315-x; pmid: 30587119
96. Y. F. Lin *et al*., Maintenance and propagation of a deleterious mitochondrial genome by the mitochondrial unfolded protein response. *Nature* **533**, 416–419 (2016). doi: 10.1038/nature17989; pmid: 27135930
97. J. C. Greene, A. J. Whitworth, L. A. Andrews, T. J. Parker, L. J. Pallanck, Genetic and genomic studies of Drosophila parkin mutants implicate oxidative stress and innate immune responses in pathogenesis. *Hum. Mol. Genet.* **14**, 799–811 (2005). doi: 10.1093/hmg/ddi074; pmid: 15689351
98. A. Postigo, P. E. Ferrer, Viral inhibitors reveal overlapping themes in regulation of cell death and innate immunity. *Microbes Infect.* **11**, 1071–1078 (2009). doi: 10.1016/j.micinf.2009.08.012; pmid: 19733680
99. M. J. White *et al*., Apoptotic caspases suppress mtDNA-induced STING-mediated type I IFN production. *Cell* **159**, 1549–1562 (2014). doi: 10.1016/j.cell.2014.11.036; pmid: 25525874

ACKNOWLEDGMENTS

I thank C. Haynes, R. Silverman, D. Narendra, and members of the Youle laboratory for thoughtful comments and H. Baldwin and A. Youle for the figures. This work was supported by the Intramural Research Program of the National Institute of Neurological Disorders and Stroke, NIH.

10.1126/science.aaw9855

RESEARCH ARTICLE SUMMARY

IMMUNE SIGNALING

Nuclear hnRNPA2B1 initiates and amplifies the innate immune response to DNA viruses

Lei Wang*, Mingyue Wen*, Xuetao Cao†

INTRODUCTION: Recognition of pathogen-derived nucleic acids by host cells is an evolutionarily conserved mechanism that induces immune defense responses to microbial infections. Most DNA viruses direct their genomic DNA into host cell nuclei, which can serve as an important molecular signature of DNA virus infection. However, little is known about the nuclear surveillance mechanisms for viral nucleic acids.

RATIONALE: Virus-induced type I interferon (IFN-I) expression depends on the TANK-binding kinase 1–interferon regulatory factor 3 (TBK1–IRF3) activation. We reasoned that nuclear DNA sensors may translocate to the cytoplasm to activate the TBK1–IRF3 pathway after recognizing viral DNA in the nucleus. Thus, we screened nuclear proteins that bound viral DNA and translocated from the nucleus to the cytoplasm after viral infection. Heterogeneous nuclear ribonucleoprotein A2B1 (hnRNPA2B1) was identified as a potential DNA sensor. We then conducted a series of in vivo and in vitro experiments to probe the biological importance and activation mechanisms of hnRNPA2B1. Additionally, we explored its relationship with known cytosolic stimulator of interferon genes (STING)–dependent DNA sensors such as cyclic GAMP synthase (cGAS).

RESULTS: hnRNPA2B1 was found to bind viral DNA in the cell nucleus during herpes simplex virus–1 (HSV-1) infection. It then translocated to the cytoplasm and activated TBK1 through the tyrosine kinase Src. Accordingly, hnRNPA2B1 knockdowns and deficiency resulted in impaired DNA virus– but not RNA virus–induced IFN-I production and prolonged viral replication. The production of proinflammatory cytokines such as tumor necrosis factor–α (TNF-α) and interleukin-6 (IL-6) was unaffected. hnRNPA2B1 became dimerized after HSV-1 infection. Mutation of the dimer interface abrogated its nucleocytoplasmic translocation upon HSV-1 infection. Thus, hnRNPA2B1 dimerization is required for its nucleocytoplasmic translocation. Additionally, hnRNPA2B1 was demethylated at Arg^{226} after HSV-1 infection, which led to its activation and the subsequent initiation of IFN-β expression. This demethylation was catalyzed by the arginine demethylase JMJD6. hnRNPA2B1 with dimer interface mutation was unable to associate with JMJD6 after HSV-1 infection and showed increased amounts of arginine methylation compared to full-length hnRNPA2B1, indicating that dimerization was required for its demethylation.

ON OUR WEBSITE

Read the full article at http://dx.doi.org/10.1126/science.aav0758

To probe the relationship between hnRNPA2B1 and the recognized DNA sensor pathways, we found that the overexpression of hnRNPA2B1 increased HSV-1–induced TBK1 activation and *Ifnb1* expression in $Cgas^{-/-}$ L929 cells. Thus, hnRNPA2B1 could induce IFN-I in a cGAS-independent manner at least in part. This is consistent with earlier evidence suggesting the existence of other IFN-I–initiating molecules in the innate response against DNA virus. Wild-type macrophages showed higher and more sustained *Ifnb1* expression than $Hnrnpa2b1^{-/-}$ macrophages in response to DNA viruses. Thus, hnRNPA2B1 was required for fully activating type I interferon production against DNA viruses mediated by cGAS, interferon-γ–inducible protein 16 (IFI16), and STING pathways. Mechanistically, hnRNPA2B1 bound *CGAS*, *IFI16*, and *STING* mRNAs and promoted their nucleocytoplasmic trafficking to amplify cytoplasmic innate sensor signaling. The translation of these mRNAs was impaired in the absence of hnRNPA2B1 after HSV-1 infection. hnRNPA2B1 was constitutively associated with fat mass and obesity-associated protein (FTO). This association was abrogated after HSV-1 infection. By this means, hnRNPA2B1 promoted the N^6-methyladenosine (m^6A) modification and nucleocytoplasmic trafficking of *CGAS*, *IFI16*, and *STING* mRNAs. Thus, hnRNPA2B1 facilitates the efficient induction of antiviral IFN-I production mediated by cGAS, IFI16, and STING.

CONCLUSION: We identified hnRNPA2B1 as an innate sensor that initiates type I IFN production upon DNA virus infection in the nucleus. hnRNPA2B1 also amplifies type I IFN responses by directly enhancing STING-dependent cytosolic DNA sensing pathways. ■

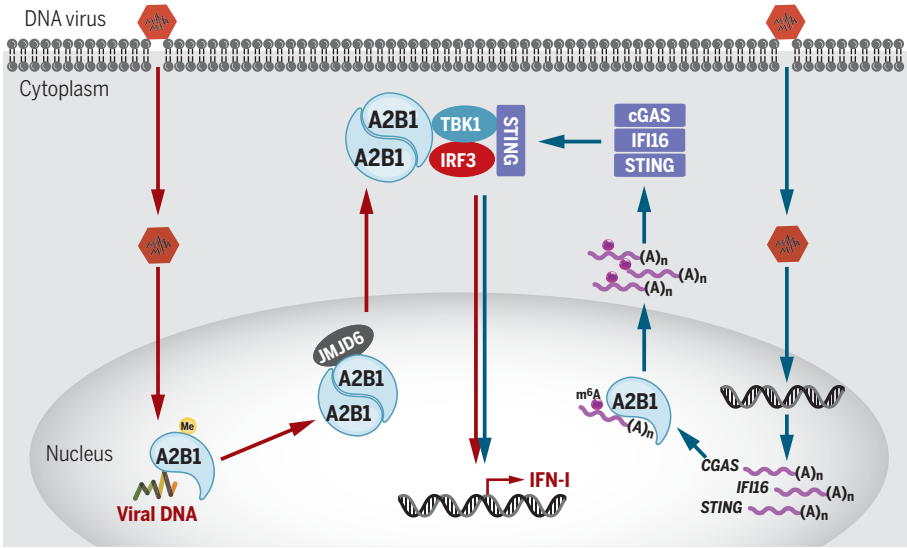

hnRNPA2B1 senses viral DNA in the nucleus and then activates and amplifies type I IFN responses. Upon entry, viral DNA is mainly enveloped within capsids. After traversing to the nucleus, DNA viruses eject their genomic DNA into the nucleus, which is recognized by hnRNPA2B1. Upon recognition of viral DNA, hnRNPA2B1 forms a homodimer, which is then demethylated by JMJD6. It consequently translocates to the cytoplasm where it activates the TBK1–IRF3 pathway and initiates IFN-α/β production. Additionally, hnRNPA2B1 promotes m^6A modification, nucleocytoplasmic trafficking, and translation of *CGAS*, *IFI16*, and *STING* mRNAs to fully ensure the activation of IFN-α/β in response to DNA virus infection.

The list of author affiliations is available in the full article online.
*These authors contributed equally to this work.
†Corresponding author. Email: caoxt@immunol.org
Cite this article as L. Wang *et al.*, *Science* **365**, eaav0758 (2019). DOI: 10.1126/science.aav0758

RESEARCH ARTICLE

IMMUNE SIGNALING

Nuclear hnRNPA2B1 initiates and amplifies the innate immune response to DNA viruses

Lei Wang[1,2]*, Mingyue Wen[2]*, Xuetao Cao[1,2,3]†

DNA viruses typically eject genomic DNA into the nuclei of host cells after entry. It is unclear, however, how nuclear pathogen–derived DNA triggers innate immune responses. We report that heterogeneous nuclear ribonucleoprotein A2B1 (hnRNPA2B1) recognizes pathogenic DNA and amplifies interferon-α/β (IFN-α/β) production. Upon DNA virus infection, nuclear-localized hnRNPA2B1 senses viral DNA, homodimerizes, and is then demethylated at arginine-226 by the arginine demethylase JMJD6. This results in hnRNPA2B1 translocation to the cytoplasm where it activates the TANK-binding kinase 1–interferon regulatory factor 3 (TBK1–IRF3) pathway, leading to IFN-α/β production. Additionally, hnRNPA2B1 facilitates N^6-methyladenosine (m^6A) modification and nucleocytoplasmic trafficking of *CGAS*, *IFI16*, and *STING* messenger RNAs. This, in turn, amplifies the activation of cytoplasmic TBK1–IRF3 mediated by these factors. Thus, hnRNPA2B1 plays important roles in initiating IFN-α/β production and enhancing stimulator of interferon genes (STING)–dependent cytoplasmic antiviral signaling.

Host innate immune responses to viruses can be triggered by the recognition of viral nucleic acids through pattern recognition receptors (PRRs). This results in the production of proinflammatory cytokines regulated by nuclear factor κB (NF-κB) signaling and type I interferons mediated by interferon regulatory factor (IRF) signaling (*1*, *2*). Typically, once DNA viruses enter a host cell, they eject and replicate their genomic DNA within host cell nuclei (*3*). The process by which pathogen-derived DNA is recognized within the nucleus remains an enigma, however. To date, only one protein, interferon-γ–inducible protein 16 (IFI16), has been proposed to recognize DNA viruses within the nucleus and activate type I interferon (IFN-I) production and inflammasome responses (*4*, *5*). Given how frequently host cells encounter nuclear pathogen–derived DNA, we therefore sought to identify other uncharacterized IFN-I initiators within the nucleus.

Many proteins that can recognize viral DNA and induce IFN-α/β production have been identified (*6*), such as RNA polymerase III, IFI16, DNA-dependent activator of interferon regulatory factors (DAI), leucine-rich repeat flightless-interacting protein 1 (LRRFIP1), LSm14A, meiotic recombination 11 homolog A (MRE11), heterotrimeric protein complex DNA-PK, high-mobility group box proteins (HMGBs), DExD/H helicase DDX41, and cyclic GMP-AMP (cGAMP) synthase (cGAS) (*7*–*16*). Nevertheless, only cytoplasmic cGAS and DNA-PK have been functionally validated as DNA sensors in vivo (*8*, *17*). Several proteins have also been reported to be involved in the DNA virus-induced inflammatory response, including absent in melanoma 2 (AIM2), IFI16, Rad50, and Sox2 (*4*, *18*–*20*). Thus, a fuller understanding of innate immune responses against DNA viruses is needed, especially regarding pathways that link the nuclear recognition of pathogen-derived DNA with the activation of cytoplasmic signaling.

We examined the nuclear proteins that bind to the genomic DNA of herpes simplex virus–1 (HSV-1) as well as translocate to the cytoplasm after viral infection. This analysis uncovered heterogeneous nuclear ribonucleoprotein A2B1 (hnRNPA2B1) as a nuclear initiator of type I interferon production that restricts DNA virus infection. After directly recognizing nuclear pathogen–derived DNA, hnRNPA2B1 translocates to the cytoplasm to initiate innate immune responses. hnRNPA2B1 then simultaneously facilitates the nucleocytoplasmic translocation and cytoplasmic expression of mRNAs such as *CGAS*, *IFI16*, and *STING* mRNA, which amplify antiviral innate immune signaling.

Results

Identification of hnRNPA2B1 as a candidate DNA sensor for type I IFN production

To identify potential nuclear DNA sensors, we biotinylated the genomic DNA of HSV-1 (F strain), precipitated the DNA-bound proteins from nuclear extracts of RAW264.7 cells, and examined the proteins that might bind HSV-1 genomic DNA by mass spectrometry (MS) (fig. S1A). Additionally, we separated the nuclear and cytoplasmic proteins after HSV-1 infection by two-dimensional (2D) SDS–polyacrylamide gel electrophoresis (SDS-PAGE), and then subjected those proteins that translocated from the nucleus to the cytoplasm 2 hours after HSV-1 infection to MS assays (fig. S1B). By integrating these two approaches, we identified 23 potential pathogen-derived DNA-binding proteins (table S1). Preliminary small interfering RNA (siRNA)–based functional screening pointed to one candidate in particular, hnRNPA2B1, as a putative IFN-I–inducing nuclear sensor. The interaction of hnRNPA2B1 with biotinylated HSV-1 DNA could be blocked competitively by unlabeled HSV-1 DNA (Fig. 1A). Human and mouse DNA also competitively blocked the binding of hnRNPA2B1 to biotinylated HSV-1 DNA. By contrast, human native nucleosomes, where genomic DNA wraps around a protein complex, could not (Fig. 1B). Thus, hnRNPA2B1 binds both self- and pathogen-derived DNA. Furthermore, chromosomal proteins block the binding of hnRNPA2B1 to self-DNA. HSV-1 DNA was precipitated through hnRNPA2B1 immunoprecipitation after HSV-1 infection, further suggesting that hnRNPA2B1 binds HSV-1 DNA during infection (Fig. 1C).

Heterogeneous nuclear ribonucleoproteins (hnRNPs) comprise a family of at least 20 abundant proteins and other less-abundant proteins in human cells. These RNA-binding proteins (RBPs) are involved in mRNA splicing, transport, and other mRNA and microRNA (miRNA) events (*21*). hnRNPA2B1 contains two tandem RNA/DNA-recognition motifs (RRMs) at the N terminus (fig. S1C), suggested to have DNA-binding capacity (*22*). Mutants lacking RRMs failed to bind biotinylated HSV-1 DNA (fig. S1D), indicating that the RRMs of hnRNPA2B1 mediate its recognition of HSV-1 DNA.

To delineate the potential roles of hnRNPA2B1 in initiating IFN-I production, we silenced hnRNPA2B1 in various mouse macrophage populations, including RAW264.7 cells, primary peritoneal macrophages (PMs), and bone marrow–derived macrophages (BMDMs) (fig. S2A). This significantly impaired HSV-1–induced mRNA expression and protein production of IFN-α, IFN-β, and CXCL10, but not interleukin-6 (IL-6) and tumor necrosis factor–α (TNF-α) (fig. S2, B to H). Thus, hnRNPA2B1 appears to play a role in DNA virus–induced IFN-I production. Knockdown of hnRNPA2B1 in PMs and BMDMS had no effect on IFN-β expression induced by RNA virus [vesicular stomatitis virus (VSV) and Sendai virus (SeV)] infections (fig. S2, I and J). A second siRNA was used to exclude off-target effects, and similar results were obtained (fig. S2, K and L). Furthermore, knockdown of hnRNPA2B1 in THP-1 cells significantly impaired HSV-1–induced but not VSV-induced *IFNA4*, *IFNB1*, *CCL5*, and *CXCL10* expression. However, *IL6* and *TNFA*

[1]National Key Laboratory of Medicinal Chemical Biology, College of Life Science, Nankai University, Tianjin 300071, China. [2]National Key Laboratory of Medical Immunology and Institute of Immunology, Second Military Medical University, Shanghai 200433, China. [3]National Key Laboratory of Medical Molecular Biology and Department of Immunology, Institute of Basic Medical Sciences, Peking Union Medical College, Chinese Academy of Medical Sciences, Beijing 100005, China.
*These authors contributed equally to this work.
†Corresponding author. Email: caoxt@immunol.org

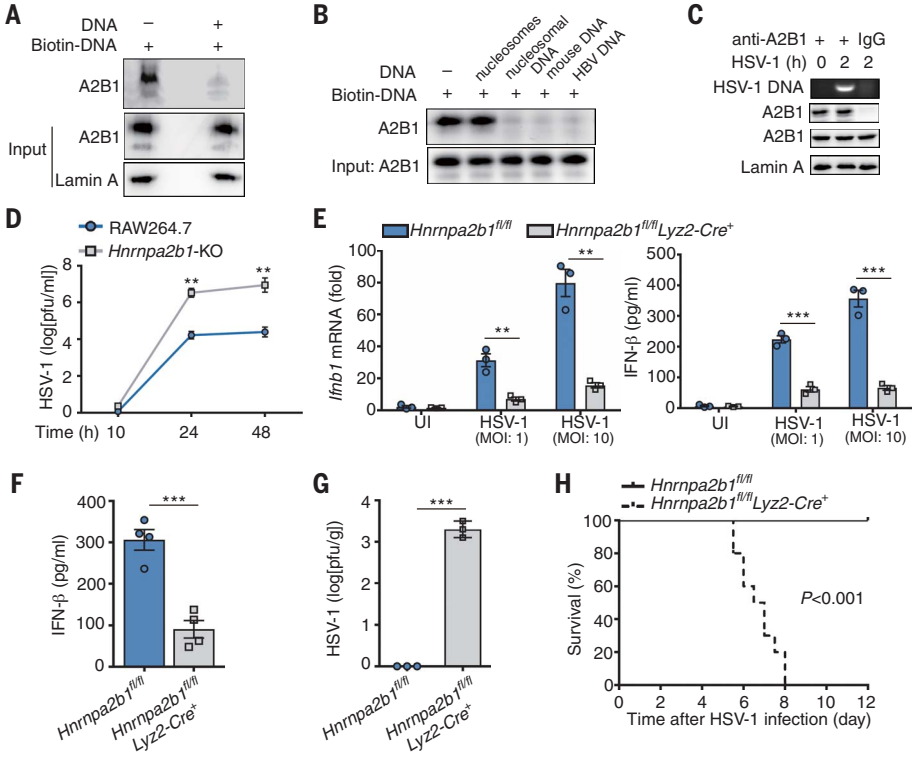

Fig. 1. hnRNPA2B1 activates antiviral defense to inhibit DNA virus replication. (**A**) Complexes obtained by nucleic acid affinity purification were examined by immunoblot in the absence or presence of unlabeled HSV-1 DNA using antibodies against hnRNPA2B1 (anti-hnRNPA2B1). (**B**) hnRNPA2B1 was pulled down and then incubated with unlabeled human native nucleosome, human nucleosomal DNA, mouse DNA, or HBV DNA. Nucleic acid affinity purification was then performed, and hnRNPA2B1 amounts were measured by immunoblot. (**C**) PCR analysis of HSV-1 DNA contained in the complex immunoprecipitated by anti-hnRNPA2B1 or IgG in macrophages infected with HSV-1 (MOI, 10) for 2 hours. (**D**) Wild-type and *Hnrnpa2b1*-KO RAW264.7 cells were infected with HSV-1 (MOI, 0.5) as indicated. Viral titers in the supernatants were measured by plaque assay. (**E**) PMs from wild-type and *Hnrnpa2b1*-cKO mice were infected with HSV-1 (MOI, 1 or 10) for 6 hours for qPCR assays of *Ifnb1* mRNA (left) and 12 hours for ELISA assays of IFN-β (right) were performed. (**F** to **H**) Wild-type and *Hnrnpa2b1*-cKO mice were intraperitoneally infected with 7×10^8 PFU of HSV-1. (F) Serum IFN-β concentrations were assayed by ELISA 6 hours after HSV-1 infection. (G) Viral titers in brains 4 days after HSV-1 infection were determined by plaque assay. (H) Kaplan–Meier survival curves of mice up to 12 days after infection. Statistical significance was determined by log-rank test (n = 10 mice per group from three independent experiments). Similar results were obtained from three independent experiments. One representative experiment is shown (A) to (C). Data are displayed as means ± SEM of three [(D), (E), or (G)] or four (F) independent experiments performed in triplicate. $^{**}P < 0.01$, $^{***}P < 0.001$, two-tailed unpaired Student's t-test [(D) to (G)]. See also figs. S1 to S5.

expression were unaffected (fig. S3, A and B). Thus, hnRNPA2B1 initiates IFN-I responses to DNA viruses in both mouse and human myeloid cells.

HSV-1–induced *Ifnb1* expression decreased significantly in *Hnrnpa2b1*-knockout (KO) RAW264.7 cells (fig. S4, A and B), where HSV-1 replication was enhanced (Fig. 1D). Moreover, *Ifnb1* expression in RAW264.7 cells induced by another DNA virus adenovirus (AdV), but not by RNA viruses (SeV and VSV) or *Listeria* bacteria, was also significantly impaired by *Hnrnpa2b1* deficiency (fig. S4C). Similar results were observed in another *Hnrnpa2b1*-KO clone (fig. S4D) and in *Hnrnpa2b1*-KO L929 fibroblasts (fig. S4, E and F). Thus, hnRNPA2B1 is important for the innate immune-mediated inhibition of DNA virus replication.

Next, we established myeloid cell-specific *Hnrnpa2b1*-conditional KO (cKO) mice (fig. S4G). Upon HSV-1 infection, both the transcription and secretion of IFN-β decreased significantly in PMs deficient in *Hnrnpa2b1* (Fig. 1E). *Ifna4* transcription was also impaired, whereas the transcription of *Il6* and *Tnfa* was not (fig. S4H). Serum IFN-β concentrations were severely attenuated in *Hnrnpa2b1*-cKO mice after HSV-1 challenge (Fig. 1F). Accordingly, much higher viral titers were detected in the brains of *Hnrnpa2b1*-cKO mice after HSV-1 infection (Fig. 1G). *Hnrnpa2b1*-cKO mice also exhibited increased mortality after HSV-1 infection compared to control mice (Fig. 1H). Serum IL-6, IFN-β, and TNF-α concentrations in *Hnrnpa2b1*-cKO mice were similar to that of wild-type mice 8 hours after RNA virus SeV infection (fig. S4I). To rule out interference by other signaling pathways, we measured several major signaling molecules. cGAS, IFI16, STING, TBK1, and IRF3 amounts were comparable in both wild-type and hnRNPA2B1-KO PMs (fig. S5A). Moreover, there were similar frequencies of $F4/80^+CD11b^+$ macrophages, natural killer (NK) cells, B cells, T cells, neutrophils, and monocytes in the spleens of wild-type and *Hnrnpa2b1*-cKO mice (fig. S5B). Thus, hnRNPA2B1 plays an important role in host innate immune defense against DNA virus infection.

hnRNPA2B1 dimerization is required for its nucleocytoplasmic translocation and initiation of IFN-α/β expression

Type I interferons in antiviral innate responses are initiated by the cytoplasmic kinase TBK1 and the subsequent activation of the transcription factor IRF3 (*23*, *24*). Thus, we hypothesized that hnRNPA2B1 must be translocated to the cytoplasm to activate the TBK1–IRF3 pathway following the recognition of viral DNA in the nucleus. hnRNPA2B1 mainly localized in the nucleus but was also present in the cytoplasm 2 hours after HSV-1 infection (Fig. 2A and fig. S6A). *Hnrnpa2b1* deficiency strongly impaired the phosphorylation of TBK1 and IRF3 (Fig. 2B), as well as decreasing the kinase activity of TBK1 after HSV-1 infection (fig. S6B). Thus, we hypothesized that TBK1 was required for the hnRNPA2B1-mediated IFN-I induction. MS assays of immunoprecipitated complexes of hnRNPA2B1 or TBK1 in RAW264.7 cells infected with HSV-1 revealed an association between hnRNPA2B1 and TBK1, which was confirmed by immunoprecipitation in mouse PMs (Fig. 2C). Similar results were obtained in THP1 cells (fig. S6C), indicating that the molecular interaction was conserved in both mouse and human cells. Furthermore, hnRNPA2B1 colocalized with TBK1 in the cytoplasm after HSV-1 infection (Fig. 2D). The overexpression of hnRNPA2B1 was unable to promote HSV-1–induced IFN-β production in $Tbk1^{-/-}$ MEFs or $Irf3^{-/-}$ macrophages (fig. S6, D and E). Thus, hnRNPA2B1 acts upstream of the TBK1–IRF3 pathway to mediate IFN-β production.

Next, we investigated the mechanisms involved in driving hnRNPA2B1 nucleocytoplasmic translocation. hnRNPA2B1 dimerized after HSV-1 infection (Fig. 3A), which was confirmed by co-immunoprecipitation of Myc- and Flag-tagged hnRNPA2B1 (Fig. 3B). Mutation of the dimer interface (DI, www.ncbi.nlm.nih.gov/Structure/cdd/cddsrv.cgi; Pro^{81}, Lys^{82}, Arg^{83}, Val^{172}, Arg^{173}, Lys^{174}) in the RRM domain abrogated dimerization and nucleocytoplasmic translocation of hnRNPA2B1 in response to HSV-1 infection (Fig. 3C and fig. S7, A and B). Thus, dimerization is required for the nucleocytoplasmic translocation of hnRNPA2B1. Variants of hnRNPA2B1

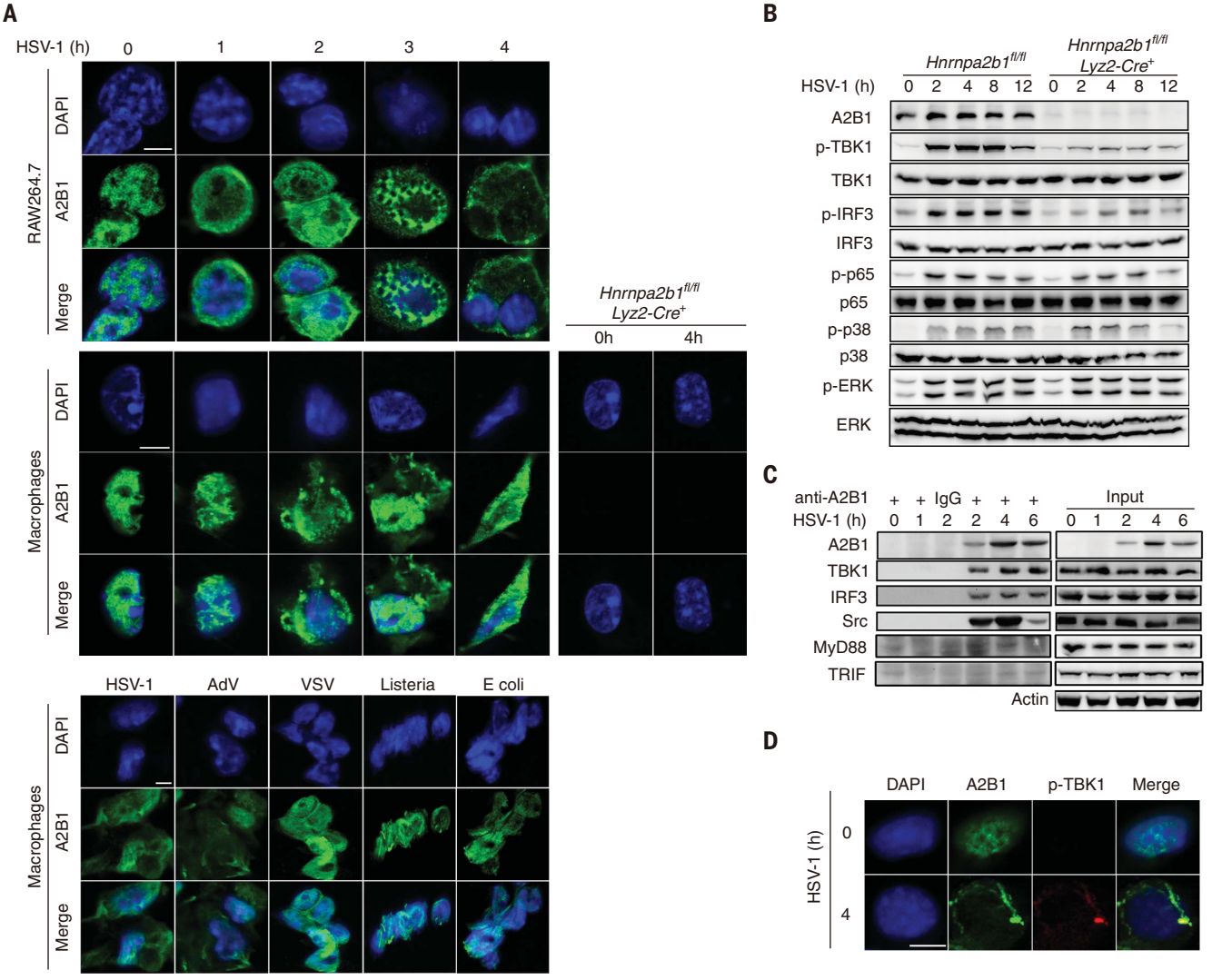

Fig. 2. DNA virus infection selectively drives nucleocytoplasmic translocation of hnRNPA2B1 to activate TBK1. (**A**) RAW264.7 cells and wild-type and *Hnrnpa2b1*-KO mouse PMs were uninfected or infected with HSV-1 (MOI, 10), AdV, VSV, *Listeria*, or *Escherichia coli* for 4 hours. hnRNPA2B1 (green) localization was then examined by confocal microscopy. Nuclei were stained with DAPI (4′,6-diamidino-2-phenylindole, blue). Scale bar, 5 μm. (**B**) PMs from wild-type and *Hnrnpa2b1*-cKO mice were infected with HSV-1 (MOI, 10) for the indicated time. Phosphorylated (p-) and total TBK1, IRF3, ERK1/2, p38, JNK, and NF-κB p65 were detected by immunoblot. (**C**) Mouse PMs were infected with HSV-1 (MOI, 10) as indicated, and cytoplasmic extracts were immunoprecipitated with anti-hnRNPA2B1 or IgG. The components in the complex were examined by immunoblot. (**D**) Confocal microscopy of colocalization of hnRNPA2B1 (green) with phosphorylated TBK1 (red) in mouse PMs infected with ultraviolet-inactivated HSV-1 (MOI, 10) for 4 hours. Nuclei were stained with DAPI (blue). Scale bar, 5 μm. Similar results were obtained for three independent experiments. One representative experiment is shown [(A) to (D)]. See also fig. S6.

carrying mutations in the dimer interface could not rescue HSV-1–induced *Ifnb1* mRNA expression (Fig. 3D) or activation of an *Ifnb1* reporter (fig. S7C). However, these dimerization mutants did not affect hnRNPA2B1 binding to viral DNA (fig. S7D). Thus, the recognition and binding of HSV-1 DNA by hnRNPA2B1 via the RRM domain appears to induce its dimerization, consequently driving its nucleocytoplasmic translocation, where it activates TBK1.

Because hnRNPA2B1 binds both viral and mammalian DNA, we examined whether hnRNPA2B1 was activated by self-DNA. Nucleofection of naked human nucleosomal DNA indeed activated *IFNB1* expression, whereas native nucleosomes did not (Fig. 3E and fig. S7E). Accordingly, hnRNPA2B1 dimers were detected after the nucleofection of naked nucleosomal DNA but not native nucleosomes (Fig. 3F). Thus, chromosomal proteins prevent the activation of hnRNPA2B1 by genomic self-DNA.

We next asked how hnRNPA2B1 activates TBK1 in response to HSV-1 infection. hnRNPA2B1 interacted with Src and STING after HSV-1 infection in mouse macrophages and human THP1 cells (fig. S8, A and B). STING and TBK1 significantly enhanced hnRNPA2B1-mediated IFN-β induction (fig. S8C). Furthermore, hnRNPA2B1 was unable to induce IFN-β in *Sting*$^{-/-}$ cells (fig. S8D). Thus, hnRNPA2B1 initiates IFN-I production by activating the STING-dependent TBK1–IRF3 pathway. Src, which has been implicated in TBK1–IRF3 activation (*25*, *26*), was activated after HSV-1 infection in mouse PMs (fig. S8E). Inhibition of Src significantly reduced serum IFN-β concentrations (fig. S8F). Thus, Src may be the upstream kinase that activates TBK1 in the hnRNPA2B1 signaling complex. As expected, phosphorylated Src colocalized with hnRNPA2B1 (fig. S8G) and active TBK1 (fig. S8H) in macrophages after HSV-1 infection. Additionally, in the absence of hnRNPA2B1, Src phosphorylation was severely impaired (fig. S8G). Src inhibitor at the concentrations used in our study did not affect HSV-1 entry into

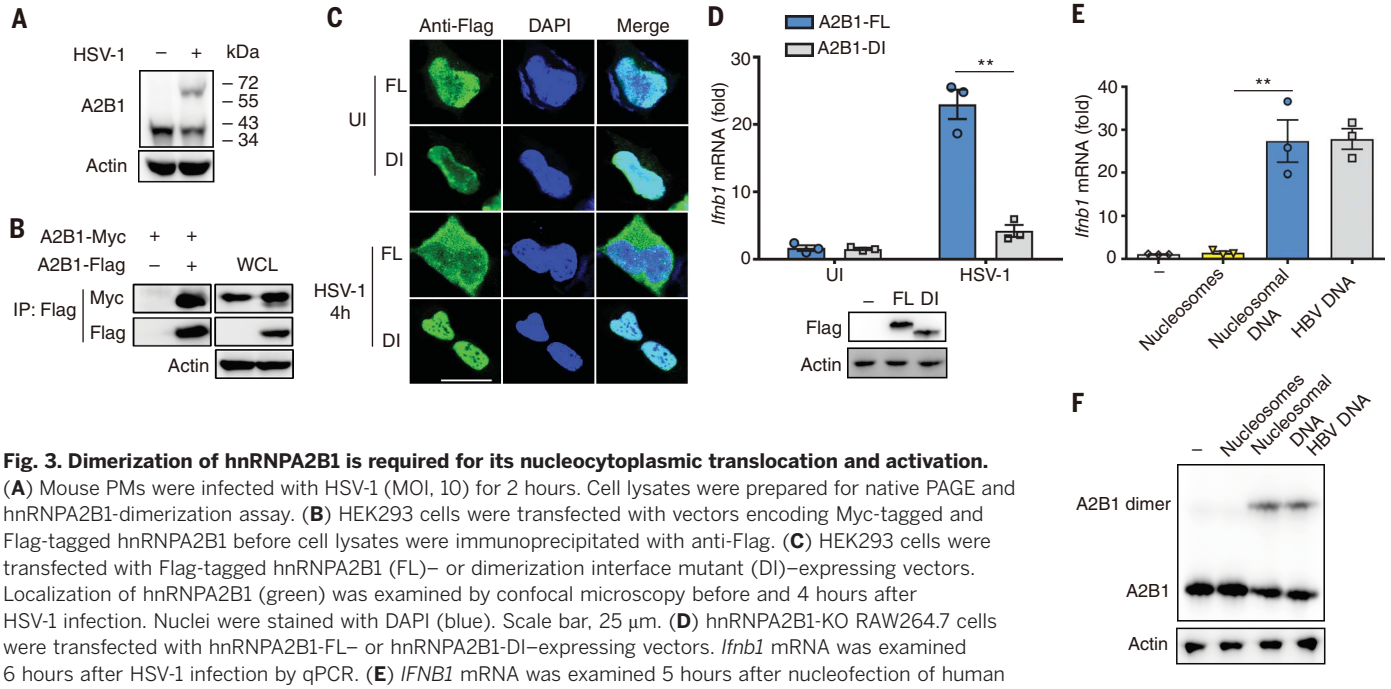

Fig. 3. Dimerization of hnRNPA2B1 is required for its nucleocytoplasmic translocation and activation. (**A**) Mouse PMs were infected with HSV-1 (MOI, 10) for 2 hours. Cell lysates were prepared for native PAGE and hnRNPA2B1-dimerization assay. (**B**) HEK293 cells were transfected with vectors encoding Myc-tagged and Flag-tagged hnRNPA2B1 before cell lysates were immunoprecipitated with anti-Flag. (**C**) HEK293 cells were transfected with Flag-tagged hnRNPA2B1 (FL)– or dimerization interface mutant (DI)–expressing vectors. Localization of hnRNPA2B1 (green) was examined by confocal microscopy before and 4 hours after HSV-1 infection. Nuclei were stained with DAPI (blue). Scale bar, 25 μm. (**D**) hnRNPA2B1-KO RAW264.7 cells were transfected with hnRNPA2B1-FL– or hnRNPA2B1-DI–expressing vectors. *Ifnb1* mRNA was examined 6 hours after HSV-1 infection by qPCR. (**E**) *IFNB1* mRNA was examined 5 hours after nucleofection of human native nucleosome or human nucleosomal DNA in PMA-differentiated THP-1 cells by qPCR. (**F**) PMA-differentiated THP-1 cells lysates were prepared for native PAGE and hnRNPA2B1 dimerization assay 2 hours after nucleofection of human native nucleosome or human nucleosomal DNA. Similar results were obtained for three independent experiments. One representative experiment is shown [(A) to (C), (F)]. Data are displayed as means ± SEM of three [(D) and (E)] independent experiments performed in triplicate. $^{**}P < 0.01$, two-tailed, unpaired Student's *t* test [(D) and (E)]. See also figs. S7 and S8.

macrophages (fig. S8I), excluding the possibility that this was due to the reduced entry of HSV-1 into macrophages. Thus, Src can bind hnRNPA2B1 and TBK1, and then activate TBK1. Together, these data demonstrate that nuclear hnRNPA2B1 forms a homodimer upon recognition of pathogen-derived DNA. This drives its translocation to the cytoplasm, where it binds and activates TBK1–IRF3 signaling via Src to initiate STING-dependent IFN-α/β expression.

JMJD6-demethylated hnRNPA2B1 dimer activates IFN-α/β expression

We next screened arginine, serine, and threonine mutations of hnRNPA2B1, and found that a mutation of Arg^{226} to Ala (R226A) within the arginine-glycine-glycine–rich (RGG) domain significantly enhanced hnRNPA2B1-induced *Ifnb1* expression (Fig. 4A). The overexpression of hnRNPA2B1-R226A in *Hnrnpa2b1*-KO RAW264.7 cells resulted in higher amounts of IFN-β mRNA and protein compared to wild-type hnRNPA2B1 (Fig. 4, B and C, and fig. S9A). Indeed, hnRNPA2B1 can be methylated at arginine residues within the RGG domain (*27*). Arginine monomethylation of hnRNPA2B1 was decreased after HSV-1 infection (Fig. 4D). Among all arginine residues, R226 was the key site for arginine monomethylation (Fig. 4E). hnRNPA2B1 was demethylated on R226 in response to HSV-1 infection in macrophages (Fig. 4F and fig. S9B). R226-demethylated hnRNPA2B1 translocated into the cytoplasm of L929 cells after HSV-1 infection (fig. S9C). Additionally, the presence of hnRNPA2B1 nuclear speckles 2 hours after HSV-1 infection suggests that hnRNPA2B1 and viral DNA colocalize. Alternatively, hnRNPA2B1 may accumulate around the nuclear pore complex when it starts to be exported into the cytoplasm. Thus, demethylation at Arg^{226} leads to hnRNPA2B1 activation and the subsequent initiation of IFN-β expression.

Our MS data suggested an association between the arginine demethylase JMJD6 and hnRNPA2B1. Immunoprecipitation experiments in mouse PMs and human THP1 cells confirmed the endogenous interaction between hnRNPA2B1 and JMJD6 upon HSV-1 infection (Fig. 5A and fig. S10A). This association was transient, as hnRNPA2B1 translocated to the cytoplasm, whereas JMJD6 remained in the nucleus (Fig. 5B). hnRNPA2B1 could be co-immunoprecipitated with JMJD6 when overexpressed in human embryonic kidney 293 (HEK293) cells (fig. S10B). JMJD6 dimerization was increased in macrophages after HSV-1 infection (fig. S10C). As the demethylation activity of JMJD6 requires its oligomerization (*28*), we hypothesized that JMJD6 may play a role in innate defense against DNA virus infection. Inhibition of JMJD6 by *N*-oxalylglycine (NOG) impaired hnRNPA2B1 demethylation in response to HSV-1 infection (Fig. 5C). HSV-1–induced *Ifnb1* expression was significantly decreased in macrophages transfected with JMJD6-specific siRNA or treated with NOG (Fig. 5D and fig. 5E). Impaired *Ifnb1* production could be rescued by the overexpression of hnRNPA2B1-R226A (Fig. 5D and fig. S10D). By contrast, JMJD6 overexpression promoted HSV-1–induced *Ifnb1* production (Fig. 5F). Thus, hnRNPA2B1 is activated by demethylation at R226 by JMJD6.

A mutation at the hnRNPA2B1 dimer interface (hnRNPA2B1-DI) led to increased arginine methylation compared to full-length hnRNPA2B1 (hnRNPA2B1-FL) (Fig. 5G). hnRNPA2B1-DI was unable to associate with JMJD6 after HSV-1 infection (Fig. 5H). Furthermore, inhibition of JMJD6 by NOG did not affect the translocation of hnRNPA2B1 in response to HSV-1 infection in macrophages (Fig. 5I). Thus, after recognizing viral DNA, hnRNPA2B1 dimerizes and then becomes demethylated by JMJD6 in the nucleus. Dimerization of hnRNPA2B1 is required for its demethylation and translocation.

hnRNPA2B1 facilitates the efficient induction of antiviral type I interferon by cGAS, IFI16, and STING

We next probed how the nuclear hnRNPA2B1 and recognized DNA sensor pathways might initiate antiviral IFN-I production. The overexpression of wild-type hnRNPA2B1 and hnRNPA2B1-R226A (the active, demethylated form of hnRNPA2B1) in $Cgas^{-/-}$ L929 cells significantly increased HSV-1–induced *Ifnb1* expression (Fig. 6A). The overexpression of hnRNPA2B1-R226A also enhanced HSV-1–induced TBK1 activation in $Cgas^{-/-}$ L929 cells (Fig. 6B), suggesting that hnRNPA2B1 can induce IFN-I at least partially in a cGAS-independent manner. This is consistent with an earlier finding that other molecules may partially compensate for the loss of cGAS (*17*).

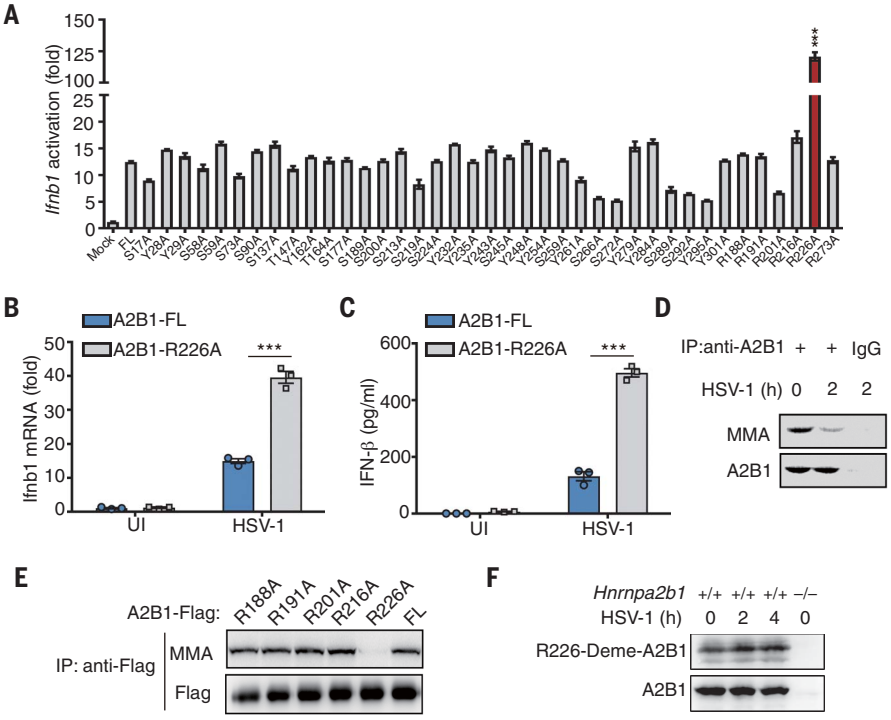

Fig. 4. Arg^{226} demethylation is essential for hnRNPA2B1-mediated type I IFN induction. (**A**) HEK293T cells were transiently transfected with hnRNPA2B1 or its mutant expression vectors with an *Ifnb1* reporter vector as indicated. The activation of the *Ifnb1* reporter was examined by dual luciferase reporter assays. (**B** and **C**) *Hnrnpa2b1*-KO RAW264.7 cells transfected with hnRNPA2B1, and mutant expression vectors were infected with HSV-1 for 7 hours (B) or 18 hours (C). *Ifnb1* mRNA was measured by qPCR (B), and IFN-β concentrations were measured by ELISA (C). (**D**) Mouse PMs were infected with HSV-1 (MOI, 10) for 2 hours. Cell lysates were immunoprecipitated with anti-hnRNPA2B1 and then examined for the level of Arg methylation by immunoblot. (**E**) HEK293T cells were transfected with the indicated vectors. Cell lysates were immunoprecipitated with anti-Flag and then examined for the level of Arg methylation by immunoblot. (**F**) The demethylation of hnRNPA2B1 was detected by using a specific antibody against R226-demethylated hnRNPA2B1 in RAW264.7 cells in response to HSV-1 infection (MOI, 10). Similar results were obtained for three independent experiments. One representative experiment is shown [(D) to (F)]. Data are displayed as means ± SEM of three [(A) to (C)] independent experiments performed in triplicate. ***$P < 0.001$, two-tailed, unpaired Student's t test [(A) to (C)]. See also fig. S9.

HSV-1–induced *Ifnb1* transcription was attenuated in *Hnrnpa2b1*-KO PMs (Fig. 6C). Vaccinia virus (VACV), another DNA virus, replicates in the cytoplasm and is sensed by cytosolic DNA sensors (*29*). VACV infection in *Hnrnpa2b1*-KO PMs induced *Ifnb1* production to a certain level after 4 hours but showed no subsequent increases in *Ifnb1* as it did in wild-type cells (Fig. 6C). Wild-type macrophages showed higher and more sustained *Ifnb1* expression than *Hnrnpa2b1*-KO macrophages in response to both viruses (Fig. 6C). Similar results were obtained in BMDMs (fig. S11). Thus, hnRNPA2B1 appears to be required for cGAS-, IFI16-, and STING-mediated pathways to fully activate type I interferon production against DNA viruses.

hnRNPA2B1 promotes nucleocytoplasmic trafficking of CGAS, IFI16, and STING mRNAs to amplify cytoplasmic innate sensor signaling

We next investigated why hnRNPA2B1 is required for the efficient induction of IFN-I by cGAS, IFI16, and STING in response to HSV-1 infection. Up to 6 hours after HSV-1 infection, the endogenous amounts of cGAS, p204 (the functional mouse ortholog of human IFI16), and STING protein were similar in both wild-type and *Hnrnpa2b1*-KO RAW264.7 cells. cGAS expression began to increase in wild-type RAW264.7 cells 6 hours after infection, whereas p204 began to increase 12 hours after infection. However, these proteins failed to increase in *Hnrnpa2b1*-KO RAW264.7 cells following HSV-1 infection (Fig. 6D). STING abundance decreased more rapidly in *Hnrnpa2b1*-KO RAW264.7 cells than in wild-type RAW264.7 cells 6 hours after infection (Fig. 6D). Thus, hnRNPA2B1 appears to be required for the efficient induction of cGAS, IFI16, and STING after DNA virus infection, which subsequently generates an antiviral IFN-I response.

We examined the effects of hnRNPA2B1 on *Cgas*, *p204*, and *Sting* mRNA expression. The transcriptional levels of these genes were similar in wild-type and *Hnrnpa2b1*-KO RAW264.7 cells, indicating that the splicing of these mRNAs was unaffected (fig. S12A). Similarly, the stability of these mRNAs did not significantly differ between these cell lines (fig. S12B). However, depletion of hnRNPA2B1 led to the nuclear retention of *Cgas*, *p204*, and *Sting* mRNAs (Fig. 7A). Analysis of mRNAs associated with hnRNPA2B1-immunoprecipitated complexes revealed that hnRNPA2B1 was able to bind *Cgas*, *p204*, and *Sting* mRNAs in macrophages after HSV-1 infection (Fig. 7B). Thus, hnRNPA2B1 appears to play a role in mediating the nucleocytoplasmic translocation of these mRNAs.

N6-methyladenosine (m^{6}A) is the predominant methylated base in mammalian mRNAs and has been recently revealed to promote mRNA translocation from the nucleus to the cytoplasm (*30*, *31*). A greater number of methylated mRNAs were precipitated after HSV-1 infection, although the amounts of methylated *Cgas*, *p204*, and *Sting* mRNA were much lower in *Hnrnpa2b1*-KO RAW264.7 cells than in controls (Fig. 7C). Thus, specific classes of mRNAs involved in antiviral response such as *Cgas, p204*, and *Sting*, undergo m^{6}A modification after DNA virus infection in an hnRNPA2B1-dependent manner.

Two RNA demethylases, alkylated DNA repair protein alkB homolog 5 (ALKBH5) and fat mass and obesity-associated protein (FTO), have been identified to date (*31*, *32*). Our MS data suggested an interaction between hnRNPA2B1 and FTO. hnRNPA2B1 was constitutively associated with FTO, and hnRNPA2B1 disassociated with FTO after HSV-1 infection in mouse PMs and human THP1 cells (Fig. 7D and fig. S12C). Knockdown of FTO led to increased HSV-1–induced *Ifnb1* expression in macrophages (Fig. 7E and fig. S12D).

The METTL3–METTL14 complex mediates mRNA m^{6}A methylation. To explore whether METTL3 was involved in the innate immune response, we studied myeloid cell–specific *Mettl3*-KO mice (*33*). *Ifnb1* expression was impaired in *Mettl3*-KO PMs and BMDMS after HSV-1 infection (fig. S12E). METTL3 deficiency did not affect hnRNPA2B1 binding with *Cgas*, *p204*, or *Sting* mRNAs (fig. S12F). *Cgas*, *p204*, and *Sting* m^{6}A levels were lower in *Mettl3*-KO macrophages than in wild-type cells (fig. S12G). Thus, METTL3 contributes to the m^{6}A modification of hnRNPA2B1-bound mRNAs in macrophages, which promotes IFN-β expression in response to DNA virus infection.

The binding of *CGAS, IFI16*, and *STING* mRNAs by demethylated hnRNPA2B1 was severely impaired compared to that by hnRNPA2B1-FL (Fig. 7F and fig. S12H). The m^{6}A levels of these mRNAs in JMJD6 inhibitor-treated cells were similar to control cells (Fig. 7G). Thus, RNA binding by hnRNPA2B1 requires Arg^{226} methylation, and demethylated hnRNPA2B1 cannot bind these mRNAs or affect their m^{6}A modification.

Analysis of RNA from nuclear and cytoplasmic fractions in both wild-type and *Hnrnpa2b1*-KO macrophages before and after HSV-1 infection revealed that hnRNPA2B1 deficiency decreased the nuclear export of mRNAs involved in several biological processes, including pheromone

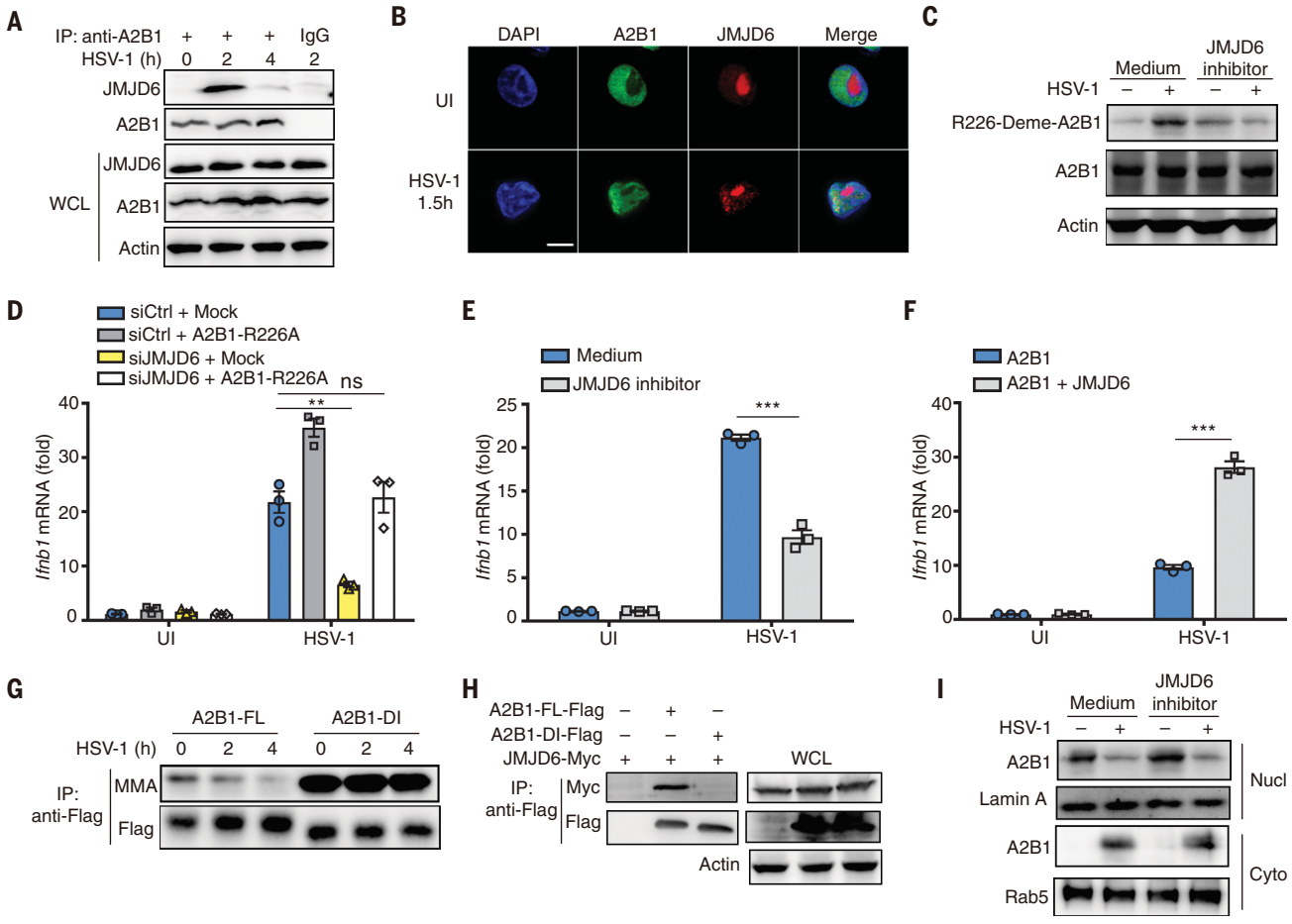

Fig. 5. JMJD6-mediated demethylation is essential for hnRNPA2B1-mediated type I IFN induction. (**A**) Mouse PMs were infected with HSV-1 (MOI, 10). Cell lysates were immunoprecipitated with anti-hnRNPA2B1 or IgG. The components in the complex were examined by immunoblot. (**B**) Mouse PMs infected with HSV-1 (MOI, 10) for 1.5 hours were examined for hnRNPA2B1 (green) and JMJD6 (red) by confocal microscopy. Nuclei were stained with DAPI (blue). Scale bar, 5 μm. (**C**) The demethylation of hnRNPA2B1 was detected by using a specific antibody against R226-demethylated hnRNPA2B1 in RAW264.7 cells after HSV-1 infection (MOI, 10) with or without JMJD6 inhibitor treatment. (**D**) Mouse PMs transfected with control siRNA or JMJD6-specific siRNAs were transfected with mock or hnRNPA2B1-R226A-expressing vector and infected with HSV-1 (MOI, 10) for 7 hours. *Ifnb1* mRNA was examined by qPCR. (**E**) Mouse PMs treated with or without JMJD6 inhibitor for 2 hours were infected with HSV-1 (MOI, 10). The *Ifnb1* mRNA was examined by qPCR. (**F**) RAW264.7 cells transfected with plasmids encoding hnRNPA2B1 or JMJD6 were infected with HSV-1 (MOI, 10). The *Ifnb1* mRNA was examined by qPCR. (**G**) HEK293T cells were transfected with Flag-tagged hnRNPA2B1-FL or -DI. Cell lysates were immunoprecipitated with anti-Flag and examined for Arg methylation by immunoblot. MMA, monomethylated arginines. (**H**) HEK293T cells were transfected with Flag-tagged hnRNPA2B1-FL or -DI and Myc-tagged JMJD6. Cell lysates were immunoprecipitated with anti-Flag and examined for Myc by immunoblot. (**I**) RAW264.7 cells were treated with or without JMJD6 inhibitor for 2 hours and then were infected with HSV-1 (MOI, 10) as indicated, and the cytoplasmic and nuclear proteins were separated. The subcellular distribution of hnRNPA2B1 was examined by immunoblot. Similar results were obtained in three independent experiments, and one representative was shown [(A) to (C), (G) to (I)]. Data are displayed as means ± SEM of three [(D) to (F)] independent experiments performed in triplicate. $^{**}P < 0.01$, $^{***}P < 0.001$; ns, not significant; two-tailed, unpaired Student's *t* test [(D) to (F)]. See also fig. S10.

receptor activity and electron transfer activity (fig. S13A). Several immune-associated genes including *Cgas* and *Sting* mRNAs were retained within the nucleus in macrophages after HSV-1 infection. By contrast, most housekeeping genes, such as *Actb* and *Gapdh*, were unaffected. Thus, not all genes were regulated by hnRNPA2B1 (fig. S13B). hnRNPA2B1 regulated more innate immune-associated genes than adaptive immune-associated genes (fig. S13C). hnRNPA2B1 appeared to affect a set of genes involved in several innate processes, including antigen presentation, the complement system, cytokine and chemokine signaling, and interferon responses (fig. S13D). Thus, hnRNPA2B1 plays a role in regulating the export of immune-associated RNAs after HSV-1 infection, especially genes involved in innate immune activation.

In conclusion, these findings suggest a dynamic interaction between hnRNPA2B1 and FTO. This interaction, in turn, affects the m^6A modification of *CGAS*, *IFI16*, and *STING* mRNAs and modulates their nucleocytoplasmic trafficking and translation in response to DNA virus infection. Thus, hnRNPA2B1 plays a crucial role in shaping the antiviral innate immune response.

Discussion

The mechanisms by which viral nucleic acids are surveilled are largely unknown. Here, we identify and validate hnRNPA2B1 as a nuclear viral DNA sensor through a series of in vitro and in vivo experiments using myeloid cell–specific *Hnrnpa2b1*-KO mice established for this study. The activities of hnRNPA2B1 illustrate the complexity, diversity, and flexibility of the nuclear innate immune response, which is at least as elaborate as cytoplasmic immune signaling. More intensive future efforts are warranted to fully understand the functional importance of nuclear

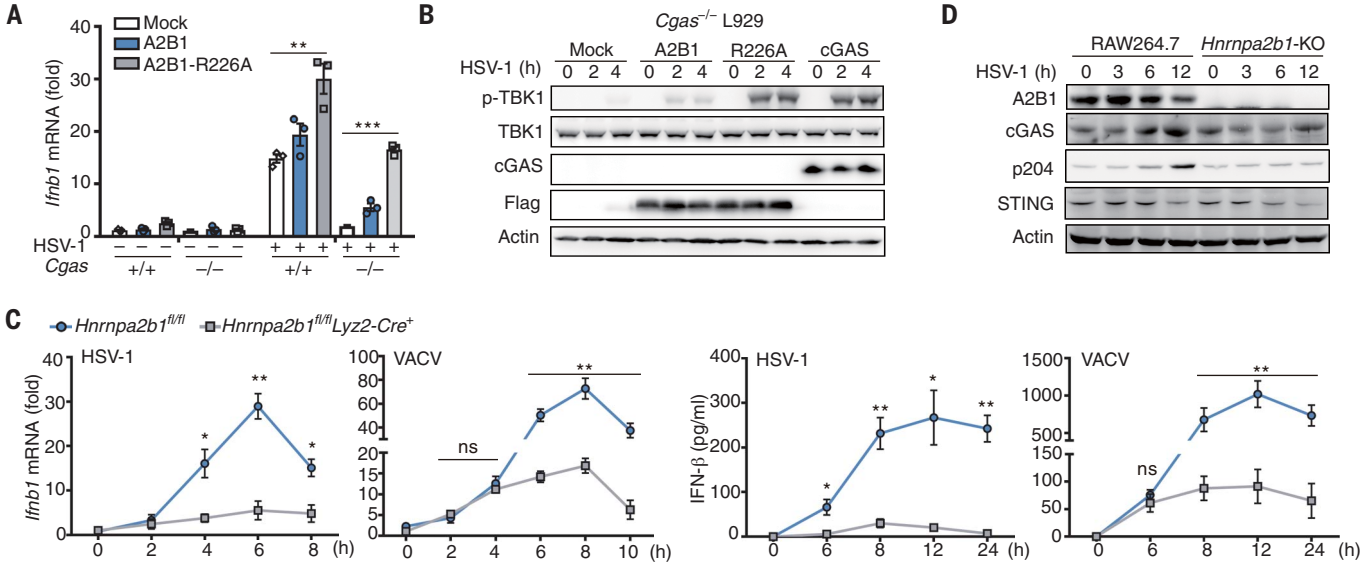

Fig. 6. hnRNPA2B1 is required for efficient type I interferon induction by cGAS, IFI16, and STING. (**A**) Wild-type and *Cgas*$^{-/-}$ L929 cells were transfected with mock, hnRNPA2B1, or hnRNPA2B1-R226A vectors for 24 hours, respectively, and then infected with HSV-1 (MOI, 10) for 7 hours. *Ifnb1* mRNA was assayed by qPCR. (**B**) Wild-type and *Cgas*$^{-/-}$ L929 cells were transfected with mock, Flag-hnRNPA2B1, Flag-hnRNPA2B1-R226A, or cGAS vectors, respectively, for 24 hours and then infected with HSV-1 (MOI, 10) as indicated. TBK1 activation was assayed by immunoblot. (**C**) Wild-type and *Hnrnpa2b1*-KO PMs were infected with HSV-1 (MOI, 1) or VACV (MOI, 1) as indicated. *Ifnb1* mRNA was assayed by qPCR and the amount of IFN-β protein was assayed by ELISA. (**D**) Wild-type and *Hnrnpa2b1*-KO RAW264.7 were infected with HSV-1 (MOI, 10) as indicated. Whole-cell lysates were prepared and examined by immunoblot for cGAS, STING, and p204 expression. Similar results were obtained for three independent experiments. One representative experiment is shown [(B) and (D)]. Data are displayed as means ± SEM of three [(A) and (C)] independent experiments performed in triplicate. *P < 0.05, **P < 0.01, ***P < 0.001; ns, not significant; two-tailed, unpaired Student's t test [(A) and (C)]. See also fig. S11.

response pathways in innate immunity and inflammation.

cGAS has been shown to have an essential role for innate response to pathogenic DNA. cGAS recognizes viral DNA in the cytoplasm, whereas hnRNPA2B1 senses viral DNA in the nucleus and initiates IFN signaling at least partially independent of cGAS. These two sensors cooperatively anchor an integrated cellular pathogen-sensing system with other known cytoplasmic sensors. We found that the overexpression of hnRNPA2B1 can increase HSV-I–induced TBK1 activation and IFN-β production in cGAS KO cells, but not increase HSV-1–induced IFN-β production in *Sting*$^{-/-}$, *Tbk1*$^{-/-}$, or *Irf3*$^{-/-}$ cells. In response to DNA virus infection, hnRNPA2B1 initiates the STING-dependent activation of TBK1-IRF3 for IFN-I production, but not NF-κB activation for IL-6 and TNF-α production. Additionally hnRNPA2B1 promotes the translocation of immune-associated mRNAs, including *CGAS*, *IFI16*, and *STING* mRNAs, and subsequently enhances their expression, ensuring the robust integration of innate immune responses. Thus, hnRNPA2B1 activity represents an important host defense mechanism by which innate antiviral responses are initiated and amplified. Our findings add insight into how this network of cellular DNA sensors efficiently launch and license innate immune responses to DNA viruses.

We found that the dimerization and dimerization-dependent demethylation mode determines whether hnRNPA2B1 functions as an IFN initiator or amplifier. In response to DNA virus infection, hnRNPA2B1 dimerizes and undergoes Arg^{226} demethylation. Demethylated hnRNPA2B1 translocates to the cytoplasm to initiate IFN-α/β production. The nuclear transport and activation of many signaling molecules requires dimerization, such as in the cases of signal transducer and activator of transcription 1 (STAT1) and STING. Here, we demonstrate that only dimerized hnRNPA2B1 can translocate to the cytoplasm. This dimer-only export of signaling molecules may be a key checkpoint for immune surveillance.

Accumulating evidence shows that there is precise epigenetic control of innate immunity (*34*). For instance, we previously demonstrated that the RNA helicase DDX46 recruits ALKBH5 to demethylate the m^{6}A of *Mavs*, *Traf3*, and *Traf6* transcripts after viral infection, consequently enforcing their retention in the nucleus and preventing their translation, which, in turn, inhibits the antiviral interferon response (*35*). hnRNPA2B1 has been primarily studied as an RNA-binding protein (RBP) (*36*–*38*). We report here that hnRNPA2B1 can also function as an m^{6}A "modulator" to promote the m^{6}A modification and nucleocytoplasmic trafficking of *CGAS*, *IFI16*, and *STING* mRNAs in response to DNA virus infection, leading to the enhanced production of type I interferons. These findings demonstrate an important role for mRNA m^{6}A modification in innate immune responses. Additional RBPs may also engage in DNA binding and affect associated biological processes.

hnRNPA2B1 binds both viral and mammalian DNA. Self genomic DNA is normally wrapped and protected by chromosomal protein complexes to prevent self-recognition. Similar mechanisms may potentially be exploited by DNA viruses by forming minichromosomes to escape sensing. cGAS and IFI16 play a role in systemic lupus erythematosus (SLE) (*39*–*42*). Similarly, autoantibodies against hnRNP-A2 have been observed in patients with SLE (*43*). A more detailed understanding of the interactions between hnRNPA2B1, pathogen-derived DNA, and host genomic DNA in physiological and pathological conditions will be necessary.

Thus, we hypothesize a highly ordered biological circuit, which critically involves hnRNPA2B1. The protein maintains its regular functions in association with RNA in the resting, infection-free state. However, upon recognizing "foreign" DNA in the nucleus, hnRNPA2B1 polarizes its function to be a nuclear sensor for viral DNA and activates innate immune response by two integrated biological functions: initiating the IFN-I response by activating TBK1 in the cytoplasm and amplifying innate signaling by regulating the transport of innate immune mRNAs in parallel or sequence. The functional "polarization" of hnRNPA2B1 then allows cells to initiate an innate immune defense program to counter DNA viruses. The nature and purpose of hnRNPA2B1 dimerization after foreign DNA

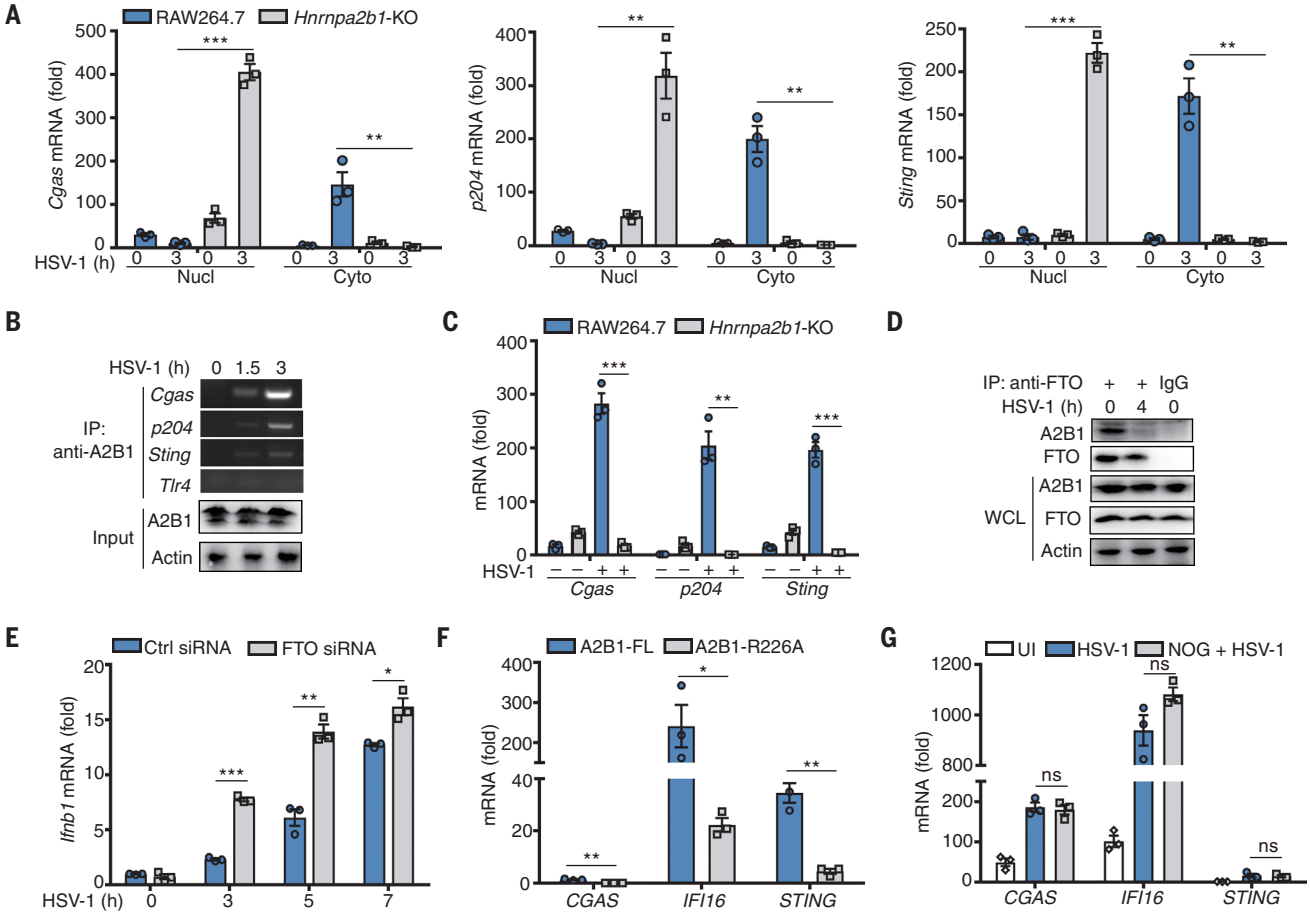

Fig. 7. hnRNPA2B1 facilitates m^{6}A modification and nucleo-cytoplasmic trafficking of *CGAS*, *IFI16*, and *STING* mRNAs upon DNA virus infection. (**A**) Wild-type and *Hnrnpa2b1*-KO RAW264.7 cells were infected with HSV-1 (MOI, 10) as indicated, and the cytoplasmic or nuclear mRNAs were extracted. *Cgas*, *p204*, and *Sting* mRNAs were detected by qPCR. The distribution of mRNA was analyzed quantitatively by densitometry of indicated mRNAs in the nucleus and cytoplasm relative to *Actb*. (**B**) Mouse PMs were infected with HSV-1 (MOI, 10) as indicated. hnRNPA2B1 was immunoprecipitated and mRNAs in the complex were detected using specific primers by PCR. (**C**) m^{6}A-containing mRNAs were immunoprecipitated with anti-m^{6}A from equal amounts of total mRNAs from wild-type and hnRNPA2B1-KO RAW264.7 cells with or without HSV-1 infection (MOI, 10) for 3 hours. *Cgas*, *p204*, and *Sting* mRNAs were assayed by qPCR. (**D**) Mouse PMs were infected with HSV-1 (MOI, 10) as indicated, and cellular extracts were immunoprecipitated with anti-FTO. hnRNPA2B1 was examined by immunoblot. (**E**) Mouse PMs transfected with control siRNA or FTO-specific siRNA were infected with HSV-1 (MOI, 10) as indicated. *Ifnb1* mRNA expression was examined by qPCR. (**F**) mRNAs were immunoprecipitated with anti-Flag from equal amounts of total mRNAs from overexpressed hnRNPA2B1-FL and -R226A HEK293 cells with or without HSV-1 infection (MOI, 10) for 3 hours. *CGAS*, *IFI16*, and *STING* mRNAs were assayed by qPCR. (**G**) m^{6}A-containing mRNAs were immunoprecipitated with anti-m^{6}A from equal amounts of total mRNAs from PMA-differentiated THP-1 cells with or without NOG treatment. Cells were infected with HSV-1 infection (MOI, 10) for 3 hours. *CGAS*, *IFI16*, and *STING* mRNAs were assayed by qPCR with specific primers. Similar results were obtained for three independent experiments. One representative experiment is shown [(B) and (D)]. Data are displayed as means ± SEM of three [(A), (C), (E) to (G)] independent experiments performed in triplicate. *P < 0.05, **P < 0.01, ***P < 0.001; ns, not significant; two-tailed, unpaired Student's t test [(A), (C), (E) to (G)]. See also figs. S12 and S13.

recognition remain open questions. Furthermore, the differences between the DNA- and RNA-binding activities of hnRNPA2B1 are still unknown. In conclusion, this study strongly suggests that nuclear DNA sensors such as hnRNPA2B1 are essential contributors to innate immune defense.

Materials and methods

Mice

C57BL/6 mice were purchased from Joint Ventures Sipper BK Experimental Animal (Shanghai, China). *Lyz2*-Cre mice were purchased from The Jackson Laboratory. To establish *Hnrnpa2b1*-conditional-knockout mice, exons 2 to 6 of the *Hnrnpa2b1* gene were trapped by insertion of loxP sequences which can be specifically recognized by CRE recombinase. *Hnrnpa2b1*$^{fl/fl}$ mice were backcrossed onto C57BL/6J background, and then crossed with *Lyz2*-Cre mice. Exons 2 to 6 were excised by CRE recombinase in myeloid cells. *Hnrnpa2b1*$^{fl/fl}$*Lyz2-Cre*$^{+/-}$ mice were mated with *Hnrnpa2b1*$^{fl/fl}$*Lyz2-Cre*$^{-/-}$ mice to generate *Hnrnpa2b1*$^{fl/fl}$*Lyz2-Cre*$^{+}$ and littermate control mice for further experiments. The mice were bred in specific pathogen-free conditions. Mice bearing a *Mettl3*^{fl} allele (*Mettl3*^{fl} mice) were from Q. Zhou (Chinese Academy of Sciences, China) and were crossed with *Lyz2*-Cre mice to obtain *Mettl3*$^{fl/fl}$*Lyz2-Cre*$^{+}$ mice. Mice at 8 weeks of age were used for in vivo experiments.

All animal experiments were undertaken in accordance with the National Institute of Health Guide for the Care and Use of Laboratory Animals, with the approval of the Second Military Medical University, Shanghai.

Cells and reagents

RAW264.7 cells, HEK293 cells, and HEK293T cells were obtained from ATCC and cultured in Dulbecco's modified Eagle's medium (DMEM) medium with 10% (v/v) fetal bovine serum (FBS)

(Gibco). Mouse peritoneal macrophages were isolated from the peritoneal cavities of mice 3 days after injection with thioglycolate medium and cultured in (DMEM) medium with 10% (v/v) FBS. *Cgas*$^{-/-}$ L929 cells and plasmids encoding *CGAS*, *STING* and *IFI16* were from Z. J. Chen (University of Texas Southwestern Medical Center). *Sting*$^{-/-}$ BMDMs and *Tbk1*$^{-/-}$ MEFs were from G. Cheng (UCLA).

VSV was a gift from W. Pan (Second Military Medical University, Shanghai, China), and Sendai virus was from B. Sun (Chinese Academy of Sciences, Shanghai, China).

Antibodies specific to hemagglutinin (HA)–tag (ab1424), Flag-tag (ab18230), Actin (Abcam 8226), cGAS (ab176177), IFI16 (ab104409) JMJD6 (ab64575) and STING (ab92605), the recombinant IRF3 (ab132091), were from Abcam Inc (Cambridge, MA). ANTI-FLAG M2 Magnetic Beads (M8823) and *N*-oxalylglycine (NOG) were from Sigma-Aldich (St. Louis, MO). Src inhibitor Saracatinib was from Selleck (Houston, TX). Antibodies specific for monomethyl arginine (Me-R4-100) (8015), IRF3 (4302), p65 (8242), Src (2123) and TBK1 (3504), and phospho-specific antibodies against IRF3 (Ser396) (4947), Src (Tyr416) (6943), TBK1 (Ser172) (5483) were from Cell Signaling Technology (Beverly, MA). Antibody against hnRNPA2B1 (anti-hnRNPA2B1) (sc-374053) was from Santa Cruz Biotechnology (Dallas, TX). Antibody specific for demethylated hnRNPA2B1 (R226) was developed using synthesized antigenic 14–amino acid peptide of deme-hnRNPA2B1 (R226): CDGYGSGRGFGDGY. Rabbit polyclonal antibodies to the peptide were purified using protein A. Finally, antibody specificity was validated using dot blot analysis.

For immunoblotting, anti-cGAS was used at 1.2 μg/ml, anti-JMJD6 at 1 μg/ml, and anti-STING at 0.5 μg/ml, and other antibodies were used at a concentration of 0.2 μg/ml. For immunofluorescence, antibodies were used at a concentration of 2 μg/ml.

HSV-1 DNA purification, biotin labeling and nucleic acid affinity purification

HSV-1 genomic DNA was purified by using ChargeSwitchg DNA Preparation Kit (Invitrogen, San Diego, CA). Approximately 5 pmol of purified viral DNA was biotinylated with a biotin 3′-end DNA labeling kit (89818, Pierce Biotechnology, Rockford, IL). Nuclear extracts from RAW264.7 cells were prepared using the Nuclear Complex Co-IP Kit (54001, Active Motif, Carlsbad, CA). Nuclear extracts were incubated with biotinylated HSV-1 DNA at 4°C overnight. The complexes were precipitated on streptavidin-coupled dynabeads (Invitrogen, 601.01), washed four times with phosphate-buffered saline (PBS) buffer and resolved on 10% SDS–PAGE gel. Differential protein bands were then selected for MS assays after silver staining.

2D electrophoresis

Nuclear and cytoplasmic extracts from RAW264.7 cells with or without infection of HSV-1 or VSV were separated on 2D SDS–PAGE gels. Isoelectric focusing was performed with ZOOM IPGRunner Kit (Invitrogen). Zoom Stripes with a pH 3 to 10 range were used overnight followed by SDS–PAGE. After silver staining, each gel was scanned on a Typhoon 9410 scanner (GE Healthcare). Each differential gel spot was excised for protein identification.

Nanospray liquid chromatography–tandem mass spectrometry

Proteins in selected bands (dots) derived from nucleic acid affinity purification, 2D electrophoresis, or immunoprecipitations were eluted and digested. Digests were analyzed by nano-ultra-performance liquid chromatography–electrospray ionization tandem mass spectrometry. Data from liquid chromatography–tandem mass spectrometry were processed through the use of ProteinLynx Global Server version 2.4 (PLGS 2.4); the resulting peak lists were used for searching the NCBI protein database with the Mascot search engine.

Sequences, plasmids constructs, transfection and RNA interference

The recombinant vectors encoding *Hnrnpa2b1* (GenBank No. NM_182650) and its mutants were constructed by PCR-based amplification from RAW264.7 cDNA and then subcloned into the pcDNA3.1 eukaryotic expression vector (Invitrogen). The pRL-TK-Renilla-luciferase plasmid was obtained from Promega (Madison, WI). Mouse DNAs for *Ifnb1* promoter were amplified from RAW264.7 cells by PCR and cloned into pGL3 plasmid (Promega) to construct *Ifnb1* luciferase reporter plasmids. The primers were: 5′-AGCTTGAATAAAATGCTAGCTAGAAGCTGTTAGAA-3′ and 5′-CAAGATGAGGCAAAGCTTCAAAGGCTGCAGTGAGAAT-3′. All constructs were confirmed by DNA sequencing.

For transient transfection of plasmids, the jetPEI reagents were used (Polyplus-transfection Company, Illkirch, France). For transient silence, the siRNA duplexes were transfected using INTERFERin reagent (Polyplus-transfection Company) according to the standard protocol. The target sequences used for transient silence were as follows: 5′-GAGGAAATTATGGAAGTGG-3′ and 5′-CCACAGAAGAAAGTTTGAGTT-3′ (siRNA2) for mouse hnRNPA2B1; 5′-CTTTGGTGGTAGCAGGAAC-3′ for human hnRNPA2B1; and 5′ CTGTGAAAGTGTATGAGAA-3′ for TBK1; 5′-TGAAGCAATTACCTGGTTTAA-3′ and 5′-GTTATCAAGGAAGTGGTATAG-3′ for mouse JMJD6; 5′-CAACGTGACTTTGCTAAAC-3′ for mouse FTO. The nonsense sequence 5′-TTCTCCGAACGTGTCACGT-3′ was used as a control siRNA.

Assay of luciferase reporter gene expression

Cells were cotransfected with the mixture of *Ifnb1* luciferase reporter plasmid, RL-TK-Renilla-luciferase plasmid, and the indicated constructs. Luciferase activities were measured with Dual-Luciferase Reporter Assay System (Promega) according to the manufacturer's instructions. Data were normalized for transfection efficiency by dividing Firefly luciferase activity with that of Renilla luciferase.

Determination of HSV-1 replication

To assess the replication of HSV-1, we infected the indicated RAW264.7 cells and L929 cells with HSV-1 [multiplicity of infection (MOI), 0.5] and the viral titers were measured by plaque assays.

In vitro kinase assay

Whole cell lysates (100 μg) were incubated with 2 ng of anti-TBK1 or immunoglobulin G (IgG) with gentle rocking at 4°C overnight. Protein G magnetic beads (Millipore) were added and incubated for additional 4 hours. The kinase activity of TBK1 was measured by using Universal Kinase Activity Kit (EA004, R&D Systems) in the presence of recombinant IRF3 as instructed.

Nucleofection

Phorbol 12-myristate 13-acetate (PMA)–differentiated THP-1 cells were transfected with 1 μg of human native nucleosomes (Millipore, 14-1057), DNA extracted from human native nucleosomes, or HBV DNA, by Amaxa Nucleofector following the manufacturer's instructions. To confirm that DNA bound to the native nucleosomes reaches the nucleus, we transfected THP1 cells with 1 μg of chicken native nucleosomes (Epicypher, 16-0019). Nuclear fractions were then separated and DNA was extracted for qPCR with chicken-specific primers.

Affymetrix GeneChip analysis

Wild-type and *Hnrnpa2b1* knockout peritoneal macrophages were infected with HSV-1 (MOI, 10) for 4 hours. RNAs from the nuclear fraction and the cytoplasmic fraction from both kinds of cells was isolated using TRIZOL. RNA samples were deoxyribonuclease I (DNase I)–treated, labeled, and hybridized on mouse GeneChip 1.0 ST arrays (Affymetrix) following standard procedures. After scanning (GeneChip Scanner 3000 7G; Affymetrix) of the arrays, the CEL files generated were analyzed using BRB Array Tool and processed using the RMA algorithm (robust multi-array average) for normalization and summarization. Gene expression ratios were processed and visualized as a heatmap.

Immunoprecipitation

For immunoprecipitation, 1 μg of specific antibodies or IgG was added per 1 mg of total proteins (1 ml of whole cell lysates) and then incubated with gentle rocking at 4°C overnight. The complexes were precipitated with Protein G magnetic beads (MILLIPORE, LSKMAGG02).

Measurements of cytokine production

Cytokine mRNA levels were assayed by quantitative real-time PCR via LightCycler (Roche, Basel, Switzerland) and SYBR RT-PCR kit (Takara, Dalian, China).

Cytokine protein levels were measured with ELISA Kits (R&D Systems, Minneapolis, MN) according to the manufacturer's instructions.

HSV-1 entry detection

Mouse peritoneal macrophages were treated with or without Src inhibitor for 30 min and infected with HSV-1 (MOI, 10) as indicated. One hour later, supernatants were removed and cells were washed with PBS for two times. Whole cell lysates were then subjected to SDS–PAGE and immunoblotted using an anti-HSV-1 major capsid protein VP5 antibody (Santa Cruz, sc-13525).

Confocal microscopy

RAW264.7 cells, HEK293 cells or L929 cells, plated on glass coverslips in six-well plates, were left uninfected or infected with HSV-1 or indicated pathogens. After being fixed in 4% (wt/vol) paraformaldehyde and treated with 0.5% (vol/vol) Triton X-100, cells were stained with primary antibodies (2 μg/ml) overnight at 4°C and then with Alexa Fluor 488- and 568-labeled secondary antibodies for 2 hours at room temperature. Cells were stained with or 4',6-diamidino-2-phenylindole (DAPI) for 5 min at room temperature and then observed with a Leica TCS SP8 confocal laser microscope with 63×/1.40 oil objective lens. Images were processed using Leica Application Suite X software (LAS X, V2.0.2.15022).

In vivo modulation of HSV-1 infection

Hnrnpa2b1$^{fl/fl}$ and *Hnrnpa2b1*$^{fl/fl}$*Lyz2-Cre*$^{+}$ mice were infected with 1×10^{8} plaque-forming units (PFU) of HSV-1 viruses intraperitoneally. Serum IFN-β concentrations were determined by enzyme-linked immunosorbent assay (ELISA) kit. HSV-1 titers were determined by plaque assays using homogenates from brains of infected mice.

Densitometry analysis

Gels were scanned by Tanon 3500B Gel Image System (Tanon, Shanghai, China) and densitometry was analyzed using software Tanonimage (V1.0).

PCR assay of specific m^{6}A-containing mRNAs

m^{6}A-containing RNAs were immunoprecipitated with anti-m^{6}A from the same amount of total RNAs of wild-type and *Hnrnpa2b1*-KO RAW264.7 cells with or without HSV-1 infection (MOI, 10). *Cgas*, *Sting*, *p204*, and *Aim2* mRNAs were assayed by qPCR. The primers were as follows: 5′-GTTCAAAGGTGTGGAGCAGC-3′ (forward) and 5′-ATTCTTTTGAATTTCACAAG-3′ (reverse) for mouse *Cgas*; 5′-GAGTGTTTACATTACACAAG-3′ (forward) and 5′-GGAGTTTATCTCCTTCCTTG-C-3′ (reverse) for *p204*; 5-GAGTGTTTACATTA-CACAAG-3′(forward) and 5′-CCTTCCTCGCAC-TTTGTTTTGC-3′ (reverse) for mouse *Aim2*; and 5′-TCAGTGGTGCAGGGAGCCGA-3′ (forward) and 5′-CGCCTGCTGGCTGTCCGTTC-3′(reverse) for mouse *Sting*.

Statistical analysis

Results are provided as means ± the standard error (SEM). All data are from at least three independent experiments performed in triplicate. Comparisons between two groups were performed using two-tailed unpaired Student's *t* test. The statistical significance of Kaplan–Meier survival curves was estimated by using the log-rank test. All statistical tests were two-sided, and significance was assigned at $P < 0.05$.

REFERENCES AND NOTES

1. T. Kawai, S. Akira, The role of pattern-recognition receptors in innate immunity: Update on Toll-like receptors. *Nat. Immunol.* **11**, 373–384 (2010). doi: 10.1038/ni.1863; pmid: 20404851
2. S. R. Paludan, A. G. Bowie, K. A. Horan, K. A. Fitzgerald, Recognition of herpesviruses by the innate immune system. *Nat. Rev. Immunol.* **11**, 143–154 (2011). doi: 10.1038/nri2937; pmid: 21267015
3. M. Marsh, A. Helenius, Virus entry: Open sesame. *Cell* **124**, 729–740 (2006). doi: 10.1016/j.cell.2006.02.007; pmid: 16497584
4. N. Kerur *et al*., IFI16 acts as a nuclear pathogen sensor to induce the inflammasome in response to Kaposi Sarcoma-associated herpesvirus infection. *Cell Host Microbe* **9**, 363–375 (2011). doi: 10.1016/j.chom.2011.04.008; pmid: 21575908
5. M. H. Orzalli, N. A. DeLuca, D. M. Knipe, Nuclear IFI16 induction of IRF-3 signaling during herpesviral infection and degradation of IFI16 by the viral ICP0 protein. *Proc. Natl. Acad. Sci. U.S.A.* **109**, E3008–E3017 (2012). doi: 10.1073/pnas.1211302109; pmid: 23027953
6. J. Wu, Z. J. Chen, Innate immune sensing and signaling of cytosolic nucleic acids. *Annu. Rev. Immunol.* **32**, 461–488 (2014). doi: 10.1146/annurev-immunol-032713-120156; pmid: 24655297
7. Y. H. Chiu, J. B. Macmillan, Z. J. Chen, RNA polymerase III detects cytosolic DNA and induces type I interferons through the RIG-I pathway. *Cell* **138**, 576–591 (2009). doi: 10.1016/j.cell.2009.06.015; pmid: 19631370
8. B. J. Ferguson, D. S. Mansur, N. E. Peters, H. Ren, G. L. Smith, DNA-PK is a DNA sensor for IRF-3-dependent innate immunity. *eLife* **1**, e00047 (2012). doi: 10.7554/eLife.00047; pmid: 23251783
9. L. Sun, J. Wu, F. Du, X. Chen, Z. J. Chen, Cyclic GMP-AMP synthase is a cytosolic DNA sensor that activates the type I interferon pathway. *Science* **339**, 786–791 (2013). doi: 10.1126/science.1232458; pmid: 23258413
10. A. Takaoka *et al*., DAI (DLM-1/ZBP1) is a cytosolic DNA sensor and an activator of innate immune response. *Nature* **448**, 501–505 (2007). doi: 10.1038/nature06013; pmid: 17618271
11. L. Unterholzner *et al*., IFI16 is an innate immune sensor for intracellular DNA. *Nat. Immunol.* **11**, 997–1004 (2010). doi: 10.1038/ni.1932; pmid: 20890285
12. H. Yanai *et al*., HMGB proteins function as universal sentinels for nucleic-acid-mediated innate immune responses. *Nature* **462**, 99–103 (2009). doi: 10.1038/nature08512; pmid: 19890330
13. P. Yang *et al*., The cytosolic nucleic acid sensor LRRFIP1 mediates the production of type I interferon via a beta-catenin-dependent pathway. *Nat. Immunol.* **11**, 487–494 (2010). doi: 10.1038/ni.1876; pmid: 20453844
14. Z. Zhang *et al*., The helicase DDX41 senses intracellular DNA mediated by the adaptor STING in dendritic cells. *Nat. Immunol.* **12**, 959–965 (2011). doi: 10.1038/ni.2091; pmid: 21892174
15. Y. Li *et al*., LSm14A is a processing body-associated sensor of viral nucleic acids that initiates cellular antiviral response in the early phase of viral infection. *Proc. Natl. Acad. Sci. U.S.A.* **109**, 11770–11775 (2012). doi: 10.1073/pnas.1203405109; pmid: 22745163
16. T. Kondo *et al*., DNA damage sensor MRE11 recognizes cytosolic double-stranded DNA and induces type I interferon by regulating STING trafficking. *Proc. Natl. Acad. Sci. U.S.A.* **110**, 2969–2974 (2013). doi: 10.1073/pnas.1222694110; pmid: 23388631
17. X. D. Li *et al*., Pivotal roles of cGAS-cGAMP signaling in antiviral defense and immune adjuvant effects. *Science* **341**, 1390–1394 (2013). doi: 10.1126/science.1244040; pmid: 23989956
18. V. A. Rathinam *et al*., The AIM2 inflammasome is essential for host defense against cytosolic bacteria and DNA viruses. *Nat. Immunol.* **11**, 395–402 (2010). doi: 10.1038/ni.1864; pmid: 20351692
19. S. Roth *et al*., Rad50-CARD9 interactions link cytosolic DNA sensing to IL-1β production. *Nat. Immunol.* **15**, 538–545 (2014). doi: 10.1038/ni.2888; pmid: 24777530
20. P. Xia *et al*., Sox2 functions as a sequence-specific DNA sensor in neutrophils to initiate innate immunity against microbial infection. *Nat. Immunol.* **16**, 366–375 (2015). doi: 10.1038/ni.3117; pmid: 25729924
21. S. P. Han, Y. H. Tang, R. Smith, Functional diversity of the hnRNPs: Past, present and perspectives. *Biochem. J.* **430**, 379–392 (2010). doi: 10.1042/BJ20100396; pmid: 20795951
22. J. Ding *et al*., Crystal structure of the two-RRM domain of hnRNP A1 (UP1) complexed with single-stranded telomeric DNA. *Genes Dev.* **13**, 1102–1115 (1999). doi: 10.1101/gad.13.9.1102; pmid: 10323862
23. K. A. Fitzgerald *et al*., IKKepsilon and TBK1 are essential components of the IRF3 signaling pathway. *Nat. Immunol.* **4**, 491–496 (2003). doi: 10.1038/ni921; pmid: 12692549
24. K. Honda, T. Taniguchi, IRFs: Master regulators of signalling by Toll-like receptors and cytosolic pattern-recognition receptors. *Nat. Rev. Immunol.* **6**, 644–658 (2006). doi: 10.1038/nri1900; pmid: 16932750
25. M. Yang *et al*., E3 ubiquitin ligase CHIP facilitates Toll-like receptor signaling by recruiting and polyubiquitinating Src and atypical PKCzeta. *J. Exp. Med.* **208**, 2099–2112 (2011). doi: 10.1084/jem.20102667; pmid: 21911421
26. X. Li *et al*., The tyrosine kinase Src promotes phosphorylation of the kinase TBK1 to facilitate type I interferon production after viral infection. *Sci. Signal.* **10**, eaae0435 (2017). doi: 10.1126/scisignal.aae0435; pmid: 28049762
27. J. D. Gary, S. Clarke, RNA and protein interactions modulated by protein arginine methylation. *Prog. Nucleic Acid Res. Mol. Biol.* **61**, 65–131 (1998). doi: 10.1016/S0079-6603(08)60825-9; pmid: 9752719
28. G. Han *et al*., The hydroxylation activity of Jmjd6 is required for its homo-oligomerization. *J. Cell. Biochem.* **113**, 1663–1670 (2012). doi: 10.1002/jcb.24035; pmid: 22189873
29. S. S. Broyles, Vaccinia virus transcription. *J. Gen. Virol.* **84**, 2293–2303 (2003). doi: 10.1099/vir.0.18942-0; pmid: 12917449
30. J. E. Harper, S. M. Miceli, R. J. Roberts, J. L. Manley, Sequence specificity of the human mRNA N6-adenosine methylase in vitro. *Nucleic Acids Res.* **18**, 5735–5741 (1990). doi: 10.1093/nar/18.19.5735; pmid: 2216767
31. G. Jia *et al*., N6-methyladenosine in nuclear RNA is a major substrate of the obesity-associated FTO. *Nat. Chem. Biol.* **7**, 885–887 (2011). doi: 10.1038/nchembio.687; pmid: 22002720
32. G. Zheng *et al*., ALKBH5 is a mammalian RNA demethylase that impacts RNA metabolism and mouse fertility. *Mol. Cell* **49**, 18–29 (2013). doi: 10.1016/j.molcel.2012.10.015; pmid: 23177736
33. K. Xu *et al*., Mettl3-mediated m^{6}A regulates spermatogonial differentiation and meiosis initiation. *Cell Res.* **27**, 1100–1114 (2017). doi: 10.1038/cr.2017.100; pmid: 28809392
34. Q. Zhang, X. Cao, Epigenetic regulation of the innate immune response to infection. *Nat. Rev. Immunol.* **19**, 417–432; Epub ahead of print (2019). doi: 10.1038/s41577-019-0151-6; pmid: 30918351
35. Q. Zheng, J. Hou, Y. Zhou, Z. Li, X. Cao, The RNA helicase DDX46 inhibits innate immunity by entrapping m^{6}A-demethylated antiviral transcripts in the nucleus. *Nat. Immunol.* **18**, 1094–1103 (2017). doi: 10.1038/ni.3830; pmid: 28846086
36. C. R. Alarcón *et al*., HNRNPA2B1 Is a Mediator of m(6)A-Dependent Nuclear RNA Processing Events. *Cell* **162**, 1299–1308 (2015). doi: 10.1016/j.cell.2015.08.011; pmid: 26321680
37. C. Villarroya-Beltri *et al*., Sumoylated hnRNPA2B1 controls the sorting of miRNAs into exosomes through binding to specific motifs. *Nat. Commun.* **4**, 2980 (2013). doi: 10.1038/ncomms3980; pmid: 24356509
38. H. Gordon *et al*., Depletion of hnRNP A2/B1 overrides the nuclear retention of the HIV-1 genomic RNA. *RNA Biol.* **10**, 1714–1725 (2013). doi: 10.4161/rna.26542; pmid: 24157614
39. D. Gao *et al*., Activation of cyclic GMP-AMP synthase by self-DNA causes autoimmune diseases. *Proc. Natl. Acad. Sci. U.S.A.* **112**, E5699–E5705 (2015). doi: 10.1073/pnas.1516465112; pmid: 26371324
40. E. E. Gray, P. M. Treuting, J. J. Woodward, D. B. Stetson, Cutting Edge: cGAS Is Required for Lethal Autoimmune Disease in the Trex1-Deficient Mouse Model of Aicardi-Goutières Syndrome. *J. Immunol.* **195**, 1939–1943 (2015). doi: 10.4049/jimmunol.1500969; pmid: 26223655
41. J. An *et al*., Expression of Cyclic GMP-AMP Synthase in Patients With Systemic Lupus Erythematosus. *Arthritis Rheumatol.* **69**, 800–807 (2017). doi: 10.1002/art.40002; pmid: 27863149
42. V. Caneparo *et al*., Anti-IFI16 antibodies and their relation to disease characteristics in systemic lupus erythematosus.

Lupus **22**, 607–613 (2013). doi: 10.1177/0961203313484978; pmid: 23612796
43. R. Fritsch-Stork *et al*., The spliceosomal autoantigen heterogeneous nuclear ribonucleoprotein A2 (hnRNP-A2) is a major T cell autoantigen in patients with systemic lupus erythematosus. *Arthritis Res. Ther.* **8**, R118 (2006). doi: 10.1186/ar2007; pmid: 16859514

ACKNOWLEDGMENTS

We thank Z. J. Chen (University of Texas Southwestern Medical Center) for providing *Cgas*$^{-/-}$ L929 cells and plasmids encoding *CGAS*, *STING*, and *IFI16*; G. Cheng (UCLA) for providing *Sting*$^{-/-}$ BMDMs and *Tbk1*$^{-/-}$ MEFs; T. Taniguchi (University of Tokyo) for providing *Irf3*$^{-/-}$ mice; Q. Zhou (Chinese Academy of Sciences) for providing *Mettl3*^{fl} mice; and T. Chen, W. Cun, and Y. Zhang for technical assistance. **Funding:** This work is supported by grants from the National Natural Science Foundation of China (81788101), National Key Research & Development Program of China (2018YFA0507403), and CAMS Innovation Fund for Medical Sciences (2016-12M-1-003). **Author contributions:** X.C. designed and supervised research; L.W. and M.W. performed the experiments; X.C., L.W., and M.W. analyzed data and wrote the manuscript. **Competing interests:** The authors declare no competing interests. **Data and materials availability:** The transcriptome microarray data are deposited in the NCBI Gene Expression Omnibus under accession number GSE129926. The *Hnrnpa2b1*$^{fl/fl}$ mouse strain, *Hnrnpa2b1*-KO RAW264.7 and L929 cell lines, and plasmids encoding *Jmjd6*, *Fto*, *Hnrnpa2b1*, and its mutants are available from the corresponding author on request as supplies permit, subject to a standard materials transfer agreement. All other data needed to support the conclusions of this manuscript are included in the main text and supplementary materials.

SUPPLEMENTARY MATERIALS

science.sciencemag.org/content/365/6454/eaav0758/suppl/DC1
Table S1
Figs. S1 to S13

11 August 2018; resubmitted 29 January 2019
Accepted 10 July 2019
Published online 18 July 2019
10.1126/science.aav0758

RESEARCH ARTICLE SUMMARY

NEUROSCIENCE

Hippocampal sharp-wave ripples linked to visual episodic recollection in humans

Yitzhak Norman, Erin M. Yeagle, Simon Khuvis, Michal Harel, Ashesh D. Mehta, Rafael Malach*

INTRODUCTION: Sharp-wave ripples (SWRs) are rapid bursts of synchronized neuronal activity elicited by the hippocampus. Extensive study of SWRs, mainly in the rodent brain, has linked these bursts to navigation, memory formation, and offline memory consolidation. However, fundamental questions remain regarding the functional meaning of this striking example of network synchrony. Perhaps the most glaring unknown is the relationship between SWRs and conscious cognition. We still do not know what cognitive process, if any, is linked to the emergence of SWRs; to put it simply, we still do not know what an animal thinks about (if anything) when the hippocampus elicits a ripple. Furthermore, the potential role of SWRs in human episodic memory is still largely unknown. Thus, studying this phenomenon in conscious, awake human patients opens a unique window, as it allows direct examination of detailed verbal reports with respect to SWR occurrences.

RATIONALE: We took advantage of the unique ability of humans to communicate verbally about their inner cognitive state to examine the role of SWRs in memory formation and retrieval, using intracranial electrophysiological recordings in patients. This approach allowed us to study free recall, the process of self-initiated, internal generation of memories. It is a uniquely powerful approach because it isolates the process of recall from external stimulation.

ON OUR WEBSITE

Read the full article at http://dx.doi.org/10.1126/science.aax1030

RESULTS: Our study revealed three major aspects linking SWRs to human declarative memory. First, the SWR rate during picture viewing (i.e., memory encoding) predicted subjects' subsequent free-recall performance. Second, a transient increase in SWR rate preceded the verbal report of recall by 1 to 2 s. This increase was content-selective, recapitulating the same picture preferences observed during viewing. Finally, during recollection, high-order visual areas showed content-selective reactivation coupled to SWR emission.

CONCLUSION: By direct recordings of electrophysiological events in the brains of individuals who could inform, in real time, on their cognitive state, we were able to demonstrate and characterize an important role of SWRs in human episodic memory. Our findings point to the involvement of hippocampal SWRs in establishing and triggering spontaneous recollections in the human brain. They implicate SWRs in the process of engraving new memories, and reveal their fundamental contribution in orchestrating the dialogue between memory centers (hippocampus) and high-level representations (cerebral cortex), which underlies the retrieval of these memories. Our study thus highlights the function of SWRs as powerful multitasking signals that contribute both to the encoding and to the spontaneous access and reinstatement of human memories. ■

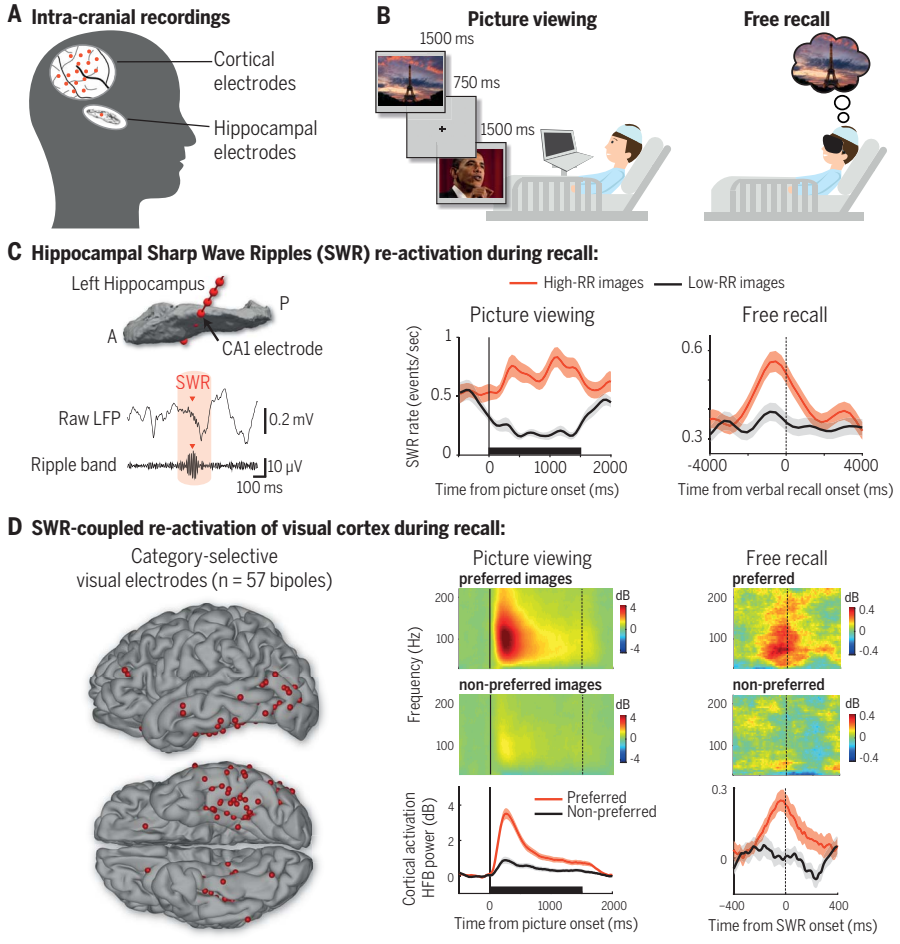

Memory reactivation coupled to hippocampal ripples during free recall. (**A**) Simultaneous intracranial recordings in hippocampus and cortex. (**B**) Patients first viewed and then freely recalled photographs of famous faces and places. (**C**) Rapid hippocampal neuronal bursts (SWRs) were identified (left). When patients freely recalled the images, a transient increase in SWR rate anticipated the onset of recall, dominated by items that generated a higher ripple rate (RR) during viewing (compare red and black lines). (**D**) Visual areas in the cortex showed SWR-coupled reactivation, recapitulating the content selectivity observed during viewing.

The list of author affiliations is available in the full article online.
*Corresponding author. Email: rafi.malach@gmail.com
Cite this article as Y. Norman *et al.*, *Science* **365**, eaax1030 (2019). DOI: 10.1126/science.aax1030

RESEARCH ARTICLE

NEUROSCIENCE

Hippocampal sharp-wave ripples linked to visual episodic recollection in humans

Yitzhak Norman[1], Erin M. Yeagle[2], Simon Khuvis[2], Michal Harel[1], Ashesh D. Mehta[2], Rafael Malach[1]*

Hippocampal sharp-wave ripples (SWRs) constitute one of the most synchronized activation events in the brain and play a critical role in offline memory consolidation. Yet their cognitive content and function during awake, conscious behavior remains unclear. We directly examined this question using intracranial recordings in human patients engaged in episodic free recall of previously viewed photographs. Our results reveal a content-selective increase in hippocampal ripple rate emerging 1 to 2 seconds prior to recall events. During recollection, high-order visual areas showed pronounced SWR-coupled reemergence of activation patterns associated with recalled content. Finally, the SWR rate during encoding predicted subsequent free-recall performance. These results point to a role for hippocampal SWRs in triggering spontaneous recollections and orchestrating the reinstatement of cortical representations during free episodic memory retrieval.

Hippocampal ripples (*1*, *2*) are brief (<150 ms) high-frequency oscillatory events, in the range of 140 to 200 Hz in rodents (*3*–*6*) and 80 to 140 Hz in primates and humans (*7*–*11*), that appear in the local field potential (LFP) of the hippocampal CA1 pyramidal layer (*3*, *5*). Conserved across a variety of species, these short-lived network oscillations constitute instances of highly synchronized neuronal activity in the brain. During a ripple, 10 to 15% of pyramidal neurons in the hippocampal-entorhinal output pathway discharge synchronously (*12*, *13*), orchestrating a network activation that has a potent impact on several cortical and subcortical targets (*10*, *14*). Because these ripples commonly co-occur with large-amplitude sharp waves appearing in CA1 stratum radiatum (*3*, *15*), it is customary to refer to them as sharp-wave ripple (SWR) complexes (*16*). SWRs occur most frequently during non–rapid eye movement sleep and quiescent wakefulness (*14*, *16*). In primates, SWRs can also be seen during attentive visual search, especially before the gaze is being directed toward a familiar target location (*17*, *18*).

Electrophysiological studies of humans and rodents have demonstrated different forms of coupling between hippocampal SWRs and cortical LFP (*9*, *11*, *19*–*22*). Extrahippocampal neuronal activations linked to previous awake experiences are reexpressed in the brief time window of the hippocampal ripple (*14*, *23*–*29*). The temporal relationship between SWRs and cortical reactivation during sleep suggests a coordinated bidirectional interaction whereby spontaneously generated patterns in the cortex bias the activity in the hippocampus, which then broadcasts, during the ripple, an integrated memory representation back to the cortex (*24*, *27*). Such hippocampal-cortical interplay has been hypothesized as an orchestration mechanism that governs the reactivation of mnemonic representations across distributed cortical networks (*24*, *27*, *30*, *31*).

Examination of the representational content of SWR events during ongoing awake behavior has revealed a structured, temporally compressed replay of hippocampal multicell sequences representing previous navigation-related experiences, as well as "preplay" of possible future paths (*32*–*38*). Awake replay/preplay points to a potential role for SWRs in reactivating mnemonic information not only during offline consolidation, but also during ongoing awake behavior that involves recall or imagination of nonpresent scenarios (*14*, *39*–*41*). However, the exact cognitive content and function of SWRs during awake behavior remains unclear. This is largely because of the difficulty of assessing detailed cognitive content in animal models. Here, we addressed this challenge by using a free-recall paradigm to examine the cognitive role of SWRs in intracranial recordings of human epileptic patients.

Free recall is a cognitive process by which previously stored items are recalled spontaneously, without externally presented cueing information. It allows the dissociation between any external stimuli and the internally driven memory process. We previously showed that hippocampal and ventral-temporal neurons reactivate in a content-specific manner during free recall (*42*, *43*). Furthermore, we were able to demonstrate a putative top-down biasing mechanism that constrains free recall to a particular category by modulating the ongoing baseline excitation of category-selective visual areas in the cortex (*44*).

One unique advantage of intracranial electroencephalography (iEEG) recordings conducted in patients is that the diagnostic procedure calls for multiple simultaneous recording sites in each patient. This allowed us to record LFP and SWR activity in the hippocampus simultaneously with high-frequency broadband (HFB; 60 to 160 Hz) signals reflecting local neuronal population activity (*45*–*47*) in task-relevant, content-specific, cortical sites.

SWR events were recorded in patients during a resting state and during a visual free-recall task (Fig. 1A). The task consisted of two runs, each beginning with a resting-state period of 200 s. Patients were then presented with vivid, full-color photographs of famous faces and places. After viewing each picture four times in pseudo-random order and completing a short interference task, patients were instructed to freely recall the pictures, targeting each category in separate blocks. To ensure reinstatement of visual content during recall, we instructed patients to describe each recalled item with two or three prominent visual features. Verbal responses during the recall phase were recorded, and the onset and offset of each verbal recall event were carefully extracted in an offline analysis. Patients were blindfolded throughout the free-recall period to completely block external visual input.

On average, patients recalled 8.8 ± 2.7 (SD) items per run; when including repeated recollections, they had 12.4 ± 5.7 "recall events" per run. There was no significant difference in recall performance between the two runs (P > 0.22, Wilcoxon signed-rank test). Recall events were defined as any verbal utterance in which patients began to describe a specific picture (see methods). The average duration of verbal recall events was 8.08 ± 6.27 s. Recall performance was similar between the two categories (average number of recalled items per run: 4.43 faces, 4.37 places; P > 0.9, Wilcoxon signed-rank test).

Sharp-wave ripple detection

A multicontact depth electrode implanted in the hippocampus was used for detection of SWR events. We used pre- and postoperative computed tomography (CT) and magnetic resonance imaging (MRI) scans to identify in each patient a hippocampal recording site located in or adjacent to the CA1/CA2 subfields, where SWR events are known to occur most prominently (*48*). The LFP in the selected site was then filtered between 70 and 180 Hz, rectified, squared, smoothed, and transformed into z-scores. Transient events that exceeded 4 SD and survived the exclusion criteria were selected as candidate SWR events (Fig. 1D; see methods).

[1]Department of Neurobiology, Weizmann Institute of Science, Rehovot 76100, Israel. [2]Department of Neurosurgery, Donald and Barbara Zucker School of Medicine at Hofstra/Northwell, and Feinstein Institute for Medical Research, Manhasset, NY 11030, USA.
*Corresponding author. Email: rafi.malach@gmail.com

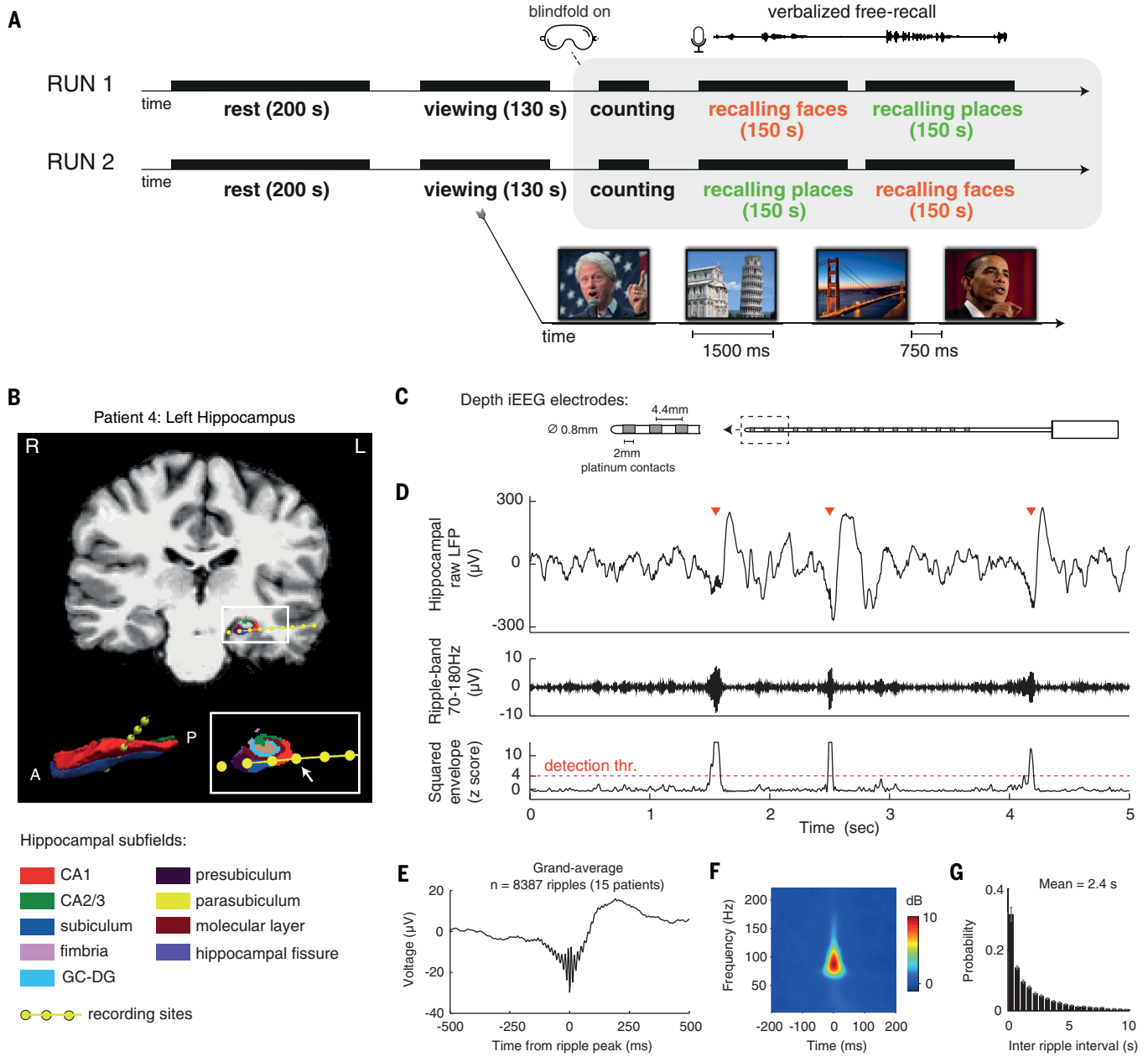

Fig. 1. Experimental design and hippocampal SWR detection. (**A**) Experimental design and stimuli (*91*). After viewing pictures of famous faces and places (see methods), participants were asked to freely recall and describe as many pictures as possible, targeting each category in separate blocks. (**B**) Coronal slice and 3D reconstruction of a hippocampal depth electrode in one representative patient. White arrow indicates CA1 recording site used for ripple detection. (**C**) Schematic diagram of depth iEEG electrodes used in our study. (**D**) Example of SWR events as they appear in the recordings. From top to bottom: raw hippocampal LFP; ripple-band filtered LFP (70 to 180 Hz); normalized ripple-band envelope used for ripple detection. (**E** and **F**) Grand average peri-ripple field potential and wavelet spectrogram centered on ripple peak (n = 8279 SWR events from 15 patients). (**G**) Overall distribution of inter-ripple intervals (n = 15 patients; error bars represent SEM).

Figure 1B shows the location of a typical CA1 recording site in one patient; Fig. 1C is a schematic drawing of the depth electrode used in our study (locations of hippocampal recording sites in each patient are depicted in fig. S1). Figure 1D shows typical SWR events as they appear in the recordings. Our dataset included 8387 SWRs obtained from 15 patients (see Fig. 1, E and F, for grand-average peri-ripple field potential and spectral decomposition and Fig. 1G for distribution of inter-ripple interval durations; see table S1 for demographic information).

We analyzed four main conditions: (i) rest, during which patients were instructed to rest with eyes closed; (ii) viewing, during which patients inspected and memorized photographs of famous faces and places; (iii) recall, referring to times within the free-recall period in which patients verbally reported recalling a specific item from the memorized set (i.e., epochs that began 3 s before the onset until the offset of each "recall event," a total of 269.5 s on average); and (iv) search, referring to all complementary time intervals between recall events, in which patients attempted to recall but did not report any recalled item (330.5 s on average).

SWR properties across cognitive states

We first examined whether the spectral signature of the SWRs varied across the different

cognitive states of the patients, or whether it remained constant (thus reflecting oscillatory events with an all-or-none behavior). We computed a peri-ripple wavelet spectrogram in a time window of −200 to 200 ms relative to the SWR peak (see methods; see fig. S2, A to D, for traces of individual SWR events and mean spectrograms, spectra, and peri-ripple field potential across conditions). A nonparametric Friedman test comparing SWR amplitude and peak frequency showed no significant differences between the main experimental conditions [fig. S2, E and F; mean peak frequency: 88.1 ± 2.1 Hz, $\chi^2(3) = 2.73$, $P > 0.43$; mean peak amplitude: 9.5 ± 1.5 dB, $\chi^2(3) = 5.00$, $P > 0.17$; $n = 15$ patients]. Similar spectral characteristics have been found in sleep SWRs in humans (*7*, *9*, *49*, *50*).

Having established that the basic spectral properties of the SWRs remained constant throughout the experiment, we next explored whether the SWR rate may have changed with the patients' cognitive state. Comparing the mean SWR rate across the different experimental conditions revealed a significant effect [$\chi^2(3) = 18.04$, $P = 0.0004$, Friedman test, $n = 15$ patients; see fig. S2G], and post hoc comparisons indicated that the basal SWR rate was slightly lower during recall and memory search (i.e., inter-recall intervals) relative to the picture-viewing and rest conditions [$P < 0.05$, pairwise Friedman tests with false discovery rate (FDR) correction; median ripple rate (events/s): 0.45 (rest), 0.47 (viewing), 0.36 (recall), 0.34 (search)].

Content-selective modulation of SWR rate

To examine whether viewing the pictures during the encoding phase influenced the SWR rate in a more transient fashion, we computed in each patient a peristimulus time histogram (PSTH) of SWRs, showing the instantaneous SWR rate in 50-ms time bins starting from −0.5 to 2.25 s relative to picture onset (Fig. 2A). Averaging across the different pictures, we found a transient general increase in SWR rate (peaking at 675 ms poststimulus) that appeared only during the first presentation of each picture. Repeated presentations of the same pictures did not evoke this nonselective time-locked response ($P < 0.01$, nonparametric cluster-based permutation test, shuffling condition labels 2000 times across patients; see fig. S3, A and B, for responses across individual presentation cycles and individual patients' data and fig. S3D for comparison between faces and places). For additional analysis examining the consistency in ripple rate across repeated presentations of the same picture, see fig. S3C.

SWRs elicited during viewing may have been reactivated later, in a content-specific manner, during the free-recall period, when patients recalled the same visual content but in the absence of any external stimulation. To examine this possibility, we pooled all items that were subsequently recalled in each patient ($n = 252$ items in total) and measured the correlation between the SWR rate evoked by each item during viewing (throughout the duration of the picture, from 50 to 1500 ms poststimulus) and the SWR rate elicited when patients freely recalled this same item (using a generic time window of 5 s centered on the onset of the verbal report of recall; repeated recollections in the same patient were averaged together). However, given the significant difference in averaged SWR rate between novel and repeated presentations described above, we analyzed the novelty-related SWRs separately from the SWRs generated during the repeated presentations.

We found a significant correlation between the SWR rates elicited by each picture during viewing and during free recall, but only for the repeated presentations—that is, when responses related to novel presentations were excluded (novel: Spearman $\rho = 0.05$, $P > 0.43$; repeated presentations: Spearman $\rho = 0.18$, $P = 0.005$; $n = 252$ successfully recalled items; fig. S4, A and B).

To investigate the temporal profile of this content-specific modulation of SWR rate during recall, we first sorted the pictures in each patient according to the number of SWRs they elicited during the repeated presentations (in a time window of 50 to 1500 ms poststimulus). We then divided the pictures into two groups: pictures that elicited a high SWR rate during viewing (above median), which we termed "high-RR" images; and pictures that resulted in low SWR rates (below median), which we termed "low-RR" images (Fig. 2B, inset).

Figure 2B depicts the average SWR rate when patients viewed the high-RR and low-RR images (red and dark contours, respectively). Note that the difference between these two signals is due to the selection process and is to be expected given the variable SWR responses across different images during viewing (see fig. S5 for further characterization of SWR responses across high-RR and low-RR images). The critical question is whether this content-specific difference during viewing reappeared during recall, in the absence of visual stimuli.

To answer this question, we computed for each patient a PSTH of SWRs, time-locked to the onset of verbal report of recall (using time bins of 200 ms from −5 to 5 s, smoothed with 1000-ms triangular window). Recall events with separation of less than 5 s from the previous recollection were excluded from the analysis. We first searched for a nonselective signal related to any recall event. We found a transient increase in SWR rate that preceded the onset of verbal report by 1 to 2 s (Fig. 2C). A nonparametric cluster-based permutation test, which compared the activation profile to 2000 shuffled PSTHs produced by circularly jittering SWR timing in each trial by a random amount, indicated that the anticipatory increase was highly significant ($P < 0.01$; cluster-defining threshold was set at ±1.96 SD from the mean rate; see also fig. S4D; significant time bins are marked in orange). Additional analysis confirmed that SWRs were not coupled to voice amplitude or instances of abrupt vocalizations (fig. S6). Movie S1 shows examples of spontaneous recall events and their relation to SWRs in three patients.

Next, we examined whether this increase during recall was content-specific. We compared SWR rates during recall of high-RR versus low-RR images (defined by the viewing responses). A nonparametric permutation test, shuffling high-RR and low-RR labels 2000 times, revealed that the SWR rate was significantly higher during recall of high-RR images ($P < 0.05$, see Fig. 2D; for raster plot and individual patients' data, see fig. S4). Here, too, the content-selective increase emerged 1 to 2 s prior to the beginning of the actual verbal report.

Ripple rate during picture viewing predicts memory performance

Could SWR dynamics during picture viewing be linked to the patients' ability to later recall these pictures? To examine this possibility, we computed a PSTH of SWRs time-locked to the onset of picture presentation, separately for the first and repeated presentations (120-ms bins smoothed by a five-point triangular window; see methods). We then computed in each patient the normalized difference in SWR rate between pictures that were later remembered or forgotten: (REM − FOR)/(REM + FOR). A cluster-based permutation test revealed that the SWR rate during picture viewing predicted the memorability of items in the subsequent free recall. Specifically, we found a higher ripple rate for remembered pictures than for forgotten pictures. This effect emerged during the poststimulus interval in the first presentation cycle ($P < 0.05$, one-sided cluster-based permutation test, Fig. 3, A and B; for individual patients' data, see fig. S7). To further examine this predictive effect, we measured in each time bin the correlation between the difference in ripple rate and the patients' memory performance during the free-recall period. We found a significant correlation, peaking during the poststimulus interval and returning back to baseline upon presentation of the next picture ($P < 0.05$, FDR correction; peak correlation: Spearman $\rho = 0.85$; Fig. 3C).

Finally, to rule out the possibility that this correlation resulted from the differences in the number of trials belonging to each group of images (remembered and forgotten), we carried out an additional permutation test, in which we shuffled the labels of the ripple rate responses 2000 times and randomly resampled the original number of remembered and forgotten trials in each patient. The results of this analysis indicated that the correlation observed in the actual data during the poststimulus interval was highly significant and did not arise from differences in the number of trials (Spearman $\rho = 0.83$, $P < 0.001$; Fig. 3D).

Ripple-triggered cortical activation

A major advantage of iEEG recordings in patients is that as a result of clinical requirements, recordings are typically obtained broadly across several cortical and medial temporal lobe (MTL)

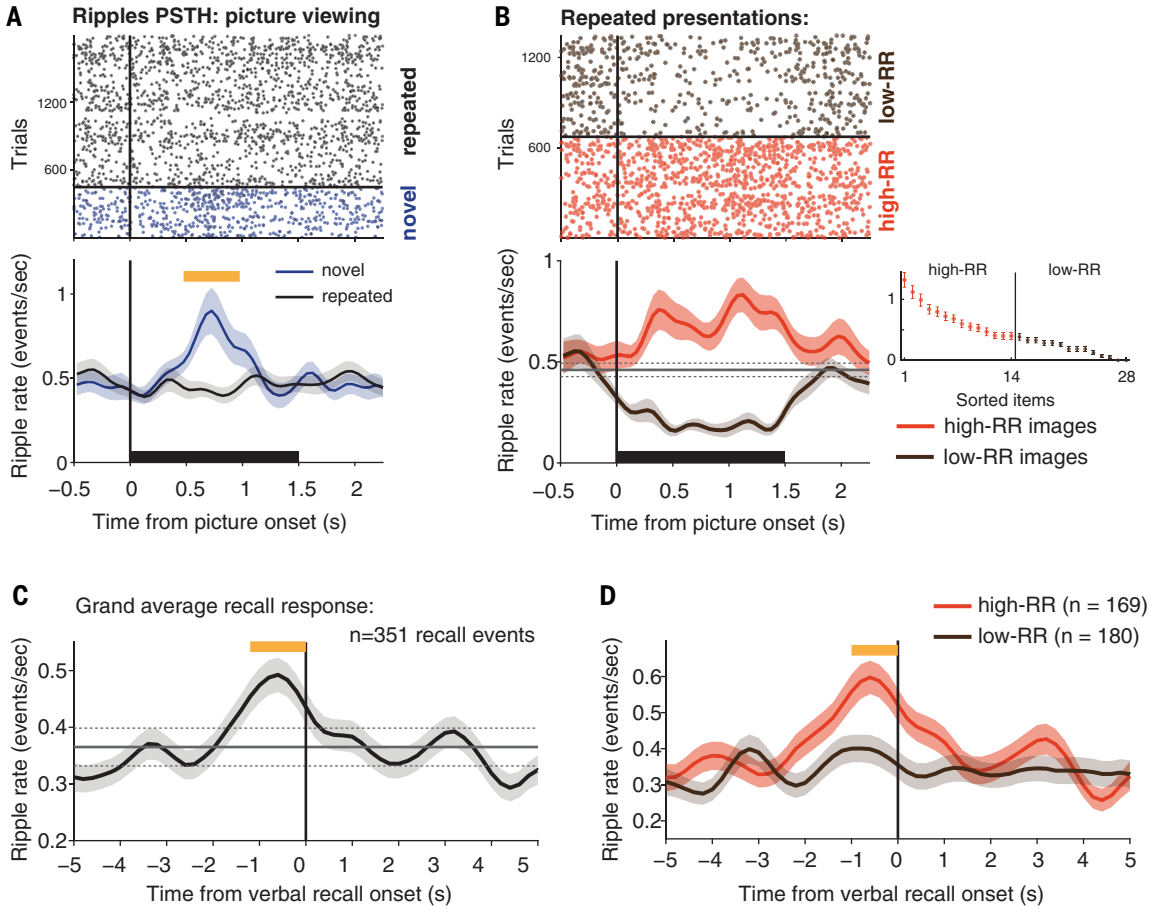

Fig. 2. Ripples PSTH during picture viewing and free recall. (**A**) SWRs raster plot and PSTH time-locked to the onset of picture presentation (n = 15 patients, each viewed 28 items × 4 presentation cycles), showing a transient increase in averaged SWR rate in response to the first but not to repeated presentations ($P < 0.01$, cluster-based permutation test). Black horizontal bars on the x axis represent stimulus on-periods. (**B**) Content selectivity of SWR rate modulation during repeated presentations, with specific images producing a higher SWR rate. Inset shows the mean rate of individual items computed over the entire stimulus period with SEM across patients. Ripple rate of high-RR images was on average 3.5 times that of low-RR images. (**C**) Grand-average ripples PSTH time-locked to the onset of verbal recall, showing a significant increase in SWR rate anticipating the onset of verbal report by 1 to 2 s ($P < 0.01$, cluster-based permutation test; see fig. S4D). (**D**) SWR rate during recall of high-RR and low-RR images (as defined during viewing), demonstrating recapitulation of the content selectivity observed during viewing ($P < 0.05$, cluster-based permutation test). Note again the anticipatory nature of the SWR rate increase. Shaded areas represent ±1 bootstrap SE computed over subjects [in (A) and (B)] or recall events [in (C) and (D)]. Gray horizontal solid/dashed lines represent mean rate (±1 SD) for the same data when SWR timing was randomly shuffled. Orange bars represent significant time bins.

areas. We took advantage of this by comparing the activity in high-order category-selective visual electrodes (i.e., selective to face or place images) during viewing to the activity in the same recording sites during free recall, when patients recalled and verbally described the electrodes' "preferred" and "nonpreferred" images. Image preference in each electrode was determined by sorting the different images according to the HFB amplitude they elicited during viewing (averaging the response over a time window of 100 to 500 ms and across the four presentations). We defined the top 10 items that evoked the strongest response during viewing as the "preferred" images and the bottom 10 items as the "nonpreferred" images. In most instances, the preferred and nonpreferred images also corresponded to the electrodes' preferred and nonpreferred categories, respectively (91% of preferred images also belonged to the electrodes' preferred category, i.e., face or place). Comparing preferred versus nonpreferred items (rather than the face/place categories) enabled us to exclude "borderline" exemplars that belonged to the optimal category yet showed a weak activation, thus enhancing the sensitivity of the analysis. Furthermore, it enabled extension of the analysis to additional visual sites, whose content selectivity was significant but not necessarily related to a clear categorical division between faces and places.

Figure 4A indicates the location of cortical recording sites that showed a significant HFB (60 to 160 Hz) power increase in response to picture presentation during the viewing session [$P_{FDR} < 0.05$, Wilcoxon signed-rank test comparing stimulus response (100 to 500 ms) versus prestimulus baseline (−400 to −100 ms)]. Visual electrodes that showed a preferential HFB response to pictures of faces or places were regarded as category-selective ($P_{FDR} < 0.05$, Wilcoxon rank-sum test, faces versus places; see methods). They were typically localized in high-order visual areas along the ventral visual stream, lateral and medial to the fusiform gyrus.

To examine the potential role of SWRs in coordinating reactivation of cortical representations during recall, we time-locked the activity in category-selective visual sites to the onset of hippocampal SWRs. Specifically, we examined whether those cortical sites were reactivated during recall-related hippocampal SWRs and whether the reactivation was content-specific (i.e., matched content preference during viewing). Shown in Fig. 4, B to D, are HFB responses in three representative category-selective recording sites during picture viewing and free recall. During recollection, these electrodes showed a small, transient modulation of HFB amplitude time-locked to the onset of hippocampal SWR

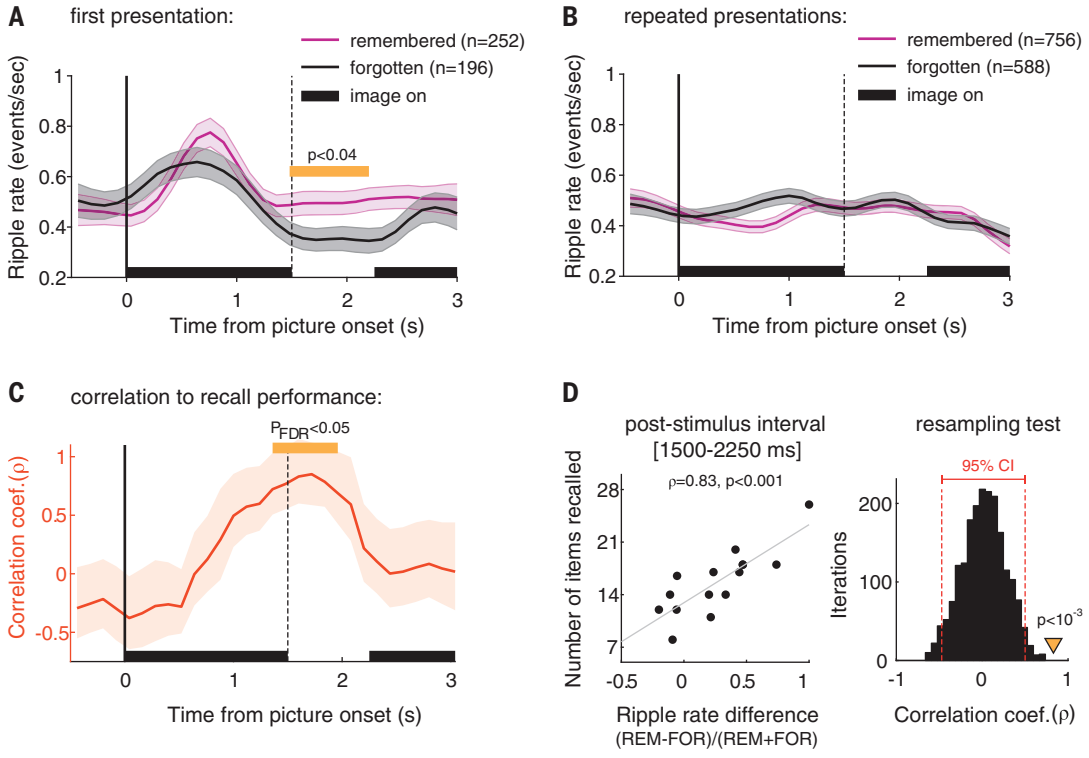

Fig. 3. Ripple rate during picture viewing predicts subsequent free-recall performance. (**A**) SWRs PSTH time-locked to onset of the first presentation of each picture shows a significantly higher ripple rate for remembered versus forgotten pictures during the poststimulus interval (P = 0.02, cluster-based permutation test; n = 15 patients). (**B**) No significant differences were observed during repeated presentations. (**C**) The difference in ripple rate between remembered and forgotten items significantly predicts subsequent recall performance across patients (P_{FDR} < 0.05; peak correlation: Spearman ρ = 0.85). Note how the correlation returns to baseline upon presentation of the next picture, attesting to the temporal specificity of this effect. (**D**) Left: Scatterplot showing the correlation between the poststimulus ripple rate difference (1500 to 2250 ms) and the subsequent recall performance (each dot represents an individual subject; gray line represents the least-squares fit). Right: Resampling test indicating that the correlation obtained in the actual data was highly significant (2000 iterations, P < 0.001) and did not arise from differences in the number of items in each group (remembered/forgotten). In (A) to (C), shaded area represents ±1 bootstrap SE computed over pooled trials [(A) and (B)] or patients (C); black horizontal bars on the x axis represent stimulus-on periods.

events. Critically, this coupled cortical activity was content-specific; that is, it occurred only when the patients recalled images from the electrodes' preferred category (preference that was revealed during viewing). In some cases, recalling the nonpreferred category led to a decrease in HFB amplitude. Thus, cortical activity coupled to hippocampal SWRs appeared most prominently when contrasting the preferred versus the nonpreferred images in each recording site.

To examine whether this peri-ripple amplitude modulation was a general phenomenon across the entire group of category-selective visual electrodes, we computed a multitaper spectrogram for each recording site during a time window of −750 to 750 ms relative to SWR onset (see methods). When patients recalled the electrodes' preferred images (i.e., top 10 images that elicited the strongest response during viewing), there was a small but highly consistent HFB activation centered around the onset of hippocampal SWRs (Fig. 5, A to C, P_{FDR} < 0.001, n = 57, Wilcoxon signed-rank test; peak normalized amplitude, 0.24 dB; SE, ±0.04). This peri-ripple cortical response involved a broadband power increase in frequencies between 50 and 180 Hz (High-Gamma), a signal known to reflect a local increase in population firing rate (*47*, *51*). This peri-ripple visual activation was significantly higher when patients recalled the electrodes' preferred images (top 10 images) as compared to the nonpreferred ones (bottom 10 images that least activated the electrodes during viewing) (P < 0.01, cluster-based nonparametric permutation test, shuffling preferred/nonpreferred labels 2000 times over electrodes; n = 57 recording sites in 13 patients, after excluding recording sites with fewer than five peri-ripple responses in each condition). Lower frequencies (1 to 30 Hz) did not exhibit content-selective power changes (no significant differences; preferred versus nonpreferred images, cluster-based permutation test; fig. S8A).

Was the SWR-triggered effect specific to overtly reported recall events? We performed the same analysis on SWRs that occurred while patients attempted to recall the electrode's preferred and nonpreferred categories but did not overtly report any recalled item (i.e., the "memory search" period). There was no content-selective peri-ripple activation during these inter-recall periods (no significant differences; fig. S8, B to D); this finding suggested that the effect was specific to conscious, reportable recall events (further comparisons among recall, memory search, and resting-state SWRs are depicted in fig. S8F). Finally, using a bootstrap sampling procedure with 2000 resamples, we estimated the latency of the maximal difference between the preferred and nonpreferred spectrograms during a [−300, 300] ms time window centered on SWR onset. The analysis showed a slight trend of an advance cortical activation [mean peak latency: −18 ms, 95% CI (−65, 29); frequency: 102.1 Hz, 95% CI (85, 118)]; however, this effect was not statistically significant.

We next examined how content-selective peri-ripple activation was distributed across the entire set of visually responsive electrodes. Figure 5D depicts the distribution of all recording sites in our dataset presented on an average cortical template. Recording sites that showed a significant visual response during the picture-viewing condition were color-coded according to their peri-ripple reactivation effect during recall. To obtain this map, we first identified the 10 images that produced the strongest and weakest responses during viewing individually in each

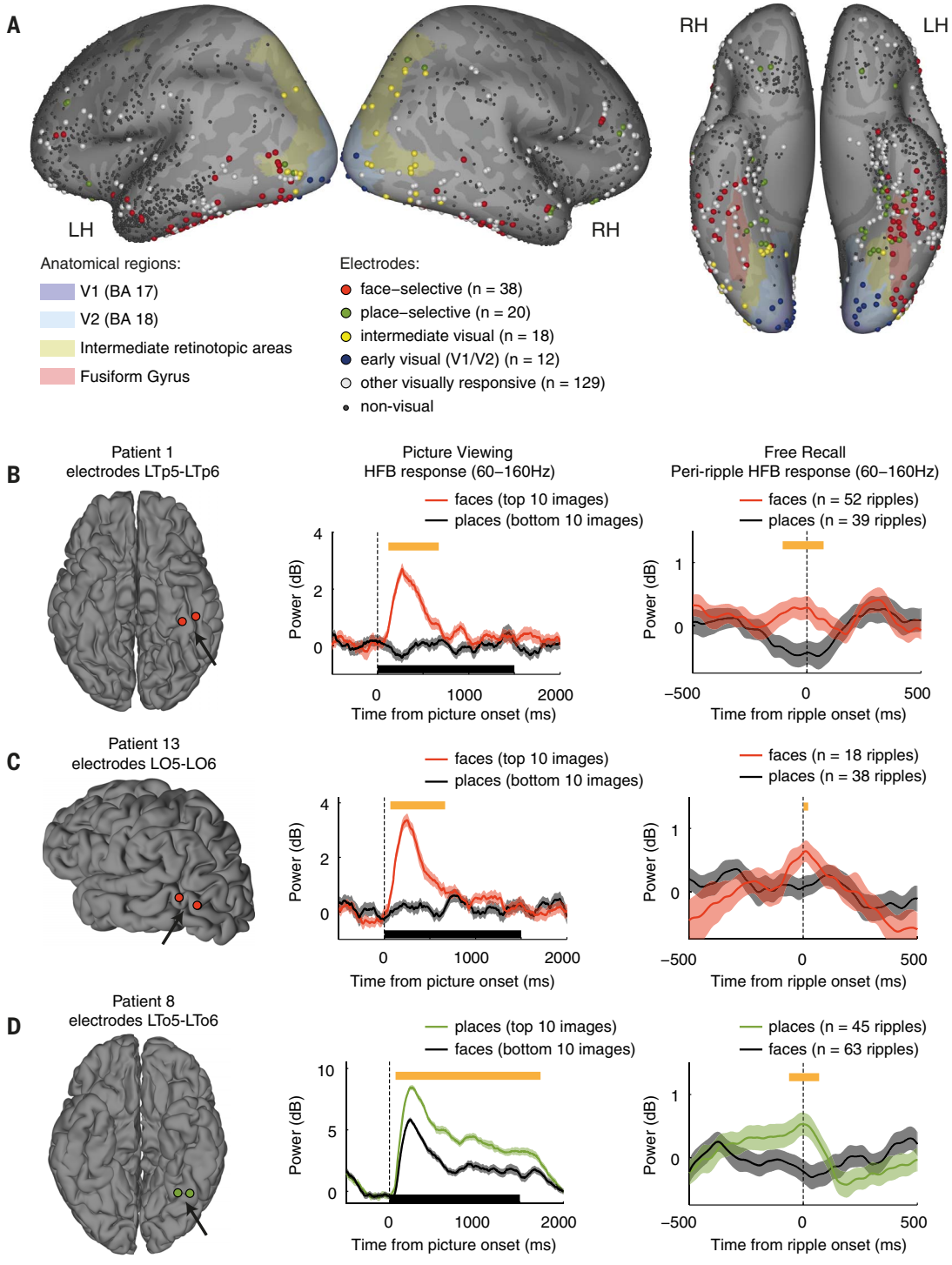

Fig. 4. Visually responsive electrodes and examples of peri-ripple visual reactivation during recall. (**A**) Multipatient electrode coverage showing the location of visually responsive electrodes in relation to early visual areas (blue), intermediate visual areas (yellow), and the fusiform gyrus (pink). Face- and place-selective bipolar electrode pairs (bipoles) are colored red and green, respectively. Each dot represents a single electrode contact taking part in a bipole. Note the clear tendency of category-selective electrodes to be localized in high-order visual areas along the ventral stream. (**B** to **D**) Category-selective peri-ripple HFB response during recall in three representative category-selective sites. Left: Anatomical location of each recording site. Center: HFB response time-locked to the onset of picture presentation (comparing face versus place images; orange bar represents significant time clusters at $P < 0.05$). Right: Peri-ripple HFB response during the verbal report of recall, when patients freely recalled the same face or place images (orange bar represents significant time points at $P < 0.05$, Wilcoxon rank-sum test). Note the category-selective modulation of HFB power around the simultaneously recorded hippocampal ripple. As can be seen in these examples, the peri-ripple cortical response involves either amplitude increase or decrease, depending on the recalled content and whether it matches the preferred representational content of the recorded site. Black bars on the *x* axis represent stimulus-on periods; shaded areas represent SEM.

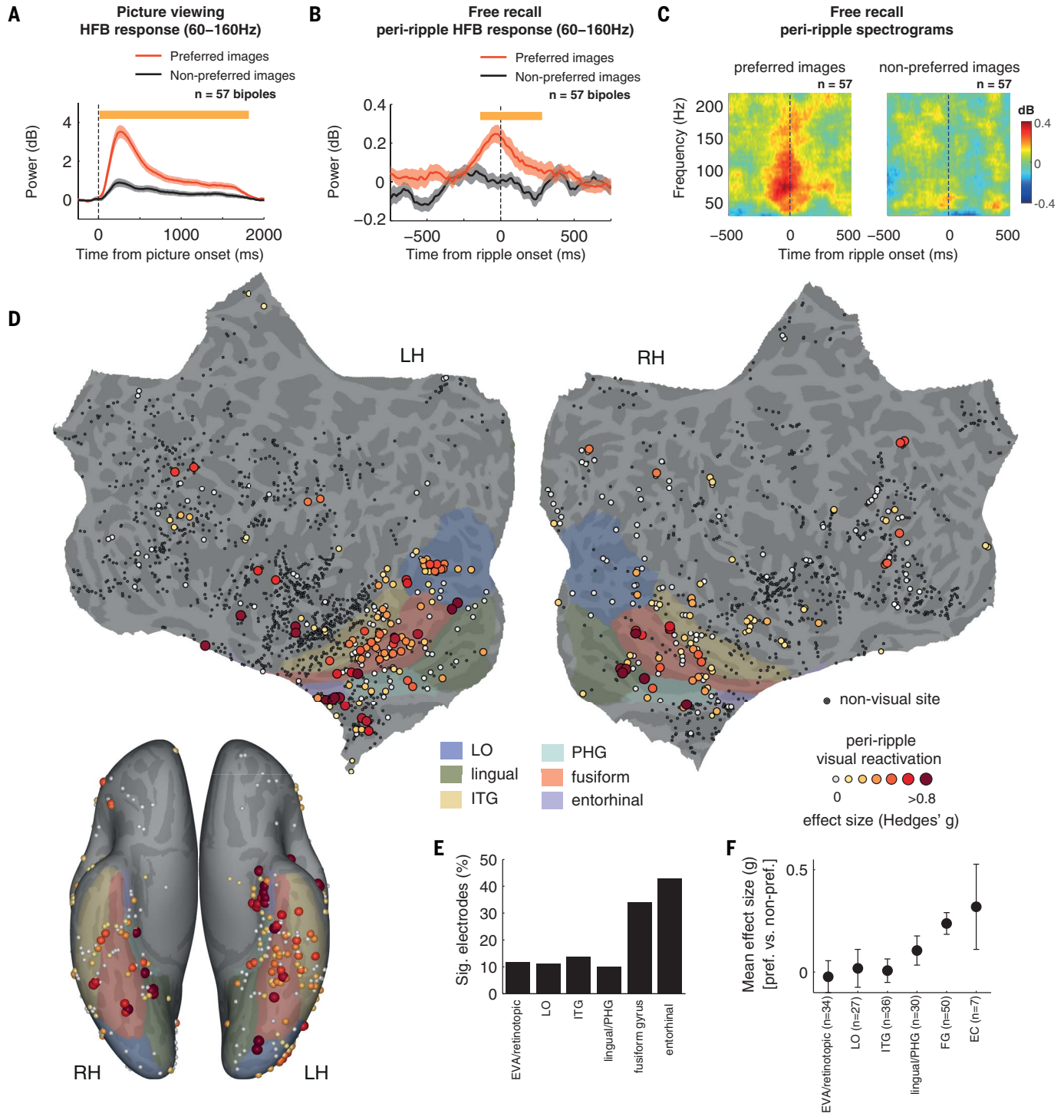

Fig. 5. Peri-ripple reactivation across the visual hierarchy during free recall. (**A**) HFB response to preferred (top 10) and nonpreferred (bottom 10) images in face/place selective recording sites during viewing. (**B**) HFB activity in the same category-selective electrodes during recall, time-locked to the onset of simultaneously recorded hippocampal ripples. Note the selective transient increase in HFB power during recall of preferred versus nonpreferred images ($P < 0.05$, cluster-based permutation test; $n = 57$ bipoles from 13 patients). (**C**) Multitaper spectrograms showing that peri-ripple cortical responses were concentrated in a broad high-frequency range (50 to 180 Hz). (**D**) Reactivation effect size (Hedges' g) in visually responsive electrodes, comparing peri-ripple responses during recall of "preferred" versus "nonpreferred" images. (**E** and **F**) Percentage of significant electrodes ($P < 0.05$, Wilcoxon rank-sum test, uncorrected) and mean effect size in each region of interest. Peri-ripple response selectivity was strongest in the fusiform gyrus and entorhinal cortex. Note the clear tendency for increased reactivation effect at more anterior-medial sites. Error bars and shaded areas represent SEM. In (A) and (B), horizontal orange bars represent significant time clusters.

recording site. Then, we computed a peri-ripple spectrogram during the verbal recall periods (similar to the analysis in Fig. 5, B and C). We separated the activations that occurred when patients recalled the electrode's preferred images from those that occurred when the patients recalled the nonpreferred ones. We then averaged the HFB power over a [−300, 300] ms time window centered on SWR onset and quantified the difference between preferred and nonpreferred images using the bias-corrected Hedges' g effect size measure (*52*), individually in each site. Recording sites with fewer than five peri-ripple responses in either the preferred or nonpreferred group were excluded. Content-selective reactivation of visual information during SWR events occurred most prominently in the fusiform gyrus as well as in downstream cortical regions including the entorhinal and perirhinal cortices. We used the anatomical atlases (*53*–*55*) included in FreeSurfer to subdivide the cortical surface into six partly overlapping regions along the visual hierarchy (*56*). Electrodes falling within these regions were grouped together. The peri-ripple reactivation was strongest in the fusiform gyrus and entorhinal cortex (i.e., the higher levels of the ventral visual hierarchy) (Fig. 5, E and F).

Memory reinstatement during SWRs

To further investigate the reinstatement of visual information during recall in relation to SWRs, we pooled together visually responsive cortical sites that showed significant content selectivity during picture viewing (see methods; see fig. S9 for electrodes' location) and constructed a multisite HFB activation pattern per each item during picture viewing and recall. We used principal components analysis (PCA) to reduce the dimensionality of the activation patterns during viewing, retaining the first 11 principal components (PCs) that accounted for 83.8% of the variation across viewed items (see methods; see Fig. 6, A and B, for PC visualization). We then applied the same linear transformation to the patterns that emerged during recall, bringing all patterns to the same 11-dimensional linear space. Next, we quantified the similarity between viewing and recall patterns. We computed the Pearson correlation using a 50-ms sliding window to examine how the similarity between patterns changed in relation to SWR timing during recall, and in relation to the onset/offset of the picture during viewing (Fig. 6, C and D). This analysis revealed a significant enhancement in pattern correlation during the SWR event ($P < 0.05$, nonparametric cluster-based permutation test; see methods). Intriguingly, there was a trend toward a second peak shortly after the disappearance of the picture; however, this peak did not survive the cluster-based permutation test.

We then asked whether we could decode the identity of recalled items on the basis of the SWR-triggered cortical HFB patterns. To perform this analysis, we trained a k-nearest neighbors (k-NN) classifier on single-trial HFB patterns during viewing and tested its classification performance on the free-recall patterns (i.e., cross-classification; see methods). Here again, the patterns' dimensionality was reduced using an out-of-sample extension of the same PCA transformation described above (Fig. 6, A and B).

Testing the classifier performance on the viewing data showed 100% accuracy in decoding the image category (using $k = 9$ NN), and 47.3% accuracy (chance level is 3.5%) in decoding exemplar identity (using $k = 1$ NN). For the cross-classification analysis, we used a 50-ms sliding window to examine the temporal profile of visual reinstatement during recall relative to the SWR onset (Fig. 6, E and F). We obtained significant decoding performance during recall for both category (82.1% accuracy, 23/28 items) and exemplar identity (21.4% accuracy, 6/28 items) ($P < 0.01$; a nonparametric cluster-based permutation test, shuffling item labels 2000 times; see methods). Decoding performance peaked together with the SWR event, suggesting a temporally precise coupling between hippocampal SWRs and cortical activity during reinstatement of visual information.

Discussion

We used a rare clinical opportunity to measure hippocampal SWRs and the associated SWR-triggered cortical activity in human patients as they memorized and freely recalled vivid photographs of famous faces and places. Our results highlight three major new aspects of SWRs' function and their relation to human episodic memory. First, a transient increase in hippocampal SWR rate preceded the onset of verbally reported recollections by 1 to 2 s. This increase was content-selective and reexpressed the same picture preferences observed during the encoding phase. Second, the SWR rate during picture viewing predicted subsequent memory performance of individual patients. Finally, during the verbal report of recall, high-order cortical visual sites showed a SWR-triggered increase in HFB activity. Again, this broadband activation was content-specific and occurred only when the patients recalled the pictures that preferentially activated the sites during viewing.

The anticipatory increase in SWR rate during recall (Fig. 2C) strongly suggests that SWRs play an important role in the initiation of self-generated recall events. Work in rodents exploring the link between awake SWRs and putative memory retrieval behaviors has demonstrated that sequences of hippocampal place cell assemblies, representing spatial and contextual information related to past experiences, are briefly replayed in the time window of the SWR (*32*, *34*, *35*, *41*, *57*). However, it was not possible to determine in these studies the actual moment of cognitive recall, and hence its temporal relationship to SWR events. Conducting the experiment in awake human patients enabled us to extend these previous studies by obtaining an estimation of when each recalled item surfaced into the patients' conscious awareness. This allowed us to establish the anticipatory nature of the SWR event.

It may be argued that this anticipatory increase could result from inaccuracies in the timing of verbal reports. However, because the SWR rate increase was transient and clearly declined at the time of the verbal report proper, such an onset "blurring" effect is unlikely. These results are intriguingly similar to the anticipatory increases in hippocampal and medial temporal neurons' firing rate observed in single-unit recordings in patients during a similar free-recall paradigm (*42*). These anticipatory hippocampal signals are compatible with a two-stage recollection process mediated by the hippocampus: a fast subconscious stage, involving reactivation of hippocampal-neocortical memory traces, and a slower conscious one, involving cortical processes that operate on the retrieved content and reinstate the mentally experienced episode (*58*). However, we cannot at this point rule out the possibility that patients thought about the recalled items prior to their verbal responses, hence contributing to the anticipatory activation.

The increase in SWR rate prior to recall onset showed visual content selectivity: Specific images that generated a higher SWR rate during the picture-viewing stage also elicited a higher SWR rate during recollection. In other words, the SWR rate during recall reexpressed the content specificity found during viewing. Thus, the phenomenon of memory reactivation is evident not only in the spike content of the SWR (e.g., content-specific sequences of hippocampal place cells) (*32*–*35*, *57*, *59*) but also in the rate of SWRs elicited during recall, which is linked to the rate of SWRs elicited during the original experience. However, it should be noted that experiences that are encoded for the first time are likely to engage a different set of memory processes (e.g., novelty detection, engram formation, etc.) that do not repeat during recall. In line with this, the link between SWR rates during the original experience and subsequent recall was found only for the repeated item presentations (fig. S4).

Our results show that SWRs play an important role in the encoding process as well. We found that the ability of patients to successfully recall a visual item was significantly linked to SWR activity during picture viewing (memory-encoding stage). This effect was observed only during the first presentation of each image and was maximal during the postpresentation period, thereby corroborating previous studies pointing to the importance of the poststimulus periods in memory encoding (*60*). Specifically, we found that the strength of the differential signal during encoding (i.e., the difference in SWR rate after presentation of recalled and forgotten items) predicted the success of patients in subsequently recalling these items. A plausible interpretation of this effect is that such differential signal during viewing may capture the process of memory trace formation, so that the larger the differential activity, the stronger the engagement of the hippocampus in the encoding process, which enhances the ability of the patient to freely recall these memories later on. Regardless of the precise mechanism, this

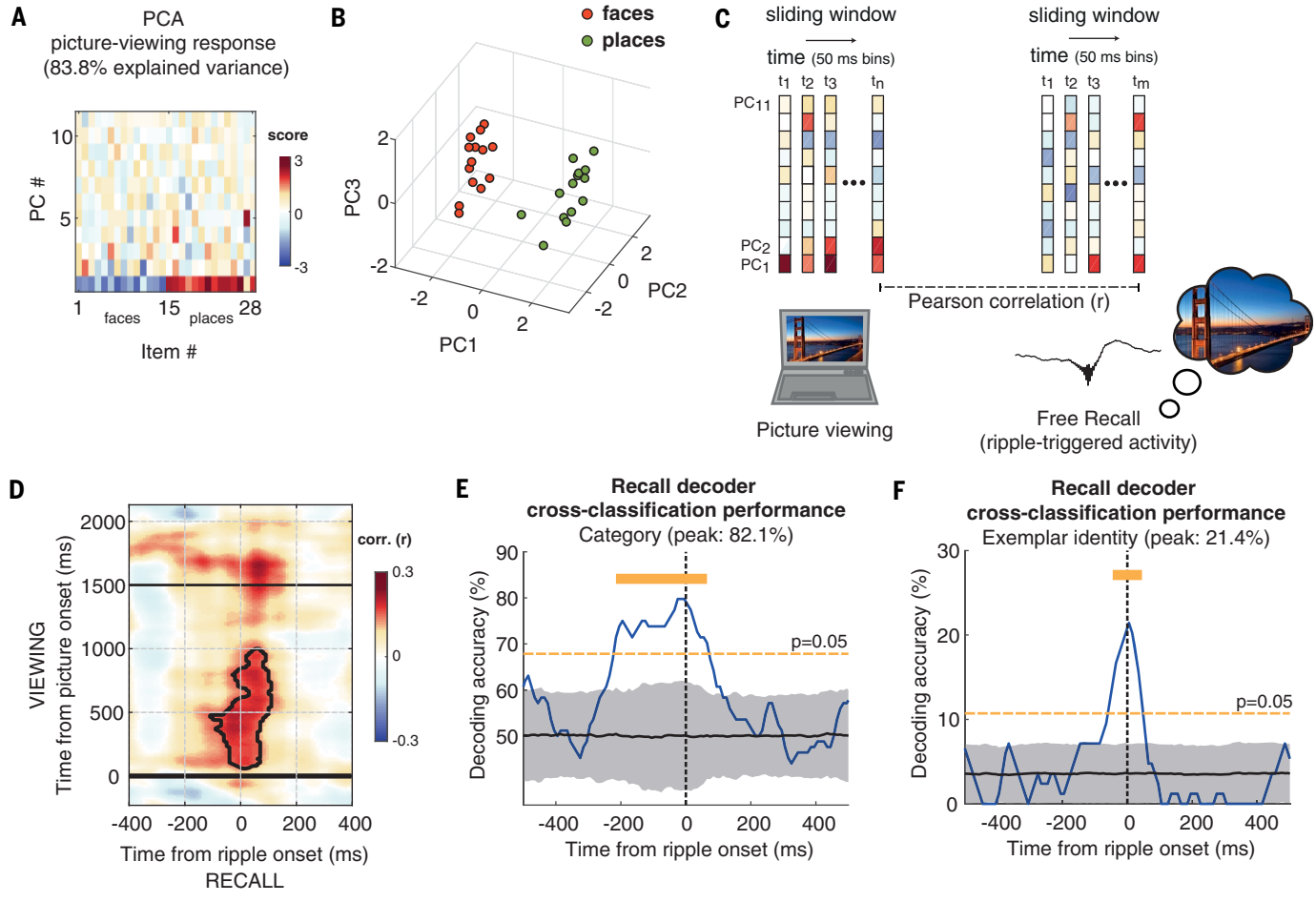

Fig. 6. Similarity between recall decoding performance and cortical activation patterns during viewing and free recall. (**A**) PCA applied to multivariate activation patterns during picture viewing. Note that the first principal component (accounting for 40% of the variance) captured the categorical difference between items. (**B**) Visualizing the patterns according to PC1, PC2, and PC3 showed a clear categorical clustering of faces and places, with some additional differentiation at the item level. (**C**) After dimensionality reduction, Pearson correlation was used to quantify the similarity between viewing and recall patterns, with a 50-ms sliding window (*91*). (**D**) Viewing-recall pattern similarity relative to the SWR event and to the onset/offset of the pictures (black horizontal lines). Significant correlation was found only during the SWR event ($P < 0.05$, cluster-based permutation test; significant clusters are contoured in black). (**E** and **F**) Performance of *k*-NN classifier trained on viewing patterns and tested on recall patterns (cross-classification). Shaded gray area shows the decoding performance for shuffled data (mean ± SD). Dashed orange lines represent the cluster-defining threshold ($P = 0.05$); significant time clusters are marked above ($P < 0.01$, cluster-based permutation test). For visualization, decoding performance was smoothed using a boxcar filter three time bins wide.

effect implicates the involvement of SWRs in memory formation.

Our observation that SWRs tend to emerge rather frequently during a visual memory task that is clearly nonspatial in nature demonstrates that SWRs are not exclusive to navigational aspects, but rather play a more general role in episodic memory (*14*). This is compatible with the occurrence of SWRs during a visual search task in primates (*18*).

Finally, an important aspect of SWR function uncovered by the current study is the content-selective coupling between SWRs and cortical activation. This content selectivity, reflected in HFB activity in high-order cortical sites, was precisely time-locked to the SWR event itself. Thus, SWR-triggered activity in high-order visual sites was significantly higher when patients recalled items that preferentially activated these sites during picture viewing. Reactivation of visual content occurred most prominently during the time window of the SWR. The SWR-triggered cortical activity was specific to the actual recall events and was not found during the search times between verbal recalls. This result further attests to the specific role of this activity in reportable, conscious recollection.

Previous work in rodents (*27*, *61*) has demonstrated a bidirectional interaction between the hippocampus and the cortex during memory consolidation and retrieval. Such studies suggested a role for the cortex in facilitating reactivation of the relevant hippocampal representation during a SWR. Consistent with these suggestions, previous work in humans (*43*) has demonstrated a slow, anticipatory activation of category-specific cortical information that precedes the actual moment of recall by several seconds (*44*, *62*). Moreover, during internal memory search, when subjects attempt to recall a particular category but fail to come up with a specific exemplar, activity in category-specific cortical sites remains slightly elevated, possibly reflecting a top-down control signal that imposes categorical boundaries on downstream memory representations in the hippocampus (*44*). Our finding of a slight trend of an advanced cortical activation prior to SWR onset is compatible with the suggested top-down cortical influence and the bidirectional nature of the hippocampal-cortical interplay in general, although further research will be required to fully characterize and confirm this interaction.

Our results are consistent with recent work by Vaz and colleagues (*63*) showing coupled ripple-band activity in MTL and temporal association cortex during successful retrieval. Both spectral

and temporal profiles of these coupled oscillatory events are compatible with the SWR-triggered HFB activation we observed.

Consistent with rodent studies reporting higher SWR rates during exploration of novel environments than of familiar ones (*14*), we observed a significantly higher increase in average SWR rate in response to the first presentation of each picture than for subsequent presentations of the same pictures. Unlike SWR activity evoked by repeated presentations, SWR rates during novel presentations were not reinstated during the subsequent recall. This pattern of results suggests the involvement of two different subtypes of SWRs elicited during viewing: one that reflects the general processing of novel information and another that reflects a mnemonic process that is more content-specific in nature (i.e., recognition memory, pattern retrieval, etc.). However, it is important to note, more generally, that processes of memory retrieval may be closely linked to processes of memory consolidation (and reconsolidation), so the observed changes in ripple rate may underlie both processes (*14*).

Together, our results demonstrate an important link between SWRs and verbally reported human episodic memory. More specifically, they reveal SWR-related reinstatement of visual representations during free recall. These results point to a process by which SWRs set up an integrated, content-specific dialogue between the hippocampus and the cortex that initiates and enables the process of recall.

Methods

Participants

Intracranial recordings were obtained from 15 patients with pharmacologically resistant epilepsy (10 females) at the North Shore University Hospital, New York. The age of the patients ranged from 22 to 57 (mean = 36.6, SD = 10.7). All patients were implanted with subdural intracranial electrodes for diagnostic purposes as part of their evaluation for neurosurgical epilepsy treatment. All participants performed the task in their native language (12 English speakers, three Spanish speakers). No clinical seizures occurred during the experimental duration. The study was conducted according to the latest version of the Declaration of Helsinki, and all participants provided a fully informed consent according to NIH guidelines, as monitored by the institutional review board at the Feinstein Institute for Medical Research.

Experimental task

The experiment was divided into two runs. Each run began with a closed-eyes resting-state period of 200 s (the first two patients performed the resting state on a different day). Immediately afterward, participants were presented with 14 different pictures of famous faces and places (seven in each category; see Fig. 1 for example stimuli). Picture duration was 1500 ms with 750-ms interstimulus intervals. Each item repeated four times in a pseudorandom order, such that each presentation cycle contained all pictures but the order of pictures was randomized within the cycle. The same picture was never presented twice consecutively. Participants were instructed to look carefully at the pictures and try to remember them in detail, emphasizing unique colors, face expressions, perspective, lighting, etc. Stimuli were presented on a standard LCD screen using Presentation software (picture size: 16.5° × 12.7° at ~60 cm viewing distance). After viewing the pictures, participants put on a blindfold and began a short interference task of counting back from 150 in steps of 5 for approximately 1 min. Upon completion, recall instructions were presented. The patients were asked to freely recall as many pictures as possible while focusing on one category at a time, starting with faces in the first run and with places in the second run.

We instructed the patients to describe each picture they recalled, as soon as it came to mind, with two or three prominent visual features. This was done to ensure that the patients also retrieved episodic visual information specific to the studied items, and not just general semantic details. The duration of the free-recall phase was 2.5 min per each category (5 min in total × two runs). In case the patients indicated that they were "through," they received a standard prompt from the experimenter (e.g., "Can you remember any more pictures?"). Each run included a new set of pictures, and the order of recalled categories was counterbalanced between the runs.

Identification of verbal recall events

Verbal responses during the free-recall phase were continuously recorded using a microphone attached to the patient's gown. The onset and offset of each recall event were extracted in an offline analysis, identifying the first/last sound wave relevant to each utterance (*44*), using Audacity recording and editing software (version 2.0.6). SWR events occurring during the verbally reported recall events, or in the 3 s that immediately preceded the events, were associated with the item that the patient described. SWR events that occurred in between recall events were regarded as "memory search" ripples and were associated only with the category that patient was instructed to recall in the beginning of the free-recall block.

Intracranial recordings

Intracranial recording sites were subdural grids, strips, or depth electrodes (Ad-Tech, Racine, WI; Integra, Plainsboro, NJ; PMT Corporation, Chanhassen, MN). Recording sites in the subdural grids and strips were 1- or 3-mm platinum disks with 4- or 10-mm intercontact spacing. Recording sites in depth electrodes implanted in the hippocampus were 2-mm platinum cylinders with 4.4-mm intercontact spacing and a diameter of 0.8 mm (see Fig. 1C). During the recordings, the intracranial EEG signal was referenced to a vertex screw/subdermal electrode and was filtered electronically between 0.1 and 200 Hz. The signal was then digitized at 500 Hz/512 Hz and stored for offline analysis using XLTEK EMU128FS/NeuroLink IP 256 systems (Natus Medical Inc., San Carlos, CA). Stimulus-triggered electrical pulses were recorded along with the iEEG data for precise synchronization with stimulus onset. All recordings were conducted at the patients' quiet bedside.

Electrode localization

Prior to electrode implantation, we obtained for each patient a T1-weighted 1-mm isometric structural MRI scan using a 3-T scanner. After implantation, a CT scan and a T1-weighted structural MRI scan at 1.5 T were acquired. The post-implantation CT and MRI scans were skull-stripped and co-registered to the preoperative anatomical MRI scan using FSL's BET and FLIRT algorithms (*64*–*66*). Concatenating these two co-registrations allowed visualization of the CT scan on top of the preoperative MRI scan while minimizing localization error due to potential brain shift caused by surgery and implantation. Individual recoding sites were then identified visually on the co-registered CT and were marked in each subject's preoperative MRI native space using BioImage Suite (*67*).

Next, preoperative structural MRI scans were processed using FreeSurfer 6.0 (*68*) to segment and reconstruct the cortical surface and hippocampal subfields in each patient. Following our previously published procedure (*44*, *69*), the three-dimensional mesh of the cortical surface in each patient was resampled and standardized using SUMA (*70*), allowing us to establish node-to-node correspondence across different surfaces. This enabled us to visualize electrodes from different patients on a single cortical template ("fsaverage") while adhering to the electrodes' location in relation to individual gyri and sulci. Finally, each cortical surface was registered onto different anatomical atlases (*54*, *55*) available in FreeSurfer, including a probabilistic atlas of visual retinotopy (*53*).

Preprocessing and data analysis

All data analysis was performed in MATLAB 2014a/2018b (MathWorks Inc., Natick, MA) using EEGLAB (*71*), Chronux (*72*), DRtoolbox (https://lvdmaaten.github.io/drtoolbox/), MES toolbox (*52*), and custom-developed analysis routines. Raw iEEG data were inspected visually and statistically to detect noisy/corrupted channels and exclude them from further analysis. The preprocessing began by converting the iEEG signals to bipolar derivations by pairing adjacent electrode contacts. Recording sites in the hippocampus were paired with a nearby white-matter electrode that was identified anatomically using FreeSurfer's segmentation (*68*). We then resampled each bipolar derivation at 500 Hz and removed the 60-Hz power line interference (including its harmonics) using zero-lag linear-phase Hamming-windowed FIR band-stop filters (3 Hz wide).

High-frequency broadband signal and spectral analysis

HFB signal was defined in the present study as the mean normalized power of frequencies

between 60 and 160 Hz (High-Gamma). This range of frequencies was used as the key electrophysiological marker of local neural population activity (45–47, 73). For analyses in which spectrograms were computed, HFB power was calculated as the average of frequency rows between 60 and 160 Hz. In all other cases, HFB power was computed by filtering the signal in 20-Hz bands between 60 and 160 Hz (using zero-lag linear-phase Hamming-windowed FIR filters) and calculating the normalized, 1/f corrected, analytic amplitude using a Hilbert transform (44). The latter method was mainly used for detecting visually responsive/category-selective recording sites and estimating their response latency [see (44) for details].

HFB data were inspected for transient electrical artifacts, defined as peaks above 5σ that appear in the HFB time series of the common average signal (i.e., the average LFP across all iEEG channels). Time windows of 200 ms around these peaks were logged for exclusion in subsequent analyses.

Spectral decomposition of SWR events in hippocampal recording sites was done using a Morlet-wavelet time-frequency method, implemented in EEGLAB. We used a window of 1 cycle at the lowest frequency (4 Hz) and up to 20 cycles at the highest plotted frequency (220 Hz), with a step size of 4 ms. Ripple-triggered spectrograms were normalized by the geometric mean power in each frequency, computed over the entire epoch length (−750 to 750 ms) and across all epochs belonging to the same condition (i.e., rest, picture viewing, recalling faces, recalling places) in a given run.

Spectral decomposition of HFB activation in cortical recording sites was done using the multitaper method (74) implemented in Chronux (http://chronux.org/) (75). For analysis of frequencies above 30 Hz, we used a combination of five tapers and a 200-ms-wide time window (advanced in 6-ms steps), resulting in frequency resolution of 20 Hz. For analysis of frequencies below 30 Hz, we used a combination of three tapers and a 500-ms-wide time window (advanced in 10-ms steps), resulting in frequency resolution of 5 Hz. Here again, the ripple-triggered spectrograms were normalized by the geometric mean power in each frequency, computed over the entire epoch length (−750 to 750 ms) and across all epochs belonging to the same condition in a given run. Stimulus-triggered spectrograms in the picture-viewing stage were normalized relative to a baseline period of −400 to −100 ms prestimulus.

Visually responsive electrodes

We identified visually responsive sites by comparing, in each bipolar electrode pair, the poststimulus HFB response (averaged over a time window of 100 to 500 ms) to the prestimulus baseline (−400 to −100 ms) using a two-tailed Wilcoxon signed-rank test. *P* values from all recording sites (across all patients) were pooled together to control the FDR (76). Bipoles that showed a significant HFB response ($P_{FDR} < 0.05$) were regarded as visually responsive. Visual bipoles that were fully contained within Brodmann areas 17/18 (V1/V2), and exhibited response latency shorter than 180 ms were labeled "early visual". To define face-selective and place-selective bipoles, we averaged the visual HFB responses over a time window of 100 to 500 ms poststimulus and compared faces versus places using a Wilcoxon rank sum test. Significant bipoles ($P_{FDR} < 0.05$) located beyond early visual areas (V1/V2) were labeled either "face-selective" or "place-selective," correspondingly. The remaining visually responsive bipoles were grouped together according to their anatomical/retinotopic location (53–55). When assigning bipoles to a specific region, we only required that one of the two contacts be located within that region, thus allowing for the same bipole to be attributed to two different regions (in cases where the bipole was located on the border between regions).

Offline ripple detection

Ripple detection was performed using a macro electrode contact located in or adjacent to the CA1/CA2 subfields, as identified anatomically in each patient using FreeSurfer's hippocampal subfields parcellation algorithm (77) (the exact anatomical location in each patient is depicted in fig. S1). For technical reasons, ripple detection in two of the patients was performed using a contact located in the subiculum [where SWR events can also be clearly identified (12)]. Prior to ripple detection, a reference signal from a nearby white-matter contact was subtracted to eliminate common noise. LFPs were then filtered between 70 and 180 Hz (zero-lag linear-phase Hamming windowed FIR filter with a transition bandwidth of 5 Hz) and instantaneous analytic amplitude was computed using a Hilbert transform. Following the procedure of (78), extreme values were clipped to 4 SD to minimize ripple rate–induced biasing. The clipped signal was then squared and smoothed (Kaiser-window FIR low-pass filter with 40 Hz cutoff), and the mean and SD were computed across the entire experimental duration to define the threshold for event detection. Events from the original (squared but unclipped) signal that exceeded 4 SD above baseline were selected as candidate SWR events. Event duration was expanded until ripple power fell below 2 SD. Events shorter than 20 ms or longer than 200 ms were excluded. Adjacent events with less than 30 ms separation (peak-to-peak) were merged. Finally, SWR peak was aligned to the trough (of the nonrectified signal) closest to the peak power.

A control detection was performed on the common average signal computed across all iEEG channels. Hippocampal SWR events that coincided with common average ripple-band peaks were removed, thus avoiding erroneous detection of transient electrical and muscular artifacts that tend to appear simultaneously on multiple channels (79, 80).

Lastly, to avoid inclusion of possible pathological events, we removed any SWR events that occurred within 50 ms from inter-ictal epileptic discharges (IEDs) (81). The latter were detected by filtering the raw hippocampal LFP between 25 and 60 Hz (zero-lag linear-phase Hamming windowed FIR filter), and similar to the above procedure, rectifying, squaring, smoothing, normalizing, and detecting events that exceeded 4 SD.

The frequency window used for ripple detection in the present study was based on previous research in humans (7, 8, 11, 82), pointing to a typical ripple-band frequency range of 80 to 140 Hz, that might occasionally reach up to 170 Hz in individual events. Thus, to minimize the possibility of filtering out genuine ripples, we used a frequency range of 70 to 180 Hz (taking into account the filter roll-off). Notably, selecting a narrower filter (e.g., 70 to 130 Hz) did not introduce any substantial changes to the main results.

SWR peristimulus time histogram

We used the following parameters to construct PSTHs of SWR events across the different experimental conditions. For picture viewing responses (Fig. 2A), we used 50-ms time bins starting from −0.5 to 2.25 s relative to picture onset, smoothed by a 5-point triangular window. To compare ripple rate between remembered and forgotten items (Fig. 3), we used a bin width of 120 ms, based on Scott's optimization method (83), to accommodate the lower number of trials. To construct PSTH during recall events, we used a bin size of 200 ms, smoothed by a 5-point triangular window.

Multivariate pattern analysis (MVPA)

Multivariate HFB activation patterns were constructed by pooling visually responsive recording sites from all subjects. For the analysis, we first defined six regions of interest along the ventral visual hierarchy, using the Desikan-Killiany atlas (54), including the lateral occipital cortex (LO), inferior temporal gyrus (ITG), lingual gyrus, parahippocampal gyrus (PHG), fusiform gyrus, and entorhinal cortex. Visually responsive electrodes that fell within these anatomical regions and showed a substantial content selectivity in their responses during picture viewing [i.e., a difference of at least 3 SD between preferred (top 10) and nonpreferred (bottom 10) images] were included in the analysis ($n = 78$ bipolar electrode pairs; electrodes' location is depicted in fig. S9).

To construct HFB activation patterns associated with the viewed images, we first computed in each recording site the instantaneous HFB power using multitaper spectrograms (as described above). In the picture-viewing condition, spectrograms were computed in a time window of −250 to 2250 ms relative to picture onset. In the free-recall condition, spectrograms were time-locked to hippocampal SWR events that occurred during the verbal report of recall (from −500 to 500 ms relative to ripple onset). Each SWR event was uniquely associated with the picture the subject was describing at the time of the event.

Next, we applied z-score transformation to the HFB power in each recording site. Z-scores were computed across all items within the same run, individually for each time point. Then, the instantaneous power was binned in 50-ms time bins (using 80% overlap). For the viewing data, power values were averaged across the four presentations of each picture, resulting in a matrix of 28 items × 78 bipoles × 236 time bins. For the recall data, power values were averaged across all SWR events associated with the same item, resulting in a matrix of 28 items × 78 bipoles × 106 time bins. For items that were not recalled by a certain patient, or did not elicit ripples, the corresponding (missing) entry in the matrix was replaced by zero (i.e., the mean).

We next averaged the viewing data over the entire stimulus duration (from 100 to 1,500 ms) to construct a "template" feature matrix of visual responses (28 items × 78 bipoles), and applied PCA to reduce the dimensionality of the features (*84*). To determine the number of PCs to retain, we estimated the true dimensionality of the data (i.e., intrinsic dimension) using a maximum likelihood estimation technique (*85*). This led us to retain the first 11 PCs, which explained 83.8% of the variation in the data (see Fig. 6, A and B).

To compute the similarity between cortical patterns that emerged during viewing and peri-ripple cortical patterns that emerged during recall, we brought all instantaneous patterns (binned in 50-ms time bins) to the same linear space by reapplying the same linear transformation that was obtained from the PCA of the averaged feature matrix described above (i.e., an out-of-sample extension of the PCA). The same linear mapping was applied to both viewing and free-recall patterns.

Finally, we used Pearson correlation to quantify the similarity between viewing and recall patterns in each 50-ms time bin. This was done to examine how the correlation changed relative to the SWR onset (during recall) and relative to the onset/offset of the picture (during viewing) (Fig. 6D). To assess statistical significance, we performed a nonparametric cluster-based permutation test, shuffling item labels 2000 times, recomputing the correlation values, and measuring the maximal cluster size after applying a threshold of $P < 0.01$ on the correlation values.

Cross-classification analysis

To test whether we could decode the identity of recalled items from the ripple-triggered cortical HFB patterns, we trained a k-nearest neighbors (k-NN) classifier on single-trial viewing patterns (28 items, each presented four times, $n = 112$ trials in total) and tested its classification performance on the peri-ripple patterns that emerged during the verbally reported recall events (i.e., cross-classification analysis; Fig. 6, E and F). For this analysis, patterns elicited during viewing were averaged over a time window of 100 to 500 ms poststimulus [where visual responses are strongest and most informative about stimulus identity (*86*, *87*)]. Here again, we reduced the dimensionality of the data using PCA, and applied the same transformation also to the peri-ripple patterns during recall, as described above for the MVPA (i.e., an out-of-sample extension of the same PCA that was applied on the viewing patterns). We used $k = 9$ nearest neighbors to decode image category and $k = 1$ nearest neighbors to decode exemplar identity. To measure classification performance in the viewing condition, we used a leave-one-out cross-validation technique. For the cross-classification analysis, decoding the recalled content, we computed classification accuracy individually in each 50-ms time bin, from −500 to 500 ms relative to the onset of the hippocampal SWR event. Statistical significance was assessed using a nonparametric cluster-based permutation test, shuffling item labels 2000 times and recomputing the cross-classification performance while measuring the size of the maximal cluster in each iteration (using a cluster-defining threshold of $P = 0.05$). FWE-corrected P values were computed as the proportion of random clusters larger than or equal to the clusters observed in the actual data.

Statistical analyses

For statistical testing, parametric methods were used for normal data. Because HFB amplitude, like other measures of population firing rate, tends to follow a log-normal distribution, amplitude values were log-transformed into decibel ($10 \times \log_{10}$) prior to any statistical testing. For non-normal data or small sample sizes, we used Wilcoxon signed-rank/rank sum tests. All statistical tests were two-sided unless stated otherwise. A Greenhouse-Geisser correction for sphericity was applied to repeated-measures analyses of variance when necessary. Multiple-comparisons correction was performed either through the Benjamini-Hochberg method (*76*) for FDR adjustment or by using nonparametric cluster-based permutation tests developed by others (*88*, *89*), in which the family-wise error rate (FWE) is inherently controlled (*90*). No statistical methods were used to predetermine sample sizes; however, sample sizes were similar to those generally used in the field. Data collection and analysis were not performed blind to the conditions of the experiments.

REFERENCES AND NOTES

1. G. Buzsáki, L.-W. S. Leung, C. H. Vanderwolf, Cellular bases of hippocampal EEG in the behaving rat. *Brain Res. Rev.* **287**, 139–171 (1983). doi: 10.1016/0165-0173(83)90037-1; pmid: 6357356
2. G. Buzsáki, Z. Horváth, R. Urioste, J. Hetke, K. Wise, High-frequency network oscillation in the hippocampus. *Science* **256**, 1025–1027 (1992). doi: 10.1126/science.1589772; pmid: 1589772
3. A. Ylinen *et al*., Sharp wave-associated high-frequency oscillation (200 Hz) in the intact hippocampus: Network and intracellular mechanisms. *J. Neurosci.* **15**, 30–46 (1995). doi: 10.1523/JNEUROSCI.15-01-00030.1995; pmid: 7823136
4. D. Sullivan *et al*., Relationships between hippocampal sharp waves, ripples, and fast gamma oscillation: Influence of dentate and entorhinal cortical activity. *J. Neurosci.* **31**, 8605–8616 (2011). doi: 10.1523/JNEUROSCI.0294-11.2011; pmid: 21653864
5. B. K. Hulse, L. C. Moreaux, E. V. Lubenov, A. G. Siapas, Membrane Potential Dynamics of CA1 Pyramidal Neurons during Hippocampal Ripples in Awake Mice. *Neuron* **89**, 800–813 (2016). doi: 10.1016/j.neuron.2016.01.014; pmid: 26889811
6. G. Buzsáki *et al*., Hippocampal network patterns of activity in the mouse. *Neuroscience* **116**, 201–211 (2003). doi: 10.1016/S0306-4522(02)00669-3; pmid: 12535953
7. A. Bragin, J. Engel Jr., C. L. Wilson, I. Fried, G. Buzsáki, High-frequency oscillations in human brain. *Hippocampus* **9**, 137–142 (1999). doi: 10.1002/(SICI)1098-1063(1999)9:2<137::AID-HIPO5>3.0.CO;2-0; pmid: 10226774
8. M. Le Van Quyen *et al*., Cell Type-Specific Firing during Ripple Oscillations in the Hippocampal Formation of Humans. *J. Neurosci.* **28**, 6104–6110 (2008). doi: 10.1523/JNEUROSCI.0437-08.2008
9. B. P. Staresina *et al*., Hierarchical nesting of slow oscillations, spindles and ripples in the human hippocampus during sleep. *Nat. Neurosci.* **18**, 1679–1686 (2015). doi: 10.1038/nn.4119; pmid: 26389842
10. N. K. Logothetis *et al*., Hippocampal-cortical interaction during periods of subcortical silence. *Nature* **491**, 547–553 (2012). doi: 10.1038/nature11618; pmid: 23172213
11. Y. Nir *et al*., Regional slow waves and spindles in human sleep. *Neuron* **70**, 153–169 (2011). doi: 10.1016/j.neuron.2011.02.043; pmid: 21482364
12. J. J. Chrobak, G. Buzsáki, High-frequency oscillations in the output networks of the hippocampal-entorhinal axis of the freely behaving rat. *J. Neurosci.* **16**, 3056–3066 (1996). doi: 10.1523/JNEUROSCI.16-09-03056.1996; pmid: 8622135
13. K. Mizuseki, G. Buzsáki, Preconfigured, skewed distribution of firing rates in the hippocampus and entorhinal cortex. *Cell Rep.* **4**, 1010–1021 (2013). doi: 10.1016/j.celrep.2013.07.039; pmid: 23994479
14. H. R. Joo, L. M. Frank, The hippocampal sharp wave-ripple in memory retrieval for immediate use and consolidation. *Nat. Rev. Neurosci.* **19**, 744–757 (2018). doi: 10.1038/s41583-018-0077-1; pmid: 30356103
15. G. Buzsáki, Hippocampal sharp waves: Their origin and significance. *Brain Res.* **398**, 242–252 (1986). doi: 10.1016/0006-8993(86)91483-6; pmid: 3026567
16. G. Buzsáki, Hippocampal sharp wave-ripple: A cognitive biomarker for episodic memory and planning. *Hippocampus* **25**, 1073–1188 (2015). doi: 10.1002/hipo.22488; pmid: 26135716
17. T. K. Leonard, K. L. Hoffman, Sharp-Wave Ripples in Primates Are Enhanced near Remembered Visual Objects. *Curr. Biol.* **27**, 257–262 (2017). doi: 10.1016/j.cub.2016.11.027; pmid: 28041797
18. T. K. Leonard *et al*., Sharp Wave Ripples during Visual Exploration in the Primate Hippocampus. *J. Neurosci.* **35**, 14771–14782 (2015). doi: 10.1523/JNEUROSCI.0864-15.2015; pmid: 26538648
19. D. Khodagholy, J. N. Gelinas, G. Buzsáki, Learning-enhanced coupling between ripple oscillations in association cortices and hippocampus. *Science* **358**, 369–372 (2017). doi: 10.1126/science.aan6203; pmid: 29051381
20. N. Maingret, G. Girardeau, R. Todorova, M. Goutierre, M. Zugaro, Hippocampo-cortical coupling mediates memory consolidation during sleep. *Nat. Neurosci.* **19**, 959–964 (2016). doi: 10.1038/nn.4304; pmid: 27182818
21. A. G. Siapas, M. A. Wilson, Coordinated interactions between hippocampal ripples and cortical spindles during slow-wave sleep. *Neuron* **21**, 1123–1128 (1998). doi: 10.1016/S0896-6273(00)80629-7; pmid: 9856467
22. Z. Clemens *et al*., Temporal coupling of parahippocampal ripples, sleep spindles and slow oscillations in humans. *Brain* **130**, 2868–2878 (2007). doi: 10.1093/brain/awm146; pmid: 17615093
23. A. Peyrache, M. Khamassi, K. Benchenane, S. I. Wiener, F. P. Battaglia, Replay of rule-learning related neural patterns in the prefrontal cortex during sleep. *Nat. Neurosci.* **12**, 919–926 (2009). doi: 10.1038/nn.2337; pmid: 19483687
24. D. Ji, M. A. Wilson, Coordinated memory replay in the visual cortex and hippocampus during sleep. *Nat. Neurosci.* **10**, 100–107 (2007). doi: 10.1038/nn1825; pmid: 17173043
25. G. Girardeau, I. Inema, G. Buzsáki, Reactivations of emotional memory in the hippocampus-amygdala system during sleep. *Nat. Neurosci.* **20**, 1634–1642 (2017). doi: 10.1038/nn.4637; pmid: 28892057
26. S. P. Jadhav, G. Rothschild, D. K. Roumis, L. M. Frank, Coordinated Excitation and Inhibition of Prefrontal Ensembles during Awake Hippocampal Sharp-Wave Ripple Events. *Neuron*

90, 113–127 (2016). doi: 10.1016/j.neuron.2016.02.010; pmid: 26971950
27. G. Rothschild, E. Eban, L. M. Frank, A cortical-hippocampal-cortical loop of information processing during memory consolidation. *Nat. Neurosci.* **20**, 251–259 (2017). doi: 10.1038/nn.4457; pmid: 27941790
28. S. N. Gomperts, F. Kloosterman, M. A. Wilson, VTA neurons coordinate with the hippocampal reactivation of spatial experience. *eLife* **4**, e05360 (2015). doi: 10.7554/eLife.05360; pmid: 26465113
29. H. Zhang, J. Fell, N. Axmacher, Electrophysiological mechanisms of human memory consolidation. *Nat. Commun.* **9**, 4103 (2018). doi: 10.1038/s41467-018-06553-y; pmid: 30291240
30. I. Skelin, S. Kilianski, B. L. McNaughton, Hippocampal coupling with cortical and subcortical structures in the context of memory consolidation. *Neurobiol. Learn. Mem.* **160**, 21–31 (2019). doi: 10.1016/j.nlm.2018.04.004; pmid: 29660400
31. G. Buzsáki, Two-stage model of memory trace formation: A role for "noisy" brain states. *Neuroscience* **31**, 551–570 (1989). doi: 10.1016/0306-4522(89)90423-5; pmid: 2687720
32. T. J. Davidson, F. Kloosterman, M. A. Wilson, Hippocampal replay of extended experience. *Neuron* **63**, 497–507 (2009). doi: 10.1016/j.neuron.2009.07.027; pmid: 19709631
33. M. P. Karlsson, L. M. Frank, Awake replay of remote experiences in the hippocampus. *Nat. Neurosci.* **12**, 913–918 (2009). doi: 10.1038/nn.2344; pmid: 19525943
34. C. T. Wu, D. Haggerty, C. Kemere, D. Ji, Hippocampal awake replay in fear memory retrieval. *Nat. Neurosci.* **20**, 571–580 (2017). doi: 10.1038/nn.4507; pmid: 28218916
35. A. C. Singer, M. F. Carr, M. P. Karlsson, L. M. Frank, Hippocampal SWR activity predicts correct decisions during the initial learning of an alternation task. *Neuron* **77**, 1163–1173 (2013). doi: 10.1016/j.neuron.2013.01.027; pmid: 23522050
36. G. Dragoi, S. Tonegawa, Preplay of future place cell sequences by hippocampal cellular assemblies. *Nature* **469**, 397–401 (2011). doi: 10.1038/nature09633; pmid: 21179088
37. K. Diba, G. Buzsáki, Forward and reverse hippocampal place-cell sequences during ripples. *Nat. Neurosci.* **10**, 1241–1242 (2007). doi: 10.1038/nn1961; pmid: 17828259
38. D. J. Foster, M. A. Wilson, Reverse replay of behavioural sequences in hippocampal place cells during the awake state. *Nature* **440**, 680–683 (2006). doi: 10.1038/nature04587; pmid: 16474382
39. D. K. Roumis, L. M. Frank, Hippocampal sharp-wave ripples in waking and sleeping states. *Curr. Opin. Neurobiol.* **35**, 6–12 (2015). doi: 10.1016/j.conb.2015.05.001; pmid: 26011627
40. M. C. Corballis, Mental time travel: A case for evolutionary continuity. *Trends Cogn. Sci.* **17**, 5–6 (2013). doi: 10.1016/j.tics.2012.10.009; pmid: 23153675
41. M. F. Carr, S. P. Jadhav, L. M. Frank, Hippocampal replay in the awake state: A potential substrate for memory consolidation and retrieval. *Nat. Neurosci.* **14**, 147–153 (2011). doi: 10.1038/nn.2732; pmid: 21270783
42. H. Gelbard-Sagiv, R. Mukamel, M. Harel, R. Malach, I. Fried, Internally generated reactivation of single neurons in human hippocampus during free recall. *Science* **322**, 96–101 (2008). doi: 10.1126/science.1164685; pmid: 18772395
43. S. Khuvis *et al*., Face-selective units in human ventral temporal cortex reactivate during free recall. bioRxiv 487686 [preprint]. 5 December 2018.
44. Y. Norman, E. M. Yeagle, M. Harel, A. D. Mehta, R. Malach, Neuronal baseline shifts underlying boundary setting during free recall. *Nat. Commun.* **8**, 1301 (2017). doi: 10.1038/s41467-017-01184-1; pmid: 29101322
45. R. Mukamel *et al*., Coupling between neuronal firing, field potentials, and FMRI in human auditory cortex. *Science* **309**, 951–954 (2005). doi: 10.1126/science.1110913; pmid: 16081741
46. J. Parvizi, S. Kastner, Promises and limitations of human intracranial electroencephalography. *Nat. Neurosci.* **21**, 474–483 (2018). doi: 10.1038/s41593-018-0108-2; pmid: 29507407
47. B. O. Watson, M. Ding, G. Buzsáki, Temporal coupling of field potentials and action potentials in the neocortex. *Eur. J. Neurosci.* **48**, 2482–2497 (2018). pmid: 29250852
48. A. Oliva, A. Fernández-Ruiz, G. Buzsáki, A. Berényi, Role of Hippocampal CA2 Region in Triggering Sharp-Wave Ripples. *Neuron* **91**, 1342–1355 (2016). doi: 10.1016/j.neuron.2016.08.008; pmid: 27593179
49. N. Axmacher, C. E. Elger, J. Fell, Ripples in the medial temporal lobe are relevant for human memory consolidation. *Brain* **131**, 1806–1817 (2008). doi: 10.1093/brain/awn103; pmid: 18503077
50. R. J. Staba, C. L. Wilson, A. Bragin, I. Fried, J. Engel Jr., Quantitative analysis of high-frequency oscillations (80-500 Hz) recorded in human epileptic hippocampus and entorhinal cortex. *J. Neurophysiol.* **88**, 1743–1752 (2002). doi: 10.1152/jn.2002.88.4.1743; pmid: 12364503
51. Y. Nir *et al*., Coupling between neuronal firing rate, gamma LFP, and BOLD fMRI is related to interneuronal correlations. *Curr. Biol.* **17**, 1275–1285 (2007). doi: 10.1016/j.cub.2007.06.066; pmid: 17686438
52. H. Hentschke, M. C. Stüttgen, Computation of measures of effect size for neuroscience data sets. *Eur. J. Neurosci.* **34**, 1887–1894 (2011). doi: 10.1111/j.1460-9568.2011.07902.x; pmid: 22082031
53. L. Wang, R. E. B. B. Mruczek, M. J. Arcaro, S. Kastner, Probabilistic maps of visual topography in human cortex. *Cereb. Cortex* **25**, 3911–3931 (2015). doi: 10.1093/cercor/bhu277; pmid: 25452571
54. R. S. Desikan *et al*., An automated labeling system for subdividing the human cerebral cortex on MRI scans into gyral based regions of interest. *Neuroimage* **31**, 968–980 (2006). doi: 10.1016/j.neuroimage.2006.01.021; pmid: 16530430
55. B. Fischl *et al*., Cortical folding patterns and predicting cytoarchitecture. *Cereb. Cortex* **18**, 1973–1980 (2008). doi: 10.1093/cercor/bhm225; pmid: 18079129
56. These six regions are the early and intermediate visual areas (including V1/V2/V3/V4 and other retinotopic areas along the dorsal stream), lateral occipital cortex, inferior temporal gyrus, lingual/parahippocampal gyrus, fusiform gyrus, and entorhinal cortex.
57. S. Takahashi, Episodic-like memory trace in awake replay of hippocampal place cell activity sequences. *eLife* **4**, e08105 (2015). doi: 10.7554/eLife.08105; pmid: 26481131
58. M. Moscovitch, R. Cabeza, G. Winocur, L. Nadel, Episodic Memory and Beyond: The Hippocampus and Neocortex in Transformation. *Annu. Rev. Psychol.* **67**, 105–134 (2016). doi: 10.1146/annurev-psych-113011-143733; pmid: 26726963
59. J. O'Neill, B. Pleydell-Bouverie, B. Dupret, J. Csicsvari, Play it again: Reactivation of waking experience and memory. *Trends Neurosci.* **33**, 220–229 (2010). doi: 10.1016/j.tins.2010.01.006
60. A. Ben-Yakov, Y. Dudai, Constructing realistic engrams: Poststimulus activity of hippocampus and dorsal striatum predicts subsequent episodic memory. *J. Neurosci.* **31**, 9032–9042 (2011). doi: 10.1523/JNEUROSCI.0702-11.2011; pmid: 21677186
61. P. Rajasethupathy *et al*., Projections from neocortex mediate top-down control of memory retrieval. *Nature* **526**, 653–659 (2015). doi: 10.1038/nature15389; pmid: 26436451
62. S. M. Polyn, V. S. Natu, J. D. Cohen, K. A. Norman, Category-specific cortical activity precedes retrieval during memory search. *Science* **310**, 1963–1966 (2005). doi: 10.1126/science.1117645; pmid: 16373577
63. A. P. Vaz, S. K. Inati, N. Brunel, K. A. Zaghloul, Coupled ripple oscillations between the medial temporal lobe and neocortex retrieve human memory. *Science* **363**, 975–978 (2019). doi: 10.1126/science.aau8956; pmid: 30819961
64. S. M. Smith, Fast robust automated brain extraction. *Hum. Brain Mapp.* **17**, 143–155 (2002). doi: 10.1002/hbm.10062; pmid: 12391568
65. M. Jenkinson, S. Smith, A global optimisation method for robust affine registration of brain images. *Med. Image Anal.* **5**, 143–156 (2001). doi: 10.1016/S1361-8415(01)00036-6; pmid: 11516708
66. M. Jenkinson, P. Bannister, M. Brady, S. Smith, Improved optimization for the robust and accurate linear registration and motion correction of brain images. *Neuroimage* **17**, 825–841 (2002). doi: 10.1006/nimg.2002.1132; pmid: 12377157
67. X. Papademetris *et al*., BioImage Suite: An integrated medical image analysis suite: An update. *Insight J.* **2006**, 209 (2006). pmid: 25364771
68. B. Fischl, FreeSurfer. *Neuroimage* **62**, 774–781 (2012). doi: 10.1016/j.neuroimage.2012.01.021; pmid: 22248573
69. T. Golan *et al*., Human intracranial recordings link suppressed transients rather than 'filling-in' to perceptual continuity across blinks. *eLife* **5**, e17243 (2016). doi: 10.7554/eLife.17243; pmid: 27685352
70. B. D. Argall, Z. S. Saad, M. S. Beauchamp, Simplified intersubject averaging on the cortical surface using SUMA. *Hum. Brain Mapp.* **27**, 14–27 (2006). doi: 10.1002/hbm.20158; pmid: 16035046
71. A. Delorme, S. Makeig, EEGLAB: An open source toolbox for analysis of single-trial EEG dynamics including independent component analysis. *J. Neurosci. Methods* **134**, 9–21 (2004). doi: 10.1016/j.jneumeth.2003.10.009; pmid: 15102499
72. H. Bokil, P. Andrews, J. E. Kulkarni, S. Mehta, P. P. Mitra, Chronux: A platform for analyzing neural signals. *J. Neurosci. Methods* **192**, 146–151 (2010). doi: 10.1016/j.jneumeth.2010.06.020; pmid: 20637804
73. K. J. Miller *et al*., Broadband changes in the cortical surface potential track activation of functionally diverse neuronal populations. *Neuroimage* **85**, 711–720 (2014). doi: 10.1016/j.neuroimage.2013.08.070; pmid: 24018305
74. P. P. Mitra, B. Pesaran, Analysis of dynamic brain imaging data. *Biophys. J.* **76**, 691–708 (1999). doi: 10.1016/S0006-3495(99)77236-X; pmid: 9929474
75. P. Mitra, *Observed Brain Dynamics* (Oxford Univ. Press, 2007).
76. Y. Benjamini, D. Yekutieli, The control of the false discovery rate in multiple testing under dependency. *Ann. Stat.* **29**, 1165–1188 (2001).
77. J. E. Iglesias *et al*., A computational atlas of the hippocampal formation using ex vivo, ultra-high resolution MRI: Application to adaptive segmentation of in vivo MRI. *Neuroimage* **115**, 117–137 (2015). doi: 10.1016/j.neuroimage.2015.04.042; pmid: 25936807
78. E. Stark *et al*., Pyramidal cell-interneuron interactions underlie hippocampal ripple oscillations. *Neuron* **83**, 467–480 (2014). doi: 10.1016/j.neuron.2014.06.023; pmid: 25033186
79. E. W. Schomburg *et al*., Theta phase segregation of input-specific gamma patterns in entorhinal-hippocampal networks. *Neuron* **84**, 470–485 (2014). doi: 10.1016/j.neuron.2014.08.051; pmid: 25263753
80. L. D. Fiederer *et al*., Electrical Stimulation of the Human Cerebral Cortex by Extracranial Muscle Activity: Effect Quantification With Intracranial EEG and FEM Simulations. *IEEE Trans. Biomed. Eng.* **63**, 2552–2563 (2016). doi: 10.1109/TBME.2016.2570743; pmid: 27448334
81. J. N. Gelinas, D. Khodagholy, T. Thesen, O. Devinsky, G. Buzsáki, Interictal epileptiform discharges induce hippocampal-cortical coupling in temporal lobe epilepsy. *Nat. Med.* **22**, 641–648 (2016). doi: 10.1038/nm.4084; pmid: 27111281
82. R. J. Staba *et al*., High-frequency oscillations recorded in human medial temporal lobe during sleep. *Ann. Neurol.* **56**, 108–115 (2004). doi: 10.1002/ana.20164; pmid: 15236407
83. D. W. Scott, On Optimal and Data-Based Histograms. *Biometrika* **66**, 605–610 (1979). doi: 10.1093/biomet/66.3.605
84. L. J. P. van der Maaten, E. O. Postma, H. J. van den Herik, Dimensionality reduction: A comparative review. *J. Mach. Learn. Res.* **10**, 66–71 (2009).
85. E. Levina, P. Bickel, Maximum likelihood estimation of intrinsic dimension. *Adv. Neural Inf. Process. Syst.* **17**, 777–784 (2004).
86. A. S. Ghuman *et al*., Dynamic encoding of face information in the human fusiform gyrus. *Nat. Commun.* **5**, 5672 (2014). doi: 10.1038/ncomms6672; pmid: 25482825
87. C. Jacques *et al*., Corresponding ECoG and fMRI category-selective signals in human ventral temporal cortex. *Neuropsychologia* **83**, 14–28 (2016). doi: 10.1016/j.neuropsychologia.2015.07.024; pmid: 26212070
88. D. M. Groppe, T. P. Urbach, M. Kutas, Mass univariate analysis of event-related brain potentials/fields I: A critical tutorial review. *Psychophysiology* **48**, 1711–1725 (2011). doi: 10.1111/j.1469-8986.2011.01273.x; pmid: 21895683
89. R. Oostenveld, P. Fries, E. Maris, J.-M. Schoffelen, FieldTrip: Open source software for advanced analysis of MEG, EEG, and invasive electrophysiological data. *Comput. Intell. Neurosci.* **2011**, 156869 (2011). doi: 10.1155/2011/156869; pmid: 21253357
90. E. Maris, R. Oostenveld, Nonparametric statistical testing of EEG- and MEG-data. *J. Neurosci. Methods* **164**, 177–190 (2007). doi: 10.1016/j.jneumeth.2007.03.024; pmid: 17517438
91. Images shown to patients are protected by copyright. Images presented in the figure are similar substitutes. Photo of Bill Clinton courtesy of Gage Skidmore; photo of the Golden Gate Bridge courtesy of Nicolas Raymond; photo of the Leaning Tower of Pisa courtesy of Josu; photo of Barack Obama courtesy of the U.S. government. All pictures are published under a Creative Commons license.

ACKNOWLEDGMENTS

We are grateful to the patients for their kind cooperation. Y.N. thanks his wife and his daughter for their continuous and loving support. We thank R. Amit, O. Sharon, R. Broday-Dvir, and

S. Grossman for intellectual support, encouragement, and helpful feedback. **Funding:** Supported by U.S.-Israel Binational Foundation grant 2017015 (R.M. and A.D.M.) and a CIFAR Tanenbaum Fellowship (R.M.). **Author contributions:** R.M. and Y.N. conceived the study and designed the experiment. Y.N. analyzed the data. R.M. supervised the analysis. E.M.Y. and S.K. ran the experiments. A.D.M. performed the surgeries and supervised the experiments and all aspects of data collection. M.H. and E.M.Y. contributed to electrode localization. Y.N. and R.M. wrote the paper. A.D.M., S.K., and E.M.Y. further contributed to the writing by reviewing and editing the manuscript. **Competing interests:** The authors declare no competing financial interests. **Data and materials availability:** The data and code that support the conclusions of this study are available upon reasonable request from Y.N. (itzik.norman@gmail.com) and are also accessible online at Zenodo (https://doi.org/10.5281/zenodo.3259369).

SUPPLEMENTARY MATERIALS

science.sciencemag.org/content/365/6454/eaax1030/suppl/DC1
Figs. S1 to S9
Table S1
Movie S1

21 February 2019; accepted 4 July 2019
10.1126/science.aax1030

RESEARCH ARTICLE

PLANT SCIENCE

Teosinte ligule allele narrows plant architecture and enhances high-density maize yields

Jinge Tian*, Chenglong Wang*, Jinliang Xia, Lishuan Wu, Guanghui Xu, Weihao Wu, Dan Li, Wenchao Qin, Xu Han, Qiuyue Chen, Weiwei Jin, Feng Tian†

Increased planting densities have boosted maize yields. Upright plant architecture facilitates dense planting. Here, we cloned *UPA1* (*Upright Plant Architecture1*) and *UPA2*, two quantitative trait loci conferring upright plant architecture. *UPA2* is controlled by a two-base sequence polymorphism regulating the expression of a B3-domain transcription factor (*ZmRAVL1*) located 9.5 kilobases downstream. *UPA2* exhibits differential binding by DRL1 (DROOPING LEAF1), and DRL1 physically interacts with LG1 (LIGULELESS1) and represses LG1 activation of *ZmRAVL1*. *ZmRAVL1* regulates *brd1* (*brassinosteroid C-6 oxidase1*), which underlies *UPA1*, altering endogenous brassinosteroid content and leaf angle. The *UPA2* allele that reduces leaf angle originated from teosinte, the wild ancestor of maize, and has been lost during maize domestication. Introgressing the wild *UPA2* allele into modern hybrids and editing *ZmRAVL1* enhance high-density maize yields.

Feeding the ever-increasing world population requires increased crop yield from limited arable lands (*1*). One solution to this challenge is to grow more plants per unit area to achieve higher productivity. However, dense planting imposes competition for water, nutrients, and light. Breeders of the cereal crop maize (*Zea mays* ssp. *mays*) have addressed this challenge by adapting plant architecture to dense planting. Plant architecture with more upright leaves (i.e., smaller leaf angle) decreases mutual shading and sustains light capture for photosynthesis despite increased plant density, thus improving the accumulation of leaf nitrogen for grain filling and increasing grain yield (*2*–*5*). With such adaptations, the planting density of maize has increased from 30,000 plants per hectare in the 1930s to >80,000 plants per hectare in the 2010s (*6*, *7*).

The ligular region, between the maize blade and sheath, consists of the ligule and auricle (*8*) and establishes leaf angle, which determines the plant's overall architecture. Mutant studies in maize have identified genes essential for development of the ligular region (*9*–*13*). *lg1* and *lg2* mutants exhibit erect leaf architecture because of defects in ligule and auricle development (*10*, *13*). Such erect leaf architecture facilitates dense planting (*3*, *4*). However, leaves in *lg* mutant plants are too erect to be useful in commercial hybrids. We searched for natural alleles that optimize plant architecture and leaf angle for dense planting.

State Key Laboratory of Plant Physiology and Biochemistry, National Maize Improvement Center, Key Laboratory of Biology and Genetic Improvement of Maize (MOA), Beijing Key Laboratory of Crop Genetic Improvement, China Agricultural University, Beijing 100193, China.
*These authors contributed equally to this work.
†Corresponding author. Email: ft55@cau.edu.cn

Upright Plant Architecture2 regulates leaf angle through *ZmRAVL1*

We mapped 12 quantitative trait loci (QTLs) for leaf angle in a population of 866 maize–teosinte BC_2S_3 recombinant inbred lines derived from a cross between the maize inbred line W22 and the teosinte accession CIMMYT 8759 (*Z. mays* ssp. *parviglumis*, hereafter referred to as 8759) (Fig. 1A and table S1). The QTL with the largest effect, *UPA2* (*Upright Plant Architecture2*), located on chromosome 2, was selected for positional cloning. The teosinte allele exhibited reduced leaf angle relative to the maize allele (fig. S1A). To verify the allelic effect, we developed a pair of near-isogenic lines (NILs) for *UPA2* (*UPA2*-NIL^{W22} and *UPA2*-NIL^{8759}) (Fig. 1B) from a recombinant inbred line that was heterozygous in the target region (fig. S1B). The two NILs differed in leaf angle in upper, middle, and lower leaves (Fig. 1C), indicating a canopy-wide effect of *UPA2* in altering plant architecture. We performed scanning electron microscopy and histological analyses for *UPA2*-NIL^{8759} and *UPA2*-NIL^{W22}, which exhibited similar size of auricle cells (fig. S2) but differed in auricle expansion. Compared with *UPA2*-NIL^{W22}, *UPA2*-NIL^{8759} with upright leaf angle had a narrower ligular band, resulting in reduced auricle size at maturity (Fig. 1, D and E, and fig. S3). Sclerenchymal layers in the ligular region provide mechanical strength for the blade. *UPA2*-NIL^{8759} contained more layers of sclerenchyma cells on the adaxial side than did *UPA2*-NIL^{W22} (Fig. 1, F and G).

To identify the genetic factor controlling *UPA2*, we generated a NIL population (n = 3180) and performed fine mapping following previously described methods (*14*, *15*). *UPA2* was narrowed down to a 240–base pair (bp) noncoding region according to the maize reference sequence (Fig. 1, H to J). *GRMZM2G102059*, encoding a B3 domain–containing protein homologous to RAVL1 in rice (*16*) (fig. S4), is located 9540 bp downstream of the 240-bp region of *UPA2* (Fig. 1, H to J). We thus named *GRMZM2G102059* "*ZmRAVL1*." The 240-bp region of *UPA2* may function as a distant cis element to regulate *ZmRAVL1* expression. Consistent with this hypothesis, *UPA2*-NIL^{8759} with small leaf angle showed lower *ZmRAVL1* expression than *UPA2*-NIL^{W22} with large leaf angle in developing leaves (fig. S5A). ZmRAVL1 is localized in the nucleus (fig. S5B). To validate the function of *ZmRAVL1*, we down-regulated *ZmRAVL1* expression by RNA interference (RNAi) and knocked out *ZmRAVL1* using CRISPR-Cas9 (*17*). In the T1 family of *ZmRAVL1*-KO#1 and *ZmRAVL1*-KO#2 carrying homozygous-null mutations (fig. S6A), Cas9-free plants were identified and propagated for phenotypic analysis and field trials. We found that both *ZmRAVL1* RNAi and knockout lines exhibited smaller leaf angle in lower, middle, and upper leaves compared with wild-type plants (Fig. 2, A and B, and fig. S6, B to D) because of decreased auricle size and increased adaxial sclerenchyma cells in the ligular region (figs. S7 and S8). By contrast, overexpressing *ZmRAVL1* led to larger leaf angle in lower, middle, and upper leaves compared with wild type (Fig. 2C and fig. S9). These results indicate that *ZmRAVL1* functions as a positive regulator of maize leaf angle.

To identify the causative sequence variant in the 240-bp region of *UPA2*, we sequenced the 240-bp region in W22 and 8759 and identified four sequence differences, including one single-nucleotide polymorphism (SNP) and three one- or two-base sequence polymorphisms, designated S1 to S4, respectively (fig. S10). We investigated whether these four sequence variants were associated with alteration of conserved regulatory sequences that may cause differential regulation by an upstream regulator. Among the four sequence variants, only S2 (TG/–) flanks a putative C2C2-binding motif (AGTGTG) (Fig. 3A and fig. S10). Maize YABBY genes *drl1* (*drooping leaf1*) and *drl2* contain a C2C2 zinc-finger domain at the N terminus (*12*). Their null mutants exhibited increased leaf angle and displayed a dropping-leaf phenotype (*12*). We tested whether DRL proteins could bind to the sequence surrounding S2 at *UPA2*. Because of the high sequence similarity between the DRL1 and DRL2 proteins (*12*), we selected DRL1 for further analysis. Electrophoretic mobility shift assay (EMSA) detected band shifts, and the probe from 8759 containing the TG nucleotides at S2 exhibited a stronger binding affinity for DRL1 compared with the probe from W22 lacking TG nucleotides (Fig. 3B and fig. S11). We also performed chromatin immunoprecipitation–quantitative polymerase chain reaction (ChiP-qPCR) using flag antibody against flag-tagged DRL1 protein. Enrichment

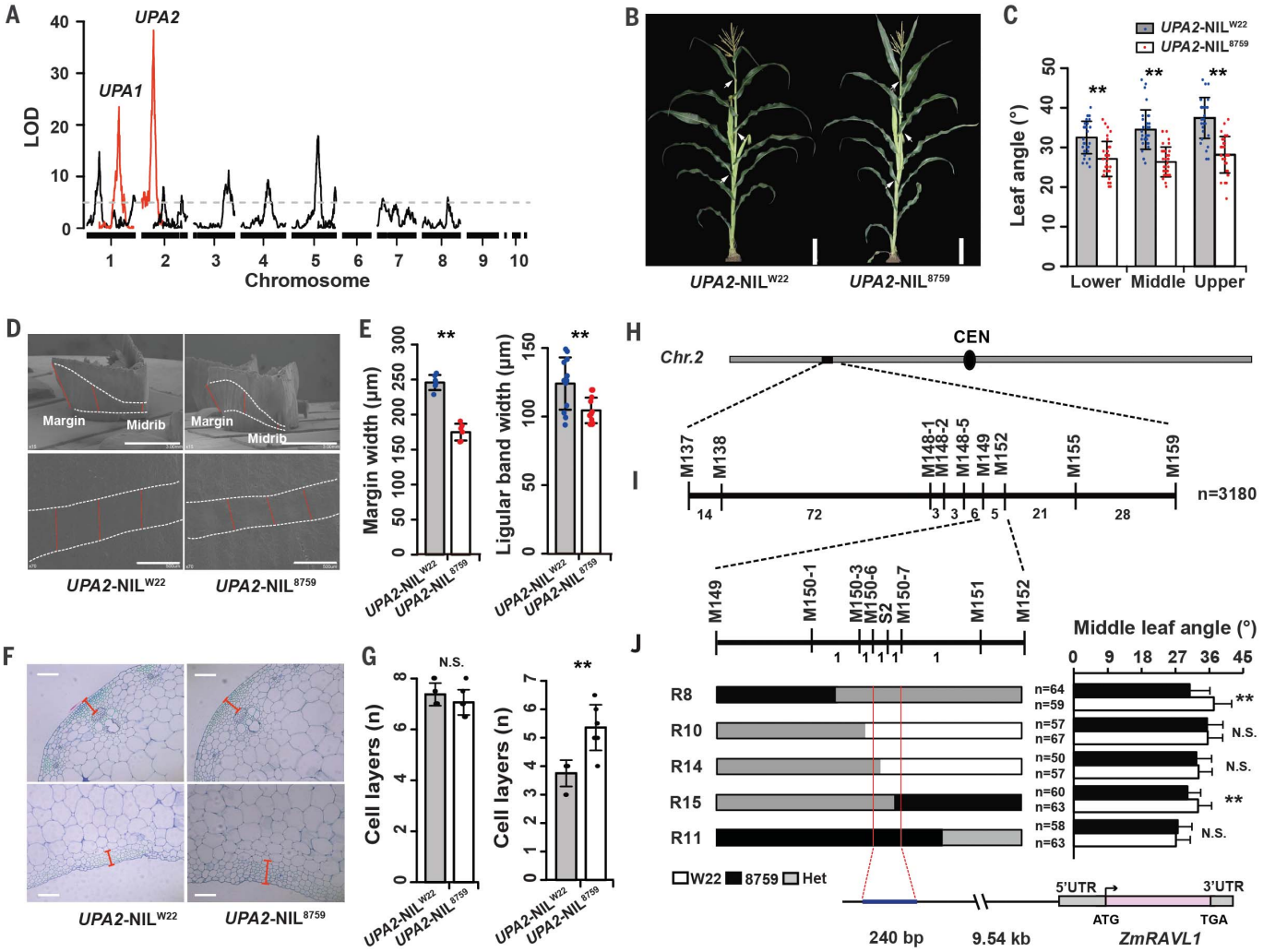

Fig. 1. Positional cloning of *UPA2*. (**A**) QTL mapping for middle leaf angle in the maize–teosinte BC_2S_3 population. LOD, logarithm of odds. *UPA2* and *UPA1* are the largest- and second-largest leaf angle QTL, respectively. The dashed gray line at LOD of 5 indicates the threshold of claiming significant QTLs. (**B**) Gross morphologies of *UPA2*-NIL^{W22} and *UPA2*-NIL^{8759}. The white arrows indicate the lower, middle, and upper leaves in which leaf angle was scored. Scale bars, 20 cm. (**C**) Comparison of leaf angle in lower, middle, and upper leaves between *UPA2*-NIL^{W22} and *UPA2*-NIL^{8759}. (**D**) Scanning electron microscopy analysis of the ligular region of *UPA2*-NIL^{W22} and *UPA2*-NIL^{8759}. The ligular band and the mature auricle region are indicated by white dashed lines. Scale bars, 3 mm (top) and 500 μm (bottom). (**E**) Comparison of the width of the ligular band and auricle margin between *UPA2*-NIL^{W22} and *UPA2*-NIL^{8759}. (**F**) Cross-sections of the mature ligular region of *UPA2*-NIL^{W22} and *UPA2*-NIL^{8759}. Top shows the abaxial side and bottom shows the adaxial side. Scale bars, 100 μm. (**G**) Comparison of number of the abaxial sclerenchyma cell layers (left) and the adaxial sclerenchyma cell layers (right) between *UPA2*-NIL^{W22} and *UPA2*-NIL^{8759}. (**H**) Location of *UPA2* on maize chromosome 2. CEN, centromere. (**I**) Fine mapping of *UPA2* using an NIL population (n = 3180). The number of recombinants between adjacent markers is indicated below the linkage map. (**J**) Progeny testing of recombinants delimited *UPA2* to a 240-bp noncoding region (red lines). The graphical genotypes of the five critical recombinants are shown on the left. White, black, and gray segments indicate regions homozygous for W22, regions homozygous for 8759, and heterozygous regions, respectively. The bar graphs on the right compare middle leaf angle between homozygous recombinants and homozygous non-recombinants within each recombinant-derived F_3 family. Black and white bars represent homozygous progenies that inherited the 8759 and W22 chromosome from the parental recombinant, respectively. The 240-bp region of *UPA2* is located 9540 bp upstream of the start codon (ATG) of *GRMZM2G102059* (*ZmRAVL1*). Pink and gray regions indicate the exon and untranslated regions (UTR), respectively. Values are means ± SD. $^{**}P < 0.01$ (Student's t test). N.S., not significant.

was detected in the fragment containing the putative C2C2-binding motif around S2 (Fig. 3C). These results indicated that the S2 variant in *UPA2* was associated with differential binding by DRL1.

lg1 and *lg2* genes establish the blade–sheath boundary, with *lg2* functioning before *lg1* (*10, 13*). To determine the regulatory relationship of *ZmRAVL1* with *lg1* and *lg2*, we examined their expression in the developing ligular region in their null mutants (fig. S12). In *lg1* and *lg2* mutants, *ZmRAVL1* expression was repressed (fig. S12, A and B), whereas in the *ZmRAVL1*-knockout line, the expression of *lg1* and *lg2* exhibited no alteration (fig. S12C). These results, together with the finding that *ZmRAVL1*-knockout lines exhibited normal ligular development and only affected auricle expansion, suggested that *ZmRAVL1* functions downstream of *lg1* and *lg2*. We next tested whether LG1 could regulate *ZmRAVL1* expression. Previous studies have shown that SBP-domain proteins recognize and bind GTAC motifs (*18*). Motif analysis identified two putative GTAC sites in the *ZmRAVL1* promoter (Fig. 3A and fig. S13A). Yeast one-hybrid assay (Y1H) (fig. S13B) and EMSA

(Fig. 3D and fig. S13C) showed that LG1 could bind the GTAC sites in the *ZmRAVL1* promoter in vitro. Further, ChIP-qPCR identified enrichment in the fragment spanning the GTAC sites in the *ZmRAVL1* promoter (Fig. 3E). Taken together, these results indicated that LG1 regulates *ZmRAVL1* expression.

Our results showed that LG1 could bind *ZmRAVL1* promoter, whereas DRL1 could bind the sequence surrounding S2 at *UPA2*, a distant cis-regulatory variant located 9.5 kb upstream of *ZmRAVL1*. To further determine how this circuit was regulated, we tested for an interaction between the LG1 and DRL1 proteins. We performed the yeast two-hybrid assay (Y2H) (Fig. 4A) and

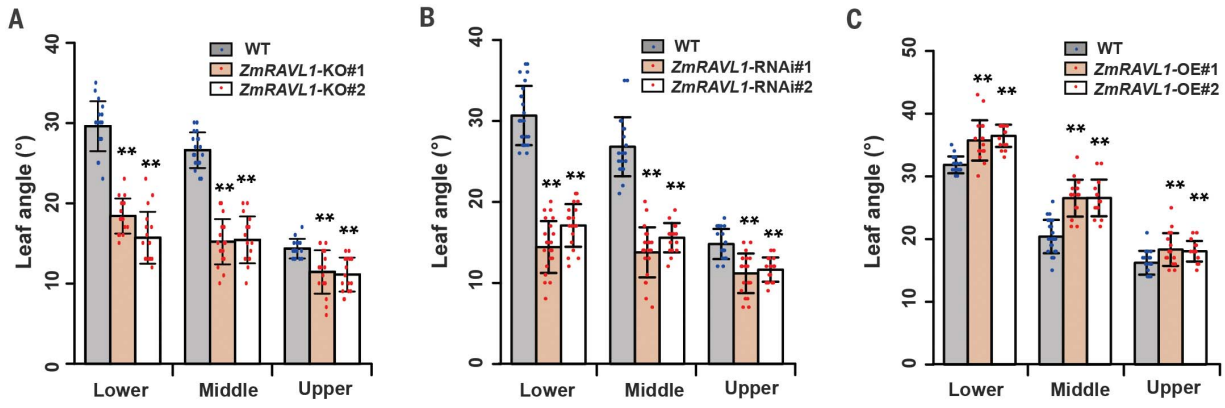

Fig. 2. *ZmRAVL1* regulates maize leaf angle. (**A**) *ZmRAVL1*-knockout lines (*ZmRAVL1*-KO#1 and *ZmRAVL1*-KO#2) exhibited reduced leaf angle in lower, middle, and upper leaves. (**B**) *ZmRAVL1* RNAi lines (*ZmRAVL1*-RNAi#1 and *ZmRAVL1*-RNAi#2) showed reduced leaf angle in lower, middle, and upper leaves. (**C**) *ZmRAVL1* overexpression lines (*ZmRAVL1*-OE#1 and *ZmRAVL1*-OE#2) exhibited increased leaf angle in lower, middle, and upper leaves. WT, wild-type. Values are means ± SD. $^{**}P < 0.01$ (Student's *t* test).

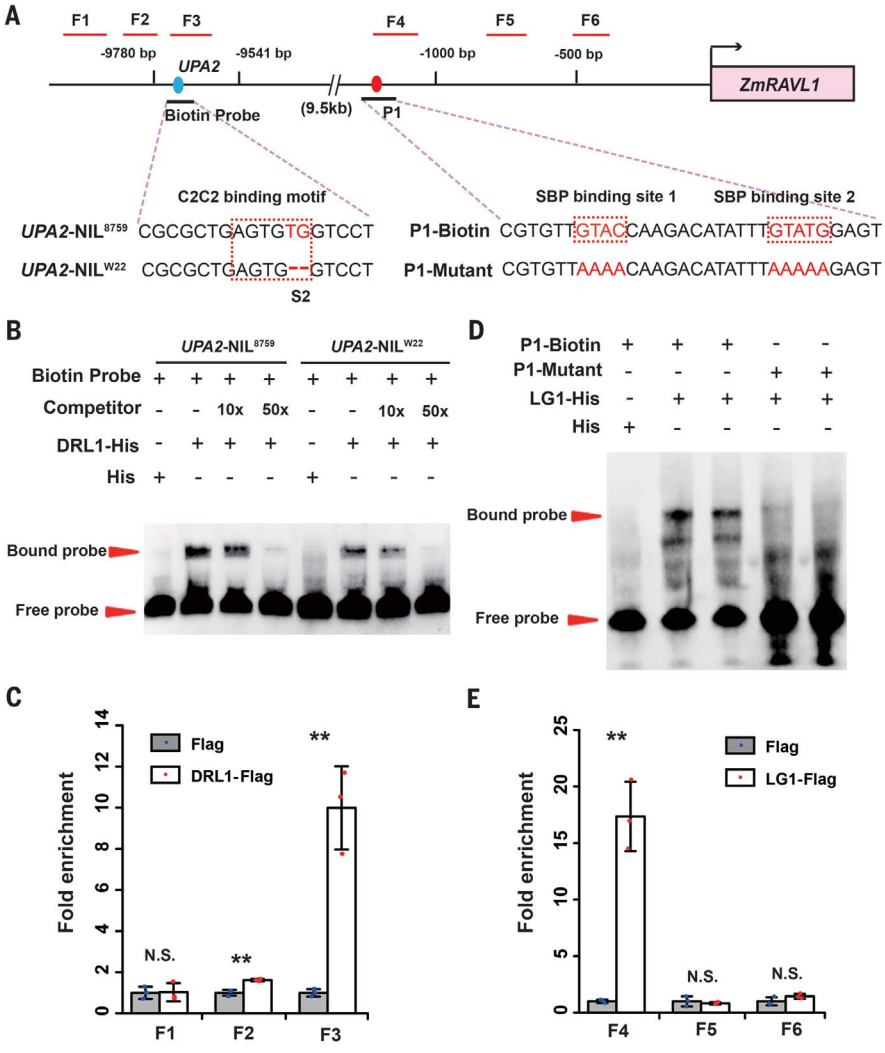

Fig. 3. DRL1 binds *UPA2* and LG1 binds *ZmRAVL1* promoter. (**A**) Relative locations of *UPA2* and *ZmRAVL1*. S2 (TG/−) flanks a putative C2C2-binding motif (red box). (**B**) EMSA shows that S2 was associated with differential binding by DRL1. The biotin-labeled probes are indicated in (A). (**C**) ChIP-qPCR indicates that DRL1 could bind the sequence surrounding S2 in vivo. The fragments used in ChIP-qPCR are indicated in (A). The F3 fragment contains the putative C2C2-binding motif surrounding S2, whereas the F1 and F2 fragments contain no putative C2C2-binding motif. (**D**) EMSA indicates that LG1 could bind the GTAC sites in the *ZmRAVL1* promoter. Biotin-labeled probes and mutant probes are indicated in (A). (**E**) ChIP-qPCR identified significant enrichment in the fragment containing the GTAC sites in the *ZmRAVL1* promoter. The fragments used in ChIP-qPCR are indicated in (A). The F4 fragment contains the putative SBP-binding motifs, whereas the F5 and F6 fragments contain no GTAC sequences. Fold enrichments in (C) and (E) were calculated relative to input. Values are means ± SD ($n = 3$ repeats) in (C) and (E). $^{**}P < 0.01$ (Student's *t* test). N.S., not significant.

the split firefly luciferase complementation assay in tobacco leaf epidermal cells (Fig. 4B). Both assays showed that LG1 and DRL1 interact in vitro and in vivo.

To investigate how DRL1 and LG1 together regulate *ZmRAVL1* expression, we performed transient expression assays in maize protoplasts, in which the coding sequence of DRL1 and LG1 driven by the *35S* promoter were used as effectors, and the UPA2 fragment (240 bp) from W22 or 8759 fused into the upstream of the luciferase (*LUC*) gene driven by a 1.7-kb *ZmRAVL1* promoter was used as the reporter (designated W22 and 8759 reporter, respectively) (Fig. 4C). When cotransforming with an empty effector construct, the 8759 reporter exhibited lower LUC activity than did the W22 reporter (Fig. 4D). Overexpressing LG1 alone induced the LUC activities of both the 8759 and W22 reporters, whereas overexpressing DRL1 alone repressed the LUC activities of the two reporters (Fig. 4D). Coexpression of LG1 with DRL1 repressed LG1-activated LUC activity (Fig. 4D). In these three cases, the 8759 reporter displayed lower LUC activity than did the W22 reporter (Fig. 4D). Thus, DRL1 physically interacts with LG1 to attenuate its effect on the transcription of *ZmRAVL1*.

Brassinosteroid C-6 oxidase underlies *UPA1*

We also performed fine mapping for the second-largest leaf angle QTL, *UPA1* on chromosome 1 (Fig. 1A and table S1). Different from *UPA2*, the teosinte allele at *UPA1* exhibited increased leaf angle relative to the maize allele (fig. S14). Phenotypic analysis of the two NILs for *UPA1* showed that *UPA1* also has a canopy-wide effect in altering leaf angles in different leaves (Fig. 5, A and B). The difference in leaf angle is due to the alteration in auricle size and the number of sclerenchyma cell layers on the adaxial side (fig. S15). Through fine mapping, *UPA1* was delimited to a 223-kb physical region containing a single gene (Fig. 5, C to E), *GRMZM2G103773*, encoding *brassinosteroid C-6 oxidase* (*brd1*), which catalyzes the final steps of brassinosteroid synthesis (*19*). We compared the *brd1* coding sequence between W22 and 8759 and identified seven SNPs, including two nonsynonymous SNPs, but not in the conserved region (fig. S16A). We compared *brd1* expression in the two NILs for *UPA1*. *UPA1*-NIL^{8759} with large leaf angle exhibited higher *brd1* expression than *UPA1*-NIL^{W22} with small leaf angle in developing leaves (fig. S16B). Indeed, a *brd1*-null mutant exhibits dwarfism and aberration in the blade–auricle border (*19*). We overexpressed *brd1* and found that the *brd1* overexpression lines exhibited normal ligular development but increased leaf angle (fig. S17) because of the enlarged auricle and the decreased number of sclerenchyma cells on the adaxial side (fig. S18). These results indicate that *brd1* is involved in the regulation of maize leaf angle.

In *ZmRAVL1*-knockout plants, *brd1* expression was down-regulated (fig. S19A), whereas in *brd1*-overexpressed lines, *ZmRAVL1* exhibited no change (fig. S19B). The two NILs for *UPA2* differed in *brd1* expression (fig. S19C), whereas *ZmRAVL1* showed similar expression in the two NILs for *UPA1* (fig. S19D). These results suggested that *brd1* functions downstream of *ZmRAVL1*. We next tested whether *ZmRAVL1* could regulate *brd1* expression. B3 transcription factors bind E-box motif (CANNTG) (*16*). We identified five putative E-box elements in the *brd1* promoter (Fig. 5F). Y1H, EMSA, and ChIP-qPCR showed that ZmRAVL1 could bind the *brd1* promoter in vitro and in vivo (Fig. 5, G and H, and fig. S20). Transient expression assay in maize protoplasts confirmed that *ZmRAVL1* activates *brd1* transcription (Fig. 5, I and J).

Of the various phytosteroids, only brassinolide and its immediate precursor, castasterone, possess biological activity in planta (*20*). *brd1* encodes a C-6 oxidase involving the conversion of 6-deoxocastasterone to castasterone (*20*). We measured endogenous brassinosteroid accumulation in the developing ligular region of the *brd1*

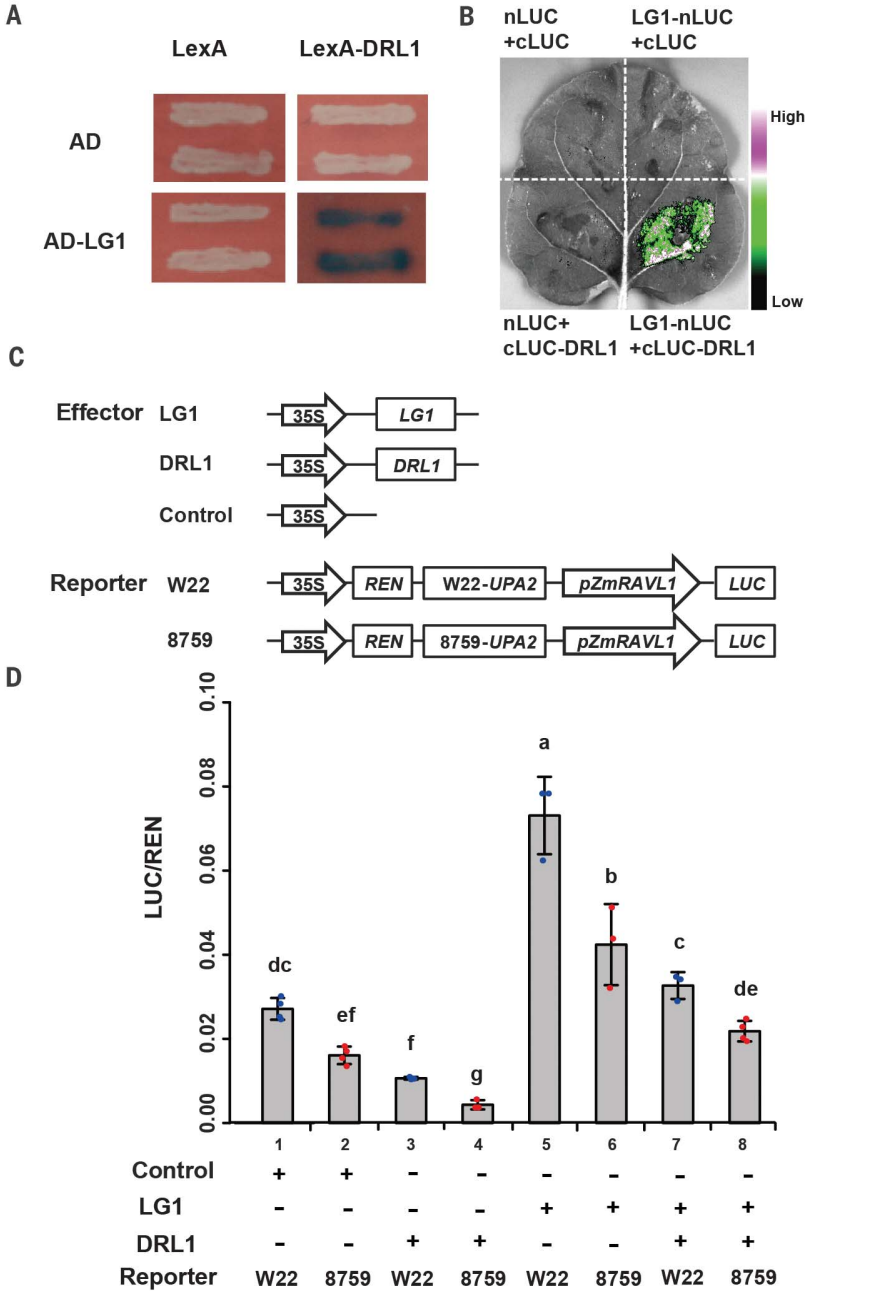

Fig. 4. DRL1 and LG1 together regulate *ZmRAVL1* expression. (**A**) Y2H indicates that LG1 and DRL1 interact in vitro. (**B**) The split firefly luciferase complementation assay shows that LG1 and DRL1 interact in vivo. (**C**) Schematic diagram shows the constructs used in the transient transcriptional activity assays. (**D**) DRL1 represses LG1 to activate the expression of *ZmRAVL1*. Values are means ± SD (n = 4 repeats). Different letters denote significant differences ($P < 0.05$) from a Duncan's multiple-range test.

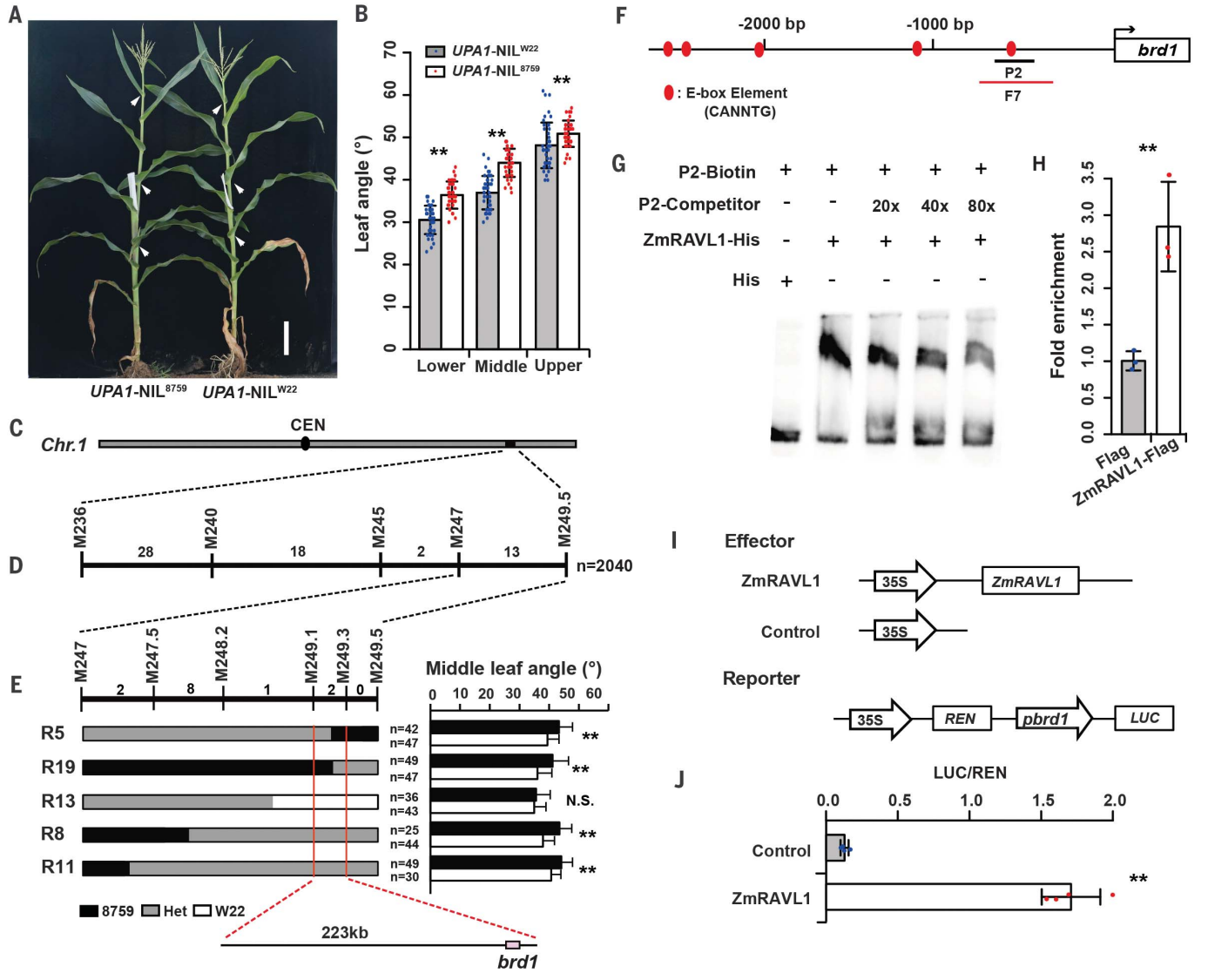

Fig. 5. Positional cloning of *UPA1*. (**A**) Gross morphologies of *UPA1*-NIL^{W22} and *UPA1*-NIL^{8759}. The white arrows indicate the lower, middle, and upper leaves in which leaf angle was scored. Scale bar, 20 cm. (**B**) Comparison of leaf angle in lower, middle, and upper leaves between *UPA1*-NIL^{W22} and *UPA1*-NIL^{8759}. (**C**) Location of *UPA1* on maize chromosome 1. CEN, centromere. (**D**) Fine mapping of *UPA1* using an NIL population (n = 2040). The number of recombinants between adjacent markers is indicated below the linkage map. (**E**) Progeny testing of recombinants delimited *UPA1* to a 223-kb physical region containing only one annotated gene, *GRMZM2G103773* (*brd1*). The graphical genotypes of the five representative recombinants are shown on the left. White, black, and gray segments indicate regions homozygous for W22, regions homozygous for 8759, and heterozygous regions, respectively. The bar graphs on the right compare middle leaf angle between homozygous recombinants and homozygous nonrecombinants within each recombinant-derived F_3 family. (**F**) Schematic diagram of the *brd1* promoter. Red dots indicate the putative E-box motif. (**G**) EMSA shows that ZmRAVL1 binds the putative E-box motif in the *brd1* promoter. The biotin-labeled probe (P2) is indicated in (F). Unlabeled probes were used in the competition assay. (**H**) ChIP–qPCR identified significant enrichment in the fragment containing the E-box motif in the *ZmRAVL1* promoter. The fragment (F7) used in ChIP-qPCR is indicated in (F). Fold enrichments were calculated relative to input. (**I**) Schematic diagram shows the effectors and reporter used in the transient transcriptional activity assays. (**J**) *ZmRAVL1* activates *brd1* expression. Values are means ± SD in (B), (H), and (J). $^{**}P < 0.01$ (Student's t test).

overexpression and *ZmRAVL1*-knockout lines. Brassinolide was not detected in our samples. Plants with *brd1* overexpression exhibited increased castasterone content (fig. S21). *ZmRAVL1*-knockout plants that showed reduced *brd1* expression had less castasterone than did wild-type plants (fig. S21). These results suggested that *ZmRAVL1* affects endogenous brassinosteroid content.

UPA2-UPA1–associated regulatory model for leaf angle

We have developed a model for how the leaf angle difference between *UPA2*-NIL^{8759} and *UPA2*-NIL^{W22} is regulated (fig. S22). We suggest that *UPA2* is controlled by a 2-bp sequence variant (TG/–) located 9.5 kb upstream of *ZmRAVL1*. Compared with the cultivated W22 allele, the wild 8759 allele containing the TG nucleotides at *UPA2* is associated with a higher binding affinity for DRL1. DRL1 physically interacts with LG1, which attenuates the transcriptional activation function of LG1 on *ZmRAVL1* expression. Low *ZmRAVL1* expression in *UPA2*-NIL^{8759} results in less expression of *brd1*, consequently decreasing endogenous brassinosteroid in the ligular region, reducing auricle expansion, and leading to smaller leaf angle. In *UPA2*-NIL^{W22},

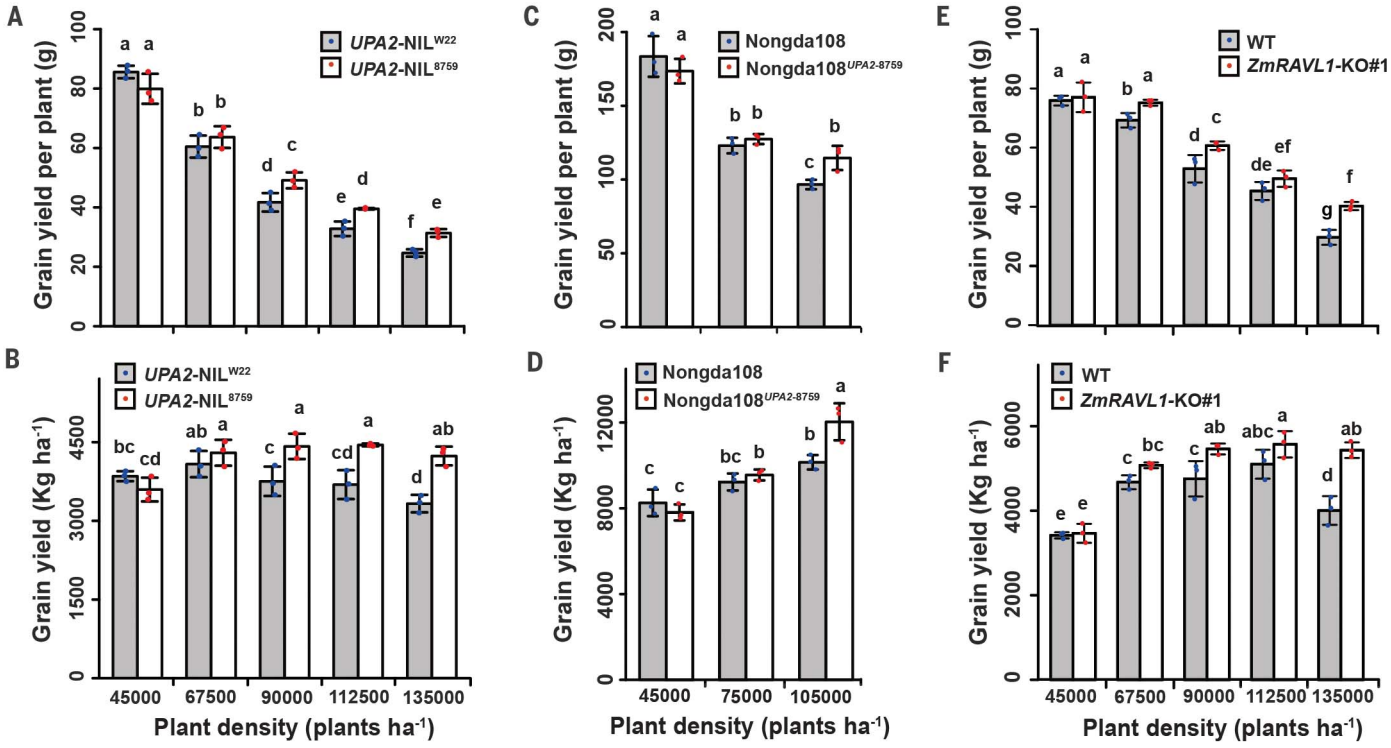

Fig. 6. Teosinte *UPA2* allele and *ZmRAVL1* edited allele enhanced maize grain yield under high planting densities. (**A** and **B**) Comparison of grain yield per plant (A) and grain yield per hectare (B) between *UPA2*-NIL^{W22} and *UPA2*-NIL^{8759} under different planting densities in the field trial in Sanya, China, in 2017. (**C** and **D**) Comparison of grain yield per plant (C) and grain yield per hectare (D) between the original Nongda108 and the improved Nongda108 carrying the 8759 *UPA2* allele under different planting densities in the field trial in Sanya, China, in 2018. (**E** and **F**) Comparison of grain yield per plant (E) and grain yield per hectare (F) between *ZmRAVL1*-KO#1 and wild-type under different planting densities in the field trial in Tieling, China, in 2018. Values are means ± SD (n = 3 replications). Different letters denote significant differences (P < 0.05) from Duncan's multiple-range tests. ha, hectare.

low binding affinity for DRL1 at *UPA2* releases LG1 to activate *ZmRAVL1* transcription, which further up-regulates *brd1* expression, resulting in increased brassinosteroid and leaf angle.

Teosinte *UPA2* and editing *ZmRAVL1* enhance maize yields

To examine the distribution of S2 at *UPA2* in the maize natural population, we genotyped S2 in 508 maize inbred lines (*21*) and 50 maize landraces (table S2). None of these maize accessions carried the TG allele at S2 (table S3). We further genotyped S2 in 45 teosinte accessions (table S4). Only two (4.4%) teosinte accessions carried the TG allele at S2 (table S3). These results suggested that S2 is a rare variant in teosinte that was lost during maize domestication.

Although the TG allele at S2 that reduces leaf angle was lost during maize domestication, this allele could be exploited for generating upright leaf architecture for dense planting in modern breeding. To test this possibility, we planted *UPA2*-NIL^{W22} and *UPA2*-NIL^{8759} under five different planting densities in two environments (Tieling and Sanya, both in China) in 2017. In both field trials, *UPA2*-NIL^{8759} with upright leaf angle out-yielded *UPA2*-NIL^{W22} under high planting densities (>67,500 and 105,000 plants per hectare in Sanya and Tieling, respectively) (Fig. 6, A and B, and fig. S23, A to F). Consistent with this result, *UPA2*-NIL^{8759} exhibited a lower rate of decrease of grain yield per plant than *UPA2*-NIL^{W22} as planting density increased (Fig. 6A and fig. S23C). To evaluate the value of *UPA2* in hybrids, we introgressed the teosinte *UPA2* allele conferring upright leaf angle, through repeated backcrossing and molecular marker assisted selection, into the two parents of Nongda108 (HuangC × Xu178), an elite maize hybrid widely planted in China. We analyzed yield in field trials of the improved Nongda108 and original Nongda108 hybrids under three different planting densities in Sanya, China, in 2018 (Fig. 6, C and D, and fig. S23, G and H). Under planting densities of 45,000 and 75,000 plants per hectare, the original Nongda108 and the improved Nongda108 exhibited similar grain yield (Fig. 6, C and D). However, as planting density increased to 105,000 plants per hectare, the improved Nongda108 showed higher grain yield than the original Nongda108 (Fig. 6, C and D). These results suggested that the teosinte *UPA2* allele can both alter the architecture of modern maize plants and improve yield potentials under dense planting.

ZmRAVL1 edited lines also displayed reduced leaf angle. We evaluated the grain yield of *ZmRAVL1*-KO#1 (Cas9-free) under five different planting densities in two locations (Tieling and Sanya) in 2018. Yield from *ZmRAVL1*-KO#1 was greater than from wild-type plants under high planting densities in both locations (Fig. 6, E and F, and fig. S24). In the *ZmRAVL1*-KO#1 T1 family, Cas9-positive plants were selected and crossed with six elite maize inbreds. In the resulting F_1 plants, the wild *ZmRAVL1* allele introduced by inbreds was edited (fig. S25). As a result, the F_1 hybrids showed reduced leaf angle compared with the control hybrids (fig. S27). We also crossed *ZmRAVL1*-RNAi#1 with the six maize inbreds. The resulting F_1 hybrids exhibited decreased *ZmRAVL1* expression compared with the control hybrids (fig. S26), leading to reduced leaf angle (fig. S27). Therefore, manipulating *ZmRAVL1* can generate upright leaf architecture for increased planting density.

REFERENCES AND NOTES

1. D. Tilman, C. Balzer, J. Hill, B. L. Befort, *Proc. Natl. Acad. Sci. U.S.A.* **108**, 20260–20264 (2011).
2. W. G. Duncan, *Crop Sci.* **11**, 482 (1971).
3. R. J. Lambert, R. R. Johnson, *Crop Sci.* **18**, 499–502 (1978).
4. J. W. Pendleton, G. E. Smith, S. R. Winter, T. J. Johnston, *Agron. J.* **60**, 422 (1968).
5. D. W. Stewart *et al.*, *Agron. J.* **95**, 1465–1474 (2003).
6. D. N. Duvick, *Maydica* **50**, 193–202 (2005).
7. F. Tian *et al.*, *Nat. Genet.* **43**, 159–162 (2011).
8. M. W. Lewis, S. Hake, *Plant Biol.* **29**, 80–86 (2016).
9. J. Moon, H. Candela, S. Hake, *Development* **140**, 405–412 (2013).

10. M. A. Moreno, L. C. Harper, R. W. Krueger, S. L. Dellaporta, M. Freeling, *Genes Dev.* **11**, 616–628 (1997).
11. G. J. Muehlbauer *et al.*, *Plant Physiol.* **119**, 651–662 (1999).
12. J. Strable *et al.*, *Plant Cell* **29**, 1622–1641 (2017).
13. J. Walsh, C. A. Waters, M. Freeling, *Genes Dev.* **12**, 208–218 (1998).
14. C. Huang *et al.*, *Proc. Natl. Acad. Sci. U.S.A.* **115**, E334–E341 (2018).
15. Y. Liang *et al.*, *New Phytol.* **221**, 2335–2347 (2019).
16. B. I. Je *et al.*, *Plant Cell* **22**, 1777–1791 (2010).
17. K. Belhaj, A. Chaparro-Garcia, S. Kamoun, N. J. Patron, V. Nekrasov, *Curr. Opin. Biotechnol.* **32**, 76–84 (2015).
18. J. Wang *et al.*, *Science* **361**, 1026–1028 (2018).
19. I. Makarevitch, A. Thompson, G. J. Muehlbauer, N. M. Springer, *PLOS ONE* **7**, e30798 (2012).
20. D. Tarkowská, O. Novák, J. Oklestkova, M. Strnad, *Anal. Bioanal. Chem.* **408**, 6799–6812 (2016).
21. Q. Yang *et al.*, *Proc. Natl. Acad. Sci. U.S.A.* **110**, 16969–16974 (2013).

ACKNOWLEDGMENTS

We thank J.F. Doebley (University of Wisconsin) for providing teosinte materials and maize landraces and valuable discussion; X. Yang (China Agricultural University) for providing the maize inbred lines; the Maize Genetics COOP Stock Center for providing the maize-teosinte BC_2S_3 population and mutants; and S. Yang (China Agricultural University) and L. Tan (China Agricultural University) for valuable discussions. **Funding**: This research was supported by the National Key Research and Development Program of China (2016YFD0100404), the National Natural Science Foundation of China (91535108), the Recruitment Program of Global Experts, and the Fundamental Research Funds for the Central Universities. **Author contributions**: J.T., C.W., and F.T. designed the research. J.T. and C.W. performed experiments and analyses. J.T., C.W., J.X., L.W., G.X., W.W., D.L., W.Q., X.H., and Q.C. collected phenotypic data. W.J. contributed to transgenic experiments. J.T., C.W., and F.T. wrote and edited the manuscript. All authors read and approved the final manuscript. **Competing interests:** A patent application related to this work has been submitted by F.T., J.T., and C.W. **Data and materials availability**: All data needed to evaluate the conclusions in the paper are present in the paper or the supplementary materials.

SUPPLEMENTARY MATERIALS

science.sciencemag.org/content/365/6454/658/suppl/DC1
Materials and Methods
Figs. S1 to S27
Tables S1 to S9
References (*22*–*33*)

2 April 2019; accepted 24 June 2019
10.1126/science.aax5482

REPORT

GRAVITATION

Relativistic redshift of the star S0-2 orbiting the Galactic Center supermassive black hole

Tuan Do[1]*, Aurelien Hees[2,1], Andrea Ghez[1], Gregory D. Martinez[1], Devin S. Chu[1], Siyao Jia[3], Shoko Sakai[1], Jessica R. Lu[3], Abhimat K. Gautam[1], Kelly Kosmo O'Neil[1], Eric E. Becklin[1,4], Mark R. Morris[1], Keith Matthews[5], Shogo Nishiyama[6], Randy Campbell[7], Samantha Chappell[1], Zhuo Chen[1], Anna Ciurlo[1], Arezu Dehghanfar[1,8], Eulalia Gallego-Cano[9], Wolfgang E. Kerzendorf[10,11,12,13], James E. Lyke[7], Smadar Naoz[1,14], Hiromi Saida[15], Rainer Schödel[9], Masaaki Takahashi[16], Yohsuke Takamori[17], Gunther Witzel[1,18], Peter Wizinowich[7]

The general theory of relativity predicts that a star passing close to a supermassive black hole should exhibit a relativistic redshift. In this study, we used observations of the Galactic Center star S0-2 to test this prediction. We combined existing spectroscopic and astrometric measurements from 1995–2017, which cover S0-2's 16-year orbit, with measurements from March to September 2018, which cover three events during S0-2's closest approach to the black hole. We detected a combination of special relativistic and gravitational redshift, quantified using the redshift parameter Υ. Our result, $\Upsilon = 0.88 \pm 0.17$, is consistent with general relativity ($\Upsilon = 1$) and excludes a Newtonian model ($\Upsilon = 0$) with a statistical significance of 5σ.

General relativity (GR) has been thoroughly tested in weak gravitational fields in the Solar System (*1*), with binary pulsars (*2*) and with measurements of gravitational waves from stellar-mass black hole binaries (*3*, *4*). Observations of short-period stars in our Galactic Center (GC) (*5*–*8*) allow GR to be tested in a different regime (*9*): the strong field near a supermassive black hole (SMBH) (*10*, *11*). The star S0-2 (also known as S2) has a 16-year orbit around Sagittarius A* (Sgr A*), the SMBH at the center of the Milky Way. In 2018 May, S0-2 reached its point of closest approach, at a distance of 120 astronomical units with a velocity reaching 2.7% of the speed of light. Within a 6-month interval of that date, the star also passed through its maximum and minimum velocity (in March and September, respectively) along the line of sight, spanning 6000 km s^{-1} in radial velocity (RV) (Fig. 1). Here we present observations of all three events combined with data from 1995–2017 (Fig. 2).

During 2018, the close proximity of S0-2 to the SMBH caused the relativistic redshift, which is the combination of the transverse Doppler shift from special relativity and the gravitational redshift from GR. This deviation from a Keplerian orbit was predicted to reach 200 km s^{-1} (Fig. 3) and is detectable with current telescopes. The GRAVITY collaboration (*9*) previously reported a similar measurement. Our measurements are complementary in the following ways: (i) We took a complete set of independent measurements with three additional months of data, doubling the time baseline for the year of closest approach and including the third turning point (RV minimum) in September 2018. (ii) We used three different spectroscopic instruments in 2018, enabling us to probe the presence of instrumental biases. (iii) To test for bias in the result, we analyzed the systematic errors that may arise from an experiment spanning more than 20 years. (iv) We publicly released the stellar measurements and the posterior probability distributions.

We used a total of 45 astrometric positional measurements (spanning 24 years) and 115 RVs (18 years) to fit the orbit of S0-2. Of these, 11 are new astrometric measurements of S0-2 from 2016 to 2018 and 28 are new RV measurements from 2017 and 2018 (Fig. 1). Astrometric measurements were obtained at the W. M. Keck Observatory by using speckle imaging (a technique to overcome blurring from the atmosphere by taking very short exposures and combining the images with software) from 1995–2005 and adaptive optics (AO) imaging (*12*) from 2005–2018. RV measurements were obtained from the W. M. Keck Observatory, Gemini North Telescope, and Subaru Telescope. All of our RV observations were taken using AO. We supplement our observations with previously reported RVs from Keck from 2000 (*7*) and the Very Large Telescope from 2003–2016 (*8*). This work includes data from two imaging instruments and six spectroscopic instruments (*13*).

We scheduled our 2018 observations using a tool designed to maximize the sensitivity of the experiment to the redshift signal (*13*). We predicted that, given the existing data (1995–2017), spectroscopic measurements at the RV maximum and minimum in 2018 would provide the most sensitivity and thus would be ideal for detecting the relativistic redshift (Fig. 3). Although they are less sensitive to the effect of the redshift, imaging observations of the sky position of S0-2 in 2018 also slightly improve the measurement of the relativistic redshift.

The RVs of S0-2 are measured by fitting a physical model (which includes properties of the star, such as its effective temperature, surface gravity, and rotational velocity in addition to RV) to its observed spectrum (*13*). The same procedure is applied to the new and archival observations; for the latter, this spectroscopic method improves the precision by a factor of 1.7 compared with previous analyses (*14*, *15*).

We also characterized additional sources of uncertainties beyond the uncertainties in the fitted model. (i) The wavelength solution, which transforms locations on the detector to vacuum wavelengths, was characterized by comparing the observed wavelengths of atmospheric OH emission lines in the spectra of S0-2 and in observations of blank sky to their known vacuum wavelengths. This comparison shows the uncertainty of the wavelength solution of the spectroscopic instruments to be ~2 km s^{-1}, with some observations from 2002–2004 having lower accuracy between 2 and 26 km s^{-1}. (ii) Reexamination

[1]Department of Physics and Astronomy, University of California, Los Angeles, CA 90095, USA. [2]Sytèmes de Référence Temps Espace, Observatoire de Paris, Université Paris-Sciences-et-Lettres, Centre National de la Recherche Scientifique, Sorbonne Université, Laboratoire National de Métrologie et d'Essais, 61 Avenue de l'Observatoire, 75014 Paris, France. [3]Department of Astronomy, University of California, Berkeley, CA 94720, USA. [4]Universities Space Research Association/Stratospheric Observatory for Infrared Astronomy, NASA Ames Research Center, Mail Stop N232-12, Moffet Field, CA 94035, USA. [5]Division of Physics, Mathematics, and Astronomy, California Institute of Technology, MC 301-17, Pasadena, CA 91125, USA. [6]Faculty of Education, Miyagi University of Education, 149 Aramaki-aza-aoba, Aoba-ku, Sendai, Miyagi 980-0845, Japan. [7]W. M. Keck Observatory, 65-1120 Mamalahoa Highway, Kamuela, HI 96743, USA. [8]Institut de Planétologie et d'Astrophysique de Grenoble, 414 Rue de la Piscine, 38400 Saint-Martin-d'Héres, France. [9]Instituto de Astrofísica de Andalucía, Consejo Superior de Investigaciones Científicas, Glorieta de la Astronomía S/N, 18008 Granada, Spain. [10]European Southern Observatory, Karl-Schwarzschild-Straße 2,85748 Garching bei München, Germany. [11]Center for Cosmology and Particle Physics, New York University, 726 Broadway, New York, NY 10003, USA. [12]Department of Physics and Astronomy, Michigan State University, East Lansing, MI 48824, USA. [13]Department of Computational Mathematics, Science, and Engineering, Michigan State University, East Lansing, MI 48824, USA. [14]Mani L. Bhaumik Institute for Theoretical Physics, Department of Physics and Astronomy, University of California, Los Angeles, CA 90095, USA. [15]Faculty of Liberal Arts, Daido University, 10-3 Takiharu-cho, Minami-ku, Nagoya, Aichi 457-8530, Japan. [16]Department of Physics and Astronomy, Aichi University of Education, 1 Hirosawa, Igaya-cho, Kariya, Aichi 448-8542, Japan. [17]National Institute of Technology, Wakayama College, 77 Noshima, Nada-cho, Gobo, Wakayama 644-0023, Japan. [18]Max Planck Institute for Radio Astronomy, Auf dem Hügel 69, D-53121 Bonn, Germany.
***Corresponding author. Email: tdo@astro.ucla.edu**

of the spectroscopic data showed that one spectroscopic instrument [Near-Infrared Camera 2 (NIRC2)] had additional systematic bias from its optical system, which resulted in a systematic offset in RV compared with other instruments. We include an RV offset parameter in the orbit fit to account for this systematic offset. (iii) We assessed systematic uncertainty by observing bright RV standard stars of the same spectral-type as S0-2 (table S3). This systematic error is 1.3 ± 1.2 km s^{-1}, smaller than the statistical uncertainties and ~17% of previous RV measurements of S0-2 (*15*). When these sources of systematic error are included in the analysis, the average RV uncertainty of S0-2 is

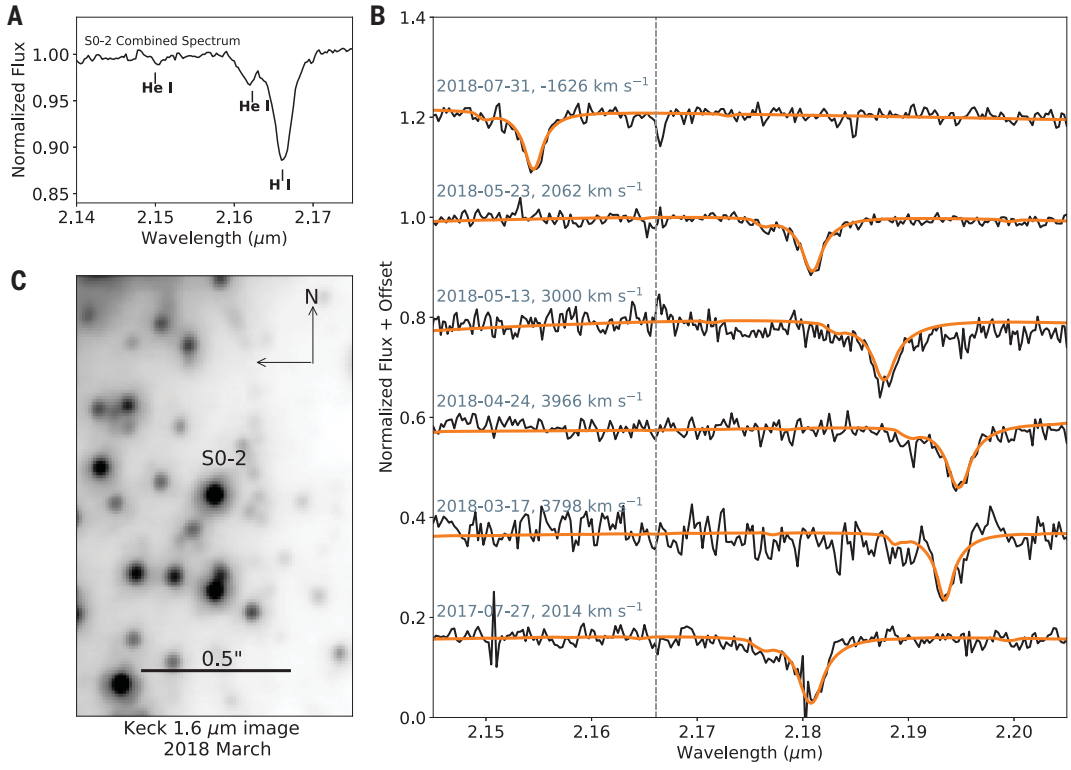

Fig. 1. Spectroscopy and imaging of the star S0-2. (**A**) Weighted-average spectrum of S0-2 from data obtained during 2006–2018 at the Keck Observatory. The strongest feature, which provides most of the RV constraint, is from the H I line at 2.1661 μm. (**B**) Sequence of S0-2 spectra observed in 2017 and 2018 (black lines). The RV of the star changes by more than 6000 km s^{-1} throughout 2018. The dashed line shows the rest wavelength of the H I line. We fit a model to the spectrum that simultaneously constrains the star's physical properties, such as effective temperature and rotation, along with the RV of the star (orange lines). This model accounts for the asymmetries in the H I feature. (**C**) Inverted Keck AO image of S0-2 (center of image) from March 2018 with the H-band filter (1.6 μm).

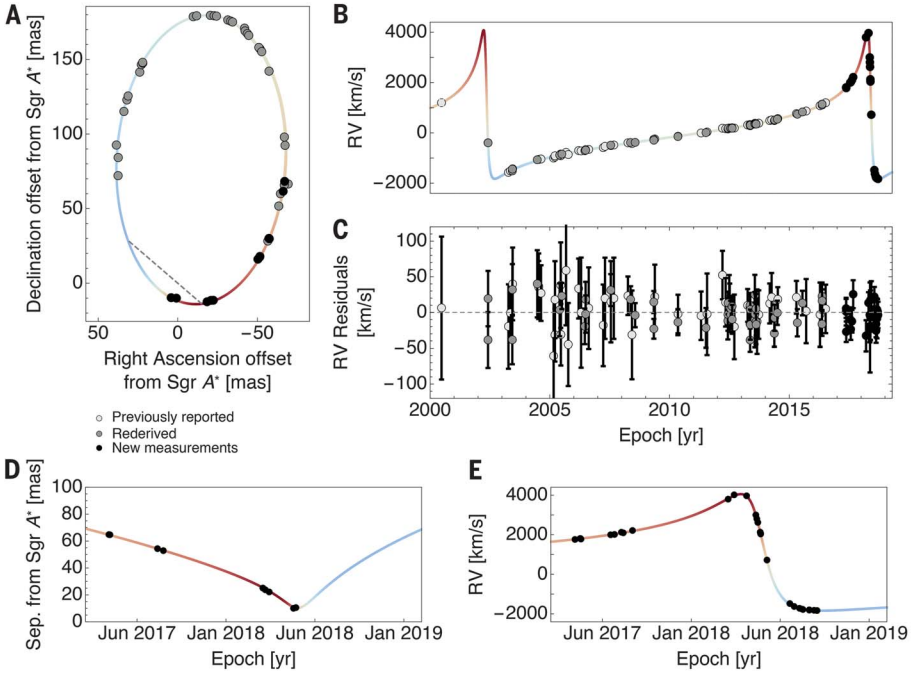

Fig. 2. GR orbit modeling of S0-2. (**A**) Astrometric measurements of the short-period star S0-2 in orbit around the SMBH Sgr A*, overlaid with our best-fitting projected orbit in the plane of the sky. The origin of the coordinate system coincides with the fitted SMBH center of mass (*13*). The *x* and *y* axes correspond to offsets in right ascension and declination, respectively, from the SMBH. We used 45 astrometric measurements from 1995–2018, of which 11 are new observations (black circles) and 34 are rederived measurements (dark gray circles). The best-fitting SMBH linear drift has been removed from the measurements. The line of nodes (dashed line) shows the intersection of the orbital plane with the plane of the sky (this line also passes through the position of the black hole). S0-2 moves clockwise in this projection; the star is behind the black hole below the line of nodes and in front of the black hole above the line of nodes. The color and intensity used in the best-fitting orbital plot represent the direction and magnitude of the line-of-sight velocity, with colors corresponding to those in (B). (**B**) RV measurements and the best-fitting RV model (colored line) using 115 RV measurements from 2000–2018. Forty-two measurements were previously reported (light gray circles), 45 were rederived for this work with improved methodology (dark gray circles), and 28 are new observations (black circles). The color of the best-fitting orbit represents the value and sign of the line-of-sight velocity. (**C**) Residuals from the best-fitting RV model. Error bars indicate 1σ uncertainties. (**D** and **E**) Observations around the three turning points, one at the closest approach to Sgr A* in the plane of the sky (D) and two RV turning points (maximum and minimum RV) (E), provide the greatest sensitivity to the relativistic redshift.

found to be 20 km s^{-1} for the Keck and Gemini observations.

The astrometric positions of S0-2 with respect to Sgr A* were placed in a common absolute astrometric reference frame by using a multistep cross-matching and transformation process. We adopted an improved methodology for obtaining precise astrometry and a more accurate absolute reference frame compared with that of previous work (*7*). This resulted in an average astrometric uncertainty for S0-2 of 1.1 milli–arc seconds (mas) for speckle imaging and 0.26 mas for AO imaging.

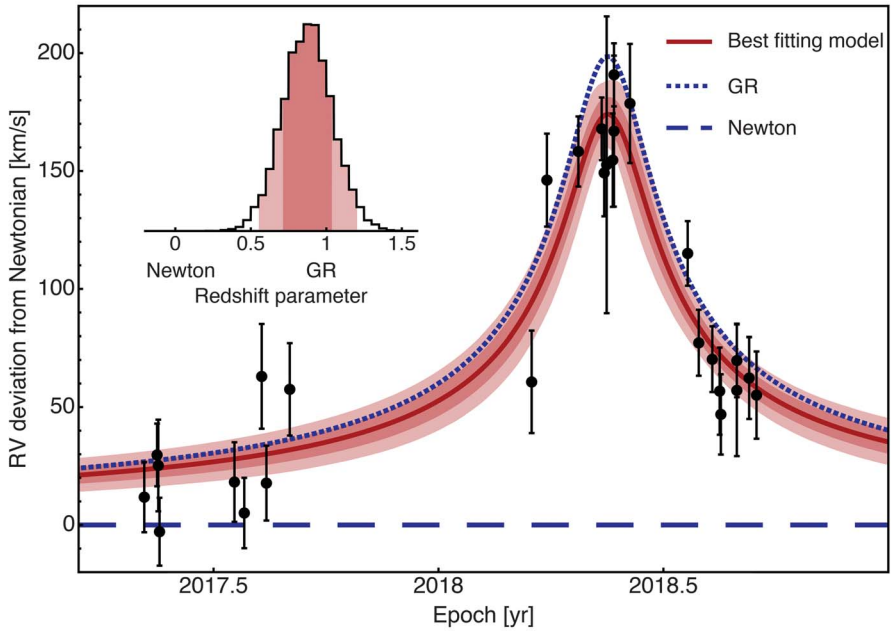

Fig. 3. Measured deviation from Newtonian predictions. The fitted deviation from Newtonian predictions, overlaid with the best-fitting orbit model (red line) corresponding to $\Upsilon = 0.88$. The inset shows the posterior probability distribution for Υ; 0.88 is the median value. The red shaded areas show the model 68 and 95% confidence intervals. The observed RVs are shown as black circles, after removing the Newtonian part of the model. Error bars indicate 1σ uncertainties. For comparison, we show the RV deviation expected for a purely relativistic signal ($\Upsilon = 1$, dotted blue line) and for a purely Newtonian model ($\Upsilon = 0$, dashed blue line) for an orbit with the same orbital parameters. Our measurement is consistent with the GR model at the 1σ confidence level, whereas the Newtonian model is excluded at >5σ confidence.

The astrometric and RV measurements are combined in a global orbital model fitting using a standard post-Newtonian approximation that includes the first-order GR corrections on the Newtonian equations of motion, the Römer time delay due to variations in the light propagation time between S0-2 and the observer, and the relativistic redshift. For the astrometric observables, we ignore the negligible effect of light deflection by the SMBH but include a two-dimensional (2D) linear drift of the gravitational center of mass. This drift accounts for systematic uncertainties in the construction of the astrometric reference frame. To our level of accuracy, the RV observable is (*13*)

$$RV = v_{z_0} + V_{Z,\mathrm{S0-2}} + \Upsilon\left[\frac{V^2_{\mathrm{S0-2}}}{2c} + \frac{GM}{cR_{\mathrm{S0-2}}}\right] \quad (1)$$

where c is the speed of light in a vacuum, v_{z_0} is a constant offset introduced to account for systematic uncertainties within our RV reduction, $V_{Z,\mathrm{S0-2}}$ is the Newtonian line-of-sight velocity of S0-2, $V^2_{\mathrm{S0-2}}/2c$ is the transverse Doppler shift predicted by special relativity depending on S0-2's velocity $\mathbf{V}_{\mathrm{S0-2}}$, and $GM/cR_{\mathrm{S0-2}}$ is the gravitational redshift predicted by GR incorporating the SMBH gravitational parameter GM (gravitational constant G and SMBH mass M) and the distance, $R_{\mathrm{S0-2}}$, between S0-2 and the SMBH. Υ is a scale parameter introduced to characterize deviations from GR; its value is 0 in a purely Newtonian model and 1 in GR (*13*). The model has 14 parameters: 6 orbital parameters for S0-2, the gravitational parameter of the SMBH (GM), the distance to the GC R_0, a 2D linear drift of the SMBH parametrized by the 2D position (x_0, y_0) and velocity (v_{x_0}, v_{y_0}) of the black hole from the

Table 1. Estimation of the model parameters. Column four (Estimation) indicates the median of the marginalized 1D posterior. Column five (Statistical uncertainty) indicates the half width of the 68% confidence interval centered on the median. Values for λ denote the +1σ and −1σ uncertainties. Column six (Systematic σ from jackknife) indicates the 1σ systematic uncertainty from the reference frame estimated from the jackknife analysis (*13*). $M_\odot$, solar mass.

Parameter	Description	Maximum likelihood	Estimation	Statistical uncertainty	Systematic σ from jackknife
$M_{\mathrm{BH}}(10^6 M_\odot)$	Black hole mass	3.984	3.975	0.058	0.026
R_0 (kpc)	Distance to GC	7.971	7.959	0.059	0.032
Υ	Redshift parameter	0.80	0.88	0.16	0.047
x_0 (mas)	x dynamical center	0.99	1.22	0.32	0.51
y_0 (mas)	y dynamical center	−0.85	−0.88	0.34	1.16
v_{x_0} (mas/year)	x velocity	−0.060	−0.077	0.018	0.14
v_{y_0} (mas/year)	y velocity	0.221	0.226	0.019	0.066
v_{z_0} (km/s)	z velocity	−3.6	−6.2	3.7	0.79
P (years)	Period	16.041	16.042	0.0016	7.8×10^{-5}
T_0 (years)	Closest approach	2018.3765	2018.3763	0.0004	1.9×10^{-5}
e	Eccentricity	0.886	0.8858	0.0004	2.8×10^{-5}
i (degrees)	Inclination	133.88	133.82	0.18	0.13
ω (degrees)	Argument of periapsis	66.03	66.11	0.24	0.077
Ω (degrees)	Angle to the ascending node	227.40	227.49	0.29	0.11
NIRC2 offset (km/s)	RV offset	80	81	19	0.8
Λ (mas)	Astrometric correlation length	21	28	$^{24.6}_{-13.6}$	11.8
p	Astrometric mixing coefficient	0.47	0.55	0.13	0.11

center of the reference frame, an offset for the RV v_{z_0}, and the redshift parameter Υ.

Several statistical tests were performed to assess systematic effects, using two different information criteria estimators— the Bayesian evidence and the expected logarithm predicted density—to compare models (*13*). We examined several sources of systematic uncertainties in the orbital fit: (i) potential offsets in RVs and astrometric positions from different instruments and (ii) potentially correlated uncertainties in astrometric measurements. On the basis of Bayesian model selection, we find that one spectrograph requires an RV offset with respect to other instruments (likely due to optical fringing) (*13*). No other instruments require an RV or astrometric positional offset. We include a parameter for the spectrograph RV offset in the model so it is fitted simultaneously. On the basis of the model selection criteria, we also find spatial correlation in the astrometric uncertainties. The correlated uncertainties are modeled with a multivariate likelihood characterized by a covariance matrix. The correlation matrix introduces a characteristic correlation length scale Λ and a mixing parameter p, both of which are simultaneously fitted with the model parameters (*13*). We validated this approach via Monte Carlo analysis, by randomly choosing one astrometric measurement per length scale to empirically estimate the effect of correlation scales. Although the inclusion of these systematic effects does not significantly affect the best-fitting Υ value, it increases the uncertainties, influencing the precision of the results.

We developed an orbit modeling software package to model the orbits. The software employs Bayesian inference for model fitting, using nested sampling to estimate the posterior probability distribution via the multinest package (*16*, *17*). We also performed Monte Carlo simulations to evaluate our fitting methodology and show that the statistical uncertainties are robust (*13*).

We initially compared a purely Newtonian model with a purely relativistic (Υ fixed to 1) model. We used the Bayes factor model selection criterion to show that the relativistic model is preferred by the data, with high confidence. The difference of the logarithm of the Bayesian evidence between these two models is 10.68. Expressed as an odds ratio, the GR model is 43,000 times more likely than the Newtonian model in explaining the observations.

We then fitted the more general model that includes the Υ redshift parameter as a free parameter. The estimated values for the 17 fitted parameters are in Table 1 (the posterior distributions are shown in figs. S10 to S13). The estimation $\Upsilon = 0.88 \pm 0.16$ and its marginal posterior is shown in Fig. 3C. We estimated the systematic uncertainties due to the astrometric reference frame construction by performing a jackknife analysis on stars used to construct the reference frame. This adds a systematic uncertainty on the redshift parameter of ~0.047, which, when added in quadrature with the statistical uncertainties, results in a total uncertainty $\sigma_\Upsilon = 0.17$. The measured redshift parameter is therefore 0.88 ± 0.17, consistent with GR at the 1σ level, whereas the Newtonian value $\Upsilon = 0$ is excluded by >5σ. Our estimation also agrees at the 1σ level with the measurement by the GRAVITY collaboration (*9*). Our experiment is independent from theirs, using a different set of measurements that includes the third turning point. We examined additional sources of systematic error that were previously not considered. The best-fitting model to the RV and the fit residuals is presented in Fig. 2. A fit using a parameter encoding deviations from GR only at the level of the gravitational redshift gives $\alpha = -0.24 \pm 0.32$, where $\alpha = 2(\Upsilon - 1)$ is the standard gravitational redshift parameter (*1*, *13*).

Our observations also constrain two other parameters: the mass of the black hole ($M_{\rm BH}$) and the distance to the GC (R_0). From our model with Υ as free parameter, the 68% marginalized confidence interval for $M_{\rm BH} = (3.984 \pm 0.058 \pm 0.026) \times 10^6 M_\odot$ and $R_0 = 7971 \pm 59 \pm 32$ pc, where the first uncertainty is the statistical uncertainty and the second uncertainty is the systematic error σ from the jackknife analysis (Table 1). If we assume GR is true, then $M_{\rm BH} = (3.964 \pm 0.047 \pm 0.026) \times 10^6 M_\odot$ and $R_0 = 7946 \pm 50 \pm 32$ pc (see supplementary text for discussion). The nested sampling chains are provided in data S3.

The gravitational redshift is a direct consequence of the universality of free fall and of special relativity (*18*), and hence of the Einstein equivalence principle, a fundamental principle of GR that provides a geometric interpretation for gravitational interactions. Violations of the equivalence principle are predicted by some theories of modified gravity motivated by the development of a quantum theory of gravitation, unification theories, and some models of dark energy (*19*). Although the gravitational redshift has been measured with higher precision within the Solar System (*20*, *21*), our results and those of the GRAVITY collaboration (*9*) extend the measurements to higher gravitational redshift and around a massive compact object, a SMBH. Sgr A* has a mass ~4×10^6 times that of the Sun. This constrains modified theories of gravitation that exhibit large nonperturbative effects around black holes but not around noncompact objects such as those in the Solar System [see (*22*–*24*) and supplementary text]. This redshift test is also performed in an environment that differs from the Solar System, where some theories predict modifications of GR to be screened or hidden (*25*).

REFERENCES AND NOTES

1. C. M. Will, *Living Rev. Relativ.* **17**, 4 (2014).
2. M. Kramer, *Int. J. Mod. Phys. D* **25**, 1630029 (2016).
3. B. P. Abbott *et al.*; LIGO Scientific and Virgo Collaborations, *Phys. Rev. Lett.* **116**, 221101 (2016).
4. B. P. Abbott *et al.*, *Astrophys. J.* **848**, L13 (2017).
5. R. Genzel, N. Thatte, A. Krabbe, H. Kroker, L. E. Tacconi-Garman, *Astrophys. J.* **472**, 153–172 (1996).
6. A. M. Ghez, B. L. Klein, M. Morris, E. E. Becklin, *Astrophys. J.* **509**, 678–686 (1998).
7. A. Boehle *et al.*, *Astrophys. J.* **830**, 17 (2016).
8. S. Gillessen *et al.*, *Astrophys. J.* **837**, 30 (2017).
9. R. Abuter *et al.*, *Astron. Astrophys.* **615**, L15 (2018).
10. D. Psaltis, in *X-Ray Timing 2003: Rossi and Beyond*, P. Kaaret, F. K. Lamb, J. H. Swank, Eds. [vol. 714 of American Institute of Physics (AIP) Conference Series, AIP, 2004], pp. 29–35.
11. T. Baker, D. Psaltis, C. Skordis, *Astrophys. J.* **802**, 63 (2015).
12. P. L. Wizinowich *et al.*, *Publ. Astron. Soc. Pac.* **118**, 297–309 (2006).
13. Materials and methods are available as supplementary materials.
14. A. M. Ghez *et al.*, *Astrophys. J.* **689**, 1044–1062 (2008).
15. D. S. Chu *et al.*, *Astrophys. J.* **854**, 12 (2018).
16. F. Feroz, M. P. Hobson, *Mon. Not. R. Astron. Soc.* **384**, 449–463 (2008).
17. F. Feroz, M. P. Hobson, M. Bridges, *Mon. Not. R. Astron. Soc.* **398**, 1601–1614 (2009).
18. L. I. Schiff, *Am. J. Phys.* **28**, 340–343 (1960).
19. T. Damour, A. M. Polyakov, *Gen. Relativ. Gravit.* **26**, 1171–1176 (1994).
20. S. Herrmann *et al.*, *Phys. Rev. Lett.* **121**, 231102 (2018).
21. P. Delva *et al.*, *Phys. Rev. Lett.* **121**, 231101 (2018).
22. G. Antoniou, A. Bakopoulos, P. Kanti, *Phys. Rev. Lett.* **120**, 131102 (2018).
23. H. O. Silva, J. Sakstein, L. Gualtieri, T. P. Sotiriou, E. Berti, *Phys. Rev. Lett.* **120**, 131104 (2018).
24. D. D. Doneva, S. S. Yazadjiev, *Phys. Rev. Lett.* **120**, 131103 (2018).
25. J. Khoury, A. Weltman, *Phys. Rev. Lett.* **93**, 171104 (2004).
26. Galactic Center Group, Orbit fitting and Scheduling Optimization Tool, Version 1.0, Zenodo (2019); 10.5281/zenodo.3305315.

ACKNOWLEDGMENTS

We thank the staff and astronomers at the W. M. Keck Observatory and the Gemini Observatory, especially G. Puniwai, J. McIlroy, S. Yeh, J. Pelletier, J. Hicock, G. Doppmann, J. Renaud-Kim, T. Ridenour, A. Hatakeyama, J. Walawender, C. Jordan, C. Wilburn, T. Stickel, H. Hershey, J. Macilroy, J. Pelletierm, J. Renauld-Kim, A. Rettura, L. Rizzi, C. Alvarez, M. Lemoine-Busserolle, M. Taylor, T. Dupuy, and M. Schwamb, for their help in obtaining the new data. The W. M. Keck Observatory is operated as a scientific partnership among the California Institute of Technology, the University of California, and the National Aeronautics and Space Administration. We wish to recognize that the summit of Maunakea has always held a very important cultural role for the Indigenous Hawaiian community. We are most fortunate to have the opportunity to observe from this mountain. We thank the Subaru Telescope staff, especially Y. Minowa, T.-S. Pyo, J.-H. Kim, and E. Mieda, for their support for the Subaru observations. The Subaru Telescope is operated by the National Astronomical Observatory of Japan. **Funding:** Support for this work was provided by NSF AAG grant AST-1412615, the W. M. Keck Foundation, the Heising-Simons Foundation, the Gordon and Betty Moore Foundation, the Levine-Leichtman Family Foundation, the Preston Family Graduate Fellowship (held by A.G.), and the UCLA Galactic Center Star Society. S.J. and J.R.L. acknowledge support from NSF AAG (AST-1518273). The W. M. Keck Observatory was made possible by the generous financial support of the W. M. Keck Foundation. S.N. acknowledges financial support by JSPS KAKENHI, grants JP25707012, JP15K13463, JP18K18760, and JP19H00695. H.S. was supported by JSPS KAKENHI grants JP26610050 and JP19H01900. Y.T. was supported by JSPS KAKENHI grant JP26800150. M.T. was supported by JSPS KAKENHI grant JP17K05439 and the Daiko Foundation. W.E.K. was supported by an ESO Fellowship and the Excellence Cluster Universe, Technische Universitat München. R.S. and E.G.-C. have received funding from the European Research Council under the European Union's Seventh Framework Programme (FP7/2007-2013)/ERC grant agreement 614922. R.S. acknowledges financial support from the State Agency for Research of the Spanish MCIU through the "Center of Excellence Severo Ochoa" award for the Instituto de Astrofísica de Andalucía (SEV-2017-0709). **Author contributions:** A.M.G., T.D., J.R.L, M.R.M., E.E.B., K.M., and A.H. contributed to conceptualization and design of the experiment. A.M.G., T.D., J.R.L., M.R.M., E.E.B., K.M., D.C., S.J., S.S., A.K.G., K.K.O., S.N., H.S., M.T., Y.T., R.C., Z.C., A.C., J.E.L., G.W., and S.C. made observations. T.D., D.C., S.N., S.C., and A.C., participated in reducing spectroscopic data and making RV measurements. J.R.L., S.J., S.S., A.K.G., Z.C., G.W., R.S., and E.G.-C. reduced imaging data and made astrometric measurements. A.M.G., T.D., A.H., G.D.M., J.R.L., D.C., S.J., R.S., E.G.-C., S.S., A.K.G., W.E.K., G.W., and A.Z. participated in methodology development for improving astrometric and RV

measurements. G.D.M., A.H., and T.D. participated in statistical modeling and model comparisons. K.M., R.C., P.W., and J.E.L. participated in building and improving instrumentation. All authors participated in writing and discussions of the paper. **Competing interests:** The authors declare no competing interests. **Data and materials availability:** Raw observational data are archived at the Keck Observatory Archive (https://www2.keck.hawaii.edu/koa/public/koa.php), the Gemini Observatory Archive (https://archive.gemini.edu/searchform), and the Subaru Mitaka Okayama Kiso Archive (https://smoka.nao.ac.jp/) under the dates and instruments listed in tables S1 and S4. Our reduced astrometric and RV measurements are provided in data S1 and S2. The nested sampling chains are provided in data S3. Software for the orbit modeling and scheduling tool is available at Zenodo (*26*).

SUPPLEMENTARY MATERIALS

science.sciencemag.org/content/365/6454/664/suppl/DC1
Materials and Methods
Supplementary Text
Figs. S1 to S18
Tables S1 to S13
References (*27*–*93*)
Data S1 to S4

26 October 2018; accepted 11 July 2019
Published online 25 July 2019
10.1126/science.aav8137

ROBOTICS

Reducing the metabolic rate of walking and running with a versatile, portable exosuit

Jinsoo Kim[1]*, Giuk Lee[2]*, Roman Heimgartner[1]†, Dheepak Arumukhom Revi[1]†, Nikos Karavas[1], Danielle Nathanson[1], Ignacio Galiana[1], Asa Eckert-Erdheim[1], Patrick Murphy[1], David Perry[1], Nicolas Menard[1], Dabin Kim Choe[1], Philippe Malcolm[3]‡, Conor J. Walsh[1]‡

Walking and running have fundamentally different biomechanics, which makes developing devices that assist both gaits challenging. We show that a portable exosuit that assists hip extension can reduce the metabolic rate of treadmill walking at 1.5 meters per second by 9.3% and that of running at 2.5 meters per second by 4.0% compared with locomotion without the exosuit. These reduction magnitudes are comparable to the effects of taking off 7.4 and 5.7 kilograms during walking and running, respectively, and are in a range that has shown meaningful athletic performance changes. The exosuit automatically switches between actuation profiles for both gaits, on the basis of estimated potential energy fluctuations of the wearer's center of mass. Single-participant experiments show that it is possible to reduce metabolic rates of different running speeds and uphill walking, further demonstrating the exosuit's versatility.

Humans can walk and run to attain a wider speed range. At low speeds, the metabolic rate of walking is lower than that of running, but this tendency is reversed at higher speeds, such that at high speeds the metabolic rate of running is lower than that of walking. The ability to switch between walking and running allows humans to adopt the gait with the lowest metabolic rate at each speed (fig. S1A) (*1*, *2*). Development of robotic assistive devices that can provide benefits for both walking and running is challenging because of the fundamentally different biomechanics of these gaits (*3*). In walking, the legs function like inverted pendulums to move the center of mass (CoM), and the gravitational potential energy and kinetic energy fluctuate out of phase (*4*). Running, meanwhile, can be modeled as a spring–mass system (*5*–*7*) with in-phase gravitational potential and kinetic energy fluctuations (*4*). In walking, the greatest internal joint moments occur at the ankle, and the hip and ankle perform approximately the same amount of positive work. In running, the greatest internal joint moments occur at the knee and ankle, and the ankle performs the largest amount of positive work, followed by the hip (*8*, *9*).

Because of these differences, most research laboratories have developed separate assistive devices for walking (*10*–*12*) and running (*3*, *13*–*15*). Robotic assistive devices have been shown to reduce the metabolic rate of walking below normal biological levels by 7 to 21% by assisting the ankle joint and/or the hip joint (*11*, *12*, *16*, *17*). Early efforts at reducing the metabolic rate of running have shown increases of 27 to 58% compared with running without an exoskeleton (*13*, *14*). These increases occur in part because the metabolic cost of carrying mass (e.g., a robotic assistive device) during running (*18*) is greater than that during walking (*19*, *20*), and the penalty for carrying mass on the limbs is further amplified due to increased limb acceleration (*21*, *22*). Nasiri *et al*. developed an unpowered exoskeleton that reduced the metabolic rate of running by 8% by applying an elastic torque at the hip as a function of interthigh angle (*23*). However, those authors noted that this design may not be effective during walking because it could disrupt the swing phase.

We hypothesize that assisting walking and running requires customized actuation profiles via an interface with low distal mass and minimal restriction of motion during the unassisted portions of the gait cycle. To achieve these design criteria, we use functional apparel to attach the device to the wearer, with cables that generate moments in concert with the combined moment that results from different biological muscles. We previously developed such an exosuit that reduces the metabolic rate of walking by 14.9% by assisting the ankle and hip (*16*). In the current study, we aimed to develop and test a lightweight, portable exosuit that assists with hip extension and can switch automatically between actuation profiles for walking and running. We chose to assist hip extension because it is important for both gaits (*8*, *9*, *24*) and does not require added mass to distal leg segments.

The textile components of the device consist of a waist belt and two thigh wraps (Fig. 1A, fig. S2, and data S1). Subjective testing of the maximum range of motion shows that the exosuit does not restrict the movements required for walking and running (Fig. 1B). Two electrical motors connected to cables via pulleys apply a tensile force between the waist belt and the thigh wraps to generate an external extension moment around the hip joint (movie S1 and data S2) (*3*). The entire exosuit weighs 5.0 kg, with 91% of the total system mass carried at the waist (table S1). This design approach minimizes the additional metabolic rate penalty when mass is added distally during walking (*25*) and running (*22*) (Fig. 1C). We programmed two separate actuation force profiles for walking and running. The timings of the walking profile and the running profile were selected on the basis of the profiles with the highest reduction in metabolic rate for walking (*26*) and running (*27*) in prior studies that used nonportable, tethered hip exosuits. The profile from the walking study was originally designed to approximate the biological hip extension moment, whereas the profile from the running study was designed to approximate the optimal profile from a muscle-driven simulation (*24*). Using these profiles as starting points, they were then slightly tailored to improve controller robustness and comfort through pilot tests. To allow the wearer to switch seamlessly between walking and running, we used an online classification algorithm that functions on the basis of potential energy fluctuations measured by inertial measurement units (IMUs) (Fig. 2, movie S1, and data S3) (*3*, *28*).

We conducted treadmill experiments at walking and running speeds ranging from 0.5 to 4.0 m s^{-1} and at gradients ranging from −10% to +20% with six male participants of similar age and build to assess the gait classification accuracy (*3*). The algorithm was 100% accurate at distinguishing between walking and running under all speed and incline conditions (data S4). Although the algorithm is based on vertical CoM acceleration at maximum hip extension, which is affected by slope, it worked accurately for steep inclines and declines.

We also conducted overground experiments on a paved outdoor course with gradual changes in speed and gait with eight male participants (fig. S3 and movie S2) (*3*). We found that the algorithm was 99.98% accurate in this protocol. Only two steps out of all trials were classified incorrectly, possibly due to altered CoM energy fluctuations in the first steps after a gait transition (Fig. 2B and fig. S4). A terrain that is more uneven than the paved outdoor course could alter the gait pattern (*29*, *30*) and affect the algorithm accuracy. However, an additional single-participant experiment on an outdoor course consisting of sloped terrain and different unpaved surfaces (mud, snow) showed 100% accuracy under such conditions (fig. S5) (*3*). Other gait classification algorithms have been developed

[1]John A. Paulson School of Engineering and Applied Sciences and Wyss Institute for Biologically Inspired Engineering, Harvard University, Cambridge, MA 02138, USA. [2]Mechanical Engineering Department, Chung-Ang University, Seoul 06974, Republic of Korea. [3]Department of Biomechanics and Center for Research in Human Movement Variability, University of Nebraska Omaha, Omaha, NE 68182, USA. *These authors contributed equally to this work. †These authors contributed equally to this work.
‡Corresponding author. Email: pmalcolm@unomaha.edu (P.M.); walsh@seas.harvard.edu (C.J.W.)

for activity logging (*31*) and controlling robotic leg prostheses (*32*), but similar accuracy has not yet been demonstrated in an exoskeleton or exosuit. Gait classification in exoskeletons or exosuits involves certain challenges, because the actuation can affect the gait pattern, which in turn can affect gait classification accuracy. To highlight the importance of accurate gait classification and gait-specific assistance, we conducted another single-participant experiment during which we applied the walking actuation profile during running and vice versa. We found that applying the opposite actuation profile deteriorated controller performance and increased metabolic rate by 33.9% (Fig. 3C) when tested during a combined walking and running condition (*3*).

The effects of the exosuit on metabolic rate during treadmill walking at 1.5 m s^{-1} and running at 2.5 m s^{-1} were evaluated on nine participants who had prior experience wearing the exosuit, as prior studies with other robotic assistive devices highlighted the importance of experience for participants to maximize the benefit they achieved from robotic assistive devices (*10*, *33*, *34*). Participants walked and ran while wearing the exosuit with assistance turned on (assist on), with assistance turned off (assist off), and without wearing the exosuit (no exo). The metabolic rate with exosuit assistance was reduced by 9.3 ± 2.2% (SEM; $P = 0.005$) for walking and by 4.0 ± 1.3% (SEM; $P = 0.017$) for running compared with that in locomotion without the exosuit ($n = 9$ participants, two-sided paired t tests with Holm-Šidák correction) (Fig. 3, A and B, and table S2) (*3*). In a previous overground experiment, we also found a reduction of 3.9 ± 1.0% (SEM; $P = 0.015$) in metabolic rate during running but no reduction ($P = 0.536$) during walking, possibly due to less strictly controlled experimental conditions ($n = 8$, two-sided paired t tests with Holm-Šidák correction) (table S3) (*3*). Additional single-participant treadmill experiments showed that it is possible to reduce the metabolic rate during higher-intensity locomotion conditions, such as walking at 1.5 m s^{-1} up a 10% slope or level running at different speeds up to 3 m s^{-1} (Fig. 3, D and E).

The mean reduction in metabolic rate of 9.3% during level treadmill walking is lower than best-in-class reductions for tethered devices [17.4% (*35*)] and powered portable devices [21.1% (*17*)] during walking and is similar to the reduction obtained with unpowered portable devices during walking [7.2% (*12*)]. The mean reduction of 4.0% in treadmill running at 2.5 m s^{-1} is of a similar magnitude as the previous best-in-class reduction obtained with a similar tethered hip exosuit [5.0% (*27*)] but about half as much as the reduction obtained with an unpowered portable hip exoskeleton [8.0% (*23*)]. The interparticipant

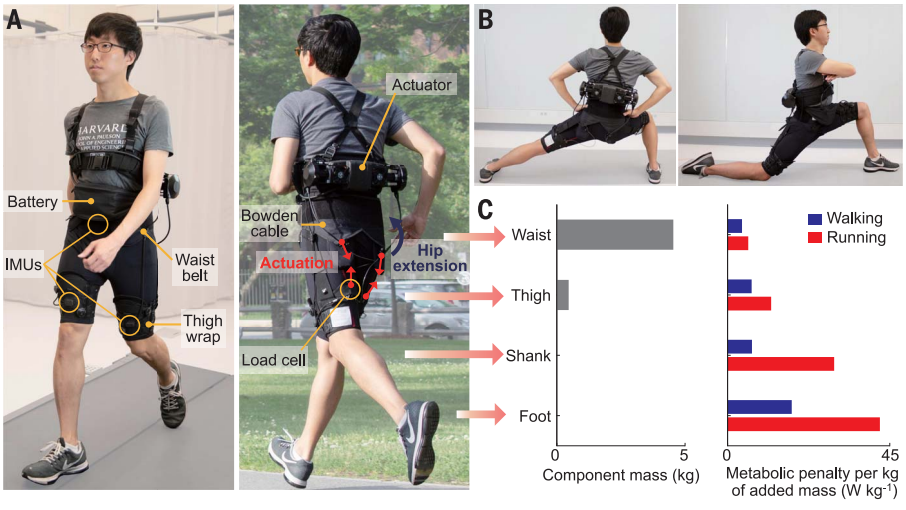

Fig. 1. Exosuit. (**A**) Components of the exosuit shown during treadmill walking and overground running. (**B**) Demonstration of the range of motion allowed by the exosuit. (**C**) Component mass and estimated penalty per kilogram of added mass for each segment, based on coefficients from the literature (table S1). The exosuit mass is concentrated around the waist, where the metabolic penalty per kilogram of added mass is the lowest. Components and mass distribution data are shown in table S1 and fig. S2. The operation of the exosuit is shown in movie S1.

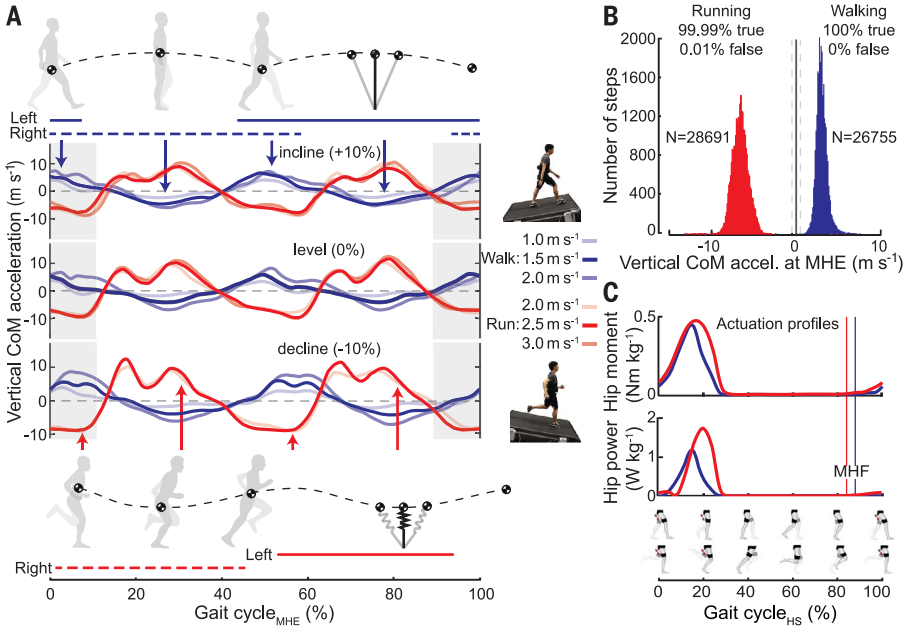

Fig. 2. Biologically inspired gait classification algorithm and actuation. (**A**) Vertical CoM acceleration during walking and running on a treadmill at different slopes and speeds ($n = 1$). Acceleration is measured by an abdomen IMU and segmented into strides on the basis of detection of maximum hip extension (MHE) via thigh IMUs. Horizontal lines represent the stance phases. The gray shaded area indicates the region used for classification. (**B**) Histogram of vertical CoM acceleration at maximum hip extension for all treadmill and overground protocols ($n = 23$). The vertical lines indicate thresholds used for classification. (**C**) Actuation profiles for walking (blue) and running (red) that were applied during the physiological and biomechanical testing on a treadmill ($n = 7$). The vertical line indicates the detection of maximum hip flexion (MHF) via thigh IMUs. Actuation profiles are segmented into strides on the basis of heel strikes (HS). Algorithm pseudocode and data of the gait classification experiments are provided in data S3 and S4.

variability of the reduction in metabolic rate during treadmill running was sizable but within the range of variabilities found in similar studies (*23*, *27*).

Humans may adapt to assistance at the hip joint by changing their coordination. To understand the effects of the actuation profiles that underlie the metabolic rate reductions, we compared differences between assist-on and assist-off conditions. We calculated the biological component of the hip moment by subtracting the moment of the exosuit from the total joint moment computed using inverse dynamics analysis of motion capture measurements in seven of the nine participants. As expected, during walking, the assist-on condition reduced the peak biological hip extension moment compared with the assist-off condition. The reduction was 14% [−0.128 ± 0.020 N·m kg^{-1} (SEM); n = 7, two-sided paired t test, P < 0.001] (Fig. 4A, table S4, and data S5). During running, there was a trend toward a reduction in peak biological hip extension moment in the assist-on compared with the assist-off condition by 12% [−0.168 ± 0.072 N·m kg^{-1} (SEM); n = 7, two-sided paired t tests, P = 0.059] (table S5). The assist-on condition reduced the peak hip extensor (gluteus maximus) activation during walking compared with the assist-off condition (−14%; n = 7, two-sided paired t tests, P = 0.043).

Even though the exosuit applied hip extension moments, it is possible that a portion of the reduction in metabolic rate comes from joints other than the hip. Muscle-driven simulations from another research laboratory predicted that robotic assistive devices can reduce activity in muscles that do not cross the assisted joints (*24*). Additionally, prior experimental work has shown that ankle exoskeletons can have effects on joints other than the ankle (*36*). In our experiment, the assist-on condition reduced the peak internal knee extension moment compared with the assist-off condition during walking and running (−12 and −3%; n = 7, two-sided paired t tests, P = 0.038 and 0.046) (Fig. 4B) and caused a trend toward reduced peak knee extensor (vastus lateralis) activation compared with that for the assist-off condition during running (−6%; n = 7, two-sided paired t test, P = 0.082). For walking, this phenomenon could be related to a reduction in knee flexion angle compared with that for the assist-off condition (n = 7, two-sided paired t test, P = 0.041), resulting in a reduction of the product of the ground reaction force and its moment arm with respect to the knee (n = 7, two-sided Wilcoxon signed rank test, P = 0.031) (Fig. 4C). This product is related to terms that add up to the total knee moment. Such an indirect strategy of assisting the knee via the hip could have applications in populations in which assisting the knee directly is challenging, such as above-the-knee amputees who rely on hip extension to compensate for the lack of knee function (*37*).

During walking, the assist-on condition also led to reductions in peak plantar flexor muscle activations (−4.5% for gastrocnemius medialis, −7.6% for soleus; n = 7, two-sided paired t test, P = 0.038 and 0.081, respectively) and an increase in stride frequency compared with the assist-off condition (+3.1%; n = 7, two-sided paired t test, P = 0.007) (table S4). This greater stride frequency may result from the exosuit actuation decelerating the swing leg before heel strike, and it may be related to the observed changes in joint moments and muscle activations during stance (*38*, *39*).

To evaluate if wearing the passive structure of the exosuit affected gait, we compared the range of motion and the effects of added mass between the assist-off and no-exo conditions. We found reductions of 2° ± 1° (SEM) in the hip range of motion for the assist-off compared with the no-exo condition in the sagittal plane during walking and in the coronal plane during running (n = 7, two-sided paired t tests, P = 0.020 and 0.010) (Fig. 4D). We found no significant differences in any other planes during walking and running (n = 7, two-sided paired t tests, P > 0.111 for all other comparisons). These differences also may have been a result of marker repositioning errors between the assist-off and no-exo conditions, but overall they highlight the minimally restrictive nature of the exosuit. The assist-off condition increased the metabolic rate by 7.0 and 3.3% [22 ± 7 and 28 ± 3 W (SEM)] above that for the no-exo condition during walking and running, respectively (n = 9, two-sided paired t tests with Holm-Šidák correction, P = 0.002 and <0.001). These increases are not significantly different from the weight penalty estimated from literature prediction formulas (n = 9, two-sided paired t tests, P = 0.972 and 0.260) (tables S1 and S6).

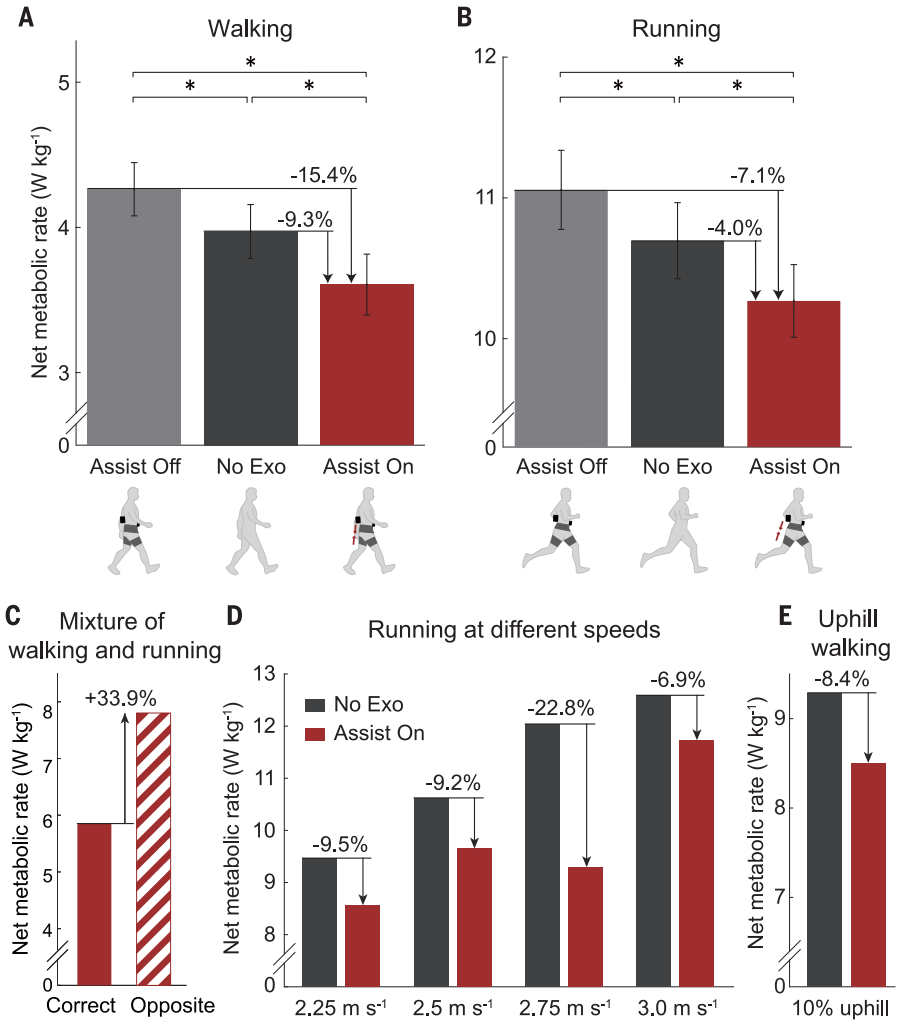

Fig. 3. Metabolic rate. (**A** and **B**) Metabolic rate for level walking at 1.5 m s^{-1} (A) and level running at 2.5 m s^{-1} (B) during the treadmill physiological and biomechanical testing protocol. Bars represent walking and running with the assistance turned off (assist off), without wearing the exosuit (no exo), and while wearing the exosuit with assistance turned on (assist on). Error bars indicate SEM. Asterisks indicate statistically significant differences (n = 9, two-sided paired t tests with Holm-Šidák correction, P < 0.05). (**C** to **E**) Metabolic rates from single-participant experiments for combined level walking and running bouts with correct or opposite actuation profiles for each gait (C), level running at different speeds (D), and 10% uphill walking at 1.5 m s^{-1} (E) (n = 1). Individual metabolic data are available in table S2.

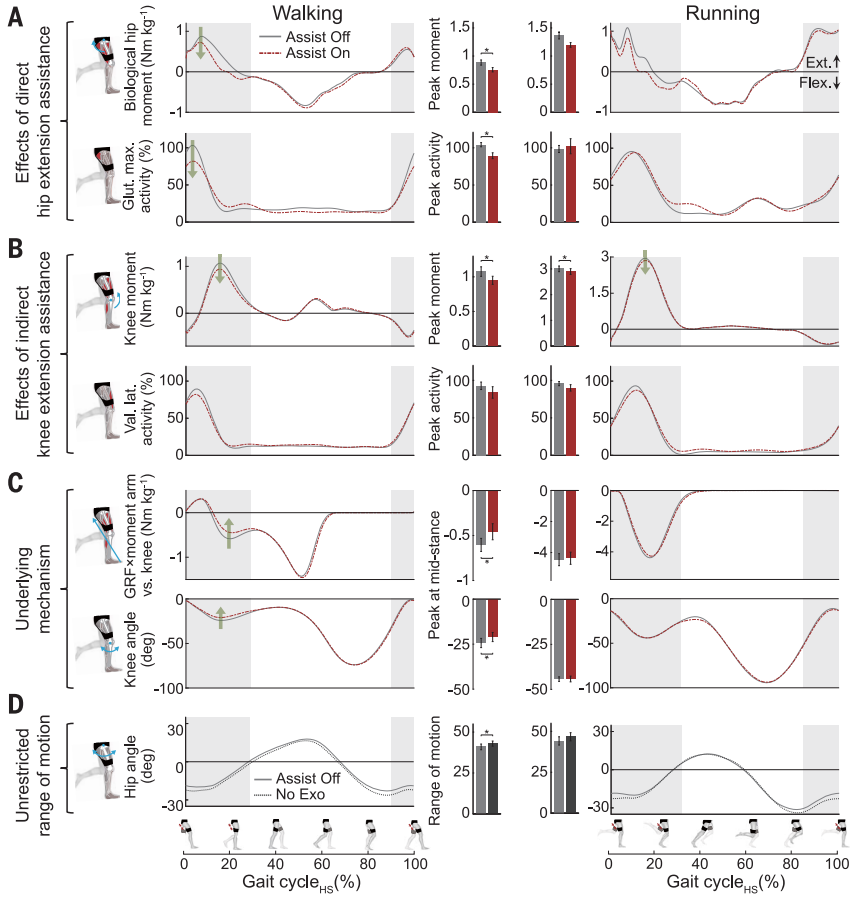

Fig. 4. Biomechanical analyses during treadmill protocol. (**A**) Effects of direct hip extension assistance on biological hip moment and gluteus maximus activation. (**B**) Effects of indirect knee extension assistance on internal knee moment and vastus lateralis activation. (**C**) Underlying mechanism. Reduction in internal knee moment could be related to decreased knee flexion, which causes a reduction of the product of the ground reaction force (GRF) and the moment arm from the knee. (**D**) Hip range of motion. All time series plots show population averages as a function of gait cycle. All extension angles and moments are positive. Green arrows indicate peak values that are analyzed in bar plots. Error bars indicate SEM. Gray shaded regions indicate the actuation period of the exosuit. Asterisks indicate statistically significant differences (n = 7, two-sided paired t tests, $P < 0.05$). Other joint- and muscle-level biomechanical summary metrics are shown in tables S4 and S5. Individual source data are available in data S5.

This work demonstrates a lightweight and minimally restrictive robotic assistive device that can reduce the metabolic rate of both walking and running. By automatically adapting assistance to the activity, the system allows the wearer to use their preferred gait for each speed. Thus, the exosuit leverages the biological versatility of human locomotion, thereby providing advantages of a wider speed range at a lower metabolic cost of transport than devices that only assist a single gait (fig. S1). To put the results in perspective, the metabolic rate reductions during walking can be compared to the effect of taking off 7.4 kg at the waist (*25*) or to reductions in metabolic rate from restorative surgery in children with cerebral palsy (*40*). The metabolic rate reductions during running can be compared to the effect of taking off 5.7 kg at the waist (*41*) or the effects of a recently designed running shoe with improved energy return (*42*). Although the changes in metabolic rate are relatively modest, they are of similar magnitude to those that have proven to be sufficient to produce changes in maximum walking and running performance. One study by Galle *et al.* (*43*) showed that an exoskeleton that reduces the metabolic rate of submaximal uphill walking by 8% significantly increases maximum performance in an incremental load test by an equal amount. Another study by Hoogkamer *et al.* (*44*) showed that increases in shoe mass that increase metabolic rate by 3.5% lead to a significant deterioration in time trial performance. Therefore, we hypothesize that our 9.3 and 4.0% reductions in the metabolic rates of walking and running, respectively, could result in proportional increases in maximal performance, for example, over a cross-country course. Moreover, additional single-participant experiments show that the exosuit is capable of providing assistance during more challenging locomotion conditions (e.g., on uphill slopes or unpaved terrain), further highlighting the versatility of the system.

REFERENCES AND NOTES

1. R. Margaria, P. Cerretelli, P. Aghemo, G. Sassi, *J. Appl. Physiol.* **18**, 367–370 (1963).
2. D. R. Carrier *et al.*, *Curr. Anthropol.* **25**, 483–495 (1984).
3. Materials and methods, supplementary text, figures, tables, movies, and datasets are available as supplementary materials.
4. G. A. Cavagna, M. Kaneko, *J. Physiol.* **268**, 467–481 (1977).
5. T. A. McMahon, G. Valiant, E. C. Frederick, *J. Appl. Physiol.* **62**, 2326–2337 (1987).
6. T. A. McMahon, G. C. Cheng, *J. Biomech.* **23** (suppl. 1), 65–78 (1990).
7. R. M. Alexander, *The Spring in Your Step: The Role of Elastic Mechanisms in Human Running*, vol. XI-A (Free University Press, 1988).
8. A. G. Schache *et al.*, *Med. Sci. Sports Exerc.* **43**, 1260–1271 (2011).
9. D. J. Farris, G. S. Sawicki, *J. R. Soc. Interface* **9**, 110–118 (2011).
10. G. S. Sawicki, D. P. Ferris, *J. Exp. Biol.* **211**, 1402–1413 (2008).
11. L. M. Mooney, E. J. Rouse, H. M. Herr, *J. Neuroeng. Rehabil.* **11**, 80 (2014).
12. S. H. Collins, M. B. Wiggin, G. S. Sawicki, *Nature* **522**, 212–215 (2015).
13. M. S. Cherry, S. Kota, A. Young, D. P. Ferris, *J. Appl. Biomech.* **32**, 269–277 (2016).
14. G. Elliott, G. S. Sawicki, A. Marecki, H. Herr, in *2013 IEEE 13th International Conference on Rehabilitation Robotics* (IEEE, 2013), document 6650418.
15. C. S. Simpson, C. G. Welker, S. D. Uhlrich, S. M. Sketch, R. W. Jackson, S. L. Delp, S. H. Collins, J. C. Selinger, E. W. Hawkes, bioRxiv 474650 [Preprint]. 30 November 2018.
16. S. Lee *et al.*, *J. Neuroeng. Rehabil.* **15**, 66 (2018).
17. J. Lee *et al.*, *IEEE Int. Conf. Rehabil. Robot.* **2017**, 498–504 (2017).
18. C. R. Taylor, N. C. Heglund, T. A. McMahon, T. R. Looney, *J. Exp. Biol.* **86**, 9–18 (1980).
19. G. M. O. Maloiy, N. C. Heglund, L. M. Prager, G. A. Cavagna, C. R. Taylor, *Nature* **319**, 668–669 (1986).
20. T. M. Griffin, T. J. Roberts, R. Kram, *J. Appl. Physiol.* **95**, 172–183 (2003).
21. E. C. Frederick, *Appl. Ergon.* **15**, 281–287 (1984).
22. M. J. Myers, K. Steudel, *J. Exp. Biol.* **116**, 363–373 (1985).
23. R. Nasiri, A. Ahmadi, M. N. Ahmadabadi, *IEEE Trans. Neural Syst. Rehabil. Eng.* **26**, 2026–2032 (2018).
24. T. K. Uchida *et al.*, *PLOS ONE* **11**, e0163417 (2016).
25. R. C. Browning, J. R. Modica, R. Kram, A. Goswami, *Med. Sci. Sports Exerc.* **39**, 515–525 (2007).
26. Y. Ding *et al.*, *J. Neuroeng. Rehabil.* **13**, 87 (2016).
27. G. Lee *et al.*, *Sci. Robot.* **2**, eaan6708 (2017).
28. J. Kim *et al.*, Autonomous and portable soft exosuit for hip extension assistance with online walking and running detection algorithm. *ICRA*, 5473–5480 (2018).
29. A. S. Voloshina, D. P. Ferris, *J. Exp. Biol.* **218**, 711–719 (2015).
30. A. S. Voloshina, A. D. Kuo, M. A. Daley, D. P. Ferris, *J. Exp. Biol.* **216**, 3963–3970 (2013).
31. S. J. Preece *et al.*, *Physiol. Meas.* **30**, R1–R33 (2009).
32. A. H. Shultz, B. E. Lawson, M. Goldfarb, *IEEE Trans. Neural Syst. Rehabil. Eng.* **23**, 403–412 (2015).
33. J. R. Koller, D. A. Jacobs, D. P. Ferris, C. D. Remy, *J. Neuroeng. Rehabil.* **12**, 97 (2015).
34. B. Wiggin, thesis, North Carolina State University (2014).
35. Y. Ding, M. Kim, S. Kuindersma, C. J. Walsh, *Sci. Robot.* **3**, eaar5438 (2018).
36. L. M. Mooney, H. M. Herr, *J. Neuroeng. Rehabil.* **13**, 4 (2016).
37. T. S. Bae, K. Choi, D. Hong, M. Mun, *Clin. Biomech.* **22**, 557–566 (2007).
38. B. R. Umberger, P. E. Martin, *J. Exp. Biol.* **210**, 3255–3265 (2007).
39. J. Doke, J. M. Donelan, A. D. Kuo, *J. Exp. Biol.* **208**, 439–445 (2005).
40. G. O. Dahlbäck, R. Norlin, *Eur. J. Appl. Physiol. Occup. Physiol.* **54**, 67–70 (1985).
41. K. J. Cureton *et al.*, *Med. Sci. Sports* **10**, 194–199 (1978).
42. W. Hoogkamer *et al.*, *Sports Med.* **48**, 1009–1019 (2017).

43. S. Galle, P. Malcolm, W. Derave, D. De Clercq, *Eur. J. Appl. Physiol.* **114**, 2341–2351 (2014).
44. W. Hoogkamer, S. Kipp, B. A. Spiering, R. Kram, *Med. Sci. Sports Exerc.* **48**, 2175–2180 (2016).

ACKNOWLEDGMENTS

The authors thank M. Athanassiu, B. M. Iwangou, D. Orzel, T. G. Goldy, L. Baker, Y. Ding, F. Panizzolo, A. Couture, Y. M. Zhou, R. Nuckols, S. Lee, J. Foster, and S. Sullivan for their contributions to this work. We thank A. A. Biewener, D. E. Lieberman, and the anonymous reviewers for their helpful suggestions for improving the manuscript. **Funding:** This material is based on work supported by the Defense Advanced Research Projects Agency (DARPA) Warrior Web program (contract no. W911NF-14-C-0051) and the National Science Foundation (award CNS-1446464). This work is also partially funded by the Wyss Institute for Biologically Inspired Engineering and the John A. Paulson School of Engineering and Applied Sciences at Harvard University. J.K. also appreciates financial support from the Samsung Scholarship. Ph.M. was supported by the Center for Research in Human Movement Variability of the University of Nebraska Omaha and the NIH (P20GM109090). C.J.W. appreciates the support of the Rolex Award for Enterprise. **Author contributions:** J.K., G.L., N.K., D.N., I.G., D.P., Ph.M., and C.J.W. conceived of the study concept and experimental methods. J.K., G.L., R.H., N.K., D.N., I.G., A.E.-E., Pa.M., D.P., N.M., and C.J.W. conceived of and implemented the hardware and control. J.K., G.L., R.H., and D.A.R. conducted the main experiments. J.K., G.L., D.A.R., A.E.-E., and D.K.C. conducted the single-participant experiments. J.K., G.L., R.H., D.A.R., and Ph.M. analyzed the system and biomechanics data. J.K., G.L., R.H., D.A.R., Ph.M., and C.J.W. prepared the manuscript. All authors revised and approved the final manuscript. **Competing interests:** Patents describing the exosuit components documented in this article have been filed with the U.S. Patent Office. J.K., D.N., I.G., and C.J.W. are inventors of at least one of the following patents and patent applications: U.S. 9,351,900, U.S. 10,278,883, U.S. 14/660,704, U.S. 15/097,744, U.S. 14/893,934, PCT/US2014/068462, PCT/US2015/051107, and PCT/US2017/042286, filed by Harvard University. Harvard University has entered into a licensing and collaboration agreement with ReWalk Robotics. C.J.W. is a paid consultant for ReWalk Robotics. The other authors declare that they have no competing interests. **Data and materials availability:** The data supporting the main conclusions of the manuscript are included in the manuscript and supplementary materials.

SUPPLEMENTARY MATERIALS

science.sciencemag.org/content/365/6454/668/suppl/DC1
Materials and Methods
Supplementary Text
Figs. S1 to S5
Tables S1 to S7
References (*45–88*)
Movies S1 to S3
Data S1 to S6

1 November 2018; accepted 17 June 2019
10.1126/science.aav7536

OPTICS

Sub–single-exciton lasing using charged quantum dots coupled to a distributed feedback cavity

Oleg V. Kozlov[1], Young-Shin Park[1,2], Jeongkyun Roh[1], Igor Fedin[1], Tom Nakotte[1,3], Victor I. Klimov[1]*

Colloidal semiconductor quantum dots (QDs) are attractive materials for realizing highly flexible, solution-processable optical gain media, but they are difficult to use in lasing because of complications associated with extremely short optical-gain lifetimes limited by nonradiative Auger recombination. By combining compositional grading of the QD's interior for hindering Auger decay with postsynthetic charging for suppressing parasitic ground-state absorption, we can reduce the lasing threshold to values below the single-exciton-per-dot limit. As a favorable departure from traditional multi-exciton–based lasing schemes, our approach should facilitate the development of solution-processable lasing devices and thereby help to extend the reach of lasing technologies into areas not accessible with traditional, epitaxially grown semiconductor materials.

Solution-processable lasers have been the subject of vigorous research, with the primary focus being on organic semiconductors (*1*) and, more recently, hybrid organic-inorganic and all-inorganic perovskites (*2*). Colloidal quantum dots (QDs) have also shown considerable promise as solution-processable lasing media with size-controlled emission wavelengths (*3*, *4*). One challenge in advancing these laboratory-based demonstrations to technologically viable devices is the multiexcitonic nature of optical gain, which leads to high lasing thresholds (*5*, *6*). The onset of optical gain corresponds to the situation of band-edge transparency, when the emitting transition is completely bleached by carriers introduced into an active medium by a pump source. In QDs, this corresponds to the regime when an average per-dot excitonic occupancy $\langle N \rangle$ is at least one (*3*). Consequently, lasing becomes possible only when a fraction of the QDs in the sample contains biexcitons and other multiexcitonic species. This leads to a major complication due to fast, nonradiative multicarrier Auger decay, wherein an electron–hole recombination energy is transferred to a third carrier residing in the same dot (*7*). This process limits optical-gain lifetimes to tens of picoseconds, which greatly complicates realization of lasing, especially in the case of continuous-wave optical and direct-current electric pumping (*5*, *6*, *8*).

Recent experiments have demonstrated that charging QDs with extra electrons can bleach the ground-state absorption and thereby reduce the optical gain threshold (*9*). This approach also extends optical-gain lifetimes, as Auger decay of a single exciton charged with one or even two additional electrons is longer than that of biexcitons (*9*), which represent the dominant optical-gain species in traditional lasing schemes. Previously, the beneficial effects of extra electrons on amplified spontaneous emission (ASE) and gain thresholds were observed by means of electrochemically charged QD samples (*10*) and, more recently, photochemically reduced QDs (*9*).

Here, we demonstrate single-mode lasing with low thresholds using a charged-QD approach. We use thick-shell, multilayered QDs with strongly suppressed Auger recombination combined with optimized second-order distributed feedback (DFB) resonators. By charging the sample with about three extra electrons per dot on average, we achieve an extremely low, sub–single-exciton lasing threshold $\langle N_{las} \rangle \approx 0.3$, which is a more than fourfold reduction compared with the neutral QDs. Further, we demonstrate a reversible tuning of the lasing threshold by controlling the degree of QD charging.

The multiexcitonic nature of optical gain in QDs is a consequence of a multifold degeneracy of band-edge electron and hole levels (*3*). In the model of twofold degenerate states, optical gain (G) is linked to the difference in the probability of a QD to contain a biexciton (P_{XX}) and that to remain in the ground state (P_0): $G \propto (P_{XX} - P_0)$ (Fig. 1A, left) (*6*). In the case where QD excitonic occupancy (N) can only be 0 (unoccupied dot, $|0\rangle$), 1 (single-exciton state, $|X\rangle$), or 2 (biexciton state, $|XX\rangle$), an optical-gain threshold ($G = 0$), or "optical transparency," is realized when every dot in the sample contains a single exciton, i.e., $\langle N_g \rangle = 1$ (Fig. 1B, left) (*6*).

By charging (doping) a QD with extra electrons, partial or even complete bleaching of the band-edge absorption can be achieved, which would reduce the optical-gain threshold (*9*). In particular, when the QD ensemble is uniformly charged with n_e electrons per dot, $\langle N_g \rangle$ decreases to 0.5 for $n_e = 1$ and to 0 for $n_e = 2$ (Fig. 1, A and B; middle and right panels, respectively). If we consider a situation of nonuniform charging and further assume Poisson statistics for both N and n_e, then the gain threshold will change to $\langle N_g \rangle = 1.15$, 0.81, and 0.46 for $\langle n_e \rangle = 0$, 1, and 2, respectively (Fig. 1C).

Suppression of Auger recombination for charged excitonic species is key to successful

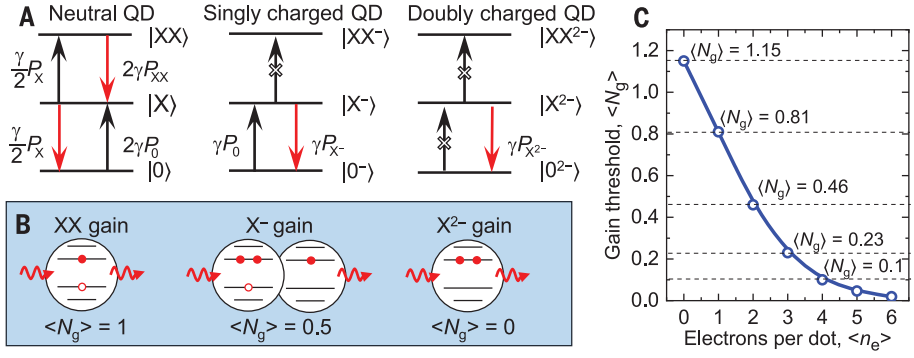

Fig. 1. Optical gain model for neutral and charged QDs. (**A**) Electronic states and optical transitions between the ground $|0\rangle$, single-exciton $|X\rangle$, and biexciton $|XX\rangle$ states for neutral (left), singly charged (middle), and doubly charged (right) QDs. Optical transitions leading to absorption and stimulated emission are shown with black and red arrows, respectively. The transition rates are indicated next to the respective transitions; γ is the probability per single spin-allowed transition (*6*). P_0, P_X, and P_{XX} denote the probabilities of the QD to be in the ground, single-exciton, or biexciton state, respectively. Singly charged and doubly charged states are denoted by superscripts "−" and "2−", respectively. P_{X^-} and $P_{X^{2-}}$ are the probabilities of the QD to be in the singly or doubly charged exciton state, respectively. (**B**) The condition of optical gain threshold ($G = 0$) for neutral (left), singly charged (middle), and doubly charged (right) QDs is met when the average per-dot number of excitons ($\langle N_g \rangle$) introduced by a pump source is, respectively, 1, 0.5, and 0. (**C**) Dependence of $\langle N_g \rangle$ on the average per-dot number of permanent electrons $\langle n_e \rangle$ for the case when both N and n_e are distributed according to Poisson statistics (*9*).

[1]Chemistry Division, C-PCS, Los Alamos National Laboratory, Los Alamos, NM 87545, USA. [2]Center for High Technology Materials, University of New Mexico, Albuquerque, NM 87131, USA. [3]Department of Chemical and Materials Engineering, New Mexico State University, Las Cruces, NM 88003, USA.
***Corresponding author. Email: klimov@lanl.gov**

realization of the charged-QD lasing scheme. An effective approach for reducing Auger decay rates is through smoothing the QD confinement potential, which leads to suppression of the intraband transition involved in the dissipation of the electron–hole recombination energy (*11*). To realize this effect practically, we enclose a small emitting CdSe core within a thick $Cd_xZn_{1-x}Se$ shell wherein x progressively decreases in the radial direction from 1 to 0 (*8*, *9*) [fig. S1 and materials and methods (*12*)]. These continuously graded QDs (cg-QDs) are completed with a final protective $ZnSe_{0.5}S_{0.5}$/ZnS layer for enhancing dot stability, improving surface passivation, and impeding defect-mediated QD discharging (*13*). The photoluminescence (PL) wavelength of the studied samples is 620 nm (inset of Fig. 2A) and the PL quantum yield (QY) is ~55% in the solution form. The single-exciton lifetime (τ_X) is ~15 ns, as inferred from PL dynamics measured using weak excitation ($<N> << 1$) (fig. S2A and supplementary text S2). The biexciton lifetime (τ_{XX}) obtained from the fast PL component emerging at high excitation powers is 1.5 ns (fig. S2, A and B). The PL measurements of photochemically doped samples (see below) indicate that the lifetime of an exciton with one extra electron (negative trion) is 4.5 ns (fig. S2A). On the basis of this value and the $n_e(n_e + 1)$ scaling of Auger time constants (*14*), the lifetime of a doubly negatively charged exciton is 2.5 ns. The PL QYs of biexcitons and charged excitons with n_e = 1 and 2 are 40, 60, and 33%, respectively (supplementary text S3). These values are considerably higher than the corresponding QYs (2.5, 10, and 3.5%, respectively) of standard CdSe QDs with a similar band gap (supplementary text S3), indicating strong suppression of Auger recombination in the cg-QD samples. The suppressed Auger decay also leads to extended optical-gain lifetimes (fig. S3 and supplementary text S4). Although this extension is observed for both neutral and charged cg-QDs, the gain dynamics in these two cases are qualitatively different. In particular, in the case of charged dots, optical gain persists in the long-time limit ($\Delta t \rightarrow \infty$), whereas in neutral dots, it exists only during a finite time window (Δt < 1.2 ns). This is an important advantage of the charged-QD gain approach, which can, in principle, simplify realization of continuous-wave lasing.

To inject a controlled number of electrons into cg-QDs, we use a modified version of a photodoping method with lithium triethylborohydride ($LiEt_3BH$) as a reducing agent (*9*, *14*, *15*) (Fig. 2B). We apply this procedure to films of cg-QDs cross-linked with bifunctional 1,8-diaminooctane molecules for improving sample stability (fig. S4 and materials and methods S1). The PL QY of film samples is 15 to 20%. It is lower than that of the QD solution because of distortion of the original surface passivation and dot-to-dot energy transfer, which results in resampling defect sites at each transfer step. In photodoping experiments, a cross-linked cg-QD sample is immersed into a solution of $LiEt_3BH$ in tetrahydrofuran (THF). QD charging is initiated by

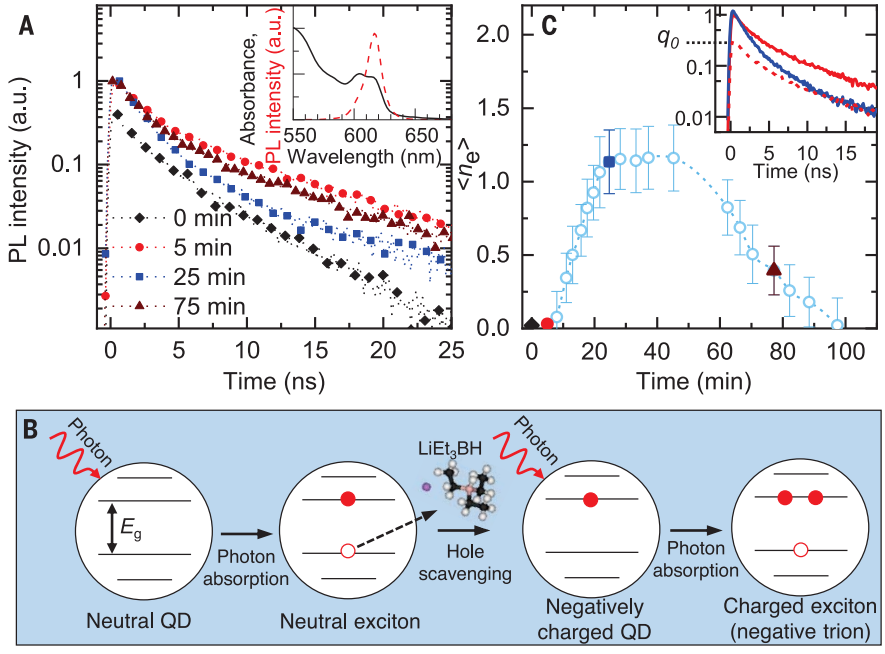

Fig. 2. Photochemical doping of QDs. (**A**) PL dynamics of a cross-linked film of cg-QDs immersed into a 0.2 M $LiEt_3BH$/THF solution as a function of time of exposure to 400-nm light of a 100-kHz laser with a per-pulse fluence (j_p) of 0.3 μJ cm^{-2} (the measurement time per trace is 30 s). Inset: the cg-QD absorption (black) and PL (red) spectra. (**B**) QD charging with an extra electron occurs by scavenging a hole from a photoexcited dot by $LiEt_3BH$ acting as a sacrificial hole acceptor. Subsequent photoexcitation of a charged dot leads to formation of a negative trion. (**C**) Average number of extra electrons per QD ($<n_e>$) as a function of photoexposure time [same conditions as in (A)]. Solid symbols correspond to the traces shown in (A) using the same symbol styles. Inset: Normalization procedure used to determine $<n_e>$. The red and blue solid traces are "raw" PL dynamics for neutral and charged QDs, respectively [same as color-matched traces in (A)]. The red dashed trace shows the dynamics of neutral dots normalized to match the long-time tail of PL from the charged dots. The normalization factor q_0 yields a relative fraction of neutral dots in the charged sample.

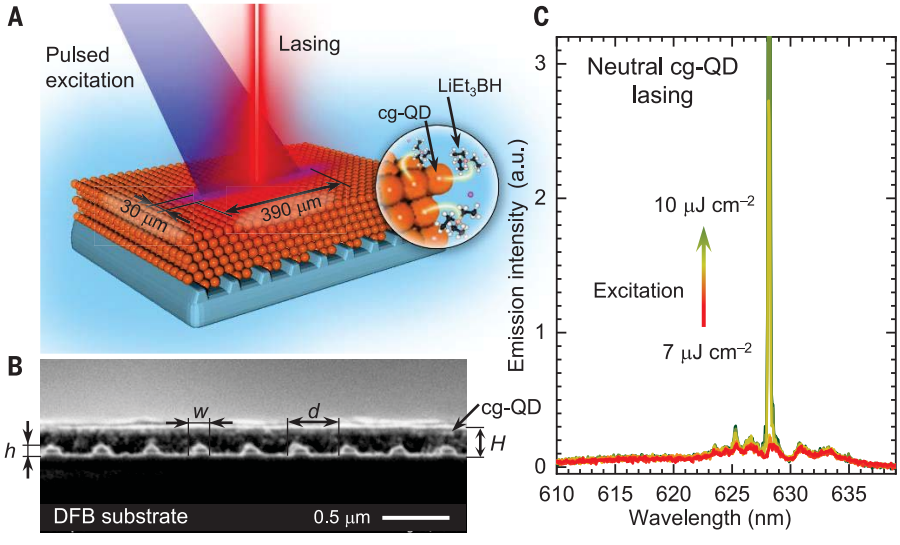

Fig. 3. Lasing studies of a device made of cg-QDs coupled to a second-order DFB grating. (**A**) Schematics of a cg-QD DFB laser. This device is immersed into a $LiEt_3BH$ solution in THF, which leads to in situ QD photodoping (inset) induced by pump pulses used to excite lasing. (**B**) Scanning electron microscopy image of a cg-QD layer (thickness H) on top of a DFB grating (period d, grove height h, and grove width w). (**C**) Example of neutral-QD lasing using a cg-QD/DFB device immersed into neat THF without the reducing agent (400-nm excitation with a femtosecond 1-kHz laser). The spectra of device surface emission for progressively increasing excitation fluences indicate a sharp transition to single-mode lasing at j_p of ~9 μJ cm^{-2}.

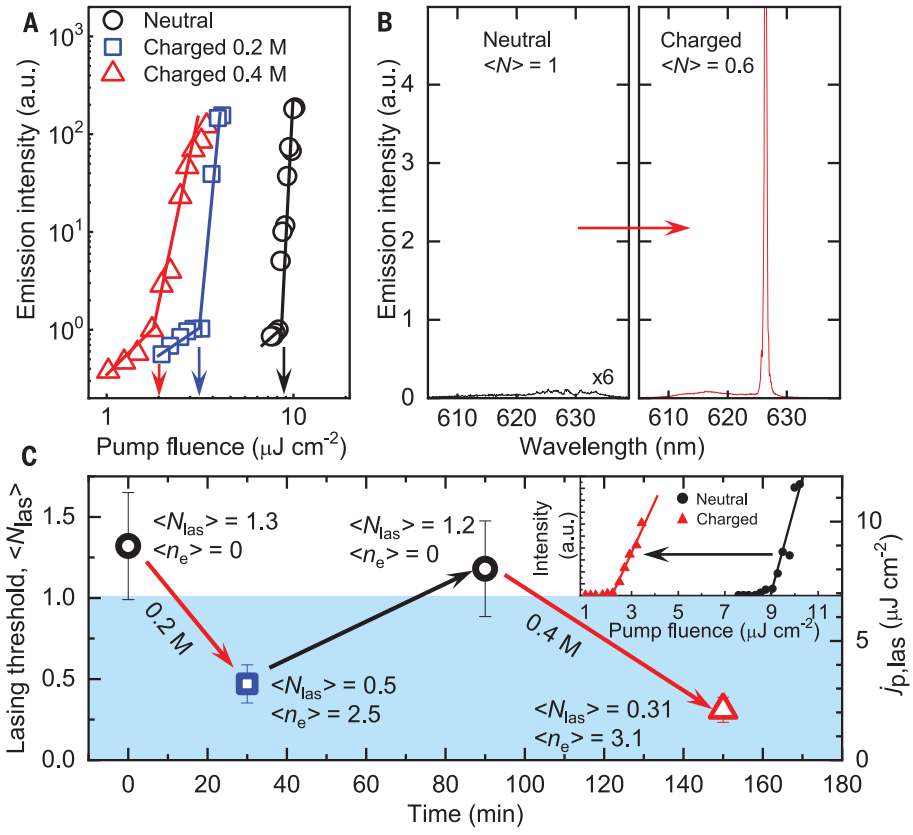

Fig. 4. Sub–single-exciton lasing realized with charged cg-QDs. (**A**) Intensity of surface emission of a cg-QD/DFB device (spectrally integrated signal around the lasing wavelength) as a function of pump fluence. Black circles are for neutral dots and blue squares and red triangles are for dots charged using 0.2 and 0.4 M $LiEt_3BH$/THF, respectively (corresponding $\langle n_e \rangle$ values are 2.5 and 3.1). As $\langle n_e \rangle$ changes from 0 to 3.1, the lasing threshold (vertical arrows) decreases from 9 to 2.1 μJ cm^{-2}; the latter corresponds to $\langle N_{las} \rangle$ = 0.31. (**B**) Before charging, the excitation level $\langle N \rangle$ = 1 does not lead to lasing (left panel). However, upon charging with $\langle n_e \rangle$ = 3.1, the same sample lases even at a lower pump level $\langle N \rangle$ = 0.6 (right panel). (**C**) Reversibility of the effect of charging on the lasing threshold. The lasing threshold decreases from $\langle N_{las} \rangle$ = 1.3 in neutral dots to 0.5 upon 30 min of exposure to 0.2 M $LiEt_3BH$ ($\langle n_e \rangle$ = 2.5). After the cg-QD sample is discharged by keeping it in the dark in neat THF for 60 min, $\langle N_{las} \rangle$ returns to its near original value of 1.2. A subsequent charging using a greater amount of $LiEt_3BH$ (0.4 M) leads to even stronger reduction of the lasing threshold to $\langle N_{las} \rangle$ = 0.31. The symbol styles are matched to the corresponding data in (A). The blue shading corresponds to sub–single-exciton lasing thresholds. The sharp, more than fourfold reduction of the lasing threshold upon charging is apparent from the inset, which shows a linear–linear plot of the surface emission intensity versus j_p for neutral (black) and charged (red, $\langle n_e \rangle$ = 3.1) cg-QDs.

exposing the QD film to pulsed 400-nm excitation (supplementary text S5). To quantify the level of charging, we monitor the PL dynamics (Fig. 2A) and determine an average per-dot number of photoinjected electrons ($\langle n_e \rangle$) from the amplitude of the slow neutral-exciton–related component (*9*) (inset of Fig. 2C). In the lasing experiments, photodoping occurs in situ because of the cg-QD film exposure to pump pulses used to excite population inversion. All photodoping and lasing experiments are conducted in the presence of ambient oxygen.

In Fig. 2A, we show PL dynamics of the cg-QD film immersed into 0.2 M $LiEt_3BH$/THF recorded at different times (t) after the onset of photoreduction. During the first 5 min, the PL peak intensity increases and the PL lifetime becomes longer (Fig. 2A, red circles), which is accompanied by an increase of the PL QY from ~15 to ~60%. These changes can be attributed to saturation of intragap surface traps by injected electrons as observed in previous QD studies (*9*, *16*). At t > 5 min, PL decay accelerates suggesting that at this point, the intragap states are fully filled, and the injected electrons begin to accumulate in intrinsic quantized states, which activates nonradiative Auger recombination (Fig. 2A, blue squares). After a quick initial growth, $\langle n_e \rangle$ stabilizes at ~1.2 (Fig. 2C), which indicates establishment of equilibrium between charging and ambient-oxygen–induced discharging. The maximal charging level depends on multiple factors, including, in particular, the $LiEt_3BH$ concentration and the excitation power (figs. S5 to S7 and supplementary text S6). Because reductant is not replenished during the measurements, eventually it becomes depleted, at which point discharging starts to overwhelm charging, leading to slowing of the PL decay (Fig. 2A).

To investigate the effect of charging on lasing performance, we deposit cross-linked cg-QD films of ~200-nm thickness H on top of SiO_2 DFB resonators fabricated by laser interferometric lithography (Fig. 3A, fig. S8, and supplementary text S7). The DFB grating parameters (Fig. 3B) are selected to provide strong in-plane feedback via second-order diffraction; this simultaneously leads to surface emission in the near-normal direction due to first-order diffraction (Fig. 3A and fig. S9) (*17*). In our lasing experiments, cg-QD/DFB resonators are immersed into a cuvette with THF and excited at 400 nm by ~130-fs laser pulses (Fig. 3A and supplementary text S7). In the absence of the photoreductant, the lasing threshold ($j_{p,las}$) is ~9 μJ cm^{-2}, as indicated by the transition from a broad PL band modulated by cavity resonances to a single narrow feature with the resolution-limited linewidth of <0.2 nm (Fig. 3C). This is accompanied by a sharp growth in the emission intensity, which increases by two orders of magnitude as j_p changes by only 20% (Fig. 4A, black circles). To quantify lasing thresholds in terms of $\langle N \rangle$, we analyze the pump-intensity dependence of long-time ($\Delta t >> \tau_{XX}$) PL and transient absorption (TA) signals (fig. S10). On the basis of this analysis, $j_{p,las}$ of 9 μJ cm^{-2} corresponds to $\langle N_{las} \rangle$ of 1.3 ± 0.3. As expected, this is slightly above the neutral-exciton gain threshold of ~1.2 estimated for our cg-QD samples (supplementary text S8).

To initiate cg-QD charging, we add 0.2 M $LiEt_3BH$ to the cuvette with the cg-QD/DFB sample. Keeping the cg-QD layer under continuous illumination with 400-nm femtosecond pulses, we wait for ~30 min, at which point the lasing threshold stabilizes at a sub–single-exciton level of 0.5 ± 0.1 (Fig. 4A, blue squares). The effect of charging on the lasing threshold is illustrated in Fig. 4B. The neutral QD sample excited with $\langle N \rangle$ = 1 does not exhibit any signatures of lasing. However, after the sample is charged, a lower pump level of $\langle N \rangle$ = 0.6 leads to intense lasing at 626.5 nm.

To test the reversibility of the effects of photodoping, we initiate sample discharging by turning off the excitation and replacing the $LiEt_3BH$ solution with neat THF. After the sample is kept in dark for an hour, the lasing threshold returns to its near original value of 1.2 ± 0.3 ($j_{p,las}$ ~8 μJ cm^{-2}; Fig. 4C), suggesting that the cg-QDs recover their precharging properties. We then repeat the photodoping procedure using a greater amount of $LiEt_3BH$ (0.4 M). After a 60-min exposure to laser light, $\langle N_{las} \rangle$ decreases again to the sub–single-exciton value, which now reaches 0.31 ± 0.07 ($j_{p,las}$ = 2.1 μJ cm^{-2}; Fig. 4C, main panel and inset). This is less than a quarter of $\langle N_{las} \rangle$ for neutral cg-QDs and almost half the value for a smaller amount (0.2 M) of $LiEt_3BH$. This indicates a more complete bleaching of ground-state absorption due to the increased level of doping. However, a further increase in the amount of $LiEt_3BH$ does not lead to an additional reduction of the lasing threshold. Indeed, the use of 1 M

$LiEt_3BH$ increased $\langle N_{las} \rangle$ to 0.5 ± 0.1 (fig. S11), indicating that at this point the benefits due to enhanced band-edge bleaching become overwhelmed by detrimental acceleration of Auger decay. Injection of extra electrons into cg-QD also leads to a considerable reduction of the ASE threshold (fig. S12 and supplementary text S9), as was previously observed in (*9*).

To relate the observed lasing thresholds to QD charging levels, we conduct measurements of PL dynamics under the same conditions as those used in the lasing experiments (fig. S13). These measurements indicate that the use of 0.2 M $LiEt_3BH$ results in $\langle n_e \rangle$ ~2.5. When the amount of $LiEt_3BH$ is increased to 0.4 M, $\langle n_e \rangle$ becomes close to ~3.1. As this corresponds to the lowest lasing threshold, $\langle n_e \rangle$ of ~3 likely represents the optimal charging level for which the band-edge absorption is strongly bleached (by nearly 90%), whereas the fraction of heavily charged dots with fast Auger recombination is still relatively low. Numerical modeling of the lasing effect using the gain model of Fig. 1 supports the assessment that a dramatic reduction of the lasing threshold down to the sub–single-exciton level is a direct consequence of the change in the optical gain mechanism, i.e., a transition from the biexciton to the charged-exciton gain (fig. S14).

Our experiments show that by using a charged-exciton gain mechanism, it is possible to realize strong lasing performance with sub–single-exciton thresholds that compare favorably (in terms of both $j_{p,las}$ and $\langle N_{las} \rangle$) with the lowest lasing thresholds previously reported for colloidal-QD–based devices (table S1). The advantageous effect of charged-exciton gain is associated with both the reduction of the gain threshold and lengthening of the gain lifetime. The benefits of a charging approach can be realized with existing QDs and previously developed lasing schemes, which should facilitate its exploitation in future QD lasing studies as well as its practical implementation in real-life lasing devices.

REFERENCES AND NOTES

1. I. D. W. Samuel, G. A. Turnbull, *Chem. Rev.* **107**, 1272–1295 (2007).
2. S. Yakunin *et al.*, *Nat. Commun.* **6**, 8056 (2015).
3. V. I. Klimov *et al.*, *Science* **290**, 314–317 (2000).
4. C. Dang *et al.*, *Nat. Nanotechnol.* **7**, 335–339 (2012).
5. F. Fan *et al.*, *Nature* **544**, 75–79 (2017).
6. Y.-S. Park, W. K. Bae, T. Baker, J. Lim, V. I. Klimov, *Nano Lett.* **15**, 7319–7328 (2015).
7. V. I. Klimov, A. A. Mikhailovsky, D. W. McBranch, C. A. Leatherdale, M. G. Bawendi, *Science* **287**, 1011–1013 (2000).
8. J. Lim, Y.-S. Park, V. I. Klimov, *Nat. Mater.* **17**, 42–49 (2018).
9. K. Wu, Y.-S. Park, J. Lim, V. I. Klimov, *Nat. Nanotechnol.* **12**, 1140–1147 (2017).
10. C. Wang, B. L. Wehrenberg, C. Y. Woo, P. Guyot-Sionnest, *J. Phys. Chem. B* **108**, 9027–9031 (2004).
11. G. E. Cragg, A. L. Efros, *Nano Lett.* **10**, 313–317 (2010).
12. See the supplementary materials.
13. W. K. Koh *et al.*, *Sci. Rep.* **3**, 2004 (2013).
14. K. Wu, J. Lim, V. I. Klimov, *ACS Nano* **11**, 8437–8447 (2017).
15. J. D. Rinehart, A. M. Schimpf, A. L. Weaver, A. W. Cohn, D. R. Gamelin, *J. Am. Chem. Soc.* **135**, 18782–18785 (2013).
16. W. van der Stam *et al.*, *Chem. Mater.* **30**, 8052–8061 (2018).
17. G. Morthier, P. Vankwikelberge, *Handbook of Distributed Feedback Laser Diodes* (Artech House, ed. 2, 2013).

ACKNOWLEDGMENTS

We thank Z. Robinson for assistance with modeling of electronic wave functions. **Funding:** The studies of charged QD photophysical properties were supported by the Solar Photochemistry Program of the Chemical Sciences, Biosciences and Geosciences Division, Office of Basic Energy Sciences, Office of Science, U.S. Department of Energy. The lasing studies were supported by the LDRD program at Los Alamos National Laboratory. **Author contributions:** V.I.K. conceived the idea. I.F. synthesized the cg-QDs and performed TEM measurements. O.V.K. conducted photocharging experiments and optical gain measurements. T.N. performed TEM and AFM measurements. J.R. designed and fabricated DFB cavities. Y.-S.P. conducted lasing experiments. V.I.K and O.V.K. wrote the manuscript with input from the other authors. **Competing interests:** The authors declare no competing interests. **Data and materials availability:** All data are available in the main text or the supplementary materials.

SUPPLEMENTARY MATERIALS

science.sciencemag.org/content/365/6454/672/suppl/DC1
Materials and Methods
Supplementary Text
Figs. S1 to S14
Table S1
References (*18*–*20*)

15 March 2019; accepted 12 July 2019
10.1126/science.aax3489

ASTROCHEMISTRY

Quantum-state–selective electron recombination studies suggest enhanced abundance of primordial HeH^+

Oldřich Novotný[1]*, Patrick Wilhelm[1], Daniel Paul[1], Ábel Kálosi[1,2], Sunny Saurabh[1], Arno Becker[1], Klaus Blaum[1], Sebastian George[1,3], Jürgen Göck[1], Manfred Grieser[1], Florian Grussie[1], Robert von Hahn[1], Claude Krantz[1], Holger Kreckel[1], Christian Meyer[1], Preeti M. Mishra[1], Damian Muell[1], Felix Nuesslein[1], Dmitry A. Orlov[1], Marius Rimmler[1], Viviane C. Schmidt[1], Andrey Shornikov[1], Aleksandr S. Terekhov[4], Stephen Vogel[1], Daniel Zajfman[5], Andreas Wolf[1]

The epoch of first star formation in the early Universe was dominated by simple atomic and molecular species consisting mainly of two elements: hydrogen and helium. Gaining insight into this constitutive era requires a thorough understanding of molecular reactivity under primordial conditions. We used a cryogenic ion storage ring combined with a merged electron beam to measure state-specific rate coefficients of dissociative recombination, a process by which electrons destroy molecular ions. We found a pronounced decrease of the electron recombination rates for the lowest rotational states of the helium hydride ion (HeH^+), compared with previous measurements at room temperature. The reduced destruction of cold HeH^+ translates into an enhanced abundance of this primordial molecule at redshifts of first star and galaxy formation.

At the beginning of the Universe, only small nuclei—mainly hydrogen, deuterium, and helium—existed. When temperatures lowered to ~2500 K, their recombination with electrons led to neutral atoms. Later, primordial molecules—mainly H_2, HD, HeH^+, and LiH—formed by radiative association and charge-exchange reactions (*1*). These molecules are crucial for the formation of the first stars, because the collisional excitation of their rotational levels and subsequent radiative emission (*2*) can cool a gas cloud to the low temperatures required for gravitational collapse. Critical for this radiative cooling is the molecular dipole moment. The dipole moment vanishes for the most abundant molecule, H_2, and is only small (0.00083 D) for the isotopically asymmetric HD molecule. However, the dipole moments are large for HeH^+ (1.66 D; HeH is unstable), HD^+ (0.9 D), and LiH (5.98 D) (*1*, *3*). Because the relative D-to-He and Li-to-He elemental abundance ratios are ~10^{-4} and ~10^{-8}, respectively, HeH^+ moves into the focus. Although a number of astronomical searches for this elementary species have been unsuccessful (*4*, *5*), HeH^+ was very recently detected in a planetary nebula (*6*).

Given that the underlying cosmological parameters and the outcome of Big Bang nucleosynthesis are known with great precision, uncertainties of the reaction rate coefficients are now perceived (*1*) as the only limitation on our understanding of primordial gas evolution. The relevant temperatures range from ~2500 K (redshift z ~ 800) to ~20 K (z ~ 6) at the end of the cosmic reionization phase. Temperatures as low as a few kelvin also apply to astrochemistry in the interstellar medium of the contemporary Universe (*7*); hence, molecular ions are crucial drivers of low-temperature gas-phase astrochemistry in all eras. Their abundance is often limited by dissociative recombination (DR) with electrons (*8*).

In this process, the ion captures a free electron while its internal degrees of freedom undergo excitation. The resulting neutral, excited compound typically dissociates on a subpicosecond time scale. The cross section of the exothermic DR reaction is strongly system dependent, as possible excitation pathways—electronic, vibrational, or rotational—vary. Extended studies (*8*–*14*) were performed on cold-electron reactions with HeH^+. Ion storage rings with an internal, merged electron beam target were used (*10*–*12*) to measure DR of molecular ions at electron temperatures that reached below 20 K. These studies and related theoretical work (*13*–*15*) revealed the strong collision energy dependence of the cross section from predissociating molecular Rydberg states, formed when the colliding electron excites vibrations and rotations of the ion core. Despite the expected strong influence of rotational excitation, all measurements to date (*9*–*12*) were performed for HeH^+ in excited rotational levels: Through the molecular dipole moment, thermal equilibrium with the blackbody radiation in the beam enclosure led to a rotational temperature of ~300 K. The present experiment, using a cryogenic ion storage ring, can finally address this rotational dependence.

Our measurements were performed in the recently completed electrostatic cryogenic ion storage ring, CSR (*16*), at the Max Planck Institute for Nuclear Physics, Heidelberg, Germany. Its vacuum chamber walls and all beam-guiding electrodes were cooled to ~6 K. HeH^+ ions from a discharge ion source were accelerated to 250 keV and injected into the cryogenic ring with four bending corners and interjacent linear sections (Fig. 1). The ions, circulating collision-free for hundreds of seconds (*16*–*18*), are merged in one of the linear sections with a quasi-monoenergetic electron beam with the same or a slightly detuned velocity [electron energy $E_0 = 27.32 \pm 0.06$ eV (±SEM) at matched velocities]. DR in the ~1-m-long overlap region leads to neutral H and He atoms that separate from the electrostatically deflected ions and impinge on a position-sensitive, multihit counting detector (*19*). At the electron beam energy $E_e = E_0$, the HeH^+ ions collide with electrons of thermal energy spread (~2 meV). Choosing, however, $E_e > E_0$, the collision energy is detuned to $E_d = (E_e^{1/2} - E_0^{1/2})^2$ and easily variable. This yields (*19*) the energy-dependent DR rate coefficient $\alpha_{DR}(E_d)$.

As demonstrated recently (*17*, *18*), rotationally excited hydride ions stored in the CSR relax by spontaneous emission of infrared photons along the energy ladder $E_J = BJ(J+1)$ in steps of $J \rightarrow J-1$, where J is the angular momentum quantum number and B is the rotational constant. For HeH^+, B/k_B = 48.2 K (k_B is the Boltzmann constant). From a comprehensive line list (*2*), we set up a radiative model for the HeH^+ rotational level populations as functions of ion storage time t. The radiation field in CSR is approximated by two components, 99% of the spectral energy density at the molecular transitions representing the 6 K wall temperature, and 1% of it representing inevitable radiation leaks from the outer (300 K) environment (*19*). In such conditions, the population of the HeH^+ J = 0 level at equilibrium ($t \gg 10$s) is 92%. In the earlier room temperature studies (*9*–*12*) of HeH^+, the equilibrium population was only ~15% for J = 0, and higher J levels were more strongly populated (Fig. 1).

In the CSR, >50% population in J = 0 is reached at t > 8 s of storage. Vibrational excitation (v) relaxes much more quickly; consistent with previous storage-ring work (*10*–*12*), a pure v = 0 population is ensured for t > 0.1 s. The CSR result for the energy-dependent DR rate coefficient $\alpha_{DR}(E_d)$ at 10 s < t < 50 s is compared with the previous storage-ring results in Fig. 2, thus displaying the effect of reducing the rotational excitation. At 20% uncertainty in the overall scaling of our data, there are minor deviations between the CSR data and previous storage-ring results between ~0.07 and 1 eV. Strong deviations, however, occur at lower energies. For the rotationally cold ions, the DR rate first assumes a sharp resonant maximum at $E_d \sim 0.044$ eV ($E_d/k_B \sim 530$ K). Below $E_d \sim 0.02$ eV ($E_d/k_B \sim 260$ K), the DR rate

[1]Max-Planck-Institut für Kernphysik, Saupfercheckweg 1, 69117 Heidelberg, Germany. [2]Faculty of Mathematics and Physics, Charles University, 18000 Praha, Czech Republic. [3]Institut für Physik, Universität Greifswald, 17487 Greifswald, Germany. [4]Rzhanov Institute of Semiconductor Physics, Novosibirsk 630090, Russia. [5]Weizmann Institute of Science, Rehovot 76100, Israel.
*Corresponding author. Email: oldrich.novotny@mpi-hd.mpg.de

becomes much smaller (by a factor up to ~8) than that for room temperature conditions and remains nearly as low down to $E_d \sim 0.001$ eV ($E_d/k_B \sim 12$K).

Substantial rotational dependence for predissociating Rydberg resonances has been predicted (*14*, *15*) for $\alpha_{DR}(E_d)$ in this energy range. We studied this concept through the storage-time dependence of the DR rate coefficient, $\alpha_{DR}(E_d, t)$. The rotational populations from the radiative cooling model reveal how the J distribution is dominated by increasingly lower levels as the storage time advances (Fig. 3A). The $\alpha_{DR}(E_d, t)$ data were analyzed in time slices adapted to some of the lower J levels (time slices I to IV for J = 3 to 0; see Fig. 3B). Although in slice I the DR rate at low collision energies is similar to the room temperature results, this level decreases as the ions cool rotationally. Moreover, later slices with dominating J = 2 or 1 indicate energy-shifted resonances below the strong peak of time slice IV.

All time-varying DR rates represent linear combinations of the time-invariant DR rates $\alpha^J_{DR}(E_d)$ for individual J levels, weighted by the average relative level populations in the various time slices. Using the data for eight separate intervals between 0.1 and 45 s and the respective average level populations from the radiative model, we deduced (*19*) state-resolved rate coefficients $\alpha^J_{DR}(E_d)$ up to J = 2 and the average DR rate from the $J \geq 3$ levels contributing at early storage times (mainly J = 3 and 4). These data (Fig. 4A) show the dominance of a single near-Lorentzian peak for J = 0. Similar peaks with maxima downshifted in E_d are seen for $J \geq 1$, where an increase of the width points to unresolved peak structure. Moreover, starting from J = 2 the rate at E_d < 0.01 eV grows. Recent theory, such as figure 13a of (*14*), predicts a similar J-dependent peak structure at ~0.01 to 0.07 eV but predicts rates up to 10 times those of the experiment at lower energy, especially for J = 0.

These energy- and state-resolved DR rates enable us to derive plasma rate coefficients for individual J levels or fully thermal ensembles. We deconvolved (*19*, *20*) the merged-beams DR rate coefficients $\alpha^J_{DR}(E_d)$ to yield DR cross sections in narrow energy bins. Subsequently, we reconvolved these J-specific cross sections to obtain plasma rate coefficients $\alpha^J_{DR,pl}(T_{pl})$ (see Fig. 4B) for Maxwellian electron energy distributions of kinetic temperature T_{pl}. These results can be state-population weighted to obtain a rate coefficient for specified rotational temperatures T_{rot} or even for fully thermalized conditions [see $\alpha_{DR,therm}(T_{rot} = T_{pl})$ in Fig. 4B]. Our results for J = 0 and J = 1 at <80 K are lower than the values (*19*) presently applied in early-Universe models (*21*, *22*) and those listed in astrochemistry databases (*23*–*25*) by factors of 15 to 80. Compared with these previous data, even the enhanced J = 2 and $J \geq 3$ average rates are lower.

A recent study (*22*) (Fig. 2) shows that, at redshifts z < 15, the only reactions essential

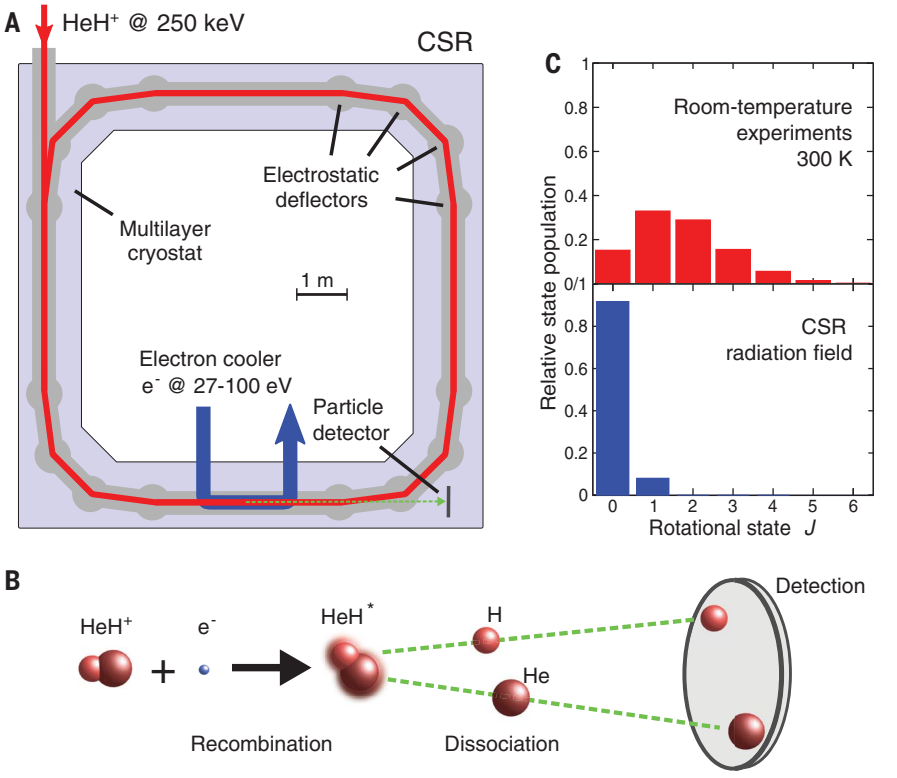

Fig. 1. Dissociative recombination in the cryogenic storage ring, CSR. (**A**) Scheme of the CSR ring structure with the injected and stored HeH^+ ion beam (red), merged electron beam (blue), reaction products (green), and particle detector. (**B**) Reaction scheme and position-sensitive detection of coincident fragments. (**C**) Equilibrium rotational state populations of HeH^+ for previous studies (300 K) and the estimated radiation field in the CSR.

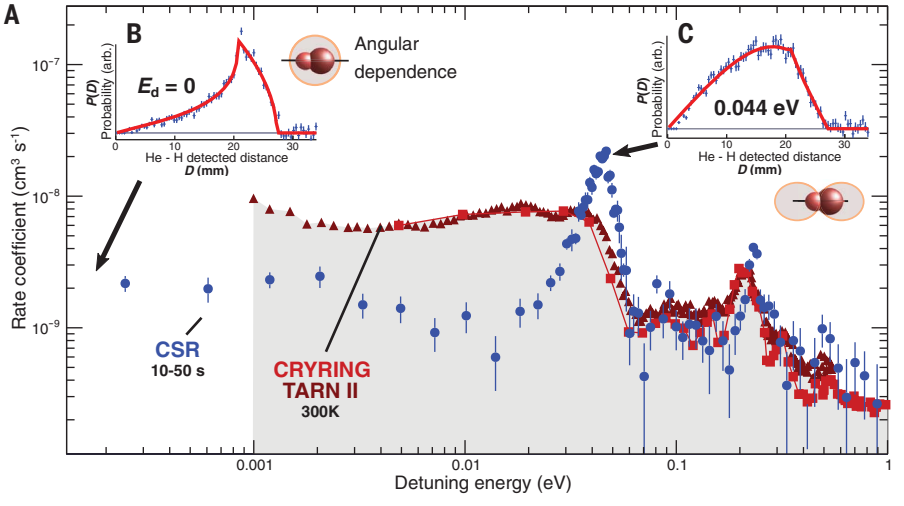

Fig. 2. DR for rotationally cold HeH^+. (**A**) Blue circles indicate the merged-beams rate coefficient α_{DR} as a function of the detuning energy E_d after relaxation to >50% J = 0 (this experiment, 10 s < t < 50 s, mean ± SD); absolute scaling uncertainty ±20% (SEM). Red symbols represent room temperature data from (*11*) (squares, absolute scaling uncertainty ±10% SEM) and from (*12*) [triangles, scaled to (*11*) at 0.03 eV]. (**B**) Fragment distance distribution projected into the detector plane for E_d = 0 (blue) with fit (*19*) for isotropic angular distribution (red). (**C**) Projected fragment distance distribution for E_d = 0.044 eV (blue) with fit (*19*) for a $|Y_{10}|^2$ angular distribution of the fragments (red). The angular dependences in (B) and (C) are indicated schematically. arb., arbitrary units.

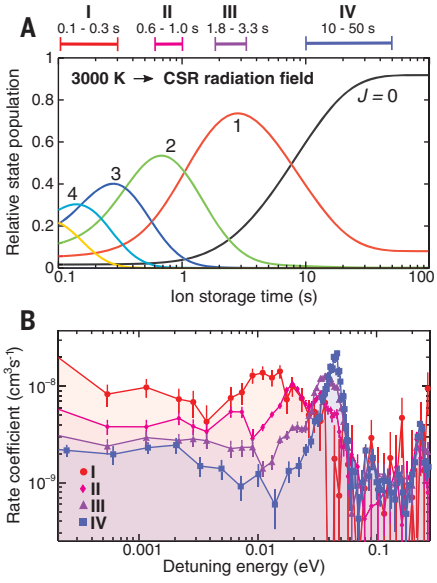

Fig. 3. DR during the rotational relaxation of HeH^+. (**A**) Relative rotational level populations as functions of ion storage time t from the radiative model (starting temperature: 3000 K; CSR radiation field: 99% at 6 K, 1% at 300 K) for J as given and with time slices I to IV in which the dominant J varies from 3 to 0. (**B**) Rate coefficient $\alpha_{DR}(E_d)$ measured in the marked time slices (mean ± SD).

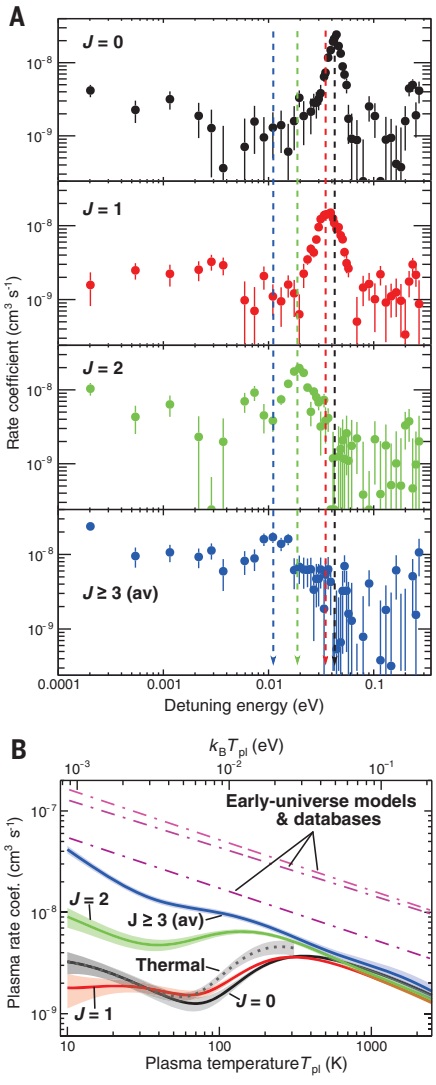

Fig. 4. Rotational-state selective DR rates for HeH^+. (**A**) Merged-beams rate coefficients $\alpha^J_{DR}(E_d)$ for $J \le 2$ and average for $J \ge 3$ (mainly 3 and 4; mean ± SD). The dashed lines mark the shift of the maximum as J increases. (**B**) Solid lines indicate single-J plasma rate coefficients $\alpha^J_{DR,pl}(T_{pl})$ for $J \le 2$ and average (av) for $J \ge 3$ (mainly 3 and 4; mean with shaded areas denoting ±SD). The dotted line represents the fully thermal rate coefficient $\alpha_{DR,therm}(T_{rot} = T_{pl})$. Dashed-dotted lines indicate values applied in early-Universe models (*21*, *22*) and astrochemistry databases (*23*–*25*). See (*19*) for further discussion, numerical fitting functions, and parameters.

for the abundance of HeH^+ are radiative association of H^+ and He for production and DR for destruction. Hence, the HeH^+ abundance from model calculations is inversely proportional to the applied DR rate coefficient. At these redshifts, a radiation temperature $T \sim 40$ K requires the $J \le 1$ levels to dominate, whereas the gas temperature is $T_{pl} \le 10$ K (*26*). Comparing for $T_{pl} = 10$ K the DR rate used by Bovino *et al.* (*22*) with our $J = 0$ and $J = 1$ rates, population-averaged for $T = 40$ K, the estimated peak HeH^+ abundance at $z \sim 15$ increases by a factor of at least 20 above the previously calculated value (*22*) (Fig. 4). This strengthens the role of HeH^+ as a potential coolant in primordial star formation and also increases the chance to observe HeH^+ from the postrecombination era at low redshifts. Furthermore, higher abundance predictions for HeH^+ indicate that the role of HeH^+ in smearing out the cosmic microwave background should be reexamined (*27*). For the HeH^+ observation in planetary nebula (*6*), high kinetic temperatures of $T_{pl} \approx 10^4$K are relevant. The absolute HeH^+ DR rate of 3.0×10^{-10} cm^3 s^{-1} used to interpret that observation (*6*) is compatible with our findings (*19*).

Considering the importance of resonant processes, our energy- and state-selective rate coefficients $\alpha^J_{DR}(E_d)$ offer a particularly clean, hitherto unavailable view on the mechanism of low-energy DR. We analyzed the emission velocities of the He and H fragments at the prominent resonance at 0.044 eV, using the position resolution of our coincidence detector, and compared them to the $E_d = 0$ behavior. Distributions $P(D)$ of the fragment distances D projected into the detector plane (Fig. 2, B and C) reflect the energy and the angular characteristic of the H and He atoms emitted in a DR reaction (*19*). For both E_d, the end points of $P(D)$ at $D \sim 27$ mm indicate an emission energy near 1.55 eV and confirm the well-known (*28*) fragmentation pathway into the atomic states 1^1S (ground state) for He and $n = 2$ for H. The shapes of $P(D)$, however, reveal different angular characteristics. At $E_d = 0$ (Fig. 2B), there is no distinct electron impact direction and the fragments are emitted isotropically. In contrast, at $E_d = 0.044$ eV (Fig. 2C), the collision direction is aligned with the beam axis and the data reveal a pure low-order multipole ($|Y_{10}|^2$) around this axis for the fragment directions. Based on the well-established axial-recoil approximation (*29*), this pure low-order multipole also applies to the DR cross section with respect to the internuclear axis, as well as to the electron partial wave that drives the DR process (*30*). We find the DR resonance of $J = 0$ HeH^+ ions at 0.044 eV to be mostly driven by an electronic partial wave with angular and magnetic quantum numbers $l = 1$, $m = 0$ ($p\sigma$ symmetry), whose importance was raised theoretically (*15*).

Our new accurate rate coefficient measurements consolidate the gas-phase chemical data on HeH^+ that govern its abundance in the post-recombination era of the early Universe. Moreover, the ability to obtain state-selective laboratory data for fundamental molecular reactions is particularly timely, considering the imminent launch of the James Webb Space Telescope (*31*). Its search for the first luminous objects and galaxies after the Big Bang will benefit greatly from reliable predictions on early-Universe chemistry. Our data show that the rotational excitation can make a substantial difference in low-temperature reaction rates of small molecules.

REFERENCES AND NOTES

1. D. Galli, F. Palla, *Annu. Rev. Astron. Astrophys.* **51**, 163–206 (2013).
2. C. M. Coppola, L. Lodi, J. Tennyson, *Mon. Not. R. Astron. Soc.* **415**, 487–493 (2011).
3. P. R. Bunker, *Chem. Phys. Lett.* **27**, 322–324 (1974).
4. I. Zinchenko, V. Dubrovich, C. Henkel, *Mon. Not. R. Astron. Soc. Lett.* **415**, L78–L80 (2011).
5. E. Zicler *et al.*, *Astron. Astrophys.* **607**, A61 (2017).
6. R. Güsten *et al.*, *Nature* **568**, 357–359 (2019).
7. A. G. G. M. Tielens, *Rev. Mod. Phys.* **85**, 1021–1081 (2013).
8. M. Larsson, A. E. Orel, *Dissociative Recombination of Molecular Ions* (Cambridge Univ. Press, 2008).
9. F. B. Yousif, J. B. A. Mitchell, *Phys. Rev. A* **40**, 4318–4321 (1989).
10. T. Tanabe *et al.*, *Phys. Rev. Lett.* **70**, 422–425 (1993).
11. C. Strömholm *et al.*, *Phys. Rev. A* **54**, 3086–3094 (1996).
12. T. Tanabe *et al.*, *J. Phys. B* **31**, L297–L303 (1998).
13. S. L. Guberman, *Phys. Rev. A* **49**, R4277–R4280 (1994).
14. R. Čurík, C. H. Greene, *J. Chem. Phys.* **147**, 054307 (2017).
15. H. Takagi, *Phys. Rev. A* **70**, 022709 (2004).
16. R. von Hahn *et al.*, *Rev. Sci. Instrum.* **87**, 063115 (2016).
17. A. O'Connor *et al.*, *Phys. Rev. Lett.* **116**, 113002 (2016).
18. C. Meyer *et al.*, *Phys. Rev. Lett.* **119**, 023202 (2017).
19. Materials and methods are available as supplementary materials.
20. O. Novotný *et al.*, *Astrophys. J.* **777**, 54 (2013).
21. D. Galli, F. Palla, *Astron. Astrophys.* **335**, 403 (1998).
22. S. Bovino, M. Tacconi, F. A. Gianturco, D. Galli, *Astron. Astrophys.* **529**, A140 (2011).
23. D. McElroy *et al.*, *Astron. Astrophys.* **550**, A36 (2013).
24. V. Wakelam *et al.*, *Astrophys. J.* **199** (suppl.), 21 (2012).
25. Gas-phase models of the Ohio State University (OSU) Astrophysical Chemistry Group, accessible via http://faculty.virginia.edu/ericherb/research.html (February 2019).
26. D. Puy, G. Alecian, J. Le Bourlot, J. Leorat, G. Pineau Des Forets, *Astron. Astrophys.* **267**, 337 (1993).

27. D. R. G. Schleicher *et al*., . *Astron. Astrophys.* **490**, 521–535 (2008).
28. J. Semaniak *et al*., *Phys. Rev. A* **54**, R4617–R4620 (1996).
29. R. N. Zare, *J. Chem. Phys.* **47**, 204–215 (1967).
30. S. L. Guberman, *J. Chem. Phys.* **120**, 9509–9513 (2004).
31. J. P. Gardner *et al*., *Space Sci. Rev.* **123**, 485–606 (2006).
32. O. Novotný, Analysis of rotationally dependent dissociative recombination rates. Edmond repository, Max Planck Society (2019); https://dx.doi.org/10.17617/3.2h.

ACKNOWLEDGMENTS

This article comprises parts of the Ph.D. thesis works of P.W., S.S., and D.P., submitted or to be submitted at the Ruprecht-Karls-Universität Heidelberg, Germany. **Funding:** This work was supported by the Max Planck Society, the Weizmann Institute of Science, the German Science Foundation (DFG Wo 1481/2-1 and DFG GE 2183/3-1), and the European Research Council (Starting Grant StG 307163). **Author contributions:** K.B., D.Z., and A.W conceived the original idea. K.B., S.G., H.K., D.Z., and A.W. provided financial support. O.N. and A.W. led the preparations, modeling, measurements, and analysis. O.N., P.W., D.P., Á.K., S.S., C.K., M.G., and A.W. performed the measurements and analyzed the data. O.N., P.W., D.P., C.K., D.A.O., M.R., A.S., A.S.T., S.V., and A.W. contributed to the design and realization of the CSR electron cooler and photocathode electron gun. O.N., S.S., A.B., C.K. and A.W. contributed to the design and realization of the detector. All other authors contributed to development and realization of further tools and methodology, as well as to preparatory measurements directly relevant for this work. O.N., H.K., and A.W. wrote the manuscript. All authors commented on the final manuscript. **Competing interests:** The authors declare no competing interests. **Data and materials availability:** The underlying data are available in the supplementary materials and Edmond, the Max Planck Society repository (*32*).

SUPPLEMENTARY MATERIALS

science.sciencemag.org/content/365/6454/676/suppl/DC1
Materials and Methods
Figs. S1 and S2
Table S1
References (*33*–*38*)

12 April 2019; accepted 1 July 2019
Published online 18 July 2019
10.1126/science.aax5921

PERVOSKITES

Thermal unequilibrium of strained black $CsPbI_3$ thin films

Julian A. Steele[1]*, Handong Jin[2], Iurii Dovgaliuk[3], Robert F. Berger[4], Tom Braeckevelt[5], Haifeng Yuan[2,6], Cristina Martin[2,7], Eduardo Solano[8], Kurt Lejaeghere[5], Sven M. J. Rogge[5], Charlotte Notebaert[9], Wouter Vandezande[1], Kris P. F. Janssen[2], Bart Goderis[9], Elke Debroye[2], Ya-Kun Wang[6], Yitong Dong[6], Dongxin Ma[6], Makhsud Saidaminov[6], Hairen Tan[6,10], Zhenghong Lu[11], Vadim Dyadkin[3], Dmitry Chernyshov[3], Veronique Van Speybroeck[5], Edward H. Sargent[6], Johan Hofkens[2]*, Maarten B. J. Roeffaers[1]

The high-temperature, all-inorganic $CsPbI_3$ perovskite black phase is metastable relative to its yellow, nonperovskite phase at room temperature. Because only the black phase is optically active, this represents an impediment for the use of $CsPbI_3$ in optoelectronic devices. We report the use of substrate clamping and biaxial strain to render black-phase $CsPbI_3$ thin films stable at room temperature. We used synchrotron-based, grazing incidence, wide-angle x-ray scattering to track the introduction of crystal distortions and strain-driven texture formation within black $CsPbI_3$ thin films when they were cooled after annealing at 330°C. The thermal stability of black $CsPbI_3$ thin films is vastly improved by the strained interface, a response verified by ab initio thermodynamic modeling.

The use of solution-processed, organic–inorganic metal halide perovskites for solar cells (*1*–*5*) is still limited by their instability within real-world devices (*6*) for two reasons. The first relates to the volatility of organic cations in methylammonium and formamidinium (FA) lead halide systems, which promotes material degradation (*7*–*9*). The second arises from their polymorphic nature, whereby a room-temperature (RT) stable black perovskite structure is not guaranteed (*10*). Implementing Cs^+ cations (i.e., $CsPbI_3$) has allowed for both high solar cell conversion efficiencies [above 17% (*11*)] and improved environmental stability (*12*, *13*). However, regarding phase stability, single-cation FA/$CsPbI_3$ systems form a thermodynamically stable yellow RT δ-phase (nonperovskite) before undergoing reversible, high-temperature phase transitions to their optically active black perovskite phases: α (cubic), β (tetragonal), and γ (orthorhombic). The thermal phase relations for $CsPbI_3$ are depicted in Fig. 1A, with the relative transitions shown in Fig. 1B. The term "black" is used to define collectively the (pseudo-)cubic phases, as they typically exhibit similar optoelectronic properties. At RT, the black phase is unstable (*14*, *15*).

As seen in Fig. 1A, the black α-$CsPbI_3$ perovskite can, depending on conditions, pass through a variety of different restructuring paths. The thermodynamically preferred cooling path (path 2) (*16*) is mediated by the series of structural distortions (Fig. 1B). When the requisite sample preparation and cooling rates are used, an RT black phase can persist (paths 3 and 4 in Fig. 1A) in the form of a pseudocubic phase. A metastable black phase will only survive at RT when the strong driving force to transform into the yellow phase (path 5) is successfully countered. For example, upon mild reheating (60 to 100°C), the metastable black phase (path 6) will normally turn yellow (*14*, *15*, *17*) once its saddle point is energetically overcome. Thus, the problem is how to form a stable black $CsPbI_3$ perovskite for near-RT device operation.

Recent findings offer a range of solutions, each following at least one of three general approaches: (i) nanocrystal formation (*18*–*21*), (ii) surface functionalization (*22*), and (iii) compositional tuning (*23*–*25*). When forming a perovskite-substrate heterojunction in thin-film device architectures, tensile strain was recently shown to manifest at RT (*26*) due to the large mismatch in thermal expansion coefficients (α_T) of the perovskite layer (~50×10^{-6} K^{-1} for lead iodide–based perovskites) and typical optically transparent substrates [both indium tin oxide (ITO) and glass reside between 4×10^{-6} and 9×10^{-6} K^{-1}]. By definition, strain will push the competing perovskite phases into a relative state of thermodynamic unequilibrium (*27*–*29*). Within this context, strain engineering can favor the formation of a desired phase or can even lead to new phases (*30*). For example, the strain introduced into $CsPbI_3$ nanocrystals processed with hydroiodic acid (*29*) has been connected to improved stability.

We report the use of interfacial clamping and strain to form an RT-stable black phase of functional $CsPbI_3$-based thin films. A combination of synchrotron-based, grazing incidence, wide-angle x-ray scattering (GIWAXS) and ab initio thermodynamic modeling revealed that substrate clamping drives texture formation (preferential alignment of domains within a polycrystalline system) and can create large biaxial strain. Strain beneficially shifted the relative free energies of the competing phases at RT. We elucidate the stabilizing roles of Br doping (≤10%) and thin-film formation [i.e., nanocrystal (NC) formation and substrate clamping], and find that strain is a key enabler in the design of stable optoelectronic devices.

We grew $CsPbI_3$ materials using a solution-processing method previously reported (*31*), with the black phase accessed through thermal annealing (see the materials and methods). Three material types were considered: powders (drop cast), thin films (spin coat), and free NCs scraped from the thin-film substrate. Figure S1 presents scanning electron microscopy data showing their differing morphologies; the thin films exhibited the formation of NC grains (50 to 200 nm), and the powders appear bulk-like.

Synchrotron-based GIWAXS was used (see fig. S2 for experimental scheme) to resolve the structural state of a $CsPbI_3$ thin film before and after thermal annealing at 330°C, as well as after thermal quenching (i.e., kinetically trapping the black phase using an RT metal slab; path 3 in Fig. 1A). Figure S3 presents the structural refinements of a δ-$CsPbI_3$ thin film at RT and its α-phase (330°C), which is consistent with the result of Trots and Myagkota (*32*). A black phase was obtained at RT by kinetically trapping the thin film, hinting at the role of the interface for suppressing the α-to-δ phase transformation. In situ GIWAXS experiments showed that the strained black thin film remained vulnerable to moisture attack, quickly destabilizing and turning yellow when exposed to moisture (fig. S4). Figure 2A displays the GIWAXS image detected from a black γ-$CsPbI_3$ thin film shortly after quenching, highlighting occurrences of anisotropic peak splitting in-plane ($q_{x,y}$) and out-of-plane (q_z) (fig. S5 shows the full GIWAXS image). This feature is a signature of crystallographic texture (preferential crystallographic orientation with distribution φ; see fig. S6) in the quenched thin film, a signature not observed before or after gradual cooling (fig. S7). Figure 2B illustrates how this split GIWAXS signal arises after cooling; the $CsPbI_3$ lattice forming an interface is lengthened in-plane when clamped, corresponding to a relative lattice reduction out-of-plane.

[1]Centre for Surface Chemistry and Catalysis, KU Leuven, Celestijnenlaan 200F, Leuven 3001, Belgium. [2]Department of Chemistry, KU Leuven, Celestijnenlaan 200F, Leuven 3001, Belgium. [3]Swiss-Norwegian Beamlines at the European Synchrotron Radiation Facility, 71 Avenue des Martyrs, F-38000 Grenoble, France. [4]Department of Chemistry, Western Washington University, 516 High Street, Bellingham, WA 98225, USA. [5]Center for Molecular Modeling (CMM), Ghent University, Technologiepark 46, 9052 Zwijnaarde, Belgium. [6]Department of Electrical and Computer Engineering, University of Toronto, 35 St. George Street, Toronto, Ontario M5S 1A4, Canada. [7]Departamento de Química Física, Facultad de Farmacia, Universidad de Castilla-La Mancha, 02071 Albacete, Spain. [8]NCD-SWEET Beamline, ALBA Synchrotron Light Source, Cerdanyola del Vallès, Barcelona 08290, Spain. [9]Polymer Chemistry and Materials, KU Leuven, Celestijnenlaan 200F, Leuven 3001, Belgium. [10]National Laboratory of Solid State Microstructures, Jiangsu Key Laboratory of Artificial Functional Materials, College of Engineering and Applied Sciences, Nanjing University, Nanjing 210093, China. [11]Department of Materials Science and Engineering, University of Toronto, 184 College Street, Toronto, Ontario M5S 3G4, Canada.
*Corresponding author. Email: julian.steele@kuleuven.be (J.A.S.); johan.hofkens@kuleuven.be (J.H.)

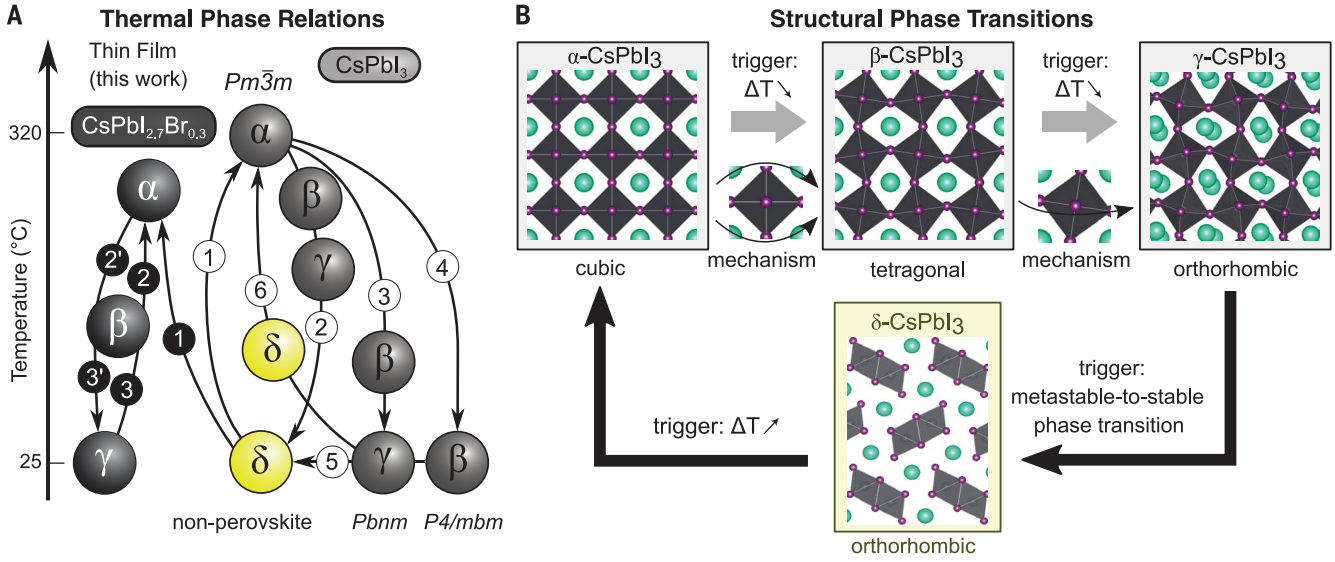

Fig. 1. Polymorphic character and metastability of $CsPbI_3$. (**A**) Thermal phase relations of $CsPbI_3$ compared with the phase behavior of strained $CsPbI_{2.7}Br_{0.3}$ thin films investigated in this work. The different path details are outlined in the text. (**B**) Crystal structure of the different phases and their relative phase transitions. The transitions between the black phases are governed by the local Pb-centered octahedral (black) distortions, depicted here using one lead atom at the center and six iodide atoms at the edges (purple), confining the cesium cations (cyan).

Figure 2C shows analysis of the 2θ scattering intensities generated along directions $q_{x,y}$, q_z, and $q_{x,y,z}$. Compared with the cubic α-phase (fig. S3), a reduction in crystal symmetry is evident from the more complex scattering pattern (*16*, *33*). Refining the $q_{x,y,z}$ data (with the Le-Bail method) using a γ-$CsPbI_3$ structure (*16*) provided an agreeable fit and yielded unit cell parameters a = 8.629 Å, b = 8.955 Å, and c = 12.636 Å (volume = 976.509 $Å^3$). Analyzing the GIWAXS image pixel intensities in Fig. 2A as a function of the azimuthal angle, we were able to quantify the degree of texturing (fig. S8). We found that the intensity of the γ(002)/(020) scattering peaks maximized in-plane, whereas the γ(200) peak was normal to this. The γ(110) peak exhibited an out-of-plane bimodal distribution (two maxima separated by ~90°), with the full width at half maxima for both being near 55°, providing a measure of the orientational distribution, φ. An illustration of the crystal texture derived from this analysis is provided in fig. S9.

The texture was imposed by the symmetry of the initial high-temperature cubic unit cell. Any phase transition that results from a reduction in symmetry (forming an anisotropic cell) is paralleled by the formation of domains, e.g., a transition from a cubic (α) to a lower-symmetry tetragonal phase (β) gives three equally probable domains. In an isotropic bulk α-$CsPbI_3$ system, the domains have the same energy upon cooling and are equally probable. However, the situation changes after the introduction of an anisotropic strain field at the interface that energetically favors some domains, causing the longer lattice b- and c-axes to remain in-plane (fig. S8).

Compared with the bulk γ-$CsPbI_3$ structure refined by Marronnier *et al.* (*16*), our thin-film γ-$CsPbI_3$ crystal was heavily distorted (fig. S10)—a result of clamping strain and rapidly cooling the material from 330°C down to RT on a glass substrate. In quantifying the extent of crystal deformation, we assessed distortions using the split low-angle peak(s) nearing 2θ = 9° (inset of Fig. 2C). These peaks arose during the α-to-γ transition through a relative doubling of the c-axis [i.e., α(001) becomes γ(002)] and a reduction in the unit-cell symmetry, whereby the (110) spacing is no longer equal to (002) in the pseudo-cubic β- or γ-phase. Considering the distortions in- and out-of-plane relative to the parent cubic, we evaluated the degree of biaxial anisotropy as follows:

$$\Delta d_{\perp} = 1 - \frac{d_{(110)}(q_z)}{d_{(001)}(q_{x,y})} \quad (1)$$

Here, d is the interplane spacing in the direction noted. Because of the relative transformation of the c-axis length during the α-to-γ transition, $d_{(001)}$ represents the normalized spacing. For a quenched RT black $CsPbI_3$ thin film, $\Delta d_{\perp}$ = 1.65%.

Two different types of strain act to increase the size of $\Delta d_{\perp}$: (i) spontaneous strain, which is introduced by a change in unit cell shape during the phase transition(s), and (ii) strain at the film/substrate interface, which is induced by the thermal expansion mismatch. Spontaneous strain can be decoupled from our measurement by using the temperature-dependent changes in the bulk $CsPbI_3$ lattice parameters, data recently reported by Marronnier *et al.* (*16*). By analyzing their data (see fig. S10), we found that $\Delta d_{\perp}$ jumped to 1.18% during the α-to-β tetragonal distortion and ceased to increase after forming an orthorhombic γ-phase. The value $\Delta d_{\perp}$ = 1.18% after the tetragonal distortion represents the spontaneous strain contribution of the RT γ-$CsPbI_3$ system, with an additional 0.47% arising in our thin film from substrate clamping. Thus, the effect of the interface is an out-of-plane structural relaxation of the same nature driven by the phase transitions (Fig. 1B), leading to texture formation and a continuation of the spontaneous strain and anisotropy.

To investigate whether the concept of strain-induced stabilization was a more general one, we explored the development of strain in the solution-processed thin films as a function of film thickness. With increasing thickness, the relative volume of the perovskite film that is subject to strain will decrease. The films shown in Fig. 2 were ~270 nm thick, so we varied the solution precursor concentration to prepare $CsPbI_3$ thin films with thicknesses ranging from 135 nm up to nearly 1 μm (an upper limit constrained by the solubility of precursor) and evaluated the structural state of their kinetically trapped RT black phase using GIWAXS (fig. S11). The strain profile and texture properties were consistent across the film thickness range studied. Further, $\Delta d_{\perp}$ retained a value close to 1.65%, although it did decrease slightly to 1.62% for the thickest films (fig. S12). For devices based on solution-processed perovskite thin films, this suggests substrate clamping and the formation biaxial strain to be centrally important.

In a second stage, the properties of the thermodynamically preferred δ-phase material formation were investigated. A slowly cooled $CsPbI_3$ thin film (–5°C/min) was tracked in situ (Fig. 1D) through an α-to-δ phase transition with GIWAXS time–temperature (*t*-*T*) profiling. The black-to-yellow phase change was identified by the introduction of δ peaks near 270°C and the fading of the black phase peak(s), which turn asymmetric with reduced crystallographic symmetry. The signals recorded in the $q_{x,y,z}$ and q_z directions are

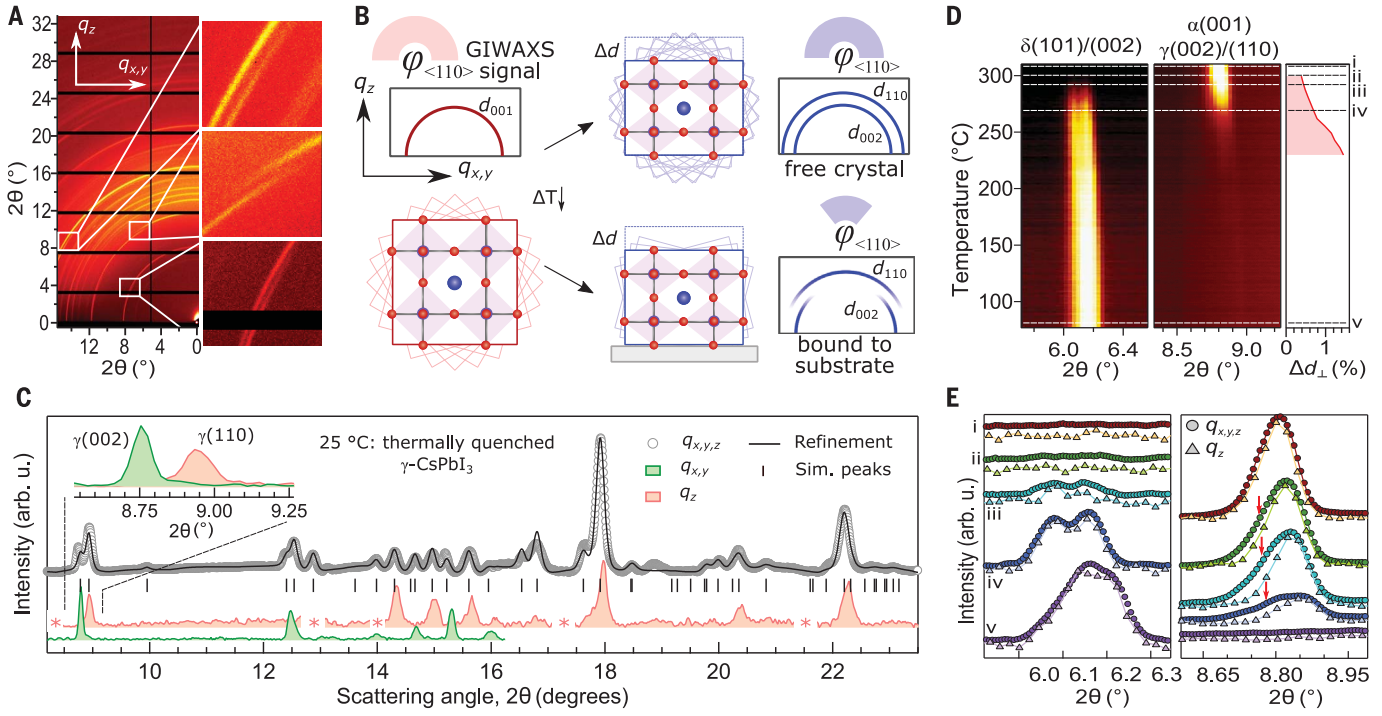

Fig. 2. Structural evaluation of substrate clamping and texture formation after the cooling of high-temperature α-$CsPbI_3$ thin films. (**A**) GIWAXS image acquired from a thermally quenched RT $CsPbI_3$ thin film, with expansions over selected diffraction peaks azimuthally split in the in-plane ($q_{x,y}$) and out-of-plane (q_z) directions. (**B**) Schematic illustration of diffraction ring splitting in the GIWAXS signal, whereby a perovskite crystal forms a heterojunction with the substrate surface at high temperature and undergoes tensile strain and texture formation (with angular distribution φ, represented by light rotated cells) upon cooling. (**C**) Comparison of GIWAXS 2θ signals generated from the image in (A), formulated by integrating over the total image ($q_{x,y,z}$) and both the $q_{x,y}$ and q_z directions. Asterisks indicate scattering blind spots between the cells of the detector. Inset is an expansion of the low-angle peaks. (**D**) GIWAXS *t*-*T* profile and calculated strain $\Delta d_\perp$ (Eq. 1) through an α-to-δ phase transition in a slowly cooled (−5°C/min) $CsPbI_3$ thin film. (**E**) Comparison of $q_{x,y,z}$ and q_z 2θ signals extracted at the points marked on the *t*-*T* profile in (D). The arrows identify the missing $q_{x,y}$ signal components detected in the $q_{x,y,z}$ direction, but not the q_z direction.

compared in Fig. 2E at the selected *t*-*T* values shown in Fig. 2D. Again, both strain and texture were established in the black phase during cooling, as seen by the distinct absence of γ(110) scattering in $q_{x,y}$. Before the black phase disappeared, $\Delta d_\perp$ increased throughout the phase change toward the expected spontaneous strain limit (~1.2% for purely spontaneous strain; see fig. S10).

The introduction of the yellow phase in Fig. 2E underwent a contrasting evolution; the growth of δ-phase peaks upon cooling was paralleled by the loss of texture and strain within the polycrystalline thin film (fig. S7). This result indicates that a sharp and clamped interface was lost once the film transformed to the yellow phase through strain release (i.e., plastic deformation), facilitated by the near-equilibrium transformation kinetics above 200°C. The constraint of the perovskite atoms at the interface was the cause for this; if the atoms were to remain affixed during a δ-phase restructuring, then there would be an increased energy penalty. The black-to-yellow phase conversion involved a marked shift in the crystal volume (*16*) (per unit formula) and a total repositioning of atomic coordinates. The in situ XRD findings of Frolova *et al.* (*15*) visualized this directly; their [001]-oriented black films (grown by vapor deposition) became disordered after a transition to the yellow phase. They also attributed the results to the large mismatch in the structure of different crystal phase layers relative to the substrate.

To investigate the influence of the strained interface on the relative stability of the α and δ phases, we monitored the local phase of a $CsPbI_3$ thin film that was partly scraped (forming free NCs), as it is thermally quenched from 330°C (Fig. 3A). From the optical images recorded in situ during the cooling ramp, the material that was still attached to the substrate became kinetically trapped at RT in the black phase, whereas the free NCs readily turned yellow below 230°C. This result confirmed the stabilizing role of the interface and its generated strain. To investigate whether the perovskite films respond in a similar way when clamped to other common interfaces, we evaluated the GIWAXS and phase behavior of $CsPbI_3$ thin films deposited on ITO-coated glass substrates (possessing a similar α_T value; see fig. S13). The root mean square roughness of the ITO (3.1 nm) is far larger than that of the bare glass (1.1 nm), yet the strain profile, crystal texture properties, and clamping-induced phase properties of thin films on the ITO surface are all comparable (fig. S13). This extends the influence of substrate clamping and improved black-phase stability across substrates possessing different roughness and chemical natures, suggesting that such parameters are unimportant in establishing a strained interface or a stable black thin film.

To understand the strain-induced shifts in the energetic stability of the competing phases, periodic density functional theory (DFT) calculations of strained and unstrained γ- and δ-$CsPbI_3$ structures were performed (Fig. 3, B and C). Our approach (see the materials and methods) first considered the average unstrained linear reduction ($\overline{\Delta L}$) of the $CsPbI_3$ crystal when it was cooled to 100°C (where the black and yellow phases strongly compete energetically), which resulted in different degrees of relative contraction for γ and δ (*16*) (Fig. 3B). Our experiments revealed that the interface in the RT black phase prevented shrinking along the in-plane direction, heavily distorting the crystal. As a result, cooling from 300° to 100°C introduced an in-plane biaxial strain of ~1%. Moreover, our DFT calculations using the SCAN (strongly constrained appropriately normed) functional (at 0 K) showed that the equilibrium volume per formula unit of δ-$CsPbI_3$ (229 $Å^3$) was substantially less than that of the γ-$CsPbI_3$ (241 $Å^3$), forcing the strain to grow to ~3% if the

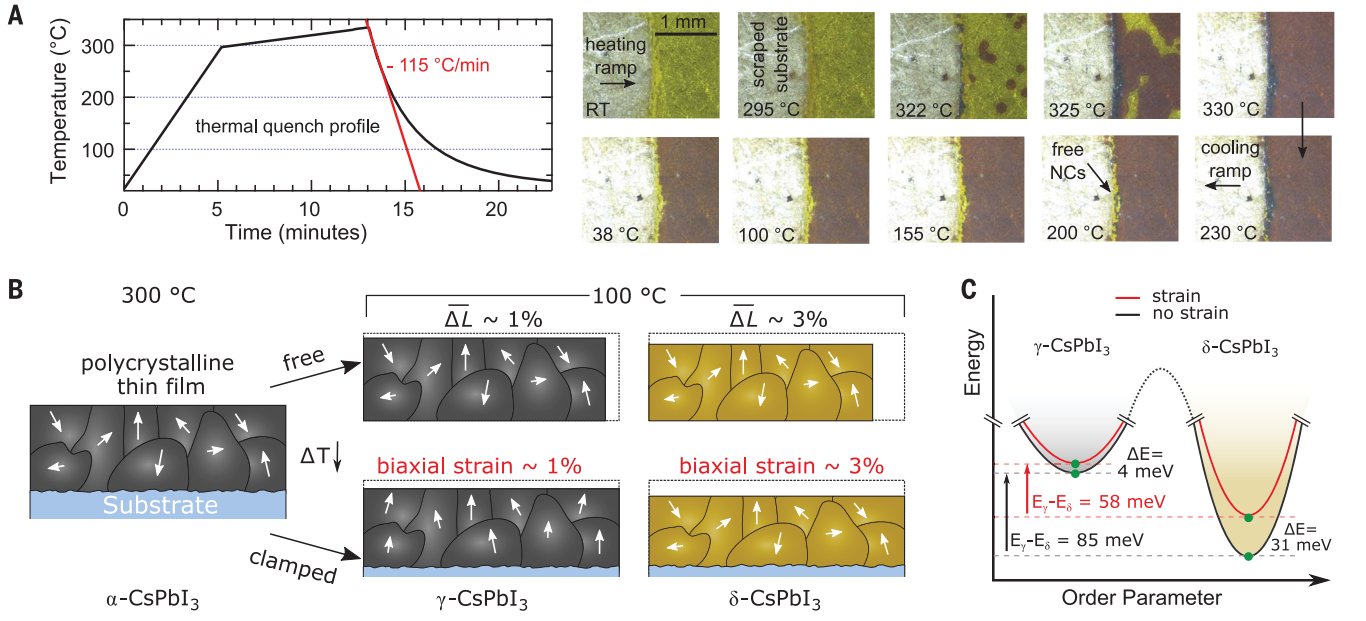

Fig. 3. Removing the interface destabilizes RT black $CsPbI_3$ thin films. (**A**) Corresponding optical images (right) of a partially scrapped $CsPbI_3$ thin-film surface (free NCs) recorded under N_2 at different temperatures during a quenching temperature profile (left). (**B**) Schematic representation of the DFT calculations used to quantify the energy of both the black γ-phase and yellow δ-phase materials that strongly compete at 100°C when cooled from the high-temperature α-$CsPbI_3$. The scenarios considered include free and clamped polycrystalline thin films (arrows reflect relative domain orientation), where the thermal change induces a reduction in the average lattice parameter length ($\overline{\Delta L}$), manifesting as biaxial strain when clamped to the substrate. (**C**) Ab initio energy diagram indicating the relative stability (at 0 K) of the black and yellow phases with and without in-plane biaxial strain, averaged out over 12 different strain directions (see table S1). The relative saddle point depth is undefined.

material underwent a γ-to-δ phase transition while remaining clamped. The quenched γ-$CsPbI_3$ thin film was polycrystalline and expressed texture, whereas the crystallographic alignment was lost in the film upon transforming to the yellow phase. To account for this, 12 different crystal orientations were considered, resulting in 12 different strained interfacial planes, with the lower-symmetry planes forming supercells (fig. S14). Their energy increase upon straining is listed in table S1 and varied only slightly across the different surface orientations.

The average relative energies determined from periodic DFT simulations (Fig. 3C) show that the unstrained yellow phase is strongly favored over the unstrained black phase, driving the γ-to-δ phase transition in free-standing crystals. However, the introduction of biaxial strain led to different energy penalties for the two phases. There was a strong relative destabilization of the strained yellow phase with respect to the strained black phase. Thus, the energy difference promoting the γ-to-δ transition was reduced, explaining in part the stabilizing influence of substrate clamping that we saw experimentally. An additional energy penalty may be present if release of the surface clamping is required, as suggested by the kinetic trapping of the $CsPbI_3$ thin film.

We never formed an RT black-phase $CsPbI_3$ thin film without kinetic trapping, with the limited lifetime of the black phase during slow cooling (Fig. 2D) preventing a detailed study of the strain-induced restructuring. For this, we used relatively light Br halide mixing to better access the temperature-dependent black-phase evolution, i.e., $CsPb(I_{1-x}Br_x)_3$, $x \leq 0.1$. These materials retain both a band-gap energy useful for solar cells (fig. S15) and comparable material morphologies (fig. S1).

Differential scanning calorimetry (DSC) studies of $CsPb(I_{1-x}Br_x)_3$ powders and NCs (fig. S16) provided two pertinent types of data. First, size-driven effects likely make the NCs formed during spin coating more stable than the bulk materials. A disparity in the surface energy between γ-CsPbI3 (0.13 J/m^2) and δ-CsPbI3 (2.57 J/m^2) is predicted (*21*) to reverse the relative magnitudes of their Gibbs free energies at crystal volumes approaching ~100 nm^3. The size of nanograins making up our thin films (fig. S1) was near this regime. Second, although Br doping helped to stabilize the black phase, the calculated enthalpies (table S2) of the reversible yellow-to-black phase transitions were comparable (13 kJ/mol) and steady across the Br mixing explored. This result suggests that the phase transitions in our mixed halide samples closely followed the thermodynamics of the parent $CsPbI_3$ system.

Figure 4A shows the GIWAXS *t-T* profile and strain state in a $CsPbI_{2.7}Br_{0.3}$ thin film through multiple phase transitions imposed during thermal cycling. The changes therein can be tracked after the successive phase transitions, whereas the emergence of texture induced by anisotropic strain results in azimuthal splitting; the latter effect can only be seen with a large area detector. Starting from δ-$CsPbI_{2.7}Br_{0.3}$, we saw the high-temperature formation of the α-phase (1), followed by β (2) and γ (3) distortion during cooling, which were reversed (2′ and 3′) upon reheating. After an initial yellow-to-black transition, a thermodynamically stable black thin film with a strained interface was realized. This is in contrast to the unstable free NCs studied by DSC (fig. S16), which do not benefit from the stabilizing strained interface. For completeness, the sequence described above for thin-film $CsPbI_{2.7}Br_{0.3}$ was compared with the nominal thermal phase relations of $CsPbI_3$ in Fig. 1A. The textured GIWAXS signal (full image shown in fig. S17) and the crystal structure of the RT γ-$CsPbI_{2.7}Br_{0.3}$ thin film is analogous to the quenched black $CsPbI_3$ thin film (fig. S4). The magnitude of $\Delta d_\perp$ in the γ-$CsPbI_{2.7}Br_{0.3}$ thin film at RT reached 1.64%, and reheating caused the strain-driven texture to be undone, reforming randomly distributed α-phase domains (see fig. S18). Thus, in addition to hindering a decay to the δ-phase (fig. S16), kinetically trapping a black $CsPbI_3$ thin film incurred no additional structural modification.

A temperature–domain structural analysis of the black $CsPbI_{2.7}Br_{0.3}$ thin film (Fig. 4B) showed no considerable hysteresis between the different restructuring pathways (fig. S19). We thus evaluated these data together; as the temperature difference (ΔT) increased, the interplanar distances d shifted relative to $d_0(\Delta T = 0)$ by $d = d_0(1 + \alpha_T \times \Delta T)$. Linear fits yielded the α_T values shown in Fig. 4B using high-temperature d_0 values. Upon cooling the black film from 300°C, the lattice *a*-axis contracted smoothly with an expansion rate comparable (*32*) to the high-temperature α-$CsPbI_3$ (α_T=4.0×10^{-5} K^{-1}). Near 200°C, the cubic

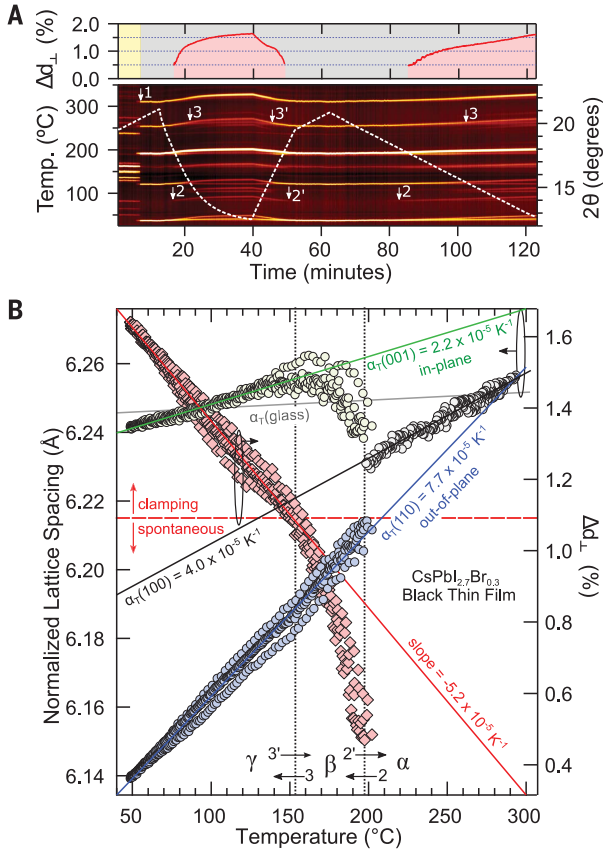

Fig. 4. Structural phase kinetics of thermally cycled strained perovskite thin film. (**A**) GIWAXS (λ = 0.95774 Å) *t-T* profile ($q_{x,y,z}$) of $CsPbI_{2.7}Br_{0.3}$ thin film through a high-temperature yellow-to-black phase transition, followed by thermal cycling. The start of the first cooling ramp (nonlinear) is ~−17°C/min and the second is −3.8°C/min. (**B**) Normalized anisotropic lattice parameters and $\Delta d_\perp$ unit cell distortions of the black phase thin film as a function of temperature. Phase changes are numerically identified in (B) and align with those depicted in (A). The linear data fits to selected segments generate the α_T values displayed. An estimate is provided for the thermal expansion of the glass substrate (*35*) ($\alpha_T = 0.37 \times 10^{-5}$ K^{-1}).

structure underwent a tetragonal distortion and the introduction of $\Delta d_\perp$ through spontaneous strain formation. The in-plane (001) lattice underwent negative thermal expansion, reverting this in-plane lattice closer to the linear expansion rate of glass. The negative thermal expansion of the *c*-axis in this temperature range agreed well with the complex bulk structural evolution detailed by Marronnier *et al.* (*16*) (see fig. S10 for full analysis) and underpinned the subsequent texture direction. Cooling through point 3 in Fig. 4B, the out-of-plane lattice continued its relatively fast reduction, whereas the in-plane spacing of the orthorhombic structure assumed positive thermal expansion [compensated by negative thermal expansion of the *b*-axis (*16*); see fig. S10]. After the β-to-γ transition, $\Delta d_\perp$ should not increase in a nonstrained system. In our clamped thin film, $\Delta d_\perp$ grew rapidly and overshot spontaneous strain contributions, being driven solely by the strained interface. With rising strain, the relative destabilization of the yellow phase was only expected to continue.

The small divergence of the in-plane $CsPbI_3$ lattice parameter (crystal *c*-axis) from the expected linear contraction of the glass suggests that the perovskite/substrate interface resulted from the adaptable nature of the perovskite crystal rather than from covalent bonding. This is supported by our studies of strained films deposited on ITO-covered glass (S13). The strong mirroring of the structural evolutions during thermal cycling signified high elastic recovery. Clamping and interfacial strain combined as key driving forces in defining both the structural texture and the improved thermal phase relations of the black phase. Thus, once a δ-$CsPbI_{2.7}Br_{0.3}$ thin film was annealed at high temperatures, it became thermodynamically trapped in an optically active black phase (Fig. 1A). Such thermal stability is highly desirable within optoelectronic devices; for instance, the energy provided by a light-emitting diode (LED)–driving current can readily destabilize the black phase (*34*). As a conceptual demonstrator, we fabricated and characterized a functioning LED device using a strained $CsPbI_{2.7}Br_{0.3}$ active layer (see fig. S20 for full details). Without any optimization, the result is a working LED device with a visibly bright (luminance of 20 cd/m^2 at 9 V) and high color purity (CIE coordinates: 0.72, 0.28) emission.

REFERENCES AND NOTES

1. M. A. Green, A. Ho-Baillie, H. J. Snaith, *Nat. Photonics* **8**, 506–514 (2014).
2. P. Meredith, A. Armin, *Nat. Commun.* **9**, 5261 (2018).
3. S. D. Stranks *et al.*, *Science* **342**, 341–344 (2013).
4. A. Walsh, A. Zunger, *Nat. Mater.* **16**, 964–967 (2017).
5. S. I. Seok, M. Grätzel, N.-G. Park, *Small* **14**, e1704177 (2018).
6. Y. Yang, J. You, *Nature* **544**, 155–156 (2017).
7. J. A. Christians, P. A. Miranda Herrera, P. V. Kamat, *J. Am. Chem. Soc.* **137**, 1530–1538 (2015).
8. B. Conings *et al.*, *Adv. Energy Mater.* **5**, 1500477 (2015).
9. G. E. Eperon *et al.*, *Energy Environ. Sci.* **7**, 982 (2014).
10. J. A. Christians, S. N. Habisreutinger, J. J. Berry, J. M. Luther, *ACS Energy Lett.* **3**, 2136–2143 (2018).
11. Y. Wang, T. Zhang, M. Kan, Y. Zhao, *J. Am. Chem. Soc.* **140**, 12345–12348 (2018).
12. M. Kulbak, D. Cahen, G. Hodes, *J. Phys. Chem. Lett.* **6**, 2452–2456 (2015).
13. J. Liang *et al.*, *J. Am. Chem. Soc.* **138**, 15829–15832 (2016).
14. S. Dastidar *et al.*, *J. Phys. Chem. Lett.* **8**, 1278–1282 (2017).
15. L. A. Frolova *et al.*, *J. Phys. Chem. Lett.* **8**, 67–72 (2017).
16. A. Marronnier *et al.*, *ACS Nano* **12**, 3477–3486 (2018).
17. T. Burwig, W. Fränzel, P. Pistor, *J. Phys. Chem. Lett.* **9**, 4808–4813 (2018).
18. D. Zhang *et al.*, *J. Am. Chem. Soc.* **138**, 13155–13158 (2016).
19. Y. Wang *et al.*, *Adv. Mater.* **27**, 7101–7108 (2015).
20. A. Swarnkar *et al.*, *Science* **354**, 92–95 (2016).
21. B. Zhao *et al.*, *J. Am. Chem. Soc.* **140**, 11716–11725 (2018).
22. Y. Fu *et al.*, *Nano Lett.* **17**, 4405–4414 (2017).
23. M. Lu *et al.*, *ACS Energy Lett.* **3**, 1571–1577 (2018).
24. Y. Hu *et al.*, *ACS Energy Lett.* **2**, 2219–2227 (2017).
25. Z. Li *et al.*, *Chem. Mater.* **28**, 284–292 (2016).
26. J. Zhao *et al.*, *Sci. Adv.* **3**, eaao5616 (2017).
27. K. M. Rabe, U. V. Waghmare, *Ferroelectrics* **194**, 119–134 (1997).
28. F. He *et al.*, *Phys. Rev. B Condens. Matter Mater. Phys.* **70**, 23405 (2004).
29. G. E. Eperon *et al.*, *J. Mater. Chem. A Mater. Energy Sustain.* **3**, 19688–19695 (2015).
30. Y. Cao *et al.*, *J. Phys. Chem. C* **122**, 9332–9338 (2018).
31. R. E. Beal *et al.*, *J. Phys. Chem. Lett.* **7**, 746–751 (2016).
32. D. M. Trots, S. V. Myagkota, *J. Phys. Chem. Solids* **69**, 2520–2526 (2008).
33. R. J. Sutton *et al.*, *ACS Energy Lett.* **3**, 1787–1794 (2018).
34. Q. Shan *et al.*, *Small* **13**, 1701770 (2017).
35. V. Craciun, D. Craciun, X. Wang, T. J. Anderson, R. K. Singh, *J. Optoelectron. Adv. Mater.* **5**, 401–408 (2003).

ACKNOWLEDGMENTS

Funding: The authors acknowledge financial support from the Research Foundation-Flanders (FWO, grant nos. G.0B39.15 and G098319N); FWO postdoctoral fellowships to J.A.S, C.M, H.Y, K.P.F.J, E.D, K.L, and S.M.J.R (grant nos. 12Y7218N, 12J1716N, 12R8718N, 12C2817N, 12O3719N, 1200117N, and 12T3519N, respectively); and an SB-FWO fellowship to T.B. (grant no. 1SC1319); the KU Leuven Research Fund (C14/15/053); the Flemish government through long-term structural funding Methusalem (CASAS2, Meth/15/04); the Hercules Foundation (HER/11/14); and the Belgian Federal Science Policy Office (IAP-VII/05). The research leading to these results has received funding from the European Research Council under the European Union's Seventh Framework Programme (FP/2007-2013)/ERC Grant Agreement (grant no. 307523 LIGHT). E.S. is grateful for the GIWAXS experimental time provided by the NCD-SWEET beamline at ALBA synchrotron. T.B. and V.V.S. acknowledge funding from the European Union's Horizon 2020 research and innovation program (consolidator ERC grant agreement no. 647755 – DYNPOR, 2015–2020). V.V.S. acknowledges the Research Board of Ghent University (BOF). The computational resources and services used were provided by Ghent University (Stevin Supercomputer Infrastructure) and the VSC (Flemish Supercomputer Center), funded by FWO. **Author contributions:** J.A.S. conceived the science, coordinated the research, and wrote the manuscript under the supervision of J.H. and M.B.J.R. I.D., V.D., W.V., K.P.F.J., E.S., and D.C. assisted with the x-ray scattering experiments and analysis. H.J., H.Y., E.H.S., and E.D. synthesized the materials under investigation, and C.M., Y.-K.W., Y.D., D.M., and Z.L. prepared and characterized the LED devices. T.B. performed the DFT calculations under supervision of S.M.J.R., K.L., and V.V.S., with support from R.F.B. C.N. and B.G. performed the DSC experiments, and M.S. and H.T. assisted in developing the science. All authors have approved the manuscript. **Competing interests:** The authors declare no competing financial interests. **Data and materials availability:** All data needed to evaluate the conclusions in this manuscript are present in the main text or the supplementary materials. Additional data or codes are available upon request to the corresponding authors. The commercial VASP software code can be licensed from the University of Vienna (see FAQ section on https://www.vasp.at). A patch with the user modifications in this article (to allow constrained cell optimizations) can be obtained from the authors upon request by VASP license holders.

SUPPLEMENTARY MATERIALS

science.sciencemag.org/content/365/6454/679/suppl/DC1
Materials and Methods
Figs. S1 to S20
Tables S1 and S2
References (*36*–*42*)

20 March 2019; accepted 10 July 2019
Published online 25 July 2019
10.1126/science.aax3878

SUPERCONDUCTIVITY

Nearly ferromagnetic spin-triplet superconductivity

Sheng Ran[1,2]*, Chris Eckberg[2], Qing-Ping Ding[3], Yuji Furukawa[3], Tristin Metz[2], Shanta R. Saha[1,2], I-Lin Liu[1,2,4], Mark Zic[2], Hyunsoo Kim[2], Johnpierre Paglione[1,2], Nicholas P. Butch[1,2]*

Spin-triplet superconductors potentially host topological excitations that are of interest for quantum information processing. We report the discovery of spin-triplet superconductivity in UTe_2, featuring a transition temperature of 1.6 kelvin and a very large and anisotropic upper critical field exceeding 40 teslas. This superconducting phase stability suggests that UTe_2 is related to ferromagnetic superconductors such as UGe_2, URhGe, and UCoGe. However, the lack of magnetic order and the observation of quantum critical scaling place UTe_2 at the paramagnetic end of this ferromagnetic superconductor series. A large intrinsic zero-temperature reservoir of ungapped fermions indicates a highly unconventional type of superconducting pairing.

Topological superconductivity has attracted great interest in condensed matter physics because of its potential application for topological quantum computing (*1*–*4*). A promising platform for topological superconductivity and Majorana fermions is the spin-triplet superconducting pairing state. For instance, the earliest theoretical model system of topological superconductivity was a one-dimensional (1D) spinless p-wave superconductor, which hosts Majorana zero modes at the ends of the chain (*5*). In 2D spinless chiral p-wave superconductors, Majorana zero modes bind to the superconducting vortices (*6*). However, triplet paring rarely exists in nature—only a dozen from the few thousand superconducting compounds discovered so far have been identified as candidate materials. Therefore, in the past decade, the experimental realization of topological superconductors has been sought in engineered topological phases, such as heterostructures in which triplet paring is induced by proximity effect with conventional s-wave superconductors (*7*). Intrinsic triplet superconductors, where the pairing state emerges by virtue of the materials' internal properties, have been underexplored owing to the limited number of candidate compounds, such as Sr_2RuO_4 (*8*–*10*) and UPt_3 (*11*, *12*).

Here, we report the discovery of a flavor of superconductivity in UTe_2 that exhibits the crucial ingredients of a spin-triplet pairing state—namely, an extremely large, anisotropic upper critical field H_{c2}; temperature-independent nuclear magnetic resonance (NMR) Knight shift; and power law behavior of electronic specific heat and nuclear spin-lattice relaxation rate in the superconducting state. In addition, UTe_2 closely resembles ferromagnetic superconductors, but with a dramatically enhanced transition temperature and upper critical field relative to known compounds (*13*–*16*), and a paramagnetic normal state; this suggests that UTe_2 is the paramagnetic end member of a ferromagnetic superconductor series.

UTe_2 crystallizes in the orthorhombic, centrosymmetric structure (space group 71 *Immm*). U atoms compose parallel linear chains oriented along the [100] a axis (Fig. 1C), which coincides with the magnetic easy axis, as seen in the magnetic susceptibility M/H, where M is magnetization and H is magnetic field strength (Fig. 2A). The low symmetry of this structure is responsible for the large magnetic anisotropy (*17*), similar to the anisotropy in the orthorhombic, ferromagnetic superconductors URhGe and UCoGe (*14*, *15*). Unlike these compounds, or the isoelectronic compound USe_2 (*18*), the temperature dependence of the magnetization and electrical resistivity show no indications of a phase transition to a magnetically ordered state (Fig. 2). The high-temperature magnetization data show paramagnetic behavior along all three crystallographic axes. A Curie-Weiss fit yields an effective moment of 2.8 bohr magnetons per unit (μ_B/U), reduced from the value of a fully degenerate $5f^2$ or $5f^3$ configuration. At low temperatures, the magnetization decreases along the b axis and becomes temperature-independent, a signature of Kondo coherence (*19*), whereas along the a axis the magnetization increases sharply and then shows a slight slope change at ~10 K, likely thanks to the Kondo coherence as well. No indication of phase transition at 10 K is observed from specific heat (see fig. S10) or resistivity measurements (Fig. 2C).

The high-temperature electrical resistivity $\rho(T)$ is typical of uncorrelated, paramagnetic moments in the presence of single-ion Kondo hybridization with the conduction band, which is responsible for the negative slope. At temperatures below a crossover marked by maximal resistivity, the Kondo hybridization yields coherent electronic bands, resulting in a metallic temperature-dependence (Fig. 2C). Although UTe_2 does not magnetically order, the low-temperature magnetic behavior shows that UTe_2 is on the verge of ferromagnetism. Below 10 K, the a axis magnetization exhibits neither conventional field/temperature (H/T) paramagnetic scaling nor Arrott-Noakes ferromagnetic critical scaling (*20*) (see fig. S7). Instead, the data scale in accordance with the Belitz-Kirkpatrick-Vojta (BKV) theory of metallic ferromagnetic quantum criticality (*21*). For temperatures < 9 K and fields < 3 T, the magnetization data scale as M/T^{β} versus $H/T^{\beta+\gamma}$ (Fig. 2D), using BKV critical exponents ($\beta = 1$, $\gamma = 0.5$, $\delta = 1.5$), behavior that has only otherwise been observed in $NiCoCr_{0.8}$ (*22*). This scaling, extending over five orders of magnitude, indicates that UTe_2 is a quantum critical ferromagnet, dominated by strong magnetic fluctuations. BKV theory applies to disordered metals and therefore, in principle, should not be applicable to UTe_2, which is in the clean limit (with a residual resistivity ratio of ~30). Instead, a ferromagnetic quantum phase transition is expected to be first order in the clean limit (*23*). Therefore, the observation of quantum criticality in UTe_2 calls for a different theory.

The transition from this correlated normal state to a superconducting ground state below the critical temperature $T_c = 1.6$ K is robust and sharp, as is evident in the low-temperature $\rho(T)$, ac magnetization $\chi(T)$ and specific heat $C(T)$ data (Fig. 3). There is a large residual value of the Sommerfeld coefficient $\gamma_0 = 55$ mJ/mol·K^2 in the superconducting state, or approximately half of the normal state value 110 mJ/mol·K^2, from which it is immediately apparent that either a large fraction of the sample is not superconducting or half of the conduction electrons at the chemical potential in this material are not gapped by the superconducting transition; the latter is indicative of an unconventional pairing mechanism, such as what occurs in UPt_3, UCoGe, and UGe_2 (*24*, *25*). There is little variation in the residual γ_0 value between samples of UTe_2 with slightly different T_c (fig. S12), suggesting that the large residual electronic density of states is likely an intrinsic, disorder-insensitive property of UTe_2. The normalized jump in $C(T)$ at T_c is $\Delta C/\gamma T_c = 2.5$, which is much larger than the conventional Bardeen-Cooper-Schrieffer value of 1.43 expected from weak coupling, placing the system in the strong coupling regime; here, γ includes only the part that superconducts below T_c and is obtained by subtracting the residual value from the full value. For temperatures below T_c, $C(T)$ follows a power law, with the exponent $n \sim 3.2$, reflecting the presence of point nodes.

Perhaps the most pronounced sign of unconventional superconductivity is obvious in the upper critical field H_{c2} of this superconductor. The resistivity as a function of temperature for different magnetic fields applied along the three principal crystal axes is shown in Fig. 4. The H_{c2}

[1]NIST Center for Neutron Research, National Institute of Standards and Technology, Gaithersburg, MD 20899, USA. [2]Department of Physics, Center for Nanophysics and Advanced Materials, University of Maryland, College Park, MD 20742, USA. [3]Ames Laboratory, U.S. Department of Energy and Department of Physics and Astronomy, Iowa State University, Ames, IA 50011, USA. [4]Department of Materials Science and Engineering, University of Maryland, College Park, MD 20742, USA.
*Corresponding author. Email: sran@umd.edu (S.R.); nbutch@umd.edu (N.P.B.)

is strongly anisotropic, with the value along b exceeding the two orthogonal directions by a factor of 4 at 1 K. The zero-temperature limit of H_{c2} along b well exceeds the highest measured magnetic field of 20 T, and we conservatively estimate a value of 40 T on the basis of the curvature of the critical field in UCoGe (*26*). The H_{c2} value is very sensitive to the alignment of magnetic field along the b axis (fig. S5).

The upper critical field of a conventional singlet superconductor is restricted by both of the orbital and paramagnetic pair-breaking effects. The zero-temperature orbital limit in superconductors is often well described by the Werthamer-Helfand-Hohenberg (WHH) theory $H_{orb} = 0.7 dH_{c2}dT_c|_{T_c} T_c$ (*27*). Although it can account for the response to field along the a axis, the WHH model otherwise disagrees drastically with our experimental results, most prominently along the b axis, where the slope of H_{c2} at T_c is ~17 T/K along b, which leads to an expected H_{orb} = 20 T for this direction. The conventional paramagnetic zero-temperature limit is given by $H_{para} = 1.86T_c$ (*28*), yielding H_{para} = 3 T for UTe_2. In the zero-temperature limit, the experimental H_{c2} value well exceeds H_{para} in all three directions and by almost an order of magnitude along the b axis, excluding spin-singlet order parameters.

The violation of the orbital limit in directions perpendicular to the magnetic easy axis (the a axis) is consistent with the behavior of the ferromagnetic superconductors (*29*) and differs qualitatively from the relatively low H_{c2} values found in other paramagnetic triplet superconductors (*8*, *30*). The unusual shape of the H_{c2} curve of UTe_2 resembles those of UCoGe (*26*) and URhGe (*31*), in which ferromagnetic spin fluctuations are believed to mediate the superconducting pairs (*25*). Although the normal state of UTe_2 is not magnetically ordered, the notable similarities suggest that its superconducting pairs are also mediated by ferromagnetic spin fluctuations, indicating that it is the end member of the series of ferromagnetic superconductors. When superconducting pairing is mediated by ferromagnetic spin fluctuations, the field dependence of the magnetization is coupled to the field dependence of the superconducting coupling strength (*32*), as verified in UCoGe and URhGe (*33*). The coupling strength λ as a function of magnetic field can be estimated based on the behavior of H_{c2} and γ (*24*). Especially prominent is the large increase in λ along the b axis of ~50% (fig. S6), which far exceeds the field-induced enhancement of λ in UCoGe (*33*).

Further confirmation of spin-triplet pairing in UTe_2 comes from NMR measurements, which are sensitive to internal magnetic fields (Fig. 3D). No change of the peak position is observed in the ^{125}Te-NMR spectra between normal and superconducting states, leading to a temperature-independent value of the ^{125}Te Knight shift K, which is proportional to the spin susceptibility of the quasiparticles forming the superconducting pairs. In singlet-paired superconductors, K decreases below T_c, whereas in UTe_2, K remains

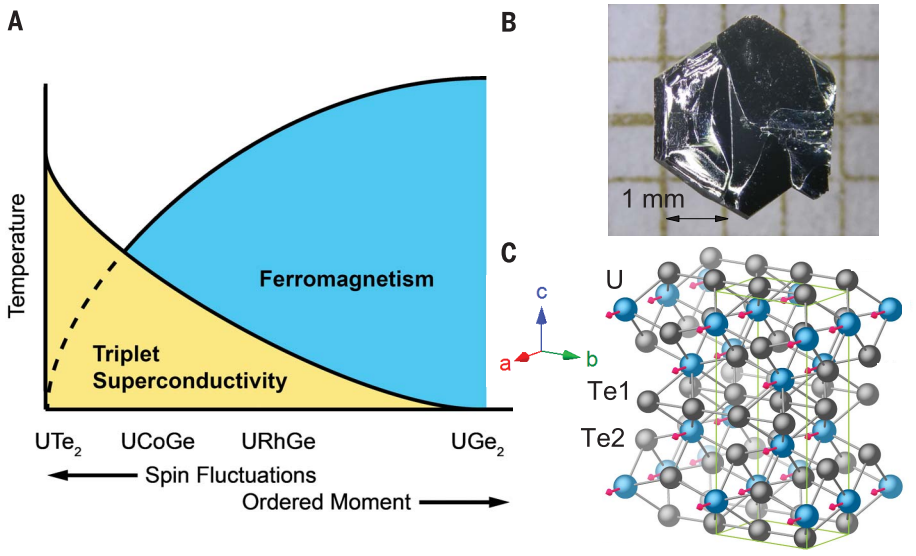

Fig. 1. Structure of UTe_2. (**A**) Global phase diagram of ferromagnetic superconductors; UTe_2 is located at the paramagnetic end of the series. (**B**) A photo of a single crystal of UTe_2 grown using chemical vapor transport method on the millimeter scale. (**C**) Crystal structure of UTe_2, with U atoms in blue and Te atoms in gray. The U atoms sit on chains parallel to the [100] a axis, which coincides with the magnetic easy axis, illustrated by the magenta arrows.

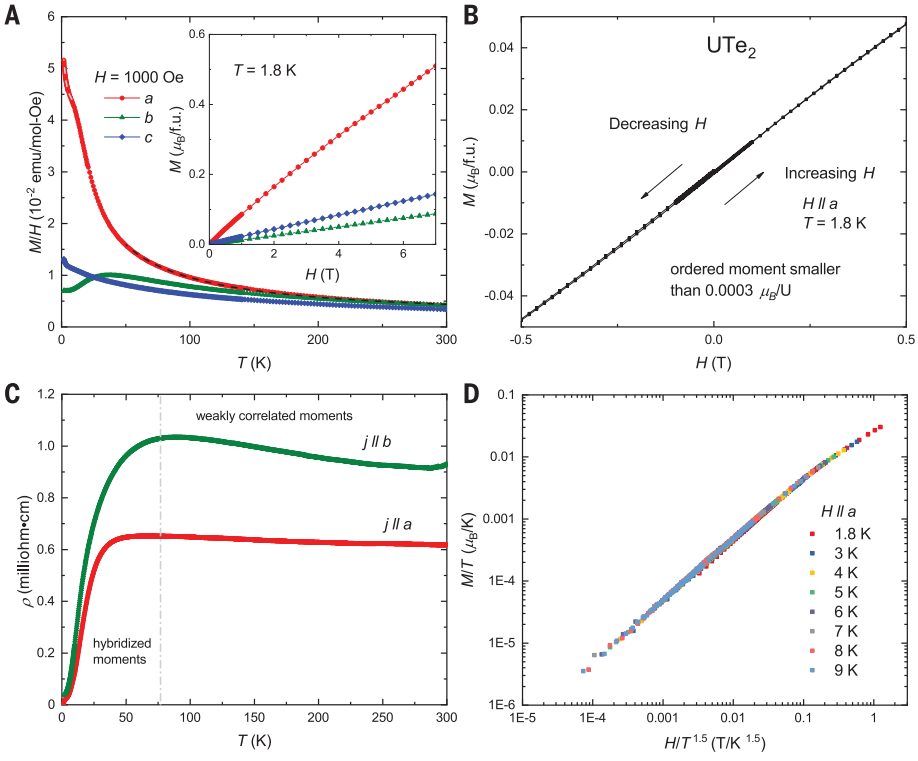

Fig. 2. Normal state properties of UTe_2. (**A**) Temperature dependence of magnetization for three different directions of magnetic field of 0.1 T. For the field in a direction, the gray dashed line is the fit to the power law in the low-temperature region, whereas the black dashed line is the fit to the Curie-Weiss law in the high-temperature region. (Inset) Magnetization as a function of applied field in three directions at 1.8 K. (**B**) Magnetization data at 1.8 K upon increasing and decreasing magnetic field in the low field range showing no hysteresis. The upper bound for an ordered moment is 0.0003 μ_B/U obtained from the zero field magnetization value. (**C**) Temperature dependence of electric resistivity data in zero magnetic field with electric current applied along a and b axes. (**D**) M/T as a function of $H/T^{1.5}$ for different temperatures. All the data collapse onto a single line. This scaling corresponds to the BKV theory of metallic ferromagnetic quantum criticality (see text).

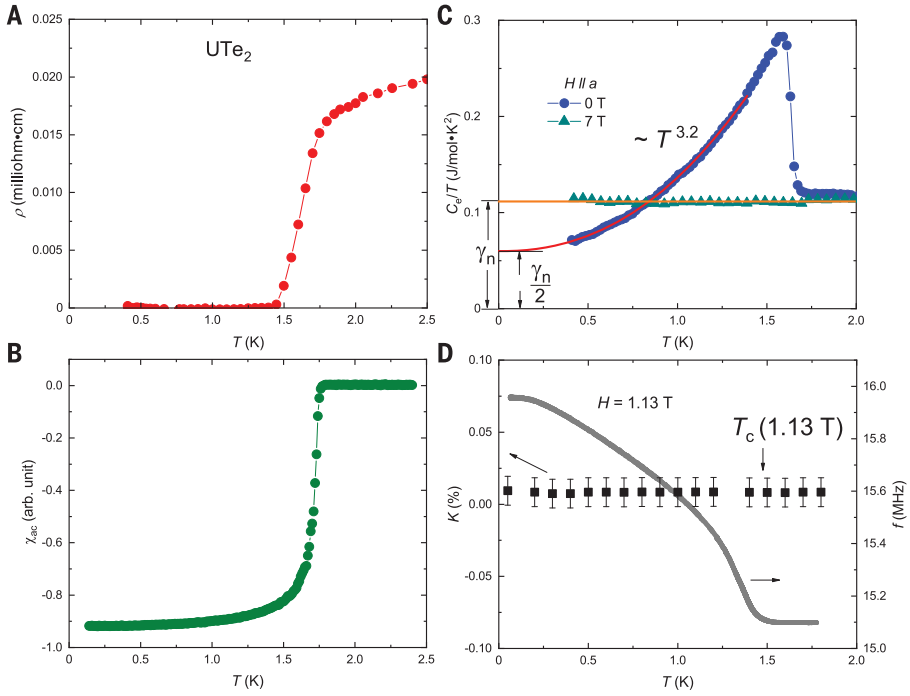

Fig. 3. Superconducting state properties of UTe_2. Temperature dependence of (**A**) resistivity and (**B**) ac magnetization data at low temperatures showing bulk superconductivity. (**C**) Electric contribution to heat capacity (phonon contribution has been subtracted as explained in the supplementary materials) in zero field and 7 T, divided by temperature, is shown as a function of temperature, illustrating γ in the superconducting and normal states. Magnetic field is applied along the *a* axis. (**D**) Temperature dependence of ^{125}Te NMR Knight shift K below and near T_c of powdered UTe_2 sample (left axis) and of the resonance frequency f of the NMR tank circuit confirming the superconducting state and T_c (right axis). H = 1.13 T.

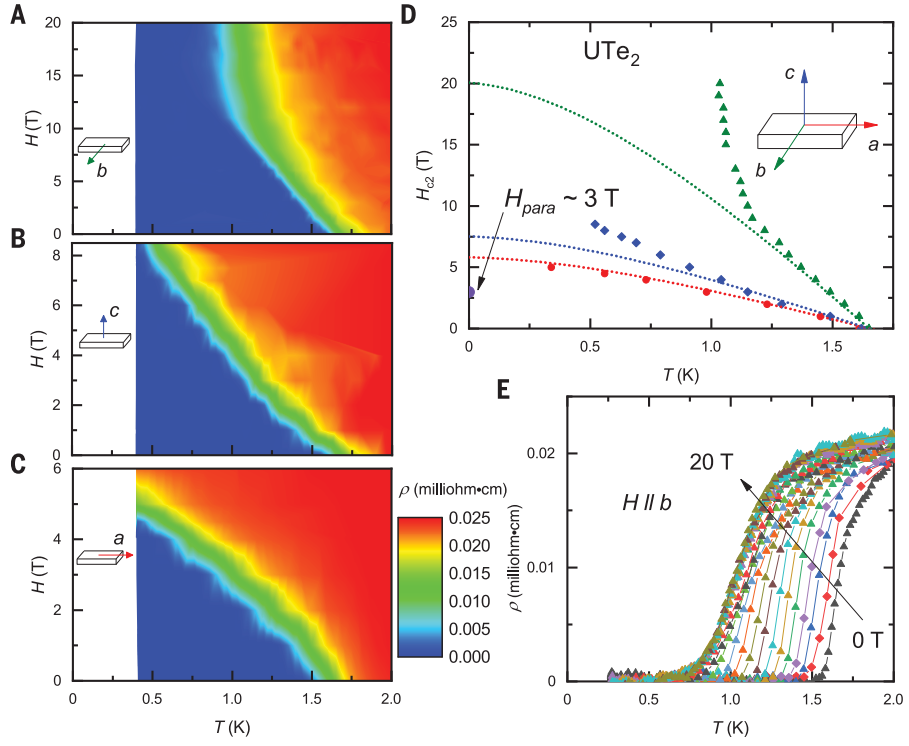

Fig. 4. Upper critical field H_{c2} of UTe_2. (**A** to **C**) Color contour plots of resistivity value as a function of temperature and magnetic field, with magnetic fields applied along (A) the *b* axis, (B) the *c* axis, and (C) the *a* axis. The current is applied along the *a* axis. (**D**) The H_{c2} value as a function of T in three directions. Dotted lines represent the WHH fit of the H_{c2} data. (**E**) Temperature-dependent resistivity data in magnetic fields applied along the *b* axis up to 20 T. Curves were measured using a constant magnetic field interval of 1 T.

constant on passing through T_c, signifying that the superconducting pair is a spin triplet (*34*, *35*). The unconventional nature of the superconductivity in UTe_2 is also observed in the temperature dependence of ^{125}Te nuclear spin-lattice relaxation rate $1/T_1$ (fig. S16). $1/T_1$ shows a steep drop below ~1 K without showing a Hebel-Slichter coherence peak in $1/T_1$ just below T_c, which is expected for conventional BSC superconductors. The temperature dependence of $1/T_1$ below T_c follows a power law behavior $1/T_1 \sim T^6$ which is close to the $1/T_1 \sim T^5$ relation expected from the point-node gap structure (*36*, *37*), consistent with the results of the specific heat measurement.

Having established clear evidence for spin-triplet pairing, one possible superconducting pairing symmetry consistent with a large fraction of ungapped electronic states of UTe_2 is the nonunitary triplet state, in which a two-component superconducting order parameter has two different energy gaps. However, such a state is generally not expected for paramagnetic, orthorhombic systems with strong spin-orbit coupling—this scenario applies to UTe_2 unless the effective spin-orbit coupling is demonstrated to be weak owing to special circumstances. No other standard archetype fits all measured properties of UTe_2, and any candidate state must account for the large field anisotropy, nodal gap structure, and the large residual electronic density of states, which are by themselves unusual. The high upper critical field itself suggests that the superconducting state resembles a condensate of equal spin pairs. One general possibility is band-selective superconductivity in a highly anisotropic electronic structure having multiple Fermi surfaces. Ongoing electronic structure measurements will help to determine whether such a description is applicable here. Regardless, explaining the relevance of ferromagnetic quantum criticality and the role of spin fluctuations will require further theoretical work.

The discovery of this superconducting state opens the door to advances in the study of spin-triplet pairing, topological electronic states, and their application to quantum information technology. As a paramagnetic version of ferromagnetic superconductors, UTe_2 is a promising topological superconductor (*38*) and may host Majorana excitations that can be detected by angle-resolved photoemission spectroscopy or scanning tunneling microscope (*39*).

REFERENCES AND NOTES

1. M. Sato, Y. Ando, *Rep. Prog. Phys.* **80**, 076501 (2017).
2. C. Beenakker, *Annu. Rev. Condens. Matter Phys.* **4**, 113–136 (2013).
3. S. D. Sarma, M. Freedman, C. Nayak, *npj Quantum Inf.* **1**, 15001 (2015).
4. J. Alicea, *Rep. Prog. Phys.* **75**, 076501 (2012).
5. A. Y. Kitaev, *Phys. Uspekhi* **44** (10S), 131–136 (2001).
6. N. Read, D. Green, *Phys. Rev. B* **61**, 10267–10297 (2000).
7. R. M. Lutchyn *et al.*, *Nat. Rev. Mater.* **3**, 52–68 (2018).
8. A. P. Mackenzie, Y. Maeno, *Rev. Mod. Phys.* **75**, 657–712 (2003).
9. C. Kallin, A. J. Berlinsky, *J. Phys. Condens. Matter* **21**, 164210 (2009).
10. Y. Maeno, S. Kittaka, T. Nomura, S. Yonezawa, K. Ishida, *J. Phys. Soc. Jpn.* **81**, 011009 (2012).
11. J. D. Strand *et al.*, *Science* **328**, 1368–1369 (2010).
12. E. R. Schemm, W. J. Gannon, C. M. Wishne, W. P. Halperin, A. Kapitulnik, *Science* **345**, 190–193 (2014).
13. S. S. Saxena *et al.*, *Nature* **406**, 587–592 (2000).

14. D. Aoki *et al*., . *Nature* **413**, 613–616 (2001).
15. N. T. Huy *et al*., *Phys. Rev. Lett.* **99**, 067006 (2007).
16. D. Aoki, K. Ishida, J. Flouquet, *J. Phys. Soc. Jpn.* **88**, 022001 (2019).
17. S. Ikeda *et al*., *J. Phys. Soc. Jpn.* **75** (suppl), 116–118 (2006).
18. H. Noël, M. Potel, R. Troc, L. Shlyk, *J. Solid State Chem.* **126**, 22–26 (1996).
19. G. R. Stewart, *Rev. Mod. Phys.* **56**, 755–787 (1984).
20. N. P. Butch, M. B. Maple, *Phys. Rev. Lett.* **103**, 076404 (2009).
21. T. R. Kirkpatrick, D. Belitz, *Phys. Rev. B* **91**, 214407 (2015).
22. B. C. Sales *et al*., *npj Quantum Materials* **2**, 33 (2017).
23. M. Brando, D. Belitz, F. M. Grosche, T. R. Kirkpatrick, *Rev. Mod. Phys.* **88**, 025006 (2016).
24. R. Joynt, L. Taillefer, *Rev. Mod. Phys.* **74**, 235–294 (2002).
25. V. P. Mineev, *Phys. Uspekhi* **60**, 121–148 (2017).
26. D. Aoki *et al*.,*J. Phys. Soc. Jpn.* **78**, 113709 (2009).
27. E. Helfand, N. R. Werthamer, *Phys. Rev.* **147**, 288–294 (1966).
28. A. M. Clogston, *Phys. Rev. Lett.* **9**, 266–267 (1962).
29. V. P. Mineev, *Phys. Rev. B* **95**, 104501 (2017).
30. Z. F. Weng *et al*., *Phys. Rev. Lett.* **117**, 027001 (2016).
31. F. Lévy, I. Sheikin, B. Grenier, A. D. Huxley, *Science* **309**, 1343–1346 (2005).
32. V. P. Mineev, *Phys. Rev. B* **83**, 064515 (2011).
33. B. Wu *et al*., *Nat. Commun.* **8**, 14480 (2017).
34. H. Tou *et al*., *Phys. Rev. Lett.* **77**, 1374–1377 (1996).
35. K. Ishida *et al*., *Nature* **396**, 658–660 (1998).
36. J. Yang, Z. T. Tang, G. H. Cao, G. Q. Zheng, *Phys. Rev. Lett.* **115**, 147002 (2015).
37. K. Katayama *et al*., *J. Phys. Soc. Jpn.* **76**, 023701 (2007).
38. A. K. C. Cheung, S. Raghu, *Phys. Rev. B* **93**, 134516 (2016).
39. J. D. Sau, S. Tewari, *Phys. Rev. B* **86**, 104509 (2012).
40. S. Ran, Replication data for: Nearly ferromagnetic spin-triplet superconductivity, Version 1, Harvard Dataverse (2019); https://doi.org/10.7910/DVN/UJAFUC.

ACKNOWLEDGMENTS

We thank W. Fuhrman, Y.-T. Hsu, T. Kong, S. Raghu, J. Sau, Y. Wang, S.-L. Xu, and V. Yakovenko for helpful discussions. We also thank H. Hodovanets for assistance during our experiments. **Funding:** Research at the University of Maryland was supported by the National Science Foundation Division of Materials Research Award DMR-1610349, U.S. Department of Energy (DOE) Award DE-SC-0019154, Air Force Office of Scientific Research Award FA9550-14-1-0332, and the Gordon and Betty Moore Foundations EPiQS Initiative through Grant GBMF4419. Research at Ames Laboratory was supported by the U.S. Department of Energy (DOE), Office of Basic Energy Sciences, Division of Materials Sciences and Engineering. Ames Laboratory is operated for the U.S. DOE by Iowa State University under Contract DE-AC02-07CH11358. **Author contributions:** S.R. and N.P.B. conceived of and designed the study. S.R. and S.R.S. synthesized the single crystalline samples. S.R., C.E., I.-L.L., H.K., and J.P. performed the electrical resistivity measurements. S.R., C.E., and T.M. performed the specific heat measurements. S.R., S.R.S., and M.Z. performed the magnetization measurements. S.R. and N.P.B. performed the neutron scattering measurements. Q.-P.D. and Y.F. performed the NMR measurements. All authors contributed to the preparation of the manuscript. **Competing interests:** The authors declare no competing interests. **Data and materials availability:** Data are available at Harvard Dataverse (*40*).

SUPPLEMENTARY MATERIALS

science.sciencemag.org/content/365/6454/684/suppl/DC1
Materials and Methods
Supplementary Text
Figs. S1 to S16

29 October 2018; accepted 12 July 2019
10.1126/science.aav8645

SOLAR CELLS

Stabilizing heterostructures of soft perovskite semiconductors

Yanbo Wang[1], Tianhao Wu[1], Julien Barbaud[1], Weiyu Kong[1], Danyu Cui[1], Han Chen[1], Xudong Yang[1,2]*, Liyuan Han[1,2,3]*

Here we report a solution-processing strategy to stabilize the perovskite-based heterostructure. Strong Pb–Cl and Pb–O bonds formed between a $[CH(NH_2)_2]_x[CH_3NH_3]_{1-x}Pb_{1+y}I_3$ film with a Pb-rich surface and a chlorinated graphene oxide layer. The constructed heterostructure can selectively extract photogenerated charge carriers and impede the loss of decomposed components from soft perovskites, thereby reducing damage to the organic charge-transporting semiconductors. Perovskite solar cells with an aperture area of 1.02 square centimeters maintained 90% of their initial efficiency of 21% after operation at the maximum power point under AM1.5G solar light (100 milliwatts per square centimeter) at 60°C for 1000 hours. The stabilized output efficiency of the aged device was further certified by an accredited test center.

The performance of perovskite solar cells (PSCs) relies on generation and extraction of charge carriers in working devices (*1*–*6*). Generally, it is the semiconductor heterostructure formed by perovskites and organic or inorganic electron-transporting layers (ETLs) and hole-transporting layers (HTLs) that enables photogenerated charge-carrier extraction. Construction of defect-free heterostructures is critical for large-scale application of perovskite-based optoelectronic devices (*7*–*9*). On the perovskite side of the heterostructure, component elements are assembled by relatively weak chemical bonds, including ionic bonds, hydrogen bonds, and van der Waals interactions (*10*–*12*). Because of their weak bonding nature, the soft crystal lattice of perovskites is easily decomposed, normally starting at the surface, and leads to great difficulties in forming stable heterostructures on perovskite surfaces. Several reports have demonstrated that perovskite components can permeate through the ETLs and HTLs, disordering the favored heterostructure and decreasing the charge extraction (*13*, *14*). Degradation of the heterostructure is accelerated by multiple factors such as illumination, heat, and electric fields (*15*–*17*).

Here we report a solution-processing strategy to stabilize the perovskite heterostructure by forming strong chemical bonds at the surface of soft perovskite films that can largely impede the loss of perovskite components, resulting in less damage to the organic HTL. In addition, the band offset of the heterostructure can benefit the hole extraction between the perovskite and the HTLs. We fabricated PSCs with efficiencies approaching 21% on an aperture area of 1.02 cm^2. The PSC with stabilized heterostructure exhibited excellent operational stability, maintaining 90% of its initial value after aging under operation conditions of AM1.5G solar light, 100 mW cm^{-2} at the maximum power point, under 60°C for 1000 hours. We also sent the aged device to a public test center [Calibration, Standards and Measurement Team at the Research Center for Photovoltaics, National Institute of Advanced Industrial Science and Technology (AIST), Japan]; a certified stabilized efficiency of 18.6% was obtained, still maintaining ~90% of its initial value.

The heterostructure consists of (i) a perovskite film with a surface rich in Pb and (ii) a chlorinated graphene oxide (Cl-GO) layer, where strong Pb–Cl and Pb–O bonds are formed to join the two layers. Figure 1A illustrates the formation of the Pb surface–rich perovskite film of $[CH(NH_2)_2]_x[CH_3NH_3]_{1-x}Pb_{1+y}I_3$ (also noted as $FA_xMA_{1-x}Pb_{1+y}I_3$). We used a dilute $Pb(SCN)_2$ solution as the Pb source that was spin-coated onto the perovskite film surface. The perovskite film with a surface rich in Pb was formed by heat treatment to remove volatile organic components like FASCN (formamidinium thiocyanate) or MASCN (methylamine thiocyanate).

We probed the surface of the perovskite film by x-ray photoelectron spectroscopy (XPS) (Fig. 1B). The peak intensity of Pb 4f core levels increased when more $Pb(SCN)_2$ was spin-coated onto the perovskite surface, whereas the peak intensity of I 3d core levels decreased (Fig. 1C), indicating the fabrication of a perovskite layer with a surface rich in Pb. The top morphology of the perovskite layer was not changed, as determined by scanning electron microscopy (Fig. 1D and fig. S1, A to E). The roughness of the Pb surface–rich perovskite layer was 25.1 ± 2.1 nm (Fig. 1E). The corresponding surface potential mapping and phase image are shown in fig. S2, A and B. Notably, $Pb(COOH)_2$ had an effect similar to $Pb(SCN)_2$, forming Pb surface–rich perovskite layers.

To form a stable heterostructure on the perovskite layer, we constructed strong chemical bonds of Pb–O and Pb–Cl by deposition of Cl-GO. A C-Cl peak at the binding energy of 289 eV appeared in the x-ray photoelectron spectrum of the C 1s core level in Cl-GO, in contrast to the x-ray photoelectron spectrum of GO (fig. S3, A and B) (*18*). We used scanning electron microscopy (SEM) to observe the perovskite/Cl-GO layer in comparison with the perovskite/GO layer. The surface of the perovskite/GO film was rough with poor uniformity (Fig. 2A), but Cl-GO spread well on the surface of perovskite film (Fig. 2B). Atomic force microscopy (AFM) over a large area (25 μm by 25 μm) on the film surface (Fig. 2, C and D) revealed surface roughnesses of 62.6 ± 24.31 nm and 24.6 ± 2.37 nm for perovskite/GO and perovskite/Cl-GO, respectively.

We also conducted Kelvin probe force microscopy (KPFM) to compare the work functions (WFs) of the corresponding three samples (figs. S2A and S4, A and B) (*19*). The surface potential distribution of perovskite/GO was relatively nonuniform compared with the potential distribution of the other two samples. After the calibration of the surface potential of the tip with Au reference (ψ_{Au}=5.10 eV), the WFs of each sample were 5.36, 5.33, and 5.43 eV, for perovskite, perovskite/GO, and perovskite/Cl-GO, respectively. The small difference in WFs between the perovskite and perovskite/GO samples was likely the result of the poor coverage or contact of GO that would not obviously change the WFs of perovskite. However, the WF of perovskite/Cl-GO was much different from that of perovskite and was near the Fermi level (E_F) of Cl-GO measured by ultraviolet photoelectron spectroscopy (UPS) (fig. S5, A and B) (*20*), indicating that Cl-GO made uniform contact with the surface of perovskite with high coverage.

We measured the x-ray photoelectron spectra of perovskite, perovskite/GO, and perovskite/Cl-GO to evaluate whether the good contact and coverage of perovskite/Cl-GO was the result of strong chemical bonding. No obvious change in the Pb 4f core level was observed between perovskite and perovskite/GO (Fig. 2E) (*21*), and we attributed this result to the poor coverage or contact of GO. However, the Pb 4f core level shifted up by 0.3 eV for perovskite/Cl-GO. We analyzed the O 1s core levels in x-ray photoelectron spectra for the pure GO, Cl-GO, perovskite/GO, and perovskite/Cl-GO (Fig. 2F). The O 1s core level of Cl-GO shifted from 532.21 to 532.52 eV, which indicates that O in Cl-GO would have stronger electron-withdrawing properties. In addition, the O 1s binding energy of perovskite/Cl-GO is ~0.10 eV lower than that of perovskite/GO, indicating that the oxidation state of O in Cl-GO is even lower than that in GO. These XPS results indicate that the Pb–O bond within perovskite/Cl-GO is stronger than that of perovskite/GO. In addition, we also observed the Cl 2p core levels of Cl-GO at 198.85 and 200.30 eV shift to 197.85 and 199.40 eV in perovskite/Cl-GO, respectively (Fig. 2G), indicating the formation of Pb–Cl bonds (*22*).

We used density functional theory (DFT) to calculate the electron density profiles of O in GO

[1]State Key Laboratory of Metal Matrix Composites, Shanghai Jiao Tong University, Shanghai 200240, China. [2]Center of Hydrogen Science, School of Materials Science and Engineering, Shanghai Jiao Tong University, Shanghai 200240, China. [3]Photovoltaic Materials Group, Center for Green Research on Energy and Environmental Materials, National Institute for Materials Science, Tsukuba, Ibaraki 305-0047, Japan.
*Corresponding author. Email: yang.xudong@sjtu.edu.cn (X.Y.); han.liyuan@sjtu.edu.cn (L.H.)

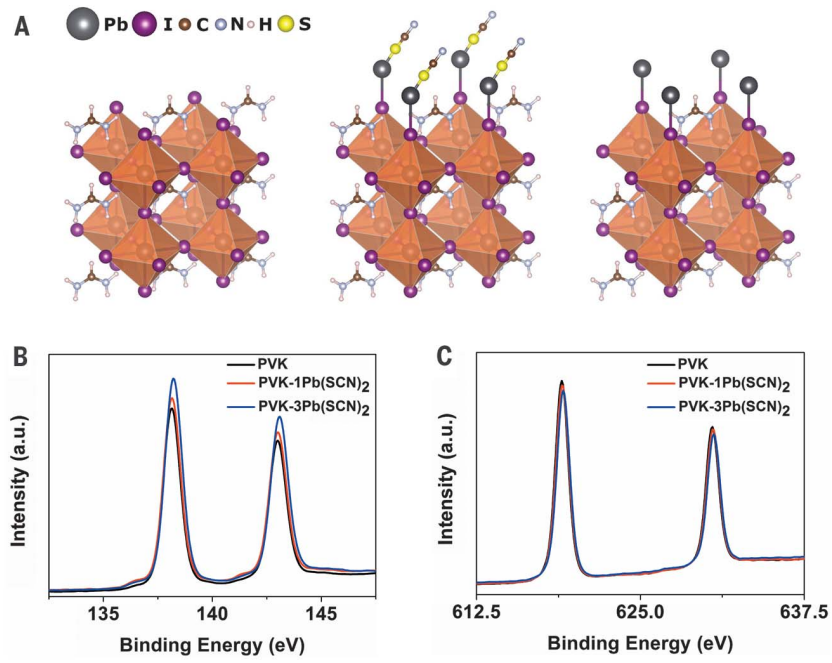

Fig. 1. Schematic of the fabrication process of the Pb surface–rich perovskite layer and characterization by XPS, SEM, and AFM. (**A**) Schematic drawing of the conversion process from the pristine perovskite layer, the layer treated with $Pb(SCN)_2$, and the Pb surface–rich perovskite layer. (**B**) XPS results of Pb 4f core levels of the pristine perovskite surface and the Pb surface–rich perovskite. PVK, perovskite; a.u., arbitrary units. (**C**) XPS results of I 3d core levels of the pristine perovskite surface and the Pb surface–rich perovskite. (**D** and **E**) (D) SEM image of the top morphology of the Pb surface–rich perovskite [Pb-1Pb$(SCN)_2$] and (E) *xy*-plane film morphology of the PVK-1Pb$(SCN)_2$ measured by AFM. PVK-1Pb$(SCN)_2$ and PVK-3Pb$(SCN)_2$ denote perovskite treated with 10 or 30 μl of a dilute solution of $Pb(SCN)_2$.

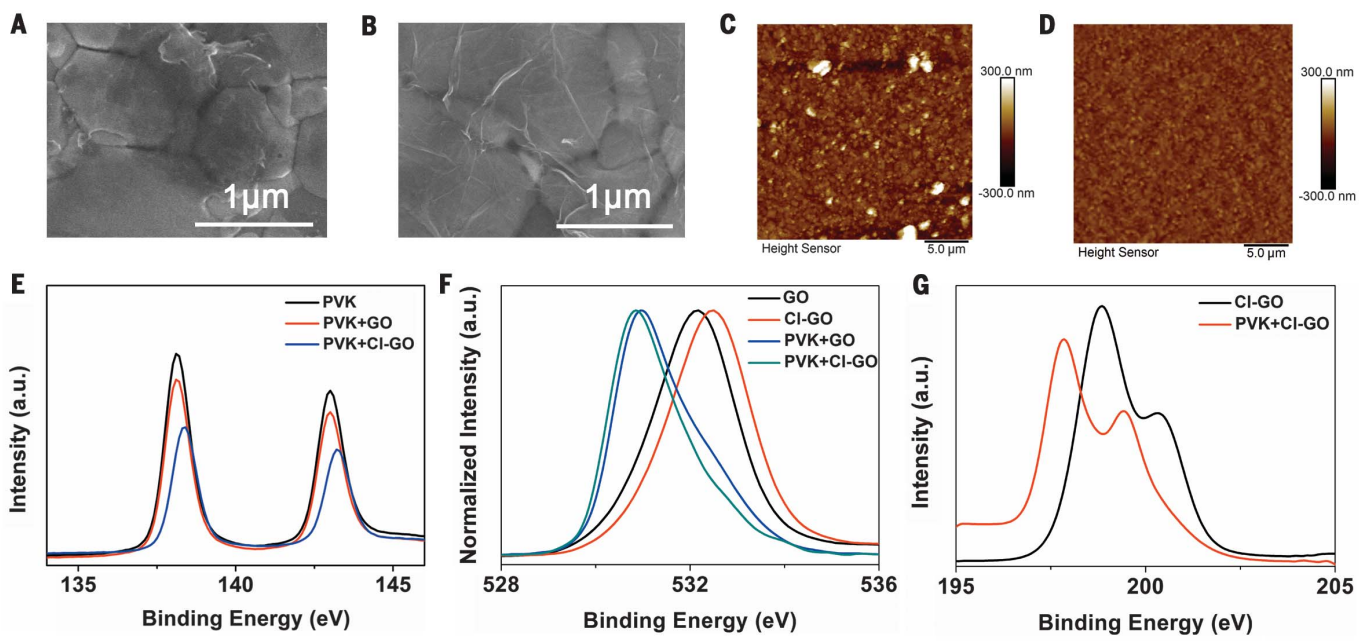

Fig. 2. Characterization of GO/Cl-GO on the surface of perovskite layer. (**A** and **B**) Top SEM image of (A) perovskite/GO and (B) perovskite/Cl-GO. (**C** and **D**) *xy*-plane film morphology of (C) perovskite/GO and (D) perovskite/Cl-GO measured by AFM. (**E**) X-ray photoelectron spectrum of the Pb 4f core level of the perovskite layer (black), perovskite/GO (red), and perovskite/Cl-GO (blue). (**F**) X-ray photoelectron spectrum of the O 1s core level of GO (black), Cl-GO (red), perovskite/GO (blue line), and perovskite/Cl-GO (green). (**G**) X-ray photoelectron spectrum of the Cl 2p core levels of Cl-GO (black) and perovskite/Cl-GO (red). For ease of comparison, the scale bars in (C) and (D) are the same as that in Fig. 1E.

(fig. S6A) and structurally optimized Cl-GO (fig. S6B). The Cl atom develops a bonding orbital with the closest carbon. We evaluated the influence of the chloride on the neighboring atoms by using projected density of states (PDOS) to verify the shift in O 1s. The PDOS of Cl-GO is the shifted image of GO, with a ~0.30-eV difference (fig. S7A). The matching of the shifted peaks (~0.31-eV shift) is shown in fig. S7B. This ~0.30-eV shift between the energies of electrons on the O 1s orbitals is in good agreement with the experimental value obtained by XPS and shows that DFT simulations confirm the influence of the Cl atom on the binding energy of the O 1s orbitals.

We further compared the energy levels of Cl-GO with other HTLs. The bandgap of Cl-GO was determined by ultraviolet-visible (UV-vis) absorption spectroscopy (fig. S8A) and calculated by the Kubelka-Munk function–converted plots (fig. S8B) (*23*). When combined with the UPS results (fig. S5), the energy levels of Cl-GO were obtained (fig. S9). The valence band maximum (VBM) of the perovskite was also measured by UPS to be −5.80 eV (fig. S10) (*24*). The highest occupied molecular orbital (HOMO) level of Cl-GO (−5.45 eV) is in the middle of the VBM of perovskite (−5.80 eV) and the HOMO level of polytriarylamines (PTAA) (−5.16 eV; fig. S11) or 2,2′,7,7′-tetrakis(*N*,*N*-di-*p*-methoxyphenylamine)-9,9′-spirobifluorene (Spiro-MeOTAD) (−5.10 eV; fig. S12), respectively (*25*, *26*), which would provide a more efficient pathway for the extraction of holes than GO (with a HOMO energy level of −5.85 eV).

To reveal the effect of perovskite/Cl-GO on the stability of heterostructure and the device, we measured the HOMO level of the HTL of a device with the structure of conducting glass/ETL/perovskite/HTL/Au electrode. The HTL was PTAA or Spiro-MeOTAD. The device was encapsulated and then aged at the maximum power point under light-soaking (AM1.5G, 100 mW cm^{-2}) for 200 hours at 60°C. We removed the package and Au electrode and measured the HTL of PTAA or Spiro-MeOTAD by UPS (figs. S11 and S12). From the high–binding energy region of the ultraviolet photoelectron spectra, we could see that the E_F of each material did not change appreciably, but the difference in the low–binding energy region indicates that the gap between the Fermi level and the HOMO energy level became larger. Thus, the aged PTAA and Spiro-MeOTAD were no longer typical p-type materials.

In contrast, we fabricated a device with a heterostructure of perovskite/Cl-GO/HTL, as well as a GO-based device as a reference. The fresh sample was first measured by AFM and KPFM to obtain the initial morphology and surface potential information (fig. S13). The corresponding devices with electrodes and encapsulation were aged with the same UPS aging test. After removing the package and Au electrode, we observed that the morphology of perovskite/PTAA and perovskite/GO/PTAA (fig. S14, A and B) differed substantially from that of the fresh perovskite/PTAA sample (fig. S13A). In contrast, the perovskite/Cl-GO/PTAA sample preserved the original morphology (fig. S14C), even though no appreciable difference in roughness was observed for all three samples. The surface potential of aged perovskite/Cl-GO/PTAA was consistent with that of the fresh sample, but the surface potential of the aged perovskite/PTAA and perovskite/GO/PTAA is 68 and 31 mV higher, respectively, than that of the fresh sample (Fig. 3, A to C). In addition, the surface potential distribution of the aged samples is analyzed in fig. S15; the aged sample with Cl-GO showed the narrowest distribution, indicating the homogeneous surface of PTAA in the perovskite/Cl-GO device. The same tendency was observed for the Spiro-MeOTAD–based samples (figs. S16 to S18). As a result, we can conclude that a stabilized heterostructure of perovskite/Cl-GO/HTL was formed.

We also analyzed the spatial distribution of perovskite components within Spiro-MeOTAD by time-of-flight secondary ion mass spectroscopy (TOF-SIMS) for the devices after the UPS aging test (fig. S19). The count of the I^- signal from the Spiro-MeOTAD layer is substantially reduced for perovskite/Cl-GO. The mapping signal of I^- in Spiro-MeOTAD was counted and presented by pixel ratio in Fig. 3, D to F. The HTL material layers in the aged control device and the perovskite/GO-based device were already fully occupied by I^-, whereas only a low signal was observed from the aged perovskite/Cl-GO sample.

We tested the thermal stability of the perovskite/Cl-GO heterostructure by aging the samples at 85°C for 150 hours under a nitrogen atmosphere.

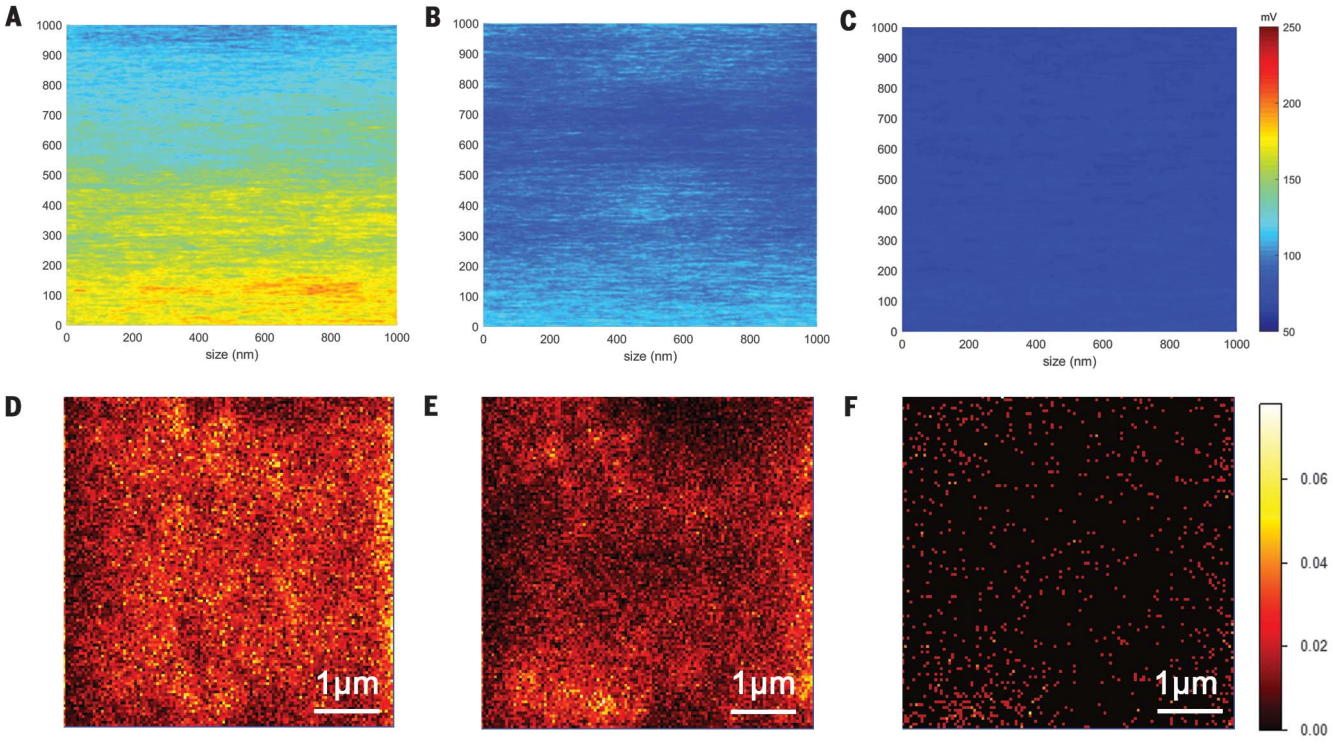

Fig. 3. Degradation of organic HLTs probed by KPFM and TOF-SIMS. (**A** to **C**) *xy*-plane potential mapping images of (A) perovskite/PTAA, (B) perovskite/GO/PTAA, and (C) perovskite/Cl-GO/PTAA measured by KPFM. (**D** to **F**) Mapping of TOF-SIMS signals of I^- in the HTLs for (D) perovskite/Spiro-MeOTAD, (E) perovskite/GO/Spiro-MeOTAD, and (F) perovskite/Cl-GO/Spiro-MeOTAD. All samples were aged after 200 hours of light-soaking at the maximum power point at 60°C.

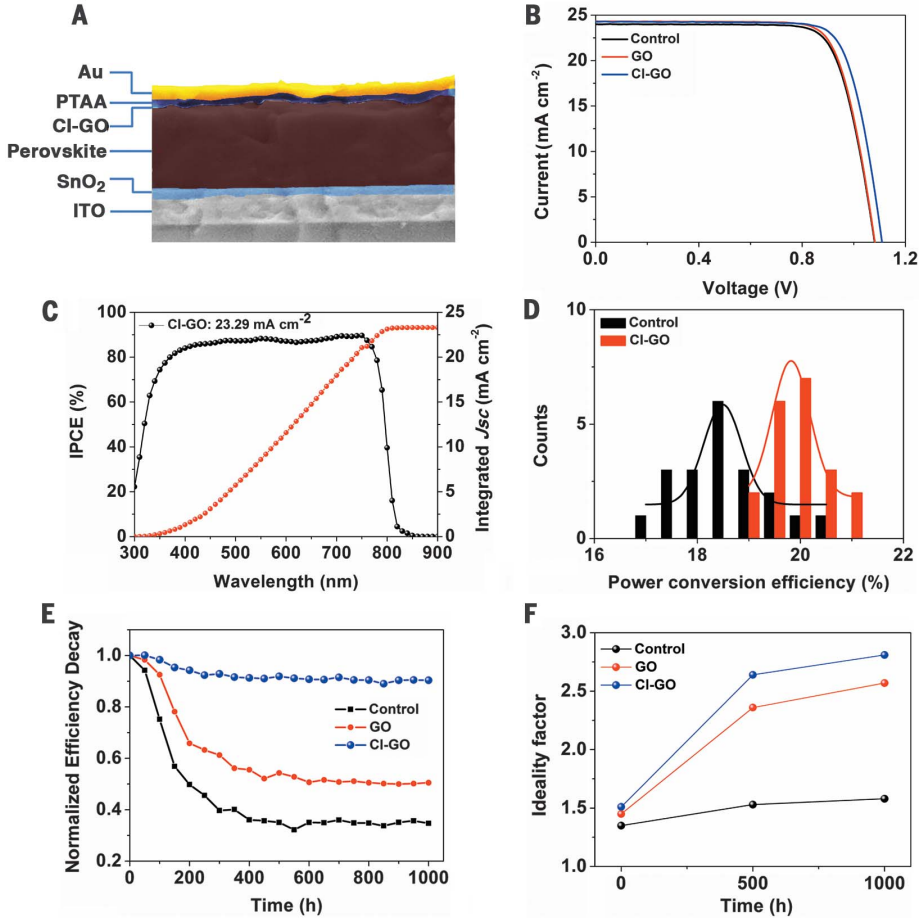

Fig. 4. Structure and performance of the PSC with an aperture area of 1.02 cm^2. (**A**) Cross-sectional SEM image of the cell. ITO, indium tin oxide. (**B**) *I-V* curves of the cells measured under forward scan. (**C**) IPCE spectrum and integrated current of the cell with perovskite/Cl-GO. *Jsc*, short-circuit current density. (**D**) Histogram of average power conversion efficiency values of the cell. (**E**) Operational stability of the control cell and the cell with GO or Cl-GO. (**F**) Ideality factors of the cells with perovskite/PTAA, perovskite/GO/PTAA, or perovskite/Cl-GO/PTAA before and after the aging test. The aging test was conducted under 1000 hours of light-soaking (AM1.5G, 100 mW cm^{-2}) at the maximum power point at 60°C. All cells were encapsulated.

The XRD patterns as well as the light absorption of perovskite/Cl-GO showed no obvious changes during the test (fig. S20). However, the UV light absorption of perovskite without Cl-GO gradually dropped during the test and the peak of PbI_2 around 500 nm became more prominent, indicating the decomposition of perovskite (fig. S20). The XRD results confirmed decomposition because the signal at 11.8° represents the arising δ phase and the signal at 12.8° could be denoted as emerging PbI_2. The contact angle with water in air rose from 50° for the perovskite sample to 76° for the perovskite/Cl-GO sample (fig. S21). This larger contact angle should enhance moisture stability, as confirmed by UV-vis absorption spectroscopy (fig. S22).

We fabricated PSCs with a perovskite/Cl-GO heterostructure on an aperture area of 1.02 cm^2. The cross-sectional SEM image is shown in Fig. 4A, and the energy levels of the cell are aligned in fig. S23. The current-voltage (*I-V*) curves of cells with different heterostructures are presented in Fig. 4B. The cell with perovskite/Cl-GO obtained a high efficiency of 21.08% under forward scan with a short-circuit current density of 23.82 mA cm^{-2}, an open-circuit voltage of 1.12 V, and a fill factor of 0.79. The detailed parameters for the other two cells can be found in table S2.

Figure 4C shows the incident photo-to-electron conversion efficiency (IPCE) of the cell with perovskite/Cl-GO; the integrated short-circuit current was calculated to be 23.29 mA cm^{-2}, which matched well with the observed short-circuit current. Twenty cells of each batch were fabricated, and the histogram of average power conversion efficiency values is presented in Fig. 4D. The cells with different heterostructures were encapsulated and aged under continuous light-soaking at the maximum power point at 60°C. The corresponding stability results are shown in Fig. 4E; the cell with the heterostructure of perovskite/Cl-GO maintained 90% of its initial value after 1000 hours, whereas the control cell and the cell with GO experienced reductions of 65 and 50%, respectively. The steady-state efficiencies across five cells with perovskite/Cl-GO were tracking at the maximum power point before and after the 1000-hour aging test (fig. S24); no obvious change in steady-state efficiency was found for either fresh or aged cells.

We also sent our aged cell with the perovskite/Cl-GO heterostructure to AIST; a certified stabilized efficiency of 18.6% was obtained on an aperture area of 1.02 cm^2 (fig. S25), which indicates that the device can operate with high efficiency for longer than 1000 hours. In addition, the Spiro-MeOTAD cells exhibited similar performance trends before and after the same aging test, indicating the effectiveness of this stable heterostructure (fig. S26).

We further calculated the ideality factors of the cells with perovskite/PTAA, perovskite/GO/PTAA, or perovskite/Cl-GO/PTAA. The photovoltaic parameters under different light intensity were first measured for each cell (fig. S27); the fresh cells for all three samples showed similar initial ideality factors ranging from 1.35 to 1.51. However, after the aging test, the ideality factor of the cell with perovskite/PTAA or perovskite/GO/PTAA increased to >2 (Fig. 4F), which indicates a serious charge-carrier recombination (*17*, *27*). The cell with the perovskite/Cl-GO heterostructure maintained an ideality factor ~1.6, indicating suppressed interface recombination and efficient charge transfer.

Compared with the perovskite/PTAA and perovskite/GO/PTAA samples, the perovskite/Cl-GO/PTAA sample exhibited the lowest steady-state photoluminescence (PL) signal (fig. S28A), consistent with time-resolved photoluminescence (TRPL) results (fig. S28B). The perovskite film itself had a decay time of 243 ns, but the lifetime in a perovskite/Cl-GO/PTAA heterostructure was 4.1 ns, compared with 5.3 ns in perovskite/GO/PTAA and 5.4 ns in perovskite/PTAA. The charge extraction was also characterized by transient photocurrent decay and photovoltage decay (fig. S28, C and D) (*28*, *29*). The photovoltage decay increased from 22.9 μs (control) to 23.7 μs (GO) and 60.4 μs (Cl-GO), and the photocurrent decay decreased from 1.87 μs (control) to 1.64 μs (GO)

and 1.25 μs (Cl-GO), respectively. These results indicated that reduced charge recombination and more-efficient charge extraction occurred in the perovskite/Cl-GO/PTAA heterostructure.

REFERENCES AND NOTES

1. A. Kojima, K. Teshima, Y. Shirai, T. Miyasaka, *J. Am. Chem. Soc.* **131**, 6050–6051 (2009).
2. J. H. Im, C. R. Lee, J. W. Lee, S. W. Park, N. G. Park, *Nanoscale* **3**, 4088–4093 (2011).
3. H. S. Kim *et al*., *Sci. Rep.* **2**, 591 (2012).
4. M. M. Lee, J. Teuscher, T. Miyasaka, T. N. Murakami, H. J. Snaith, *Science* **338**, 643–647 (2012).
5. E. Edri *et al*., *Nat. Commun.* **5**, 3461 (2014).
6. V. Roiati *et al*., *Energy Environ. Sci.* **7**, 1889–1894 (2014).
7. J. Y. Jeng *et al*., *Adv. Mater.* **25**, 3727–3732 (2013).
8. Y. Wu *et al*., *Nat. Energy* **1**, 16148 (2016).
9. Q. Jiang *et al*., *Nat. Photonics* **13**, 460–466 (2019).
10. A. Amat *et al*., *Nano Lett.* **14**, 3608–3616 (2014).
11. C. Motta *et al*., *Nat. Commun.* **6**, 7026 (2015).
12. F. El-Mellouhi *et al*., *ChemSusChem* **9**, 2648–2655 (2016).
13. S. Kim *et al*., *Sci. Rep.* **7**, 1200 (2017).
14. Y. C. Zhao *et al*., *J. Phys. Chem. C* **121**, 14517–14523 (2017).
15. H. F. Zarick, N. Soetan, W. R. Erwin, R. Bardhan, *J. Mater. Chem. A* **6**, 5507–5537 (2018).
16. G. Y. Kim *et al*., *Nat. Mater.* **17**, 445–449 (2018).
17. W. Tress *et al*., *Energy Environ. Sci.* **11**, 151–165 (2018).
18. G. Beamson, D. Briggs, *High Resolution XPS of Organic Polymers: The Scienta ESCA 300 Database* (Wiley, 1992).
19. R. J. Davis *et al*., *J. Mater. Chem.* **21**, 1721–1729 (2011).
20. D. Konios *et al*., *J. Mater. Chem. A* **4**, 1612–1623 (2016).
21. W. Z. Li *et al*., *J. Mater. Chem. A* **2**, 20105–20111 (2014).
22. H. Zhao *et al*., *Nanotechnology* **27**, 495405 (2016).
23. H. C. Hsu *et al*., *Nanoscale* **5**, 262–268 (2013).
24. D. Luo *et al*., *Science* **360**, 1442–1446 (2018).
25. Z. Hawash, L. K. Ono, S. R. Raga, M. V. Lee, Y. B. Qi, *Chem. Mater.* **27**, 562–569 (2015).
26. J. Luo *et al*., *Energy Environ. Sci.* **11**, 2035–2045 (2018).
27. M. Cai *et al*., *Joule* **2**, 296–306 (2018).
28. Y. Li *et al*., *J. Am. Chem. Soc.* **137**, 15540–15547 (2015).
29. B. Chen, M. Yang, S. Priya, K. Zhu, *J. Phys. Chem. Lett.* **7**, 905–917 (2016).

ACKNOWLEDGMENTS

We thank H. Li and J. Liu from the Instrumental Analysis Center of Shanghai Jiao Tong University (China) for assistance with AFM and KPFM measurements, Z. Bao from the Instrumental Analysis Center of Shanghai Jiao Tong University (China) for assistance with SEM measurements, Y. Han and Y. Zhang from the Instrumental Analysis Center of Shanghai Jiao Tong University (China) for assistance with TOF-SIMS measurements, and Y. Wu from East China University of Science and Technology (China) for assistance with PL and TRPL measurements. **Funding:** This work was supported by the National Natural Science Foundation of China (grant nos. 11574199, 11674219, and 11834011), the Program for Professor of Special Appointment (Eastern Scholar) at Shanghai Institutions of Higher Learning, and a KAKEHI Grant of Japan (grant no. 18H02078). **Author contributions:** Y.W., X.Y., and L.H. conceived of the work. Y.W. and W.K. fabricated and characterized solar cells. Y.W. conducted the SEM, AFM, KPFM, UPS, TOF-SMIS, XRD, UV-vis, PL, and TRPL measurements. T.W. synthesized the GO and Cl-GO and performed the XPS measurements. J.B. conducted the DFT calculation and participated in the discussion of KPFM. D.C. participated in the discussion of UPS results. H.C. assisted with measurement of transient photocurrent and transient photovoltage. Y.W. wrote the first draft of the manuscript. Y.W., X.Y., and L.H. revised the manuscript. All authors analyzed the data and reviewed the manuscript. **Competing interests:** None declared. **Data and materials availability:** All data needed to evaluate the conclusions in the paper are present in the manuscript or the supplementary materials.

SUPPLEMENTARY MATERIALS

science.sciencemag.org/content/365/6454/687/suppl/DC1
Materials and Methods
Supplementary Text
Figs. S1 to S28
Tables S1 and S2
References (*30*–*36*)

25 April 2019; accepted 17 July 2019
10.1126/science.aax8018

GEOCHEMISTRY

Primordial and recycled helium isotope signatures in the mantle transition zone

S. Timmerman[1]*†, M. Honda[1], A. D. Burnham[1], Y. Amelin[1], S. Woodland[2], D. G. Pearson[2], A. L. Jaques[1], C. Le Losq[1], V. C. Bennett[1], G. P. Bulanova[3], C. B. Smith[3], J. W. Harris[4], E. Tohver[5]

Isotope compositions of basalts provide information about the chemical reservoirs in Earth's interior and play a critical role in defining models of Earth's structure. However, the helium isotope signature of the mantle below depths of a few hundred kilometers has been difficult to measure directly. This information is a vital baseline for understanding helium isotopes in erupted basalts. We measured He-Sr-Pb isotope ratios in superdeep diamond fluid inclusions from the transition zone (depth of 410 to 660 kilometers) unaffected by degassing and shallow crustal contamination. We found extreme He-C-Pb-Sr isotope variability, with high $^3He/^4He$ ratios related to higher helium concentrations. This indicates that a less degassed, high-$^3He/^4He$ deep mantle source infiltrates the transition zone, where it interacts with recycled material, creating the diverse compositions recorded in ocean island basalts.

Wide ranges of Sr-Nd-Hf-Pb isotopic compositions for ocean island basalts (OIBs) and continental plume–related basalts indicate the existence of different geochemical reservoirs in the mantle (*1*, *2*). This is also evident from their widely variable helium (He) isotope composition of 4.3 to 50 (*1*, *3*, *4*), with $^3He/^4He$ ratios expressed as R/Ra, the ratio of $^3He/^4He_{sample}$ to the $^3He/^4He_{air}$ standard (1.4×10^{-6}). The chemical evolution, nature, and scale of these different reservoirs remain problematic. By contrast, mid–ocean ridge basalts (MORBs) are formed by shallow melting of the upper mantle and show much more uniform helium isotope compositions [8 ± 1 R/Ra (SD)] (*5*) and more homogeneous Sr-Nd-Hf-Pb isotope compositions. The higher R/Ra values of plume-related basalts relative to MORBs are taken as key evidence of a primordial undegassed reservoir with high $^3He/^4He$ ratios present in Earth's lower mantle (*6*–*10*). However, the preservation of such a reservoir over the Earth's history has been questioned on the basis of geophysical evidence of slab subduction into the lower mantle and mantle convection models (*11*). An upper mantle location for the high-$^3He/^4He$ reservoir has also been suggested on the basis of seismic anomalies, heterogeneities sampled by small degrees of melt, and modeled low–U-Th/^3He domains formed through melt depletion (*1*, *12*–*17*). Resolving the existence and location of a long-term preserved, primordial, undegassed, high-$^3He/^4He$ reservoir, and where it interacts with other reservoirs in the mantle, is key to understanding the evolution of Earth and deep mantle convection.

Diamonds are physically and chemically robust, allowing retention of He isotope signatures that reflect their formation environment (*18*–*20*). Here, we present helium isotope data of fluid inclusions from sublithospheric diamonds; these data provide an unparalleled perspective on He isotopes from transition zone depths (410 to 660 km). We studied 24 diamonds (1.3 to 6 mm in size) from the Juina-5 and Collier-4 kimberlites and São Luiz River (Juina, Brazil). The Juina area is renowned for the unusually predominantly sublithospheric origin of its diamonds (*21*–*23*). Our diamonds have physical features and properties that are consistent with other diamonds from Earth's transition zone (410 to 660 km depth), including dislocations or diffuse growth zones (database S1) and no detectable nitrogen (N) or fully aggregated N defects (database S2) (*24*). The diamonds contain mineral inclusions seen in other transition zone diamonds (*21*, *25*, *26*), including breyite (database S3 and fig. S1, A and B), coesite, carbonates, sulfides, and amorphous silicate (fig. S1, C and D). Although only diamond C4-106 has a confirmed superdeep origin, on the basis of its breyite mineral inclusions, all diamonds show typical sublithospheric features. After establishing the sublithospheric origin for our diamonds, we measured helium isotopes of the fluid inclusions. We combined these data with picogram analyses of Pb-Sr isotopes of fluid inclusions, trace-element patterns of fluid inclusions, and carbon isotope values of the diamond hosts (*24*).

Helium is trapped in submicrometer fluid inclusions (database S1), as the Juina diamonds are relatively young, likely formed less than 500 million years ago (*23*, *27*), and He diffusion through diamond is extremely slow (*19*). Preservation of He and its isotope signatures in diamond is supported

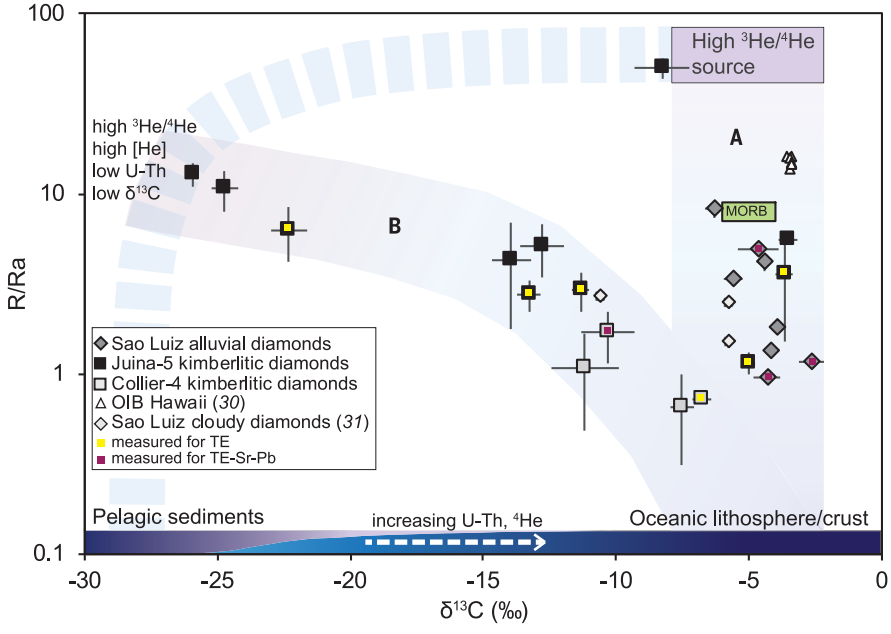

Fig. 1. Helium isotope compositions (R/Ra) of fluid inclusions and carbon isotope compositions ($\delta^{13}C$) of their diamond hosts. Two trends (A and B) are observed in the studied sublithospheric Brazilian diamonds. Values for São Luiz cloudy diamonds (*31*), OIBs from Hawaii (*30*), and MORBs (*5*) are shown for comparison. R/Ra values are shown with 1 SD uncertainty, and the $\delta^{13}C$ values are averages ± 1 SD variations of multiple analyses across the diamond.

[1]Research School of Earth Sciences, Australian National University, 142 Mills Road, Acton, ACT 2601, Australia. [2]Earth and Atmospheric Sciences, University of Alberta, 116 Street and 85 Avenue, Edmonton, Alberta T6G 2R3, Canada. [3]School of Earth Sciences, University of Bristol, Queens Road, Bristol BS8 1QU, UK. [4]School of Geographical and Earth Sciences, Gregory Building, University of Glasgow, Glasgow G12 8QQ, UK. [5]University of Sao Paolo, Sao Paolo, Brazil.
*Corresponding author. Email: suzette.timmerman@anu.edu.au
†Present address: Institut für Mineralogie, University of Münster, Corrensstrasse 24, 48149 Münster, Germany.

by He heterogeneities within individual diamonds (*18*, *20*). We removed the outer rim of the diamond to eliminate any ^{4}He implantation [up to 30 μm from the diamond surface (*19*)] from the surrounding matrix, either from the mantle or the kimberlite. The potential impact of production of radiogenic ^{4}He within the diamond generally results in an R/Ra shift of <0.8, based on low U-Th-Sm concentrations measured on 10 of the studied diamonds (database S2) and assuming a diamond formation age of 500 million years ago (fig. S2). Cosmogenic production of ^{3}He at Earth's surface may also modify He isotope compositions, which is a concern for diamonds from alluvial sources (São Luiz River). The highest R/Ra value for our diamonds was from the Juina-5 kimberlite, and it coincides with the R/Ra of 49.8 from Baffin Island picrites (*4*), the highest observed in basalts. Diamonds recovered from kimberlite pipes are less likely to have been exposed to cosmic rays, but we cannot exclude exposure entirely, as the diamonds from Collier-4 and Juina-5 kimberlite pipes were likely recovered from the near-surface oxidized yellow ground kimberlite material. Thus, our studied diamonds provide the most direct and undegassed evidence of the variation in helium isotope compositions in Earth's transition zone.

Previous studies of δ^{13}C-δ^{18}O diamond-mineral inclusion correlations (*25*) and major and trace-element abundances of mineral inclusions (*23*, *28*) have established the presence of subducted material in the transition zone under the Juina region. The He isotopic signatures released from the sparse fluid inclusions vary from 0.7 to 49.9 R/Ra (Figs. 1 and 2). This range is larger than the variation found in plume-related basalts. Lead isotope ratios also bear similarities to plume-related basalts (Fig. 3, fig. S3, and database S2) and, along with trace-element patterns (Fig. 4 and fig. S4), provide evidence for the involvement of subducted material. Furthermore, the large range in ^{87}Sr/^{86}Sr ratios (0.7051 to 0.7260) (Fig. 3) suggests the involvement of old continental crust [enriched mantle (EMII) component]. Low Rb/Sr ratios that do not support the observed radiogenic Sr can be caused by subduction-related loss of Rb relative to Sr. A negative Nb anomaly characterizing the involvement of subducted material is present in all the trace-element patterns of our studied samples. This anomaly implies that a recycled crustal component, and not the ambient mantle, dominates the trace-element budget in the fluid inclusions. Furthermore, the negative Y/Ho, negative Sr, and positive Eu anomalies and the Zr-Hf depletion measured in our samples are all best explained by shallow (crustal) processes (*24*). Eu anomalies range from 0.01 to 3.2 Eu/Eu* and correlate positively with La/Nd ratios. We found no correlation of trace-element ratios with diamond host C or fluid He isotope compositions, indicating decoupling of volatile from lithophile elements.

The carbon isotope compositions of the diamonds form two arrays with the R/Ra values (Fig. 1). The large range in R/Ra values (trend A, Fig. 1) could be the result of mixing of various mantle reservoirs and oceanic crust–lithosphere with different R/Ra ratios (*29*) but with typical mantle carbon isotope values centered around −5‰. Similar ranges in He isotope composition were observed in a compilation of MORBs (*5*), OIBs (*30*), and two cloudy São Luiz diamonds (*31*). We also found diamonds that presented a negative correlation between δ^{13}C and R/Ra (trend B, Fig. 1). Although unexpected, a high-^{3}He/^{4}He source dominating the isotope ratio could explain why the R/Ra values are higher than those found for MORBs. This would be most visible in rocks that have low helium concentrations and low U-Th-Sm contents, such as recycled pelagic sediments strongly depleted in almost all their helium and U-Th during subduction; indeed, the low δ^{13}C values of some Juina diamonds have previously been related to subducted pelagic sediments (*23*). The diamonds that showed mantle-like carbon and low R/Ra values may be related to oceanic lithosphere, which would likely be more retentive of U-Th than sediments would, given their lower water content and diminished propensity to form melt. Mixing between fluids

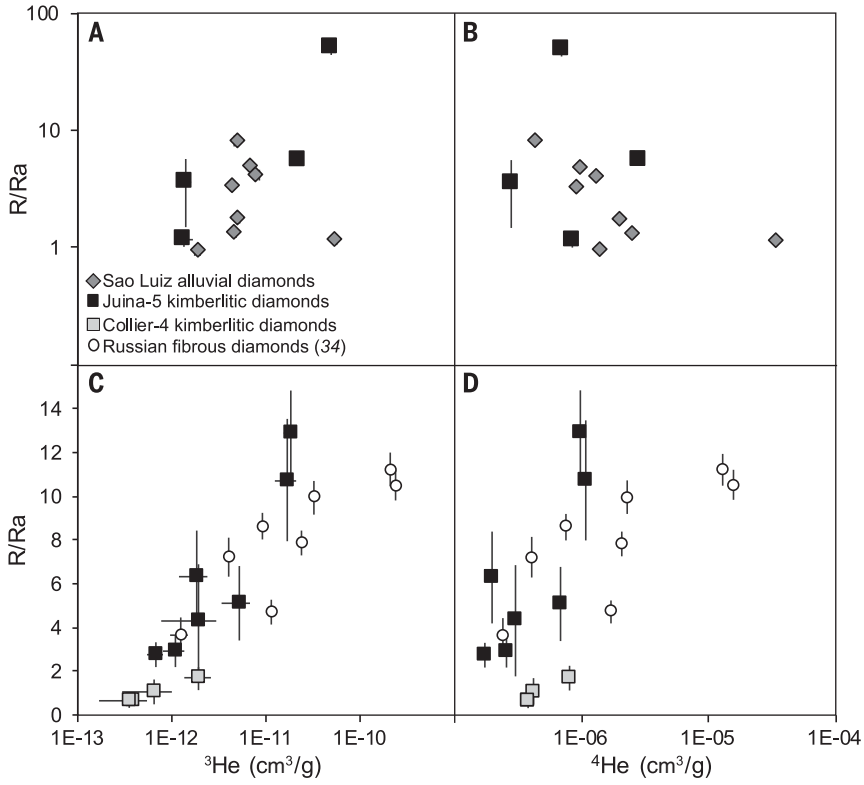

Fig. 2. Helium isotopic composition of the fluid inclusions. (**A** and **B**) R/Ra versus He concentrations of the fluid inclusions in alluvial and Juina-5 sublithospheric diamonds from array A. (**C** and **D**) R/Ra versus He concentrations of fluid inclusions in Collier-4 and Juina-5 sublithospheric diamonds from array B. Helium data from lithospheric fibrous diamonds (*34*) with a plume component are given for comparison. As most of the noble gases are contained in fluid inclusions in diamond, some of the variability in He concentrations can be attributed to differences in fluid inclusion population densities between diamonds. Errors are 1 SD. Helium concentrations are in cubic centimeters per gram (cm^3/g).

Fig. 3. Strontium ^{87}Sr/^{86}Sr versus ^{206}Pb/^{204}Pb isotopic compositions of fluid inclusions. The data support the presence of enriched mantle (EMII component) in three of the diamonds and a HIMU component in one diamond. Strontium isotope compositions shown are for present day and with a correction for 500 million years of ^{87}Sr ingrowth from ^{87}Rb decay. Data for OIB and MORB fields are from (*38*). Errors are 2 SD.

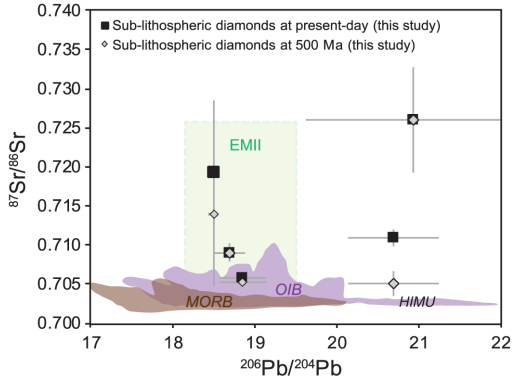

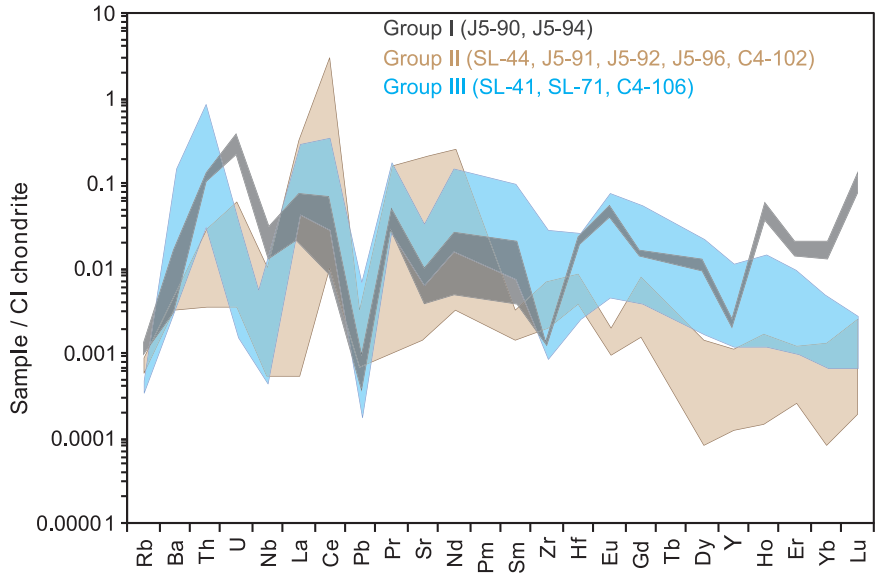

Fig. 4. Trace-element patterns of fluid inclusions. Three different groups of patterns were observed, revealing anomalies consistent with the influence of recycled material. Individual patterns are shown in fig. S4.

from oceanic lithosphere (mantle $\delta^{13}C$, high U-Th/^{3}He, low R/Ra) and pelagic sediments contaminated by high-^{3}He/^{4}He material (low $\delta^{13}C$, low U-Th, high R/Ra) could explain trend B. Helium is trapped in fluid inclusions during diamond precipitation, likely caused by an interaction between a low-degree oxidized melt from subducted material and ambient reduced mantle or plume material (*32*). Several additional lines of evidence support a high-^{3}He/^{4}He source, potentially delivered by a mantle plume that may have originated from the African Large Low Shear Velocity Province (*33*). A clear increase in ^{3}He concentrations and, to a lesser extent, in ^{4}He concentrations, is accompanied by higher ^{3}He/^{4}He ratios for the Collier-4 and Juina-5 diamonds (Fig. 2, C and D). This observation requires that the high-^{3}He/^{4}He source has higher He abundances than reservoirs with low ^{3}He/^{4}He ratios and thus supports the presence of a primordial ^{3}He plume. A similar conclusion was reached for fibrous lithospheric diamonds from Russia (*34*). Further, a high-^{3}He/^{4}He component could be related to a Cretaceous mantle plume in the Juina area. The contemporaneous formation of alkaline rocks and the Trindade plume track (32) with the young diamond formation age of a sublithospheric Collier-4 diamond [101 ± 7 million years (*23*)] along with the kimberlite eruption ages around 93 million years ago in the Juina area (*35*) all provide evidence for a deep high-^{3}He/^{4}He source delivered by a plume. Transportation of superdeep diamonds to shallower depths also has been suggested to occur by a mantle plume (*22*). Evidence from seismic tomography indicates that this plume-related mantle remains coupled to the lithosphere beneath Brazil today (*36*).

The complexity of isotope compositions observed in oceanic basalts has attracted development of a variety of models to explain them. Central to these models has been the problem of constraining the heterogeneous He isotope compositions of the OIB source, because these compositions seem to be largely decoupled from those of other radiogenic isotopes. Resolving this issue is critical, because He in particular has been used to define large-scale mantle structures (*3*) despite debate about the depth of the high-^{3}He/^{4}He source region tapped by OIB (*1*, *6*–*17*). The He isotopic data for fluid inclusions in superdeep diamonds presented here resolve this issue by showing direct evidence that the high-^{3}He/^{4}He source must be present in the deep mantle, beneath a depth of 410 km. Further, the wide-ranging Sr-Pb-C isotope compositions of the superdeep diamond-forming fluids document the extreme variability in the Earth's transition zone due to recycled crustal inputs. This recycled material is also recorded by C-N-O isotopes in other superdeep diamonds and their mineral inclusions (*25*, *37*) and clearly has the potential to generate much of the isotopic variation found in OIBs. Our results show that the transition zone is an important heterogeneous reservoir sampled by ascending plumes, ultimately forming OIBs with less extreme isotope compositions due to mixing.

REFERENCES AND NOTES

1. C. Class, S. L. Goldstein, *Nature* **436**, 1107–1112 (2005).
2. A. Hofmann, in *Treatise on Geochemistry*, vol. 3, R. W. Carlson, Ed. (Elsevier Science, ed. 2, 2014), pp. 67–101.
3. D. Hilton, D. Porcelli, in *Treatise on Geochemistry*, vol. 2, R. W. Carlson, Ed. (Elsevier, 2003), pp. 327–353.
4. F. M. Stuart, S. Lass-Evans, J. G. Fitton, R. M. Ellam, *Nature* **424**, 57–59 (2003).
5. D. W. Graham, *Rev. Mineral. Geochem.* **47**, 247–317 (2002).
6. M. G. Jackson, J. G. Konter, T. W. Becker, *Nature* **542**, 340–343 (2017).
7. H. M. Gonnermann, S. Mukhopadhyay, *Nature* **459**, 560–563 (2009).
8. H. M. Gonnermann, S. Mukhopadhyay, *Nature* **449**, 1037–1040 (2007).
9. D. Porcelli, G. Wasserburg, *Geochim. Cosmochim. Acta* **59**, 4921–4937 (1995).
10. L. Kellogg, G. Wasserburg, *Earth Planet. Sci. Lett.* **99**, 276–289 (1990).
11. R. D. van der Hilst, S. Widiyantoro, E. Engdahl, *Nature* **386**, 578–584 (1997).
12. S. W. Parman, *Nature* **446**, 900–903 (2007).
13. A. Meibom *et al.*, *Earth Planet. Sci. Lett.* **208**, 197–204 (2003).
14. R. L. Christiansen, G. Foulger, J. R. Evans, *Geol. Soc. Am. Bull.* **114**, 1245–1256 (2002).
15. G. Foulger *et al.*, *Geophys. J. Int.* **146**, 504–530 (2001).
16. G. Foulger, D. Pearson, *Geophys. J. Int.* **145**, F1–F5 (2001).
17. D. L. Anderson, *Proc. Natl. Acad. Sci. U.S.A.* **95**, 4822–4827 (1998).
18. S. Timmerman, M. Honda, D. Phillips, A. L. Jaques, J. W. Harris, *Mineral. Petrol.* **112** (suppl. 1), 181–195 (2018).
19. D. Shelkov, A. Verchovsky, H. Milledge, C. Pillinger, *Chem. Geol.* **149**, 109–116 (1998).
20. M. D. Kurz, J. J. Gurney, W. J. Jenkins, D. E. Lott III, *Earth Planet. Sci. Lett.* **86**, 57–68 (1987).
21. A. Thomson *et al.*, *Contrib. Mineral. Petrol.* **168**, 1081 (2014).
22. M. J. Walter *et al.*, *Science* **334**, 54–57 (2011).
23. G. P. Bulanova *et al.*, *Contrib. Mineral. Petrol.* **160**, 489–510 (2010).
24. Supplementary materials.
25. A. Burnham *et al.*, *Earth Planet. Sci. Lett.* **432**, 374–380 (2015).
26. F. Kaminsky, *Earth Sci. Rev.* **110**, 127–147 (2012).
27. B. Harte, S. Richardson, *Gondwana Res.* **21**, 236–245 (2012).
28. A. Thomson *et al.*, *Lithos* **265**, 108–124 (2016).
29. T. Hanyu, I. Kaneoka, *Nature* **390**, 273–276 (1997).
30. D. R. Hilton, G. M. McMurtry, R. Kreulen, *Geophys. Res. Lett.* **24**, 3065–3068 (1997).
31. R. Burgess, L. Johnson, D. Mattey, J. Harris, G. Turner, *Chem. Geol.* **146**, 205–217 (1998).
32. A. R. Thomson, M. J. Walter, S. C. Kohn, R. A. Brooker, *Nature* **529**, 76–79 (2016).
33. T. H. Torsvik, K. Burke, B. Steinberger, S. J. Webb, L. D. Ashwal, *Nature* **466**, 352–355 (2010).
34. M. Broadley *et al.*, *Geochem. Perspect. Lett.* **8**, 26–30 (2018).
35. F. V. Kaminsky *et al.*, *Lithos* **114**, 16–29 (2010).
36. J. C. VanDecar, D. E. James, M. Assumpção, *Nature* **378**, 25–31 (1995).
37. M. Palot, D. Pearson, R. Stern, T. Stachel, J. Harris, *Geochim. Cosmochim. Acta* **139**, 26–46 (2014).
38. A. Stracke, M. Bizimis, V. J. Salters, *Geochem. Geophys. Geosyst.* **4**, 8003 (2003).

ACKNOWLEDGMENTS

P. Holden, X. Zhang, S. Zink, E. Kristianov, M. Regier, and M. Krebs are thanked for analytical assistance. **Funding:** This research is supported by AGRTP and Ringwood scholarships and an IAGC Elsevier Ph.D. student research grant to S.T., ARC-DP140101976 to M.H. and A.L.J., and a CERC to D.G.P. **Author contributions:** S.T. carried out all the analyses and wrote the first version of the paper, with the exceptions of six He sample analyses carried out by M.H. and Raman analyses at ANU performed by C.L.L. G.P.B., C.B.S., J.W.H., and E.T. supplied the samples. All authors contributed to data discussions and the paper. **Competing interests:** The authors declare no competing interests. **Data and materials availability:** All data are available in the main text or the supplementary materials.

SUPPLEMENTARY MATERIALS

science.sciencemag.org/content/365/6454/692/suppl/DC1
Materials and Methods
Figs. S1 to S5
Tables S1 to S4
Databases S1 to S4
References (*39*–*71*)

31 March 2019; accepted 16 July 2019
10.1126/science.aax5293

NEUROSCIENCE

Specialized cutaneous Schwann cells initiate pain sensation

Hind Abdo[1]*, Laura Calvo-Enrique[1]*, Jose Martinez Lopez[1], Jianren Song[2], Ming-Dong Zhang[1], Dmitry Usoskin[1], Abdeljabbar El Manira[2], Igor Adameyko[3], Jens Hjerling-Leffler[1], Patrik Ernfors[1]†

An essential prerequisite for the survival of an organism is the ability to detect and respond to aversive stimuli. Current belief is that noxious stimuli directly activate nociceptive sensory nerve endings in the skin. We discovered a specialized cutaneous glial cell type with extensive processes forming a mesh-like network in the subepidermal border of the skin that conveys noxious thermal and mechanical sensitivity. We demonstrate a direct excitatory functional connection to sensory neurons and provide evidence of a previously unknown organ that has an essential physiological role in sensing noxious stimuli. Thus, these glial cells, which are intimately associated with unmyelinated nociceptive nerves, are inherently mechanosensitive and transmit nociceptive information to the nerve.

The ability to detect and protect from damage-causing (noxious) stimuli relies on the existence of sensory afferents, called nociceptors (*1*–*6*). Nociceptive nerves are generally unmyelinated and associate with Remak glial cells that protect and metabolically support the axons (*7*, *8*). The unmyelinated nerve endings are activated by noxious stimuli and, hence, represent the pain receptors in the skin. We used genetic labeling to address how cutaneous glia (Schwann cells) distribute and interact with nociceptive nerve terminals. Neural-crest and glia-specific Cre lines (Plp-CreERT2, Sox10-CreERT2, Sox2-CreERT2) coupled to the Rosa26-enhanced YFP ($R26R^{YFP}$) or $R26R^{tdTOMATO}$ ($R26R^{TOM}$) reporter lines were used. Recombination in Schwann cells and staining for nerves with PGP9.5 revealed cutaneous Schwann cells in a static location in the dermis, close to the dermal/epidermal border in both glabrous and hairy skin, and were closely associated with ascending nerve fibers in both Plp-YFP (Fig. 1A and fig. S1, A and C) and Sox10-TOM mice. The latter also revealed epidermal Schwann cell processes attached to nerves, likely because of brighter fluorescence (Fig. 1B and fig. S1, B and D). Consistent with Schwann cells, these were Plp^{YFP+}, $SOX10^{+}$, and $S100\beta^{+}$ cells with extensive radial processes into epidermis (Fig. 1A). Transmission electron microscopy revealed that nerve terminals emerged from the soma of Schwann cells located a few micrometers from the border to epidermis with the glia as the only source of cytoplasmic sheaths. Ascending immediate subepidermis nerves branched with radial Schwann cell processes, ensheathing progressively fewer nerves. In intraepidermal endings, smaller parts of nerve terminals were in contact with glia processes (Fig. 1C and fig. S2A). Nerve and Schwann cell processes were surrounded by a thick layer of fibrillar collagen oriented in the direction of the glio-neural complex and distinct from the rest of collagen. These morphologically distinct glia also carried high expression of Aquaporin1 (Fig. 1E) and were associated with $CGRP^{+}$, $P2RX3^{+}$, and transient receptor potential $V1^{+}$ nociceptive fibers (Fig. 1F and fig. S2B). Immunoelectron microscopy for TOMATO in Sox10-TOM mice confirmed Tomato

[1]Department of Medical Biochemistry and Biophysics, Division of Molecular Neurobiology, Karolinska Institutet, Stockholm 17177, Sweden. [2]Department of Neuroscience, Karolinska Institutet, Stockholm 17177, Sweden. [3]Department of Physiology and Pharmacology, Karolinska Institutet, Stockholm 17177, Sweden.
*These authors contributed equally to this work.
†Corresponding author. Email: patrik.ernfors@ki.se

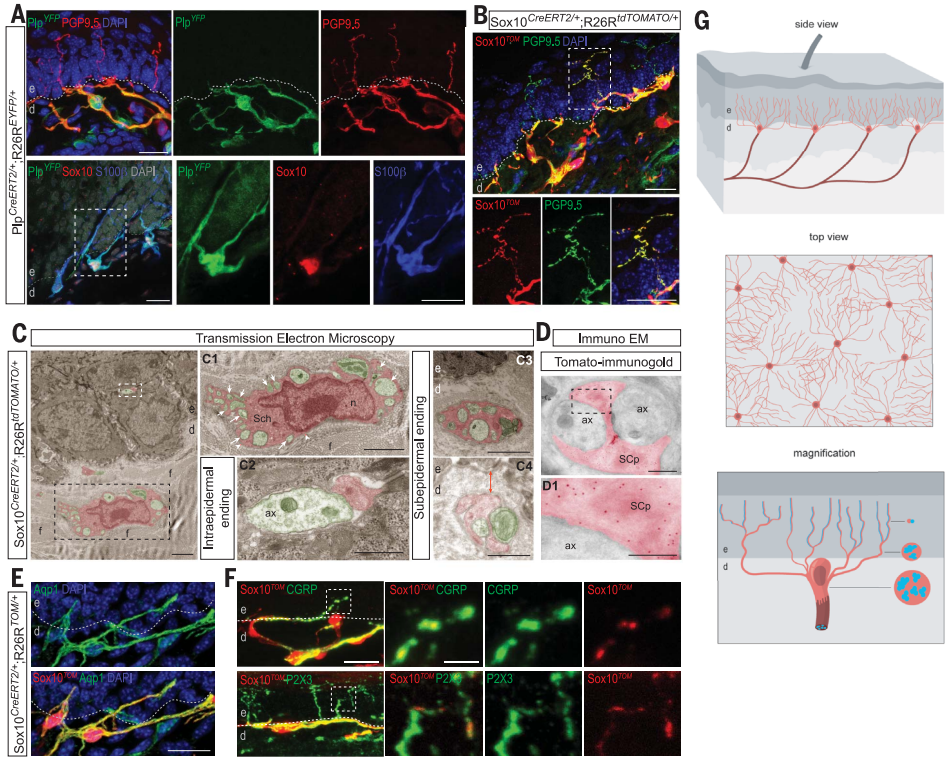

Fig. 1. Cutaneous Schwann cells form a glio-neural end organ in the skin. (**A** and **B**) Cutaneous Schwann cells in the subepidermal border with radial processes into epidermis ensheath unmyelinated nerve endings. Genetically labeled Schwann cells in Plp-YFP (A) and Sox10-TOM (B) mice associate with unmyelinated nerves ($PGP9.5^{+}$) and express glia markers SOX10 and S100β. Insets show higher magnification. (**C** and **D**) Transmission electron microscopy of the glio-neural complex. Images were pseudo-colored (axons, green and cutaneous Schwann cell and its processes, red). (C1) Subepidermal border and (C2) epidermis are higher magnification of boxed area in (C). Arrowheads point to basal lamina on the abaxonal surface, and arrows point to axons. (C3 and C4) Subepidermal Schwann cell processes enfold few (C4) or several axons (C3) close to the epidermis (red arrow is 1 μm in C4). (D) Immuno–electron microscopy (EM) with anti-dsRed antibody (red dots) shows specific expression of TOMATO in Schwann cell process and not by the axons. (**E**) Immunohistochemistry for Aquaporin1 (Aqp1). (**F**) Immunohistochemistry for CGRP and P2X3. (**G**) Schematic illustration of the glio-neural complex in the subepidermal border and epidermis (nociceptive Schwann cell, red and nerves, blue). Hatched line indicates dermal-epidermal border. ax, axon; d, dermis; DAPI, 4′,6-diamidino-phenylindole; e, epidermis; f, fibrillar collagen; n, nucleus; Sch, cutaneous Schwann cell; SCp, Schwann cell process.

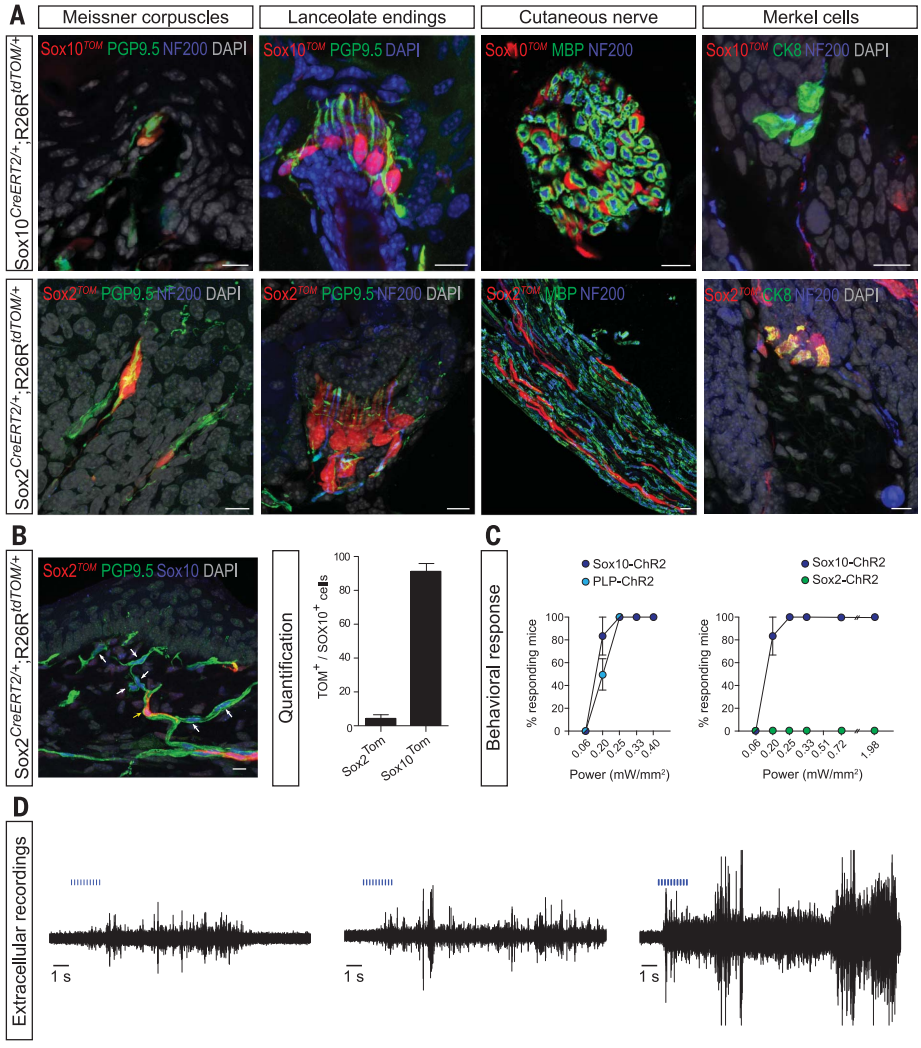

Fig. 2. Nociceptive Schwann cells can initiate pain-like behavior and are sufficient to elicit action potential propagation. (**A**) Immunohistochemistry reveals recombination in LTMR end-organ glia and in Remak glia of nerves in Sox10-TOM and Sox2-TOM mice, and in the latter also in Merkel cells. (**B**) Sox10-TOM but rarely Sox2-TOM mice recombine in nociceptive Schwann cells ($SOX10^+$). White arrows indicate non-recombined and yellow arrow indicates occasional recombined $SOX10^+$ Schwann cell in Sox2-TOM mice. Quantification is on right. (**C**) Optogenetic stimulation of nociceptive Schwann cells results in nocifensive behavior. Sox10-ChR2 and Plp-ChR2 mice but not Sox2-ChR2 mice respond to blue-light application. (**D**) Activation of nociceptive Schwann cells results in nerve electrical activity. Extracellular recording from the palmar nerve after optogenetic stimulation (blue marks) of the skin in Sox10-ChR2 mice. MBP, myelin basic protein; NF200, neurofilament 200.

in ultrastructurally identified glial cells (Fig. 1D and fig. S2C). Thus, a morphologically and molecularly specialized type of Schwann cells (hereafter termed nociceptive Schwann cells) form a mesh-like network in the subepidermal border that constructs a glio-neural complex through an intimate association with nociceptive nerves (Fig. 1G, schematic illustration) that is insulated by structural support of collagen fibers.

To determine whether nociceptive Schwann cells contribute to pain perception, we first analyzed recombination in various glia compartments of Plp-YFP, Sox10-TOM, and Sox2-TOM mice. Both Plp-YFP and Sox10-TOM mice recombine in nociceptive Schwann cells and terminal Schwann cells of Meissner corpuscles, lanceolate endings, and glia in nerves but not Merkel cells or dorsal root ganglion neurons (Fig. 2A and fig. S3). By contrast, Sox2-TOM mice largely failed to recombine nociceptive Schwann cells (Fig. 2B) but recombined in all other compartments seen for Sox10-TOM as well as Merkel cells (Fig. 2A and fig. S4). Thus, if crossed to light-sensitive channels, these driver strains can be used to manipulate Schwann cell activity without direct stimulation of sensory nerves and thereby resolve the role of nociceptive versus other cutaneous Schwann cell types.

The driver strains were crossed to Channelrhodopsin-2 (ChR2)–enhanced YFP mice to generate Plp-ChR2 and Sox10-ChR2 mice. We wanted to determine whether optogenetic stimulation of nociceptive Schwann cells is sufficient to elicit pain-like responses. A light power–dependent increase in limb withdrawal was observed in both strains (Fig. 2C). Extracellular recording from the palmar nerve after light stimulation of the palmar skin revealed increased firing with increased length of light pulses (1, 10, or 50 ms), including C-fiber mass activity and maybe also A-fiber high-amplitude bursts (Fig. 2D). The low-threshold mechanoreceptors (LTMRs) terminating as lanceolate endings in hair follicles and innervating Merkel cells and Meissner corpuscles elicit sensations of hair deflection, touch, pressure, flutter, or vibration but not pain behavior (*9*). However, in chronic pain, light touch–activated neurons can contribute to mechanical allodynia (*10*–*12*). In contrast with Sox10-ChR2 positive control mice that displayed a robust light intensity–dependent response, optogenetic stimulation of LTMR terminal Schwann cells in Sox2-ChR2 mice failed to evoke a withdrawal response (Fig. 2C) and therefore do not contribute to the withdrawal response.

To ascertain that the reflexive defensive responses are caused by pain, we assayed coping behavior that may serve to soothe suffering (*13*). Optogenetic stimulation led to robust licking, shaking, and paw-guarding behavior (Fig. 3A).

To resolve the sensory modalities nociceptive Schwann cells modulate, optogenetic activation that is subthreshold to elicit behavior was combined with cold, heat, and mechanical stimuli. We reasoned that coincident subthreshold light could sensitize to the physiological stimuli that it modulates. Coping-behavior subthreshold stimulation significantly increased sharp 2-g von Frey coping behavior, whereas paw-withdrawal subthreshold stimuli did not affect touch sensitivity, measured by the cotton swab withdrawal assay (*14*) (Fig. 3, B and C), although they elevated the response to cold stimuli in both Plp-ChR2 and Sox10-ChR2 mice (Fig. 3, D and E, and fig. S5, B and C). In Sox10-ArchT mice generated to silence nociceptive Schwann cells, no difference in cold response was seen (Fig. 3F and fig. S5D). Withdrawal subthreshold optogenetic stimulation in Plp-ChR2 and Sox10-ChR2 potentiated heat-evoked

responses (Fig. 3, G and H, and fig. S5, A and E), but silencing did not result in any difference of the thermal threshold (Fig. 3I and fig. S5F). Plp-ChR2 mice displayed dose-dependent reduction of the mechanical withdrawal threshold by increasing the length of subthreshold light trains (Fig. 3J), confirmed in Sox10-ChR2 mice after coincident activation of Schwann cells (Fig. 3K and fig. S5G). Unlike for cold and heat, silencing resulted in a significantly increased mechanical threshold, which was reversed after 24 hours (Fig. 3L and fig. S5H).

Electrical properties of nociceptive Schwann cells were examined in dissociated Sox10-TOM–expressing nociceptive Schwann cells by whole-cell current-clamp electrophysiological recordings. Stepwise current injections revealed two-phase linear I-V relationships around the resting membrane potential (Fig. 4, A and B), with a clear knee precisely around their resting membrane potential (average of –32.56 ± 1.36 mV) (Fig. 4C). The decreased resistance upon depolarization (Fig. 4, D and E) indicates an intrinsic (nonmechanical) opening of channels, pulling the membrane potential toward resting value. The passive membrane properties indicated a slow time constant, within the range of neurons (Fig. 4F).

We measured electrical responses to mechanical stimuli to determine whether nociceptive Schwann cells are mechanically active. Whole-cell voltage response to mechanical force in steps of 40 nm with five or 10 steps at ~60 Hz, a pause, and thereafter five or 10 steps out was measured. Mechanical stimulation produced a transient depolarization (n = 9) (Fig. 4, G and H). Four cells did not return all the way to baseline, possibly because of the mechanical force affecting the integrity of the seal. In the remaining cells, the decay was essentially complete during continued force application, suggesting that the mechanoreceptive response adapts to sustained force over time. Both response and adaptation were very rapid, resulting in similar responses in the subsequent stimuli. The cells tracked the maximum frequency of stimuli that we could generate (60 Hz). Releasing the force also depolarized the cells (Fig. 4G). Thus, nociceptive Schwann cells responded to both positive and negative changes in force but much less to sustained force. Peak mean amplitude was 25.5 ± 2.1 mV (Fig. 4I), and 50% depolarization duration (half-width) was 6.7 ± 1.5 ms (Fig. 4J), with time at the beginning of the rising phase to the peak (rise time) of 1.4 ± 0.2 ms (Fig. 4K). This time course of the mechanoreceptor potential may reflect that of the underlying mechanoreceptor current. This suggests very fast gating mechanisms, similar to what has been described in sensory neurons (*15*, *16*).

We provide evidence for a specialized glial cell type that builds a sensory organ in the skin, initiating the sensation of pain. The nociceptive Schwann cells display a mesh-like network of cytoplasmic sheaths around nerves in the subepidermal border with radial processes entering into the epidermis abutting to unmyelinated nociceptive nerves. The nociceptive Schwann cells are the cellular equivalents of the ignored Remak Schwann

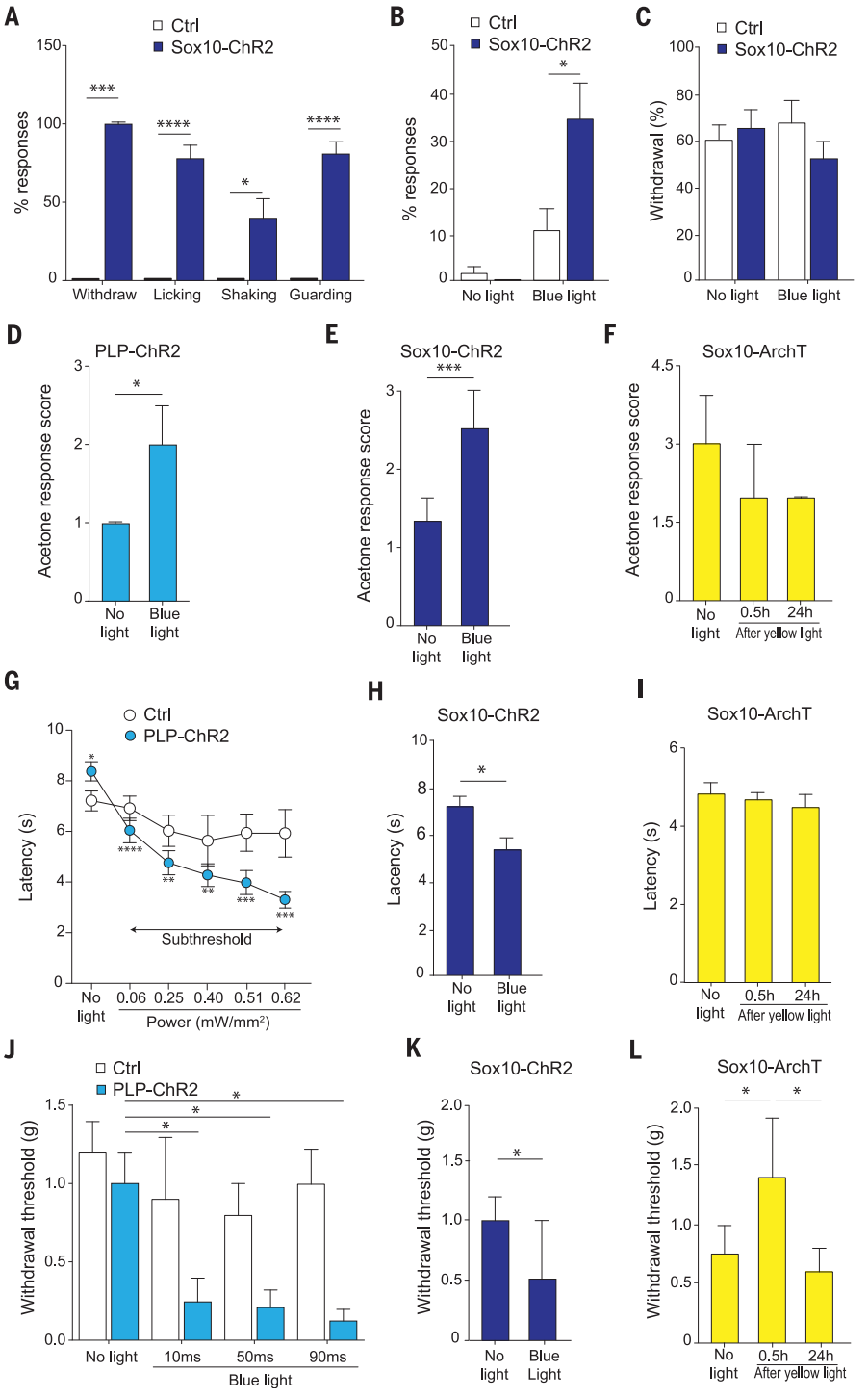

Fig. 3. Nociceptive Schwann cells determine the sensitivity threshold for mechanosensation. (**A**) Suprathreshold photoactivation of nociceptive Schwann cells evokes coping behavior associated with pain. (**B** to **L**) Blue bars, subthreshold optogenetic activation of nociceptive Schwann cells combined with natural stimuli and yellow bars before and after optogenetic inhibition. (B) Coping response to nociceptive mechanical stimuli (2-g von Frey). (C) Withdrawal to cotton swab. (D to F) Response to cold. (G to I) Withdrawal latency to heat. (J) Mechanical threshold without light or with increased length of subthreshold blue-light trains. (K) Mechanical threshold. (L) Mechanical threshold before or after optogenetic inhibition. Ctrl, control. Statistics text and *P* values can be found in the supplementary materials, material and methods.

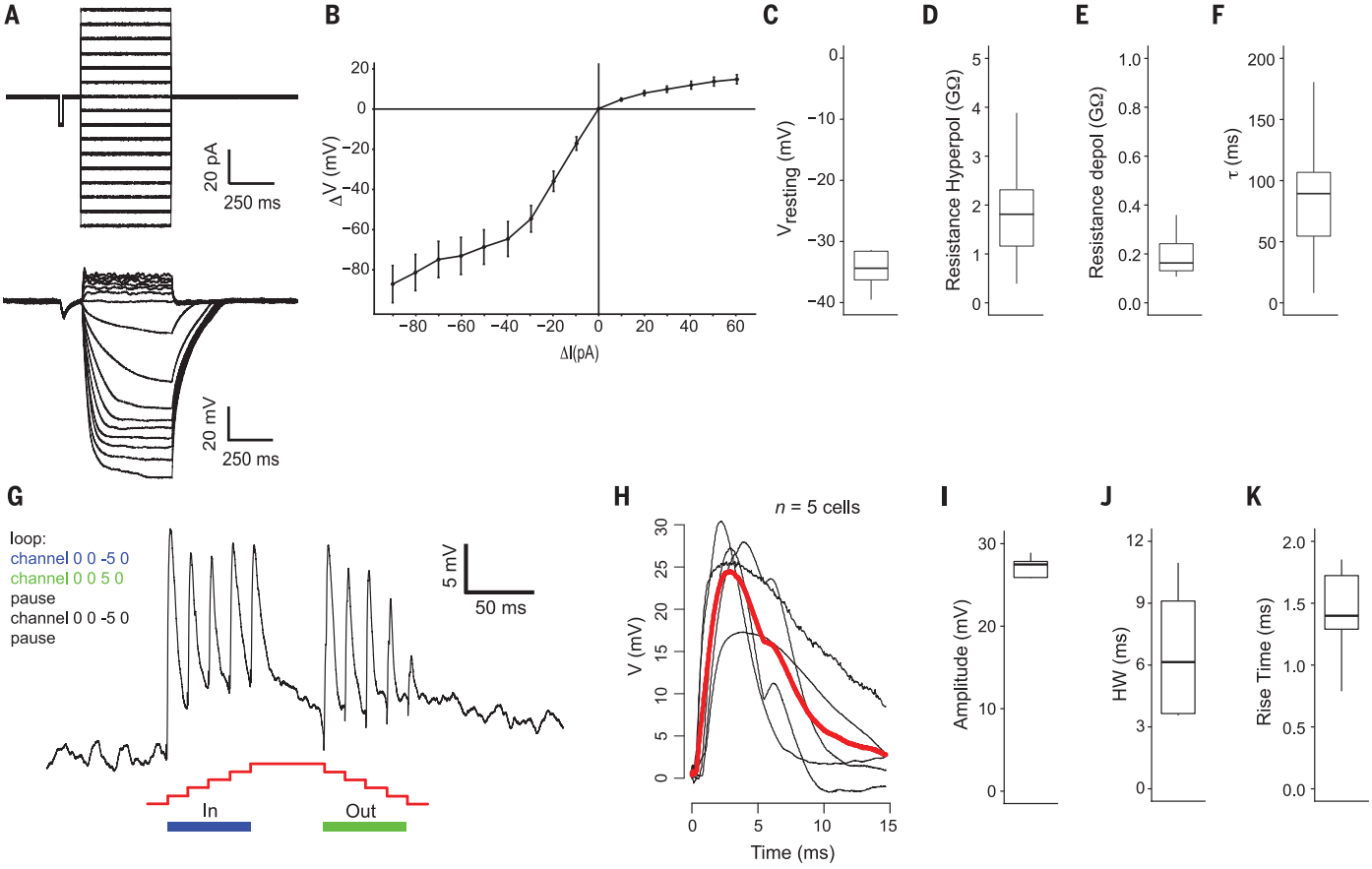

Fig. 4. Nociceptive Schwann cells are mechanosensory cells. (**A**) Voltage signal detected during whole-cell current-clamp recordings evoked current steps. (**B**) Two-phase linear I-V relationships during hyperpolarization and depolarization. (**C**) Resting membrane potential of nociceptive Schwann cells. (**D**) Resistance of cells calculated during hyperpolarizing current injections. (**E**) Resistance of cells calculated during depolarizing current injections. (**F**) Time constant (τ). (**G**) Mechanical stimulation of nociceptive Schwann cells during whole-cell current-clamp recordings; example of inward steps and subsequent outward steps applied as indicated. (**H**) Mechanically evoked depolarization (red, average). (**I**) Amplitudes of depolarization. (**J**) Half-width of depolarization. (**K**) 10 to 90% rise time of the depolarization. depol, depolarization; HW, half-width; Hyperpol, hyperpolarization.

cells described in the subepidermal border of the skin some 45 years ago. At that time, nerve fibers were thought to lose their glia attachment and enter epidermis as free nerve endings (*17*). The nociceptive Schwann cells are highly mechanosensitive with rapid adaptation and respond to both positive and negative changes in force, similar to "on" and "off" mechanoreceptor responses observed in *Caenorhabditis elegans* (*18*). They transduce nociceptive stimuli into electrical signals that translate into pain-like behavior. The nociceptive nerve endings in skin also gate responses to various noxious stimuli (*1*–*6*). Hence, nociceptive nerves and nociceptive Schwann cells form a nociceptive glio-neural complex with two sensor-receptor cell types, the glia and the nerve, both likely influencing the sensation of pain. Most or all types of nociceptors appear to contribute to the nociceptive glio-neural complex, and consistently, both mechanical and thermal nociception is potentiated in gain-of-function experiments. However, loss-of-function experiments indicate either that activation of thermosensitive ion channels in primary afferents (*19*–*22*) is sufficient by itself or, alternatively, that nociceptive Schwann cells contribute to a submodality not captured in our behavioral tests. By contrast, nociceptive Schwann cells are physiologically contributing to sensation of mechanical stimuli, as the threshold was affected in both gain- and loss-of-function experiments. This could suggest a broader response profile of discrete nociceptive neuron types than that predicted from their molecular profiles (*23*–*26*). Functional implications of our findings are vast if nerve and glial cell receptor types mediate different aspects of thermal and mechanical nociceptive transduction, as has been proposed for Merkel cells participating in non-noxious touch sensation (*27*–*29*).

REFERENCES AND NOTES

1. V. E. Abraira, D. D. Ginty, *Neuron* **79**, 618–639 (2013).
2. M. Costigan, J. Scholz, C. J. Woolf, *Annu. Rev. Neurosci.* **32**, 1–32 (2009).
3. F. Lallemend, P. Ernfors, *Trends Neurosci.* **35**, 373–381 (2012).
4. Y. Liu, Q. Ma, *Curr. Opin. Neurobiol.* **21**, 52–60 (2011).
5. C. Peirs *et al.*, *Neuron* **87**, 797–812 (2015).
6. S. A. Prescott, Q. Ma, Y. De Koninck, *Nat. Neurosci.* **17**, 183–191 (2014).
7. B. L. Harty, K. R. Monk, *Curr. Opin. Neurobiol.* **47**, 131–137 (2017).
8. K. R. Jessen, R. Mirsky, *J. Physiol.* **594**, 3521–3531 (2016).
9. C. J. Woolf, T. P. Doubell, *Curr. Opin. Neurobiol.* **4**, 525–534 (1994).
10. R. Dhandapani *et al.*, *Nat. Commun.* **9**, 1640 (2018).
11. M. Koltzenburg, L. E. Lundberg, H. E. Torebjörk, *Pain* **51**, 207–219 (1992).
12. C. Peng *et al.*, *Science* **356**, 1168–1171 (2017).
13. T. Huang *et al.*, *Nature* **565**, 86–90 (2019).
14. S. S. Ranade *et al.*, *Nature* **516**, 121–125 (2014).
15. K. Poole, R. Herget, L. Lapatsina, H. D. Ngo, G. R. Lewin, *Nat. Commun.* **5**, 3520 (2014).
16. Y. Song *et al.*, *J. Physiol. Biochem.* **74**, 207–221 (2018).
17. N. Cauna, *J. Anat.* **115**, 277–288 (1973).
18. R. O'Hagan, M. Chalfie, M. B. Goodman, *Nat. Neurosci.* **8**, 43–50 (2005).
19. M. J. Caterina *et al.*, *Nature* **389**, 816–824 (1997).
20. D. D. McKemy, W. M. Neuhausser, D. Julius, *Nature* **416**, 52–58 (2002).
21. A. M. Peier *et al.*, *Cell* **108**, 705–715 (2002).
22. I. Vandewauw *et al.*, *Nature* **555**, 662–666 (2018).
23. C. Li, S. Wang, Y. Chen, X. Zhang, *Neurosci. Bull.* **34**, 200–207 (2018).
24. C. L. Li *et al.*, *Cell Res.* **26**, 83–102 (2016).
25. D. Usoskin *et al.*, *Nat. Neurosci.* **18**, 145–153 (2015).
26. A. Zeisel *et al.*, *Cell* **174**, 999–1014.e22 (2018).
27. R. Ikeda *et al.*, *Cell* **157**, 664–675 (2014).

28. S. Maksimovic *et al*., *Nature* **509**, 617–621 (2014).
29. S. H. Woo *et al*., *Nature* **509**, 622–626 (2014).

ACKNOWLEDGMENTS

We thank M. Karlén for schematic illustrations. **Funding**: P.E. received the ERC (PainCells 740491), the Swedish MRC, KAW Scholar and project grant, and Welcome Trust (200183). M.-D.Z. received a brain foundation post-doc fellowship. **Author contributions**: Conceptualization: P.E. and I.A.; mouse models/behavior/experimental design: H.A. and L.C.-E.; electrophysiology: J.M.L. and J.H.-L.; nerve recording: J.S. and A.E.M.; Immuno: H.A., L.C.-E., and M.-D.Z.; animal platforms: D.U.; writing (H.A., L.C.-E., and P.E.) and revision (L.C.-E. and P.E.) of the manuscript with input from all authors: L.C.-E. and P.E.; and supervision and funding: P.E. **Competing interests**: No competing interests. **Data and materials availability:** All data are available in the manuscript or the supplementary material. The Sox10-CreERT2 mice were obtained under an MTA from MRC.

SUPPLEMENTARY MATERIALS

science.sciencemag.org/content/365/6454/695/suppl/DC1
Materials and Methods
Supplementary Text
Figs. S1 to S5

10 April 2019; accepted 2 July 2019
10.1126/science.aax6452

NEUROSCIENCE

Bright and photostable chemigenetic indicators for extended in vivo voltage imaging

Ahmed S. Abdelfattah[1]*, Takashi Kawashima[1]*†, Amrita Singh[1,2], Ondrej Novak[1,3], Hui Liu[1], Yichun Shuai[1], Yi-Chieh Huang[4], Luke Campagnola[5], Stephanie C. Seeman[5], Jianing Yu[1], Jihong Zheng[1], Jonathan B. Grimm[1], Ronak Patel[1], Johannes Friedrich[6,7,8], Brett D. Mensh[1], Liam Paninski[6,7], John J. Macklin[1], Gabe J. Murphy[5], Kaspar Podgorski[1], Bei-Jung Lin[4], Tsai-Wen Chen[4], Glenn C. Turner[1], Zhe Liu[1], Minoru Koyama[1], Karel Svoboda[1], Misha B. Ahrens[1]‡, Luke D. Lavis[1]‡, Eric R. Schreiter[1]‡§

Genetically encoded voltage indicators (GEVIs) enable monitoring of neuronal activity at high spatial and temporal resolution. However, the utility of existing GEVIs has been limited by the brightness and photostability of fluorescent proteins and rhodopsins. We engineered a GEVI, called Voltron, that uses bright and photostable synthetic dyes instead of protein-based fluorophores, thereby extending the number of neurons imaged simultaneously in vivo by a factor of 10 and enabling imaging for significantly longer durations relative to existing GEVIs. We used Voltron for in vivo voltage imaging in mice, zebrafish, and fruit flies. In the mouse cortex, Voltron allowed single-trial recording of spikes and subthreshold voltage signals from dozens of neurons simultaneously over a 15-minute period of continuous imaging. In larval zebrafish, Voltron enabled the precise correlation of spike timing with behavior.

Animal behavior is produced by patterns of neuronal activity that span a wide range of spatial and temporal scales. Understanding how neural circuits mediate behavior thus requires high-speed recording from ensembles of neurons for long periods of time. Although the activity of large numbers of neurons can now be routinely recorded using genetically encoded calcium indicators (GECIs) (*1*), the slow kinetics of calcium signals complicate the measurement of action potentials, and subthreshold voltage signals are missed entirely (*1*–*3*). Voltage imaging using genetically encoded voltage indicators (GEVIs) can overcome these challenges, enabling imaging of fast spikes and subthreshold dynamics in genetically defined neurons (*4*, *5*). The high imaging speed and excitation intensity required for voltage imaging, combined with the smaller volume of the cellular membrane, place increased demands on voltage indicators relative to GECIs. Extant GEVIs rely on fluorescence from either microbial rhodopsins (*6*–*8*) or fluorescent proteins (*9*–*13*). These fluorophores lack the brightness and photostability to allow in vivo voltage imaging from large fields of view over time scales of many behavioral events, precluding the millisecond–time scale analysis of neural circuits. Improved rhodamine dyes such as the Janelia Fluor (JF) dyes can be used in complex biological experiments because of their high brightness and photostability (*14*), compatibility with self-labeling protein tags (*15*, *16*), and ability to traverse the blood-brain barrier for in vivo delivery (*17*). We describe a "chemigenetic," or hybrid protein–small molecule, GEVI scaffold that we call Voltron, which irreversibly binds these synthetic fluorophore dyes. Voltron provides an increased photon yield that enables in vivo imaging of neuronal spiking and subthreshold voltage signals in model organisms with order-of-magnitude improvement in the number of neurons imaged simultaneously over substantially longer durations.

Our design for a chemigenetic voltage indicator combines a voltage-sensitive microbial rhodopsin domain (*6*, *7*, *11*) with a dye-capture protein domain (Fig. 1A) that irreversibly binds a synthetic fluorophore dye ligand (*14*, *15*) (Fig. 1B), analogous to previously reported voltage indicators that use fluorescent proteins (*10*, *11*, *18*). Transmembrane voltage–dependent changes in the absorption spectrum (*6*, *19*) of the rhodopsin domain of Voltron reversibly modulate the degree of fluorescence quenching of the nearby bound dye through Förster resonance energy transfer (FRET). We investigated the modularity of this approach, finding that three different rhodopsin domains—QuasAr1 (*7*), QuasAr2 (*7*), and Ace2N (*11*, *20*)—modulated the fluorescence of the rhodamine dye Janelia Fluor 549 (JF_{549}) after binding to either HaloTag (*15*) or SNAP-tag (*21*) dye-capture protein domains (figs. S1 to S8). Removing a small number of amino acid residues at the junction of the rhodopsin and self-labeling tag domains increased the amplitude of fluorescent voltage signals (fig. S1), presumably by decreasing average distance and thus increasing FRET efficiency between the dye and rhodopsin retinal cofactor. The configuration providing the best signal-to-noise ratio (SNR) for spikes was Ace2N fused to HaloTag with five amino acids removed at their junction (Fig. 1, A and B, and fig. S2), hereafter referred to as Voltron.

We tested several Voltron-dye combinations in cultured rat neurons and acute mouse brain slices with high-speed imaging and simultaneous whole-cell patch clamp electrophysiology (Fig. 1C, figs. S6 and S9 to S13, and tables S1 and S2). Voltron could detect neuronal action potentials and subthreshold potential changes with a variety of JF dye ligands with emission maxima between 520 nm and 660 nm using fluorescence imaging with one-photon excitation (Fig. 1, C to E, and fig. S6) but was not compatible with two-photon imaging, as described previously for rhodopsin-containing GEVIs (*22*, *23*). Voltron bound to JF_{525} ($Voltron_{525}$) exhibited the highest sensitivity, giving a fluorescence change of −23 ± 1% $\Delta F/F_0$ for a voltage step from −70 mV to +30 mV (Fig. 1E and fig. S9); $Voltron_{549}$ showed similar sensitivity. $Voltron_{525}$ responded to voltage steps with submillisecond on and off time constants (table S3 and fig. S10). We compared the brightness and photostability of Voltron in neuronal cultures with those of two other fluorescent protein–based GEVIs: Ace2N-mNeon (*11*) and ASAP2f (*13*). Both $Voltron_{525}$ and $Voltron_{549}$ were brighter than Ace2N-mNeon (by a factor of 3 to 4) and ASAP2f (by a factor of 16 to 18) (Fig. 1F) in cell culture. This difference did not result from differences in expression; we compared the brightness of $Voltron_{549}$ and Ace2N-mNeon at the single-molecule level and observed a similar brightness difference (factor of 3 to 4) (Fig. 1G). $Voltron_{525}$ and $Voltron_{549}$ were also more photostable in ensemble measurements (Fig. 1H, tables S4 and S5, and figs. S14 and S15) as well as in single-molecule assays, in which photobleaching times were longer for $Voltron_{549}$ than those of Ace2N-mNeon by a factor of 8 (Fig. 1I). Overall, the improved brightness and photostability of Voltron increased the photon yield by at least a factor of 10 in neurons relative to existing GEVIs that rely on fluorescent proteins.

In vivo, Voltron could be reliably expressed and labeled with dye in mice, larval zebrafish, and adult fruit flies (Figs. 1 to 4 and figs. S16 to S19 and S21 to S45). Simultaneous in vivo electrophysiology and Voltron imaging in each of these organisms confirmed the detection of individual action potentials (Fig. 1, J and K, and figs. S17 to S19). For imaging in the mouse brain,

[1]Janelia Research Campus, Howard Hughes Medical Institute, Ashburn, VA 20147, USA. [2]Solomon H. Snyder Department of Neuroscience, Johns Hopkins University, Baltimore, MD 21205, USA. [3]Department of Auditory Neuroscience, Institute of Experimental Medicine, Academy of Sciences of the Czech Republic, Prague, Czech Republic. [4]Institute of Neuroscience, National Yang-Ming University, Taipei 112, Taiwan. [5]Allen Institute for Brain Science, Seattle, WA 98109, USA. [6]Department of Statistics and Center for Theoretical Neuroscience, Columbia University, New York, NY 10027, USA. [7]Department of Neuroscience and Grossman Center for the Statistics of Mind, Columbia University, New York, NY 10027, USA. [8]Center for Computational Biology, Flatiron Institute, New York, NY 10010, USA.
*These authors contributed equally to this work. †Present address: Department of Neurobiology, Weizmann Institute of Science, Rehovot, Israel. ‡These authors contributed equally to this work.
§Corresponding author. Email: schreitere@janelia.hhmi.org

we used a variant of Voltron appended with a 63–amino acid sequence from the rat potassium channel Kv2.1 that restricts expression to the membrane of the cell body and proximal dendrites (*24*, *25*) (Voltron-ST; fig. S20). The rapid kinetics of Voltron$_{525}$-ST allowed clear observation of action potentials in fast-spiking parvalbumin (PV)–expressing interneurons in the CA1 region of the mouse hippocampus (Fig. 2, A to G, and fig. S21). We measured the orientation tuning of the spiking and subthreshold responses of cortical layer 2/3 pyramidal neurons in mouse primary visual cortex in response to the mouse observing directional movement of light and dark stripes, a benchmark for new indicators (*1*, *11*) (Fig. 2, H to L, and figs. S22 to S24), and confirmed that spiking activity showed sharper orientation selectivity than did subthreshold voltage signals

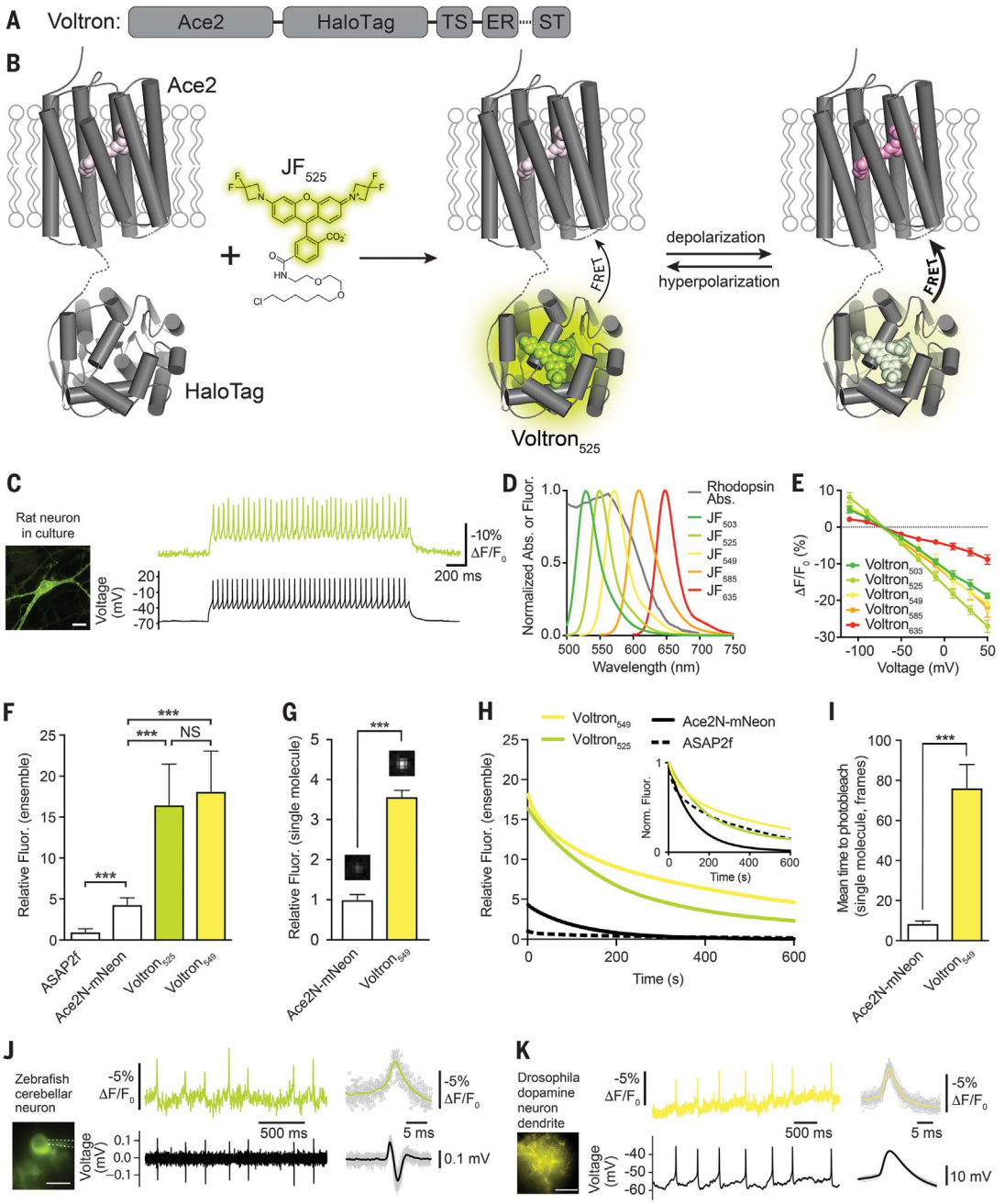

Fig. 1. Development of the chemigenetic voltage indicator Voltron. (**A**) Schematic of Voltron sequence: A rhodopsin (Ace2) is fused to a self-labeling tag domain (HaloTag) with additional sequences added to improve or localize membrane targeting: Golgi export trafficking sequence (TS), endoplasmic reticulum export sequence (ER), and somatic targeting sequence (ST). (**B**) Model of Voltron mechanism. (**C**) Left: Cultured rat hippocampal neuron expressing Voltron and labeled with JF$_{525}$. Scale bar, 20 μm. Right: Single-trial recording of action potentials and subthreshold voltage signals from current injections in primary neuron culture using 400-Hz imaging (top, fluorescence) or electrophysiology (bottom, membrane potential). (**D**) Fluorescence emission spectra of different JF dyes overlaid with the absorbance spectrum of Ace2N. (**E**) Fluorescence change as a function of membrane voltage with different JF dye–Voltron conjugates. (**F**) Relative fluorescence of ASAP2f, Ace2N-mNeon, Voltron$_{525}$, and Voltron$_{549}$ in cultured neurons (n = 70, 68, 48, and 62 measurements, respectively, from five independent transfections for each construct). Illumination intensity was ~10 mW/mm^2 at imaging plane. ***P < 0.001 [one-way analysis of variance (ANOVA) followed by Bonferroni test on each pair]; NS, not significant. Fluorescence was normalized to ASAP2f mean intensity. (**G**) Relative single-molecule brightness of Ace2N-mNeon and Voltron$_{549}$. ***P < 0.001 (two-tailed Student t test). (**H**) Bleaching curves for ASAP2f, Ace2N-mNeon, Voltron$_{525}$, and Voltron$_{549}$ in primary neuron culture. Illumination intensity was ~23 mW/mm^2 at imaging plane. Bleaching curves were normalized to mean cellular fluorescence from (F) or normalized to the zero-time value (inset). (**I**) Mean time to bleach of Ace2N-mNeon and Voltron$_{549}$ during single-molecule imaging, 100-ms frames. ***P < 0.001 (two-tailed Student t test). (**J** and **K**) Simultaneous in vivo Voltron imaging (300 and 800 Hz, top) and electrophysiology (bottom) in larval zebrafish (extracellular) and adult *Drosophila* (whole-cell), respectively. Spike-triggered averages are shown at the right. Scale bars, 20 μm.

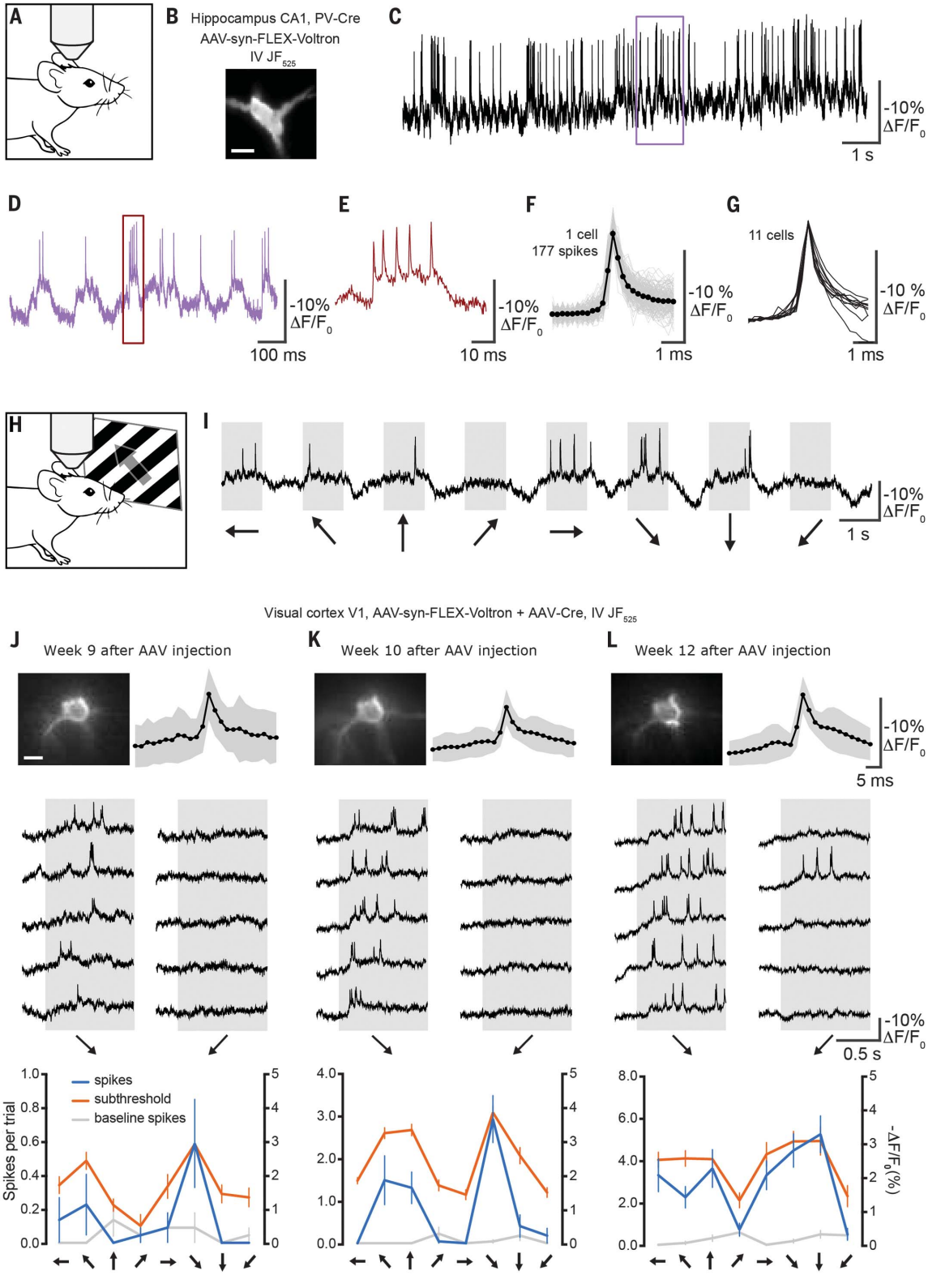

Fig. 2. Using Voltron to measure membrane voltage dynamics in hippocampal PV neurons and visual cortex pyramidal neurons of mice. (**A**) Schematic of imaging of spontaneous activity in the CA1 region of the hippocampus of an awake mouse. (**B**) Image of hippocampal PV neuron expressing Voltron labeled with JF_{525}. Scale bar, 20 μm. (**C** to **E**) $Voltron_{525}$ raw $\Delta F/F_0$ traces showing spontaneous spikes of a PV neuron (B) located at a depth of 60 μm in the hippocampal CA1 region of a fully awake mouse imaged at 3858 frames per second. Color-coded boxes indicate regions shown at expanded time scales. (D) is a zoom of the boxed region from (C); (E) is a zoom of the boxed region from (D). (**F**) Overlay of 177 spikes detected during a 15-s period (gray) and their average (black). (**G**) Spike shape of 11 PV neurons. (**H**) Schematic of imaging of primary visual cortex of an anesthetized mouse during display of drifting grating visual stimuli. (**I**) Example trace showing 500-Hz Voltron fluorescence during one trial of a sequence of visual stimuli. Arrows below represent the direction of movement of the drifting grating. (**J** to **L**) Top left: Images of a pyramidal cell at a depth of 148 μm, imaged three times over a period of 4 weeks at the indicated number of weeks after virus injection. Scale bar, 10 μm. Top right: Average of all spikes in session (black) and SD (gray). Middle: Raw $\Delta F/F_0$ trace for five repetitions in each session, showing two orthogonal orientations (indicated with arrows below) from the neuron pictured at top left. Bottom: Orientation tuning to full-frame drifting gratings of the neuron pictured at top left, displayed as number of spikes during trials (blue), number of spikes during preceding intertrial intervals (gray), and subthreshold $\Delta F/F_0$ (right *y* axis) after low-pass filtering traces using a 10-point median filter. For each orientation, subthreshold response is calculated by averaging the low-pass–filtered trace between 100 and 400 ms after trial onset, and baseline is calculated by averaging the low-pass–filtered trace from 80 ms preceding trial onset to 20 ms after trial onset. Data are displayed as response minus baseline. Error bars represent SEM (20 to 22 repetitions per session).

(*26*). We extended the imaging period over several consecutive weeks by injecting additional JF_{525} HaloTag ligand before each imaging session (Fig. 2, J to L, and fig. S24).

Next, we attempted to image larger areas containing more neurons for longer times in vivo in mouse cortex (Fig. 3). By wide-field microscopy at illumination intensities between 3 and 20 mW/mm^2, we could clearly identify and distinguish action potentials from nearby neurons throughout 15 min of continuous imaging (SNR = 5.3 during the first minute, 4.4 during the final minute) (Fig. 3, B to E). We expanded the field of view to include dozens of cortical interneurons labeled with Voltron$_{525}$-ST in a transgenic mouse line (NDNF-Cre) (*27*) while imaging at 400 Hz (Fig. 3, F and G, and figs. S25 to S42). Overall, we imaged a total of 449 neurons (12 fields of view in three mice), demonstrating routine voltage imaging of populations of neurons in superficial mouse cortex (Fig. 3G and figs. S25 to S42). This scale of in vivo voltage imaging enabled analysis of membrane potential correlations between many neuron pairs (fig. S26).

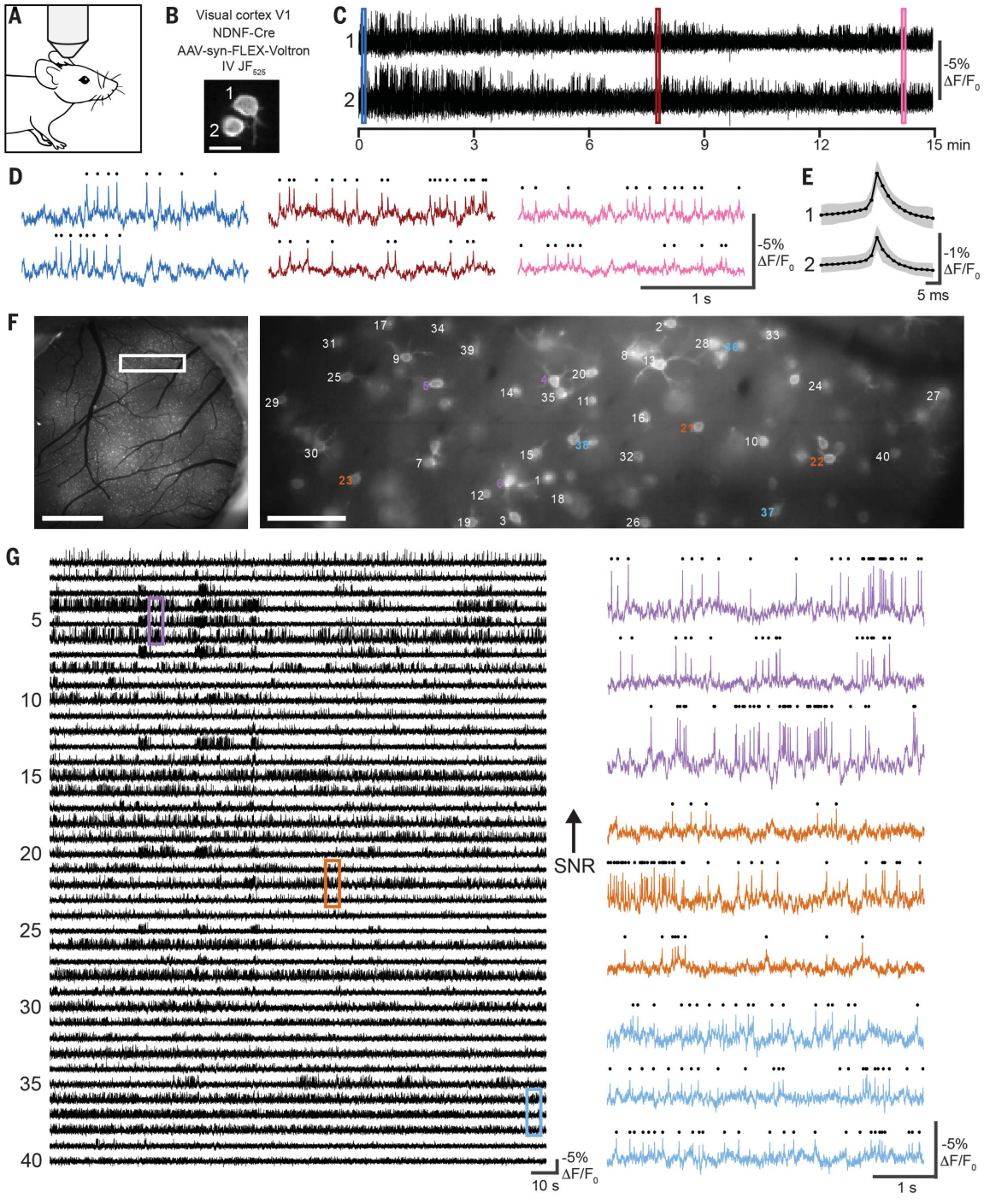

Fig. 3. Imaging of voltage activity in large fields of view of the mouse neocortex over long durations. (**A**) Schematic of the imaging setup. (**B**) Image of two neurons expressing Voltron$_{525}$-ST in layer 1 of the visual cortex of an NDNF-Cre mouse. Scale bar, 10 μm. (**C**) $\Delta F/F_0$ traces from neurons in (B), recorded over 15 min at 400 Hz. (**D**) Color-coded zooms of indicated regions of the traces in (C), with detected action potentials indicated by black dots above the fluorescence traces. (**E**) Average of all spikes in session (black) and SD (gray). (**F**) Left: Fluorescence image of a cranial window over primary visual cortex (V1) in an NDNF-Cre mouse showing Cre-dependent expression of Voltron$_{525}$-ST (bright spots). Scale bar, 1 mm. Right: Zoomed image of left panel in the area indicated by the white rectangle, with neuron labels corresponding to fluorescence traces in (G). Scale bar, 100 μm. (**G**) Left: $\Delta F/F_0$ traces during 3 min of recording at 400 Hz from neurons pictured in (F), in decreasing order of SNR. Right: Zooms of $\Delta F/F_0$ traces from color-coded regions of (G) with detected action potentials represented as black dots above, illustrating representative traces with high (top), medium (middle), and low (bottom) SNR. Traces have been background-subtracted, which removes shared subthreshold membrane potential fluctuations (compare to fig. S25 without subtraction).

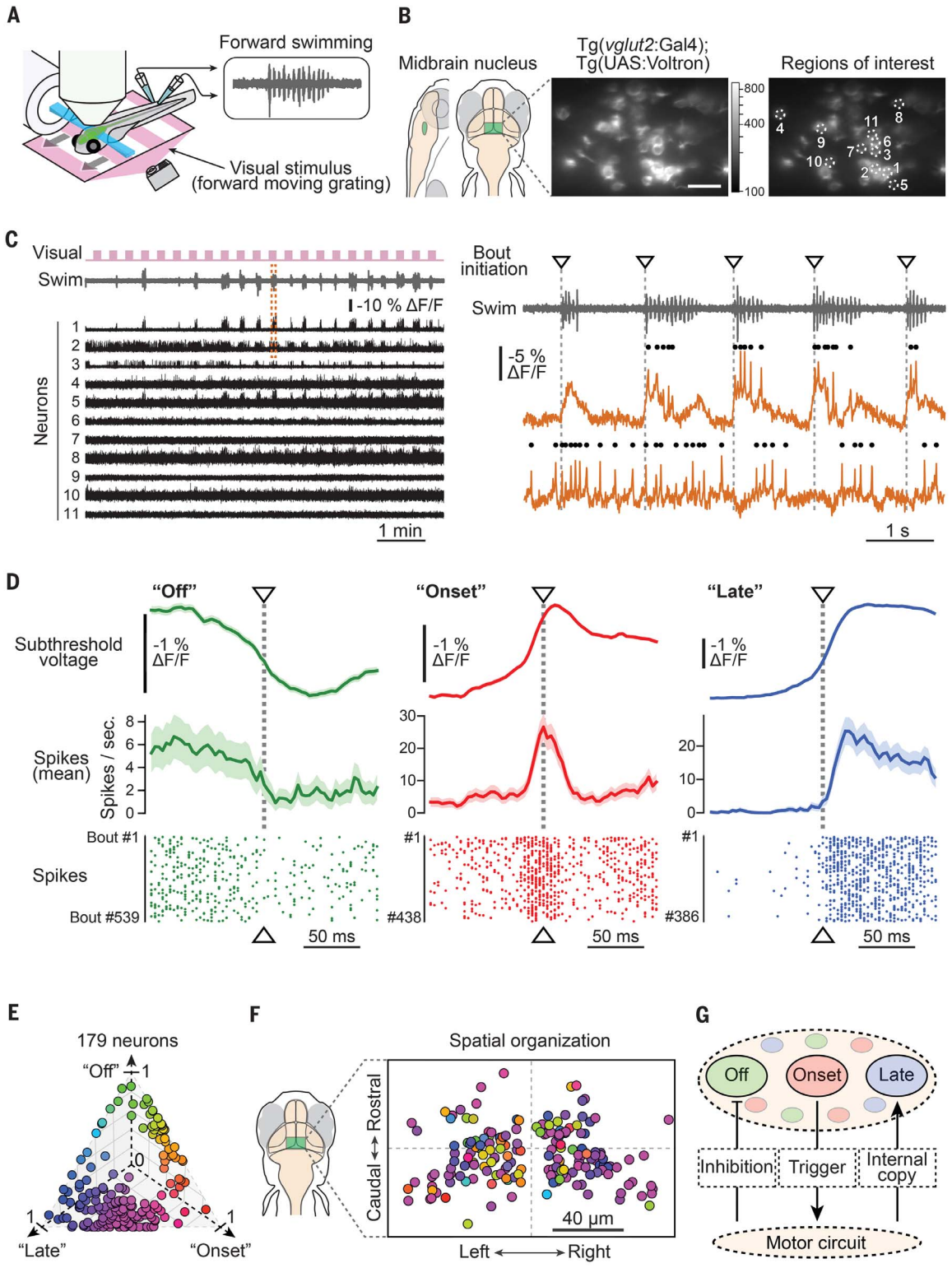

Fig. 4. Voltron reveals millisecond–time scale neural dynamics during swimming behavior in zebrafish. (**A**) Schematic illustration of the setup. An immobilized zebrafish is placed under the light-sheet microscope, and the motor signals (inset) from its tail are recorded using a pair of electrodes. Visual stimuli (forward-drifting gratings) for eliciting swimming responses are presented below the fish. (**B**) Left: Anatomical location of the imaged brain region (midbrain nucleus; see fig. S44A). Center: Representative field of view of the imaged region expressing Voltron. Scale bar, 20 μm. Right: Position of neurons analyzed in (C). (**C**) Left: Periods of visual motion (pink) and swim signals (gray) are plotted above Voltron fluorescence traces (black) simultaneously recorded from 11 neurons shown in (B). Right: Zoom of swimming signals (top) and Voltron fluorescence traces from two representative neurons (bottom) are expanded from the dashed box in the left panel. Dots at the top of each trace represent action potentials recognized by the algorithm described in fig. S45, A and B. Inverted triangles and dotted gray lines indicate initiation of each swim bout. (**D**) Mean subthreshold signal (top), mean frequency of action potentials (middle), and raster plots of action potentials (bottom) near the initiation of swim bouts from three representative neurons: "Off" (green), "Onset" (red), and "Late" (blue). Shadows in the top and middle panels represent SEM across swim events. (**E**) Classification of recorded neurons by their mean subthreshold signals near the initiation of swim bouts; 179 neurons recorded from 43 fish were classified using non-negative matrix factorization and colored according to the weights for three factors: "Onset" (red), "Off" (green), and "Late" (blue). See supplementary materials for details of this classification. (**F**) Spatial organization of the same population of neurons as in (E). Neurons from multiple fish are superimposed on a single map according to the distance from the center of this midbrain nucleus. (**G**) Hypothetical model of neural activity modulation in this midbrain nucleus.

We used Voltron to image zebrafish larvae, which respond to visual input with fast, directed swim bouts that are tailored to the details of the stimulus (*28*). We sought to uncover how this sensory-to-motor transformation unfolds in neuronal populations at fine time scales that are inaccessible with calcium imaging. We verified that Voltron could detect action potentials and subthreshold voltage signals in live zebrafish after labeling with several different colors of dye ligands (figs. S17 and S43). We then used Voltron$_{525}$ to monitor neural activity during swim bouts induced by visual motion (Fig. 4A). We recorded Voltron signals from 179 neurons across 43 fish in a motor-sensory nucleus in the tegmental area of the midbrain (Fig. 4B and fig. S44), yielding data on subthreshold membrane voltage modulation as well as automatically detected spike times (Fig. 4C and fig. S45). We found neuron populations with different temporal activity patterns, including neurons whose firing rate increased ~1 s before the fish started swimming (fig. S44, B and C, "Ramp"), neurons whose firing rate was suppressed each time the fish swam (Fig. 4D, "Off"), and neurons that fired each time the fish swam (Fig. 4D, "Onset" and "Late"). Of the latter types, some fired just before swimming (~20 ms before swim onset, "Onset") and others fired just after swimming (~10 ms after swim onset, "Late"). There was a change in subthreshold voltage that preceded these firing rate changes by tens of milliseconds (Fig. 4D and fig. S44D). The neuron types were spatially intermingled within this midbrain nucleus (Fig. 4, E and F). The existence of neurons that fired before swimming and neurons that fired after swimming may indicate that this nucleus both partakes in the generation of swim bouts and is influenced by the motor output (Fig. 4G). Thus, Voltron allows for the dissection of population motor coding and sensorimotor integration circuits in ways that neither single-cell electrophysiology nor population calcium imaging can.

We tested Voltron in adult *Drosophila* in vivo by expressing the protein in a pair of dopaminergic neurons, one in each brain hemisphere, which innervate a single compartment in the mushroom body. We detected strong spiking signals from axons and dendrites of these neurons with Voltron$_{549}$ (Fig. 1K and fig. S18). The fluorescence signals matched action potentials detected using electrophysiology. In some neuronal cell types in *Drosophila*, calcium indicators located in the cell body have failed to exhibit fluorescence changes even under conditions where high spike rates are expected (*29*). However, spikes were clearly detectable when imaging from the soma of dopamine neurons with Voltron (fig. S18E). We could clearly distinguish spikes from the two neurons according to the amplitude of the spiking signals even when imaging from neuropil where their axons overlap extensively, likely because each bilaterally projecting cell contributes a denser innervation of the mushroom body in the ipsilateral hemisphere (fig. S18D).

Combining the molecular specificity of genetically encoded reagents with the superior photophysics of chemical dyes is an established path to improved imaging reagents (*14*). However, previous attempts to create hybrid protein–small molecule indicators by various approaches have not been successful for in vivo imaging (*30*). We engineered a modular sensor scaffold in which the targeting and sensor domains are genetically encoded and only the fluorophore and its protein-binding anchor are synthetic. The resulting chemigenetic indicator, Voltron, exhibits increased photon output, enabling in vivo voltage imaging of many more neurons over longer times—approximately 10^2 more neuron-minutes than other sensors. This improvement enables imaging experiments that can help to reveal how the precise electrical dynamics of neuronal populations orchestrate behavior over different time scales.

REFERENCES AND NOTES

1. T. W. Chen *et al*., *Nature* **499**, 295–300 (2013).
2. K. Svoboda, W. Denk, D. Kleinfeld, D. W. Tank, *Nature* **385**, 161–165 (1997).
3. V. Emiliani, A. E. Cohen, K. Deisseroth, M. Häusser, *J. Neurosci.* **35**, 13917–13926 (2015).
4. Y. Xu, P. Zou, A. E. Cohen, *Curr. Opin. Chem. Biol.* **39**, 1–10 (2017).
5. M. Z. Lin, M. J. Schnitzer, *Nat. Neurosci.* **19**, 1142–1153 (2016).
6. J. M. Kralj, A. D. Douglass, D. R. Hochbaum, D. Maclaurin, A. E. Cohen, *Nat. Methods* **9**, 90–95 (2011).
7. D. R. Hochbaum *et al*., *Nat. Methods* **11**, 825–833 (2014).
8. Y. Adam *et al*., *Nature* **569**, 413–417 (2019).
9. L. Jin *et al*., *Neuron* **75**, 779–785 (2012).
10. P. Zou *et al*., *Nat. Commun.* **5**, 4625 (2014).
11. Y. Gong *et al*., *Science* **350**, 1361–1366 (2015).
12. A. S. Abdelfattah *et al*., *J. Neurosci.* **36**, 2458–2472 (2016).
13. H. H. H. Yang *et al*., *Cell* **166**, 245–257 (2016).
14. J. B. Grimm *et al*., *Nat. Methods* **12**, 244–250 (2015).
15. G. V. Los *et al*., *ACS Chem. Biol.* **3**, 373–382 (2008).
16. L. P. Encell *et al*., *Curr. Chem. Genomics* **6**, 55–71 (2012).
17. J. B. Grimm *et al*., *Nat. Methods* **14**, 987–994 (2017).
18. Y. Gong, M. J. Wagner, J. Zhong Li, M. J. Schnitzer, *Nat. Commun.* **5**, 3674 (2014).
19. J. M. Kralj, D. R. Hochbaum, A. D. Douglass, A. E. Cohen, *Science* **333**, 345–348 (2011).
20. T. Wada *et al*., *J. Mol. Biol.* **411**, 986–998 (2011).
21. A. Keppler *et al*., *Nat. Biotechnol.* **21**, 86–89 (2003).
22. S. Chamberland *et al*., *eLife* **6**, e25690 (2017).
23. D. Brinks, A. J. Klein, A. E. Cohen, *Biophys. J.* **109**, 914–921 (2015).
24. C. A. Baker, Y. M. Elyada, A. Parra, M. M. L. Bolton, *eLife* **5**, e14193 (2016).
25. S. T. Lim, D. E. Antonucci, R. H. Scannevin, J. S. Trimmer, *Neuron* **25**, 385–397 (2000).
26. S. L. Smith, I. T. Smith, T. Branco, M. Häusser, *Nature* **503**, 115–120 (2013).
27. B. Tasic *et al*., *Nat. Neurosci.* **19**, 335–346 (2016).
28. M. B. Ahrens *et al*., *Nature* **485**, 471–477 (2012).
29. T. Hige, Y. Aso, G. M. Rubin, G. C. Turner, *Nature* **526**, 258–262 (2015).
30. A. Wang, J. Feng, Y. Li, P. Zou, *ACS Chem. Neurosci.* **9**, 639–650 (2018).

ACKNOWLEDGMENTS

We thank the Vivarium, Cell Culture, Instrument Design and Fabrication, Imaging, Molecular Biology, and Virus Production facilities at Janelia for assistance. Specifically, we thank B. Shields, D. Walpita, J. Cox, C. McGlynn, D. Alcor, A. Taylor, J. Rouchard, K. Ritola, X. Zhang, and J. Towne. We thank Z. Wei for discussions on data analysis. **Funding:** Supported by HHMI (A.S.A., T.K., A.S., O.N., H.L., Y.S., J.Y., J.Z., J.B.G., R.P., B.D.M., J.J.M., K.P., G.C.T., Z.L., M.K., K.S., M.B.A., L.D.L., and E.R.S.), Simons Collaboration on the Global Brain research awards 325171 and 542943SPI (M.B.A. and L.P.), IARPA MICRONS D16PC00003 (L.P.), NIH R01EB22913 (L.P.), Taiwan Ministry of Science and Technology MOST106-2628-B-010-004, MOST105-2628-B-010-005, MOST106-2320-B-010-012 and Taiwan National Health Research Institute NHRI-ex-107-10509NC (T.-W.C. and B.-J.L.), and the Allen Institute for Brain Science (L.C., S.C.S., and G.J.M.). **Author contributions:** A.S.A., L.D.L., and E.R.S. conceived the project. A.S.A. engineered Voltron. A.S.A., H.L., J.Z., J.B.G., R.P., J.J.M., Z.L., L.D.L., and E.R.S. performed and analyzed in vitro experiments. T.K., J.F., L.P., M.K., and M.B.A. performed and analyzed experiments in larval zebrafish. A.S., O.N., Y.-C.H., L.C., S.C.S., J.Y., G.J.M., K.P., B.-J.L., T.-W.C., and K.S. performed and analyzed mouse experiments. Y.S. and G.C.T. performed and analyzed experiments in *Drosophila*. L.P., J.J.M., G.J.M., K.P., B.-J.L., T.-W.C., G.C.T., Z.L., M.K., K.S., M.B.A., L.D.L., and E.R.S. supervised various aspects of this work. A.S.A. and E.R.S. wrote the manuscript with input and assistance from B.D.M. and all other authors. **Competing interests:** A.S.A., L.D.L., and E.R.S. have filed for a patent on chemigenetic voltage indicators. **Data and materials availability:** All data are available in the manuscript or the supplementary materials. Plasmids and AAVs are available from Addgene (www.addgene.org), transgenic *Drosophila* stocks are available from the Bloomington Drosophila Stock Center (https://bdsc.indiana.edu), and transgenic zebrafish are available from the Zebrafish International Resource Center (https://zebrafish.org/). J.B.G. and L.D.L. are inventors on U.S. Patents 9,933,417, 10,018,624, and 10,161,932 as well as U.S. Patent Application 16/211,388 held/submitted by HHMI; these cover azetidine-containing fluorophores such as JF$_{525}$. A.S.A., L.D.L., and E.R.S. are inventors on patent application WO2018102577A1 submitted by HHMI that covers chemigenetic voltage indicators. DNA plasmids and AAVs, transgenic zebrafish, and transgenic flies described in this manuscript are available from Addgene, ZIRC, and the Bloomington Drosophila Stock Center, respectively, under a material agreement with HHMI.

SUPPLEMENTARY MATERIALS

science.sciencemag.org/content/365/6454/699/suppl/DC1
Materials and Methods
Tables S1 to S5
Figs. S1 to S45
References (*31*–*62*)

5 October 2018; accepted 17 July 2019
Published online 1 August 2019
10.1126/science.aav6416

CELL BIOLOGY

Active cell migration is critical for steady-state epithelial turnover in the gut

Denis Krndija[1]*, Fatima El Marjou[1], Boris Guirao[2], Sophie Richon[1], Olivier Leroy[2], Yohanns Bellaiche[2], Edouard Hannezo[3]†, Danijela Matic Vignjevic[1]†

Steady-state turnover is a hallmark of epithelial tissues throughout adult life. Intestinal epithelial turnover is marked by continuous cell migration, which is assumed to be driven by mitotic pressure from the crypts. However, the balance of forces in renewal remains ill-defined. Combining biophysical modeling and quantitative three-dimensional tissue imaging with genetic and physical manipulations, we revealed the existence of an actin-related protein 2/3 complex–dependent active migratory force, which explains quantitatively the profiles of cell speed, density, and tissue tension along the villi. Cells migrate collectively with minimal rearrangements while displaying dual—apicobasal and front-back—polarity characterized by actin-rich basal protrusions oriented in the direction of migration. We propose that active migration is a critical component of gut epithelial turnover.

The gut epithelium is the largest mucosal surface of the body (*1*) and one of the most rapidly renewing tissues (3 to 5 days) in adult mammals (*2*). A single layer of columnar cells lines the villi (finger-like evaginations that project into the gut lumen) and the crypts (small invaginations into the connective tissue). Stem cells in the crypts give rise to transit-amplifying cells, which divide four to five times before terminal differentiation (*2*). After exiting the crypt, differentiated epithelial cells migrate for ~3 days, until they reach the top of the villus, where they get extruded (*2*). Continuous migration of cells between the spatially distant functional compartments of cell division and loss is a major component in gut epithelial renewal. The predominant theory is that cells migrate passively, driven by a pushing force resulting from cell division (i.e., mitotic pressure) (*3*, *4*). However, irradiation and mitotic inhibitor treatment do not block gut epithelial migration, despite causing substantial cell loss in the crypts (*5*, *6*), raising the possibility of active migration. In this study, we investigated the mechanism(s) of epithelial cell migration during homeostatic renewal in the small intestine.

To quantitatively test the contribution of mitotic pressure in epithelial cell migration along the villi, we performed 5-ethynyl-2′-deoxyuridine (EdU) pulse-chase assays in mice injected with hydroxyurea (HU), a specific S-phase inhibitor (*7*, *8*). A low dose of HU (HU^{lo}) efficiently inhibited mitosis, without affecting cell migration along the villi (Fig. 1, A to C, and figs. S1, A to D, and S2, A to C). This suggests that cell division per se is not the principal driving force for cell migration. High concentrations of HU (HU^{hi}) were shown to inhibit cell migration but are proapoptotic (*5*). As expected, HU^{hi} reduced crypt cellularity (fig. S1, A to D), but cell migration was decreased only in the lower villus region (Fig. 1, A to C, and fig. S2, A, B, and D). Together, these data suggest that the acting range of mitotic pressure is limited to crypts and the lower villus region.

We next investigated the alternative possibility that cells could migrate actively. Because of the potentially complex spatial interplay between passive and active migratory forces, we developed a biophysical model for gut epithelium renewal. This minimal continuum theory for migrating and proliferating cells (*9*, *10*) (Fig. 1D, fig. S3, and theory note in the supplementary materials) predicted that proliferation forces alone would result in a gradual decrease in cell density toward the villus, whereas active migration would cause a density increase because of cell overcrowding near the villus top (Fig. 1E). We measured one-dimensional (1D) density profiles along the villus axis [as well as 2D density (fig. S4)] and observed that cell density first gradually decreased toward the middle of the villus and then increased in the top region of the villus (Fig. 1, F to H), in good qualitative agreement with the active migration model (Fig. 1E). We thus hypothesized that cell migration along the villus operates according to a two-tier migration system: proliferation forces dominate close to the crypt, whereas active migration forces become predominant in the upper part of the villus. By fitting the active migration force in our model, we obtained a good quantitative prediction for the nonmonotonous cell density profile along the villus (Fig. 1H and fig. S3G). Moreover, simulating a short-term mitotic pressure inhibition predicted a density decrease only at the villus bottom, which was quantitatively confirmed, with HU^{hi} treatment decreasing cell density only at the bottom 10% of the villus (Fig. 1, I to K, and fig. S1, F and G). These data strongly suggested the existence of an active migratory mechanism, in addition to mitotic pressure, which contributes to cell migration along the villi.

The model also predicted an increase in cell speed along the villus axis, dependent on the strength of the active migration force (Fig. 2A). Using EdU pulse-chase assays, we found greater cell displacements in the middle villus compared with the villus bottom (Fig. 2B). To measure cell speed directly, we performed live imaging of gut explants derived from Villin:$CreER^{T2}$/mTmG reporter mouse (*11*–*13*), where membrane-targeted green fluorescent protein (GFP) is expressed mosaically in the epithelium (Fig. 2, C to E, and fig. S5A). Cells accelerated as they progressed along the villus axis (Fig. 2D and movie S1). Ex vivo speed profiles, together with in vivo EdU pulse-chase data, correlated well with model predictions for an active migratory mechanism (Fig. 2E).

We then characterized collective cell dynamics, with the tracked patch of cells retaining cohesiveness during migration and extending ~10% along the villus axis without simultaneously shrinking laterally (Fig. 2F, fig. S5B, and movie S4). This could be almost entirely accounted for by cell extension along the villus axis; contributions due to junction remodeling from cell rearrangements and delamination were limited, and, as expected, no divisions were observed (Fig. 2F). The observed cohesiveness, consistent with the clonal ribbons observed previously (*14*), could be well explained by a minimal 2D model of cells performing biased random walks toward the villus top, with cell-cell interactions minimizing cell dispersion and allowing collective migration (fig. S5, C to F).

Forces driving epithelial migration have been best characterized quantitatively in culture (*15*–*19*), where active migration results in a buildup of tension in the colony center (*16*). Similarly, an active migration model predicts a buildup of mechanical tension in the villus bottom, driven by cell traction forces toward the top. Conversely, if proliferation forces acted alone, pressure should be highest (and tension lowest) close to the crypt, while dissipating along the crypt-villus axis as a result of friction with the basement membrane. Spatial differences in tissue tension can thus be used to infer how and where forces act during cell migration (*16*, *20*–*23*). We imaged mice with GFP-tagged endogenous nonmuscle myosin IIA heavy chain (*24*) to highlight the apical actomyosin belt associated with E-cadherin–containing adherens junctions (*25*) (fig. S5G). To map tensile forces, we made circular laser cuts of epithelial adherens junctions at the lower and upper villus regions (fig. S5H). The epithelium recoiled isotropically after the laser cut, indicating that it was always under tension (Fig. 2, G and H, and fig. S5H). The recoil speed was significantly higher in the lower villus region (Fig. 2H, fig. S5I, and movies S2 and S3). This further supported a model of active migration forces causing a crowding or increased pressure effect at the top and leaving the villus bottom under higher tension.

[1]Institut Curie, PSL Research University, CNRS UMR 144, F-75005 Paris, France. [2]Institut Curie, PSL Research University, U934/UMR3215, F-75005 Paris, France. [3]Institute of Science and Technology Austria (IST Austria), Am Campus 1, 3400 Klosterneuburg, Austria.
*Corresponding author. Email: denis.krndija@curie.fr
†These authors contributed equally to this work.

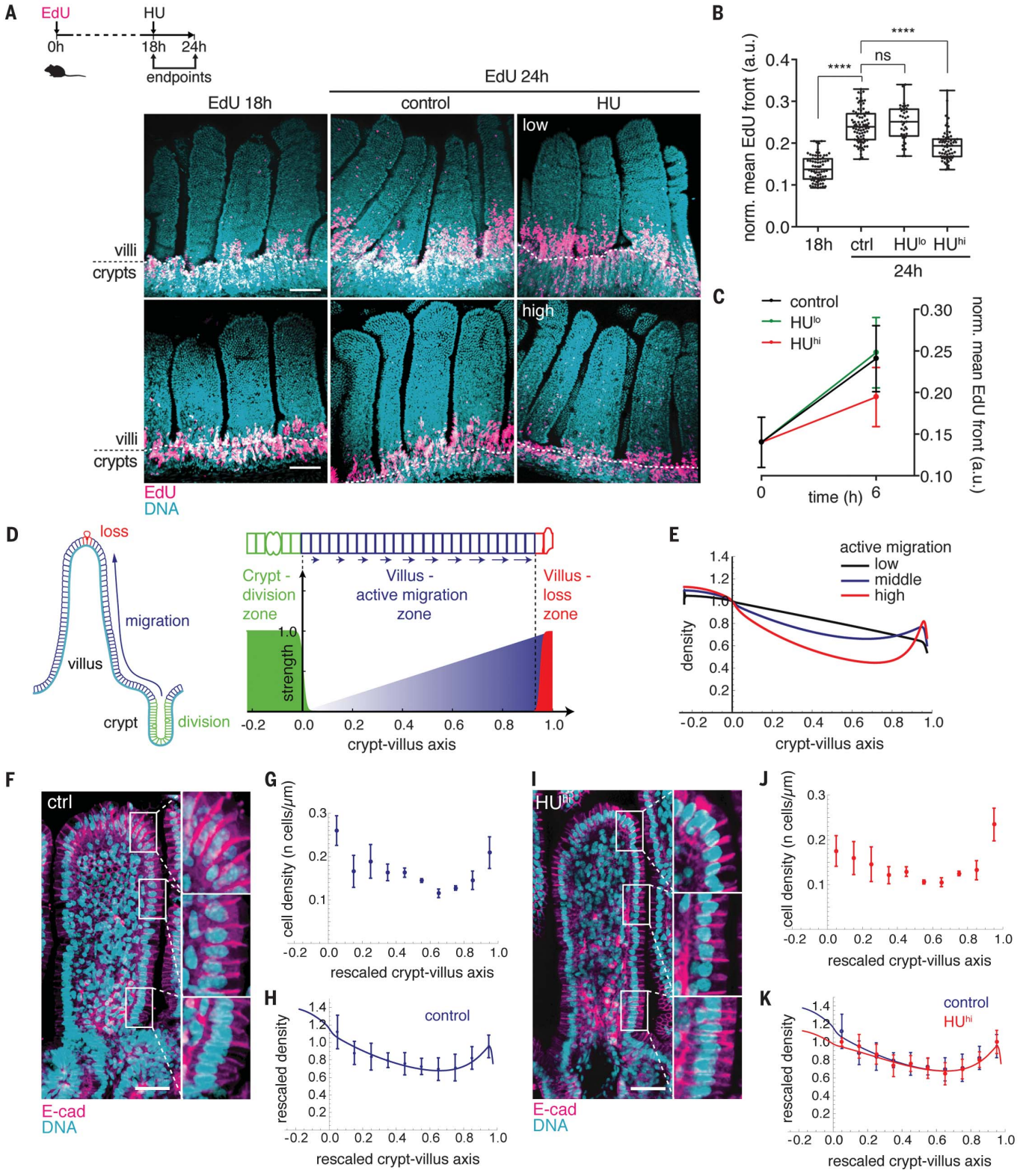

Fig. 1. Epithelium continues migrating during mitotic block. (**A**) Top: EdU and HU injection scheme with EdU chase time points. Bottom: Maximum Z projections (30 to 50 μm range). Dashed line in bottom panels indicates the crypt-villus interface. Scale bars, 50 μm. (**B**) Box-and-whisker plot corresponding to (A). ****$P < 0.0001$; ns, not significant; au, arbitrary units. (**C**) EdU fronts plotted as a function of time. (**D**) Theoretical model for epithelial renewal during gut homeostasis. (**E**) Predicted cell density profiles along the crypt-villus axis depending on the level of active migratory force. (**F**) Control villus—longitudinal section. Boxed regions are shown in high magnification. Scale bar, 40 μm. (**G**) Cell density profile of the villus shown in (F). E-cad, E-cadherin. (**H**) Model fit to average density profile. (**I**) HU^{hi} treatment—longitudinal section. Boxed regions are shown in high magnification. Scale bar, 40 μm. (**J**) Cell density profile of the villus shown in (I). (**K**) Average density profiles for control (blue) and HU^{hi} (red), with their theoretical predictions (lines).

Actively migrating cells generate protrusive forces through lamellipodia or filopodia, which are driven by actin polymerization (*26*). Gut epithelial cells are columnar, apicobasally polarized, and not known to have lamellipodia. To assess if gut epithelial cells have cryptic protrusions, we generated a mouse that mosaically expresses LifeAct-mCherry in the gut epithelium, to follow F-actin in individual cells (Fig. 3A). We found that enterocytes have small, F-actin–rich basal feet in contact with the basement membrane, pointing in the direction of cell movement (Fig. 3, B to D). Membrane-targeted GFP also highlighted basal protrusions in Villin:CreER^{T2}/mTmG reporter mice (fig. S6A). Radial distance map

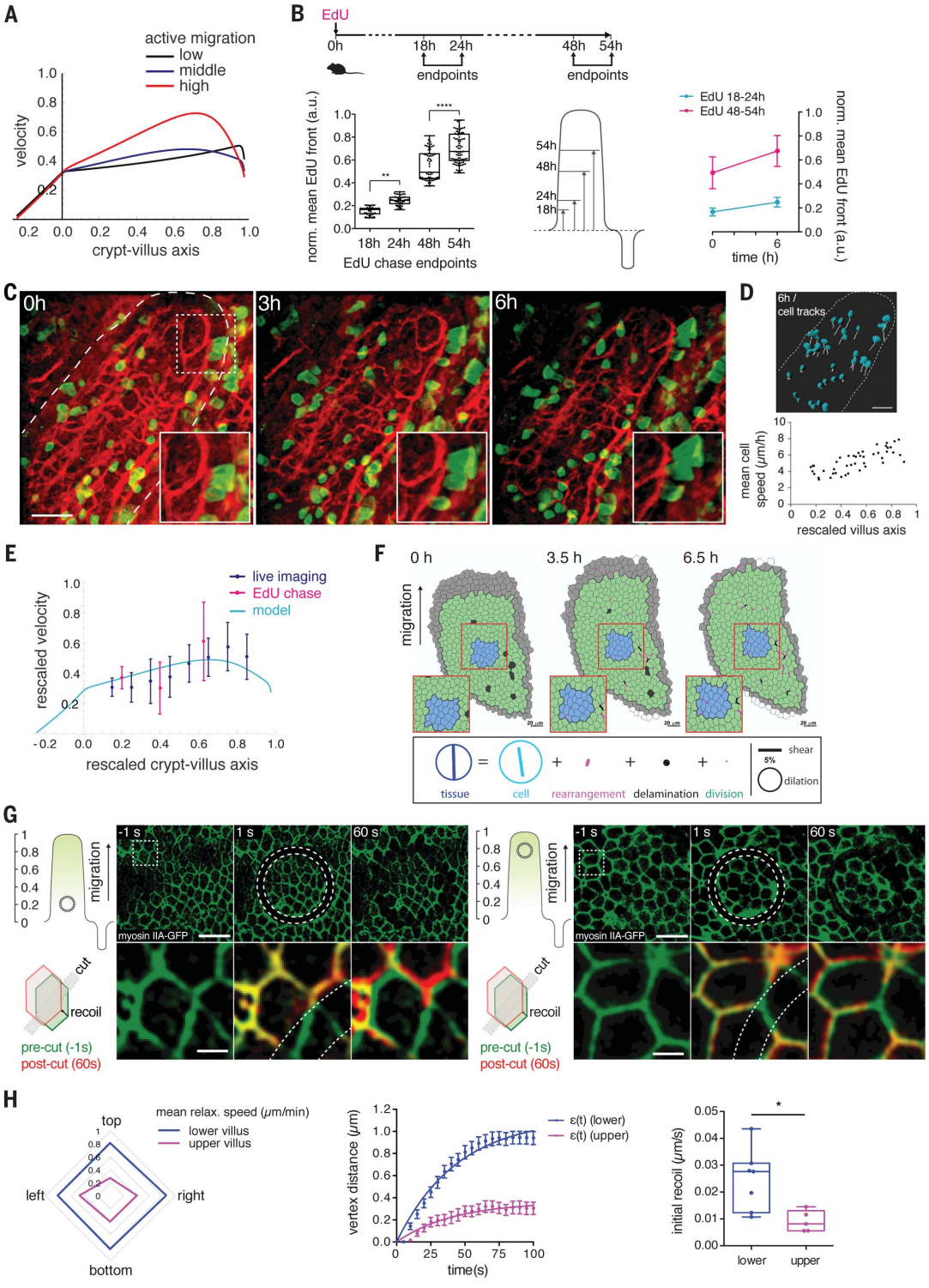

Fig. 2. Epithelial cells migrate collectively with increasing velocity and create a gradient of tissue tension along the villi. (**A**) Predicted cell velocity profiles along the crypt-villus axis depending on the level of active migratory force. (**B**) EdU pulse-chase assay (top); box-and-whisker plot (bottom left) and EdU fronts' position (scheme; bottom middle); EdU fronts plotted as a function of time (bottom right). (**C**) Montage from a time-lapse movie of gut explants (Villin:CreER^{T2}/mTmG; maximum projection of 50 μm); dashed line, villus. (Inset) A magnified region. Scale bar, 50 μm. (**D**) Top: Cell segmentation (cyan) and cell tracks (white) from the experiment shown in (C). Dashed line, villus. Scale bar, 50 μm. Bottom: Mean cell speeds plotted against relative cell position. (**E**) Average cell velocity plotted against villus axis, overlaid with model predictions. (**F**) Top: Skeletonized and tracked images from a time-lapse movie. Newly formed junctions (magenta), junctions formed after rearrangements (black), delamination (green), or division (none). Inset shows a magnified region. Scale bars, 20 μm. Bottom: Analysis of tissue deformation. Circles represent size change; bars represent pure shear (contraction-elongation). (**G**) Montage showing images before and after laser ablation in lower villus (left-hand panel) and upper villus (right-hand panel). Scale bars, 20 μm. Magnified regions: Postablation images (post-cut, red) overlaid with preablation images (pre-cut, green). Scale bars, 5 μm. (**H**) Left: Radar chart showing mean relaxation speed per four directions in lower (blue) and upper (purple) villus regions [as schematized in (G)]. Middle: Vertex separation $\varepsilon(t)$ plot in function of time, for lower (purple) and upper (blue) villus region. Right: Initial recoil speed for lower and upper villus region. *$P < 0.05$.

analysis (fig. S6, B and C) confirmed that these protrusions were front-back polarized, analogous to the front-back polarity described in migrating cells (Fig. 3, D to F, and fig. S6C). As actin-based protrusions typically require the actin-related protein 2/3 (Arp2/3) complex (*27*, *28*), we tested whether a specific Arp2/3 inhibitor, CK-*666* (*29*), disrupted basal protrusions and migration in vivo. Integrity of cell-cell adhesions, crypt cellularity, and mitosis were not affected during this short-term CK-*666* treatment, excluding potential confounding effects on cell migration (fig. S7, B to D). In CK-666–treated mice, apicobasal polarity and the total protrusion area were not affected, but basal front-back polarity was lost (Fig. 3, D to G, and fig. S6D). Accordingly, CK-*666* treatment inhibited cell migration along the villi (Fig. 4, A and B). Next, we generated an inducible, gut epithelium–specific

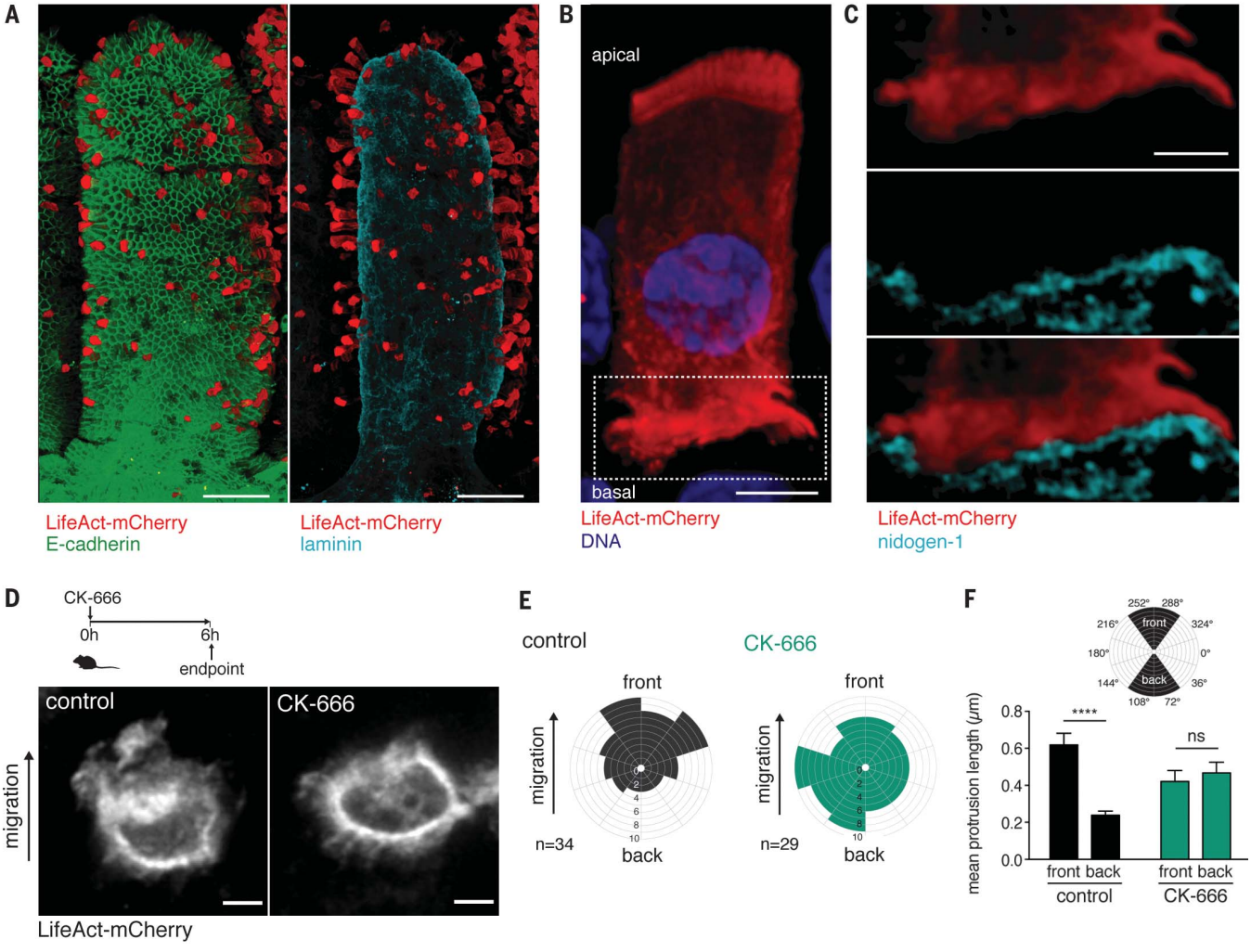

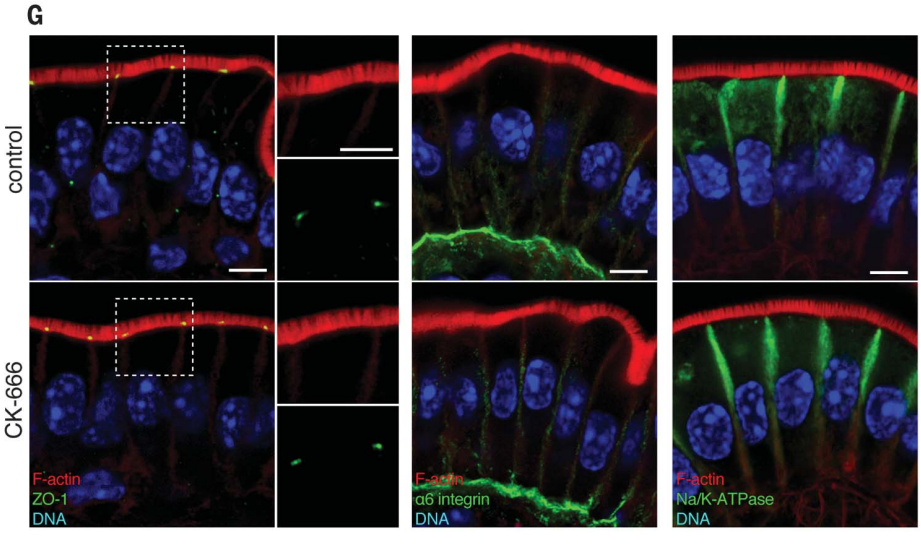

Fig. 3. Epithelial cells display actin-rich basal protrusions oriented in the direction of migration. (**A**) Mosaic expression of LifeAct-mCherry (red) in the intestinal epithelium. Maximum intensity projection (Z range, 30 μm). Scale bars, 50 μm. (**B**) Super-resolution 3D image (Z range, 2.4 μm) of a LifeAct-mCherry-expressing enterocyte. Scale bar, 4 μm. (**C**) Magnified 2D image of the boxed region shown in (B). Scale bar, 2 μm. (**D**) Maximum Z projections of basal part of enterocytes (Z range, 2.6 μm) expressing LifeAct-mCherry, control [dimethyl sulfoxide (DMSO)] or CK-666–treated. Scale bars, 2 μm. (**E**) Rose plots with average normalized radial distances for protrusions. n, number of cells analyzed. (**F**) Bar chart showing protrusion length with respect to front-back orientation. ****$P <$ 0.0001. (**G**) Super-resolution images; apical marker ZO-1 (left) and basolateral markers α6 integrin (middle) and Na/K-ATPase (right). Boxed regions are shown in high magnification. Scale bars, 5 μm.

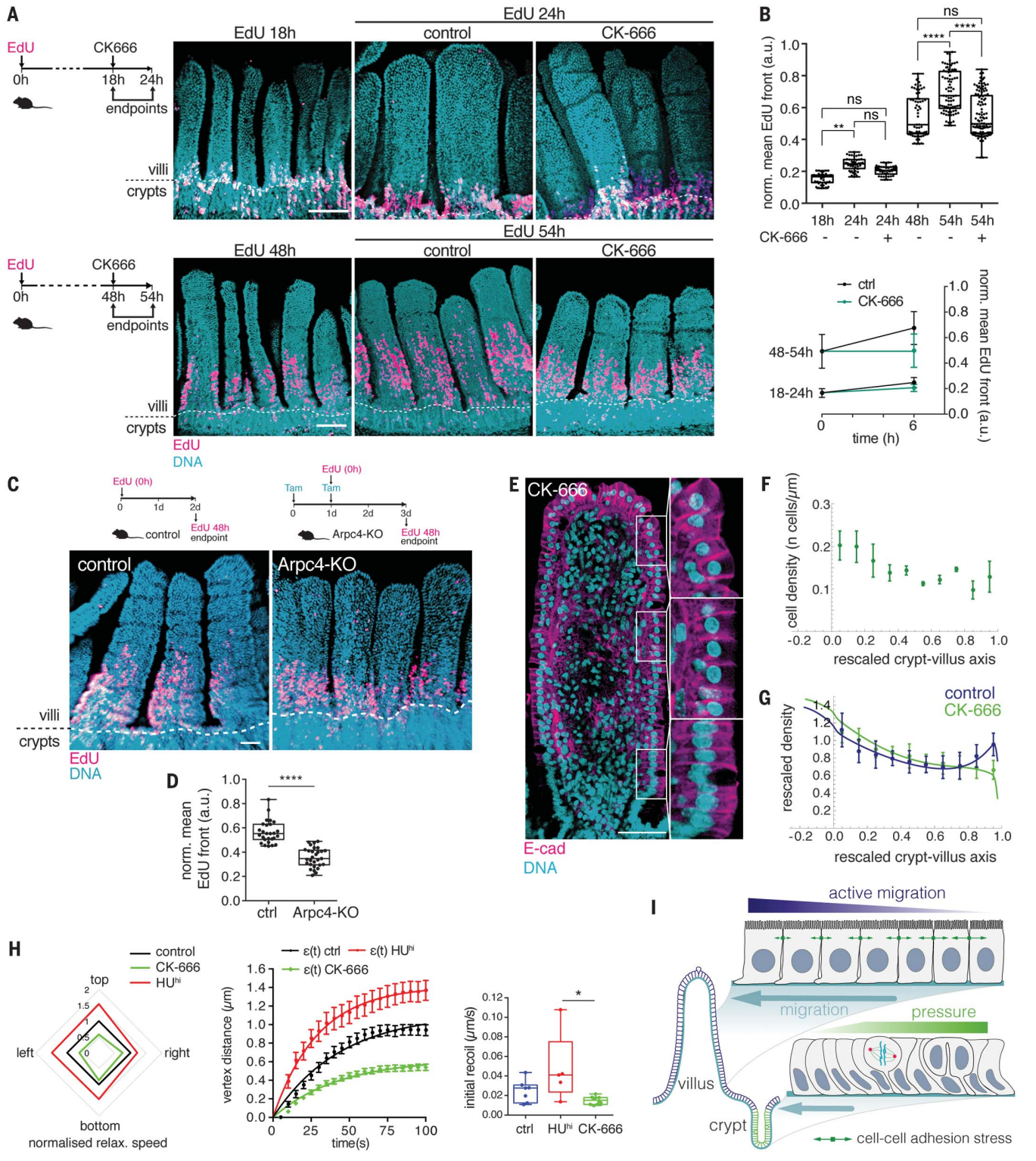

Fig. 4. Epithelial cell migration is driven by Arp2/3. (**A**) EdU pulse-chase assays; maximum Z projections (30 to 50 μm). Dashed line indicates the crypt-villus interface. Scale bars, 100 μm. (**B**) Top: Box-and-whisker plot for EdU fronts. $^{**}P < 0.01$, $^{****}P < 0.0001$. Bottom: EdU fronts plotted against time. Control, DMSO. (**C**) EdU pulse-chase assays; maximum Z projections (30 to 50 μm). Tam, tamoxifen. Scale bar, 50 μm. (**D**) Box-and-whisker plot for EdU fronts. $^{****}P < 0.0001$. (**E**) CK-666 treatment—longitudinal section. Boxed regions are shown in high magnification. Scale bar, 50 μm. (**F**) Cell density profile of the villus shown in (E). (**G**) Average density profiles. Control (blue, same as Fig. 1H); CK-666 (green); theoretical prediction (lines). (**H**) Left: Radar chart displaying relaxation speed in HU^{hi}- or CK-666–treated mice, along four indicated directions. Middle: Vertex separation $\varepsilon(t)$, in function of time. Right: Initial recoil speed, box-and-whisker plot. Control: DMSO or saline, for CK-666 and HU, respectively. $^{*}P < 0.05$. (**I**) Mechanical model for epithelial migration in the small intestine.

Arp2/3 knockout (KO) mouse by crossing the $Arpc4^{fl/fl}$ mouse (*30*) with the Villin:$CreER^{T2}$ line. Arpc4 depletion (fig. S8A) also decreased cell displacement along the villi (Fig. 4, C and D), without affecting crypt cell numbers, cell-cell junction integrity, or the apicobasal polarity (fig. S8, B to E). Inhibition of migration after CK-666 treatment was more pronounced in the upper than in the lower villus region (Fig. 4B). This agreed with the theoretical model, which predicted that inhibition of active migration would have a more pronounced effect in the upper villus region (fig. S7A).

Furthermore, the CK-666–treated tissue density profile matched our model prediction, abrogating the density increase at the villus top seen in controls (Fig. 4, E to G, and fig. S7, E and F). Arpc4-KO produced a similar cell density profile as CK-666 (fig. S8F), whereas the villus length was unaffected in both cases (figs. S7G and S8G). To validate the predicted roles of mitotic pressure and active migration in generating pressure and tension forces, respectively, we performed laser cut experiments. HU^{hi} treatment led to an increase in tissue tension (i.e., decrease in pressure) on villi, whereas Arp2/3 inhibition led to a decrease in tissue tension (Fig. 4H). This supports our two-tier model of mitotic pressure and Arp2/3-dependent tensile migratory forces (Fig. 4I).

Maintenance of a functional intestinal barrier (*31*) requires tightly regulated epithelial renewal. Dysregulation of either proliferation, migration, or extrusion could lead to pathologies, such as inflammatory diseases and tumor formation (*32*). Here, we showed that Arp2/3-driven active migration occurs along the villus. We showed that intestinal epithelial cells exhibit dual polarity—apicobasal and front-back—characterized by actin-rich basal protrusions oriented in the direction of migration. We propose that active migratory forces are a key component in the homeostatic renewal of the adult gut epithelium.

REFERENCES AND NOTES

1. L. W. Peterson, D. Artis, *Nat. Rev. Immunol.* **14**, 141–153 (2014).
2. L. G. van der Flier, H. Clevers, *Annu. Rev. Physiol.* **71**, 241–260 (2009).
3. H. Cheng, C. P. Leblond, *Am. J. Anat.* **141**, 461–479 (1974).
4. A. Parker *et al*., *FASEB J.* **31**, 636–649 (2017).
5. P. Kaur, C. S. Potten, *Cell Tissue Kinet.* **19**, 601–610 (1986).
6. N. A. Wright, M. Alison, *The Biology of Epithelial Cell Populations* (Oxford Univ. Press, 1984).
7. S. E. Pfeiffer, L. J. Tolmach, *Cancer Res.* **27**, 124–129 (1967).
8. K. Ijiri, C. S. Potten, *Br. J. Cancer* **55**, 113–123 (1987).
9. J. Ranft *et al*., *Proc. Natl. Acad. Sci. U.S.A.* **107**, 20863–20868 (2010).
10. E. Hannezo, A. Coucke, J.-F. Joanny, *Phys. Rev. E* **93**, 022405 (2016).
11. F. El Marjou *et al*., *Genesis* **39**, 186–193 (2004).
12. M. D. Muzumdar, B. Tasic, K. Miyamichi, L. Li, L. Luo, *Genesis* **45**, 593–605 (2007).
13. R. Staneva, J. Barbazan, A. Simon, D. M. Vignjevic, D. Krndija, *Methods Mol. Biol.* **1749**, 163–173 (2018).
14. C. Lopez-Garcia, A. M. Klein, B. D. Simons, D. J. Winton, *Science* **330**, 822–825 (2010).
15. R. Farooqui, G. Fenteany, *J. Cell Sci.* **118**, 51–63 (2005).
16. X. Trepat *et al*., *Nat. Phys.* **5**, 426–430 (2009).
17. D. T. Tambe *et al*., *Nat. Mater.* **10**, 469–475 (2011).
18. R. Moore, S. Carlson, J. L. Madara, *Lab. Invest.* **60**, 237–244 (1989).
19. F. Ubelmann *et al*., *Proc. Natl. Acad. Sci. U.S.A.* **110**, E1380–E1389 (2013).
20. Z. Liu *et al*., *Proc. Natl. Acad. Sci. U.S.A.* **107**, 9944–9949 (2010).
21. V. Maruthamuthu, B. Sabass, U. S. Schwarz, M. L. Gardel, *Proc. Natl. Acad. Sci. U.S.A.* **108**, 4708–4713 (2011).
22. M. P. Sheetz, D. P. Felsenfeld, C. G. Galbraith, *Trends Cell Biol.* **8**, 51–54 (1998).
23. J. D. Hood, D. A. Cheresh, *Nat. Rev. Cancer* **2**, 91–100 (2002).
24. Y. Zhang *et al*., *Blood* **119**, 238–250 (2012).
25. J. L. Madara, *Am. J. Physiol.* **253**, C171–C175 (1987).
26. D. A. Lauffenburger, A. F. Horwitz, *Cell* **84**, 359–369 (1996).
27. P. Suraneni *et al*., *J. Cell Biol.* **197**, 239–251 (2012).
28. C. Wu *et al*., *Cell* **148**, 973–987 (2012).
29. B. J. Nolen *et al*., *Nature* **460**, 1031–1034 (2009).
30. W. C. Skarnes *et al*., *Nature* **474**, 337–342 (2011).
31. J. M. Blander, *FEBS J.* **283**, 2720–2730 (2016).
32. E. R. Fearon, B. Vogelstein, *Cell* **61**, 759–767 (1990).

ACKNOWLEDGMENTS

We thank J.-F. Joanny, D. Louvard, G. Montagnac, J. Rosenblatt, R. Galupa, and all members of the DMV lab for helpful discussions and critical reading of the manuscript. We thank A. M. Lennon-Dumenil for providing the $Arpc4^{fl/fl}$ mouse strain and R. Adelstein for the GFP-NMHCII-A strain. We thank O. Renaud for help with imaging and image processing. We acknowledge the Cell and Tissue Imaging facility (PICT-IBiSA) and Animal Facility, Institut Curie. **Funding:** This work was supported by ERC-2012-StG_20111109 grant STARLIN (D.M.V.) and ANR-16-CE13-0016-01 grant HOMEOGUT (D.M.V.). **Author contributions:** D.K. and D.M.V. conceived of the study and designed all experiments. Experiments were performed by D.K., S.R., and F.E.M. Data analysis was done by D.K., B.G., and E.H. Mouse colony management and transgenesis was done by F.E.M. Modeling was done by E.H. O.L. wrote a macro for protrusion orientation analysis. D.K., Y.B., E.H., and D.M.V. wrote the manuscript. **Competing interests:** The authors declare no competing interests. **Data and materials availability:** All data in the paper are presented in the main text or in the supplementary materials.

SUPPLEMENTARY MATERIALS

science.sciencemag.org/content/365/6454/705/suppl/DC1
Materials and Methods
Theory Note
Figs. S1 to S8
Table S1
References (*33*–*51*)
Movies S1 to S4

2 July 2018; resubmitted 6 May 2019
Accepted 3 July 2019
10.1126/science.aau3429

Cytokine Panel

The Bio-Plex Pro Human Immunotherapy Panel 20-plex covers biologically researched cytokine targets that are associated with immunotherapy research. It is a ready-to-use, 1 × 96-well kit that contains premixed magnetic capture beads and detection antibodies, standards, and buffers that produce results for 20 different cytokines using only 12.5 µL of sample. The Bio-Plex Panel maximizes laboratory efficiency by generating key actionable data in a single experiment. The kit is compatible with other Bio-Rad platforms, including the Bio-Plex 200, Bio-Plex 3D Suspension Array Systems, and other xMAP platforms.

Bio-Rad
For info: 800-424-6723
www.bio-rad.com

Coomassie Stain

InstantBlue has a unique mechanism that stains proteins in 15 min while leaving a clear background, eliminating the need to fix, wash, or destain. It is formulated for safe use and easy disposal. InstantBlue is a nontoxic formulation and does not contain any methanol or acetic acid, making it compatible with mass spectrometry protocols. With extended stability, InstantBlue has a shelf life of two years that will not compromise the high sensitivity of the protein bands, as 5 ng can be detected per band.

Expedeon
For info: 844-611-3656
www.expedeon.com

Protein Analysis Platform

Jess automates the protein separation and immunodetection of traditional Western blotting, eliminating many of the tedious, error-prone steps typical of this technique. Just load your samples and reagents into the microplate, and Jess separates your proteins by size, while precisely managing antibody additions, incubations, washes, and even detection steps. Come back to fully analyzed results in 3 h. Go further with multiplexing—Jess's fluorescent detection gets all the information you need in one shot. Jess—she's like Western blot meets ELISA all-in-one.

ProteinSimple
For info: 888-607-9692
proteinsimple.com/jess.html

Secondary Antibodies

TrueBlot monoclonal secondary antibodies recognize the native, nonreduced form of immunoglobulin G (IgG) over its reduced form in a variety of species. This unique ability makes TrueBlot secondary antibodies the ideal solution when performing Western blot detection of immunoprecipitated proteins (IP/Western blot), as their use reduces interference by the ~55-kDa heavy-chain and ~23-kDa light-chain of the immunoprecipitating antibody, enabling unhindered detection of your blotted-protein band of interest. It is available in horseradish peroxidase (HRP)-conjugated forms that target mouse, rabbit, goat, or sheep IgG, or fluorescent-conjugated forms that target mouse or rabbit IgG.

Rockland
For info: 800-656-7625
rockland-inc.com

Synthetic sgRNA

Edit-R CRISPR-Cas9 synthetic single-guide RNAs (sgRNAs) greatly simplify the workflow of permanently knocking out genes by eliminating the time-consuming cloning of individual guide RNA expression vectors. Our chimeric sgRNAs contain both CRISPR RNA (crRNA) and transactivating crRNA in one molecule, which arrives ready-to-use and is ideal for experiments when a single molecule is preferable. Edit-R synthetic sgRNA provides the functionality and reliability of Dharmacon RNA oligos. sgRNAs can be designed to target any gene using the CRISPR Design Tool. The sgRNA is synthesized using patented Dharmacon 2'-ACE chemistry, which provides faster, more efficient coupling rates than standard RNA synthesis chemistries, resulting in more full-length product. Our synthetic sgRNA are column-purified, deprotected, and desalted to deliver highly functional, ready-to-use molecules. For larger quantities and additional purification options for sgRNAs, the custom single-strand RNA synthesis tool can be used for ordering.

Dharmacon
For info: 800-235-9880
dharmacon.horizondiscovery.com

siRNA/miRNA Transfection Kit

With the Exo-Fect siRNA/miRNA Transfection Kit, you get powerful new technology for loading small RNA cargo into extracellular vesicles (EVs). Unlike electroporation, a common method for introducing small RNAs into EVs, the Exo-Fect workflow does not require access to specialized equipment or the same time-consuming optimization of voltage and timing. Instead, it leverages our proprietary Cell-Penetrating Peptide (CPP) technology to transfer small interfering RNAs (siRNAs) or microRNAs (miRNAs) to the inside of your EVs. The Exo-Fect is highly efficient, and a posttransfection cleanup step ensures low background. You get clean, ready-to-use, RNA-loaded EVs. Try the Exo-Fect and turn your EVs into small RNA–delivering machines.

System Biosciences
For info: 888-266-5066
www.systembio.com

Cooling Base

The DrySyn ChilliBlock from Asynt allows you to undertake sensitive biological assays in a temperature-controlled manner, vastly reducing the risk of expensive biological samples, reagents, or enzymes degrading due to adverse temperature conditions. Traditionally, methods of cooling biological assays have relied upon direct immersion in insulated ice buckets, which are prone to considerable temperature variability, sample contamination, and loss of wetted labels. In addition, using this methodology can only maintain a cooled temperature for a limited time, and requires staff to periodically monitor and add new coolant (ice). Modular in design, the ChilliBlock base can be simply attached to most laboratory heating/cooling circulators, thereby enabling stable temperature control at important biological temperatures, such as 0°C or 37°C, for long periods of time. Designed for versatility, the ChilliBlock has interchangeable blocks for tubes, vials, and plates as well as custom DrySyn blocks to fit any Eppendorf tube or vial.

Asynt
For info: +44-(0)-1638-781709
www.asynt.com/product/drysyn-chilliblock-system

Electronically submit your new product description or product literature information! Go to www.sciencemag.org/about/new-products-section for more information.

Newly offered instrumentation, apparatus, and laboratory materials of interest to researchers in all disciplines in academic, industrial, and governmental organizations are featured in this space. Emphasis is given to purpose, chief characteristics, and availability of products and materials. Endorsement by *Science* or AAAS of any products or materials mentioned is not implied. Additional information may be obtained from the manufacturer or supplier.

TALENT
Doctoral Fellowship Programme

Third call opens on
15 Aug. **and closes 1 Oct. 2019**

Read more
talent.ku.dk

UNIVERSITY OF COPENHAGEN
FACULTY OF SCIENCE

EUROPEAN UNION

HORIZON 2020
This project has received funding from the European Union's Horizon 2020 research and innovation programme under the Marie Skłodowska-Curie grant agreement No 801199.

ScienceCareers
FROM THE JOURNAL SCIENCE AAAS

Confused about your next career move?

Download Free Career Advice Booklets!

ScienceCareers.org/booklets

FIND YOUR HAPPIER PLACE.

Find your next job at ScienceCareers.org

There's scientific proof that when you're happy with what you do, you're better at what you do. Access career opportunities, see who's hiring and take advantage of our proprietary career-search tools. Get tailored job alerts, post your resume and manage your applications all in one place: sciencecareers.org

ScienceCareers
FROM THE JOURNAL SCIENCE AAAS

Chemistry and Chemical Engineering at Nanjing University

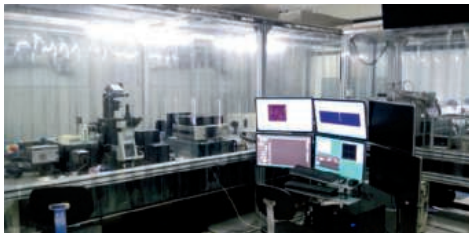

The School of Chemistry and Chemical Engineering (SCCE) at Nanjing University (NJU) is amongst the oldest colleges and departments in China. The Chemistry Department can be traced back to 1920, and was later amalgamated by the Chemistry Department of the former Central University and the Chemistry Department of the former Jinling University. SCCE was set up in 1993, and is now composed of three departments:

- *Department of Chemistry*
- *Department of Chemical Engineering*
- *Department of Polymer Science and Engineering*

SCCE has 161 faculty members, including 109 full professors, 4 members of the Chinese Academy of Sciences, 13 Chang Jiang Scholars of Ministry of Education (MOE), 20 winners of National Science Foundation of China (NSFC) fund for Distinguished Young Scholars. SCCE has a student body of about 1,680, of which are 430 undergraduate students and near 1,250 MSc and Ph.D. students.

SCCE has a state key discipline, and hosts the State Key Laboratory of Coordination Chemistry, the State Key Laboratory of Analytical Chemistry for Life Science, the Key Laboratory of Mesoscopic Chemistry of Ministry of Education and the Key Laboratory of High Performance Macromolecule Materials and Technology of Ministry of Education. It is authorized to confer degrees in 1 Ph.D. program, 1 master program and 2 undergraduate programs.

SCCE has a strong tradition in research. Over 40 members of the Chinese Academy of Sciences once studied or worked in the school. More than 140 awards including the National Science Award and the Ministerial and Provincial Awards have been won by SCCE. It has become one of the most attractive and competitive bases for personnel cultivation and scientific research in the country.

SCCE has established extensive international cooperation and academic exchanges with foreign institutions. It has hosted and sponsored a number of international conferences, symposiums and workshops on various topics. Many world leading chemists including several Nobel laureates have been invited to present lectures. Faculty members have been regularly invited to give plenary and keynote talks in the international conferences and symposiums.

SCCE seeks outstanding faculty candidates in the following research fields:

- *Inorganic Chemistry,*
- *Analytical Chemistry,*
- *Organic Chemistry,*
- *Physical Chemistry,*
- *Polymer Chemistry and Physics,*
- *Applied Chemistry,*
- *Chemical Biology*

Consideration will be given to candidates at all levels of faculty positions, including tenured full/associate professors and tenure-track assistant professors.

Qualified faculty candidates should have a Ph.D. in a relevant discipline, post-doctoral experience with an extensive publication record in high quality journals, a commitment to excellence in research and teaching, and the ability to engage with broader chemistry themes for the purpose of achieving transformative and translational research gains. Competitive recruitment packages are available with salary and faculty rank based on qualifications. All newly hired tenured faculty members will be provided sufficient startup resources and necessary research infrastructures. Annual salaries for assistant professors will be commensurate with work experience and research performance.

Qualified applicants are asked to send the following documents:

- *Cover letter*
- *Curriculum Vitae with Publication list*
- *Teaching statement*
- *Research statement*
- *Two or more reference letters (the signed letter to be submitted by the reference writers by email)*

Mr. Feng Peng
(H. R. Secretary of SCCE)
Email: fengpeng@nju.edu.cn

CAREER FEATURES:

Faculty Careers

Issue date: September 13
Book ad by August 29
Ads accepted until Sept. 6 if space allows

Issue date: October 11
Book ad by September 26
Ads accepted until Oct. 4 if space allows

Deliver your message to a global audience of targeted, qualified scientists.

129,564
subscribers in print every week

473,652
monthly unique browsers on ScienceCareers.org

55%
of our weekly readers are Ph.D.s

Why choose these features for your advertisement?

- Relevant ads lead off these career sections with a special faculty careers banners.

Expand your exposure by posting your print ad online:

- Link on the job board homepage to a landing page for faculty careers jobs
- Additional marketing driving relevant job seekers to the job board.

What makes *Science* the best choice for recruiting?

- Read and respected by 400,000 readers around the globe
- Your ad dollars support AAAS and its programs, which strengthens the global scientific community.

Faculty recruiting opportunities

Whatever your timing, we've got two special opportunities for your faculty ads this fall. The September 13 feature article focuses on how to navigate moving a research lab to another country. The October 11 job focus highlights faculty job opportunities in print and online.

To book your ad, contact:
advertise@sciencecareers.org

The Americas
202 326 6577
Europe
+44 (0) 1223 326527
Japan
+81 3 6459 4174
China/Korea/Singapore/ Taiwan
+86 131 4114 0012

Science Careers
AAAS
SCIENCECAREERS.ORG

Produced by the *Science*/AAAS Custom Publishing Office.

FOR RECRUITMENT IN SCIENCE, THERE'S ONLY ONE *SCIENCE*.

DISCOVER THE FUTURE

a leading position at SciLifeLab

To further strengthen our research environment and complement research areas already present at SciLifeLab, we are now looking to recruit an outstanding young group leader to a new SciLifeLab Fellows position.

The fellow will become an associate at the SciLifeLab research center, as well as contract a position at Stockholm University.

SciLifeLab Fellows position / Assistant Professor in Neurochemistry

Focused on molecular techniques to visualize and manipulate activity in the nervous system.

Read more at: www.scilifelab.se/fellows.

Application deadline: September 10, 2019.

About SciLifeLab

As a national hub for molecular biosciences in Sweden, SciLifeLab (Science for Life Laboratory) facilitates cutting-edge, multi-disciplinary life science research and promotes its translation to the benefit of society. The center focuses on both health and environmental research and is jointly operated by its four founder universities: KTH Royal Institute of Technology, Karolinska Institutet, Stockholm University, and Uppsala University. About 200 research groups, 1500 researchers and 40 national infrastructure facilities are associated with SciLifeLab.

10 ways that *Science* Careers can help advance your career

1. Register for a free online account on **ScienceCareers.org**.
2. Search thousands of job postings and find your perfect job.
3. Sign up to receive e-mail alerts about job postings that match your criteria.
4. Upload your resume into our database and connect with employers.
5. Watch one of our many webinars on different career topics such as job searching, networking, and more.
6. Download our career booklets, including Career Basics, Careers Beyond the Bench, and Developing Your Skills.
7. Complete an interactive, personalized career plan at "my IDP."
8. Visit our Employer Profiles to learn more about prospective employers.
9. Research graduate program information and find a program right for you.
10. Read relevant career advice articles from our library of thousands.

Visit **ScienceCareers.org** today — all resources are free

SCIENCECAREERS.ORG

ScienceCareers
FROM THE JOURNAL SCIENCE AAAS

ScienceCareers online @sciencecareers.org

University of Missouri
DIRECTOR OF BIOLOGICAL SCIENCES

The University of Missouri (MU) invites nominations and applications for the position of Director of the Division of Biological Sciences (DBS). DBS is housed in the College of Arts and Science, the largest and most academically diverse unit on campus, and the Director will report to the Dean.

The new Director will have the opportunity to lead an established and vibrant biological sciences Division with a strong and successful commitment to research, undergraduate and graduate education, and outreach to the broader community. We seek an individual who will support and contribute to the Division's strategic vision that builds on its demonstrated strengths in research, teaching, and commitment to inclusive excellence.

The Director is responsible for all aspects of the Division. We seek a dynamic individual who will provide vision, leadership, and guidance for academic and research programs; recruit high-caliber faculty, students and staff; develop resources to strengthen the long-term viability, efficiency, and effectiveness of the Division's research and teaching programs; promote collaborative research within the Division and across MU; lead inclusion and diversity efforts within the Division; administer the Division's budget; collaborate with the dean on fundraising; be an advocate for the department; and mentor faculty at different stages of their careers.

The successful candidate will have an earned doctorate in an appropriate discipline.

In addition, the ideal candidate would have a record that could include:

- An established record of excellence in research and teaching in an area that complements departmental strengths
- Program leadership
- Experience with strategic planning, budgetary responsibilities and human resources
- Promoting intra- and inter-departmental collaboration
- Working cooperatively with faculty with a transparent, approachable leadership style respectful of the principles of shared governance
- Experience with alumni and donor relations
- Understanding of the dual missions of a Land Grant and AAU Research 1 university
- Experience advancing inclusion and diversity for faculty, staff and students
- Leading graduate and undergraduate training programs
- Familiarity with national trends in undergraduate and graduate education
- Be qualified for tenure at the rank of professor at MU.

The Division of Biological Sciences at MU is noted for its excellence in research and teaching. We are distinctive in the breadth and depth of our research and the integrative approaches we take to fundamental problems in biology, ranging from genomes to ecosystems, using a diversity of organisms. We share faculty with an interdisciplinary Life Sciences Center as well as with the Donald Danforth Plant Sciences Center in St. Louis; are active research partners with faculty in engineering, veterinary medicine, agriculture and natural resources, as well as with research scientists from state and federal agencies, including the Missouri Department of Conservation, the USGS, and USDA-ARS; and are active members of various interdisciplinary academic programs and groups, including the Interdisciplinary Plant Group, the Interdisciplinary Neuroscience Program, the Genetics Area Program, the MU Informatics Institute, the Missouri Maize Center, and the Evolution and Social Sciences Group.

Our faculty members are internationally known researchers and prize-winning teachers and include a Nobel Laureate, a National Academy of Sciences member, a Presidential Early Career Award for Scientists and Engineers recipient, 6 AAAS Fellows, and multiple members of disciplinary societies and honorary organizations.

Our undergraduate major attracts a large (~1100 majors), diverse (12% URM), and talented pool of students, including those interested in graduate, medical and other professional schools. Our graduate program is also vibrant and diverse (22% URM). All of our graduate students receive a competitive stipend, health insurance, and tuition.

Additional information about the Division can found at biology.missouri.edu.

Please apply online at **https://hrs.missouri.edu/find-a-job/academic**. Use the online application and be prepared to upload (compiled into a single PDF) a detailed curriculum vitae; cover letter summarizing your experience in higher education; a description of research plans and teaching interests; a diversity statement describing your professional experience advancing inclusion within an academic setting; and the names and contact information of three referees willing to write a letter if solicited. Applicants should contact the chair of the search committee (bioscifacultysearch@missouri.edu) with questions about the position and MU Human Resource Services (muhrs@missouri.edu) with questions about the online application process.

Review of application materials will begin **October 1, 2019**. To ensure full consideration, applications should be complete by this date. The position will remain open until filled.

An Equal Opportunity/Access/Affirmative Action/Pro-disabled and Veteran Employer.

By **Mikel Haggadone**

How running redefines success

"YOU ARE AMAZING." Those three words adorned the final slide of my most recent Research in Progress Seminar, which Ph.D. candidates in my program give annually to fellow students, postdocs, and faculty members. It's an unconventional way to end a scientific talk. The inspiration comes from my experiences as an ultrarunner—an athlete who completes runs longer than a standard marathon. The core philosophy of the team I run with—the Some Work, All Play Adventure Team—is that the courage required to pursue any scary adventure is to be celebrated, independent of the outcome. This mentality has helped me tremendously in both my professional and personal pursuits, but it's all too rare in the scientific community.

When I started to work toward my Ph.D. 5 years ago, my mindset was completely different. I believed we are defined by results. So, when I made the painful decision to leave my first Ph.D. program after spending my first year battling depression, anxiety, and disordered eating, I couldn't help but see myself as a failure who was incapable of handling the challenges of graduate school. Despite knowing that my mental illness was neither a sign of weakness nor my fault, I felt as far from amazing as humanly possible. My love for research persisted, but I would need to make significant changes if I was ever going to thrive in academia.

I chose to continue my Ph.D. studies at my undergraduate institution, where I would be closer to family, friends, and familiar support networks. But my myopic pursuit of the perfect CV still left me unfulfilled, endlessly chasing outcomes that I expected would finally make me feel like a "successful" scientist.

That started to change when one of my classmates invited me to run a half-marathon. I had never run a race that long, but I decided to give it a go. I wasn't the fastest finisher—far from it. But I was immensely proud that I had the courage to venture into unknown territory. For the first time in my life, I realized that embarking on a challenge can yield fulfillment, regardless of the outcome. I was hooked. Less than a year later, I was racing ultradistance trail events of up to 50 miles.

As any ultrarunner will attest, the highs of endurance sports do not come without extreme lows, too. By participating in a sport where setbacks are more common than successes, I developed a new relationship with failure. Perhaps it seems paradoxical, but when a hip injury forced me to walk at the end of a recent 50-mile race, my slowest miles were accompanied by my biggest smiles.

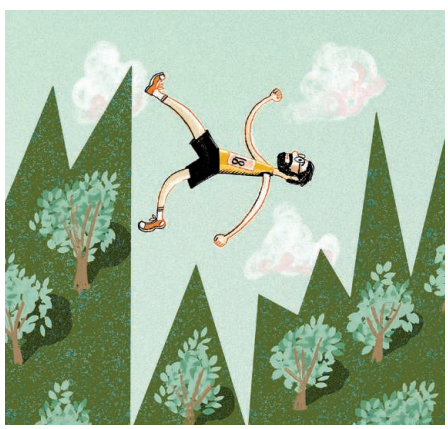

"To be amazing is to have the courage to embark on a scary, uncertain adventure."

Earlier in my Ph.D., when experiments failed to support major hypotheses, I would shut down, unwilling to consider the possibility that embedded in the setback was an opportunity to try something new. These days, I still don't like getting negative data. Who does? But I have become more resilient, perceiving obstacles as essential to achieving growth and finding meaning. The adage in ultrarunning is that a race is "life in a day," because of all the highs and lows an endurance adventure brings. I prefer to think of a race as "a Ph.D. in a day." Embracing this way of thinking has been transformative.

But I know that many of my fellow scientists struggle to acknowledge missteps or vulnerability, as I once did, which makes it far too easy to feel alone in "failing." This is why I now end my talks with a "YOU ARE AMAZING" slide. To be amazing does not require achieving recognition, awards, or major publications. To be amazing is to have the courage to embark on a scary, uncertain adventure and journey into the vast unknown.

When this slide comes up, many audience members give an unmistakably authentic smile. Some talk to me afterward; others send messages thanking me. I've even received a few hugs along the way. Of course, some may quietly scoff at the slide. But they, too, are amazing. ■

Mikel Haggadone is a Ph.D. candidate at the University of Michigan in Ann Arbor. He runs with the SWAP Adventure Team and the nonprofit organization Bigger Than The Trail, which advocates for mental health. Send your career story to SciCareerEditor@aaas.org.

ILLUSTRATION: ROBERT NEUBECKER

Published by AAAS